UNIVERSITY OF HULL

Perovskite Nanoparticles as Contrast Agents for Molecular Imaging and Anti-Cancer Theranostics

Being a Thesis submitted for the Degree of

Doctor of philosophy (PhD)

In the University of Hull

By

Salim Khalfan Suroor AL Habsi

BSc. MSc

(September 2019)

ABSTRACT

Nanoparticles (NPs) offer diagnostic and therapeutic capabilities not accessible with microscale particles. As the field of molecular imaging has risen up out of the mixing of molecular biology with medicinal imaging, the use of NPs as imaging contrast agents is progressively increasing. Super paramagnetic iron oxide (SPIONs) are investigated and used as T_2 contrasting agents for *MRI* respectively, due to their paramagnetic properties. Contrast agents are used to highlight the targeted tumour regions in the molecular tissues in order to offer a great visibility, either lighter or darker during *MRI* diagnosis. Typically, SPION influence T_2 relaxation time of the water molecules protons, whereas Gd-based complexes are the main contrast agents influencing T_1 relaxation type. However, SPIONs present some drawbacks such as difficulties in distinguishing molecular regions with weak signals based on a bright contrast. Several efforts are being devoted towards construct T_1 and T_2 dual-modes contrast agents to overcome the disadvantages of the single contrast agents modalities. Hence, a synergetic combination of T_1 and T_2 contrast enhanced imaging can potentially offer more detailed and comprehensive imaging information which provide higher diagnostic accuracy.

The aim of the present study is to prepare perovskite mixed metal compounds with general formula KMF_3 (M = Mn, Fe, Co) and test their applicability as contrast agents. The advantage of using perovskite mixed metal compounds is that their crystal structure and formulas offer flexibility for chemical modification, thus tuning of magnetic properties and, therefore, improved contrast agents. Furthermore, $KMnF_3$ has been reported as a biocompatible, promising T_1 contrast agent.

NPs of KMF_3 (M =Mn, Fe, Co) were prepared *via* co-precipitation (bare NPs) and solvothermal methods (oleate-capped NPs). Powder x-ray diffraction (PXRD), and TEM analysis were undertaken to determine the crystal structure and the particle size. To allow for compatibility in aqueous medium, the NPs were functionalised with a variety of ligands such as 11-aminoundecanoic acid, alendronic acid, polyethylene glycol (PEG) and oleylamine. IR spectroscopy was utilised to ascertain the occurrence of functionalisation.

Both methods were effective in synthesising KMF_3 (M=Mn, Fe, Co) NPs with cubic unit cell, although some impurities are present when oleate-capped NPs are prepared *via* solvothermal method.

NPs obtained *via* co-precipitation underwent decomposition during the functionalisation process with 11-aminoundecanoic acid, alendronic acid and PEG ligands. NPs obtained *via* solvothermal methods showed improved stability under the ligand exchange process with oleylamine ligand, leading to functionalisation with alendronic acid.

Ultra-small nanoparticles (USNPs) with an average hydrodynamic diameter of 2 nm were obtained thanks to the tuning of the synthetic method. *In-vitro MRI* test showed a unique dual mode weighted T_1 *and* T_2 *MR* imaging effect for $KMnF_3$ with relatively high relaxivity (r_1) and moderately high (r_2) of 6 and 51 $mM^{-1}s^{-1}$ respectively. These values are comparable to that of the Gd-based complexes and SPIONs. Functionalised $KFeF_3$ NPs were unstable and, at some stage during the characterisation, decomposed partially to Fe_3O_4 in air, while $KCoF_3$ showed a negative *MRI* effect.

Using the developed T_1/T_2 dual-mode coated alendronate $KMnF_3$ a theranostic system was developed *via* a successful conjugation process to DOX, a drug used in chemotherapy to treat various types of cancers. Furthermore, conjugation to the over expressed VEGFR anti-body to specifically target VEGFR, the over expressed protein in cervical and colorectal cancer cell lines was successfully achieved.

After a successful detection of VEGFR and EGFER in cervical (HeLa) and colorectal (HT-29 and HCT-116) cancer cell lines, the toxicity of the new theranostic system was tested against these cell lines using MTS colorimetric test. The cells uptake and localisation of the NPs were evaluated by fluorescence using flow cytometry and confocal microscopy.

Acknowledgments

Praises to Allah, who gave me the power, patients to complete this project and gave me the ability to proceed successfully. Pursuing a PhD. project is an arduous yet, enjoyable experience. It is just like gaining beautiful flavour gradually accompanied by hardships, bitterness, frustration, trust, encouragement and surrounded by love and help with greater people. During my arrival to the final stage enjoying the wonderful scenery. I realised that, it was in fact, a team work that got me there. Though it would not be sufficient to express my feeling in words towards all those great people who helped me. I would definitely still would like to give my high degree of appreciation to every single one of them.

First and foremost, I would like to offer my sincere gratitude to my esteemed supervisors, Dr M. Grazia Francesconi and Dr Graeme J. Stasiuk, who expertly supported me throughout my project with their patience and knowledge whilst allowing me to work in my own way and develop an understanding of the project, giving me the opportunity to enhance my project knowledge by interacting with large number of professionals and researchers at various kind of training courses and conferences either in solid state chemistry or in molecular imaging and theranostic here in the UK or overseas.

I would also like to express my thanks and gratitude to all technical staff in the department of chemistry at the University of Hull for their technical supports by providing me all the necessary equipment and excellent support that facilitated the completion of this project.

Special thanks to the Royal Court Affairs in Oman for the financial support provided to run this research as well as to complete my PhD at the University of Hull. I also would like to thank all staff at the department of development and training in Royal Court Affairs and people at the Omani embassy in London for their enormous support and massive help in releasing all obstacles that I have encountered throughout my study period in the UK.

Finally, I am indebted to my loving family including my wife Jamila AL Khalili who is my hero and blessed me with a life of joy in the hours when the light of lab was off. My children Abdullah, Omar, Arwa and AL Yazen for their constant encouragement, immense patience and understanding, without which it would have been impossible to complete this work.

Conferences attended (PhD 2015-2019)

No	*Conference*	*Place and Date*
1.	Northern Regional Dalton Meeting 2016	University of Hull. UK 30.6.2016
2.	MERCIA Meeting	School of pharmacy and Biomolecular Science, John Moores University. (Liverpool). UK 14.12.2016
3.	12th European Molecular Imaging Meeting	Germany (Koln) 5-7.4.2017 University of Koln
4.	Northern Regional Dalton Meeting 2017	Sheffield 29.6.2017 University of Sheffield. UK
5.	North of England Cell Biology Forum 2017	HY medical school University of Hull Business school UK 15.9.2017
6.	The 37th RSC Solid State Group Christmas Meeting	University of Reading. UK, 18-19/12/2017
7.	RSC Dalton Division Northern Regional Meeting 2018	University of Leeds. UK, 29.6.2018
8.	World Molecular Imaging Congress 2018	United State of America (USA) Seattle - Washington 12-15/9/2018
9	Solid State Chemistry Group Charismas Meeting 2018	University College London UK 17-18/12/2018
10	RSC Dalton Division Regional Meeting 2019	University of York UK 13/6/2019
11	Approaches to modelling disorder course	University of Southampton 28/6/2019
12	Heart start course	Hull and York medical school 1.7.2019

Oral presentation

Ultra-small $KMnF_3$ nanoparticles as dual-probe contrast agents for Magnetic Resonance Imaging (*MRI)*.

Postgraduate Colloquium – University of Hull 15.7.2019

Prizes

Postgraduate Poster presentation 1st prize award.

Title: Perovskite Fluorides as contrast agents for Magnetic Resonance Imaging (*MRI*)

Conference: International Women's day 2019

Venue: University of Hull

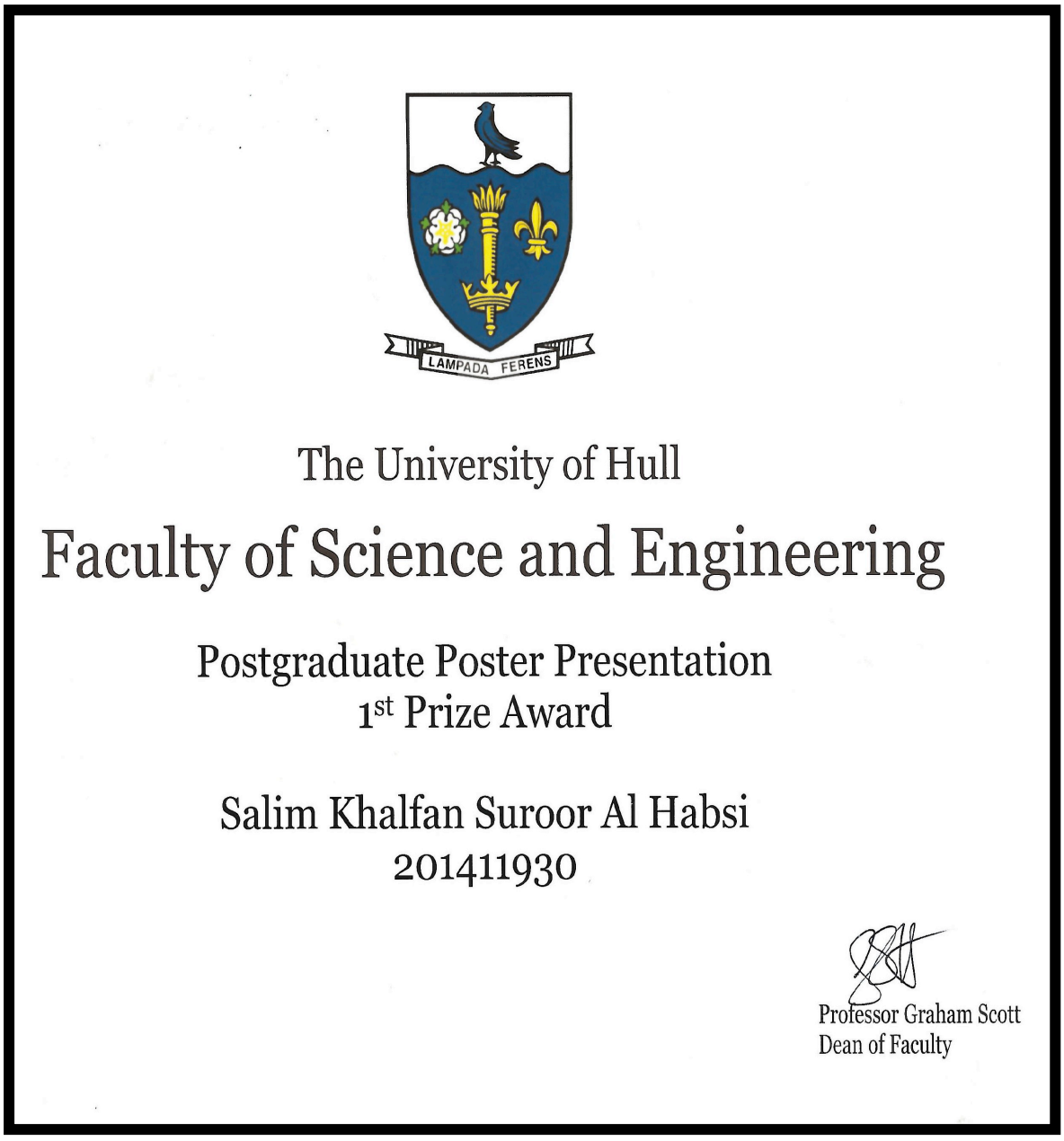

Abbreviations

NPs	Nano-particles
FDA	Food and drug administration
ICP	Inductively coupled plasma
ICP-OES	Inductively coupled plasma-optical emission spectroscopy
SPION	Super-Paramagnetic Iron Oxide Nanoparticles
RKKY	Ruderman, Kittle, Kasuya and Yasida interaction
NTA	Nano sight tracking analysis
RF	Radio Frequency
UC	Up conversion
LSS	Liquid-Solid-Solution
MR	Magnetic Resonance
ODA	Orthodecyamine
OAM	Oleylamine
HDM	Hexadecylamine
THF	Tetrahydrofuran
PXRD	Powder X-ray Diffraction
TGA	Thermo-Gravimetric Analysis
TEM	Transmission Electron Microscopy
T_1	Longitudinal or spin-lattice relaxation time
T_2	Transverse or spin-spin relaxation time
T^*	(T-star) transverse relaxation rate
r_1	Longitudinal or spin-lattice relaxation rate
r_2	Transverse or spin-spin relaxation rate
UV	Ultra-Violet

t_{2g}	Triply degenerate orbitals
e_g	Doubly degenerate orbital
γ	Gamma
α	Alpha
β	Beta
CAs	Contrast Agents
Gd-DOTA	Dotarems contrast agent
Gd-DTPA	Magnevists contrast agents
MRI CAs	Magnetic Resonance Imaging Contrast Agents
SBM	Solomon-Bloembergen-Morgan theory
q	Bound water molecules
τ_R	Rotational correlation time
τ_M	Water residence time
K_{ex}	Proton relaxitivity of feast water exchange
NSF	Nephrogenic Systemic Fibrosis
USNPs	Ultra-Small Nanoparticles
Es-MIONs	Extremely small Magnetic iron oxide nanoparticles
PEG	Polyethylene Glycol
DLS	Dynamic Light Scattering
TEM	Transform Electron Microscopy
DOX	Doxorubicin
EGFR	Epidermal Growth Factor
VEGFR	Vascular Endothelial Growth Factor
HNSCC	Head and Neck Squamous Carcinoma Cells
RGD	Arg-Gly-Asp peptide

SeNPs	Selenium Nanoparticles
HUVECs	Human Unbiblical Vein Endothelial Cells
FL	Fluorescence
FACS	Flow Cytometry Analysis
FL	Flow Channel
FSC	Forward Scatter
SSC	Side Scatter
HeLa	Human Cervical cancer cell lines
HCT-116	Human colorectal cancer cell lines
HT-29	Human colorectal cancer cell lines
EDTA	ethylenediaminetetraacetic acid
GDO	Gadolinium Dysprosium Oxide
MRI	Magnetic resonance imaging
NMR	Nuclear magnetic resonance
FTIR	Fourier transform **infrared** spectroscopy
(DSSCs)	Dye-sensitized solar cells
T	Tesla
R_A	Radius of A atom
R_B	Radius of B atom
R_O	Radius of O atom
ROI	Region of interest
^{1}H	Proton
^{11}B	Boron 11 isotope
^{13}C	Carbon 13 isotope
^{19}F	Fluorine 19 isotope

^{31}P	Phosphorous 31 isotope
LSS	Liquid-Solid-Solution
^{1}H NMR	Proton nuclear magnetic resonance
^{11}B NMR	Boron nuclear magnetic resonance
$1^{3}C$ NMR	Carbon nuclear magnetic resonance
^{31}P NMR	Phosphorus nuclear magnetic resonance
B_0	External magnetic field
ω	Larimore frequency
HPLC	High performance liquid chromatography
hkl	Miller indices
RT	Room temperature

Table of Contents

ABSTRACT ii

Acknowledgments iv

Conferences attended (PhD 2015-2019) v

Oral presentation vi

Prizes vii

Abbreviations viii

Table of Contents xii

Table of Figures xix

List of Tables xxviii

1 Introduction 2

1.1 NPs as Molecular Imaging with Theranostics 2

1.2 Magnetic Nanoparticles 3

1.3 Metal Oxides 5

1.3.1 Direct exchange interactions 5

1.3.2 Super exchange interactions 6

1.3.3 Indirect exchange interactions 8

1.4 Iron Oxide Nanoparticles 9

1.5 Perovskite Structure 9

1.5.1 Perovskite fluorides 11

1.5.2 Synthesis of Alkali metal fluorides 12

1.5.3 Tolerance Factors in Perovskites 12

1.5.4 Different Types of Perovskite Symmetry 13

1.5.4.1 Ideal Cubic Structure 14

1.6 Synthesis Methods for Perovskite Nanomaterials 19

1.6.1 Co-Precipitation Method 20

1.6.2 Thermal Decomposition Method 20

1.6.3 Microemulsion method 21
1.6.4 Hydrothermal Method 21
1.6.5 Sol-gel synthesis 23
1.7 Protection/Stabilization of Magnetic Nanoparticles 25
1.7.1 Oleylamine in nanoparticles synthesise 26
1.8 Magnetic Resonance Imaging (*MRI*) 27
1.8.1 Basic Principle of MRI 27
1.9 Magnetic nanoparticles as *MRI* contrast agents 29
1.9.1 T_1 contrast agents 29
1.9.2 T_2 contrast agents 32
1.9.3 Dual-mode T_1/T_2 contrast agents 36
1.10 Colorectal cancer 39
1.10.1 The hallmarks of cancer 41
1.11 Theranostics 41
1.11.1 Drug delivery 44
1.12 References 50
2 Experimental 60
2.1 General instrumentation and techniques 60
2.1.1 Power X-Ray Diffraction (PXRD) 60
2.2 Nanoparticles Tracking Analysis (NTA) 63
2.3 Fourier Transform Infra-red spectroscopy (FT-IR) 64
2.4 Transmission Electron Microscopy (TEM) and Energy Dispersive X-ray spectroscopy (EDX) 65
2.5 Optical emission Inductively Coupled Plasma (ICP) 66
2.6 Zeta potential and hydrodynamic size measurements 66
2.7 C H N analysis 67
2.8 NMR instrument 67
2.9 UV-visible spectrometry 68

2.10 Fluorescence measurements 68
2.11 Flow cytometry 68
2.12 Confocal fluorescence microscopy 69
2.13 Biological analysis 70
2.13.1 Cell line and cell culture 70
2.13.2 Media growth preparation 71
2.13.3 Cell passaging 71
2.13.4 Cell Counting 72
2.14 References 74
3 Introduction 76
3.1 Co-precipitation synthesis of NPs method 76
3.2 Experimental 77
3.2.1 Synthesis of maghemite (γ-Fe_2O_3) NPs 77
3.2.2 Synthesis of KMF_3 (M = Mn, Fe Co, Ni, Cu) 77
3.2.3 Functionalisation of synthesised NPs 79
3.3 Results and Discussion 83
3.3.1 Co-precipitation synthesis of γ-Fe_2O_3 NPs 83
3.3.2 Synthesis of perovskite KMF_3, where M = Mn, Fe, Co, Zn, Cu and Ni 87
3.3.3 Synthesis of $GdFeO_3$ 101
3.4 Functionalisation of NPs 104
3.4.1 PXRD analysis for standard 11-aminoundecanoic acid and sodium alendronate trihydrate 107
3.4.2 Functionalisation of NPs with 11-aminoundecanoic acid 108
3.4.3 Zeta potential 117
3.4.4 Thermal Gravimetric analysis 119
3.4.5 Rate of Relaxation measurements 123
3.4.6 Functionalisation of KMF_3 (M = Mn, Fe, Co) with alendronate 129
3.5 Conclusions 130

3.6 References 131
4 Introduction 135
4.1 Experimental 135
4.1.1 Synthesis of polyethylene glycol coated KMF_3 NPs (PEGylated KMF_3) (M = Mn, Fe, Co, Cu and Ni) 135
4.2 Results and Discussion 138
4.2.1 PXRD analysis of PEGylated $KMnF_3$ 138
4.2.2 PXRD analysis of PEGylated $KFeF_3$ 139
4.2.3 PXRD analysis of PEGylated $KCoF_3$ 140
4.2.4 PXRD analysis of PEGylated $KZnF_3$ and $KCuF_3$ 140
4.2.5 FTIR analysis of coated K-oleate $KMnF_3$ NPs 142
4.2.6 FTIR analysis of PEGylated KMF_3 (M = Mn, Fe, Co) NPs 144
4.2.7 Nano Tracking Analysis (*NTA*) 147
4.3 Synthesis and functionalisation of KMF_3 (M = Mn, Fe, Co) using ligand exchange between K-oleate and Na-alendronate 150
4.3.1 PXRD analysis of coated alendronate $KMnF_3$ 150
4.3.2 PXRD analysis of coated alendronate $KFeF_3$ 151
4.3.3 PXRD analysis of coated alendronate $KCoF_3$ 152
4.3.4 FTIR analysis 153
4.3.5 Nano Tracking Analysis (NTA) 155
4.4 Conclusions 157
4.5 References 158
5 Introduction 160
5.1 Experimental 163
5.1.1 Solvothermal synthesis of coated oleylamine KMF_3 (M = Mn, Fe, Co) NPs 163
5.1.2 Solvothermal synthesis of coated alendronate KMF_3 (M= Mn, Fe, Co) after being ligand exchanged with oleylamine ligand 163
5.2 Results and Discussion 163

5.3 Solvothermal Synthesis of KMF_3 NPs (M = Mn, Fe and Co) 163
5.3.1 Synthesis of coated alendronate $KMnF_3$ 163
5.3.2 PXRD analysis 166
5.3.3 FTIR analysis 167
5.3.4 Nano Tracking Analysis (NTA) 169
5.3.5 Zeta-potential measurements 169
5.3.6 Relaxation rates 170
5.3.7 Synthesis of coated alendronate $KFeF_3$ 174
5.3.8 Synthesis of coated alendronate $KCoF_3$ 187
5.4 Conclusions 196
5.5 References 197
6 Introduction 201
6.1 Experimental 202
6.1.1 Synthesis of $DyFeO_3$ 202
6.1.2 Functionalisation with tetra ethyl orthosilicate 203
6.1.3 Functionalisation of silica core shell $DyFeO_3$ with APTES 204
6.2 Results and discussions 204
6.2.1 PXRD analysis 204
6.3 TEM images 206
6.4 Zeta potential 207
6.5 Functionalisation of $DyFeO_3$ with silica 207
6.6 FTIR analysis 209
6.7 TEM analysis 210
6.8 Zeta potential 216
6.9 Relaxitivity 217
6.10 Conjugation of APTES with silica coated $DyFeO_3$ 219
6.11 TEM images 222
6.12 Conjugation with doxorubicin (DOX) 224

6.13 FT-IR spectrum of conjugated DOX/$DyFeO_3$ NPs 226
6.14 Zeta potential of DOX conjugated $DyFeO_3$ 227
6.15 Conclusions 227
6.16 References 229
7 Introduction 232
7.1 Conjugation of Doxorubicin (DOX) to coated alendronate $KMnF_3$ NPs 232
7.2 Experimental 232
7.2.1 Conjugation of sodium alendronate coated $KMnF_3$ with DOX 232
7.2.2 MTS Assay 235
7.2.3 Fluorescence properties measurement of DOX 236
7.2.4 Detection of EGFR and VEGFR-1 on Hela, HCT116 and HT-29 cell lines determined by FACS 236
7.2.5 Cellular uptake studies 237
7.3 Results and discussion 237
7.3.1 Conjugation of DOX to coated alendronate $KMnF_3$ NPs 237
7.3.2 Dynamic Light Scattering (DLS) and Nano Tracking Analysis (NTA) 241
7.3.3 Zeta potential 242
7.3.4 Cytoxicity study 243
7.3.5 Fluorescence DOX 248
7.3.6 Detection of over expressed EGFR and VEGFR proteins by flow cytometry 249
7.3.7 Conjugation of anti-VEGFR to DOX-$KMnF_3$ 252
7.3.8 Cellular uptake 253
7.3.9 Confocal microscopy 256
7.3.10 Cytotoxicity of $KMnF_3$-DOX-anti-VEGFR 261
7.4 Conclusions 263
7.5 References 265
8 Conclusion 268

Future work 271

Appendix I

Table of Figures

Figure 1-1: Alignment of individual magnetic moments in range magnetic phenomena..... 4
Figure 1-2: The magnetization (M) vs. the external magnetic field alteration (H) in different types of NPs sizes.[9]..... 5
Figure 1-3: Direct exchange interactions between metal centres in metal oxide (a) anions are close together (b) anions are further apart..... 6
Figure 1-4: Super exchange interactions through non-metal (violet) to metal ion..... 6
Figure 1-5: schematic diagram for antiferromagnetic coupling in metal oxides..... 7
Figure 1-6: Ferromagnetic super exchange interactions in metal oxides, 180-degree interaction(a), 90-degree interaction (b) 8
Figure 1-7: Indirect exchange interactions usually takes place between metal canters in metal oxides..... 9
Figure 1-8: Unit cell of $CaTiO_3$, which shows an orthorhombic unit cell. [26] 10
Figure 1-9: Unit cell of cubic $SrTiO_3$.[57] 14
Figure 1-10: Unit cell of Tetragonal $BaTiO_3$.[58] [59] 15
Figure 1-11: Rhombohedral unit cell of $LaAlO_3$. [60] 16
Figure 1-12: Orthorhombic unit cell of $GdFeO_3$.[62] 17
Figure 1-13: Monoclinic unit cell of $BaBiO_3$.[65] 18
Figure 1-14: Triclinic unit cell of $BiMnO_3$. 19
Figure 1-15: The liquid-solid-solution (LSS) phase-transfer synthetic strategy. Reproduced with kind permission from reference.[93] 23
Figure 1-16: The Reaction Pathway for the Production of Metal Oxide Nanostructures in the Sol–Gel Method.[95] 24
Figure 1-17: Chemical structure of oleylamine 26
Figure 1-18: Schematic illustration of the mechanisms of MRI. (a) Protons precess ω under an external magnetic field B0. (b) After the introduction of the RF pulse, protons are excited, removing the RF pulse relaxation process occurs (c) Representation of T_1 and T_2 relaxation time 29
Figure 1-19: Currently used gadolinium-based contrast agents in medical field..... 31
Figure 1-20: Physical parameters influencing the relaxation rate efficiency of contrast agents at molecular level.[117] 32
Figure 1-21: Parts of digestive system in human body.[182] 40
Figure 1-22: Different passive and active strategies used for drug conjugated NPS delivery to cancer cell lines 45
Figure 1-23: Scattering of X-rays by atoms in successive parallel plans. Constructive interference occurs when the path difference between scattered waves is equal to an integral number of wavelengths. 61
Figure 1-24: Schematic diagram of X-ray scattering by a powder sample..... 61
Figure 1-25: Some representive planes in cubic crystalline structure 63
Figure 1-26: Basic principle of FTIR system drawn by chemdraw software 65
Figure 1-27: Schematic diagram of flow cytometry. 69
Figure 1-28: Diagram to illustrate the fluorescence spectroscopy process..... 70

Figure 1-29: Schematic diagram followed for cells splitting, suspension of cell in growth media (a), removal of the old media (b), centrifuging and removal of media (c) and dispersion of the splitted new cells in new media (d). *72*
Figure 1-30: Injection of the Trypan blue cells suspension in haemocytometer (a) and cell counting strategy (b&c) *73*
Figure 3-1: Different steps involved in the synthesis and functionalisation of KMF_3 NPs with 11-aminoundecanoic acid ligand. *80*
Figure 3-2: Different steps involve in the synthesis and functionalisation of KMF_3 NPs with sodium alendronate trihydrate ligand. *82*
Figure 3-3: PXRD pattern of γ-Fe_2O_3 (blue) compared to the model (red) *83*
Figure 3-4: Unit cell of spinel cubic maghemite structure [22] *84*
Figure 3-5:FT-IR spectrum obtained for γ-Fe_2O_3 NPs. *85*
Figure 3-6: TEM images of the γ-Fe_2O_3 NPs with the diameter of ca. 5 nm obtained in the absence of 11-aminoundecanoic acid or sodium alendronate ligands *86*
Figure 3-7: Crystal size vs concentration plot obtained by Nano Tracking Analysis (NTA) for bare γ-Fe_2O_3 NPs. *87*
Figure 3-8: Suspension of the prepared NPs in water filtered under vacuum. *88*
Figure 3-9: Picture taken for $KCoF_3$ NPs after washing with methanol where white layer of KBr was formed *89*
Figure 3-10: Picture taken for $KCoF_3$ NPs after washing with HPLC water indicating the removal of KBr layer *89*
Figure 3-11: Powder X-ray diffraction patterns of the prepared unfunctionalised $KMnF_3$ NPs compared (blue) to the standard bulk $KMnF_3$ (red). *90*
Figure 3-12: Powder X-ray diffraction patterns of the prepared unfunctionalised $KFeF_3$ NPs compared to the standard bulk $KFeF_3$. *91*
Figure 3-13: Powder X-ray diffraction patterns of the prepared unfunctionalised $KCoF_3$ NPs compared to the standard bulk $KCoF_3$. *91*
Figure 3-14: Powder X-ray diffraction patterns of the prepared unfunctionalised $KZnF_3$ NPs compared to the standard bulk $KMnF_3$ *92*
Figure 3-15: Powder X-ray diffraction patterns of the prepared unfunctionalised $KNiF_3$ NPs compared to the standard bulk $KNiF_3$. *92*
Figure 3-16: Powder X-ray diffraction patterns of the prepared unfunctionalised $KCuF_3$ NPs compared to the standard bulk $KCuF_3$. *93*
Figure 3-17: Estimation of crystal size of the synthesised Nano particles using 3 different techniques. .. *94*
Figure 3-18: Crystal size vs relative intensity plots obtained by Nano Tracking Analysis (NTA) for bare synthesised NPs. (a) $KMnF_3$, (B) $KFeF_3$, (c) $KCoF_3$ and (d) $KZnF_3$ *95*
Figure 3-19: TEM image obtained for: (a) $KMnF_3$, (b) $KFeF_3$, (c) $KCoF_3$ and (d) $KZnF_3$. *96*
Figure 3-20: Atomic % of elemental composition obtained by EDX for bare NPs(a) $KMnF_3$, (b) $KFeF_3$, (c) $KCoF_3$ and (d) $KZnF_3$ *97*
Figure 3-21: Elemental composition obtained by ICP analysis for all bare NPs (a) $KMnF_3$, (b) $KFeF_3$, (c) $KCoF_3$ and (d) $KZnF_3$ *98*

Figure 3-22 : Ideal cubic unit cell of the perovskite structure of KMF_3 where M = Mn, Fe, Co, Ni, Cu and Zn. 99
Figure 3-23: FIR spectrum of bare $KMnF_3$. 100
Figure 3-24: FIR spectrum of bare $KFeF_3$. 100
Figure 3-25: FIR spectrum of bare $KCoF_3$. 101
Figure 3-26: FIR spectrum of $KZnF_3$. 101
Figure 3-27: Powder X-Ray diffraction patterns of GdFeO3at different incubation temperature range from 500 to 900°C compared to the model. 103
Figure 3-28: $GdFeO_3$ nanocrystal formation scheme exemplified by the forming of $GdFeO_3$ under the heat treatment of co-precipated initial mixture in air. I - the mechanism of co-precipated hydroxides simultaneous dehydration with $GdFeO_3$ formation; II - the scheme of step-by-step transformations of co-precipitated components with spatial-isolated Fe_2O_3 and Gd_2O_3 NPs formation followed by solid state interaction for $GdFeO_3$ production.[44] 104
Figure 3-29: Chemical structures of ligands used in the functionalisation of the investigated NPs process: (a) 11-aminoundecanoic acid, (b) alendronate sodium trihydrate 105
Figure 3-30: Structures of NPs functionalised with (a) 11-aminoundecanoic acid and (b) Alendronic acid ligands. 106
Figure 3-31: PXRD pattern of 11-aminoundecanoic acid ligand used (red) compared to its available model in literature (blue) 107
Figure 3-32: PXRD pattern of Alendronate sodium trihydrate ligand used (red) compared to its available model in literature (blue). 108
Figure 3-33: PXRD patterns of $KMnF_3$ 2-hours functionalisation with 11-aminoundeacnoic acid (blue) compared to bare $KMnF_3$ (red) and 11-aminoundecanoic acid (yellow). 109
Figure 3-34: PXRD patterns of $KFeF_3$ 1-hour functionalisation with 11-aminoundeacnoic acid (red) compared to bare $KFeF_3$ (yellow) and 11-aminoundecanoic acid (blue). 109
Figure 3-35: PXRD patterns of $KCoF_3$ 2-hours functionalisation with 11-aminoundeacnoic acid (red) compared to bare $KCoF_3$ (yellow) and 11-aminoundecanoic acid (blue) 110
Figure 3-36: PXRD patterns of $KZnF_3$ 1-hour functionalisation with 11-aminoundeacnoic acid (red) compared to bare $KZnF_3$ (yellow) and 11-aminoundecanoic acid (blue). 110
Figure 3-37: Crystal sizes obtained of functionalised NPs using 3 different techniques 112
Figure 3-38: TEM images obtained for functionalised NPs with 11-aminoundecanoic acid: (a) $KMnF_3$, (b) $KFeF_3$, (c) $KCoF_3$ and (d) $KZnF_3$. 114
Figure 3-39: Atomic % of elemental composition obtained by EDX for functionalised NPs with 11-amino undecanoic acid (a) $KMnF_3$, (b) $KFeF_3$, (c) $KCoF_3$ and (d) $KZnF_3$ 115
Figure 3-40: FTIR spectrum for functionalised $KMnF_3$ and $KFeF_3$ with 11-amino undecanoic acid compared to the bare compounds and ligand: (a) $KMnF_3$ and (b) $KFeF_3$ NPs 116
Figure 3-41: FTIR spectrum for functionalised $KMnF_3$ and $KFeF_3$ with 11-amino undecanoic acid compared to the bare compounds and ligand: (a) $KCoF_3$ and (b) $KZnF_3$ NPs 117
Figure 3-42: Thermogravimetric analysis for 11-aminoundecanoic acid. 120
Figure 3-43: Thermal gravimetric analysis graphs for functionalised NPs (blue) compared to the bare NPs (red): a ($KMnF_3$), B ($KFeF_3$) and c ($KCoF_3$) 122
Figure 3-44: Longitudinal relaxation rate measurement for γ-Fe_2O_3 with 11-aminoundecanoic acid. 124

Figure 3-45: Transverse relaxation rate measurement for γ-Fe_2O_3 with 11-aminoundecanoic acid..... 124
Figure 3-46: Longitudinal relaxation rate measurement for $KMnF_3$ with 11-aminoundecanoic acid.... 125
Figure 3-47: Transverse relaxation rate measurement for $KMnF_3$ with 11-aminoundecanoic acid. 126
Figure 3-48: Longitudinal relaxation rate measurement for $KFeF_3$ with 11-aminoundecanoic acid..... 127
Figure 3-49: Transverse relaxation rate measurement for $KFeF_3$ with 11-aminoundecanoic acid..... 127
Figure 3-50: Longitudinal relaxation rate measurement for $KCoF_3$ with 11-aminoundecanoic acid..... 128
Figure 3-51: Transverse relaxation rate measurement for $KCoF_3$ with 11-aminoundecanoic acid..... 128
Figure 4-1: Different steps involve in the hydrothermal synthesis of PEGylated KMF_3 (M = Mn, Fe and Co) 137
*Figure 4-2: PXRD pattern of PEGylated $KMnF_3$ (a) compared to bare $KMnF_3$ (b), PEG (c) and K-Oleate (d). The peaks highlighted by * correspond to unknown impurities..... 138*
*Figure 4-3: PXRD pattern of PEGylated $KFeF_3$ (a) compared to bare $KFeF_3$ (b), PEG (c) and K-Oleate (d). The peaks highlighted by * correspond to unknown impurities..... 139*
*Figure 4-4: PXRD pattern of PEGylated $KCoF_3$ (a) compared to bare $KCoF_3$ (b), PEG (c) and K-Oleate (d). The peaks highlighted by * correspond to unknown impurities..... 140*
*Figure 4-5: PXRD pattern of PEGylated $KZnF_3$ (a) compared to bare $KZnF_3$ (b), PEG (c) and K-Oleate (d). The peaks highlighted by * correspond to unknown impurities..... 141*
*Figure 4-6: PXRD pattern of PEGylated $KCuF_3$ (a) compared to bare $KCuF_3$ (b), PEG (c) and K-oleate (d). The peaks highlighted by * correspond to unknown impurities..... 142*
Figure 4-7: FTIR spectrum of $KMnF_3$ coated with oleic acid (blue) compared to pure oleic acid (red) 143
Figure 4-8: FTIR spectrum of $KFeF_3$ coated with K-oleate (red) compared to pure K-oleate (black) ... 143
Figure 4-9: FTIR spectrum of $KCoF_3$ coated with K-oleate(black) compared to pure K-oleate (red).... 144
Figure 4-10: Ligand exchange mechanism between Poly Ethylene Glycol (PEG) ligand with potassium oleate..... 145
Figure 4-11: FTIR spectrum of $KMnF_3$ coated with PEG (a) compared to pure PEG (b) 146
Figure 4-12: FTIR spectrum of $KFeF_3$ coated with PEG (a) compared to pure PEG (b) 146
Figure 4-13: FTIR spectrum of $KCoF_3$ coated with PEG (black) compared to pure PEG (red)..... 147
Figure 4-14: Nano Tracking analysis (NTA) size distribution graph obtained for the PEGylated $KMnF_3$ NPs..... 148
Figure 4-15: Nano Tracking analysis (NTA) size distribution graph obtained for the PEGylated $KFeF_3$ NPs..... 149
Figure 4-16: Nano Tracking analysis (NTA) size distribution graph obtained for the PEGylated $KCoF_3$ NPs..... 149
Figure 4-17: Nano Tracking analysis (NTA) size distribution graph obtained for the standard silica particles of 100 nm dispersed in water..... 150
*Figure 4-18: PXRD pattern of coated alendronate $KMnF_3$ (a) compared to bare $KMnF_3$ (b), alendronate (c) and K-Oleate (d). The peaks highlighted by * correspond to unknown impurities..... 151*
*Figure 4-19: PXRD pattern of coated alendronate $KFeF_3$ (a) compared to bare $KFeF_3$ (b), alendronate (c) and K-Oleate (d). The peaks highlighted by * correspond to unknown impurities..... 152*
*Figure 4-20: PXRD pattern of coated alendronate $KCoF_3$ (a) compared to bare $KCoF_3$ (b), alendronate (c) and K-Oleate (d). The peaks highlighted by * correspond to unknown impurities..... 153*

Figure 4-21: FTIR spectrum of $KMnF_3$ coated with alendronate (a) compared to pure alendronate (b) and coated oleate $KMnF_3$ (c). *154*
Figure 4-22: FTIR spectrum of $KFeF_3$ coated with alendronate (a) compared to pure alendronate (b) and coated oleate $KFeF_3$ (c). *154*
Figure 4-23: FTIR spectrum of $KCoF_3$ coated with alendronate (a) compared to pure alendronate (b) and coated oleate $KCoF_3$ (c). *155*
Figure 4-24: Nano Tracking analysis (NTA) size distribution graph obtained for the alendroted $KMnF_3$ NPs. *156*
Figure 4-25: Nano Tracking analysis (NTA) size distribution graph obtained for the alendronated $KFeF_3$ NPs. *156*
Figure 4-26: Nano Tracking analysis (NTA) size distribution graph obtained for the alendronated $KCoF_3$ NPs. *157*
Figure 5-1: General Perovskite structure of KMF_3 (M = Mn, Fe, Co) *161*
Figure 5-2: HERTEM images obtained for coated alendronate $KMnF_3$with different magnification scale obtained at different area *165*
Figure 5-3: Elemental composition of alendronate coated $KMnF_3$ NPs obtained via EDS *166*
Figure 5-4: d-spacing measurement for the coated alendronate $KMnF_3$ crystal lattice. *166*
Figure 5-5: PXRD patterns of functionalised $KMnF_3$ with oleylamine and sodium alendronate compared to the standard $KMnF_3$ PXRD pattern. *167*
Figure 5-6: FT-IR spectra of the functionalised NPs compared to the pure oleylamine and sodium alendronate. *169*
Figure 5-7: Hydrodynamic radius for $KMnF_3$ USNPs coated with Na-alendronate obtained by Nano tracking analysis (NTA). *170*
Figure 5-8: Zeta potential value obtained for coated alendronate $KMnF_3$ NPs. *170*
Figure 5-9: T_1 relaxation rate of coated alendronate $KMnF_3$ *172*
Figure 5-10: T_2 relaxation rate of coated alendronate $KMnF_3$ *172*
Figure 5-11: T_1/T_2 MRI effect of coated alendronate $KMnF_3$ at 3 T. *172*
Figure 5-12: T_1 and T_2 mapping for coated alendronate $KMnF_3$ NPs. *173*
Figure 5-13: Squid measurements for perovskite coated alendronate $KMnF_3$ NPs *174*
Figure 5-14: schematic diagram for the synthesis of coated oleylamine $KFeF_3$ NPs. *175*
Figure 5-15: Optimisation of the long chain oleylamine ligand on $KFeF_3$ NPs surface. *175*
Figure 5-16: PXRD patterns obtained for $KFeF_3$ (a), coated oleylamine $KFeF_3$ (b) and coated alendronate $KFeF_3$ (c) *176*
Figure 5-17: TEM picture to show the d-spacing of the coated alendronate $KFeF_3$ NPs. *177*
Figure 5-18: FTIR spectrum for oleylamine (red), coated oleylamine $KFeF_3$ (black), pure sodium alendronate (purple) and coated alendronate $KFeF_3$ (green) *178*
Figure 5-19: TEM images of the alendronate coated $KFeF_3$ of different magnification taken at different part of the dispersed NPs. *179*
Figure 5-20: Size distribution graph for coated alendronate $KFeF_3$ NPs obtained by origin software. *180*
Figure 5-21: size of individual coated alendronate $KFeF_3$ NPs. *180*
Figure 5-22: EDS analysis obtained for coated alendronate $KFeF_3$ NPs. *182*
Figure 5-23: Zeta potential value measured for coated alendronate $KFeF_3$ NPs *182*

Figure 5-24: T_1 relaxation rate of coated alendronate $KFeF_3$. 183
Figure 5-25: Transverse relaxation rate of coated alendronate $KFeF_3$ NPs 184
Figure 5-26: T_1 and T_2 weighted images obtained for coated alendronate $KFeF_3$ NPs as concentration of Fe ion increases 185
Figure 5-27: T_1 and T_2 mapping obtained for coated alendronate $KFeF_3$ NPs as concentration of Fe ion increases 185
Figure 5-28: PXRD pattern comparison between the coated alendronate $KFeF_3$ and single phaseFe_3O_4 NPs 186
Figure 5-29: Squid measurements for the prepared coated alendronate $KFeF_3$. 187
Figure 5-30: PXRD pattern of single phase $KCoF_3$ (a), coated oleylamine $KCoF_3$ (b) and Coated alendronate $KCoF_3$ after being ligand exchange with oleylamine ligand (c). 188
Figure 5-31: FTIR spectrum of single-phase coated alendronate $KCoF_3$ NPs and pure alendronate used as a coating ligand 189
Figure 5-32: TEM images of coated alendronate NPs taken at different parts with different magnification 190
Figure 5-33: Distribution of NPs size for coated alendronate $KCoF_3$ constructed by origin software... 191
Figure 5-34: Hydrodynamic size of coated alendronate $KCoF_3$ obtained by NTA 191
Figure 5-35: Elemental analysis of coated alendronate $KCoF_3$ NPs obtained by EDX 192
Figure 5-36: Longitudinal relaxation rate of coated alendronate $KCoF_3$ NPs. 193
Figure 5-37: Transverse relaxation rate of coated alendronate $KCoF_3$ NPs. 194
Figure 5-38: T_1 and T_2 weighted images obtained for the prepared coated alendronate $KCoF_3$ NPs (a) compared to negative standard image (b). 194
Figure 5-39: T_2-mapping image obtained for the prepared coated alendronate $KCoF_3$ NPs. 195
Figure 5-40: Squid measurements for coated alendronate $KCoF_3$ NPs. 196
Figure 6-1: Chemical structure of citric acid 202
Figure 6-2: PXRD patterns of $DyFeO_3$ heated at 500°C for different times (a) 23h, (b) 25h and (c) 30 h compared to the (d) standard pattern for bulk $DyFeO_3$ 205
Figure 6-3: TEM images for bare $DyFeO_3$ at different magnifications. 206
Figure 6-4: Apparent zeta potential of $DyFeO_3$ NPs surface prior to coating with TEOS 207
Figure 6-5: PXRD pattern of silica coated $DyFeO_3$ compared to bare $DyFeO_3$ and standard $DyFeO_3$. 209
Figure 6-6: FTIR spectrum of silica coated $DyFeO_3$ (a) compared to bare ligand (b) and bare $DyFeO_3$ (c). 210
Figure 6-7: TEM images for unfiltered coated silica $DyFeO_3$ NPs when 0.6 g ETOS added over an hour. 212
Figure 6-8: TEM images for filtered silica coated $DyFeO_3$ NPs when 0.6 g ETOS added over an hour 213
Figure 6-9: TEM images of unfiltered $DyFeO_3$ with half amount of silica added over 24 hours using a burette. 214
Figure 6-10: TEM images of filtered $DyFeO_3$ with half amount of silica added over 24 hours using a burette 214
Figure 6-11: Elemental composition of unfiltered(a) and filtered(b) silica coated $DyFeO_3$ NPs when 0.6 g ETOS added over an hour. 215

Figure 6-12: Elemental composition of unfiltered and filtered silica coated $DyFeO_3$ NPs when 0.3 g ETOS added over 24 hours. 216
Figure 6-13: Apparent zeta potential of the silica coated $DyFeO_3$ nanoparticle surface 217
Figure 6-14: Longitudinal relaxation rates of $DyFeO_3$ and silica coated $DyFeO_3$ 218
Figure 6-15: Transverse relaxation rates of $DyFeO_3$ and silica coated $DyFeO_3$ 219
Figure 6-16: Functionalisation of $DyFeO_3$ with APTES ligand 220
Figure 6-17: PXRD patterns of APTES coated $DyFeO_3$ (a) compared to silica coated $DyFeO_3$ (b) and standard $DyFeO_3$ (c). 221
Figure 6-18: FTIR spectrum of APTES coated $DyFeO_3$ compared to silica coated $DyFeO_3$ and standard $DyFeO_3$. 222
Figure 6-19: TEM images obtained for APTES conjugated $DyFeO_3$ at different crystal parts. 223
Figure 6-20: EDX spectra obtained for APTES conjugated DyFeO3 at different crystal parts. 223
Figure 6-21: Conjugation of DOX with APTES coated $DyFeO_3$ mechanism 225
Figure 6-22: FTIR spectrum of $DyFeO_3$/DOX compared to DOX and $DyFeO_3$/APTES 226
Figure 6-23: Zeta potential of $DyFeO_3$ conjugated with DOX 227
Figure 7-1: Schematic diagram for the synthesis for conjugated DOX into the coated alendronate $KMnF_3$ via and O,O′ -Bis[2-(N-Succinimidylsuccinylamino)ethyl]polyethylene glycol linker that activates the carbonyl group 234
Figure 7-2: The appearance of the three 96 well plates when MTS assay was performed 235
Figure 7-3: Reduction of yellow Tetrazolium compound to water soluble purple Formazan for alive cells using MTS protocol 236
Figure 7-4: FT-IR spectrum for conjugated DOX with coated alendronate $KMnF_3$ NPs compared to DOX spectrum. 238
Figure 7-5: comparison of UV-visible spectrum for DOX, loaded DOX NPs, linker and unloaded DOX NPs. 239
Figure 7-6: Determination of loaded DOX into coated alendronate $KMnF_3$ NPs using UV-visible spectroscopy 240
Figure 7-7: Calibration curve obtained for the determination of loaded DOX into coated alendronate $KMnF_3$ NPs using UV-visible spectrometry measurements. 240
Figure 7-8: Hydrodynamic size of conjugated DOX with coated alendronate $KMnF_3$ obtained by NTA 242
Figure 7-9: Apparent zeta potential for conjugated DOX with coated alendronate $KMnF_3$ NPs. 243
Figure 7-10: Cytotoxicity effect of synthesised coated alendronateKMnF3 NPs against HeLa cervical cancer cell lines. 244
Figure 7-11: Cytotoxicity effect of DOX against HeLa cervical cancer cell lines. 244
Figure 7-12: Cytotoxicity effect of DOX-conjugated $KMnF_3$ NPs against HeLa cervical cancer cell lines. 244
Figure 7-13: Cytotoxicity effect of synthesised coated alendronate$KMnF_3$ NPs against HT-29 colorectal cancer cell lines. 245
Figure 7-14: Cytotoxicity effect of DOX against HT-29 colorectal cancer cell lines. 246
Figure 7-15: Cytotoxicity effect of DOX-coated alendronate $KMnF_3$ NPs against HT-29 colorectal cancer cell lines. 246

Figure 7-16: Cytotoxicity effect of synthesised coated alendronate$KMnF_3$ NPs against HCT-116colorectal cancer cell lines. *247*
Figure 7-17: Cytotoxicity effect of DOX against HCT-116 colorectal cancer cell lines. *247*
Figure 7-18: Cytotoxicity effect of DOX-coated alendronate $KMnF_3$ NPs against HCT-116 colorectal cancer cell line *248*
Figure 7-19: Emission and excitation fluorescence spectra of DOX. *249*
Figure 7-20: FACS analysis to show the existence of EGFR (green) and VEGFR (pink) compared to the negative control (purple) on Hela cells lines *250*
Figure 7-21: FACS analysis results to show the existence of negative control (dark purple), EGFR (green) and VEGFR (Indigo) on HCT-116 colorectal cells lines. *250*
Figure 7-22: FACS analysis results to show the existence of negative control (dark purple), EGFR (green) and VEGFR (Indigo) on HT-29 colorectal cells lines. *251*
Figure 7-23: FACS analysis to show the existence of EGFR (green) and VEGFR (pink) compared to the negative control (purple) on Colo 320 cells lines *251*
Figure 7-24: Average hydrodynamic size of DOX-$KMnF_3$-antiVEGFR nanoconjugate. *252*
Figure 7-25: Zeta potential of VEGFR dissolved in HPLC water *253*
Figure 7-26: Zeta potential of conjugated DOX-$KMnF_3$-VEGFR anti-body. *253*
Figure -7-27: Hela cells uptake by (Violet) cell only, (green) $KMnF_3$ NPs, (brown) DOX only, (blue) $KMnF_3$ and DOX, (Purple) $KMnF_3$-DOx-VEGFR anti body using FL_2 flow cytometry channel *254*
Figure-7-28 Colorectal HT-29 cells uptake by (Violet) cell only, (green) $KMnF_3$ NPs, (brown) DOX only, (blue) $KMnF_3$ and DOX, (Purple) $KMnF_3$-DOx-VEGFR anti body using FL_2 flow cytometry channel .. *255*
Figure -7-29: HCT116 cells uptake by (Violet) cell only, (green) $KMnF_3$ NPs, (brown) DOX only, (blue) $KMnF_3$ and DOX, (Purple) KMnF3-DOx-VEGFR anti body using FL2 flow cytometry channel *255*
Figure 7-30: Bright field (c), dark field(a) and merge (b) images of HeLa cells incubated with coated alendronate $KMnF_3$ NPs only for one hour *257*
Figure 7-31: Bright field (c), dark field(a) and merge (b) images of HT-29 cells incubated with coated alendronate $KMnF_3$ NPs only for one hour *257*
Figure 7-32: Bright field (c), dark field(a) and merge (b) images of HCT-116 cells incubated with coated alendronate $KMnF_3$ NPs only for one hour *257*
Figure 7-33: Bright field (c), dark field(a) and merge (b) images of HeLa cells incubated with coated DOX only for one hour *258*
Figure 7-34: Bright field (c), dark field(a) and merge (b) images of HT-29 cells incubated with DOX only for one hour *258*
Figure 7-35: Bright field (c), dark field(a) and merge (b) images of HCT-116 cells incubated with DOX only for one hour *258*
Figure 7-36: Bright field (c), dark field(a) and merge (b) images of HeLa cells incubated with $KMnF_3$-DOX for one hour *259*
Figure 7-37 Bright field (c), dark field(a) and merge (b) images of HT-29 cells incubated with $KMnF_3$-DOX for one hour *259*
Figure 7-38: Bright field (c), dark field(a) and merge (b) images of HCT-116 cells incubated with $KMnF_3$-DOX for one hour *259*

Figure 7-39: Bright field (c), dark field of Alex Flour 488 anti-VEGF(a), dark field of DOX(b) and merge (d) images of HeLa cells incubated with $KMnF_3$-DOX-anti-VEGFR for one hour..... 260
Figure 7-40: Dark field of Alex Flour 488 anti-VEGF(a), dark field of DOX(b)images of HT-29 cells incubated with $KMnF_3$-DOX-anti-VEGFR for one hour..... 260
Figure 7-41: Bright field Alex Flour 488 anti-VEGF(a), bright field of DOX(b), dark field (c) and merge (d) images of HT-116 cells incubated with $KMnF_3$-DOX-anti-VEGFR for one hour..... 261
Figure 7-42: Cytotoxicity effect of DOX-coated alendronate $KMnF_3$ NPs and anti-VEGFR against Hela cervical cancer cell lines. 262
Figure 7-43: Cytotoxicity effect of DOX-coated alendronate $KMnF_3$ NPs and anti-VEGFR against HT-29 colorectal cancer cell lines..... 263
Figure 7-44: Cytotoxicity effect of DOX-coated alendronate $KMnF_3$ NPs and anti-VEGFR against HCT-116 colorectal cancer cell line..... 263
Figure 0-1: PXRD patterns for standard $KMnF_3$ (a) compared to coated alendronate $KMnF_3$ (b) and sodium alendronate trihydrate (c) obtained at 2 hours..... I
Figure 0-2: PXRD patterns for standard $KMnF_3$ (a)compared to coated alendronate $KMnF_3$ (b) and sodium alendronate trihydrate (c) obtained at 1 hour. I
Figure 0-3: PXRD patterns for standard $KMnF_3$ (a)compared to coated alendronate $KMnF_3$ (b) and sodium alendronate trihydrate (c) obtained at 48hours..... II
Figure 0-4: PXRD patterns for standard $KFeF_3$ (a) compared to coated alendronate $KFeF_3$ (b) and sodium alendronate trihydrate (c) obtained at 1hour. II
Figure 0-5: PXRD patterns for standard $KFeF_3$ (a) compared to coated alendronate $KFeF_3$ obtained at 2hours. III
Figure 0-6: PXRD patterns for standard $KCoF_3$ (a) compared to coated alendronate $KCoF_3$ obtained at 2hours and sodium alendronate trihydrate (c)..... III
Figure 0-7: PXRD patterns for standard $KZnF_3$ (a) compared to coated alendronate $KZnF_3$ obtained at 2hours and sodium alendronate trihydrate (c)..... IV
Figure 0-8: MTS graph for coated alendronate $KMnF_3$ against Colo320 cancer cell line plotted by graph prism pad software IV
Figure 0-9: MTS graph for coated alendronate $KCoF_3$ against Colo320 cancer cell line plotted by graph prism pad software V
Figure 0-10: MTS graph for coated alendronate $KZnF_3$ against Colo320 cancer cell line plotted by graph prism pad software V
Figure 0-11: MTS graph for coated alendronate $KMnF_3$ against Caco cancer cell line plotted by Excel. VI
Figure 0-12: MTS graph for coated alendronate $KFeF_3$ against Caco cancer cell line plotted by Excel.. VI
Figure 0-13: MTS graph for coated alendronate $KFeF_3$ against Colo320 cancer cell line plotted by Excel. VII

List of Tables

Table 1-1: Goldschmidt tolerance factor (t) for some types of common perovskite oxide structures.[55] 13
Table 1-2: Conditions for the seven different crystal system. [56] 13
Table 1-3: Brief comparison for nanoparticle synthesis methods. 25
Table 3-1: C, H and N analysis for functionalised NPs 114
Table 3-2: Zeta potential of functionalised and bare NPs 118
Table 3-3: Calculated ligands per one NPs for functionalised NPs with 11-aminoundecanoic acid 121
Table 3-4: The obtained longitudinal and transverse relaxitivity at 9.4 T for γ-Fe_2O_3 123
Table 3-5: The obtained longitudinal and transverse relaxitivity at 9.4 T for $KMnF_3$. 125
Table 3-6: The obtained longitudinal and transverse relaxitivity at 9.4 T for $KFeF_3$. 126
Table 3-7: The obtained longitudinal, transverse relaxitivity at 9.7 T for $KCoF_3$. 128
Table 3-8: r_1 and r_2 relaxivity for gadolinium related contrasting agents available in the literature. 129
Table 3-9: r_1 and r_2 relaxitivity for the studied perovskite KMF_3 coated with 11-aminoundecanoic acid. 129
Table 4-1: The obtained unit cell parameters results for the investigated compounds compared to the literature reference standards. 140
Table 6-1: Different samples prepared to optimise the hydrodynamic size of the prepared coated silica $DyFeO_3$ NPs. 203
Table 6-2: The refined unit cell parameters of $DyFeO_3$ NPs calcinated at 500°C for different time compared to the model values obtained by High score software 205

CHAPTER 1

Introduction

1 Introduction

1.1 NPs as Molecular Imaging with Theranostics

Nanoparticles (NPs) offer diagnostic and therapeutic capabilities not available with small molecules or microscale tools. As the field of molecular imaging has emerged from the blending of molecular biology with medical imaging, NP imaging is increasingly common for both therapeutic and diagnostic applications.[1] The term theranostic describes multifunctional technology that combine targeting, diagnostic and therapeutic within a single nanoscale complex.[2] The theranostic capabilities of paramagnetic nanoparticles have attracted tremendous attention of scientists over the past decades as a promising candidate for cancer bioimaging enhancement and as medication transporter for therapy. The primary advantages of these NPs are the low toxicity, depth insensitive nature of *MRI* detection and long periods of flow t time. Super paramagnetic iron oxide (SPIO) and Ultra-small paramagnetic iron oxide (USPIO) decrease T_1 and T_2 relaxation times in a dose-dependent manner. They are utilized as contrast agents for bone marrow contrast and contrast agents for lymphography and angiography or as a perfusion agent of the brain and kidney. Although NPs have been FDA approved for clinical use as transport vehicles for nearly 15 years, full mechanisms of their theranostic potential is incomplete.[1] However, NPs have shown remarkable success in the areas of drug delivery and magnetic resonance imaging.

Diagnosis with NPs in molecular imaging involves the correlation of the signal with a phenotype. The location and intensity of NP signals emanating from a living subject indicate the disease stage, area's size and biochemical signature. Therapy with NPs uses the image for resection or delivery of a small molecule or RNA therapeutic. Ablation of the affected area is also possible via heat or radioactivity.

Recently, T_1–T_2 dual-mode contrast agents have been developed and actively studied because they have the ability to validate reconstruction and visualization of the data in an accurate and reliable manner, and to acquire complementary and self-confirmed information to permit meaningful interpretation.[3] It is well known that Gd (III) complexes work as a T_1 contrast agents, while SPIOs as T_2 contrast agents.[4] However, as single-mode MRI only offers T_1 images or T_2 images, it cannot provide accurate results about the lesion location sometimes when there are false *MRI* contrast signals caused by respiratory and other motion artefacts. Therefore, it is meaningful to develop T_1–T_2 dual-mode contrast agents.

The ideal theranostic NP includes the following features: (1) it selectively and rapidly accumulates in diseased tissue; (2) it reports biochemical and morphological

characteristics of the area; (3) it delivers an effective therapeutic; and (4) it is safe and biodegrades with nontoxic by products.[1] Such a system contains a central imaging core surrounded by small molecule therapeutics. The system targets *via* ligands such as IgG and is protected from immune scavengers by a cloak of protective polymer. Although no NP has achieved all of the above criteria, many NPs possess one or more of these features. While the most clinically translatable NPs have been used in the field of magnetic resonance imaging, other types in development are quickly becoming more biocompatible through methods that modify their toxicity and biodistribution profiles.[1]

1.2 Magnetic Nanoparticles

Over the last few decades the study of magnetisation processes in nanoparticles (NPs) has increased. The most extensively used metal in the composition of metallic core NPs is Iron (Fe), in particular oxides such as Fe_3O_4 and γ-Fe_3O_4.[5, 6]

Due to their unpaired electrons on the *d* orbitals, Fe^{3+} or Fe^{2+} have strong magnetic moment. **Error! Reference source not found.** represents the wide range of magnetic states which can appear in inorganic solids.[7]The characteristic feature of diamagnetic materials is that their magnetic moments tend to align opposite to an external magnetic field (B_0) and in consequence are repelled by the applied magnetic field.[7] In the paramagnetic states, the atomic magnetic moments are not aligned or adjusted with respect to each other and the crystal has roughly negligible net magnetic moment. When an external magnetic field is applied, the crystal exhibits a small magnetic moment because some of its numerous individual magnetic moments will align in the same direction. In a ferromagnetic state all the magnetic moments are aligned, even if there is no an external magnetic field, so the overall crystal has a strong magnetic moment. A different magnetic state appears when the magnetic moments are antiparallel and of equal strengths, the state is antiferromagnetism and has no net magnetic moment.[8] [9] In ferrimagnetic materials unpaired electrons orientate anti-parallel. However, there is a greater magnetic moment in one direction causing the material exhibit magnetic properties in the absence of the magnetic field. These materials behave as permanent magnet, but do not become paramagnetic above the critical temperature.

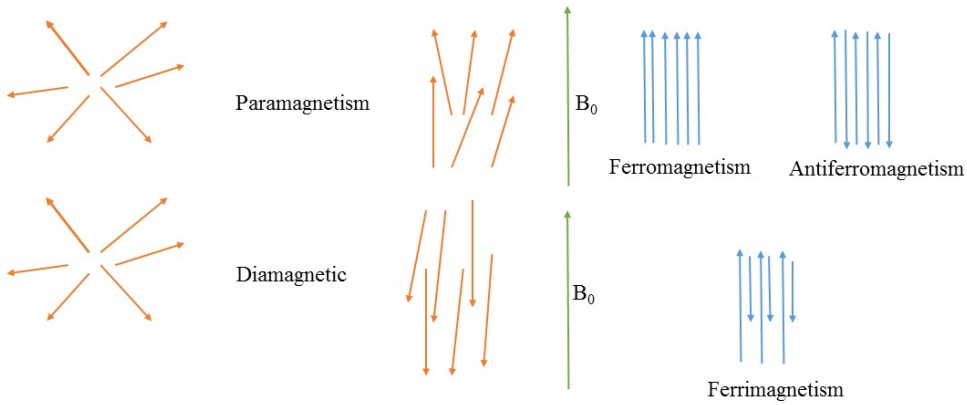

Figure 1-1: Alignment of individual magnetic moments in range magnetic phenomena

Super para-magnetism is another important type of magnetic behaviour. It occurs in materials with specific size, shape and chemical composition.[10] These parameters allow for a single domain ferri- or ferromagnetic system with paramagnetic behaviour possessing a large magnetic moment. To evaluate magnetic properties, magnetization (M) can be measured as a function of external magnetic field alteration (H) characteristic can be performed (**Error! Reference source not found.**) (b). One of the parameters that can be obtained from these measurements is coercivity, i.e. the energy which is required to demagnetize the material. It is commonly known that coercivity of magnetic materials varies with size. The variation of coercivity with NP size is presented in **Error! Reference source not found.** (a). A single magnetic domain material has zero coercivity and is said to be superparamagnetic, until a particular size ($\leq$ 10 nm), then the coercivity increases as the particle size increases, and becomes a single- or multidomain ferri- or ferromagnetic system.[11] At the point when a ferromagnetic material is magnetized in one direction, it will not return to zero magnetization when the applied magnetic field is expelled. It must be driven back to zero by a field the opposite direction. If an alternating magnetic field is applied to the material, its magnetization will trace out a loop known as hysteresis loop. This hysteresis loop differs for extremely small SPIONs (or single paramagnetic ions), SPIONs and ferromagnetic NPs. Due to very a small magnetic moment, extremely small SPIONs exhibit almost a linear relationship between magnetization and magnetic field, and the saturation magnetization appears at very high magnetic field **Error! Reference source not found.** (b). SPIONs do not exhibit coercivity due to fluctuations of magnetic moments and ferromagnetic NPs exhibit coercivity as displayed **Error! Reference source not found.** (c) and (d) respectively.

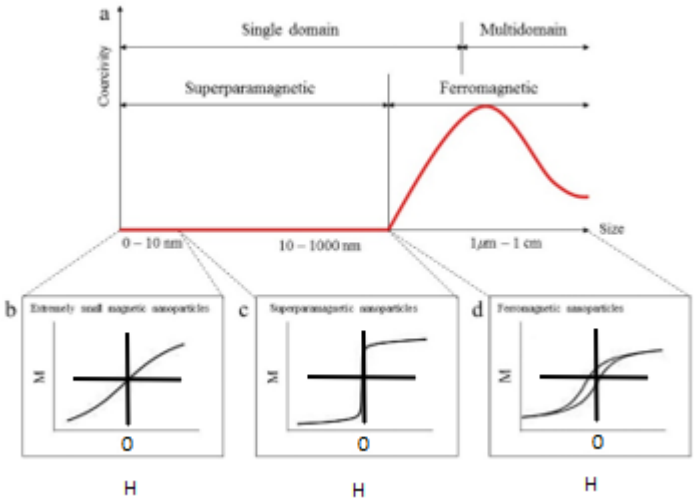

Figure 1-2: The magnetization (M) vs. the external magnetic field alteration (H) in different types of NPs sizes.[9]

1.3 Metal Oxides

The structure of metal oxide solids normally consists of an oxygen anion lattice with metal ions filling the coordination sites.[12, 13] The ordering of the cations and anions changes according to the nature of the crystal structure. Due to the closeness of ions within the unit cell, different magnetic properties can appear. These properties are highly dependent on the coupling interactions and the degree of their atomic orbital overlap.[14, 15]Three types of magnetic exchange interaction can occur in metal oxides. Direct exchange interactions, super exchange interactions and indirect interactions. A brief explanation of each of these are given below:

1.3.1 Direct exchange interactions

This interaction normally takes place between two metals which are close to each other without any other cation/anion in between (**Error! Reference source not found.**) (a). According to the Pauli Exclusion Principle, the electrons in both metals should have opposing spins. As the distance between the metals increases, the coupling effect get weaker and the spins of electron become free to alter their direction (**Error! Reference source not found.**) (b).[14, 15]

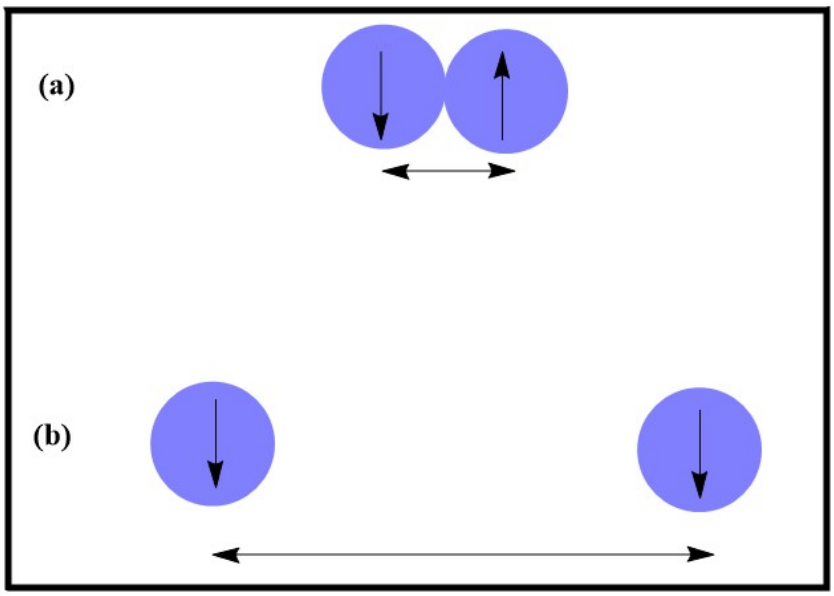

Figure 1-3: Direct exchange interactions between metal centres in metal oxide (a) anions are close together (b) anions are further apart

1.3.2 Super exchange interactions

This kind of interaction (**Error! Reference source not found.**) is subject to the coupling of electrons spins, where a non-metal intermediate ion (usually oxygen or halide) is located between the metal cations.[14, 15] This can give rise to two types of coupling:

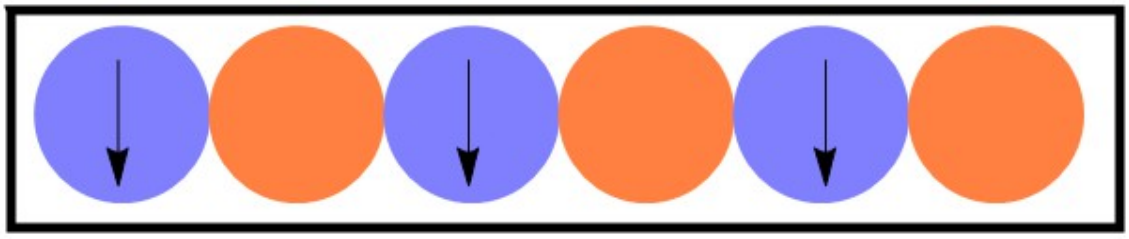

Figure 1-4: Super exchange interactions through non-metal (violet) to metal ion

1.3.2.1 Antiferromagnetic coupling

. The unpaired *d* electrons in $3d_{x^2-y^2}$ orbital has a covalent interaction with an electron in a filled *p* orbital of the oxygen anion, but if the electrons have opposed spins. The oxygen spin down electron will interact with d-orbital in which the electron spins up. **Error! Reference source not found.** represent this coupling interactions.[14, 15]

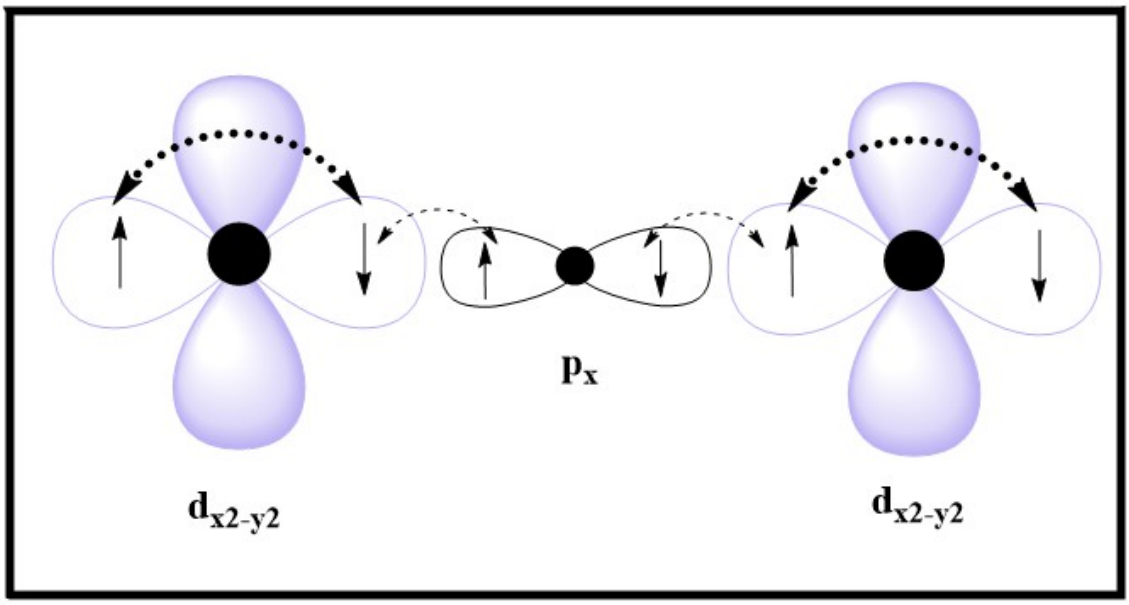

Figure 1-5: schematic diagram for antiferromagnetic coupling in metal oxides.

1.3.2.2 Ferromagnetic coupling

This occurs when one orbital of the O^{2-} anion overlaps with a half-filled e_g orbital of the metal and the other orbital of the anion overlaps with the half-filled t_{2g} orbital of the metal ion.[16] This can take two types of interaction called 180 degree and 90 degree interaction and explained below:

180-degree interaction: occurs when an electron of the O^{2-} ion undergoes a sigma interaction with e_g orbital of the paramagnetic metal and undergo direct exchange interaction, while the other electron of O^{2-} hopes into the t_{2g} orbital of another metal to undergo week pi-interaction with the Px orbital of the anion.

90-degree interaction: occurs when the t_{2g} orbitals of the metal lies 90-degree from the p orbitals of the anion. This interaction is exactly opposite to the 180-degree interaction. Generally, this types of superexchange interaction is much weaker, however the compound still exhibits enough ferromagnetic character.

Figure demonstrates both ferromagnetic interactions for two Fe^{4+} and one intervening O^{2-}.

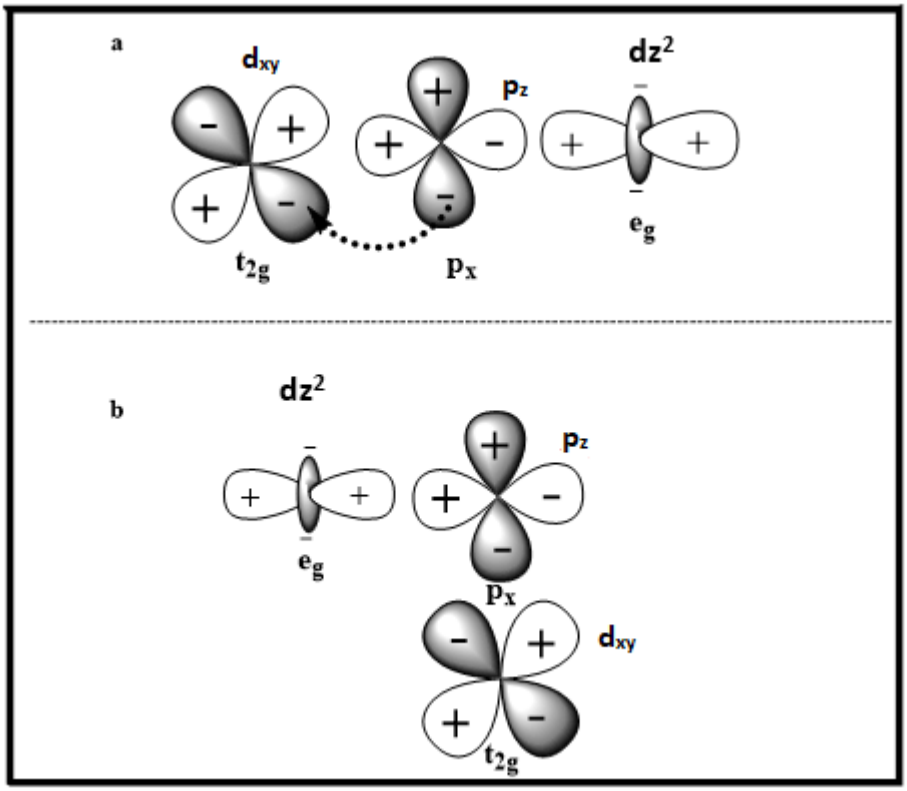

Figure 1-6: Ferromagnetic super exchange interactions in metal oxides, 180-degree interaction(a), 90-degree interaction (b)

1.3.3 Indirect exchange interactions

The final type of coupling is through indirect exchange coupling. These are also called RKKY (Ruderman, Kittel, Kasuya and Yasida) interactions.[17, 18] This takes place when two paramagnetic metal centres force their neighbouring spin to align antiparallel. This will result in a parallel alignment of the next metal centre.[14, 15] The schematic diagram in **Error! Reference source not found.** illustrates this interaction.

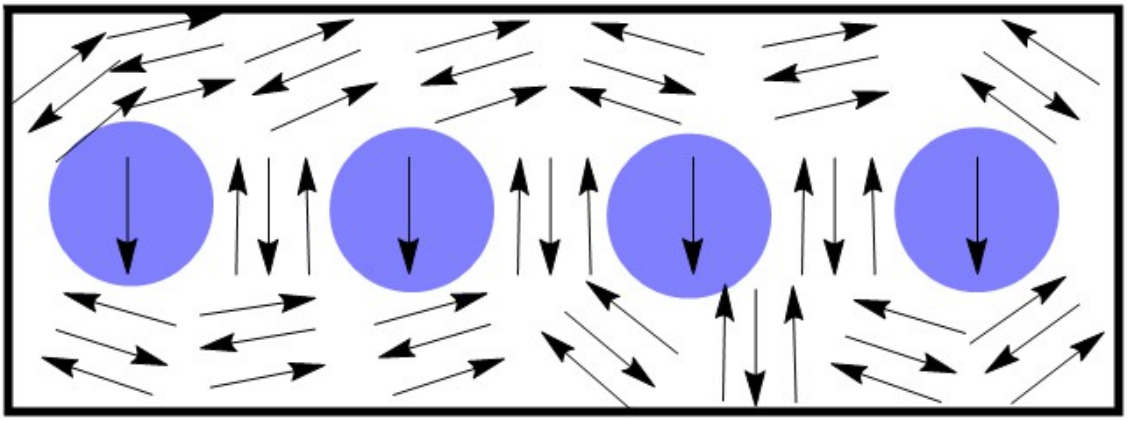

Figure 1-7: Indirect exchange interactions usually takes place between metal canters in metal oxides.

Transition metal oxides all have d valence electrons, therefore the overlap of these d orbital is highly dependent on the closeness of the metal centres to each other. The coupling between the transition metal 3d orbital and lanthanides lanthanide 4f orbitals is hindered and difficult to occur due to the different angles of the 3d orbitals as well as to the 4f orbitals in lanthanides are shielded by the 5s and 5 d electron shells. Thus transition metal –lanthanides coupling can only occurs through indirect coupling only.[13, 15]

1.4 Iron Oxide Nanoparticles

Superparamagnetic iron oxide nanoparticles (SPIONs) have been utilized in a broad range of applications over recent years.[19] Iron oxide is found in number of different phases such as hematite (α-Fe_2O_3), magnetite (Fe_3O_4) and maghemite (γ-Fe_2O_3). Among these phases, Fe_3O_4 is the most extensively used in gas sensors[20], catalytic application[21] and polymeric membrane to improve adsorptive removal of heavy metals from water resources[22] and as biohybrid materials.[22] It plays a crucial role in biomedical application for example as drug delivery vehicles, hyperthermia agents and *MRI* contrast agents.[21]

1.5 Perovskite Structure

The first compounds discovered to show the perovskite structure, $CaTiO_3$, is named after the Russian mineralogist L.A. Perovski.[23] The perovskite structure is frequently adopted by materials of general stoichiometry ABX_3 where A and B are metals, with A larger than B and X is a non-metal. It belongs to a series of crystal structures displayed by ternary inorganic solids i.e. solids formed by two cations and one anion. The structure is Built build up from a packing of X anions (oxide or fluoride anions). Usually with B taking coordination four to six and A coordination eight or twelve.[24] Small cations of 1, 2, 3, 4, 5 or 6 valence oxidation states can occupy the octahedral B sites, whereas the A sites 1, 2 or 3 valent larger-sized cations are located.[24] **Error! Reference source not found.**

shows the crystalline unit cell of $CaTiO_3$. Many studies presented the different aspects of the crystalline perovskite-type compounds.[24, 25]

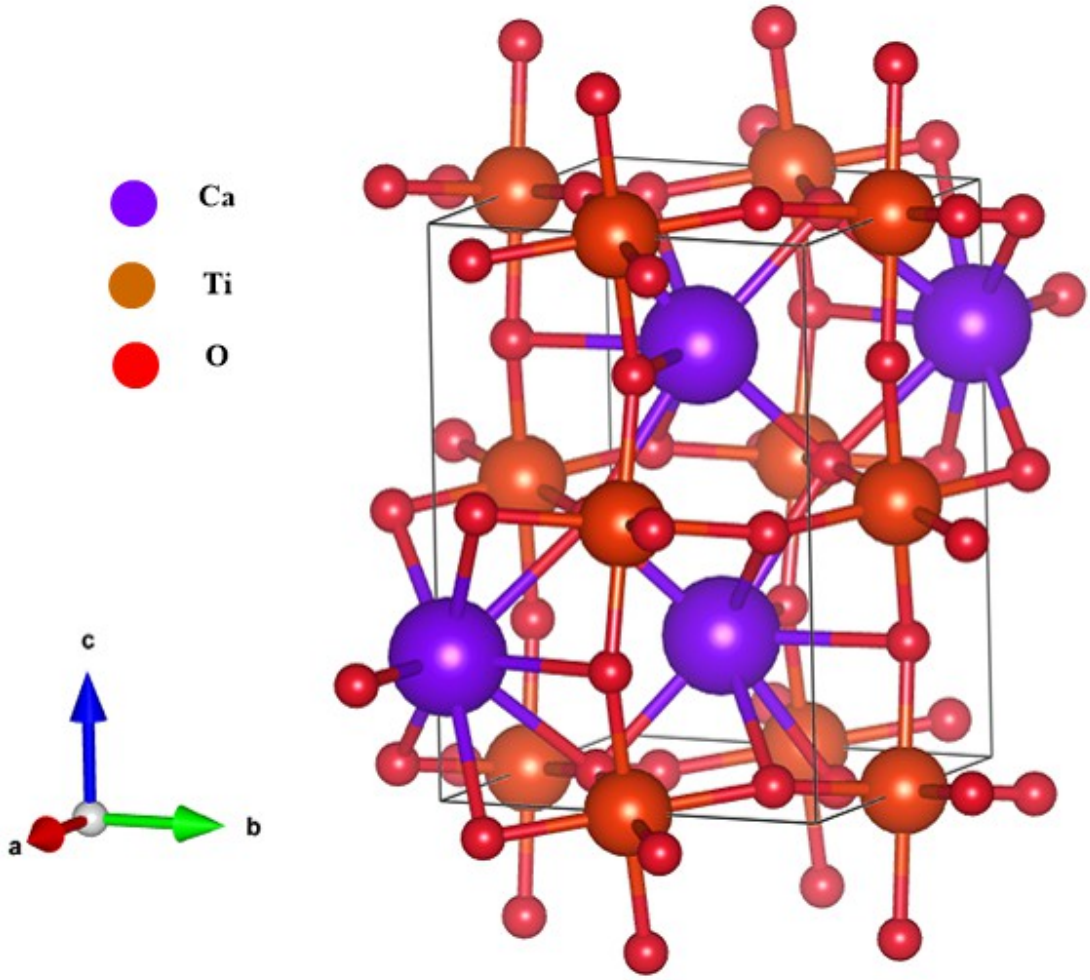

Figure 1-8: Unit cell of $CaTiO_3$, which shows an orthorhombic unit cell. [26]

Ferroelectric storage memory, magnetic bubble memory systems and electrically erasable read-only memory which were invented to replace magnetic core memory are of the important uses of ferroelectric materials showing the perovskite structure. Other application includes, for example microsensors and microactuators, ferroelectric devices such as tuneable microwave devices[27] and solar energy conversion. $PbTiO_3$, $SrTiO_3$, $KTaO_3$, $NaTaO_3$, $BaTiO_3$, $CaTiO_3$, La_2TiO_5, $BiFeO_3$ etc.[28] are the perovskite materials investigated for the use of solar energy storage. In addition, industry for the production of oxygen under UV conditions[28] utilizes perovskite $BiFeO_3$. .Another example is the Solar electricity application is where the Dye-sensitized solar cells (DSSCs) that were developed by Grätzel.[29]

1.5.1 Perovskite fluorides

Materials possessing perovskite structure have received enormous attention over the last few decades because of their interesting and fascinating properties such as colossal magneto resistance and high temperature superconductivity.[30] Perovskite materials have been known to possess magnetic properties as a results of their unique and specific ordering of occupied d-orbital. In particular, halogen-based cubic perovskite crystals ABX_3 (where A and B are cations and X is a monovalent halogen anion) are a subject of interest due to their relatively simple and flexible crystal structure and ease of synthesis *via* different rapid, cheap and environmentally friendly preparation methods .[30] Furthermore, they can be easily doped with different ions and their electrical, magnetic and optical properties are the key factors for their wide range of applications.[31]

KMF_3 (M = Mn, Fe, Co, Ni and Zn) perovskites have been actively researched due to their super-ionic behaviour, high-temperature and physical properties such as nonmagnetic insulator behaviour, piezoelectric characteristics and ferromagnetism.[32-34] It is also well known that alkali metal fluorides have wide applications in the organo fluorine chemistry both as a catalyst and as a fluorinating agent in various reactions.[35, 36] The alkali metal perovskite fluorides possess a cubic crystal structure with space group$Pm\bar{3}m$. In the cubic structure of KMF_3 (M = Mn, Fe, Co and Ni), the M atom is located at the center of an octahedron of six fluoride ions.[37]M-3d states are partially filled and F-2p states are completely filled. The M-t_{2g} states are lower in energy than M-e_g states and hence the overlapping of e_g with F-2p is stronger. [37]

Hayutallh *et al*. predicted using the full-potential linearized augmented plane wave (FP-LAPW) method within the density functional theory (DFT), $KMnF_3$, $KFeF_3$, $KCoF_3$ and $KNiF_3$ compounds are elastically stable, and their elastic properties play an important role in providing valuable information on the stability and stiffness of these materials.[38] Based on their calculated elastic constants, $KMnF_3$ is ductile and the remaining compounds are found to be brittle. The band gap increases from Mn to Ni in KMF_3 due to the decrease in the hybridization of the 3d orbital of M (M = Mn, Fe, Co and Ni) and F-2p. Furthermore, these Compounds show mixed ionic and covalent bonding.[38]

Hayatallah et al. stated that these compounds possess ferromagnetic and antiferromagnetic magnetic behaviours, however the anti-ferromagnetic state is energetically higher than the ferromagnetic state. Hence the anti-ferromagnetic behaviour is the predominant. Based on magnetic moment measurements, a gradual decrease in the

magnetization in going from $KMnF_3$ to $KNiF_3$ due to the hybridization of M-3d and F-2p states and transfer of electrons from M to F atoms.[38]

Due to half metallicity and ferromagnetic behaviour these compounds can be used for spintronic applications.[38]

1.5.2 Synthesis of Alkali metal fluorides

Manganese nanostructures or inorganic Mn-containing compounds have been recognized as a magnetic resonance contrast agents due to their paramagnetic properties for ultrasensitive T_1-weighted magnetic resonance imaging (MRI) and anticancer drug releasing.[39, 40] In the past few decades, much work has been focused to fabricate various nanostructures of manganese oxides such as MnO_2 nanosheets, MnO nanoplates, MnO nanocrystals, Mn_3O_4 nanoparticles and water-coordinated Mn(II) complex.[41-47] In addition, biocompatible fluoroperovskite $KMnF_3$ nanoparticles have been fabricated and used as an efficient *MRI* contrast agent.[48-50] Sheng *et al*. demonstrated a controllable hydrothermal method at 120°C to prepare microspheres and hollow microspheres of cubic coated PEG and citric acid $KMnF_3$ NPs.[51] The initial colloids restricted by the long-chains and modulated by citric acid which results in mono dispersed spherical aggregates in order to lower their surface energy.[52] As the reaction time proceeds, the loose spherical aggregates increase in their hydrodynamic size. Simultaneously, the contents of aggregates changed to form $KMnF_3$ due to the thermodynamic stability. Liu *et al.* reported an oil-based procedure to synthesize lanthanide-doped $KMnF_3$ nanocrystals with single-band up conversion (UC) that exhibit anti-Stokes emission which is important for applications of photonics, photovoltaics, biological imaging, and therapeutics .[53] Prof. Tang and his co-workers developed a facile one-pot synthetic process to fabricate water soluble PEGylated fluoroperovskite $KMnF_3$ nanoparticles with high longitudinal relaxivity (r_1 = 23.15 mM^{-1} s^{-1}). Ultrathin oleylamine coated nanowires of $KMnF_3$ are synthesised by Hao and his workers.[54] The oleylamine ligand works as an efficient structure directing agent that played an important role in the nucleation of this morphology.[54]The ultrafine as-prepared nanowires and nanoparticles of $KMnF_3$ showed a great potential to work as a contrast agents for Magnetic Resonance Imaging (*MRI*) and tumour targeting.

1.5.3 Tolerance Factors in Perovskites

The first description of the tolerance factor for the perovskite structure was made by Victor Moritz Goldschmidt in 1926.[24] This factor is used as an indicator for ternary and more complex oxides of whether the perovskite structure is a perfect or distorted. It is given

by the expression $t = (R_A + R_O)/\sqrt{2}(R_B + R_O)$.[24]Where R_A is the radius of the A metal, R_B is the radius of B metal and R_o is the radius of oxygen or halide. Empirically, if $0.9 \leq t \leq 1$, the structure is undistorted and remains cubic. Distortion can only take place when t deviates from unity. There are two main well-known cases for distortion:

1- When $t > 1$, the A ion is too big and the B ion is too small. This produces hexagonal structure.[55]
2- When $t < 0.9$, the A ion is too small and the B ion is too big. This would result in an orthorhombic / rhombohedral structure. **Error! Reference source not found.** represents Goldschmidt's tolerance factors for common perovskite oxides.[55]

Table 1-1: Goldschmidt tolerance factor (t) for some types of common perovskite oxide structures.[55]

Composition	*t*	*Space group*
$SrTiO_3$	1	Pm3m
$BaTiO_3$	1.062	P4mm
$CaTiO_3$	0.966	Pnma
$PbTiO_3$	1.026	Pm3m

1.5.4 Different Types of Perovskite Symmetry

According to the literature, Perovskites Perovskite crystals show unit cells of different crystal systems from cubic (high symmetry) to triclinic (very low symmetry)[24]. **Error! Reference source not found.** shows the conditions of the 7 crystal systems.

Table 1-2: Conditions for the seven different crystal system. [56]

Crystal System	*Cell Edges*	*Cell Angles*
Cubic	$a = b = c$	$\alpha = \beta = \gamma = 90°$
Tetragonal	$a = b$	$\alpha = \beta = \gamma = 90°$
Orthorhombic	$a \neq b \neq c$	$\alpha = \beta = \gamma = 90°$
Rhombohedral	$a = b = c$	$\alpha = \beta = \gamma \neq 90°$
Hexagonal	$a = b \neq c$	$\alpha = \beta = 90°, \gamma = 120°$
Monoclinic	$a \neq b \neq c$	$\alpha = \gamma = 90° \neq \beta$
Triclinic	$a \neq b \neq c$	$\alpha \neq \beta \neq \gamma \neq 90°$

The well-known and important structure examples are described in the following sections.

1.5.4.1 Ideal Cubic Structure

When t = 1, the perfect (cubic) perovskite structure exists.[24] The ideal cubic structure can be seen in $BaTiO_3$ and $SrTiO_3$. For $SrTiO_3$, Sr^{2+} and O^{2-} ions forming a cubic close-packed lattice with Ti^{4+} ions occupying the octahedral holes created by the oxygens. The perovskite structure has a three-dimensional net of corner sharing [TiO_6] octahedral with Sr^{2+} ions in the twelve-fold cavities in between the polyhedral. In the cubic ABX_3 perovskite structure (a = 0.3905 nm, space group *Pm-3m*, Z = 1), where Z is the number of atoms per unit formula.

For example, the ideal cubic perovskite $SrTiO_3$ represented in Figure 1-9 has t = 1.00, r_A = 1.44 Å, r_B = 0.605 Å and r_O =1.40 Å.[24]

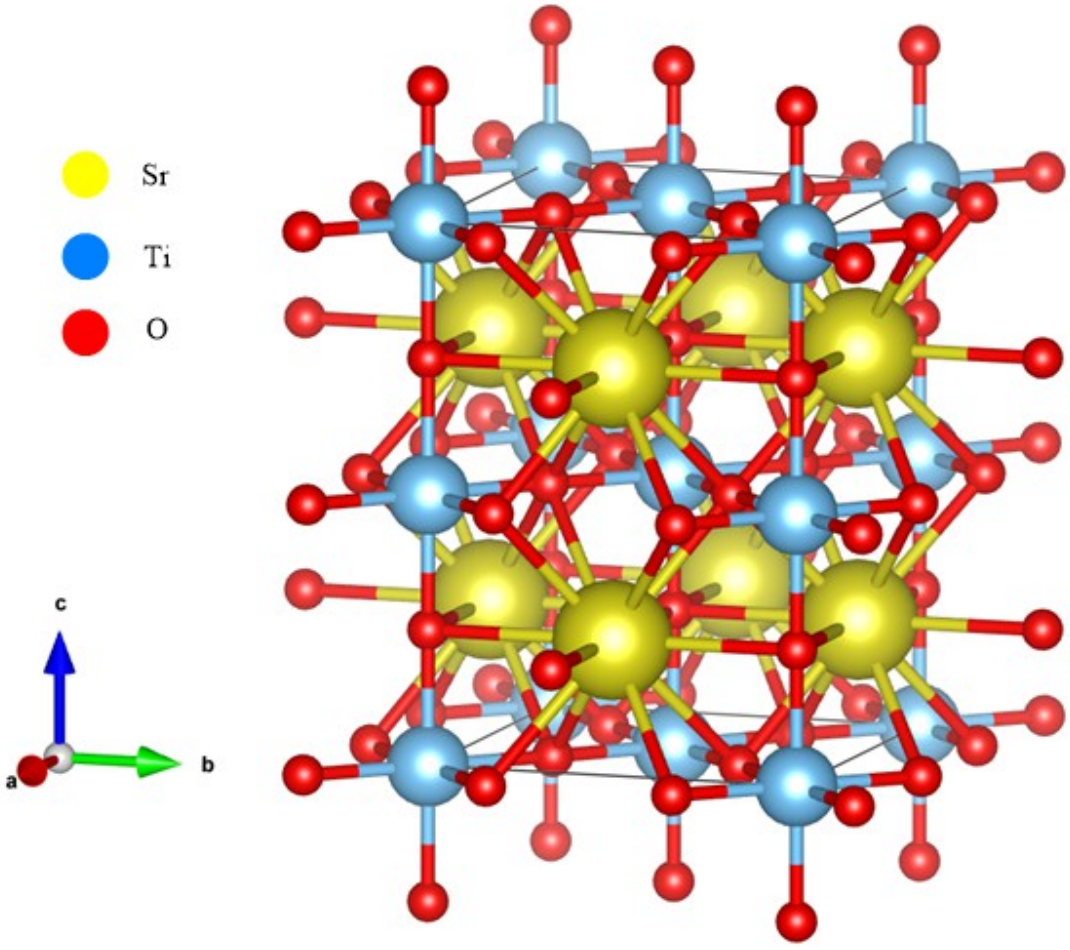

Figure 1-9: Unit cell of cubic $SrTiO_3$.[57]

1.5.4.2 Tetragonal-Type Perovskite Structures

One of the most important compounds of this class is $BaTiO_3$.The Ba-O octahedral bond is distorted and an increase along the c axis occurs when t is more than 1. It has a space group *P4mm*, $c_0 = 0.4038$ nm, $a_0 = 0.3994$ nm and Z = 1. As can be seen from the chemical structure of this compound in **Error! Reference source not found.**. Another example of tetragonal perovskite structure is the compound of $PbTiO_3$ that has higher distortion. In this compound, the increase of the volume of the A cation is combined with the lone-pair nature of the Pb^{2+} cation, showing one of the biggest tetragonality values c_0/a_0 for a perovskite-type structure.[24]

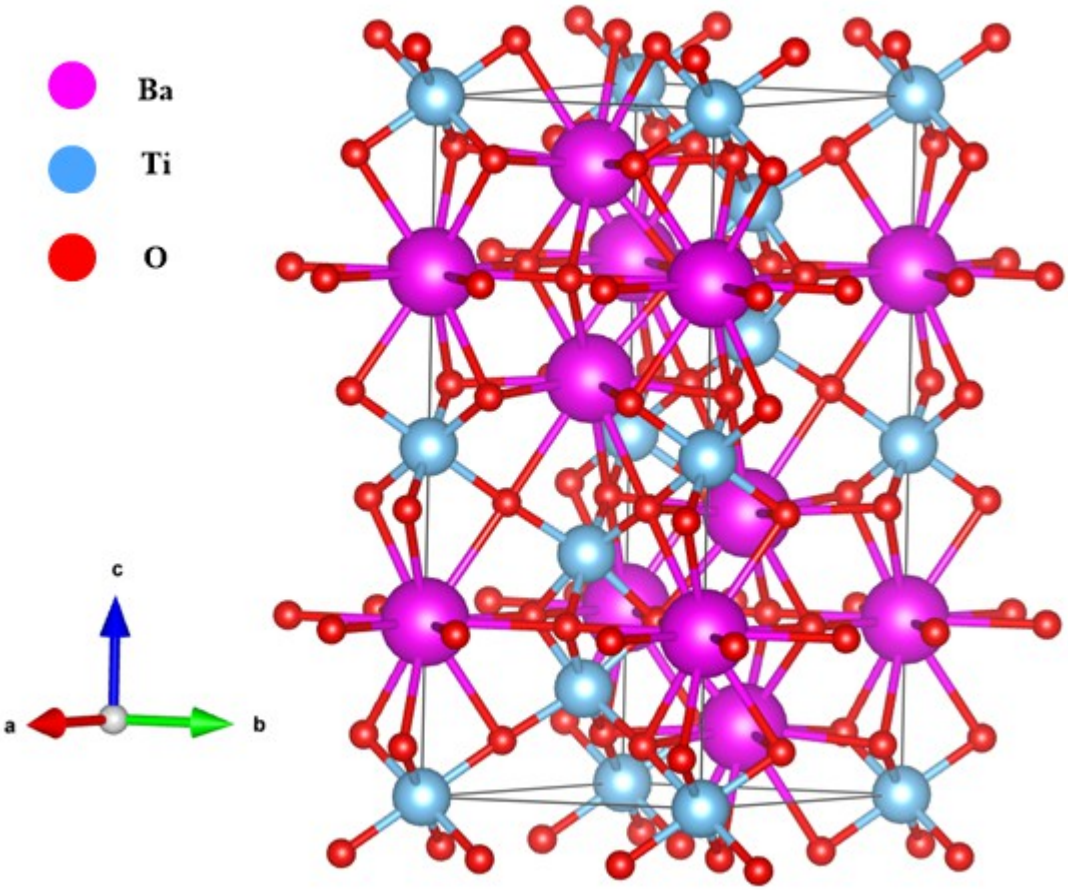

Figure 1-10: Unit cell of Tetragonal $BaTiO_3$.[58] [59]

1.5.4.3 Rhombohedrally Distorted Perovskite

One of the most commons compounds that exhibits a rhombohedral distortion is $LaAlO_3$. Generally, $LaAlO_3$ has a primitive lattice at room temperature with Z = 2 corresponding

to a hexagonal cell with Z = 6. However, the distortion is small and sometimes it can be explained as a face-centred pseudo cubic cell, with Z = 8 as seen in **Error! Reference source not found.**. Similar compounds are $LnAlO_3$ with Ln = Ce, Nd and Pr. The aluminates crystallize with orthorhombic structure when the ionic radius of the rare-earth cations cation decrease.[24]

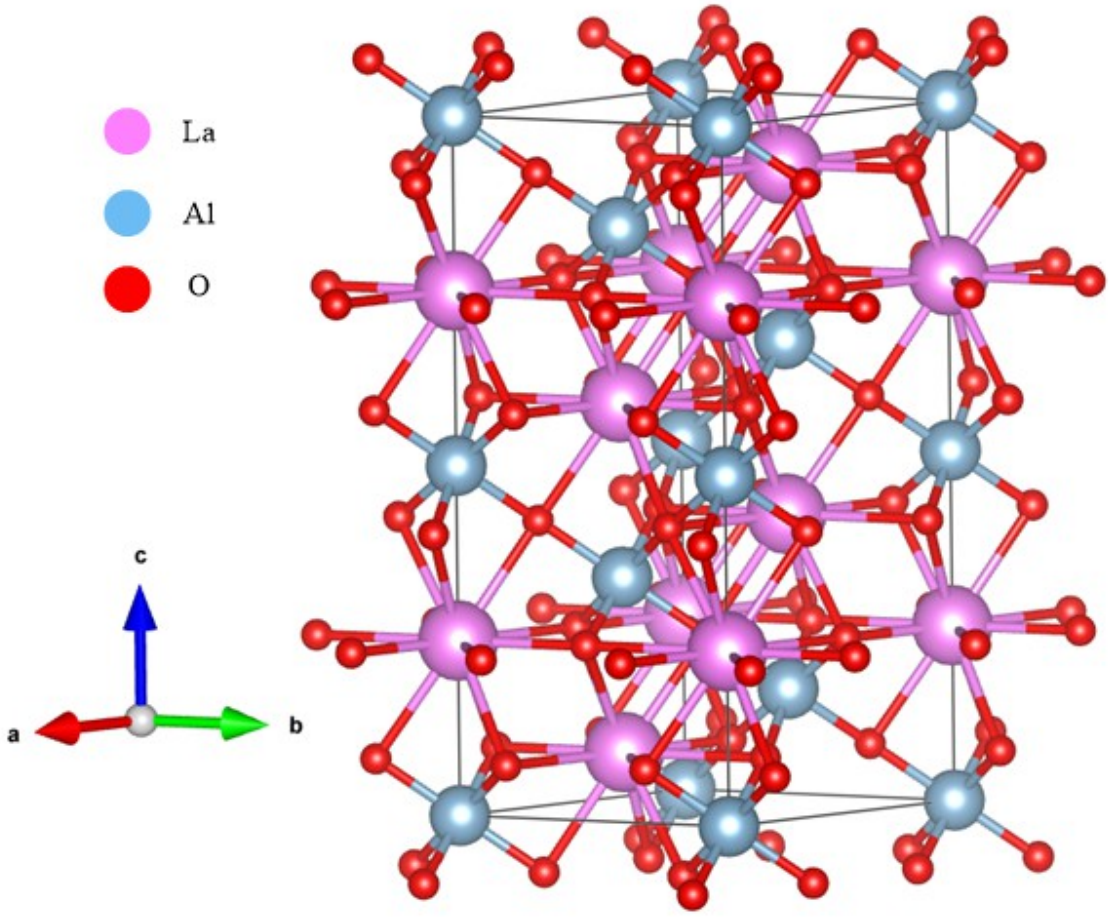

Figure 1-11: Rhombohedral unit cell of $LaAlO_3$. [60]

1.5.4.4 Orthorhombic Perovskite Compounds

$GdFeO_3$ is probably the most common type of orthorhombically distorted perovskite. It crystallizes with space group *Pbnm* and Z = 4. The cell parameters are related to a pseudo cubic cell of $a^{/}$ parameter, by $a_0 \sim \sqrt{2}a_0 \sim c_0$ z $2a_0$ and b_0.

As summarized in the tables of Muller and Roy,[61] this structure is extremely common among ABX_3 perovskite-type compounds, it includes many $LnMO_3$ compounds in which Ln is a trivalent rare-earth and M a trivalent cation (Al, Mn, Fe, V, Cr, Ga) .As a result of the small A cation radius, an orthorhombically distorted perovskite is produced, for which the 12-fold site is hard to accomplish. When these cations stabilized to achieve the lowest energy level, the B-X octahedral groups must tilt about the pseudo-cubic (**Error!**

Reference source not found.). The orthorhombically distorted structure is the largest number of distorted perovskites

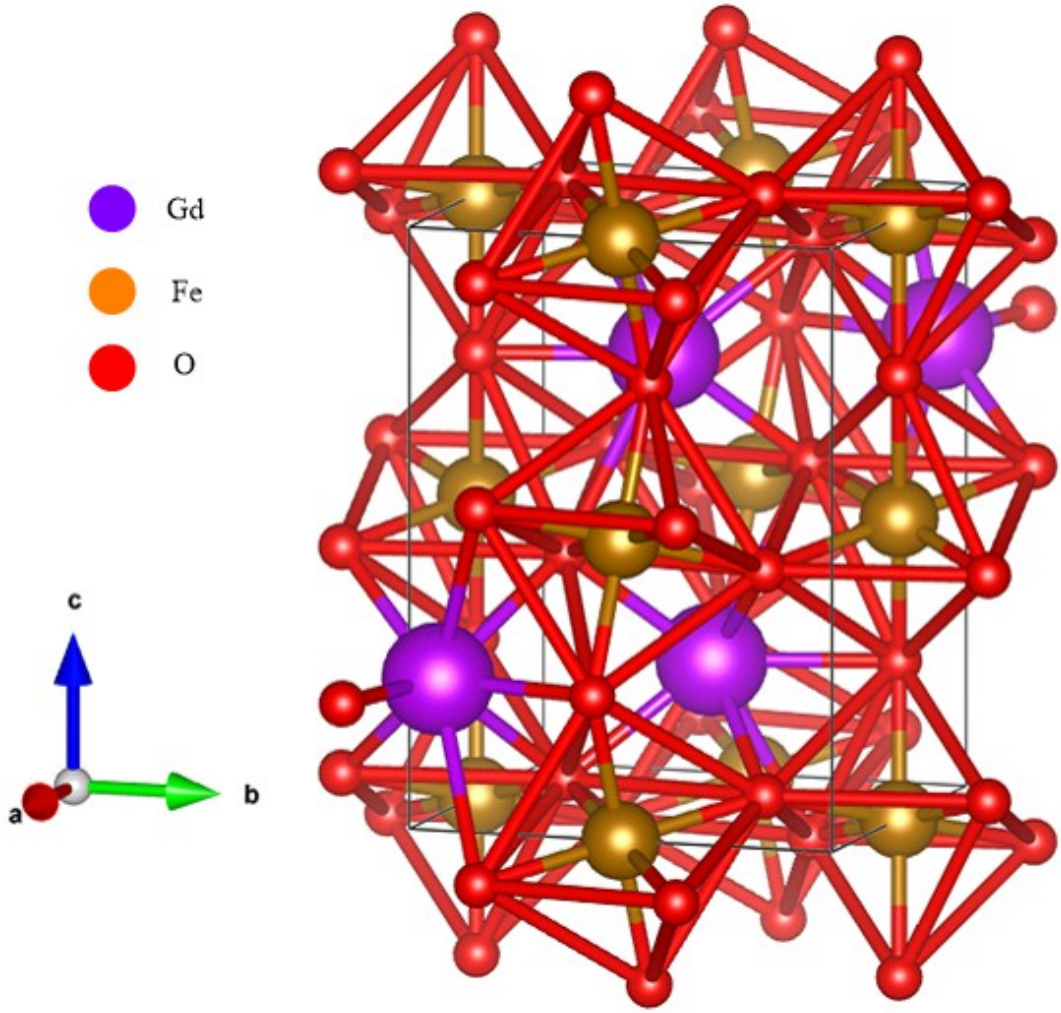

Figure 1-12: Orthorhombic unit cell of $GdFeO_3$.[62]

1.5.4.5 Monoclinic Symmetry

The perovskite structure of $BaBiO_3$ in **Error! Reference source not found.** shows a monoclinic distortion. This natural perovskite exists a controversy about the monoclinic or orthorhombic structures. $BaBiO_3$ is a better example of monoclinic structure.[63]

1.5.4.6 Triclinic Perovskite Compounds

The $BiMnO_3$ structure shown in **Error! Reference source not found.** is an example of triclinic perovskite that has high degree of distortion, in which the Mn^{3+} cation has a

strong Jahn Teller character and further more distortion arises from the Bi^{3+}lone pair. Other examples that show a triclinic distorted structure are the double-perovskite compounds of the general formula $A_2B'B''O_6$.[64] In which the perovskite B sites are occupied alternately by different cations B' and B''. As a result of the Presence of a Mn^{3+} cation with a strong JahneTeller effect, crystalline structures with a high degree of distortion are formed. Because of this reason, in $LnMnO_3$ compounds, a hexagonal structure is formed when the Ln ionic radius decreases, and the perovskite structure is only obtained by high-energy procedures.[61]

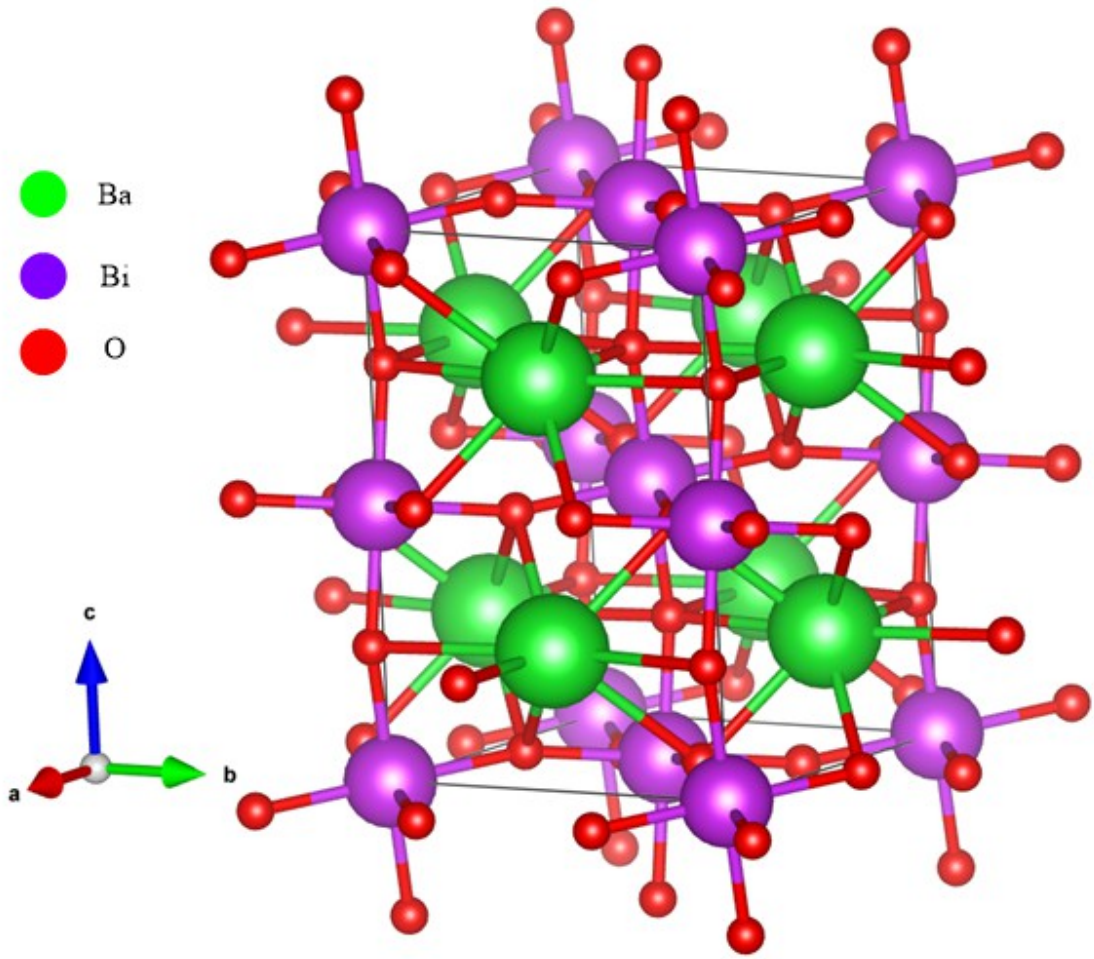

Figure 1-13: Monoclinic unit cell of $BaBiO_3$.[65]

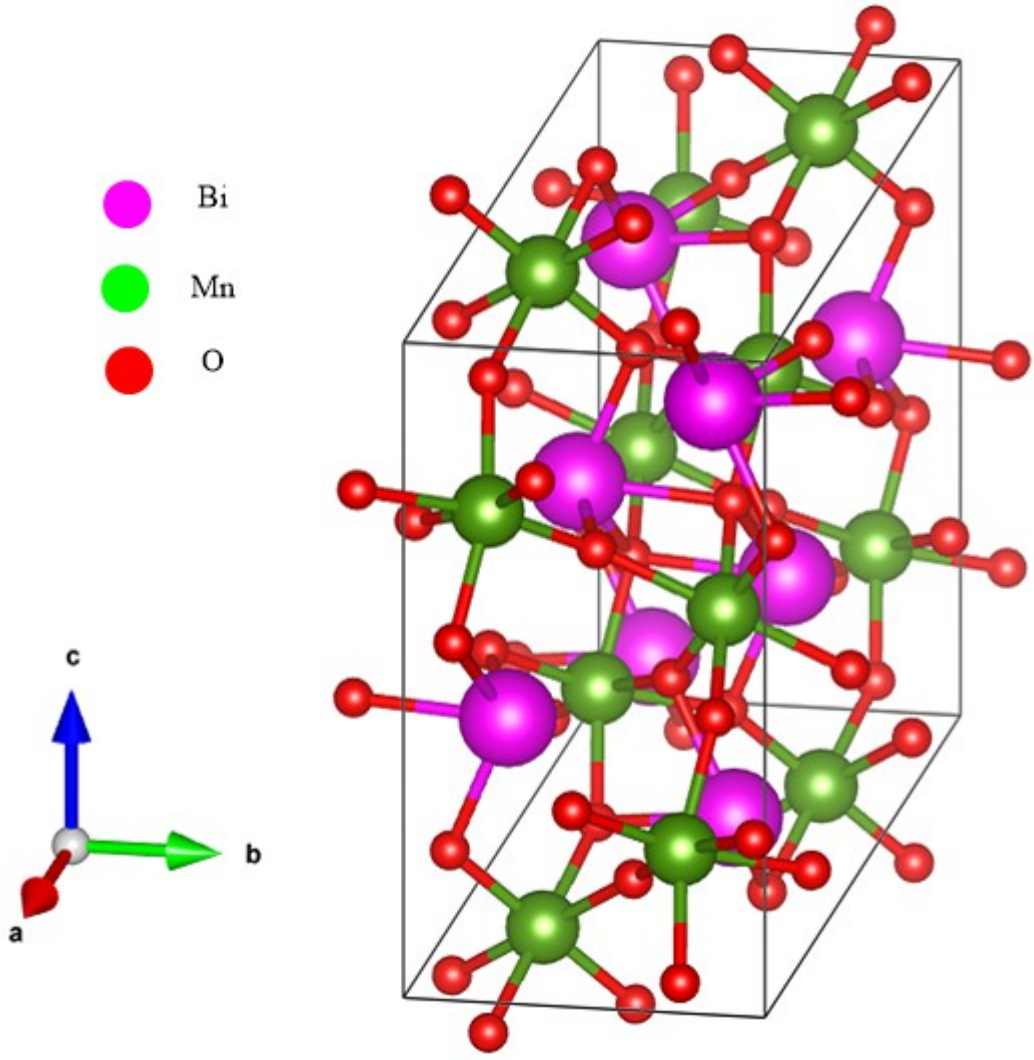

Figure 1-14: Triclinic unit cell of $BiMnO_3$.

1.6 Synthesis Methods for Perovskite Nanomaterials

In the recent decade, nanomaterials have been largely investigated from scientific and engineering perspectives. Due to their small size and large surface-to-volume area, they exhibit different properties from those of bulk materials, and have become promising candidates for nanometre scale electronic, optical, and mechanical and biomedical devices.[28]

Ceramic techniques were generally used to deliver perovskite ABX_3 structures in the past.[28] Binary metal oxide components are stoichiometrically combined and heated to form the perovskite structure. Since this approach requires high temperatures and long diffusion paths, this strategy leads to inadequate control of grain size, crystal morphology, and grain shape of the material. Furthermore, ceramic techniques can affect the quality of

the formed materials in terms of their crystal purity and presence of defects.[66] More importantly, the conventional ceramic method leads to polycrystalline compounds with micro size particles and it is not possible to control the size. To improve these methods and produce homogenous and nanocrystalline materials, several methods have been developed.[28]

These methods incorporate co-precipitation, `sol–gel technique[67], hydrothermal synthesis[68], solvo thermal synthesis,[69] vapour evaporation method method,[70] deposition method[25], electrospinning method,[71],supercritical fluids,[72] liquid–solid–solution (LSS) phase transfer,[73] sol precipitation,[74] decomposition of bi-metallic alkoxide precursors in the presence of coordinating ligands,[75] pyrolysis and composite-hydroxide-mediated approach, bioinspired synthesis methods.[76] Some of these approaches are described in the following sections.

1.6.1 Co-Precipitation Method

This method is widely used for synthesizing Super Paramagnetic Iron Oxide Nanoparticles (SPIONs). This involves the precipitation of aqueous solution mixture containing ferric and ferrous salts (in a 2:1 stoichiometric ratio), at room or elevated temperatures (70-90℃), in the absence of oxygen using a base such as NaOH.[77] A higher yield of monocrystalline can be obtained by this method in a short time, however this method typically results in a lack of well-defined nanocrystalline size, stoichiometry, and magnetism. Factors such as Fe^{2+}/Fe^{3+} ratio, ionic strength of the media, pH, reaction temperature and the type of precursor salts used (chlorides, sulphates, nitrates) can greatly affect the shape, size and composition of the magnetic nanoparticles.[77] To produce monodisperse particles, short burst of nucleation and subsequent slow controlled growth is crucial.[77] The production of monodisperse SPIONs to maintain acceptable MR signal-enhancing effect depends on controlling these processes. Ammonia, urea, ammonium carbonate and ammonium oxalate are some of the most common reagents used for precipitation.[78]

1.6.2 Thermal Decomposition Method

Synthesis of magnetic particles with control over size and shape have been created by many comparative techniques.[79] Thermal decomposition of organometallic compounds in organic solvents containing stabilizing surfactants is used to prepare monodisperse nanocrystals with narrow size.[80] The organometallic compounds include metal cupferronates M_xCupx (Cup=N-nitrosophenylhydroxylamine, $C_6H_5N(NO)O$-, M=metal) particle,[81] acetylacetonates, [M(acac)n], (acac=acetylacetonate, M = Fe, Mn, Co, Ni, Cr;

n = 2 or 3,), metal or carbonyls.[82] Oleic acid,[83] fatty acids,[84] and hexadecylamine[85] are regularly utilized as surfactants. To control the size and morphology of the nanoparticles, the proportions of the starting reagents including surfactant and organometallic mixes are important parameters. Furthermore, the reaction time and temperature may likewise be critical for the exact control of morphology and size.

1.6.3 Microemulsion method

A microemulsion is a thermodynamically stable isotropic dispersion consisting of two immiscible fluids, where an interfacial film of surfactant molecules can be used to stabilize the microemulsion of either or both fluids.[86] In water-in-oil microemulsions, the aqueous phase is dispersed as microdroplets (commonly 1–50 nm in distance across) bounded by a monolayer of surfactant atoms in the continuous hydrocarbon phase. Using the molar proportion of water to surfactant, the bulk of the reverse micelle can be measured.[87] The microdroplets will continuously collide, combine, and break once more, and finally a precipitate forms in the micelles by mixing two miscible water-in-oil microemulsions containing the preferred reactants.[88] The precipitate can be extracted by centrifuging or filtering the mixture by adding solvents, for example, acetone or ethanol, to the microemulsions, accordingly, a microemulsion can be used as a nanoreactor for the preparation of nanoparticles.[88]

This method is quite complicated due to the low yield of magnetic nanoparticles in contrast to other methods, such as co-precipitation and thermal decomposition[89] and to synthesise the desired amounts of nanoparticles, large amounts of solvent are necessary. It is therefore difficult to scale-up and not a very effective technique.

1.6.4 Hydrothermal Method

The fundamental principle of the hydrothermal synthesis is to carry out the reaction in an aqueous medium or suspense the precursors at a specific temperature and high pressure.[90] In many cases, crystalline powders can be produced using this method without calcination. In the past, this method was used to prepare $BaTiO_3$ and many other perovskites compounds. The size and shape of the NPs can be changed by controlling the concentration of the starting materials, reaction temperature and the pH of the solution.[90] $BaTiO_3$ was recently synthesized at low temperatures using an electric field in a hydrothermal vessel at known temperatures (100 and 200 °C).[90] Other scientists were able to synthesise it using an electric field to further reduce of the hydrothermal synthesis temperature.[90]

Wide ranges of nanostructured materials can be formed under hydrothermal conditions. *Li et al*. reported an ideal technique for the synthesis of various nanoparticles by a liquid–solid–solution reaction. Their work involved the use of metal linoleate as solid, an ethanol–linoleic acid as a liquid phase, and water–ethanol as a solution under hydrothermal conditions at various reaction temperatures as shown in **Error! Reference source not found.** .[91] This procedure depends on the separation mechanism happening at the interfaces of the liquid, solid, and solution phases and general phase exchange happened throughout the synthesis stages.[73]

Li et al. also used a hydrothermal reduction method to synthesise hydrophilic, monodisperse single-crystalline ferrite microspheres.[92] The reaction was carried out by mixing ethylene glycol, $FeCl_3$, polyethylene glycol and sodium acetate. The mixture was stirred vigorously until a clear solution was formed. This solution was then sealed in a Teflon-lined stainless-steel autoclave, and heated to and maintained at 200 °C for 8–72 h. Monodisperse samples with sizes ranging from 200–800 nm spheres were collected with. To direct the synthesis Li *et al*. used multicomponent reaction mixtures, consisting of sodium acetate, ethylene glycol and polyethylene glycol with sodium acetate as the electrostatic stabilizer to prevent particle agglomeration, polyethylene glycol as a surfactant against particle agglomeration and ethylene glycol as a high-boiling-point reducing agent, which was known from the polyol process to produce monodisperse metal or metal oxide nanoparticles. This multicomponent approach seems to be powerful in directing the formation of desired materials, even though the mechanism is not fully clear to date.

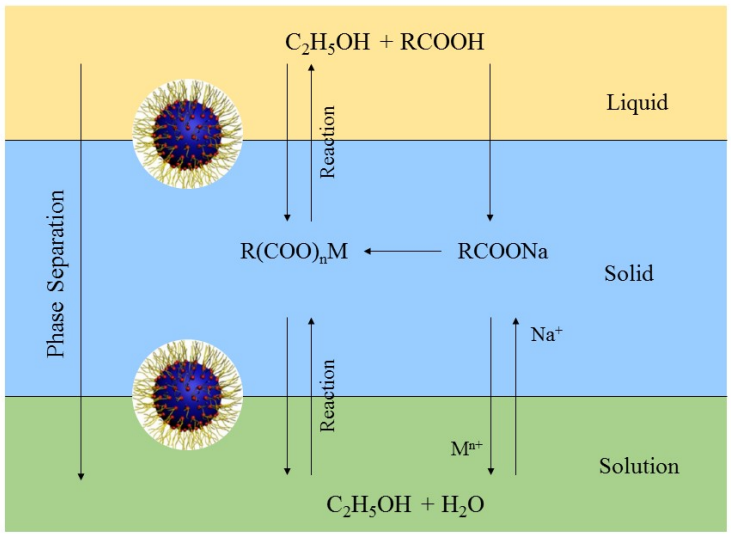

Figure 1-15: The liquid-solid-solution (LSS) phase-transfer synthetic strategy. Reproduced with kind permission from reference.[93]

1.6.5 Sol-gel synthesis

Several studies have reported many methods for the synthesis of nanoparticles. Among these methods, the sol-gel method is one of the powerful synthetic approaches to synthesise metal oxide and mixed metal oxide composite NPs. The Sol-gel method involves a few steps to produce the metal oxides: hydrolysis, condensation and drying.[94] Initially the corresponding metal precursor undergoes rapid hydrolysis to produce the metal hydroxide solution, and then an immediate condensation which leads to the formation of three-dimensional gels. Finally, the obtained gel undergoes a drying process, and formed product is readily converted to an **Aerogel** or a **Xerogel** based on the mode of drying.[95] A schematic diagram for the production of metal oxide NPs *via* the sol-gel method is illustrated in **Error! Reference source not found.**.

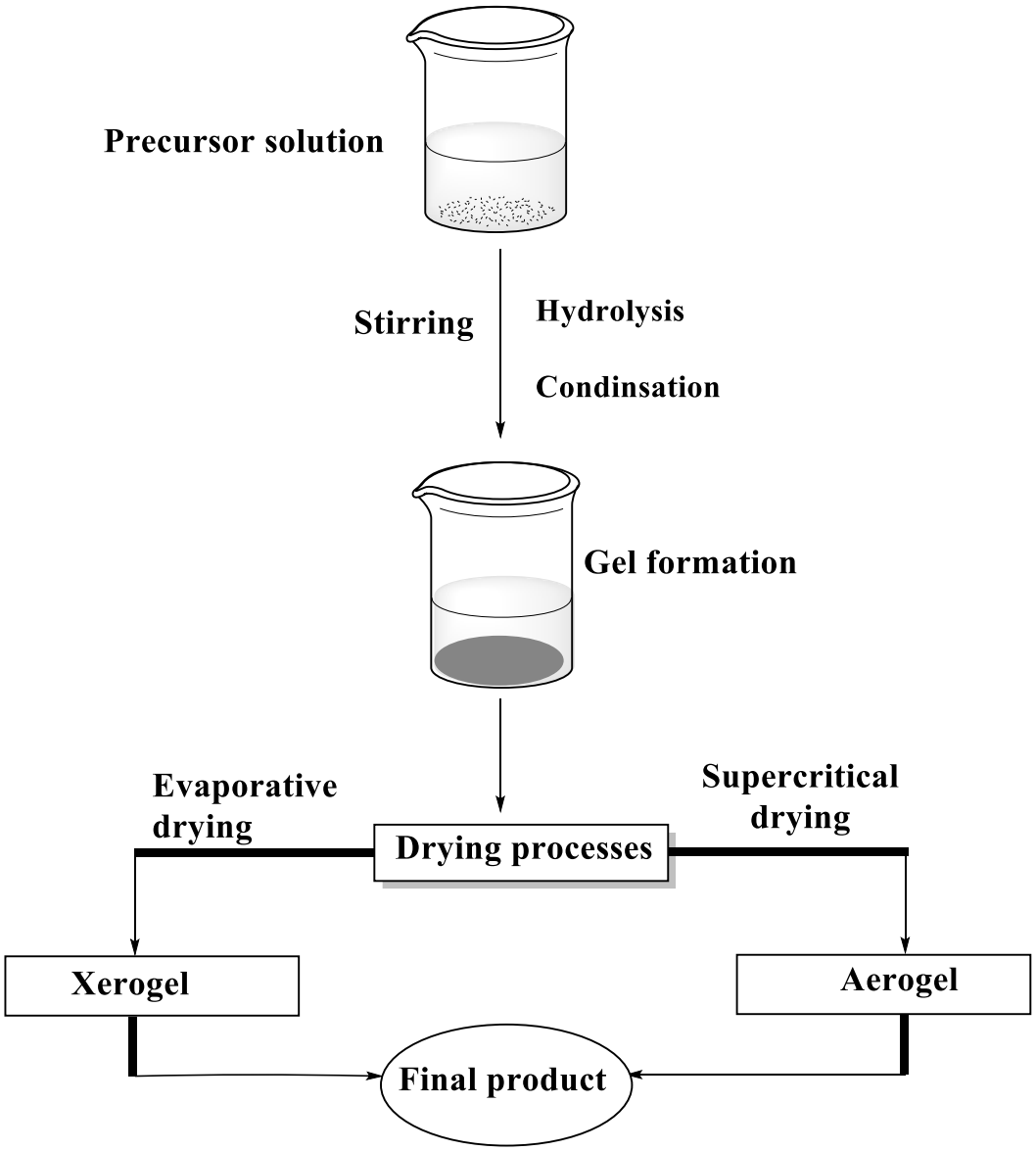

Figure 1-16: The Reaction Pathway for the Production of Metal Oxide Nanostructures in the Sol–Gel Method.[95]

The advantages and disadvantages of the mentioned synthetic techniques are briefly outlined in table 3. Regarding size and morphology control of the nanoparticles, thermal decomposition appears to be the best technique known to date.[89] In terms of simplicity of the technique, co-precipitation is the favoured method. Hydrothermal synthesis needs further investigation for the synthesis of magnetic nanoparticles. As an option, micro emulsions can likewise be utilized to synthesize monodispersed nanoparticles with different morphologies. However, this technique requires a large amount of solvent. To date, magnetic nanoparticles are mostly prepared from co-precipitation and thermal decomposition. Using these methods, large scale preparation of magnetic nanoparticles can be acheived.[89]

Table 1-3: Brief comparison for nanoparticle synthesis methods.

Synthetic method	*Synthetic Conditions*	*Reaction Temperature (°C)*	*Time (s)*	*Solvent*	*Size distribution*	*Shape control*	*Yield*
Co-Precipitation	Ambient	20-90	Minutes	Water	Relatively Narrow	Poor	High/scalable
Thermal Decomposition	Inert atmosphere	100-320	Hours/Days	Organic	Narrow	Good	Low
Micro emulsion	ambient	20-50	Hours/Days	Organic	Narrow	Good	low
Hydrothermal	High pressure	220	Hours/Days	Water-Ethanol	Very Narrow	Good	Medium

1.7 Protection/Stabilization of Magnetic Nanoparticles

There have been numerous significant improvements in the synthesis of nanoparticles with inorganic materials and improving the stability of these particles without precipitation or agglomeration is a critical issue. Nanoparticles with cores made out of inorganic materials, for example, noble, magnetic metals, their alloys, semiconductors and oxides have been investigated for a wide range of application, for biomedicine, from diagnostics to treatment of diseases. The impacts of nanoparticles must be controllable, predictable and deliver the desired result with least cytotoxicity.[96] Thus, improving the chemical stability of magnetic nanoparticles is necessary to develop efficient strategies. Specific interactions with biomolecules of interest can only take place when the nanoparticle surface is chemically modified.[96]

Careful tailoring of the ligand shell can be met *via* these criteria, allowing specific targeting, recognition and stabilisation of biochemical species.

Polymers or surfactants can be physically adsorbed or chemically attached on magnetic nanoparticles to produce a single or double layer.[97, 98] These layers create repulsive (mainly as steric repulsion) forces to balance the van der Waals and magnetic attractive forces acting on the nanoparticles. Thus, the stabilization of the magnetic nanoparticles is highly depending on this steric repulsion. Polymers containing functional groups, such as phosphates, carboxylic acids, sulphonate and sulphatetes, can bind to the surface of iron oxide NPs.[99] Some suitable polymers for coating include poly(alkylcyanoacrylates), poly(aniline) poly(pyrrole), poly(methylidene malonate), and polyesters, such as, poly (glycolic acid), poly(lactic acid), poly(ε-caprolactone), and their copolymers.[100-102] Furthermore, ligands such as sodium alendronate, oleylamine, poly ethylene glycol are widely used to coat the surface of the nanoparticles and reduce the static interactions between the individual NPs. Chemically surface-modified magnetic nanoparticles with specific biocompatible polymers are intensively studied for magnetic-field as contrast agents for magnetic resonance imaging and as directed drug targeting.[103, 104]

1.7.1 Oleylamine in nanoparticles synthesise

Oleylamine (OAm) is a versatile reagent for the synthesis of various nanoparticles.[105] As a long-chain primary alkylamine, it can work as a template, a coating and an electron donor at high temperatures.[105]Other examples includes ODA and HAD. Furthermore, OAm is liquid in nature at room temperature, which may facilitate the washing process that follow the chemical synthesis of nanoparticles. The molecular structure of OAm is depicted in **Error! Reference source not found.**. The double bond (C=C) in the middle of the molecule is another special feature of the compound. Although ODA and OAm exhibit similar basicity and affinity to metals through their NH_2 functional groups, the resulting morphology and crystallinity of the produced nanoparticles are significantly different.[105]

Figure 1-17: Chemical structure of oleylamine

1.8 Magnetic Resonance Imaging (*MRI*)

Magnetic resonance imaging (*MRI*) scanning is a medical non-invasive, non-radioactive investigation technique that uses radio frequency waves and strong magnet to generate images of internal tissues and organs.[106, 107]

Tissue, for example, bone, fat and muscles have distinctive densities and water content, that create different signal intensities. Correspondingly, pathological tissue will vary from healthy tissue and appear on the scanner as darker or brighter than normal. Uses of contrast agents such as iron oxide and gadolinium chelates significantly enhance the signal in the MRI to differentiate tissues and body structures.

MRI is viewed as one of the first line imaging instruments for clinical diagnosis. This is due to its unique features, including no radiation risk, high spatial resolution and tissue contrast. Nonetheless, the naturally poor sensitivity of *MRI* remains an impediment for the exact recognition of molecular targets, for example, small mutation changes or tumours in early stage disease. To address this sensitivity issue, Magnetic nanoparticles have been utilized as *MRI* contrast agents.[106]

1.8.1 Basic Principle of MRI

Like (NMR), nuclei such as ^{1}H, ^{11}B, ^{13}C, ^{19}F, or ^{31}P can be used as a rich hotspot for the *MRI* signal. Water protons (^{1}H) are the most understood source in the present diagnostic *MRI* technique among these.[108] Proton nuclear spin are distributed parallel or anti-parallel to the direction of the external magnetic field ($B_{0)}$, when an external magnetic field is applied simultaneously, the proton nuclear spins precess with a Larmor frequency of $\omega_0 = \gamma B_0$ (γ is gyromagnetic ratio). When a radiofrequency (RF) of ω_0 is applied, the spins aligns antiparallel to B_0 due to the energy absorbed.[108]

Immediately after the excitation by RF source, the excited spin of the water protons falls down into the ground state to relax. This involve emitting the energy picked up from the RF source. This relaxation continues by means of two different processes: T_1 longitudinal relaxation or T_1 recovery in which the nuclei can return to the ground state only by dissipating their excess energy to their surrounding (biological tissues have T_1 values of half a second or several seconds at 1.5 T), this is why this relaxation is called spin-lattice relaxation. The time constant for this relaxation is called T_1 and is dependent on the internal motion of the molecules and the strength of the external magnetic field B_0.[109]

T_2 transverse relaxation (spin-spin relaxation), is the decay of transverse magnetization due to the loss of coherence of the spin (dephasing). Transverse relaxation differs from

longitudinal relaxation in that the spins do not dissipate energy to their surrounding but instead exchange energy with each other. Both processes take place simlutanously.[110] The overall result is a cumulative loss of phase. It is a process due to pure spin-spin interaction. Dephasing occurs with the time constant T_2 and is more or less independent of the strength of the external magnetic field, B_0.[111]

The second type of transverse relaxation is T_2^* which occurs due to the intrinsic inhomogeneity of the magnetic field, this also contributes to the dephasing, resulting in an overall signal decay that is even faster.[111] Most of the inhomogeneity that produce the T_2* effect occurs at tissue borders, particularly at air/tissue interfaces, or are induced by local magnetic fields (e.g. iron particles). T_2* effects can be avoided by using spin echo sequences. In other words, T_2 represents the process of energy transfer between spins, while T_2* denotes to the effects of additional field inhomogeneities contributing to dephasing.[111]

As a result of these relaxation forms, *MRI* produces grey scale pictures. To generate *MRI* images, two well-known methods are used: 1- T_1-weighted images and a quicker T_1 relaxation rate gives a brighter contrast. 2- T_2-weighted images and faster T_2 relaxation rate generates a darker image.[108]

Error! Reference source not found. represents a schematic diagram of the mechanism of *MRI:* (a) proton precess on under external magnetic field (b) spin excitation after introducing RF pulse, spin relaxation after removal of RF pulse and representation of T_1 and T_2 weighted relaxation times.

The rate of water proton relaxation in different biological tissues and organs can be differentiated by their different water proton densities and tumbling rates, and causes them to exhibit distinct *MRI* contrast. However when this differentiation in the pathological and the ordinary tissues is peripheral, an *MRI* contrast agent can shorten the T_1 or T_2 relaxation time (accelerate the relaxation rate) in the region of interest to build up the contrast between them.[108]

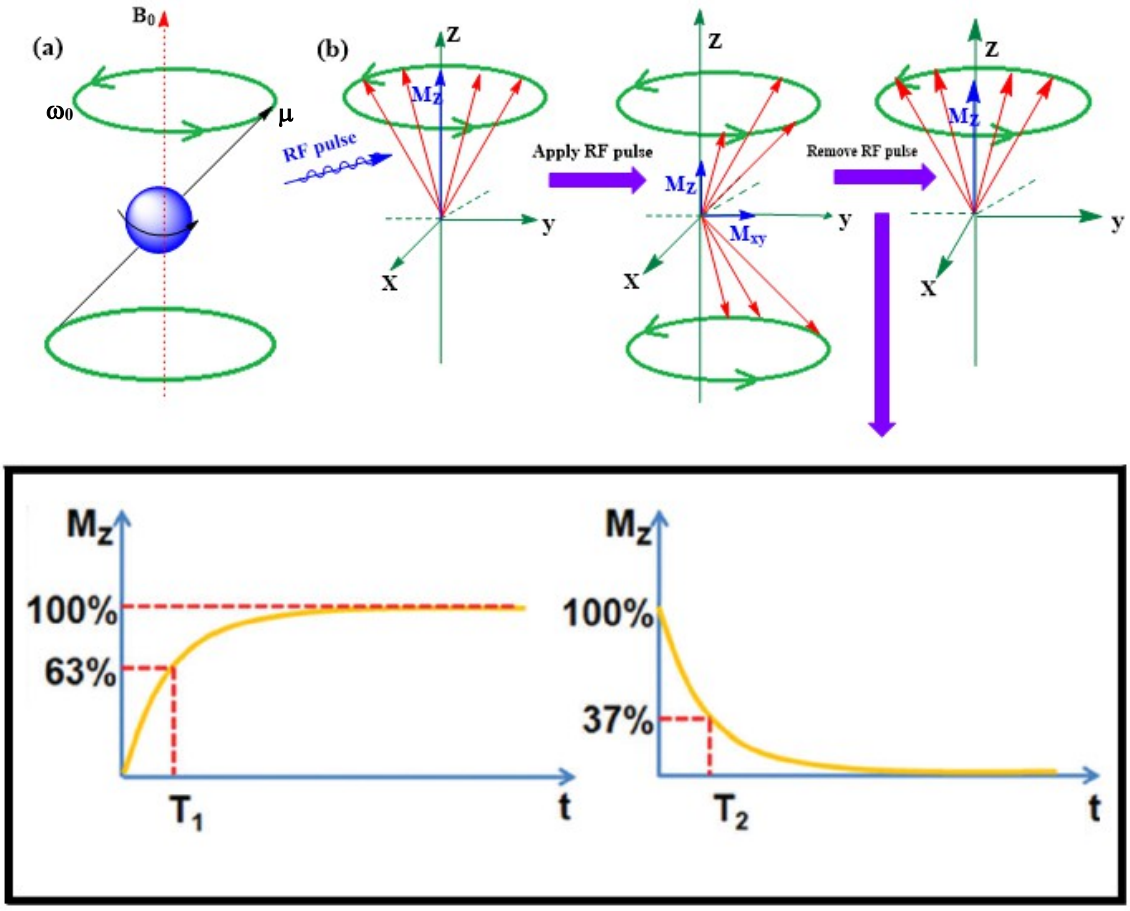

Figure 1-18: Schematic illustration of the mechanisms of MRI. (a) Protons precessω under an external magnetic field B0. (b) After the introduction of the RF pulse, protons are excited, removing the RF pulse relaxation process occurs (c) Representation of T_1 and T_2 relaxation time

1.9 Magnetic nanoparticles as *MRI* contrast agents

Based on their relaxivity (r_1 or r_2), *MRI* contrast agents are categorized into T_1 or T_2 agents. The relaxivity coefficients is defined as the ability of the contrasting agent to enhance the relaxation rate of the water proton in different biological tissues. A high r_2 value is crucial for an effective T_2 *MRI* contrast agent. In correlation, a high r_1 and a low r_2/r_1 are prerequisites for a T_1 agent.[112] Longitudinal and transverse relaxation rates r_1 and r_2 are the slopes calculated from $1/T_1$ and $1/T_2$ as a function of contrast agent concentrations respectively. Therefore, the easy tuning or controlling the nanoparticles magnetism enables them to have ideal r_1, r_2 values and r_2/r_1 ratio.

1.9.1 T_1 contrast agents

The majority *MRI* contrasting agents are chelates of paramagnetic metals of the rare earth series, Gd^{3+} complexes being the most widely studied as a T_1 contrasting agent.[113] Gd^{3+} is commonly used in biological application. This is due to its seven unpaired electrons with that have relatively long electronic relaxation time and result in large and long-

lasting paramagnetic relaxation effect. However, free Gd (III) is toxic, therefore the use of Gd (III)$^{3+}$ chelates is important to reduce its toxicity. The first generation of Gd(III) chelates was derived from linear or macrocyclic polyaminopoly carboxylates, such as diethylene triaminepentaacetic acid ([DTPA(Gd)(H2O)]2−) and 1,4,7,10-tetraazacyclododecane-1,4,7,10- tetra acetic acid ([DOTA(Gd)(H2O)]−).[113]

T_1 CAs are normally more dominant than the *T_2* CAs in the medical field as the enhanced brightening effect of the area of interest can be easily distinguished from other healthy tissues.[114] In addition, *T_1* agents usually produce higher spatial resolution images and could efficiently neglect the false signal reading of *T_2* modalities.[115]Currently, the most widely used *T_1* CAs are paramagnetic gadolinium ion complexes, in which small-molecule gadolinium chelates, such as , Gd-DOTA (Dotarems) and Gd-DTPA (Magnevists) , have been widely employed in clinical imaging. These gadoliniums based CAs and some others are displayed in **Error! Reference source not found.**

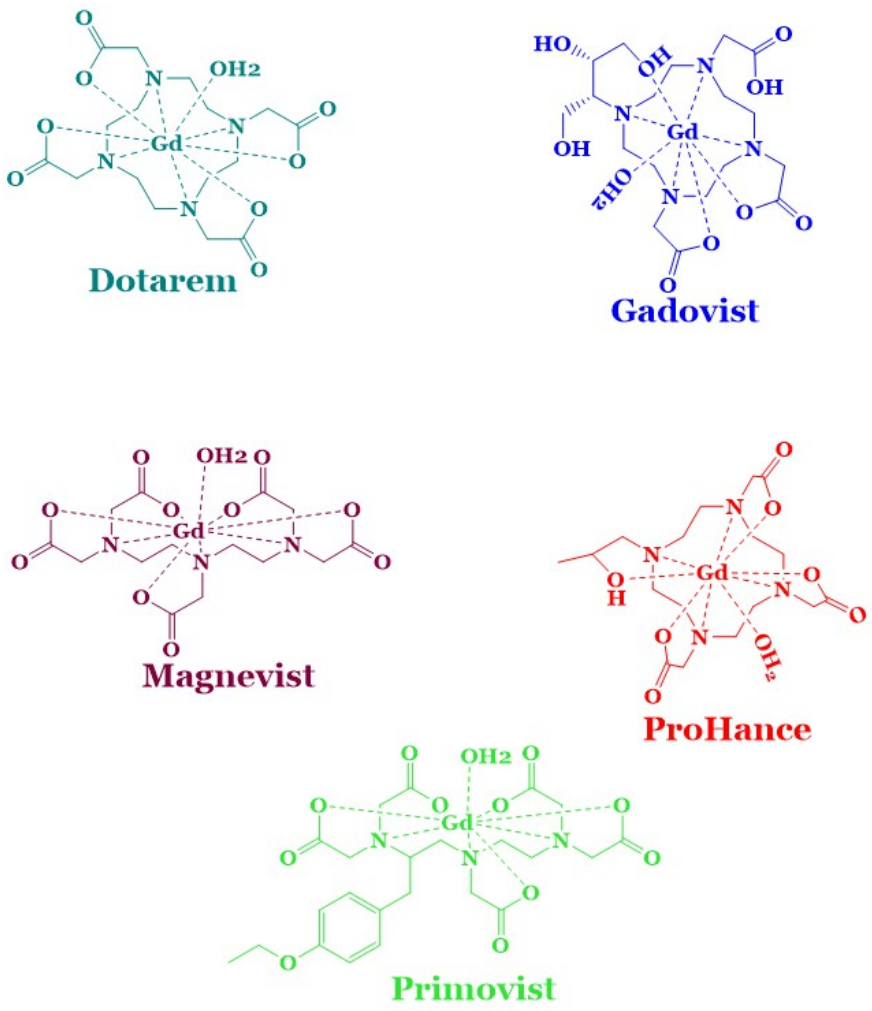

Figure 1-19: Currently used gadolinium-based contrast agents in medical field

Gadolinium is relatively able to offer long electron relaxation times. This is due to it is high magnetic moment (7.94 μB), and its symmetric $^{8}S_{7/2}$ ground state.[116] These characteristics are the key factors which make Gd^{3+} an excellent candidate for *MRI* CAs. In the presence of Gd compounds, the relaxation time of the solvent (water) protons would be shortened and hence the relaxation rate gets enhanced as a result of the dipole–dipole interactions between the proton nuclear spin and the local magnetic field generated by the unpaired electron spins. Some factors affecting the relaxivity efficiency of gadolinium complexes are displayed in **Error! Reference source not found.**.[117] The closest regions to the paramagnetic metal ion which are highly related to the relaxitivity efficiency are divided into 3 regions: an inner sphere and outer sphere. In the inner sphere, water molecules are directly bounded to Gd^{3+}, whereas in the outer sphere, the bulky water molecules get diffused in the near environment. In each region, water molecules are greatly influenced by the gadolinium ion. Moreover, in the second sphere where water molecules are hydrogen bonded to the chelating unit is considered in some cases.

According to the classical Solomon–Bloembergen– Morgan (SBM) theory for T_1 CAs.[118-120 121]. The enhancement of the relaxation process is caused by increasing the number of bound water molecules (q), enhancing rotational correlation time (τ_R), and optimizing water residence time (τ_M). In the region of the inner sphere, the main parameters are the hydration number of water molecules (q) and the longitudinal and transverse electronic relaxation times (T_{ie}, i = 1 and 2). Another crucial parameter is the rotational correlation time τ_R which is time needed for reorientation of the metal–proton vector.[117] The higher value of τ_R represents slower molecular tumbling which results in a high enhancement in the proton relaxivity. The parameter τ_M (with $k_{ex} = 1/\tau$) represents the time required for the water molecules to reside in the inner sphere, which is highly favourable for proton relaxivity in the case of fast water exchange (high k_{ex}).[117]

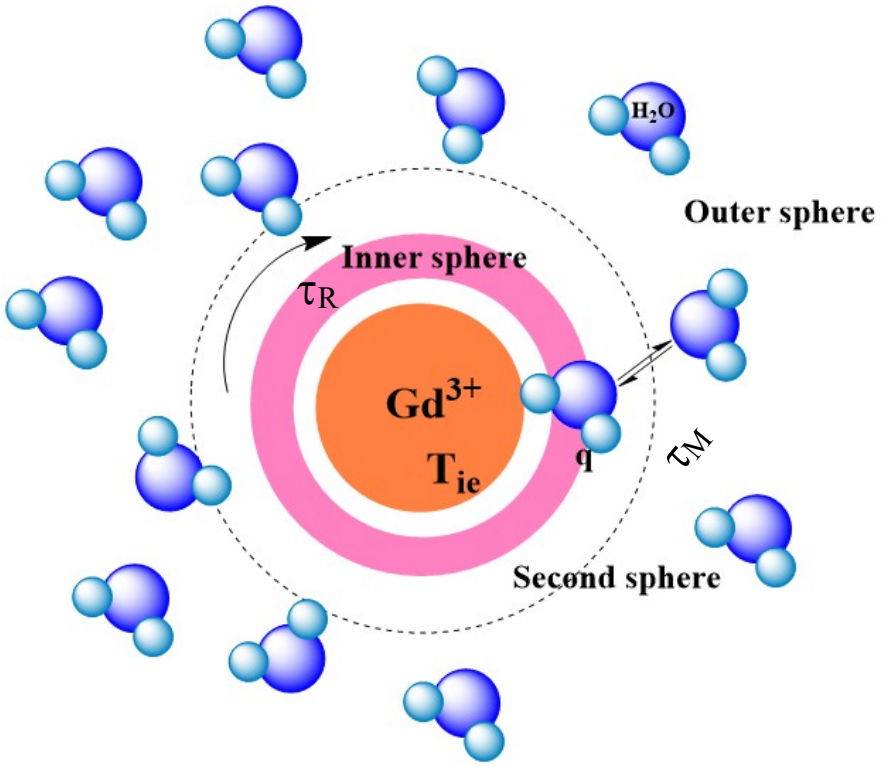

Figure 1-20: Physical parameters influencing the relaxation rate efficiency of contrast agents at molecular level.[117]

1.9.2 T_2 contrast agents

The other type of the *MRI* contrast agents is the negative contrast agents agent which can shorten the transverse relaxation time (T_2) of the proton spin and results in darker T_2 weighted images.[122] At present, most of the available contrast agents used in the medical field are gadolinium chelates based contrast agents.[122] However, several studies reported

that the use of gadolinium chelates may lead to nephrotoxicity due to the formation of strong intermediate complexes with biological matrices in *vivo*.[123-125] Hence, The Federal Drug Administration (FDA) has clarified their side effects and issued a general warning against their use in all patients with acute renal insufficiency. Gadolinium chelate contrast agents are more likely to be abandoned in the next future due to the gadolinium associated nephrogenic systemic fibrosis (NSF). Compared to gadolinium chelate, magnetic iron oxide nanoparticles (MIONs) contrast agents have excellent biocompatibility and safety as iron is one of the crucial elements in the human body whereas Gd (III) is not. Hence, in the past few decades MIONs were subjected to many investigations.

Several methods were reported for the synthesis of commercial MION contrast agents., Among these synthesis, Co-precipitation method is the most popular due to many important factors such as simplicity, mild conditions, cheap and easy to scale up, produces high yield, and being environmentally friendly as no toxic reagent are used.[89, 126] Finally, the formed MIONs usually have hydrophilic surfaces, making them water soluble and compatible for biological applications. Massart *et al.* were the first who to report and synthesise of MIONs by this method.[127] Their procedures involve mixing Fe^{2+} and Fe^{3+} in the presence of sodium hydroxide or ammonium hydroxide. This leads to the precipitation of MIONs.[128] To obtain ideal MIONs yield with an excellent water solubility (or colloidal stability), regular morphologies, uniform sizes, good monodispersity and high saturation magnetization are needed. Recently many studies were performed in order to optimise the synthesis conditions such as the ratio of the starting material salts used, pH of the solution, reaction temperature and reaction time.[129-132]

Due to the failure in synthesising uniform and well dispersed MIONs using co-precipitation method, further investigations such as functional surface modification or filtering should be performed.

Another well-known method to synthesise MIONs is the Polyol method. This method is known to synthesise water soluble NPs and it is simply similar to the thermal decomposition method. Using this method, Hu *et al.* prepared MIONs in diethylene glycol using a one pot reaction.[133] The formed NPs were ultra-small with an average diameter range of 3 to 6 nm with uniform size, regular morphology and excellent water solubility. The drawback of this method lies in scale up due to the difficulties in removing the organic solvent and surfactants used in the reaction. It is worth to noting that the size of the MIONs is an importing factor that affect the relaxitivity efficiency of the water proton in molecular tissues. It has been reported that MIONs larger than 10 nm can be

used as negative contrast agents and those smaller than 5 nm have the potential to work as positive contrast agents.[134] In some studies, these smaller nanoparticles can also work as dual-mode T_1 and T_2 contrast agents. Brief detail about contrast agents are given in the following sections:

1.9.2.1 MION negative contrast agents

Ferumoxide and Ferucarbotan are the two popular MION formulations that are available in the market and used as negative T_2 weighted contrast agents. Ferumoxide is also known as Feridex in the United States and Endorem in Europe. Normally, Ferumoxide is a stable MIONs MION collide surrounded by a low molecular mass dextran ligand. Its hydrodynamic size ranges from 120 to 180 nm. The longitudinal (r_1) and transverse (r_2) relaxation rates are 24 and 98 $mM^{-1}s^{-1}$ respectively.[135] Ferucarbtan(Resovist). MION are coated with the carboxydextarne ligand. The hydrodynamic size ranges from 45 to 60 nm, which is smaller in size than that of Ferumoxide. The r_1 and r_2 are 25 and 125 $mM^{-1}s^{-1}$ respectively.[136]

These MION T_2 negative contrast agents are specific with excellent performance to obtain clear images for liver or spleen and can be cleared from blood to liver by the RES after several intravenous administration.[137-139] Another advantage, is that these formulations are nontoxic and safe as they can be metabolised *via* lysosomes and converted into nonmagnetic iron ions which can be also utilized in the formation of ferritin and haemoglobin in the blood.[140-142]

However, Resovist is the only currently available commercial negative contrast agent in several countries including Japan and the USA. All other negative MIONs have been removed from the market.[136] The most probable reasons for this action are:

The negative contrast agents lead to dark images that can be difficult to distinguish with the signals of other pathogenic conditions, including calcification, hemorrhage, and metal deposits, for example endogenous iron. The relatively high magnetic moments of the negative MIONs MION contrast agents could results in susceptibility artefacts such as distortion of the magnetic field on the surrounding of disease regions, or background distortion), this could significantly destroys the background around diseased regions and produce unclear images.[114, 143] Another reason is related to the relatively large particle sizes of the negative MION contrast agents, which affect the metabolism process and therefore take a long time for rapid clearance from the body and accordingly may cause long-term side effects.[144] The final reason is due to the long relaxation time mechanism

to produce T_2-weighted images compared to time needed to create the T_1-weighted *MR* images .

1.9.2.2 Synthesis of extremely small MIONs (Es-MIONs) positive contrast agents

To avoid the negative drawbacks of MION contrast agents, Tautetz and his workers first prepared extremely small NPs that have less than 5 nm in diameter size.[145] The formed products showed a potential to work as positive MION contrast agents with a large longitudinal relaxation rate 2 to 50 $mM^{-1}s^{-1}$ and r_2/r_1 ratio smaller than 5 . Hereafter the synthesis of extremely small MION received higher attention and much research has been conducted to investigate the properties of the Es-MIONs. Several methods have been documented for the synthesis of this type of NPs, and mainly include co-precipitation, thermal decomposition, polyol or reduction precipitation methods.

In 2004, Sun and workers reported a thermal decomposition method using $Fe(acac)_3$, $Co(acac)_2$, or $Mn(acac)_2$ as starting materials to prepare monodispersed MFe_2O_4 (M = Mn, Fe, Co) nanoparticles. Their work was focused on preparing single phase NPs of a controllable size. They synthesised Fe_3O_4 nanoparticles with an average size smaller than 5 nm.[146]

Based on this thermal decomposition method, in 2009, Tromsdorf *et al*. systematically prepared superparamagnetic PEGylated ESMIONs of 4 nm core size and applied them as potential blood pool T_1-weighted *MRI* contrast agents. According to the NPs cytotoxicity and stability under physiological conditions, the size of the core ES-MIONs, density and length of PEG coating were optimized. The formed NPs had reasonably high r_1 relaxivity (7.3 mM^{-1} s^{-1}) with relatively low r_2/r_1 ratio (2.4). The observed r_1 value is doubled of the reported value of Magnevist (Gd-DTPA), which is clear evidence that the formed USNPs could be used as a potential positive contrast agent.[147]

In 2011, Kim *et al*. prepared highly dispersed and uniform ES-MIONs *via* a thermal decomposition method using iron−oleate complex in the presence of oleic acid and oleyl alcohol. The size of the ES-MIONs was very uniform could be controlled from 1.5 to 3.7 nm with high crystallinity.[148]

Park *et al*. developed a polyol method to prepare water soluble and monodispersed PEG coated ES-MIONs in triethylene glycol. The average particle size was 1.7 nm using TEM microscopy, and the hydrodynamic diameter is determined to be 5.4 nm using dynamic light scattering (DLS). The squid measurements were carried out and the M−H curves revealed that the PEG coated ES-MIONs exhibit ferromagnetic behaviour at 5 K, but are

superparamagnetic at 300 K. Moreover, the PEG coated ES-MIONs possess a relatively high r_1 of 4.46 mM^{-1} s^{-1} and low r_2/r_1 ratio of 3.4. These values reveal that the formed NPs can be used as T_1-weighted *MRI* contrast agents.[149]

The Co-precipitation method was also utilized by Li *et al*. to prepare water-soluble ES-MIONs. He used thiol coated poly- (methacrylic acid) (PMAA−PTMP) as a stabilizer. Different salts of $FeCl_3$ and $FeSO_4$ were used as iron source precursors to react with ammonia solution. The average particle size of the formed ESMIONs estimated by HR-TEM was 3.3 ± 0.5 nm and the hydrodynamic diameter determined by DLS was 7.5 nm. The M−H curve revealed that the ES-MIONs were superparamagnetic with a magnetization of 16 emu g^{-1} at room temperature. The efficiency of the formed NPs as a contrast agent was determined by performing NMR experiments. The r_1 relaxivity value was 8.3 mM^{-1} s^{-1}, which is also double the value of the commercial T_1- weighted *MRI* contrast agent Gd-DTPA (r_1 = 4.8 mM^{-1} s^{-1}). Furthermore, the r_2/r_1 ratio of the formed NPs is 4.2 which is also relatively small, indicating their potential as a T_1-weighted *MRI* contrast agents.[150] Generally, the magnetic properties of ES-MIONs are highly dependent on the size of the particles. NPs show superparamagnetic properties when the particle size is larger than 2.2 nm. However, when the size is reduced to 1.5 nm, they show paramagnetic behaviours.

The low magnetization of the ES-MIONs is normally related to the spin canting effect. The brightness effect of the T_1 ES-MIONs contrast agents is proportional to their concentration. For further investigation, Kim *et al* prepared different samples of ES-MIONs with different particle sizes of 12, 3, and 2.2 nm. Their r_1 relaxivities were 2.37, 4.77, and 4.78 $mM^{-1}s^{-1}$, respectively and the r_2/r_1 ratios were 24.8, 6.12, and 3.67 respectively. The obtained results are clear indication of the correlation between particles sizes and T_1 enhancement. In other words, the smaller the size of the NPs, the better the T_1 contrast.[148]

1.9.3 Dual-mode T_1/T_2 contrast agents

The combination of multiple imaging modalities can yield complementary diagnostic information and offer synergistic advantages over single modality.[151-155] The T_1/T_2 dual-modal strategy for *MRI* has attracted considerable interest because it can give highly accurate diagnostic information by the beneficial contrast effects in both T_1 imaging with high tissue resolution and T_2 imaging with high feasibility on detection of for example a

lesion.[156] For Example Rivas and colleagues developed a dual-mode contrast agent based on Rhodamine DO3A conjugate.[157] The DO3A unit was coordinated to Gd(III). The probe showed the capability to penetrate the HEK cells and localised in the mitochondria. Furthermore, it has a pH sensitivity to acidic microenvironments and is tumour specific. Generally, T_1 and T_2 images exhibits bright and dark images contrasts, respectively, that occurs due to recovered (T_1) or decayed (T_2) magnetization after a specific pulse sequence.[158-161] In terms of application, *T_1 MRI* is normally useful for imaging liquid retaining concrete structures such as joints or fat tissue, which are challenging and quite complicated by *T_2 MRI*. On the other hand, *T_2 MRI* is powerful in imaging water-rich structures or local inflammation, which usually appear as bright signals in this sequence.[156] The faster the T_1 relaxation, the brighter the T_1 image and the faster the T_2 relaxation, the darker the T_2 image and vice versa.[156] Frankly speaking T_1 contrast agents are normally paramagnetic metals such as Gd^{3+}, Mn^{2+} chelating complexes and T_2 contrast agents are super magnetic nanoparticles such as Fe_3O_4.[158, 159, 161] Despite the fact that T_1 and T_2 contrast agents have their individual r_1 and r_2 values, few of them exhibits dual-mode T_1/T_2 contrast due to several reasons such as: 1) The lower r_2 (< 10 $mM^{-1}s^{-1}$) value for most Gd^{+3} T_1 contrast agents, results in limited effect such as percentage change on T_2 relaxation value, 2)T_2 contrast agents normally have high r_2 values, ranging from hundreds to a few thousand $mM^{-1}s^{-1}$ which force the T_1 contrast, although their R_1 relaxation rates values are not necessarily low.[156]

Several strategies have been reported in designing and constructing T_1/T_2 dual-mode contrast agents for different applications. The synthesis of this kind of contrast agent is usually subdivided into the following categories : (1) conjugation of T_1 contrast materials onto T_2 contrast materials[162-165] (2) doping T_1 contrast materials onto T_2 contrast materials[151, 166-170] (3) magnetic nanomaterials with specific magnetisation and appropriate size[150, 171, 172] and (4) clustering T_1 contrast materials with nonmagnetic porous materials.[4, 173-175] The enhancement in the longitudinal and transverse relaxation times relies on the inner and outer sphere regimes respectively.[176] Therefore, conjugation of T_1 contrast materials with T_2 contrast materials would result in an increase in the T_1 contrast ability, where T_2 realxitivity can be maintained at the same level.

Cheon *et al.* investigated the ability of silica coated paramagnetic Gd species as T_1/T_2 dual-modal contrast agents.[162] Their work involve a flexible tuning of T_2 quenching to T_1 relaxation by altering the thickness of the SiO_2 layer.[162, 163] Using this approach, they also recently reported a tuning strategy that depends on distance for imaging a wide range

of biological targets.[177] In order to change the quenching effect to T_1 relaxivity using strong magnetization of T_2 paramagnetic materials, Gao *et al.* documented steps of synthetic routes to incorporate paramagnetic nanocrystals into superparamagnetic iron oxide nanoparticles. Their observation revealed that the incorporated mixture exhibited a mutal T_1 and T_2 contrast ability enhancement compared to the single contrast agents.[166-169, 178] The relatively larger size of lanthanide atoms compared to iron play an important role in the formation of small nanocrystals rather than substituting vacancy of the iron oxide crystals. The incorporated T_1 contrast materials of Gd_2O_3 or EuO NPs show parallel spin ordering with the same direction of magnetic field induced by the T_2 contrast agents. As a result , longitudinal and transverse relaxivities can both be enhanced due to the contrast agents effect, therefore synergistically increased T_1 and T_2 contrast abilities would be observed.[178]

Many studies show that magnetic nanoparticles with appropriate magnetizations and sizes inherently display both T_1 and T_2 contrasts.[150, 171, 179] Dai and his co-workers synthesised FeCo nanoparticles with diameters of 4 and 7 nm. These developed NPs showed both T_1 and T_2 contrast agent's capability. The synthesis mechanism is still controversial .[171] More recently, Lu *et al*. reported that iron oxide nanoparticles with an average diameter of 5 nm are also able to exhibit T_1 and T_2 dual contrast .[150] Further decrease in the average size of iron oxide nanoparticles to ~3 nm favours T_1 contrast efficiency.[148] The most probable reasons for the dominant T_1 effect are more likely attributed to the reduced magnetization, that decreases the T_2 spin dephasing effect, and due to the increase in the surface-to-volume ratio and therefore a large number of paramagnetic centres would be provided on the NPs surface to interact with the water molecules. Similarly, studies on both types of iron oxide NPs with metal-rich Fe_3O_4(111) and Fe_3O_4(100) facets showed T_1/T_2 dual-modal contrast potential.[166, 176]

Another strategy that is widely used to construct paramagnetic enhanced T_1/T_2 contrast agents is achieved by clustering of T_1 contrast materials in nonmagnetic matrices such as porous silica, polymers, or organic frameworks or proteins.[4, 173-175] These types of contrast agents can enhance the longitudinal and transverse relaxitivites in two ways. Firstly, the diffusion of water molecules around the complex is constrained upon clustering. This leads to a significant change in the overall motional effect of T_2 relaxation and subsequently shortens the T_2 relaxation times of water protons.[174] Secondly, the building nature of the developed complex results in constrained coordination and

chemical exchange for surrounding water molecules and, therefore, an enhanced T_1 effect, known as the geometrical confinement effect would be observed.[180]

To construct an ideal T_1-T_2 dual mode contrast agent, a few general rules could be applied to assess the correlations between T_1 and T_2 contrasts. Initially, due to the overlap that occurs between T_1 relaxation by T_2 decaying effects, optimisation of NPs with moderate R_2 values could control the T_2 decaying effect with T_1 relaxation, without it, the T_1 contrast effect could be diminished.[163] Secondly, The longitudinal and transverse relaxitivities of T_1 and T_2 contrast agents can be highly effected by altering their structural and physical parameters, for example surface, size morphology, aggregation state and crystallization. Controlling such parameters could result in a highly effective T_1-T_2 dual-mode contrasts.[163]

1.10 Colorectal cancer

Colorectal cancer is the third most common cancer and the third leading cause of cancer death in men and women in the United States. It causes significant suffering and economic disasters worldwide.[181] It is a well-known disease that starts in the colon and rectum. These two organs are crucial parts of the large intestine which is the most important part of the digestion system as shown in **Error! Reference source not found.**. They exist at the lower part of the body's digestive system.

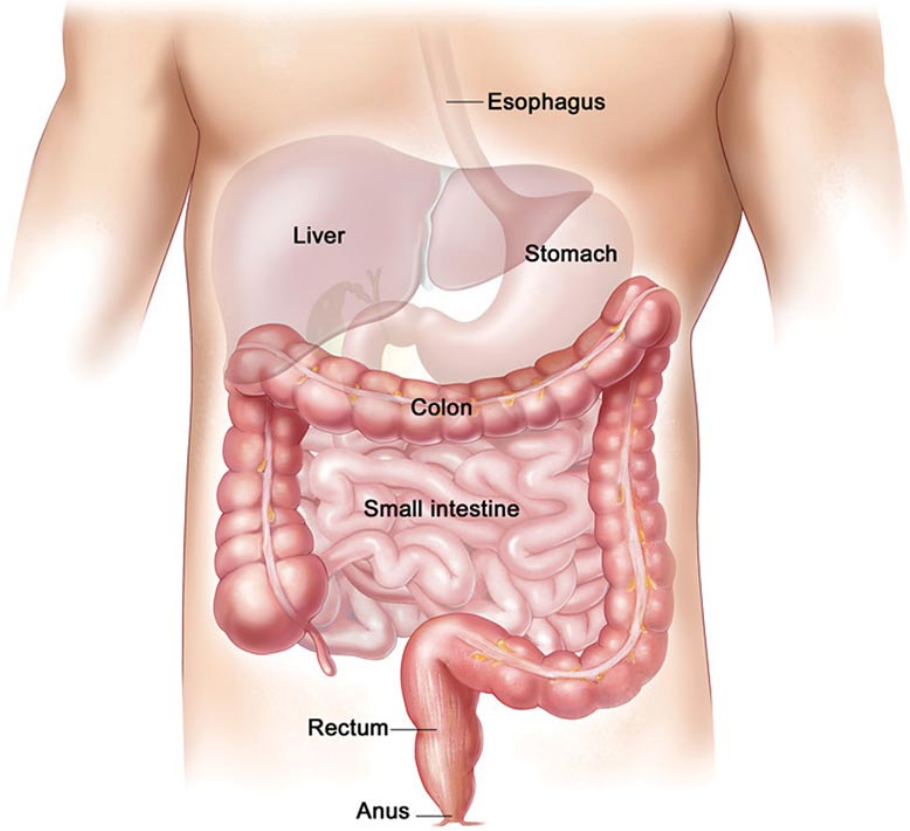

Figure 1-21: Parts of digestive system in human body.[182]

Most colorectal cancer are adenocarcinomas (cancers that begin in cells that are responsible for releasing or making mucus and other unusual fluids).[181] The initial stage of colorectal cancer begins by the growth of polyps that could form on the inner wall either of the colon or rectum. Over time, some polyps become cancerous, therefore early diagnosis and treatment can prevent colorectal cancer cases significantly.

According to the American cancer society statistics carried out in 2017, the estimated numbers of new cases in the United State were 71,420 and 64,010 for males and females respectively, with 50,260 deaths over all the 51 states in America and with 655,000 death worldwide per year.[183] This considerable values not only made the colorectal cancer the fourth most common form of cancer in USA but also the third leading cause of cancer related death in western world. The world health organisation declared in 2018 that the number of the new male's colorectal cancer cases in Oman were 262 (13.12%) cases. This value was the highest among the other cancer cases in the region. In contrast, the new female's colorectal cancer cases lied thirdly after the breast and thyroid cases and

found around 106 (8%) cases. Both percentages are significantly high compared to the number of populations.

1.10.1 The hallmarks of cancer

The hallmarks of cancer consist of six biological processes during the multistep required for the growth and proliferation of the cancer cells in to develop human tumours. These hallmarks include sustaining proliferative signalling, evading growth suppressors, resisting cell death, enabling replicative immortality, inducing angiogenesis and activating invasion and metastasis. As a result of cancer research progress, in the last decade two hallmarks of energy metabolism and evading immune destruction were added to this list. Each of these hallmarks gives a significant contribution to the cancer cell formation using different signalling and mechanisms which stimulate the overexpressed proteins in the tumour.

Vascular endothelial growth factor (VEGF) and epidermal growth factor receptor (EGFR) are two proteins that are greatly linked to the formation of colorectal cancer cells.[184] VEGFR works as a nutrient supplier for the tumours to form new blood vessels in a process known as angiogenesis. Thus of the well-known method to treat this type of cancer is to target this protein using drugs usually given by infusion to the patient such as Bevacizumab (Avastin), Ramucirumab (Cyramza) or Ziv-aflibercept (Zaltrap) in order to stop it working.[184] On the other hand, EGFR is a protein that usually formed in high amounts on the surface of the colorectal cancer cells, giving them the energy to grow and survive. Some advanced and metastasis colon or rectal cancer can also be treated by targeting this protein using Cetuximab (Erbitux) or Panitumumab (Vectibix).[184] These drugs have been approved by the U.S Food and Drugs Administration.

1.11 Theranostics

Advances in paramagnetic nanoparticle affect the improvement of both imaging and therapeutic functions. Over the previous decade, tools and concepts related to nanotechnology have been connected to beat the traditional strategies for advanced diagnosis and therapy. Specifically, advances in nanoparticle innovation have made new standard for theranostics. The term theranostics is defined as the combination of diagnostic agents and therapeutics within a single probe.[185] It takes advantage of the high ability of Nano systems to work as contrast agents and drug carrier. The targeted imaging and therapy are made achievable by attaching or conjugating a variety of imaging and therapeutic materials. Therefore, many efforts have been devoted to improve the

sensitivity and accuracy for clear cancer diagnosis especially at the most complicated early stages and possibly for better efficacy therapeutic methods. A real example of theranostic system is IONPs-Dox-CRGD-micelles, developed by Nasongkla and co-workers in 2006.[186] Their work involves the conjugation of doxorubicin to the core of poly(ethylene glycol)-Poly(D, L-Lactide)(PEG-PLA) micelles. Moreover, a cyclic Arginine-Glycine-Aspartic Acid (CRGD) as a targeting ligand was attached to specifically target the over-expressed a, β_3 receptor on the endothelial cells. This probe showed itself to be an excellent theranostics system, with an integrated capability to be utilized as an *MRI* imaging agent and drug delivery carrier, making it a candidate for future cancer diagnosis and therapy. Similarly, Choi *et al*. recently developed a theranostics application using coated human serum albumin (HAS) iron oxide nanoparticles.[187] The developed system was delivered to the tumour targeted site *via* passive means.[188] Moreover, doxorubicin as a therapeutic drug was conjugated to the dopamine-HAS matrices.[189] The overall system demonstrated excellent tumour targeting. This was proved by obtaining a clear image by *MRI* in real time. Simultaneously, intravenous treatment revealed that the release of free doxorubicin from the probe into the tumour site causes a significant suppression of tumour growth. Interestingly, the anticancer activity of the developed system was comparable to commercial Doxil, a liposome-based DOX formula used in the current medical applications to treat various cancer types. Hence, the developed system showed was shown to be promising theranostics nanoplatform for simultaneous cancer imaging and therapy.

Beside magnetic nanoparticles, Single Wall Carbon nanotubes (SWCNTs) are widely reported in Raman and photoacoustic imaging and drug delivery.[190-192] One of the unique properties of CNTs is their ability to be functionalised with various biomolecules imaging agents and drug delivery either by covalent conjugation or noncovalent adsorption through their graphene surface.[193] Generally cisplatin and paclitaxel are conjugated to the functional groups on the CNTs surface or to the polymer coating of CNTs *via* cleavable bonds.[194, 195] Bhirde *et al.* reported that the unique Raman properties of CNTs in combination with a portable handheld device can be used to create a theranostic platform for cancer therapy.[196] They showed that SWCNTs can be delivered to ovarian cancer cells grown in two-dimensional cell culture or three-dimensional environment. They can be selectively irradiated and distinguished in cancer cells using a simple handheld Raman instrument. SWCNTs provide an effective theranostics system, due to their capability to increase the

cellular temperatures allowing for easy detection. Moon *et al.* proved that the collective treatments of SWNT and NIR irradiation causes eradication of tumours with no observation of reappearance over six months in a human epidermoid mouth carcinoma cell line.[197] In addition, Liu *et al.* reported that *in vivo* photothermal tumour ablation was made possible using SWCNT conjugates after intravenous injection followed by NIR laser irradiation.[198]

Gold-based nanomaterials (GNMs), gold nanorods (GNRs) and gold nanocages (GNC) have been recently utilized as cancer theranostics agents.[199-205] They are bio-inert and can be easily modified with various biomolecules or chemical moieties. Besides that, they can be excited in relatively deeper tissues by near infra-red irradiation.[187] Due to such properties, GNMs have been used as contrast agents for many imaging modalities.[187, 206] Furthermore, they have been considered as efficient therapeutic agents for drug or gene delivery systems or photothermal therapy. West et al. showed that by controlling the gold nanoparticles shell, it was possible to image and destroy breast carcinoma cancer cells in animal models simultaneously.[206] Furthermore, Chen and his co-workers developed NP systems which composed of a silica core embedded with magnetite and coated with a gold shell containing a fluorophore indocyanine green (ICG) for dual mode imaging and photothermal therapy.[207] The developed gold nanosystem was effective as a theranostics imaging and therapeutic probe.

Another form that is extensively utilized is the use of polymeric nanoparticles as nanocarriers to create theranostics systems.[187] This is due to the physical and chemical nature of these polymers, as their surface charge, particle size or degradation can be easily modified. In addition, their surface can be easily engineered with different targeting molecules, where imaging probes and therapeutic agents can be easily conjugated.[208, 209] More recently, polymersomes coated with hydrophobically modified maghemite NPs and conjugated with DOX within their membrane were fabricated as a potential theranostics nanocarriers for magnetic resonance (*MRI*) imaging and magneto-chemotherapy.[210] The developed polymersomes demonstrated enhanced *MRI* contrast properties. Upon bombarding with radiofrequency magnetic hyperthermia, DOX release was triggered, showing a promising potential of the nanoplatform for magneto-chemotherapy.

Nanomaterials are normally categorised into organic and inorganic materials, where organic materials including polymer-drug conjugates, dendrimers and polymeric micelles are commonly used for drug delivery.[185] For instance, Abraxane, NPs bound to albumin, is the first class of this type that is used as an antitumor drug for treatment of breast cancer and approved by the US Food and Drug Administration (FDA).[211] With the benefits of enhanced drug delivery and low toxicity, currently numerous organic system drugs have been engineered and tested in medical applications.[211] On the other hand, inorganic nanomaterials have unique and characteristic physical properties which are related to their size and composition.[212] Specifically, paramagnetic nanoparticles show fascinating material properties that enable them to be an excellent system for cell targeting , imaging diagnosis, and therapy, and render them perfect platform materials for theranostics.[213]

In chemotherapy, the active anti-cancer drug is normally delivered to the tumour with poor specificity and high degree of toxicity. Administration of these drugs through conventional drug delivery methods such as oral administration or intravenous routes could result in disorderly pharmacokinetics due to their strong interaction with the metabolic routes in the body.[214] This means that higher dose need to be used which could enhance the toxicity.[215] NP drug delivery that are coated or attached to biodegradable ligands or polymers offer an efficient and less toxic solution to overcome this issue.

1.11.1 Drug delivery

The delivery of a drug through nanoparticles can be made possible by either active or passive strategies.[216] (Passive delivery refers to NP transport through leaky tumour capillary fenestrations into the tumour interstitium and cells by passive diffusion or convection).[216] Selective accumulation of NP and drug then occurs by the EPR effect taking the advantage of the tumour permeability. Many examples of this passive drug delivery method have been reported in the literature. These include the following examples:

1.11.1.1 Leaky vasculature

This method relays on polymer nanoparticles that known for their enhanced permeability and retention. This method was first described by Maeda and Matsumura.[217]They stated that when a chemotherapeutic drug is conjugated to a suitable polymer using a degradable linker and administered into the body, it would enhance the concentration of the carried drug 10 to 100 times within the tumour tissue compared to the administration of the pure drug on its own.

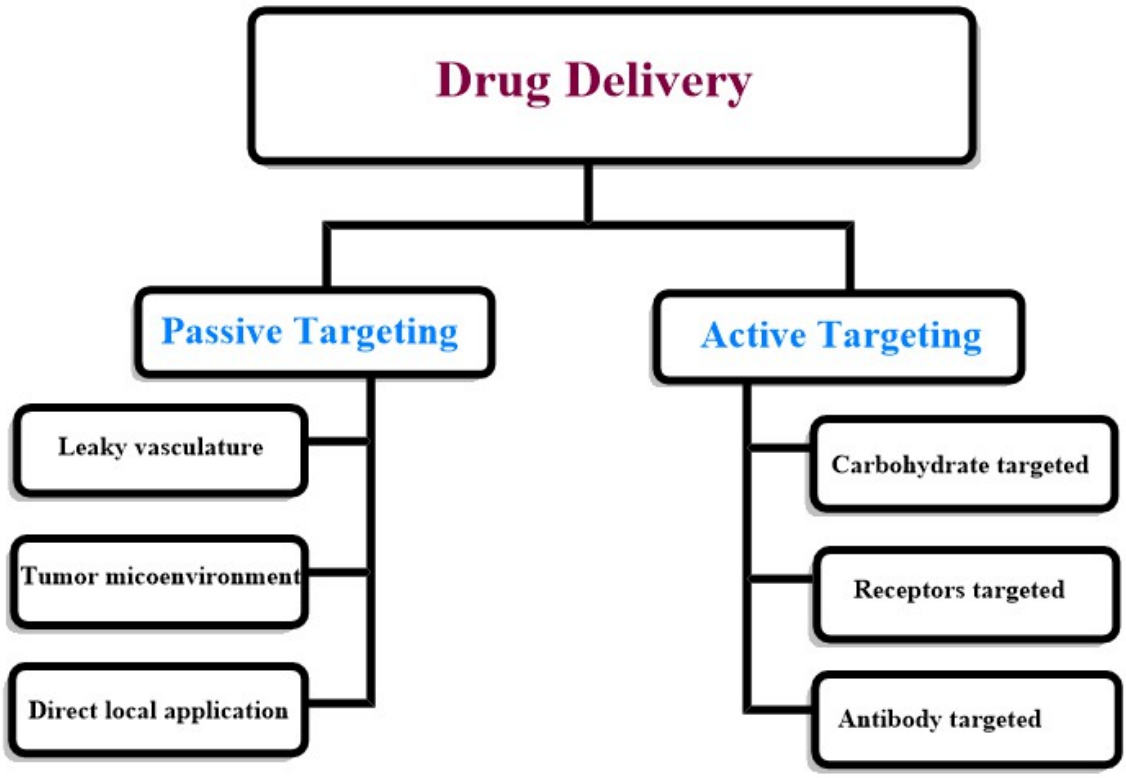

Figure 1-22: Different passive and active strategies used for drug conjugated NPS delivery to cancer cell lines

1.11.1.2 Tumour microenvironment

This type of passive drug targeting depends on the nature of the tumour environment. The drug is normally coupled to a tumour specific material. Upon reaching the targeted location, the tumour environment converts it to an active substance.[218] Mansour and his collaborators synthesised a hydrophilic maimed derivative of doxorubicin conjugated with a metalloprotenose-2-spicific peptide sequences.[219] This is also called tumour-activated prodrug therapy. The formulated pro-drug conjugate had a strong capability to attach to the cysteine-34 position of circulating albumin, which in turn rapidly cleaved by the matrix metallo-protease-2 and releasing free doxorubicin. Furthermore, factors such as redox potential and pH have been widely known as drug release triggers at tumour site.[220] Shin *et al* have developed an *in vitro* 3D tumour model by adapting the hydrogel template strategy to culture uniformly sized spheroids in a hydrogel scaffold containing microwells.[221] The *in vitro* 3D tumour model was to closely simulate an *in vivo* solid tumour and its microenvironment for evaluation of anticancer drug delivery systems. His Their finding provided many information that was useful to improve and optimise the drug delivery system to more effective chemotherapy.

1.11.1.3 Local drug application

In this method, the anti-cancer drug is delivered directly to the tumour tissue, avoiding systematic circulation in the body. Localized drug delivery through intratumoral administration solves the problems raised by conventional approaches used for drug delivery, which require exposure to higher concentrations of anticancer agents. For instance, injecting mitomycin directly in the tumour tissue leads to an enhancement in the drug concentration in the tumour site and less toxicity.[222] Human breast carcinoma cell line (MDA-MB-435S) transfected with wild-type p53 DNA-loaded NPs demonstrated sustained and significantly greater antiproliferative activity than those with naked wild-type p53 DNA or with wild-type p53 DNA complexed with a commercially available transfecting agents (Lipofectamine).[223] In addition, (Onyx), the 55-kilodalton (kDa) protein from the E1B-region of adenovirus binds to and inactivates the p53 gene, which is mutated in half of human cancers.[224] Onyx is an important anti-cancer agent that is administered in several ways. Most of these ways allow the drug to be delivered directly into tumour tissue sites. It has been clinically investigated to treat neck and head cancer, pancreatic cancer and metastatic colorectal cancer, ovarian cancer and advanced sarcomas.[225-229] Moreover, Lamrecht and colleagues showed that Tacrolimus (FK506) entrapped in NPs administered either orally or rectally to male Wister rats suffering from pre-existing experimental colitis, results in enhanced and selective drug penetration into in the inflammation site as opposed to surrounding healthy tissue.[230] The relative drug concentration into the inflamed tissue was nearly 3 times higher compared with healthy tissue when using nanoparticles as drug carriers. This method prevents the anti-cancer agents from spreading or circulating throughout the body and can be excreted through metabolism processes, however the drawbacks of this method is the poor accessibility for certain lung cancers, it can be highly intensive and sometimes tumour localisation is not feasible.

Active targeting involves drug delivery to a specific site based on molecular recognition. Conjugation of the ligand or antibody to a NP causes the ligand or antibody to specifically interact with their receptor or antigenic receptor at the target cell site. This approach is used to direct nanoparticles and chemotherapeutic drugs to cell surface carbohydrates (Lectin), receptors, or antigens.

A real example of active targeting strategy is the conjugation of folate to coated polyethylene glycol nanoparticles targeting the folate receptor. Many of the cancer cells overexpress folate receptors on their surface. For example, the folate receptor is a highly

selective tumour marker overexpressed in greater than 90% of ovarian carcinomas. Normally, these receptors have a higher binding affinity for the NP folate bound protein than for free folate.[231, 232] The folate conjugated nanoparticles undergo receptor mediated endocytosis and localizes in the cell cytoplasm, causing the conjugated anti-cancer drug, to be cleaved from the NP to kill the target cells. Bhirde *et al.* developed a single wall carbon nanotube (SWNT) attached to cis-platin and anti-EGFR as a drug delivery vehicle that specifically target the overexpressed epidermal growth factor receptor on head and neck squamous carcinoma cells (HNSCC).[233] They compared the anticancer activity on these cell lines with a control which was SWNT-cisplatin without EGFR antibody. Results showed that HNSCC cells treated with SWNT−cisplatin−EGF were killed selectively, while control systems that did not feature EGF-EGFR binding did not influence cell proliferation. Their *in vivo* examination in mice showed that significant regression of tumour growth was rapid when treated with targeted SWNT−cisplatin−EGF relative to nontargeted SWNT-cisplatin, revealing the importance of the selective EGF-EGFR binding

Several studies have characterized the over-expression of Vascular Endothelial Growth Factor (VEGFR) receptor in human tumours and highlighted the importance of VEGF in tumour angiogenesis, the process of new blood vessel growth.[234, 235] Blocking of VEGF has been confirmed to inhibit tumour growth and metastasis.[236, 237] Consequently, VEGFR is currently considered as an ideal target for antiangiogenesis intervention. Recently, RGD (Arg-Gly-Asp)-peptide coated with Se nanoparticles and loaded with anti-cancer drug doxorubicin (RGD-NPs) significantly enhanced the cellular uptake and antiangiogenic activities of SeNPs *in vitro* and *in vivo*. This nanosystem inhibited angiogenesis through induction of apoptosis and cell cycle arrest in human umbilical vein endothelial cells (HUVECs) *via* suppression of VEGF-VEGFR2-ERK/AKT signalling axis.[238] Furthermore, RGD-NPs were also found to be effective in inhibiting MCF-7 tumour growth and angiogenesis in nude mice via down-regulation of VEGF-VEGFR2.[238]

These examples of specific targeted over-expressed receptors on various cancer cell lines are efficient drug delivery methods documented in literature to achieve an effective cancer therapy and cancer-targeted antiangiogenesis.

Research in nanotechnology is expected to accelerate the development of multifunctional, novel, and sophisticated applications which can lead to a clear recognition for the various cancer cells, direct and deliver anti-cancer drugs to target tissue, help in monitoring the cancer therapy, offer real-time assessment of surgical and therapeutic efficacy, and most

importantly, marking intracellular variations to prevent and avoid precancerous cells from becoming malignant.

The aim of this project is to synthesise perovskites ultra-small nanoparticles such as γ-Fe_2O_3, $GdFeO_3$ and KMF_3 (M = Mn, Fe, CO, Ni, Cu, Zn) using different method strategies such as coprecipitation, hydrothermal, solvothermal and sol-gel. Nanoparticles exhibit unique physical properties that are couple with size range commensurate with biomolecular and cellular systems. These features make them attractive materials for therapeutic and diagnostic applications. The formed nanoparticles are then functionalised by different ligands either directly using 11-aminoundecanoic acid or sodium alendronate tetrahydrate or using ligand exchange method where nanoparticles are first coated by potassium oleate, poly ethylene glycol or oleylamine and then subjected to ligand exchange mechanism with sodium alendronate ligand. The purpose of the functionalisation process is to provide a monolayer on the surface of the nanoparticles that can control the interaction between them and the biomacromolecules in the human tissues, in order to enhance the cellular internalization ability, non-cytotoxicity, and improved payload binding capacity necessary for effective intracellular delivery. The coated nanoparticles are then characterised by different analytical techniques such as Powder X-ray diffraction (PXRD), Fourier Transform Infra-red (FTIR), Transmission Electron Microscopy (TEM), Energy dispersive X-ray (EDX), Nano Tracking Analysis (NTA) and inductively coupled plasma spectroscopy (ICP), to validate their purity, structure stability, coating process, morphology and size to be utilised in biomedical applications.

Upon successful functionalisation, the efficiency of these nanoparticles to work as T_1 or T_2 contrast agents would be tested by measuring their relaxation time, hence their relaxation rates would be calculated. *MRI* phantom analysis would also be used to validate these tests.

Biomolecule coated NPs provide specific attributes that are difficult or impossible to achieve using synthetic materials, such as providing efficient delivery of biomolecules with minimal toxicity. Therefore, the functionalised NPs would be conjugated with doxorubicin, the most known drug used for treatment of various cancer cells, using a linker.

Furthermore, the present study investigated comparative in-vitro cytotoxicity against colorectal and cervical cancer cells for the bare, functionalised with alendronate and doxorubicin conjugated NPs. This would highlight the safest concentration of the probes to be used as theranostic agents.

This project will also describe a method to provide a useful tool for targeting NPs for imaging and drug delivery (Theranostic). This can be done by conjugating this project would describe a method to provide a useful tool for targeting nanoparticles for imaging and drug delivery (Theranostic). This can be done by conjugating them with antibodies such as such as EGFR and VEGFR receptors to specifically targeted them to bind with the overexpressed protein on the cells surface. The anti-VEGFR nanoconjugates are expected to bound specifically to the cancerous cells with six-fold greater affinity than to non-cancerous control cells.

The final part of this project is to investigate the colocalization of the all formed nanoparticles in colorectal cancer cell lines (HCT-116, HT-29) and cervical cancer cell lines (Hela) to highlight the impact of these probes in theranostic enhancement for sensitive diagnostic and effective therapy

1.12 References

1. J. V. Jokerst and S. S. Gambhir, *Accounts of chemical research*, 2011, **44**, 1050-1060.
2. R. Bardhan, S. Lal, A. Joshi and N. J. Halas, *Accounts of chemical research*, 2011, **44**, 936-946.
3. G. Huang, H. Li, J. Chen, Z. Zhao, L. Yang, X. Chi, Z. Chen, X. Wang and J. Gao, *Nanoscale*, 2014, **6**, 10404-10412.
4. L. Wang, H. Lin, L. Ma, J. Jin, T. Shen, R. Wei, X. Wang, H. Ai, Z. Chen and J. Gao, *Nanoscale*, 2017, **9**, 4516-4523.
5. W. Wu, Q. He and C. Jiang, *Nanoscale research letters*, 2008, **3**, 397.
6. J. Vidal-Vidal, J. Rivas and M. López-Quintela, *Colloids and Surfaces A: Physicochemical and Engineering Aspects*, 2006, **288**, 44-51.
7. A. S. Teja and P.-Y. Koh, *Progress in Crystal Growth and Characterization of Materials*, 2009, **55**, 22-45.
8. D. L. J. Thorek, A. Chen, J. Czupryna and A. Tsourkas, *Annals of Biomedical Engineering*, 2006, **34**, 23-38.
9. M. H. Bryl, PhD, ADAM MICKIEWICZ UNIVERSITY, 2013.
10. M. Knobel, W. C. Nunes, L. M. Socolovsky, E. De Biasi, J. M. Vargas and J. C. Denardin, *J Nanosci Nanotechnol*, 2008, **8**, 2836-2857.
11. C. S. a, J. S. H. L. b. and M. Z. a. , *Advanced Drug Delivery Reviews*, 2008, **60**, 1252–1265.
12. R. M. Cornell and U. Schwertmann, *The iron oxides: structure, properties, reactions, occurrences and uses*, John Wiley & Sons, 2003.
13. L. E. Smart and E. A. Moore, *Solid state chemistry: an introduction*, CRC press, 2016.
14. R. J. Tilley and R. Tilley, *Understanding solids: the science of materials*, Wiley Online Library, 2004.
15. G. F. Dionne, *Magnetic oxides*, Springer, 2009.
16. *Angewandte Chemie*, 2011, **50**, 12547-12550.
17. M. A. Ruderman and C. Kittel, *Physical Review*, 1954, **96**, 99-102.
18. K. Yosida, *Physical Review*, 1957, **106**, 893-898.
19. I. Karimzadeh, H. R. Dizaji and M. Aghazadeh, *Journal of Magnetism and Magnetic Materials*, 2016, **416**, 81-88.
20. R. N. Bhargava, Gallagher, D., Hong, X. and Nurmikko, A., *Physical Review Letters*, 1994, **72**, 416-419.
21. P. I. P. Soares, C. A. T. Laia, A. Carvalho, L. C. J. Pereira, J. T. Coutinho, I. M. M. Ferreira, C. M. M. Novo and J. P. Borges, *Applied Surface Science*, 2016, **383**, 240-247.
22. N. Ghaemi, S. S. Madaeni, P. Daraei, H. Rajabi, S. Zinadini, A. Alizadeh, R. Heydari, M. Beygzadeh and S. Ghouzivand, *Chemical Engineering Journal*, 2015, **263**, 101-112.
23. S. A. Bhalla, R. Guo and R. Roy, *Material Research Innovations*, 2000, **4**, 3-26.
24. C. Moure and O. Peña, *Progress in Solid State Chemistry*, 2015, **43**, 123-148.
25. T. Salim, S. Sun, Y. Abe, A. Krishna, A. C. Grimsdale and Y. M. Lam, *Journal of Materials Chemistry A*, 2015, **3**, 8943-8969.
26. S. Sasaki, C. T. Prewitt, J. D. Bass and W. Schulze, *Acta Crystallographica Section C: Crystal Structure Communications*, 1987, **43**, 1668-1674.
27. C. Andy, D. Jamal, L. Jeong-Soo and M. Meyyappan, *Nanotechnology*, 2010, **21**, 412001.

28. N. Nuraje and K. Su, *Nanoscale*, 2013, **5**, 8752-8780.
29. B. O'Regan and M. Gratzel, *Nature*, 1991, **353**, 737-740.
30. M. P. J. Punkkinen, *Solid State Communications*, 1999, **111**, 477-481.
31. M. G. Brik, G. A. Kumar and D. K. Sardar, *Materials Chemistry and Physics*, 2012, **136**, 90-102.
32. M. Eibschütz, H. J. Guggenheim, S. H. Wemple, I. Camlibel and M. DiDomenico Jr, *Physics Letters A*, 1969, **29**, 409-410.
33. A. H. Cooke, D. A. Jones, J. F. A. Silva and M. R. Wells, *Journal of Physics C: Solid State Physics*, 1975, **8**, 4083-4088.
34. R. A. Heaton and C. C. Lin, *Physical Review B*, 1982, **25**, 3538-3549.
35. G. G. Yakobson and N. E. Akhmetova, *Synthesis*, 1983, **1983**, 169-184.
36. M. Sahnoun, M. Zbiri, C. Daul, R. Khenata, H. Baltache and M. Driz, *Materials Chemistry and Physics*, 2005, **91**, 185-191.
37. in *Handbook of Magnetism and Advanced Magnetic Materials*, DOI: 10.1002/9780470022184.hmm411.
38. Hayatullah, G. Murtaza, R. Khenata, S. Muhammad, A. H. Reshak, K. M. Wong, S. Bin Omran and Z. A. Alahmed, *Comput. Mater. Sci.*, 2014, **85**, 402-408.
39. Z.-j. Liu, X.-x. Song and Q. Tang, *Nanoscale*, 2013, **5**, 5073-5079.
40. Z. Zhao, X. Wang, Z. Zhang, H. Zhang, H. Liu, X. Zhu, H. Li, X. Chi, Z. Yin and J. Gao, *ACS Nano*, 2015, **9**, 2749-2759.
41. Z. Zhao, H. Fan, G. Zhou, H. Bai, H. Liang, R. Wang, X. Zhang and W. Tan, *Journal of the American Chemical Society*, 2014, **136**, 11220-11223.
42. Y. Chen, D. Ye, M. Wu, H. Chen, L. Zhang, J. Shi and L. Wang, *Advanced Materials*, 2014, **26**, 7019-7026.
43. M. Park, N. Lee, S. H. Choi, K. An, S.-H. Yu, J. H. Kim, S.-H. Kwon, D. Kim, H. Kim, S.-I. Baek, T.-Y. Ahn, O. K. Park, J. S. Son, Y.-E. Sung, Y.-W. Kim, Z. Wang, N. Pinna and T. Hyeon, *Chemistry of Materials*, 2011, **23**, 3318-3324.
44. Y. Lu, L. Zhang, J. Li, Y.-D. Su, Y. Liu, Y.-J. Xu, L. Dong, H.-L. Gao, J. Lin, N. Man, P.-F. Wei, W.-P. Xu, S.-H. Yu and L.-P. Wen, *Advanced Functional Materials*, 2013, **23**, 1534-1546.
45. H. Yang, Y. Zhuang, H. Hu, X. Du, C. Zhang, X. Shi, H. Wu and S. Yang, *Advanced Functional Materials*, 2010, **20**, 1733-1741.
46. X. Ding, J. Liu, J. Li, F. Wang, Y. Wang, S. Song and H. Zhang, *Chemical Science*, 2016, **7**, 6695-6700.
47. B. Phukan, A. B. Patel and C. Mukherjee, *Dalton Transactions*, 2015, **44**, 12990-12994.
48. X.-x. Song, X.-z. Xu, H.-p. Wan and Q. Tang, *RSC Advances*, 2014, **4**, 55003-55009.
49. X.-x. Song, Z.-j. Liu, X.-z. Xu and Q. Tang, *New Journal of Chemistry*, 2014, **38**, 3813-3818.
50. Z.-j. Liu, X.-x. Song, X.-z. Xu and Q. Tang, *Nanotechnology*, 2014, **25**, 155101.
51. J. Sheng, K. Tang, D. Su, S. Zeng, Y. Qi and H. Zheng, *Journal of Fluorine Chemistry*, 2009, **130**, 742-748.
52. M. Mo, J. C. Yu, L. Zhang and S.-K. A. Li, *Advanced Materials*, 2005, **17**, 756-760.
53. J. Wang, F. Wang, C. Wang, Z. Liu and X. Liu, *Angewandte Chemie International Edition*, 2011, **50**, 10369-10372.
54. L.-N. Hao, K. Liu, S. Cheng, Y. Wang, Y.-J. Xu and H.-S. Qian, *Materials Letters*, 2017, **196**, 145-148.
55. L. Li, 2015.

56. T. O. Peter Atkins, Jonathan Rourke, Mark Weller, Fraser Armstrong, *Shriver & Atkins' Inorganic Chemistry*, Oxford University Press, Fifth edition edn., 2010.
57. G. M. N. Meyer, R.J.; Hutton, J., *Ferroelectrics*, 1978 **21**, 461-462.
58. R. Buttner and E. Maslen, *Acta Crystallographica Section B: Structural Science*, 1992, **48**, 764-769.
59. R. H. M. Buttner, E.N., *Acta Crystallographica, Section B: Structural Science* 1992, **48**, 764-769.
60. J. R. Zhao, N.L.; Angel, R.J., *Journal of Physics: Condensed Matter* 2004, **16**, 8763-8773.
61. O. Muller and R. Roy, *The major ternary structural families*, Springer, 1974.
62. N. L. Z. Ross, J.; Angel, R.J., *Journal of Steroid Biochemistry* 2004, 768- 3775.
63. C. A. Triana, L. T. Corredor, D. A. Landínez Téllez and J. Roa-Rojas, *Physica B: Condensed Matter*, 2012, **407**, 3150-3154.
64. A. A. Belik, S. Iikubo, T. Yokosawa, K. Kodama, N. Igawa, S. Shamoto, M. Azuma, M. Takano, K. Kimoto, Y. Matsui and E. Takayama-Muromachi, *Journal of the American Chemical Society*, 2007, **129**, 971-977.
65. C. R. Chaillout, J.P.; Santoro, A.; Marezio, M., *olid State Communications* 1985, **56**, 829-831.
66. W. Eerenstein, N. D. Mathur and J. F. Scott, *Nature*, 2006, **442**, 759-765.
67. N. Rajput, *International Journal of Advances in Engineering & Technology*, 2015, **7**, 1806-1811.
68. X. Zhu, Z. Liu and N. Ming, *Journal of Materials Chemistry*, 2010, **20**, 4015-4030.
69. D. R. Modeshia and R. I. Walton, *Chemical Society Reviews*, 2010, **39**, 4303-4325.
70. J. Chen, S. Zhou, S. Jin, H. Li and T. Zhai, *Journal of Materials Chemistry C*, 2016, **4**, 11-27.
71. J. Yuh, J. C. Nino and W. M. Sigmund, *Materials Letters*, 2005, **59**, 3645-3647.
72. R. Helen, A. Cyril, L.-S. Anne, E. Catherine, M. Mario and C. François, *Nanotechnology*, 2005, **16**, 1137.
73. X. Wang, J. Zhuang, Q. Peng and Y. Li, *Nature*, 2005, **437**, 121-124.
74. F. Guangneng, H. Lixia and H. Xueguang, *Journal of Crystal Growth*, 2005, **279**, 489-493.
75. S. O'Brien, L. Brus and C. B. Murray, *Journal of the American Chemical Society*, 2001, **123**, 12085-12086.
76. H. Liu, C. Hu and Z. L. Wang, *Nano Letters*, 2006, **6**, 1535-1540.
77. A. H. Lu, E. e. L. Salabas and F. Schüth, *Angewandte Chemie International Edition*, 2007, **46**, 1222-1244.
78. D. Pérez-Coll, P. Núñez, J. R. Frade and J. C. C. Abrantes, *Electrochimica Acta*, 2003, **48**, 1551-1557.
79. C. B. Murray, D. J. Norris and M. G. Bawendi, *Journal of the American Chemical Society*, 1993, **115**, 8706-8715.
80. S. H. Sun, H. Zeng, D. B. Robinson, S. Raoux, P. M. Rice, S. X. Wang and G. X. Li, *Journal of the American Chemical Society*, 2004, **126**, 273-279.
81. J. Rockenberger, E. C. Scher and A. P. Alivisatos, *Journal of the American Chemical Society*, 1999, **121**, 11595-11596.
82. D. Farrell, S. A. Majetich and J. P. Wilcoxon, *Journal of Physical Chemistry B*, 2003, **107**, 11022-11030.
83. A. C. S. Samia, K. Hyzer, J. A. Schlueter, C. J. Qin, J. S. Jiang, S. D. Bader and X. M. Lin, *Journal of the American Chemical Society*, 2005, **127**, 4126-4127.
84. N. R. Jana, Y. F. Chen and X. G. Peng, *Chemistry of Materials*, 2004, **16**, 3931-3935.

85. A. P. Alivisatos, *Science*, 1996, **271**, 933.
86. D. Langevin, *Annual Review of Physical Chemistry*, 1992, **43**, 341-369.
87. B. K. Paul and S. P. Moulik, *Current Science*, 2001, **80**, 990-1001.
88. S. Mornet, S. Vasseur, F. Grasset, P. Veverka, G. Goglio, A. Demourgues, J. Portier, E. Pollert and E. Duguet, *Progress in Solid State Chemistry*, 2006, **34**, 237-247.
89. A.-H. Lu, E. L. Salabas and F. Schüth, *Angewandte Chemie International Edition*, 2007, **46**, 1222-1244.
90. E. A. R. Assirey, *Saudi Pharmaceutical Journal*, 2019, DOI: https://doi.org/10.1016/j.jsps.2019.05.003.
91. X. Wang, J. Zhuang, Q. Peng and Y. D. Li, *Nature*, 2005, **437**, 121-124.
92. H. Deng, X. L. Li, Q. Peng, X. Wang, J. P. Chen and Y. D. Li, *Angewandte Chemie-International Edition*, 2005, **44**, 2782-2785.
93. C. M. Sorensen, *Nanoscale Materials in Chemistry*, Wiley, New York, 2001.
94. A. E. Danks, S. R. Hall and Z. Schnepp, *Materials Horizons*, 2016, **3**, 91-112.
95. B. G. Rao, D. Mukherjee and B. M. Reddy, in *Nanostructures for novel therapy*, Elsevier, 2017, pp. 1-36.
96. C. Queffélec, M. Petit, P. Janvier, D. A. Knight and B. Bujoli, *Chemical Reviews*, 2012, **112**, 3777-3807.
97. L. F. Shen, P. E. Laibinis and T. A. Hatton, *Langmuir*, 1999, **15**, 447-453.
98. M. H. Sousa, F. A. Tonrinho, J. Depeyrot, G. J. da Silva and M. Lara, *Journal of Physical Chemistry B*, 2001, **105**, 1168-1175.
99. U. S. R. M. Cornell, *The Iron Oxides: Structure, Properties, Reactions, Occurrence and Uses*, VCH, Weinheim, 1996.
100. G. Barratt, *Cellular and Molecular Life Sciences*, 2003, **60**, 21-37.
101. M. D. Butterworth, S. A. Bell, S. P. Armes and A. W. Simpson, *Journal of Colloid and Interface Science*, 1996, **183**, 91-99.
102. M. X. Wan and J. C. Li, *Journal of Polymer Science Part a-Polymer Chemistry*, 1998, **36**, 2799-2805.
103. L. A. Harris, J. D. Goff, A. Y. Carmichael, J. S. Riffle, J. J. Harburn, T. G. St Pierre and M. Saunders, *Chemistry of Materials*, 2003, **15**, 1367-1377.
104. A. F. Thunemann, D. Schutt, L. Kaufner, U. Pison and H. Mohwald, *Langmuir*, 2006, **22**, 2351-2357.
105. S. Mourdikoudis and L. M. Liz-Marzan, *Chemistry of Materials*, 2013, **25**, 1465-1476.
106. R. Alford, M. Ogawa, P. L. Choyke and H. Kobayashi, *Molecular BioSystems*, 2009, **5**, 1279-1291.
107. C. Sanjai, S. Kothan, P. Gonil, S. Saesoo and W. Sajomsang, *Carbohydrate Polymers*, 2014, **104**, 231-237.
108. T.-H. Shin, Y. Choi, S. Kim and J. Cheon, *Chemical Society Reviews*, 2015, **44**, 4501-4516.
109. M. M. Yaseen, *Magnetic Resonance Imaging MRI*, Al - Najah Printing & Publishing Est, Cairo - Egypt, 4th edn., 2012.
110. V. D. K. Dominik Weishaupt, Borut Marincek, *How Does MRI work?*, Springer-Verlag, Berlin, 2008.
111. What is MRI I what is magnetic resonance imaging I mri imaging, https://mrimaster.com/index.7.html, (accessed May 2017, 2017).
112. S. Tong, S. Hou, Z. Zheng, J. Zhou and G. Bao, *Nano Letters*, 2010, **10**, 4607-4613.
113. E. Pérez-Mayoral, V. Negri, J. Soler-Padrós, S. Cerdán and P. Ballesteros, *European Journal of Radiology*, 2008, **67**, 453-458.
114. H. B. Na, I. C. Song and T. Hyeon, *Advanced Materials*, 2009, **21**, 2133-2148.

115. C.-T. Yang, P. Padmanabhan and B. Z. Gulyás, *RSC Advances*, 2016, **6**, 60945-60966.
116. Y. Cao, L. Xu, Y. Kuang, D. Xiong and R. Pei, *Journal of Materials Chemistry B*, 2017, **5**, 3431-3461.
117. E. Debroye and T. N. Parac-Vogt, *Chemical Society Reviews*, 2014, **43**, 8178-8192.
118. P. Caravan, J. J. Ellison, T. J. McMurry and R. B. Lauffer, *Chemical reviews*, 1999, **99**, 2293-2352.
119. S. Aime, M. Botta, M. Fasano and E. Terreno, *Chemical Society Reviews*, 1998, **27**, 19-29.
120. I. Solomon, *Physical Review*, 1955, **99**, 559.
121. D. Ni, W. Bu, E. B. Ehlerding, W. Cai and J. Shi, *Chemical Society Reviews*, 2017, **46**, 7438-7468.
122. G.-P. Yan, L. Robinson and P. Hogg, *Radiography*, 2007, **13**, e5-e19.
123. H. Ersoy and F. J. Rybicki, *Journal of Magnetic Resonance Imaging*, 2007, **26**, 1190-1197.
124. M. A. Perazella, *Clinical Journal of the American Society of Nephrology*, 2009, **4**, 461-469.
125. X.-H. Ma, A. Gong, L.-C. Xiang, T.-X. Chen, Y.-X. Gao, X.-J. Liang, Z.-Y. Shen and A.-G. Wu, *Journal of Materials Chemistry B*, 2013, **1**, 3419-3428.
126. C.-C. Huang, K.-Y. Chuang, C.-P. Chou, M.-T. Wu, H.-S. Sheu, D.-B. Shieh, C.-Y. Tsai, C.-H. Su, H.-Y. Lei and C.-S. Yeh, *Journal of Materials Chemistry*, 2011, **21**, 7472-7479.
127. R. Massart, *IEEE Transactions on Magnetics*, 1981, **17**, 1247-1248.
128. X. Liu, Z. Ma, J. Xing and H. Liu, *Journal of Magnetism and Magnetic Materials*, 2004, **270**, 1-6.
129. C. Hui, C. Shen, T. Yang, L. Bao, J. Tian, H. Ding, C. Li and H. J. Gao, *Journal of Physical Chemistry C - J PHYS CHEM C*, 2008, **112**.
130. J. Mürbe, A. Rechtenbach and J. Töpfer, *Materials Chemistry and Physics - MATER CHEM PHYS*, 2008, **110**, 426-433.
131. B. L. Cushing, V. L. Kolesnichenko and C. J. O'Connor, *Chemical Reviews*, 2004, **104**, 3893-3946.
132. L. Vayssières, C. Chanéac, E. Tronc and J. P. Jolivet, *Journal of Colloid and Interface Science*, 1998, **205**, 205-212.
133. F. Hu, K. W. MacRenaris, E. A. Waters, T. Liang, E. A. Schultz-Sikma, A. L. Eckermann and T. J. Meade, *J Phys Chem C Nanomater Interfaces*, 2009, **113**, 20855-20860.
134. Z. Shen, A. Wu and X. Chen, *Molecular pharmaceutics*, 2016, **14**.
135. Y.-X. J. Wang, *Quant Imaging Med Surg*, 2011, **1**, 35-40.
136. Y.-X. J. Wang, *World J Gastroenterol*, 2015, **21**, 13400-13402.
137. L. Zeng, L. Xiang, W. Ren, J. Zheng, T. Li, B. Chen, J. Zhang, C. Mao, A. Li and A. Wu, *RSC Advances*, 2013, **3**, 13915-13925.
138. L. Zeng, L. Luo, Y. Pan, S. Luo, G. Lu and A. Wu, *Nanoscale*, 2015, **7**, 8946-8954.
139. L. Zeng, W. Ren, L. Xiang, J. Zheng, B. Chen and A. Wu, *Nanoscale*, 2013, **5**, 2107-2113.
140. Z. Shen, H. Wu, S. Yang, X. Ma, Z. Li, M. Tan and A. Wu, *Biomaterials*, 2015, **70**, 1-11.
141. X. Ma, A. Gong, B. Chen, J. Zheng, T. Chen, Z. Shen and A. Wu, *Colloids and Surfaces B: Biointerfaces*, 2015, **126**, 44-49.
142. Y.-X. J. Wang, S. M. Hussain and G. P. Krestin, *European Radiology*, 2001, **11**, 2319-2331.

143. J. W. M. Bulte and D. L. Kraitchman, *NMR in Biomedicine*, 2004, **17**, 484-499.
144. L. Gu, R. H. Fang, M. J. Sailor and J.-H. Park, *ACS nano*, 2012, **6**, 4947-4954.
145. J. Schnorr, S. Wagner, C. Abramjuk, I. Wojner, T. Schink, T. J. Kroencke, E. Schellenberger, B. Hamm, H. Pilgrimm and M. Taupitz, *Investigative radiology*, 2004, **39**, 546-553.
146. Z. Liu, X. Wang, K. Yao, G. Du, Q. Lu, Z. Ding, J. Tao, Q. Ning, X. Luo and D. Tian, *Journal of Materials Science*, 2004, **39**, 2633-2636.
147. U. I. Tromsdorf, O. T. Bruns, S. C. Salmen, U. Beisiegel and H. Weller, *Nano letters*, 2009, **9**, 4434-4440.
148. B. H. Kim, N. Lee, H. Kim, K. An, Y. I. Park, Y. Choi, K. Shin, Y. Lee, S. G. Kwon and H. B. Na, *Journal of the American Chemical Society*, 2011, **133**, 12624-12631.
149. J. Y. Park, P. Daksha, G. H. Lee, S. Woo and Y. Chang, *Nanotechnology*, 2008, **19**, 365603.
150. Z. Li, P. W. Yi, Q. Sun, H. Lei, H. Li Zhao, Z. H. Zhu, S. C. Smith, M. B. Lan and G. Q. Lu, *Advanced Functional Materials*, 2012, **22**, 2387-2393.
151. Z. Zhou, D. Huang, J. Bao, Q. Chen, G. Liu, Z. Chen, X. Chen and J. Gao, *Advanced Materials*, 2012, **24**, 6223-6228.
152. J. Cheon and J.-H. Lee, *Accounts of Chemical Research*, 2008, **41**, 1630-1640.
153. J. R. McCarthy and R. Weissleder, *Advanced Drug Delivery Reviews*, 2008, **60**, 1241-1251.
154. J. Gao, H. Gu and B. Xu, *Accounts of Chemical Research*, 2009, **42**, 1097-1107.
155. X. He, J. Gao, S. S. Gambhir and Z. Cheng, *Trends in Molecular Medicine*, 2010, **16**, 574-583.
156. Z. Zhou, R. Bai, J. Munasinghe, Z. Shen, L. Nie and X. Chen, *ACS nano*, 2017, **11**, 5227-5232.
157. C. Rivas, G. J. Stasiuk, J. Gallo, F. Minuzzi, G. A. Rutter and N. J. Long, *Inorganic chemistry*, 2013, **52**, 14284-14293.
158. N. Lee, D. Yoo, D. Ling, M. H. Cho, T. Hyeon and J. Cheon, *Chemical reviews*, 2015, **115**, 10637-10689.
159. A. J. L. Villaraza, A. Bumb and M. W. Brechbiel, *Chemical reviews*, 2010, **110**, 2921-2959.
160. L. Zhang, R. Liu, H. Peng, P. Li, Z. Xu and A. K. Whittaker, *Nanoscale*, 2016, **8**, 10491-10510.
161. N. Lee and T. Hyeon, *Chemical Society Reviews*, 2012, **41**, 2575-2589.
162. J.-s. Choi, J.-H. Lee, T.-H. Shin, H.-T. Song, E. Y. Kim and J. Cheon, *Journal of the American Chemical Society*, 2010, **132**, 11015-11017.
163. T.-H. Shin, J.-s. Choi, S. Yun, I.-S. Kim, H.-T. Song, Y. Kim, K. I. Park and J. Cheon, *ACS nano*, 2014, **8**, 3393-3401.
164. F. Li, D. Zhi, Y. Luo, J. Zhang, X. Nan, Y. Zhang, W. Zhou, B. Qiu, L. Wen and G. Liang, *Nanoscale*, 2016, **8**, 12826-12833.
165. G. H. Im, S. M. Kim, D.-G. Lee, W. J. Lee, J. H. Lee and I. S. Lee, *Biomaterials*, 2013, **34**, 2069-2076.
166. Z. Zhou, C. Wu, H. Liu, X. Zhu, Z. Zhao, L. Wang, Y. Xu, H. Ai and J. Gao, *ACS nano*, 2015, **9**, 3012-3022.
167. Z. Zhou, L. Wang, X. Chi, J. Bao, L. Yang, W. Zhao, Z. Chen, X. Wang, X. Chen and J. Gao, *ACS nano*, 2013, **7**, 3287-3296.
168. X. Wang, Z. Zhou, Z. Wang, Y. Xue, Y. Zeng, J. Gao, L. Zhu, X. Zhang, G. Liu and X. Chen, *Nanoscale*, 2013, **5**, 8098-8104.
169. L. Yang, Z. Zhou, H. Liu, C. Wu, H. Zhang, G. Huang, H. Ai and J. Gao, *Nanoscale*, 2015, **7**, 6843-6850.

170. Z. Zhou, H. Liu, X. Chi, J. Chen, L. Wang, C. Sun, Z. Chen and J. Gao, *ACS applied materials & interfaces*, 2015, **7**, 28286-28293.
171. W. S. Seo, J. H. Lee, X. Sun, Y. Suzuki, D. Mann, Z. Liu, M. Terashima, P. C. Yang, M. V. McConnell and D. G. Nishimura, *Nature materials*, 2006, **5**, 971.
172. L. Wang, J. Huang, H. Chen, H. Wu, Y. Xu, Y. Li, H. Yi, Y. A. Wang, L. Yang and H. Mao, *ACS nano*, 2017, **11**, 4582-4592.
173. D. Niu, X. Luo, Y. Li, X. Liu, X. Wang and J. Shi, *ACS applied materials & interfaces*, 2013, **5**, 9942-9948.
174. T. Courant, V. G. Roullin, C. Cadiou, M. Callewaert, M. C. Andry, C. Portefaix, C. Hoeffel, M. C. de Goltstein, M. Port and S. Laurent, *Angewandte Chemie International Edition*, 2012, **51**, 9119-9122.
175. Y. Chen, K. Ai, J. Liu, X. Ren, C. Jiang and L. Lu, *Biomaterials*, 2016, **77**, 198-206.
176. Z. Zhou, Z. Zhao, H. Zhang, Z. Wang, X. Chen, R. Wang, Z. Chen and J. Gao, *ACS nano*, 2014, **8**, 7976-7985.
177. J.-s. Choi, S. Kim, D. Yoo, T.-H. Shin, H. Kim, M. D. Gomes, S. H. Kim, A. Pines and J. Cheon, *Nature materials*, 2017, **16**, 537.
178. Z. Zhou, D. Huang, J. Bao, Q. Chen, G. Liu, Z. Chen, X. Chen and J. Gao, *Advanced materials*, 2012, **24**, 6223-6228.
179. V. K. Sharma, A. Alipour, Z. Soran-Erdem, Z. Aykut and H. V. Demir, *Nanoscale*, 2015, **7**, 10519-10526.
180. J. S. Ananta, B. Godin, R. Sethi, L. Moriggi, X. Liu, R. E. Serda, R. Krishnamurthy, R. Muthupillai, R. D. Bolskar and L. Helm, *Nature nanotechnology*, 2010, **5**, 815.
181. N. C. I. a. t. N. I. o. Health, National cancer institute, https://www.cancer.gov/types/colorectal, (accessed 5/7/2017, 2017).
182. N. i. o. h. a. t. f. o. n. l. o. madicine, Colorectal Cancer: Symptoms, Diagnosis and Treatment, https://medlineplus.gov/magazine/issues/spring09/articles/spring09pg7-8.html, (accessed 5/7/2017, 2017).
183. A. C. Society, Estimated Number of New Cases for the Four Major Cancers by Sex and Age Group, 2017, https://www.cancer.org/content/dam/cancer-org/research/cancer-facts-and-statistics/annual-cancer-facts-and-figures/2017/estimated-new-cases-for-the-four-major-cancers-by-sex-and-age-group-2017.pdf, (accessed 5/7/2017, 2017).
184. S. Hu, H. Dai, T. Zhang, W. Fu, S. D. Berezov, C. Chen, D. Jorissen, H. Takeda and A. N. Bethune, *Cancer Letters*, 2017, **401**, 81.
185. D. Yoo, J.-H. Lee, T.-H. Shin and J. Cheon, *Accounts of Chemical Research*, 2011, **44**, 863-874.
186. N. Nasongkla, E. Bey, J. Ren, H. Ai, C. Khemtong, J. S. Guthi, S.-F. Chin, A. D. Sherry, D. A. Boothman and J. Gao, *Nano letters*, 2006, **6**, 2427-2430.
187. K. Y. Choi, G. Liu, S. Lee and X. Chen, *Nanoscale*, 2012, **4**, 330-342.
188. J. Xie, K. Chen, J. Huang, S. Lee, J. Wang, J. Gao, X. Li and X. Chen, *Biomaterials*, 2010, **31**, 3016-3022.
189. Q. Quan, J. Xie, H. Gao, M. Yang, F. Zhang, G. Liu, X. Lin, A. Wang, H. S. Eden and S. Lee, *Molecular pharmaceutics*, 2011, **8**, 1669-1676.
190. Z. Liu, W. Cai, L. He, N. Nakayama, K. Chen, X. Sun, X. Chen and H. Dai, *Nature nanotechnology*, 2007, **2**, 47.
191. Z. Liu, C. Davis, W. Cai, L. He, X. Chen and H. Dai, *Proceedings of the National Academy of Sciences*, 2008, **105**, 1410-1415.
192. A. A. Bhirde, G. Liu, A. Jin, R. Iglesias-Bartolome, A. A. Sousa, R. D. Leapman, J. S. Gutkind, S. Lee and X. Chen, *Theranostics*, 2011, **1**, 310.

193. Z. Liu, J. T. Robinson, S. M. Tabakman, K. Yang and H. Dai, *Materials today*, 2011, **14**, 316-323.
194. S. Dhar, Z. Liu, J. Thomale, H. Dai and S. J. Lippard, *Journal of the American Chemical Society*, 2008, **130**, 11467-11476.
195. Z. Liu, K. Chen, C. Davis, S. Sherlock, Q. Cao, X. Chen and H. Dai, *Cancer research*, 2008, **68**, 6652-6660.
196. A. A. Bhirde, G. Liu, A. Jin, R. Iglesias-Bartolome, A. A. Sousa, R. D. Leapman, J. S. Gutkind, S. Lee and X. Chen, *Theranostics*, 2011, **1**, 310-321.
197. H. K. Moon, S. H. Lee and H. C. Choi, *ACS nano*, 2009, **3**, 3707-3713.
198. X. Liu, H. Tao, K. Yang, S. Zhang, S.-T. Lee and Z. Liu, *Biomaterials*, 2011, **32**, 144-151.
199. M.-C. Daniel and D. Astruc, *Chemical reviews*, 2004, **104**, 293-346.
200. C. M. Cobley, J. Chen, E. C. Cho, L. V. Wang and Y. Xia, *Chemical Society Reviews*, 2011, **40**, 44-56.
201. X. Huang, I. H. El-Sayed, W. Qian and M. A. El-Sayed, *Journal of the American Chemical Society*, 2006, **128**, 2115-2120.
202. L. Tong, Q. Wei, A. Wei and J. X. Cheng, *Photochemistry and photobiology*, 2009, **85**, 21-32.
203. K. Y. Choi, H. Chung, K. H. Min, H. Y. Yoon, K. Kim, J. H. Park, I. C. Kwon and S. Y. Jeong, *Biomaterials*, 2010, **31**, 106-114.
204. G. D. Moon, S.-W. Choi, X. Cai, W. Li, E. C. Cho, U. Jeong, L. V. Wang and Y. Xia, *Journal of the American Chemical Society*, 2011, **133**, 4762-4765.
205. M. S. Yavuz, Y. Cheng, J. Chen, C. M. Cobley, Q. Zhang, M. Rycenga, J. Xie, C. Kim, K. H. Song and A. G. Schwartz, *Nature materials*, 2009, **8**, 935.
206. L. R. Hirsch, R. J. Stafford, J. Bankson, S. R. Sershen, B. Rivera, R. Price, J. D. Hazle, N. J. Halas and J. L. West, *Proceedings of the National Academy of Sciences*, 2003, **100**, 13549-13554.
207. W. Chen, R. Bardhan, M. Bartels, C. Perez-Torres, R. G. Pautler, N. J. Halas and A. Joshi, *Molecular cancer therapeutics*, 2010, **9**, 1028-1038.
208. M. Ferrari, *Nature reviews cancer*, 2005, **5**, 161.
209. D. Peer, J. M. Karp, S. Hong, O. C. Farokhzad, R. Margalit and R. Langer, *Nature nanotechnology*, 2007, **2**, 751.
210. C. Sanson, O. Diou, J. Thevenot, E. Ibarboure, A. Soum, A. Brûlet, S. Miraux, E. Thiaudière, S. Tan and A. Brisson, *ACS nano*, 2011, **5**, 1122-1140.
211. W. J. Gradishar, S. Tjulandin, N. Davidson, H. Shaw, N. Desai, P. Bhar, M. Hawkins and J. O'Shaughnessy, *Journal of Clinical Oncology*, 2005, **23**, 7794-7803.
212. A. P. Alivisatos, *The Journal of Physical Chemistry*, 1996, **100**, 13226-13239.
213. Q. A. Pankhurst, J. Connolly, S. Jones and J. Dobson, *Journal of physics D: Applied physics*, 2003, **36**, R167.
214. J. Williams, R. Lansdown, R. Sweitzer, M. Romanowski, R. LaBell, R. Ramaswami and E. Unger, *Journal of Controlled Release*, 2003, **91**, 167-172.
215. J.-C. Leroux, E. Allémann, F. De Jaeghere, E. Doelker and R. Gurny, *Journal of Controlled Release*, 1996, **39**, 339-350.
216. F. Yuan, 1998.
217. H. Maeda and Y. Matsumura, *Critical reviews in therapeutic drug carrier systems*, 1989, **6**, 193-210.
218. R. V. Chari, *Advanced drug delivery reviews*, 1998, **31**, 89-104.
219. A. M. Mansour, J. Drevs, N. Esser, F. M. Hamada, O. A. Badary, C. Unger, I. Fichtner and F. Kratz, *Cancer research*, 2003, **63**, 4062-4066.
220. X. Guo and F. C. Szoka, *Accounts of chemical research*, 2003, **36**, 335-341.

221. C. S. Shin, B. Kwak, B. Han and K. Park, *Molecular Pharmaceutics*, 2013, **10**, 2167-2175.
222. T. Nomura, A. Saikawa, S. Morita, T. Sakaeda, F. Yamashita, K. Honda, Y. Takakura and M. Hashida, *Journal of controlled release*, 1998, **52**, 239-252.
223. S. Prabha and V. Labhasetwar, *Molecular pharmaceutics*, 2004, **1**, 211-219.
224. D. D. Barker and A. J. Berk, *Virology*, 1987, **156**, 107-121.
225. F. R. Khuri, J. Nemunaitis, I. Ganly, J. Arseneau, I. F. Tannock, L. Romel, M. Gore, J. Ironside, R. MacDougall and C. Heise, *Nature medicine*, 2000, **6**, 879.
226. J. R. Hecht, R. Bedford, J. L. Abbruzzese, S. Lahoti, T. R. Reid, R. M. Soetikno, D. H. Kirn and S. M. Freeman, *Clinical Cancer Research*, 2003, **9**, 555-561.
227. T. Reid, E. Galanis, J. Abbruzzese, D. Sze, L. M. Wein, J. Andrews, B. Randlev, C. Heise, M. Uprichard and M. Hatfield, *Cancer research*, 2002, **62**, 6070-6079.
228. P. Vasey, L. Shulman, S. Campos, J. Davis, M. Gore, S. Johnston, D. Kirn, V. O'neill, N. Siddiqui and M. Seiden, *Journal of clinical oncology*, 2002, **20**, 1562-1569.
229. E. Galanis, S. H. Okuno, A. Nascimento, B. Lewis, R. Lee, A. Oliveira, J. A. Sloan, P. Atherton, J. Edmonson and C. Erlichman, *Gene therapy*, 2005, **12**, 437.
230. A. Lamprecht, H. Yamamoto, H. Takeuchi and Y. Kawashima, *Journal of pharmacology and experimental therapeutics*, 2005, **315**, 196-202.
231. J. F. Kukowska-Latallo, K. A. Candido, Z. Cao, S. S. Nigavekar, I. J. Majoros, T. P. Thomas, L. P. Balogh, M. K. Khan and J. R. Baker, *Cancer research*, 2005, **65**, 5317-5324.
232. J. Sudimack and R. J. Lee, *Advanced drug delivery reviews*, 2000, **41**, 147-162.
233. A. A. Bhirde, V. Patel, J. Gavard, G. Zhang, A. A. Sousa, A. Masedunskas, R. D. Leapman, R. Weigert, J. S. Gutkind and J. F. Rusling, *ACS Nano*, 2009, **3**, 307-316.
234. S.-Y. Cheng, H. Huang, M. Nagane, X.-D. Ji, D. Wang, C. Shih, W. Arap, C.-M. Huang and W. K. Cavenee, *Proceedings of the National Academy of Sciences*, 1996, **93**, 8502-8507.
235. L. F. Brown, B. Berse, R. W. Jackman, K. Tognazzi, A. J. Guidi, H. F. Dvorak, D. R. Senger, J. L. Connolly and S. J. Schnitt, *Human pathology*, 1995, **26**, 86-91.
236. K. J. Kim, B. Li, J. Winer, M. Armanini, N. Gillett, H. S. Phillips and N. Ferrara, *Nature*, 1993, **362**, 841.
237. M. Skobe, P. Rockwell, N. Goldstein, S. Vosseler and N. E. Fusenig, *Nature medicine*, 1997, **3**, 1222.
238. X. Fu, Y. Yang, X. Li, H. Lai, Y. Huang, L. He, W. Zheng and T. Chen, *Nanomedicine: Nanotechnology, Biology and Medicine*, 2016, **12**, 1627-1639.

CHAPTER 2

CHARACTERISATION TECHNIQUES

2 Experimental

2.1 General instrumentation and techniques

2.1.1 Power X-Ray Diffraction (PXRD)

PXRD patterns were collected for the NP samples to determine their purity as well as to indicate their unit cell dimensions due to its high sensitivity, relatively simple analysis of results and none destructive nature. As a result of the constructive interference between the electromagnetic waves, diffraction occurs when an object is blocking the path of constructive waves. Beams of electrons are scattered in various directions at specific angles when x-rays interact with them. For the reflected signals to be strong enough to be detected all reflections need to be in phase with one another. For this to occur there must be an integral spacing between the path lengths of the reflected x-rays, where difference in pathlength = 2dsinθ. This is shown by the Bragg equation and determines the interplanar spacing within the crystal.

Thus, for an integral number of wavelength (n) the Bragg equation can be formed:

The Bragg equation below explains the relationship between the angle of incidence, wavelength of the incident x-ray, and spacing between the crystal lattice of atoms. This equation is known as Bragg's law and determines the interplanar spacing within crystal.[1] It is expressed as:

$$n\lambda = 2d\sin\theta \qquad \textit{Equation 1-1}$$

Where λ is the wavelength of the incident x-rays, n (an integer) is the order of diffraction, d is the interplanar spacing between the crystal atomic layers and θ is the angle between incidence x-ray and the surface of the crystalline materials. Figure 1-23 illustrate the principle of the powder x-ray diffraction technique.

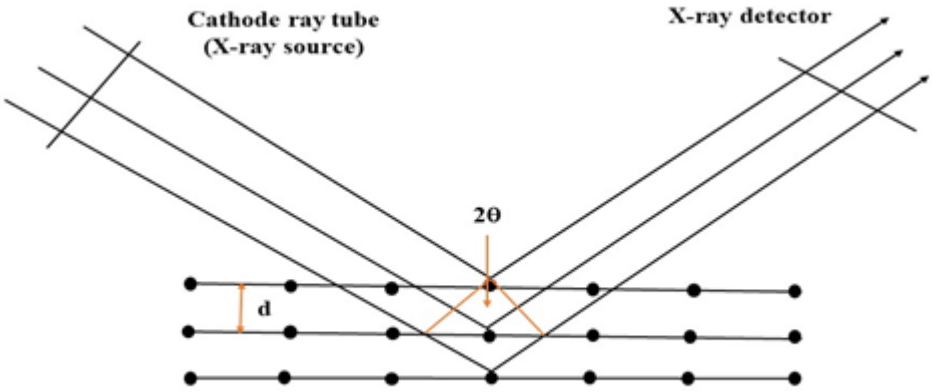

Figure 1-23: Scattering of X-rays by atoms in successive parallel plans. Constructive interference occurs when the path difference between scattered waves is equal to an integral number of wavelengths.

In PXRD, a cone is formed due to the x-ray scattering as illustrated in Figure 1-24. Each cone represents a plane of diffraction and the obtained data would be useful to explore the sample structure and composition.[2, 3] The crystalline sample is scanned at a range of 2θ angle. As a result of random orientation of the crystalline powder materials, all diffraction directions are eventually encompassed. Peaks formed are shown as a plot of intensity versus the angle of the detector.

PXRD patterns were collected for the sample using PANalytical (Empyrean series 2) X-Ray diffractometer instrument. As it was fixed slit, a nickel filter was used to minimize the fluorescence that might arise due to closeness of Mn, Fe and Co elements from the copper in the periodic table. The angle range was 20-80°C, step size 0.026260°, time per step 1518.015 s, scan speed 0.004402 °/s and number of steps 2285.

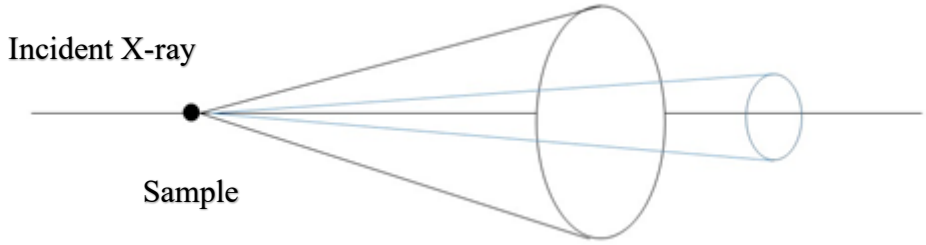

Figure 1-24: Schematic diagram of X-ray scattering by a powder sample.

In crystallography, the lattice planes are represented by hkl integers.[3] These integers indicate the different planes in the crystal structure. Planes have different arrangements of atoms and different density of atoms. The hkl integers can be identified by determining

the reciprocals of the intercept of the lattice planes along the x, y and z axes.[3] The well-known general rules are, when the Miller index is zero, the plane is parallel to that axis and when it is small, the plane is more parallel to that axis, while when it is big, the plane is usually perpendicular to that axis. In such a structure, the interplanar spacing d_{hkl} for cubic geometry can be correlated to the lattice parameter a using the following equation:

$$\frac{1}{d_{hkl}^2} = \frac{h^2+k^2+l^2}{a^2} \qquad \textit{Equation 1-2}$$

When combining the Bragg equation with equation 2-2, a new equation is produced to express the relationship between the angle at which the X-rays diffracted with the lattice parameter a.

$$sin^2\theta = \frac{4\lambda^2}{a^2}\,(\,h^2 + k^2 + l^2\,) \qquad \textit{Equation 1-3}$$

Using equation 2-3, the specific angle at which an X-ray beam is diffracted defined by a known set of planes can be calculated. The intensity of scattered X-rays is highly dependent on the nature and number of atoms within the plane. In general, a linear relationship between the amount of the scattered light and the atomic number of the element. Due to this reason PXRD patterns are characteristic for each compound. Figure 1-25 shows six different Miller indices examples for different planes in a crystalline structure.

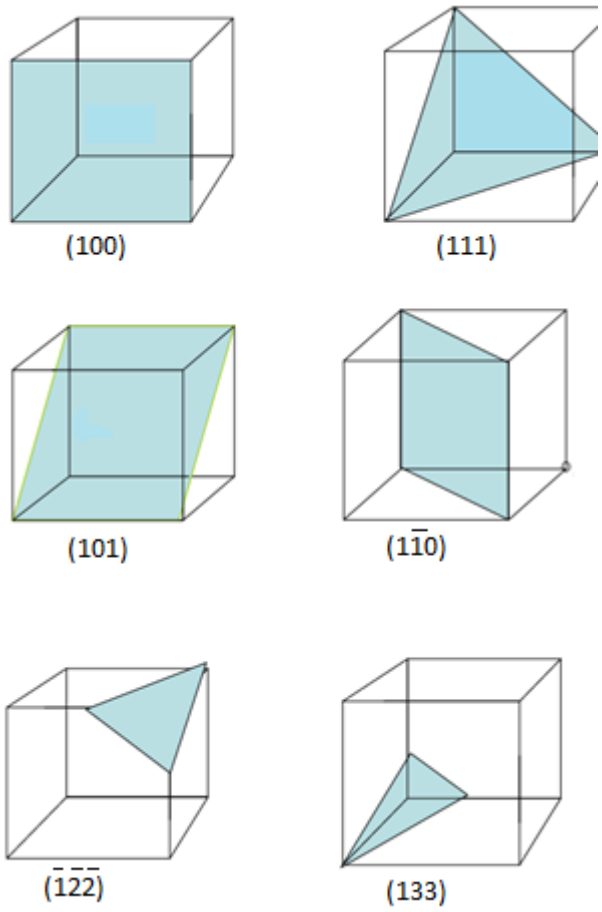

Figure 1-25: Some representive planes in cubic crystalline structure

2.2 Nanoparticles Tracking Analysis (NTA)

An LM10-HS microscope from Nano sight was used to collect NTA measurements. The instrument was used with a 75-mW laser at 532 nm (green), equipped with a sample chamber. The samples were injected in the sample chamber with sterile syringe until the liquid reached the tip of the nozzle. All measurements were performed at room temperature. The concentration of the sample was adjusted before analysis to a specific dilution with HPLC water. This technique utilises the fundamentals of both Brownian motion and light scattering in order to determine the particle size distributions of samples that are suspended in a liquid medium such as water or methanol in the case of the medium used in this project.[4] The particles that move under Brownian motion can be visualised by eye in two ways, either directly by a microscope or *via* a small camera that is connected directly to the microscope.

NTA software records a video file (of typically 30-60 s duration) of the particles viewed and then simultaneously identifies and tracks the centre of each particle on a frame-by-

frame basis. The image analysis software then determines the average distance moved by each particle using the Stokes-Einstein equation:

$$D_t = \frac{TK_B}{3\pi\eta d} \qquad \textit{Equation 1-4}$$

Where (D_t) is the particle diffusion coefficient to be calculated, (T) is the sample temperature, K_B is a constant, (η) is the solvent viscosity and (d) is the hydrodynamic diameter of the particle.[4]

2.3 Fourier Transform Infra-red spectroscopy (FT-IR)

FTIR spectroscopy is a powerful technique that yields information about chemical structure by utilizing an infra-red electromagnetic radiation.[5] The importance of the FTIR spectroscopy in the identification of molecular structures originates from the much information contents obtained and the possibility to assign certain absorption bands related to its functional groups. The detector analyses the variations in energy versus time transmitted wavelength using Fourier equation series. The application of Fourier transform give rise to a spectrum of wavenumber versus intensity

An FTIR instrument consists of a radiation source, beam splitter, static and moveable mirrors and photodetector. The sample is normally placed in front of a detector. When monochromatic infrared radiation emitted from the source reaches the splitter (partially transparent mirror), some of the radiation passes through it and the other part is reflected. These two beams then reach both mirrors, where they reflected back to the beam splitter. At the splitter those beams are split again, causing the part of radiation reflected from the moving mirror to recombine and pass through the sample into the detector. The other part of the reflected radiation goes back to the radiation source. Both mirrors are set at equal distance from the splitter, this causes the two beams reaching the detector to be in the same phase, which leads to constructive interference.[6] At this point, the radiation reaching the detector has the highest intensity. However, if one of the mirrors moves by a short distance, then the intensity of radiation reaching the detector will suddenly drop. This is because the two recombining beams are no longer in the same phase and cancel each other out (destructive interference). The constructive and destructive interference leads to the formation of an interferogram.[7] This interferogram can be converted into a spectrum by a process called Fourier Transformation. The overall schematic diagram of this process is shown in Figure 1-26.

The analysis of FTIR was carried out using a Nicolet FT-IR spectrometer with smart orbit, Dimond ATR. Analysis was carried out using the EZ OMNIC software. A spectrum of the background was recorded first and then the sample spectrum was obtained.

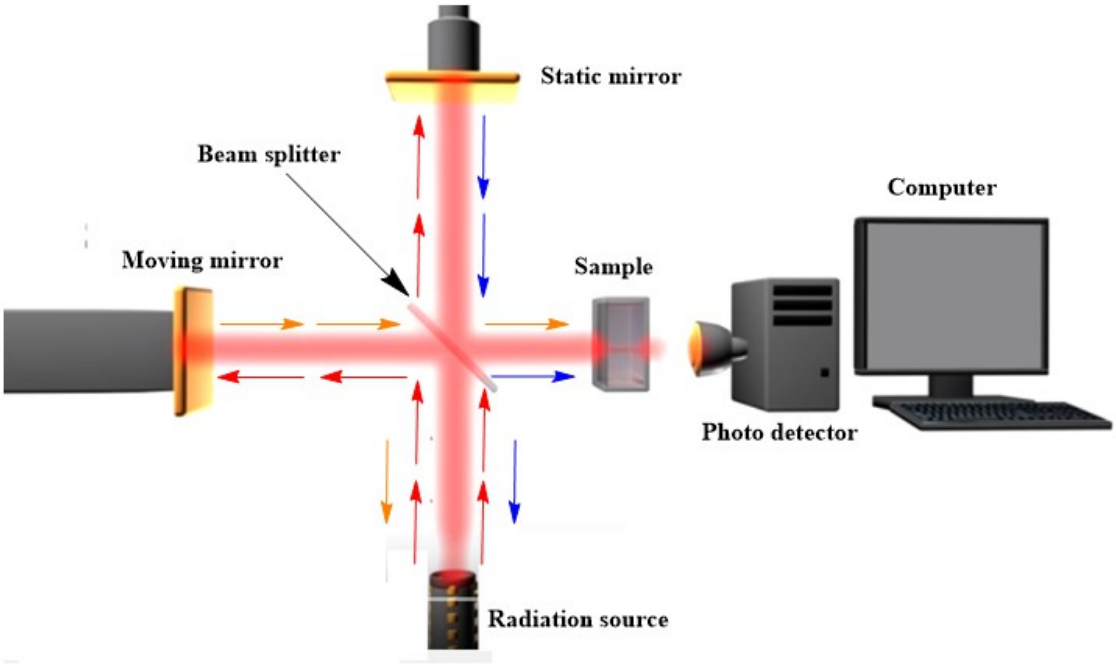

Figure 1-26: Basic principle of FTIR system drawn by chemdraw software

2.4 Transmission Electron Microscopy (TEM) and Energy Dispersive X-ray spectroscopy (EDX)

Electron microscopy is well known technique for imaging materials at the microscale or nanoscales. Normally, electron microscopes are combined with EDX to detect the elemental composition of the analysed samples. In comparison to TEM which is used to image the internal structure of the samples, SEM is only limited to image the external surfaces. The atomic ratio of the elemental composition available in the samples can be quantitatively identified by EDX.

In TEM, an electron source is usually generated from a lanthanum hexaboride (LaB_6) crystal filament. The electrons produced are directed through a vacuum chamber and transmitted through a sample. All sample regions that have higher mass scatter electrons to greater extent. As a result of the electron interaction with the analysed sample, a grayscale image is produced, which can be magnified on to imaging device.

Once the above described process takes place, a fraction of ground state electrons of the sample increase in energy due to the high electron bombardment of the sample. This

forms an electron hole in their place. This causes an electron from a higher energy to relax in order to occupy this vacancy accompanied with emission of energy similar to that of an X-ray. In EDX, these emissions are collected. These energies differ from element to element and therefore the elemental composition can be determined.

TEM analysis was performed with a JEOL 2010 instrument, running at 200 KV with a lanthanum hexaboride crystal filament. Images were taken with a Gatan Ultrascan 4000, a 64-megapixel camera operated using Digital Micrograph.

TEM sample preparation can be complex as the samples to be analysed should not be more than 100 nm of thick. samples are dispersed in water and deposited onto the TEM grids and allowed to dry.

2.5 Optical emission Inductively Coupled Plasma (ICP)

ICP is a spectroscopy technique used to determine the elemental composition of samples.[8] It is widely utilized due to its speed and accuracy and has the ability to determine multiple elements simultaneously as compared to atomic absorption spectroscopy, where only one element can be analysed at a time.[9] ICP spectroscopy involves the use of inert gas (Argon) and high temperature (10,000 K) to excite the elemental atoms in the presence of electric field.[10] When atoms are excited, they return to low energy positions and emission rays are released. These produced rays can be used to estimate the different type of elements in the sample.

Elemental analysis was carried out using Inductively Coupled Optical Emission Spectroscopy (ICPOEs) with a Perkin Elmer Optima 5300 DV. All the samples were digested with 0.1 M HNO_3 using a microwave system prior to the analysis. The digested samples and calibration standards of various elements were diluted by same 0.1 M HNO_3 to obtain the desired concentrations. All calibration standards were prepared using 1000 ppm concentrations of iron, manganese, potassium, silicon, dysprosium and tin which were purchased from Romail UK.

2.6 Zeta potential and hydrodynamic size measurements

The Zeta (ξ) potential is defined as the electrostatic potential that exists at the shear plane of a particle, and is caused by both local environment of the particle and the surface charge.[11] The Zeta potential was determined with a Zetasizer Nano series Nano ZS from Malvern Instruments. Measurements were recorded at 25°C on samples suspended in water which is placed in a universal dip cell. The Zeta (ξ) potential was automatically calculated from electrophoretic mobility based on the Smoluchowski equation:[12]

$$v = (\varepsilon . E / \eta) . \xi \qquad \textit{Equation 1-5}$$

Where v is the measured electrophoretic velocity, η is the viscosity, ε is the electrical permittivity of the electrolytic solution and E is the electric field.

The hydrodynamic size of the prepared NPs was measured using DLS instrument. Each measurement was made in triplicate, while the NPs were dispersed in 5 ml of deionised *HPLC* water at 25℃.

2.7 C H N analysis

Simultaneous determination for CHN in NP samples was carried out using an EA 1108 CHN Elemental Analyser. The technique relies on the combustion of the samples and the amount of products are measured. Usually a known amount of sample is weighed in a fully sealed aluminium or tin capsule and then placed in the analyser under controlled conditions. The sample passes into a pyrolysis tube where combustion takes place at 900°C under pure oxygen atmosphere. This results in converting carbon, hydrogen and nitrogen into CO_2, H_2O and nitrogen oxides. These produced gasses are then carried by a stream of helium to a chamber containing heated copper, where NO_2 is reduced to N_2 and excess oxygen is removed. After this conversion, the mixture of CO_2, H_2O and N_2 gasses is transported *via* the helium carrier gas to an analysing chamber where a specialised type of gas chromatography is preformed which does not require a mobile phase for separation. The separated gasses are then detected by a thermal conductivity detector and then percentages of C, H and N can be determined.[13]

2.8 NMR instrument

To identify the relaxation (T_1/T_2) values of the synthesised NPs, NMR spectroscopy instrument was used. All atomic nuclei exhibit an intrinsic value of spin. When an electric field is applied they absorb electromagnetic radiation, they release this radiation in a radiofrequency which related to their spin value.

The longitudinal (T_1) and transverse relaxivity (T_2) measurements were carried out using a JEOL ECP400 (9.4T) NMR spectrometer operating at 400 MHz. Both T_1 and T_2 measurements involve the use of Evan's method, where sample is dissolved in *HPLC* water, and was placed into a sealed capillary tube. This tube was inserted in an NMR tube which was filled with 1 ml D_2O. The T_1 measurements were made using linear inversion recovery 90 deg pulse. T_2 measurements were made using nonlinear spin lock 90 deg pulse. The computer program Delta was used to plot the time versus signal intensity to get an exponential plot, T_1 and T_2 were calculated from the plot. The

longitudinal (r_1) was calculated by dividing $1/T_1$ over the concentration of the ion in each compound and transverse relaxitivity (r_2) was calculated by dividing $1/T_2$. The slopes of each plot were considered as the relaxation rates. These graphs were plotted using origin software.

2.9 UV-visible spectrometry

Based on Bouguer-Lambert-Beer law, the basic mathematical physical concept to perform light absorption measurements on gases or solutions in the visible or infra-red regions is expressed by the equation:

$$Absorbance = Log \frac{I_0}{I} = \varepsilon cd \qquad \text{Equation 1-6}$$

Where I_0 is the intensity of the light entering the sample and I is the intensity of light emerging from the sample, ε is the molar extinction coefficient, c is the concentration of light absorbing sample and d is the pathlength of the sample in cm.[14]

UV-visible spectrometry was used to determine the concentration of DOX conjugated to the synthesised NPs. A series of standard DOX concentrations were prepared to plot the calibration graph. All UV spectra for both standards and samples were plotted using origin software.

2.10 Fluorescence measurements

Fluorescence measurement of DOX was made using a Horiba Fluromax-4P spectrofluorometer in a 10 mm quartz cuvette. Emission and Excitation for DOX spectra were recorded in aqueous medium. Excitation and emission wavelengths were collected on the plasmonic resonance at 499 and 594 nm respectively using a Becker and Hickl HPM-100 detector.

2.11 Flow cytometry

Detection of EGFR and VEGFR as performed via (BD FACS calibur, USA) equipped with a single 488 nm argon-ion excitation laser, and three fluorescence reading channels FL_1(530 nm), FL_2 (585 nm) and FL_3 (670 nm). The three main parts of flow cytometry instrument are fluidics, optics and electronics.[15] The main role of fluidics is to transport cells to the laser beam for integration. For accurate measurements it is important that cell particles are passed to the laser beam one at a time.[15] Most flow cytometers accomplish this by injecting the sample stream containing the cells into a flowing stream of sheath solution. The sample stream becomes compressed to allow a single cell to be excited by the laser beam. This phenomena is called Hydrodynamic focusing.[16] When cells are

passed through a laser light, they scatter light in different direction with different angles (Forward scatter –FSC) and (side scatter – SSC). The forward scattered light is directly proportional to the cell relative size and surface area, and the side scattered light is also proportional to the relative granularity of complexity of cells. In addition, if the particles of cell are tagged by fluorescent molecule such as fluurochrome, they reflect light to low angles and give a relative fluorescence intensity that can be easily detected by a detector. Figure 1-27 illustrates how flow cytometry work.

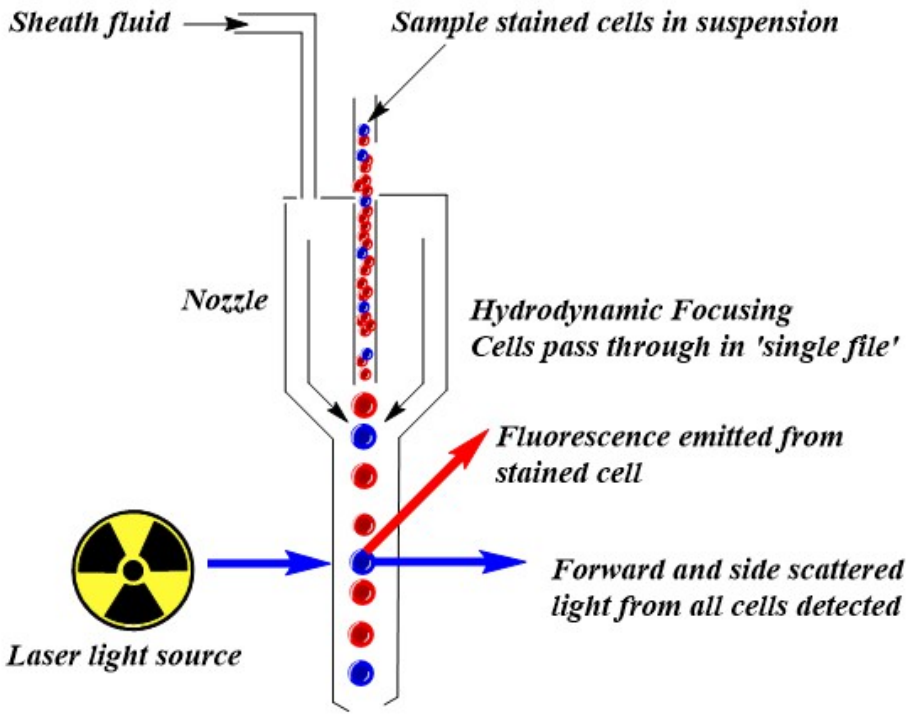

Figure 1-27: Schematic diagram of flow cytometry.

2.12 Confocal fluorescence microscopy

Fluorescence microscopy is one of the extensively used techniques to visualise the localisation of small molecules within cells. This is due to its high sensitivity, specificity and reliability. It relays on the basic principle of florescence spectroscopy as shown in Figure 1-28. Fluorophores such as dyes, antigens or anti-bodies fluoresce if they are bombarded by a light of specific wavelength, and an electronic transition from the molecular ground singlet state into the first excited singlet state takes place. The electron in the excited state remains for a certain time and then returns back to the ground state. During this transition, energy is released in the form of emission. This phenomenon is called fluorescence. The transition involves loss of energy, higher wavelength and different colours compared to the original light absorbed.

The Fluorescence microscope utilises a very powerful light source and a dichroic mirror which can reflect light at specific excitation/emission wavelengths. This specific light is then passed through an objective which is focused into the sample. The light emitted by the sample is then passed into a detector for image digitalization. Fluorescence imaging was observed using a ZEISS AXIO Vert.A1 florescent microscope and Zen lite software was used to create micrographs.

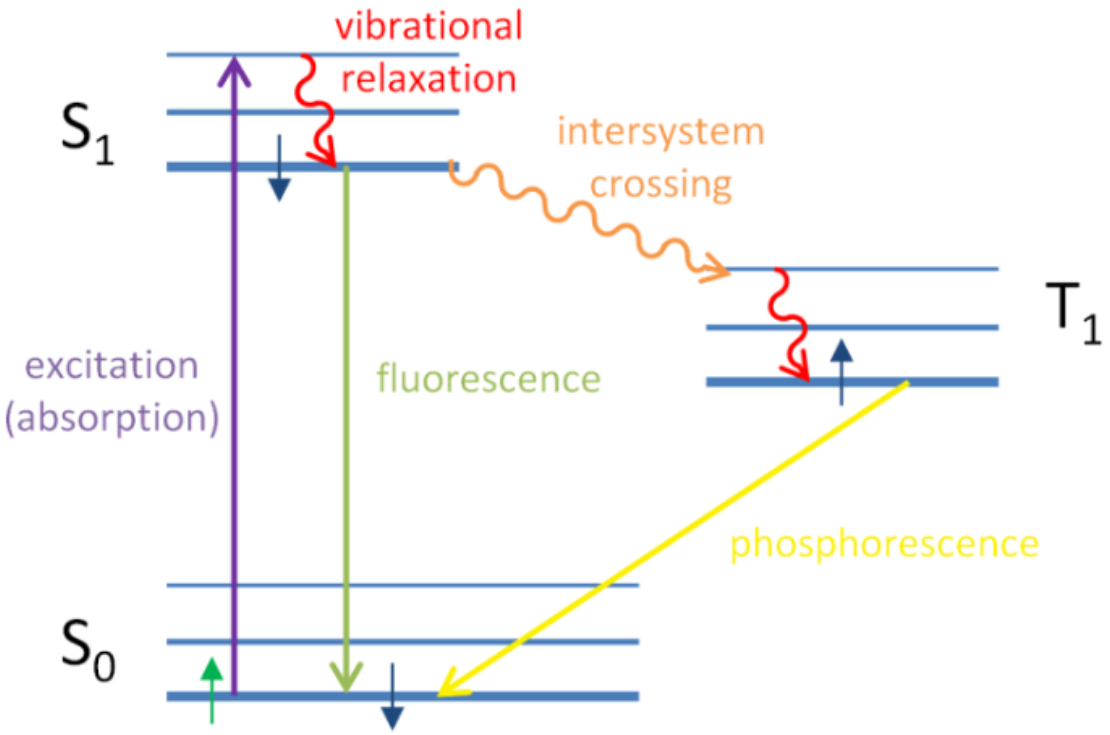

Figure 1-28: Diagram to illustrate the fluorescence spectroscopy process.

2.13 Biological analysis

2.13.1 Cell line and cell culture

The human cervical cancer cell line (HeLa), colon cancer HCT-116 and colon cancer (HT-29) were purchased from Scientific Laboratory Supplies. The Hela cells were grown in RPMI 1640, whereas HCT-116 and HT-29 cells were grown in Macoys media. All Media contain L-glutamine (500 ml) (Lonza) supplemented with 50 ml 10 % Fetal Bovine Serum (FBS) (Lonza) and 5 ml 1% streptomycin sulfate (PenStrep) (Lonza).

All cell types were grown in 25 ml culture flasks and were incubated at 37˚ C in humidified atmosphere with 5% CO_2.

2.13.2 Media growth preparation

Media (500 ml), P/S (5 ml) and FBS (50 ml) were warmed up to 37°C using a thermostatic water bath. These along with sterilised 20 ml syringes and 45 µl filters were first sprayed with 70% ethanol and then placed into a biosafety cabinet. These syringes and filter were used to take up the FBS and P/S supplements and filter them into a media bottle. The media bottle containing these supplements was then shaken to ensure good mixing and placed in a fridge for further use.

2.13.3 Cell passaging

Cell lines are extensively used in biomedical field research. This protocol describes the method used to change medium and cell splitting or passaging. Providing fresh nutrient is essential to keep the cell healthy, while cell splitting is extremely vital for optimum cell growth. This protocol was carried out in a biosafety cabinet. When the confluency of the incubated cells is not 80%, and media turns cloudy, the media was changed using a sterilised 10 ml pipette and cells were then rinsed with 10 ml PBS. After removing PBS, the media immediately replaced by a new volume of fresh warmed media. The flask was returned back to incubator at 37°C, under 5% CO_2 for continues growth. In the case of cell splitting, initially media and trypsin (with EDTA) were warmed up in a water bath at 37°C. A flask containg the adhered cells was checked under a microscopy to confirm 80-90% confluency. In a biosafety hood, the flask was tilted and the old media was discarded into a virkon waste flask using a 10 ml pipette. The cells were then rinsed with 10 ml PBS to remove any remaining serum that may exist in the flask. 3 ml dissociation reagent (Trypsin with EDTA) was then added to remove cells from the base of the flask, making sure this solution covered all the cells. The flask was then incubated for 3 minutes or until all cells started to detach. The flask was gently tapped to accelerate the cell detaching process and to confirm the total release of cells from the flask. 3 ml of the corresponding media was added to inhibit the further action of trypsin. Using 5 ml pipette, the contents were transferred to a 25 ml centrifuge tube and centrifuged at 1500 rpm at room temperature for 3 minutes. A well-formed pellet was formed. The media was then removed and discarded into the virkon solution. The pellets were re-suspended into 3 ml of media. Continuous pipetting ensures a homogenous dispersion solution of single cells. These cells were now ready for splitting. 1 ml of the suspended cells were transferred in a new 25 ml culture flask containing 17 ml of corresponding media. The flask was then incubated at 37°C, under 5% CO_2 until confluent for further splitting or use in assay. Figure 1-29 represents the systematic cell splitting protocol used.

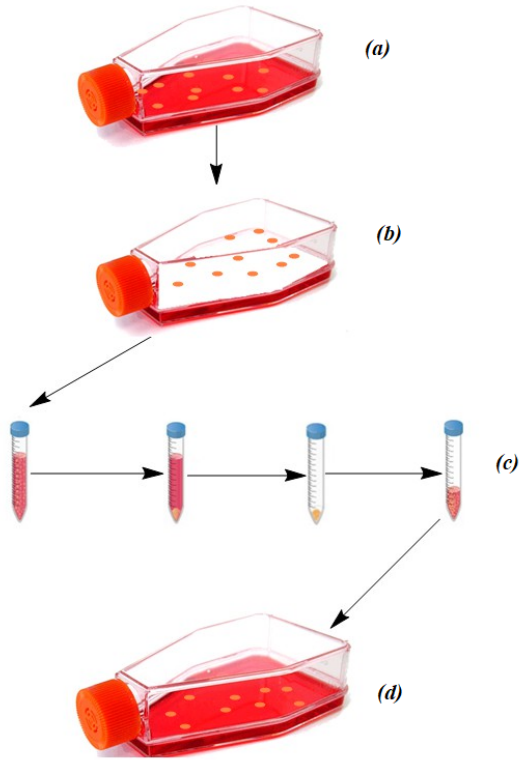

Figure 1-29: Schematic diagram followed for cells splitting, suspension of cell in growth media (a), removal of the old media (b), centrifuging and removal of media (c) and dispersion of the splitted new cells in new media (d).

2.13.4 Cell Counting

Outside the biosafety cabinet, a haemocytometer was removed from its box, sprayed with 70% ethanol and dried using tissues. A clean cover slip was then moisturised using tissues sprayed with 70% ethanol. The cover slip was then placed on the haemocytometer, making sure that it did not slide off. Using a micro pipette, 10 µl cell suspension was mixed with 10 µl trypan blue in a clean vial. The mixture was then mixed two to three times using the same micro pipette to ensure a homogenous suspension. Using a Glison pipette, 10 µl of this suspension was then placed underneath the cover slip by carefully touching the edge of the cover slip with the pipette tip, allowing the chamber to fill by capillary action as shown in Figure 1-30(a). The prepared haemocytometer was then placed under a phase contrast microscope at ×20 magnification. All cells were counted by focusing the microscopic objective on the four outer squares in the grid, each at a time, using a manual cell counter (Figure 1-30 10(b). Each square contains 16 smaller squares, Figure 1-30(c). Cells on top and left touching middle lines were included, whereas cells touching the middle line at bottom and right were not counted. When there were too many or too few cells to count, the procedure was repeated either by concentrating or diluting the original suspension as appropriate. For accurate determination, the total number of

cells overlying 1 mm^2 should be between 15 and 50 cells. Live cells appear colourless and bright under phase contrast (refractile), while dead cells stain blue and are non-refractile. The total number of viable cells was counted, recorded and calculated using the following equations:

$$Viable\ cells/ml = Average\ viable\ cells\ counter\ per\ square \times Dilution\ factor \times 10^4 \qquad Equation\ 1\text{-}7$$

Where:

$$Average\ viable\ cells\ counter\ per\ square = \frac{Total\ number\ of\ viable\ cells\ in\ 4\ squares}{4} \qquad Equation\ 1\text{-}8$$

$$Dilution\ factor = \frac{Total\ volume\ (sample+diluting\ liquid)}{volume\ of\ sample} \qquad Equation\ 1\text{-}9$$

$$Therefore,\ Total\ viable\ cells\ /\ sample = viable\ cells/ml \times the\ original\ volume\ of\ fluid\ from\ which\ the\ sample\ was\ removed \qquad Equation\ 1\text{-}10$$

This value was then used to determine the volume of media required to dilute 1 ml of the original sample to achieve a specific number of cells for an experiment.

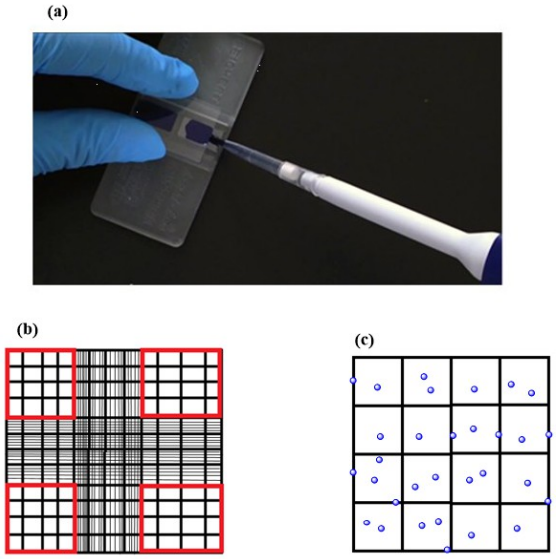

Figure 1-30: Injection of the Trypan blue cells suspension in haemocytometer (a) and cell counting strategy (b&c)

2.14 References

1. L. E. Smart and E. A. Moore, *Solid state chemistry: an introduction*, CRC press, 2016.
2. H. P. Klug and L. E. Alexander, *X-Ray Diffraction Procedures: For Polycrystalline and Amorphous Materials, 2nd Edition, by Harold P. Klug, Leroy E. Alexander, pp. 992. ISBN 0-471-49369-4. Wiley-VCH, May 1974.*, 1974, 992.
3. R. J. Tilley and R. Tilley, *Understanding solids: the science of materials*, Wiley Online Library, 2004.
4. J. G. Walker, *Measurement Science and Technology*, 2012, **23**, 065605.
5. O. Faix, in *Methods in lignin chemistry*, Springer, 1992, pp. 83-109.
6. in *Kirk‐Othmer Encyclopedia of Chemical Technology*, DOI: 10.1002/0471238961.0914061810151405.a01.pub3, pp. 1-18.
7. C. Pasquini, *Journal of the Brazilian chemical society*, 2003, **14**, 198-219.
8. H. Niu and R. S. Houk, *Spectrochimica Acta Part B: Atomic Spectroscopy*, 1996, **51**, 779-815.
9. C. D. Palmer, M. E. Lewis, C. M. Geraghty, F. Barbosa and P. J. Parsons, *Spectrochimica Acta Part B: Atomic Spectroscopy*, 2006, **61**, 980-990.
10. A. Montaser and D. W. Golightly, 1987.
11. N. Wangoo, J. Kaushal, K. Bhasin, S. Mehta and C. R. Suri, *Chemical Communications*, 2010, **46**, 5755-5757.
12. A. Sze, D. Erickson, L. Ren and D. Li, *Journal of Colloid and Interface Science*, 2003, **261**, 402-410.
13. C. Sharpec, *Inorganic chemistry*, Pearson education limited, Scotland, fourth edittion, 2012.
14. W. Mäntele and E. Deniz, *Spectrochimica Acta Part A: Molecular and Biomolecular Spectroscopy*, 2017, **173**, 965-968.
15. A. L. Givan, *Methods in Molecular Biology: Flow Cytometry Protocols, TSHaRG Hawley, Editor, Humana Press Inc*, 1992, 1-31.
16. G.-B. Lee, C.-I. Hung, B.-J. Ke, G.-R. Huang, B.-H. Hwei and H.-F. Lai, *Transactions-American Society of Mechanical Engineers Journal of Fluids Engineering*, 2001, **123**, 672-679.

CHAPTER 3

Co-precipitation synthesis of nanoparticles

3 Introduction

3.1 Co-precipitation synthesis of NPs method

Magnetic NPs have been extensively used in various applications such as in catalysis, magnetic fluids and biomedical applications.[1-3] Size and shape are two important factors that affect the magnetic properties of the NPs.[3] Currently, magnetic oxide and fluoride NPs are fascinating, unique and are of significant interest because of their multiple applications, ranging from fundamental research to industrial use.[4] An example of the many types of NPs that are currently gaining much interest are γ-Fe_2O_3, $GdFeO_3$ and KMF_3 (M = Mn, Fe, Co, Ni, Cu) NPs due to their fascinating magnetic, catalytic and optical properties.[5-7] Several methods can be used to synthesize magnetic NPs, such as the sol-gel, hydrothermal, co-precipitation, auto-combustion and aerosolization methods.[8-11] Our NPs were prepared by the co-precipitation method. This method can be affected by many factors such as reaction time, stirring time and type and concentration of alkaline bases used to form the NPs.[12] Controlling these parameters will lead to a single phase and pure NPs. This method is easy, rapid, environmentally friendly and can produces high yields. However, it has many disadvantages that may obstruct the formation of the targeted products such as low degree of crystallinity, broad particles sizes with uninform dispersitivity. Ultimately, these properties could obstruct their use as contrast agents for Magnetic Resonance Imaging (*MRI*) and as carriers for drug delivery. Stability and biocompatibility are other characteristics that make these particles potentially useful for a broad range of applications.[13] Therefore, optimising these factors would result in a highly sensitive probes to be used as contrast agents and drug delivery. In this chapter we aim to prepare different cubic perovskite NPs such as γ-Fe_2O_3, $GdFeO_3$ and KMF_3 (M= Mn, Fe, Co, Ni, Cu) in order to be utilized as contrast agents for Magnetic Resonance Imaging (*MRI*). The formed NPs were first functionalised using organic ligands such as 11-aminoundecanoic acid or sodium alendronate trihydrate to make them biocompatible in aqueous medium and applicable for biological application. The formed NPs were fully characterised using different techniques to examine their stability and their use as contrast agents for Magnetic Resonance Imaging (*MRI*). This involve powder X-Ray diffraction, FT-IR analysis, Nano Tracking Analysis (NTA), thermal gravimetric analysis, Transmission Electron Microscopy (TEM) and Energy Dispersive X-Ray Spectroscopy (EDX).

3.2 Experimental

3.2.1 Synthesis of maghemite (γ-Fe_2O_3) NPs

The synthesis of γ-Fe_2O_3 was performed according to the previously reported method with few modifications.[14]

The synthesis procedure was done according to the following reaction:

$$2\,Fe^{3+} + Fe^{2+} + 8OH^- \xrightarrow{\text{heat}} Fe_3O4 + 4H_2O \qquad \textit{Equation 3-1}$$

$$2Fe_3O_4 + H_2O_2 \longrightarrow 3Fe_2O_3 + H_2O \qquad \textit{Equation 3-2}$$

$FeCl_3$ (0.1662 g, 0001 mol) and $FeCl_2.4H_2O$ (0.099 g, 0.0005 mol) in the ratio of (2:1) were mixed in 50 ml ethylene glycol and heated to 80 °C. A 5 M solution of NaOH (~85 ml) was added dropwise until the pH of the solution reached 10. The beaker containing the solution was placed on a heating plate, the temperature was then increased to 120 °C while the solution was stirred vigorously. After 1 hour, the heat was removed and the solution was cooled to room temperature. 10 ml of hydrogen peroxide solution (H_2O_2: H_2O) in the ratio of (1:1) was then added dropwise to the solution with vigorous stirring. NPs precipitated and were then filtered using a Buchner funnel and washed with warm water before being dried in an oven at 100°C overnight. Finally, the NPs were collected magnetically by placing a magnetic bar underneath the beaker and decanting the liquid.

3.2.2 Synthesis of KMF_3 (M = Mn, Fe Co, Ni, Cu)

3.2.2.1 Synthesis of $KMnF_3$

The following method described below has been modified from the previous report.[15]

$MnBr_2$ (2.405 g, 0.0112 mol) dissolved in 50 ml methanol was placed in a round bottom flask and KF (1.952 g, 0.0336 mol) dissolved in 25 ml methanol was added. The solution was left to stir (20 minutes) and the suspension formed was left overnight to settle. The excess methanol was decanted and the $KMnF_3$ formed was then filtered under vacuum using a fritted funnel and left to dry at room temperature. The sample was then ground and then washed with methanol 3 times followed by 50 ml of water for 10 times.

3.2.2.2 Synthesis of $KCoF_3$

The following method is similar to the method used for the synthesis of $KMnF_3$ NPs, however $CoBr_2$ was used instead of $MnBr_2$.[15]

$CoBr_2$ (2.405 g, 0.0112 mol) dissolved in 50 ml methanol was placed in a round bottom flask and KF (1.952 g, 0.0336 mol) dissolved in 25 ml methanol was added. The solution

was left to stir (20 minutes) and the suspension formed was left overnight to settle. The excess methanol was decanted and the $KCoF_3$ formed was filtered under vacuum using a fritted funnel and left to dry at RT. The sample was then ground and then washed with methanol 3 times followed by 50 ml of water for 10 times.

3.2.2.3 Synthesis of $KFeF_3$

The method used in this experiment was similar to a previously published co-precipitation method and a slight modification has been made.[16]

KF (6.972g, 0.12 mol) was dissolved in a minimum volume of water containing three drops of concentrated nitric acid. This solution was heated on a hot plate to boiling and kept near boiling while a solution of divalent $FeCl_2.4H_2O$ (7.9524g, 0.04 mol) was added dropwise. The divalent iron chloride was made by dissolving $FeCl_2.4H_2O$ (7.9524g, 0.04 mol) in a minimum volume of water. A few additional millilitres of water may be used to wash the last residue of this solution into the fluoride solution. Once all of the chloride solution was added, the beaker was removed from the hot plate, and 30 ml of cool water was added. The precipitate was allowed to settle and the supernatant was decanted and discarded, the solid was washed twice with ethanol, twice with acetone, and 10 times with *HPLC* water. The precipitate was then dried at room temperature.

A modification was done to this preparation method as iron (II) is air oxidized rather readily. This may lead to a problem where oxidation of Fe^{2+} to Fe^{3+} ion during the synthesis may take place. This problem was overcome by adding 75 ml of 0.5 M $SnCl_2$ solution (in 3 M HCl) dropwise to the iron (II) solution until any traces of yellow colour due to iron (III) disappear, leaving clear green iron (II) solution. Then ten drops of excess tin (II) solution were added. Tin (II) may be also added to the fluoride solution to assure that the iron remained in the reduced form. The iron in solid $KFeF_3$ may be oxidized if the solid is wet. To minimize this oxidation the washing was done as rapidly as possible or under an inert atmosphere.

3.2.2.4 Synthesis of $KNiF_3$ and $KCuF_3$

The syntheses of $KNiF_3$ and $KCuF_3$ were carried out using the same method described for $KCoF_3$, however $NiBr_2$ and $CuCl_2$ salts were used for the synthesis of $KNiF_3$ and $KCuF_3$ respectively.

3.2.2.5 Synthesis of $GdFeO_3$

The synthesis of GdFeO3 was performed using the previously published method by Li *et.al.*[17] $GdFeO_3$ samples were prepared by the precipitation method from aqueous

solutions of stoichiometric amounts of $Gd(NO_3)_3.6H_2O$ (1M) and $Fe(NO_3)_3.9H_2O$ (1M). Aqueous 10% wt NH_4OH was used as precipitating medium. To the NH_4OH medium, the aqueous solutions of gadolinium and iron nitrates were added dropwise manner while adjusting the pH value to 8-9 using 1M NaOH. The co-precipitated mixtures were filtered immediately after preparation to remove traces of NO_3^-. $GdFeO_3$ mixture was then dried at room temperature in air and then divided equally into 5 portions. Each mixture portion of $GdFeO_3$ was then pressed and calcined in air individually at 500-900˚C.

3.2.3 Functionalisation of synthesised NPs

3.2.3.1 Direct Functionalisation of Nano-Particles with 11-Aminoundecanoic acid

The method used is same as the previously published method with a slight modification.[18] Prior to the ligand exchange, (0.0102 mg) of the original NPs for each (γ-Fe_2O_3, $KMnF_3$, $KFeF_3$, $KCoF_3$, $GdFeO_3$) solution were washed extensively three times with methanol, and twice each with ethanol and acetone (5 ml each), followed by centrifugation for 5 minutes at 13000 rpm. Finally, the sample was resuspended in THF (4 ml) and mixed with water (4 ml) containing 11-aminoundecanoic acid (50 mg, 0.24 mmol). The solution was stirred for either 48, 24, 2 or 1 hours and then directly centrifuged at room temperature for 5 minutes at 13000 RPM, the supernatant was discarded and the pellet was washed with a 1:1 mixture of THF: water (2 mL THF: 4 ml Water). Following 5 minutes centrifuge spin, the solution was decanted and the pellet was further re-suspended in 2 mL THF: Water until the pellet had been washed with a total of 6 mL THF: Water or until a 15-minute total wash time had been reached. Finally, the solid pellet was transferred onto a watch glass and allowed to dry overnight in a desiccator at room temperature (25°C) ready for PXRD measurements. Each functionalised compound was evaluated by FT-IR (600 cm^{-1}- 4000 cm^{-1}) using Dimond ATR, TEM, NMR and Nano Tracking Analysis.

Figure 3-1 illustrates the ligand exchange process *via* 11-aminoundecanoic acid ligand.

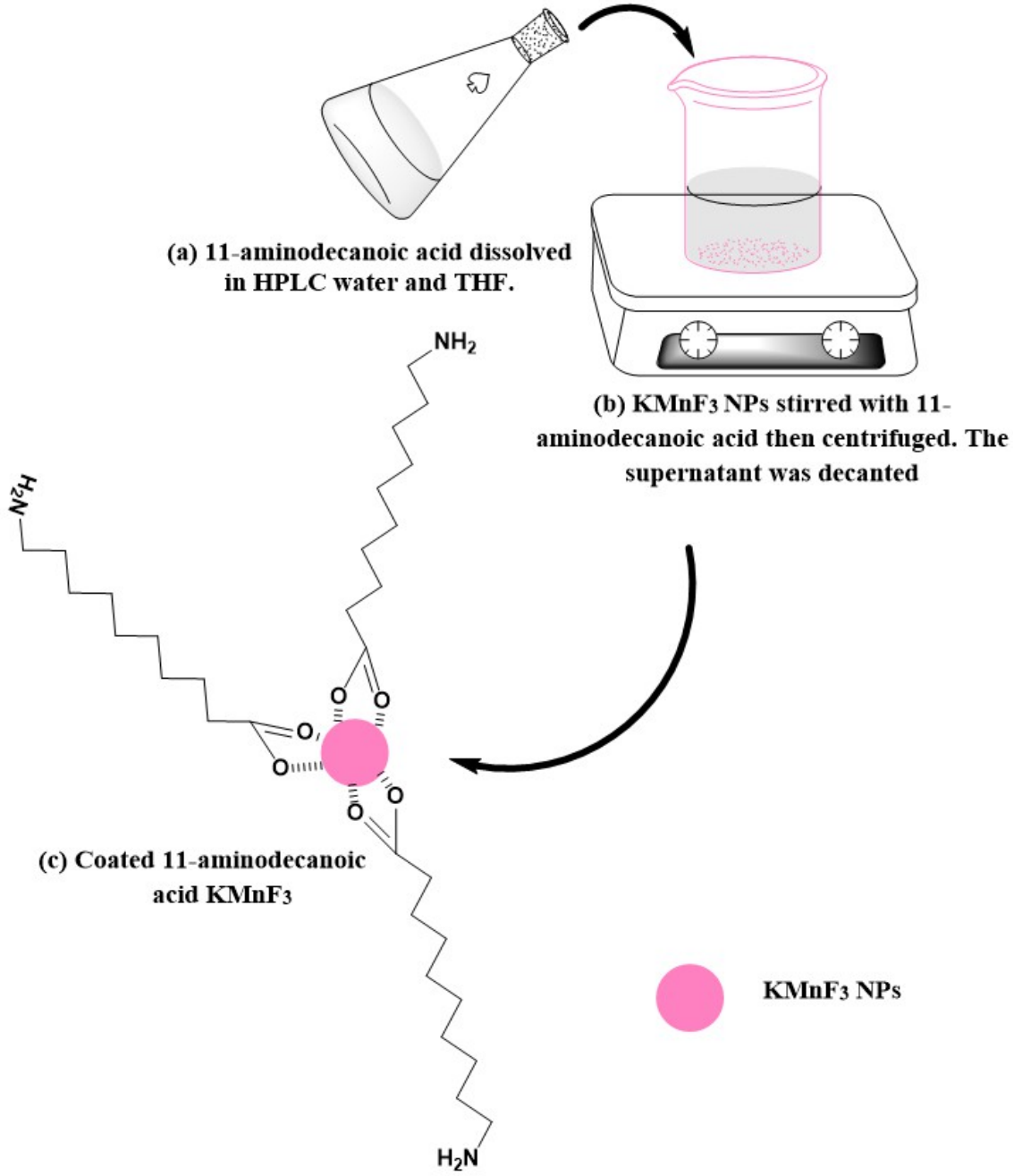

Figure 3-1: Different steps involved in the synthesis and functionalisation of KMF_3 NPs with 11-aminoundecanoic acid ligand.

3.2.3.2 Direct Functionalisation of Perovskite Nano-particles with sodium alendronate tri hydrate ligand

0.012g of the KMF_3 sample was suspended in THF (4mL). In a separate flask, 0.05g of sodium alendronate tri-hydrate was dissolved in water (4mL) using a magnetic stirrer and the pH was adjusted to 9 with 1M potassium hydroxide. The ligand solution was added

to the solution with the KMF_3 sample and THF and left to stir at room temperature for either 48, 24, 2 or 1 hour. The formed solution was centrifuged for 10 minutes at room temperature. The unwanted supernatant was discarded and the pellet was washed with acetone (max 10 ml broken down into 2ml per centrifuge spin). Using 1M KOH, the pH of the formed solution was checked and adjusted to ensure that it remained at pH 9. As a final stage, the solid pellet was transferred onto a watch glass and allowed to dry in a desiccator overnight at room temperature (25°C). This solid was scanned using Powder X-ray Diffraction (PXRD). Each functionalised compound was evaluated by FT-IR (600 cm^{-1} - 4000 cm^{-1}) using a Diamond ATR, TEM and Nano Tracking Analysis (NTA). Figure 3-2 represents a schematic diagram for this functionalisation method.

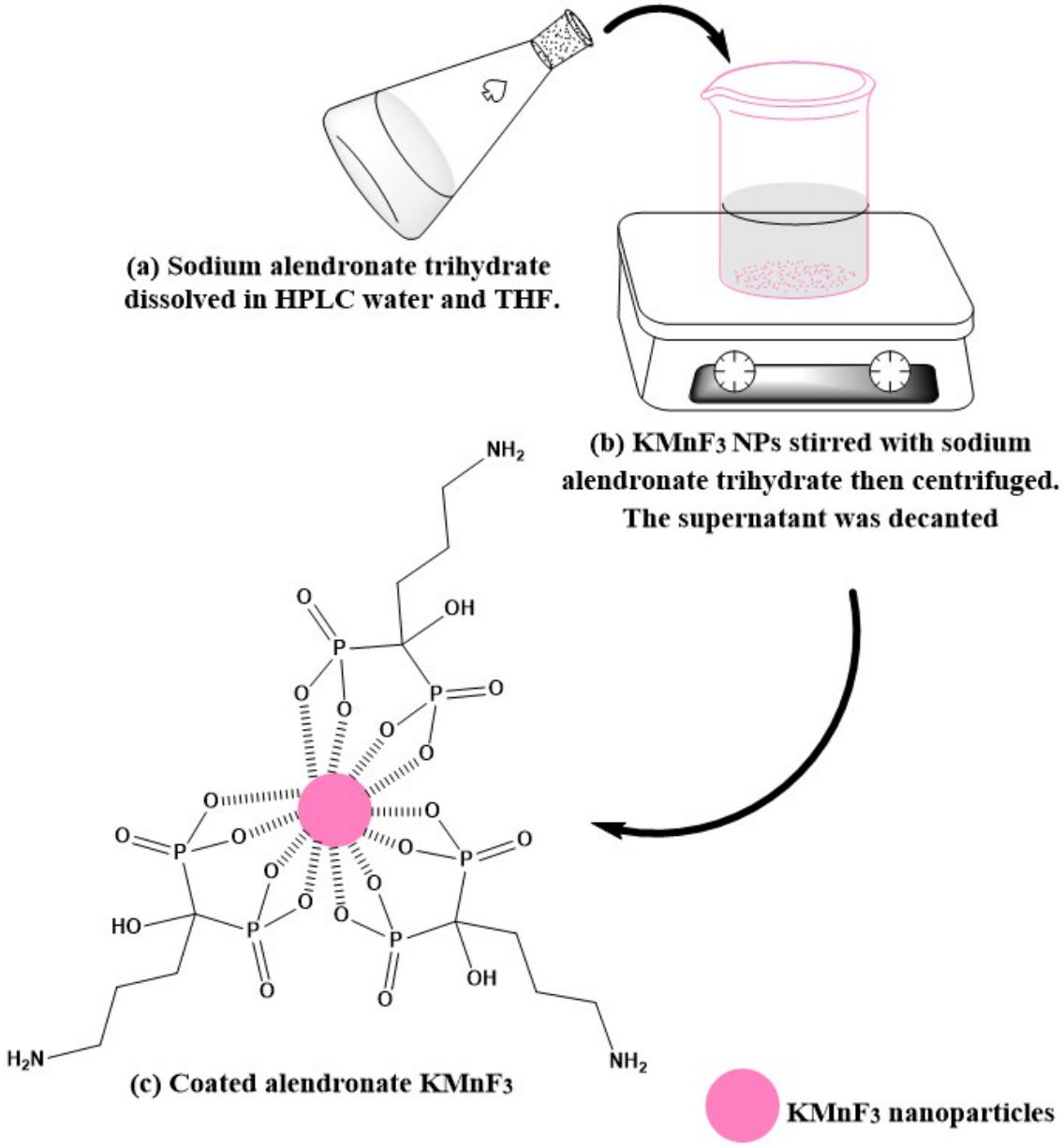

Figure 3-2: Different steps involve in the synthesis and functionalisation of KMF_3 NPs with sodium alendronate trihydrate ligand.

3.3 Results and Discussion

3.3.1 Co-precipitation synthesis of γ-Fe_2O_3 NPs

3.3.1.1 Powder X-ray diffraction (PXRD)

Synthesis of γ-Fe_2O_3 was carried out to obtain a good standard for magnetic NPs. Synthesis and functionalisation of γ-Fe_2O_3 have been reported in previous studies.[14]

The purity and the crystalline structure of the γ-Fe_2O_3 was characterised by Powder-X-ray diffraction. PXRD measurement for maghemite NPs compared to the bulk γ-Fe_2O_3 is shown in

Figure 3-3. All diffraction peaks correspond to the γ-Fe_2O_3 crystalline planes (hlk) (220, 311, 222, 400, 422, 511, 440 and 531) were observed and they are consistent with the standard structure of maghemite.[19] The unit cell parameter was found a = 8.338(2) Å corresponding to cubic spinel structure of γ-Fe_2O_3 as shown in Figure 3-4. [20] This confirms that the obtained NP is γ-Fe_2O_3 and not Fe_3O_4, which has trigonal unit cell structure.

Traditionally magnetite NPs are transformed to γ-Fe_2O_3 by using hydrogen ferric nitrate at 100°C because maghemite has similar magnetic properties to magnetite and better stability[21]. In this experiment H_2O_2 was used as an oxidizing agent to transform all Fe^{2+} to Fe^{3+}. The addition of (1:1) hydrogen peroxide: water dropwise to the reaction mixture under vigorous stirring causes the colour of the powder change from black to brown indicating the phase transformation from Fe_3O_4 to γ-Fe_2O_3.

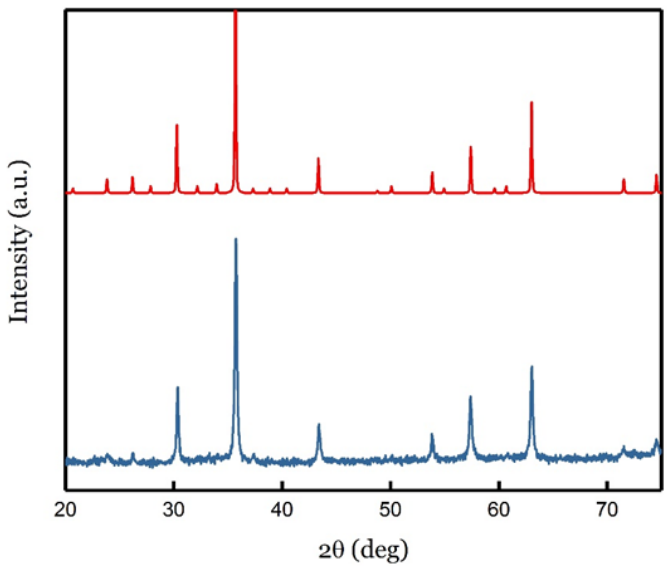

Figure 3-3: PXRD pattern of γ-Fe_2O_3 (blue) compared to the model (red)

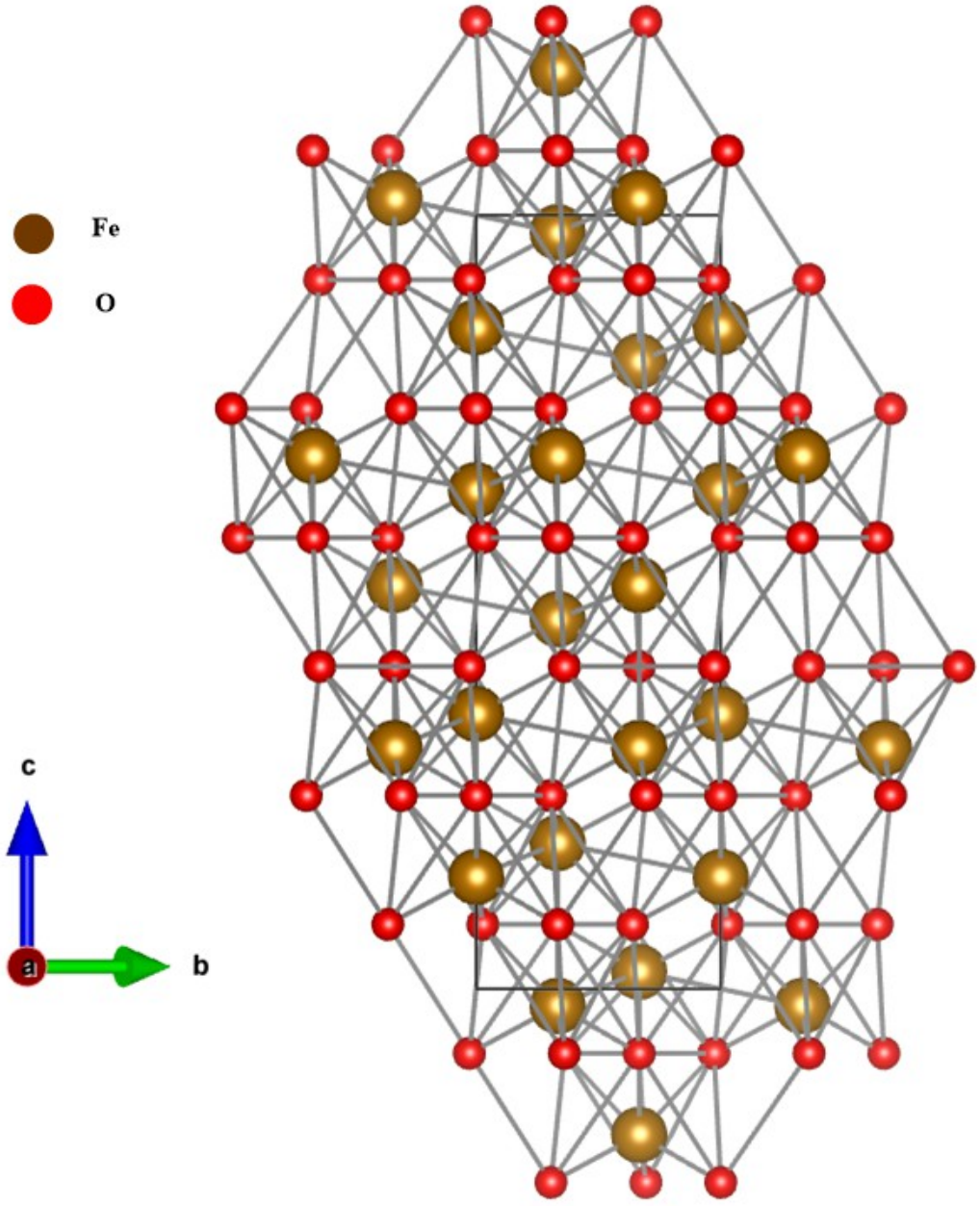

Figure 3-4: Unit cell of spinel cubic maghemite structure [22]

ICP analysis showed that the formed γ-Fe_2O_3 contains 55.60% iron with a contamination of Na (1.84%), detected. This value is lower than the theoretical value (~70%), indicating the existence of impurities. Most studies did not show the exact contents of iron in γ-Fe_2O_3, however the iron content of two samples of maghemite NPs after being functionalised by polyrhodanine ligand was measured in a previous study by ICP-OES and found 4.15 and 4.219 %.[23]

Figure 3-5 represents the FT-IR spectrum of the prepared γ-Fe_2O_3 NPs. FT-IR analysis reveal that the γ-Fe_2O_3 was successfully synthesised. The absorption band at 900 cm^{-1} can be assigned to vibration of the Fe-O functional group. In addition, the two peaks at about 3420 cm^{-1} and 2362 cm^{-1} come from the hydroxyl group (OH^{-1}) and (CO_2) that might be present in the atmosphere. The peak at 1663 cm^{-1} is related to hydroxide group that is attached to the surface of the material.[24]

The morphology and average particle size were investigated with transmission electron microscope. Figure 3-6 shows the TEM images of γ-Fe_2O_3 NPs at different parts of the images. It shows somewhat irregularly shaped particles from spheres to more oval in shape and narrow size distribution of γ-Fe_2O_3. The average size of NPs is 5 nm. This value is smaller than the value reported in previous study for the bare single phase γ-Fe_2O_3 (13 nm).[14] Agglomeration of the NPs was observed. This agglomeration phenomenon occurs due to the increase in the large ratio of surface area to volume, therefore the attractive force between the NPs increases, hence agglomeration of the NPs take place[25]. To examine the validity of TEM result, this particles size of γ-Fe_2O_3 was also determined by NTA as seen in Figure 3-7 and found to be 42 nm, the difference in size compared to the value of average diameter size obtained by TEM analysis is attributed to the higher degree of agglomeration. From Figure 3-7, it can be seen that almost mono dispersed crystal particles were obtained in some parts of the tested sample.

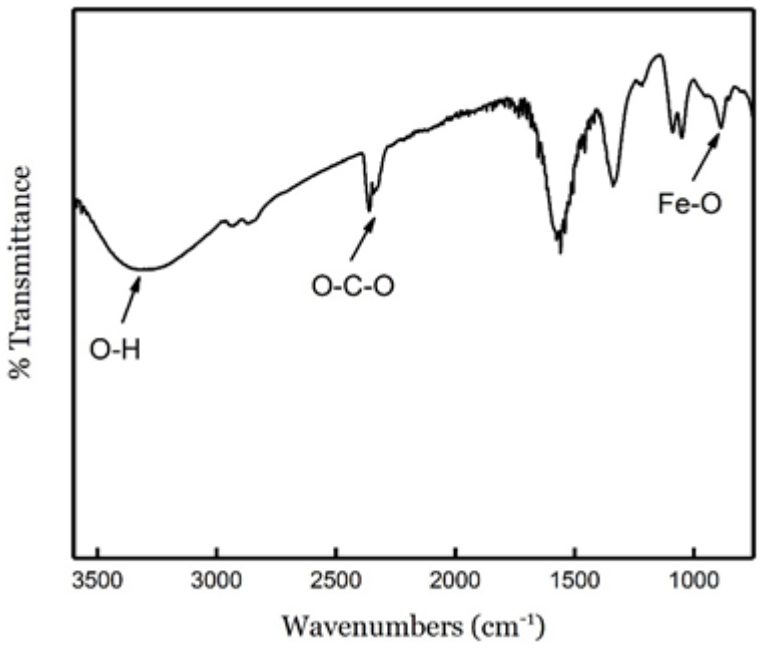

Figure 3-5:FT-IR spectrum obtained for γ-Fe_2O_3 NPs.

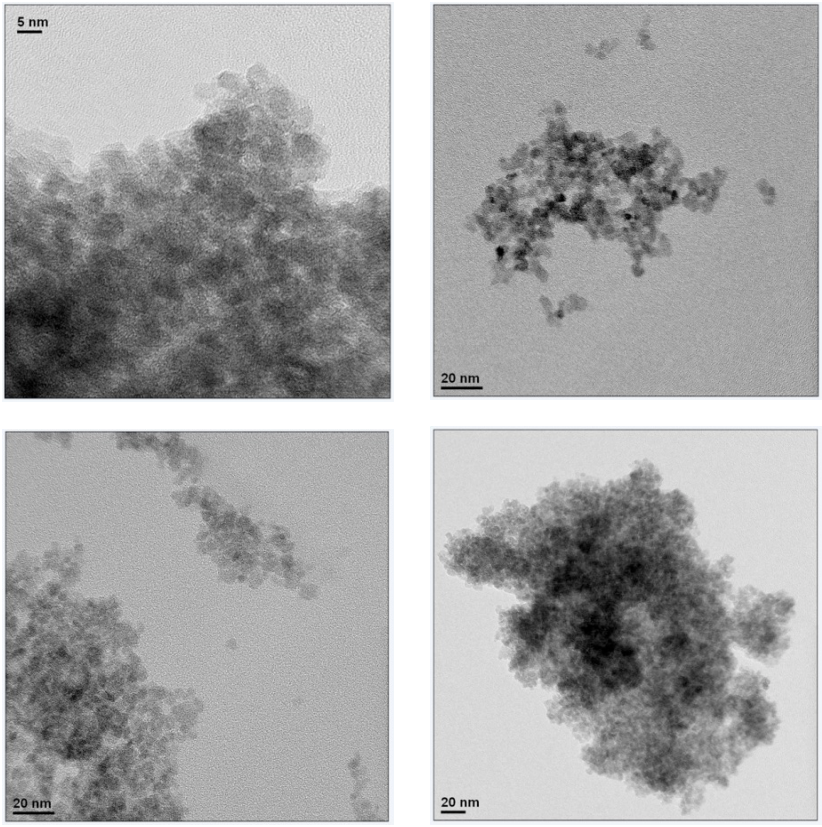

Figure 3-6: TEM images of the γ-Fe_2O_3 NPs with the diameter of ca. 5 nm obtained in the absence of 11-aminoundecanoic acid or sodium alendronate ligands

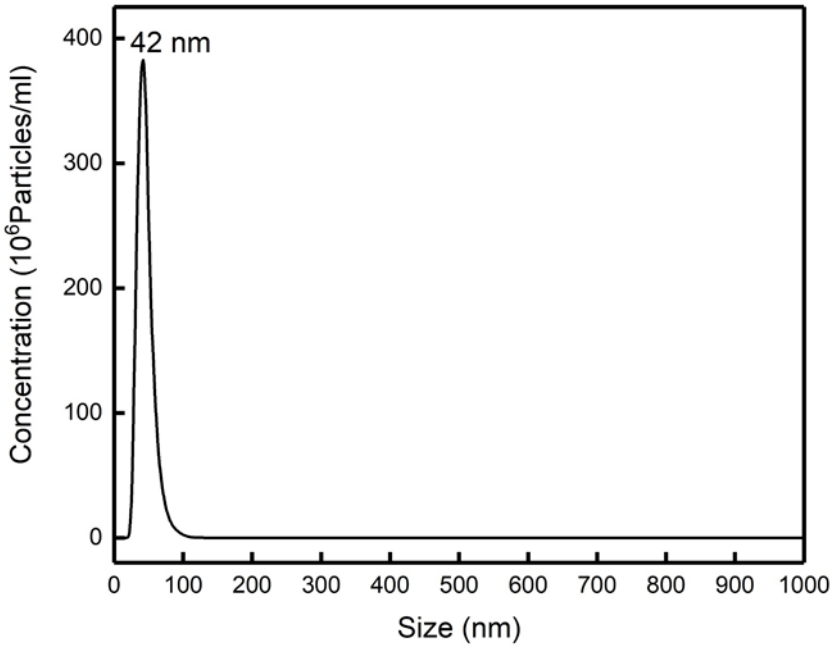

Figure 3-7: Crystal size vs concentration plot obtained by Nano Tracking Analysis (NTA) for bare γ-Fe_2O_3 NPs.

3.3.2 Synthesis of perovskite KMF_3, where M = Mn, Fe, Co, Zn, Cu and Ni

The procedure employed in the synthesis of the fluoride perovskites is similar to the literature co-precipitation method.[26] Deficiency in potassium and fluoride is one of the main problem in the formed product.[27] During synthesis, excess KBr was observed and it was difficult to get a single phase structure. To remove the excess KBr, the formed NPs were washed with a large volume of *HPLC* water. A similar problem of a high percentage of KCl in the synthesis of perovskite fluoride was reported by Richard et al.[27] In addition. The same previous study has mentioned that this method tends to produce Iron (III) contamination with the formed $KFeF_3$ NPs. It is possible to produce pure materials by different methods, however the employed methods are, in general time consuming, fairly extreme, have severe hazards and are susceptible to explosion.[27] The ICP analysis confirmed the theoretical stoichiometric ratio for $KFeF_3$ [K(0.62 mol) : (Fe (0.65 mol)], $KMnF_3$ [K(0.80 mol) : Mn(0.62 mol)], $KCoF_3$[K(0.55 mol : Co(0.57) and $KZnF_3$ [K(0.76) : Zn(0.80)] the obvious variation in the ratio of K and Mn elements might be attributed to the present of KBr contamination.[28] Reducing oxidized iron impurities using the modified method to form $KFeF_3$ seems to be very effective. $Sncl_2$ was used to reduce any possible reduction Fe^{3+} to Fe^{2+} ions, so that all iron ions must be in the Fe^{2+} oxidation state. However, there was a little contamination by tin (0.5 %, 0.004 mol)). The reasons for selecting non-aqueous media for the synthesis of KMF_3 (where M = Mn, Fe, Co, Zn,

Cu and Ni) were for safety issues as well as to reduce the loss of fluoride contents during synthesis in order to make them suitable for biological application.

Usually $KFeF_3$ is very light tan in colour, the change in its colour to brown is an indication for an oxidation process. The other compounds do not seem to vary in colour, $KMnF_3$ is very light pink, $KCoF_3$ is bright pink, $KZnF_3$ is colourless and $KCuF_3$ is light green.[12] Figure 3-8 represents the different colours of the investigated NPs dispersed in methanol. Furthermore, problems may also arise in the synthesis if the solutions are not saturated, if the heating is continued very long after the last of the chloride solution has been added or if there is high volume of acid.[26] A study showed that the manganese compound tends to hydrolyse during its synthesis by this method,[26] however such a problem did not appear to arise. In addition, the oxidation process of the final dry $KFeF_3$ was very slow, and did not encountered any problem.

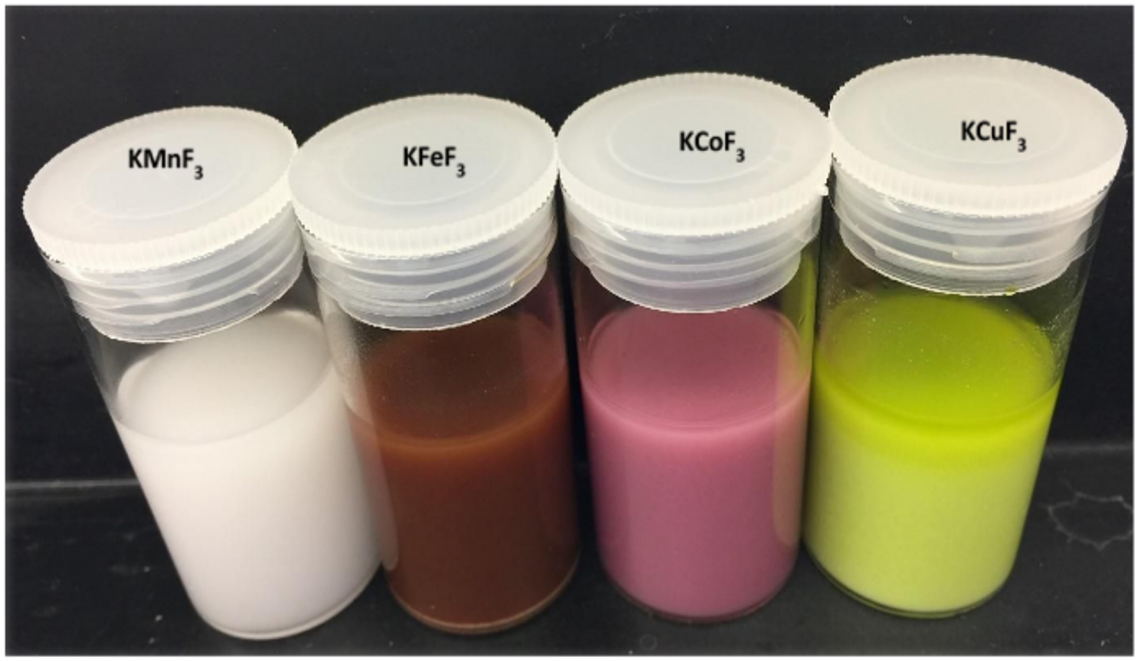

Figure 3-8: Suspension of the prepared NPs in water filtered under vacuum.

It was noticed when NPs were filtered and then washed with THF and acetone, a KBr layer was formed after centrifugation, as shown in Figure 3-9. KBr salt is insoluble in organic solvents, therefore it was important to wash with *HPLC* water several times to dissolve KBr in order to obtain a pure single-phase nanoparticle. Figure 3-10 Shows samples after washing.

Figure 3-9: Picture taken for $KCoF_3$ NPs after washing with methanol where white layer of KBr was formed

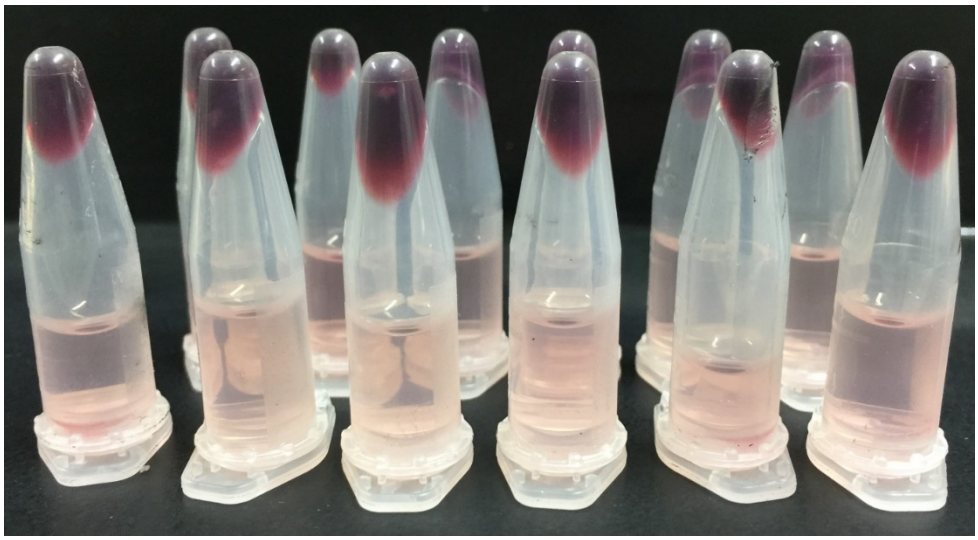

Figure 3-10: Picture taken for $KCoF_3$ NPs after washing with HPLC water indicating the removal of KBr layer

3.3.2.1 Powder X-ray Diffraction of ternary fluorides compounds of KMF_3 (where M =Mn, Fe, Co and Zn)

Figure 3-11 to Figure 3-16 represent the Powder X-ray diffraction patterns of KFM_3 (M = Mn, Fe, Co, Zn, Ni and Cu) respectively.

Figure 3-11Figure 3-11 to Figure 3-15 reflect the cubic structure of KMF_3(M= Mn, Fe, Co, Zn and Ni respectively, whereas Figure 3-16 reflects the structure of $KCuF_3$ which possesses a trigonal distorted structure due to the Jahan Teller effect, the unit cell constants of the ternary fluoride structures obtained from PXRD analysis were (4.1843(3), 4.153(2) , 4.056(2), 4.058(2) Å for $KMnF_3$(00-017-0116), $KFeF_3$(01-072-0110), $KCoF_3$(00-072-1000) and $KZnF_3$(01-078-1962) respectively and they agreed well with the reported values of their bulk material.[27, 29, 30] whereas the PXRD patterns for $KNiF_3$ and $KCuF_3$ did not match with their bulk patterns available in the literature. [31] This could be attributed to the unknown impurities detected in their compositions. Another reason for not obtaining the single-phase structure for $KNiF_3$ and $KCuF_3$ could be the use of $NiCl_2$ and $CuCl_2$ as a starting material instead of $NiBr_2$ and $CuBr_2$. Due to the above reasons, $KCuF_3$ and $KNiF_3$ NPs will not discussed any further in this chapter.

The PXRD patterns demonstrate that all the typical peaks belong to KMF_3 have appeared for $KMnF_3$, $KFeF_3$, $KCoF_3$ and $KznF_3$, indicating that each sample of the NPs is in its single phase and no peaks belonging to other compounds could be recognized. All peaks of hkl values (100, 110, 111, 200, 210, 211, 220 and 310) have appeared, indicating primitive lattice types.

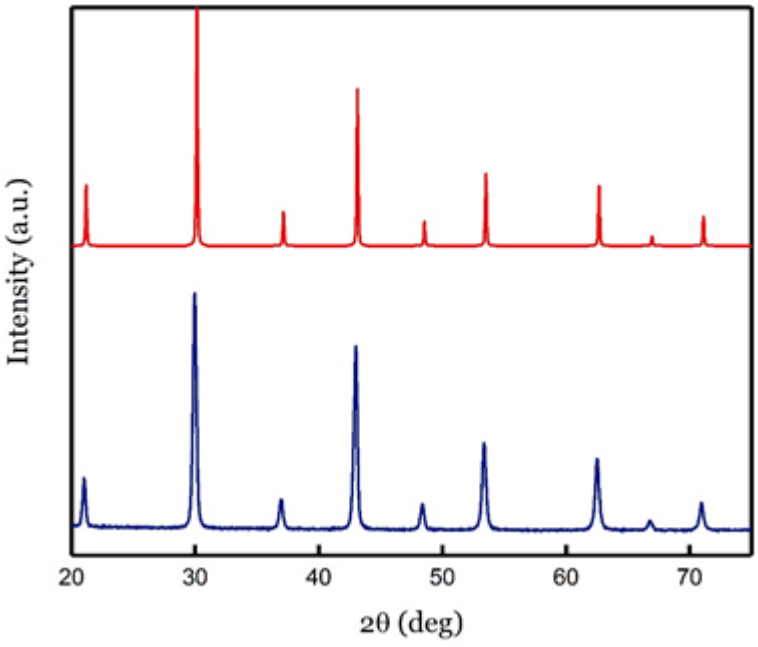

Figure 3-11: Powder X-ray diffraction patterns of the prepared unfunctionalised $KMnF_3$ NPs compared (blue) to the standard bulk $KMnF_3$ (red).

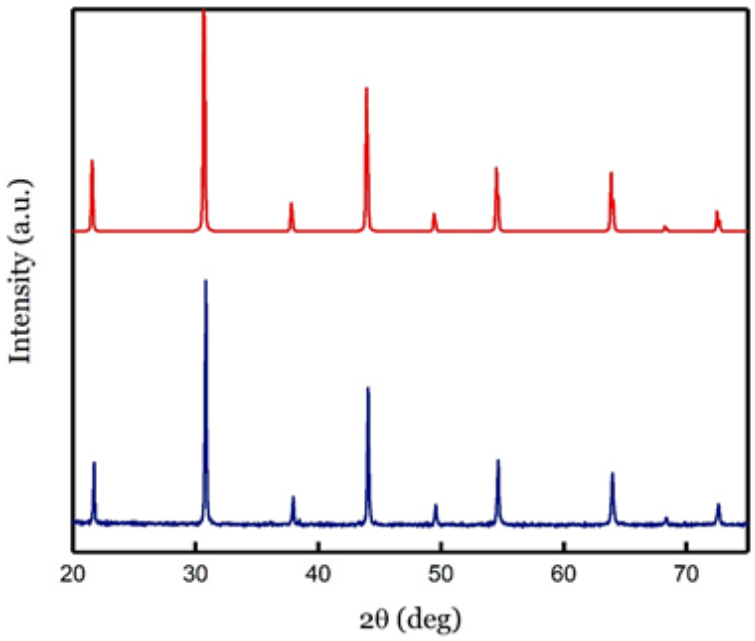

Figure 3-12: Powder X-ray diffraction patterns of the prepared unfunctionalised $KFeF_3$ NPs compared to the standard bulk $KFeF_3$.

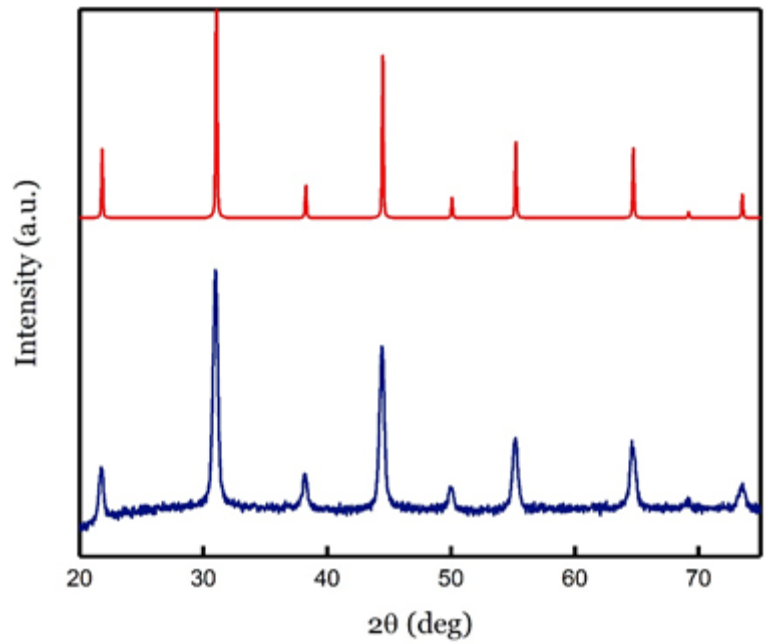

Figure 3-13: Powder X-ray diffraction patterns of the prepared unfunctionalised $KCoF_3$ NPs compared to the standard bulk $KCoF_3$.

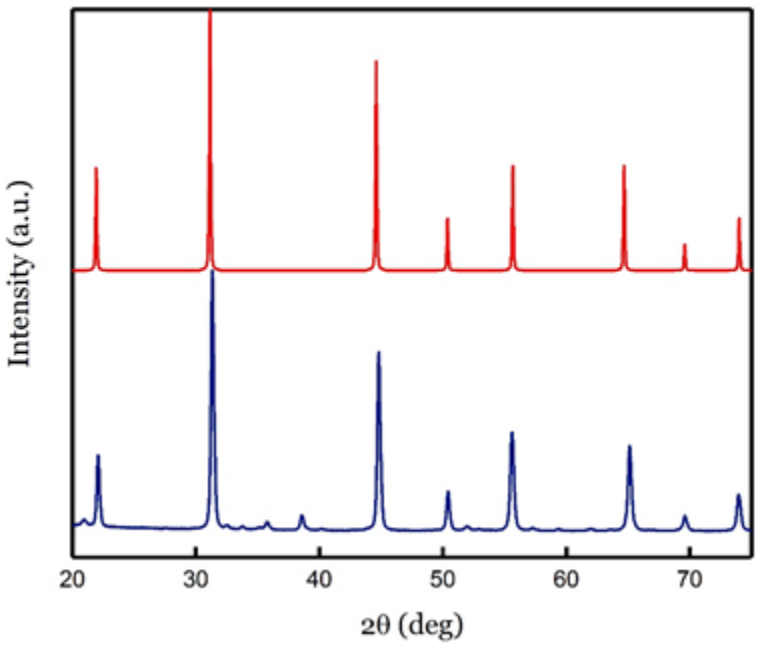

Figure 3-14: Powder X-ray diffraction patterns of the prepared unfunctionalised $KZnF_3$ NPs compared to the standard bulk $KMnF_3$

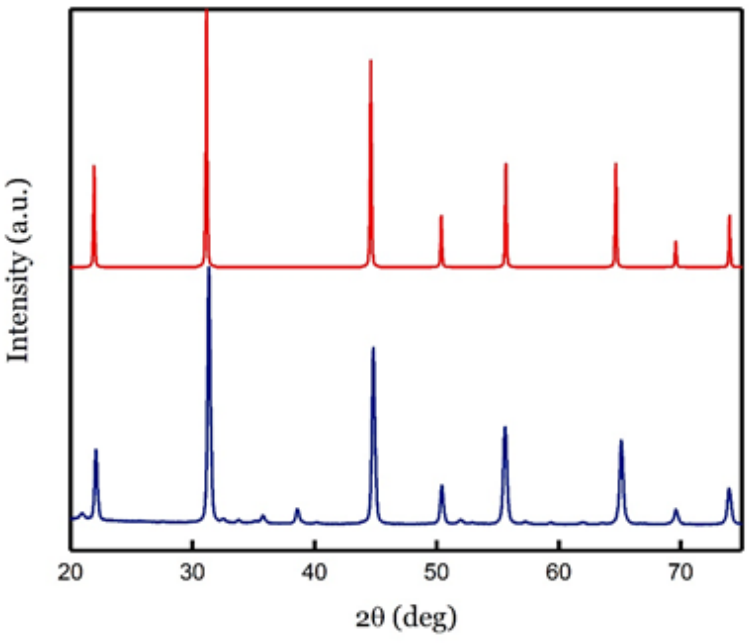

Figure 3-15: Powder X-ray diffraction patterns of the prepared unfunctionalised $KNiF_3$ NPs compared to the standard bulk $KNiF_3$.

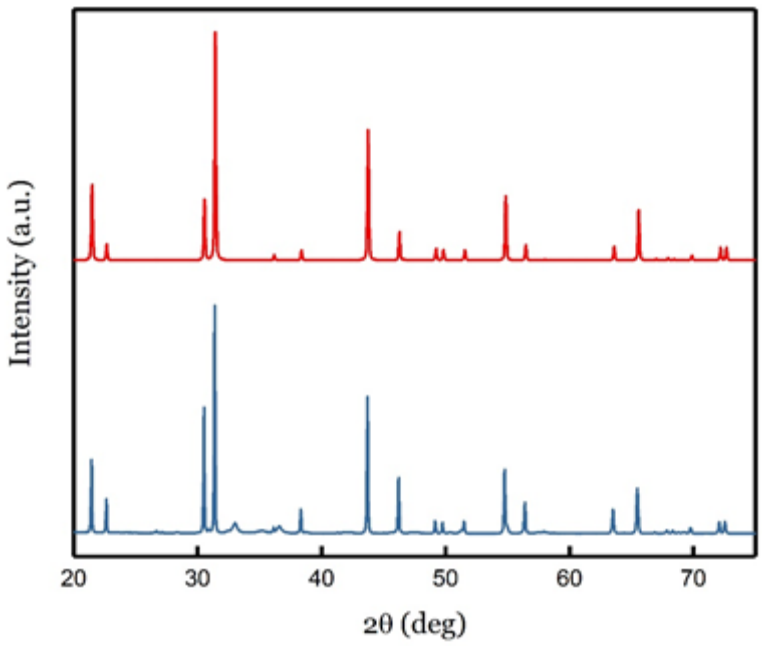

Figure 3-16: Powder X-ray diffraction patterns of the prepared unfunctionalised $KCuF_3$ NPs compared to the standard bulk $KCuF_3$.

Cu K-alpha of wavelength 1.54056 Å is the most widely used anode to produce X-rays in diffractometers, because the wavelength of Copper K-alpha radiation is intense, monochromatic and is of the order of the lattice spacing found in crystalline solids to produce efficient diffraction pattern. However, samples that are rich in Fe, Mn, Cr will fluoresce under the incident Cu Ka beam and create polychromatic radiation. This leads to strange shaped and elevated backgrounds affecting the PXRD pattern. To solve this problem a nickel filter was used. The main purpose of the nickel filter used is to remove Kβ wavelength and decrease the effect of high fluorescence that might Mn, Fe Co or Zn demonstrate. The average crystal's size for $KMnF_3$ and $KFeF_3$, $KCoF_3$ and $KZnF_3$ were measured using 3 different instruments, Transform Electron Microscopy (TEM), Powder X-ray diffraction (PXRD) and Nano Tracking Analysis (NTA). Figure 3-17 shows a comparison in the average crystal's size for each nanoparticle compound obtained by these three techniques. The results obtained were comparable and almost same. The observed slight variation in the crystal size could be attributed to the nature of the dispersive medium in the sample or to the formation of aggregation.

Transmission Electron Microscopy (TEM), Dynamic Light Scattering (DLS) and Nano Tracking Analysis (NTA) are some of the techniques that have been used to measure dispersity, size and shape from a suspension of particles. Some of these are cost effective and user friendly while others are time consuming and labour intensive. The most common used and user friendly for the measurement of NP size is DLS.[32] This technique

measures the crystal size based on the fluctuations in the scattered light intensity due to the movement of NP under Brownian motion. However, the analysis is assessed towards larger particle size that is formed due to aggregates which bias the particle size distribution. Therefore, inaccurate size measurement would be obtained. Using NTA that has lower concentration detection limit in comparison with DLS which measures the particle size on the basis of particle by particle, offer a significant method for characterisation and visualisation of NPs in suspension. Figure 3-18 illustrates the plots of crystal size as a function of intensity for the prepared NPs. It is clear from these graphs that the higher majority of the particles are mono dispersed in the aqueous medium, despite using the co-precipitation synthesis method. In addition, a smaller degree of agglomeration was observed and this was attributed to the physical and chemical nature of the NPs.

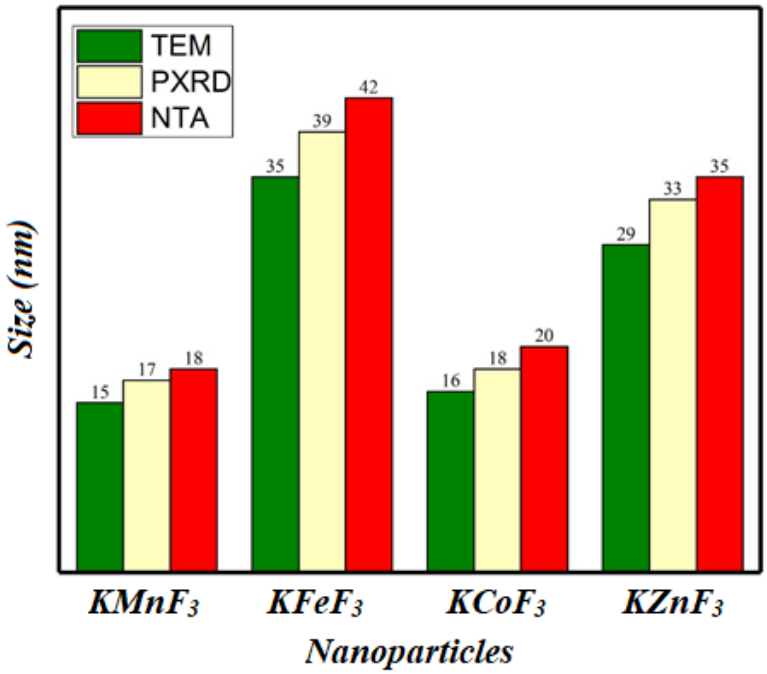

Figure 3-17: Estimation of crystal size of the synthesised Nano particles using 3 different techniques.

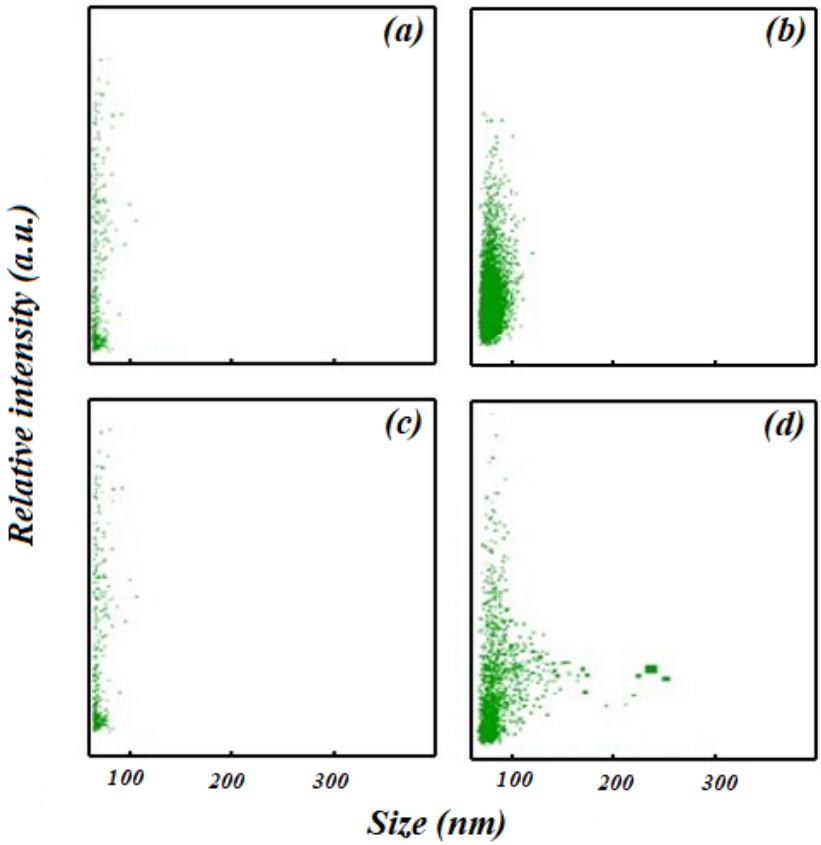

Figure 3-18: Crystal size vs relative intensity plots obtained by Nano Tracking Analysis (NTA) for bare synthesised NPs. (a) $KMnF_3$, (B) $KFeF_3$, (c) $KCoF_3$ and (d) $KZnF_3$

Figure 3-19 displays the TEM images obtained for the prepared NPs. Clearly, the particles within the molecules are clustered together. This is as expected to the perovskites being attractive and thusly being hard to separate due to agglomeration. It was unrealistic to measure the size of the particles from TEM for some images as the particles were 'clustered together'. The images do demonstrate that the particles size appears to be uniform and the morphology is roughly cubic. A study has demonstrated that, $KMnF_3$ or $KCoF_3$ prepared or washed by distilled water contained hydroxyl, oxy groups or the hydrates.[28] EDX analysis was carried out for all synthesised NPs and the estimated elemental composition for each compound is illustrated in Figure 3-20.

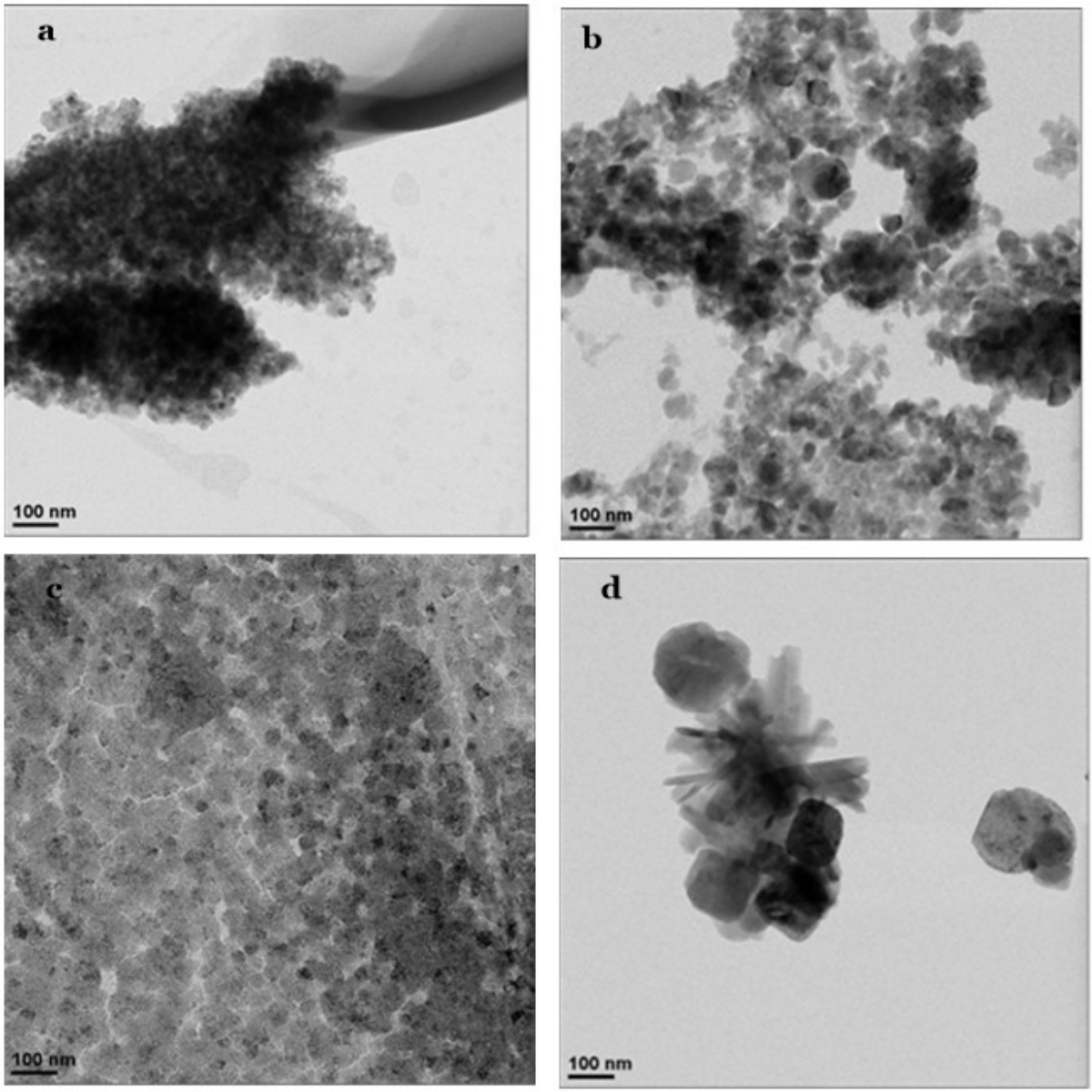

Figure 3-19: TEM image obtained for: (a) $KMnF_3$, (b) $KFeF_3$, (c) $KCoF_3$ and (d) $KZnF_3$.

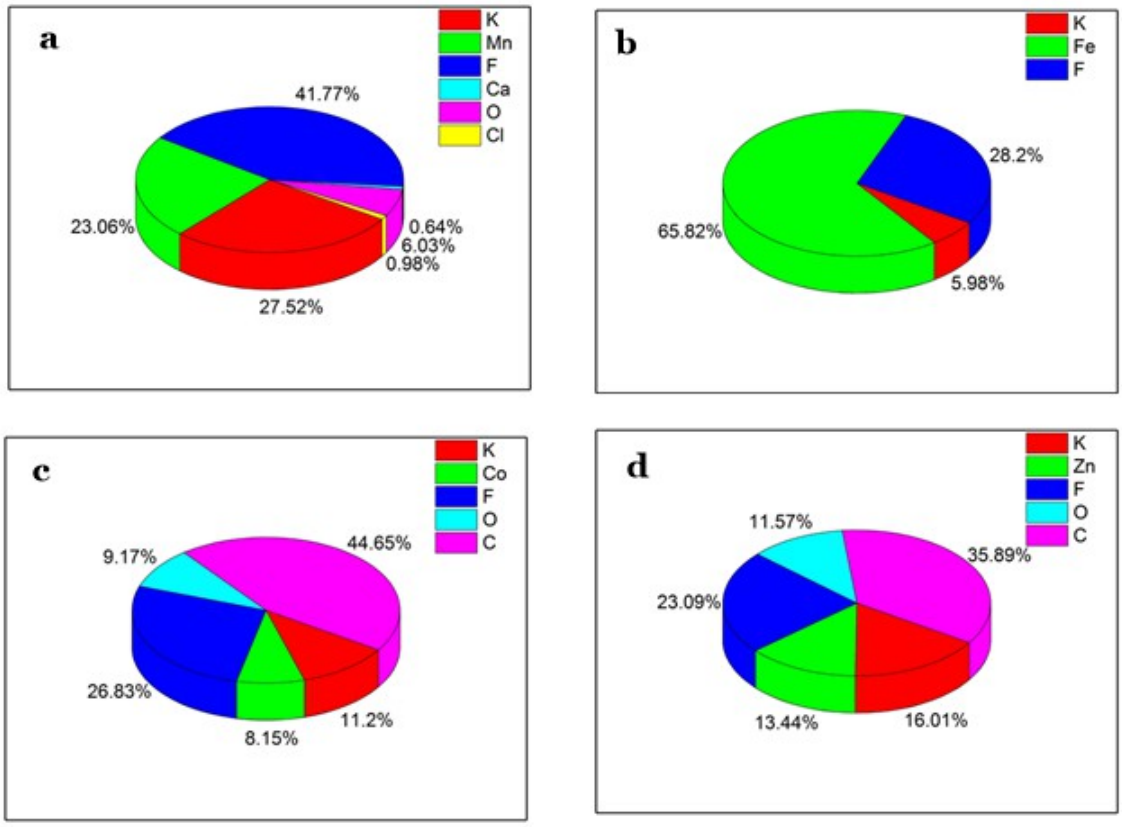

Figure 3-20: Atomic % of elemental composition obtained by EDX for bare NPs(a) $KMnF_3$, (b) $KFeF_3$, (c) $KCoF_3$ and (d) $KZnF_3$.

As can be seen in Figure 3-20, the potassium and M (M = Mn, Fe, Co, Zn) atomic percentages in $KMnF_3$, $KFeF_3$, $KCoF_3$ and $KZnF_3$ are different and do not matches with the theoretical values for these compounds, however the atomic % of the fluorine has the higher atomic percentage. This was unexpected for the chemical stoichiometric ratio of the compounds. This indicates that the theoretical stoichiometric ratio was not obtained, it could be attributed to the EDX technique, where it is only able to provide localised information on the sample that may not be representative of the whole sample or it might be due to the wrong positioning of the sample in the instrument chamber, where sample should be totally flat to get precise measurements.

The elemental composition of the bare NPs was further investigated quantitatively with the Inductively Coupled Plasma spectroscopy (ICP), where different elemental standards were used. This is to confirm the validity of the EDX data. The results obtained in Figure 3-21 confirmed the expected stoichiometric ratio of the prepared compounds and contradict the previously obtained results by EDX. The amount of the tin associated with

the reducing agent used in the synthesis of $KFeF_3$ was only 0.5%. Further analysis is needed to confirm the accuracy of the EDX measurements for the fluoride ion.

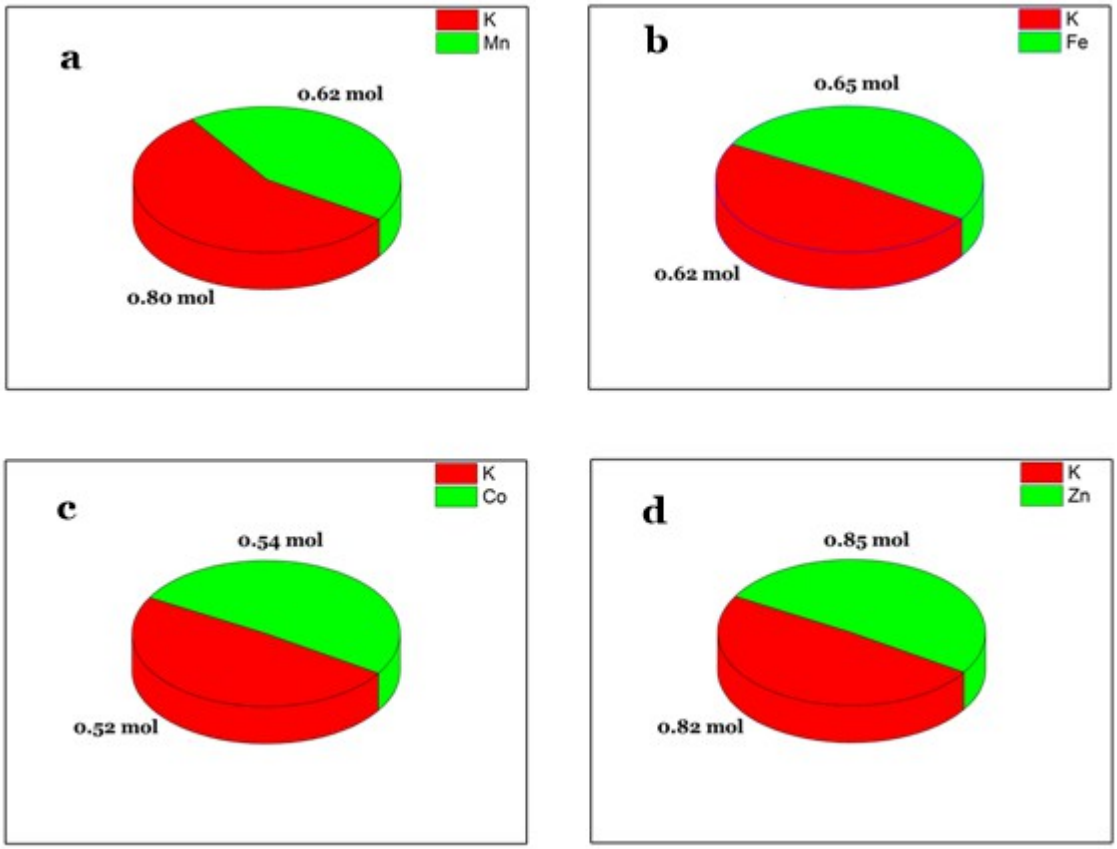

Figure 3-21: Elemental composition obtained by ICP analysis for all bare NPs (a) $KMnF_3$, (b) $KFeF_3$, (c) $KCoF_3$ and (d) $KZnF_3$

The ideal cubic perovskite structure for KMF_3 (M = Mn, Fe, CO, Zn) is displayed in Figure 3-22. Furthermore, the prepared NPs were analysed by Far infrared analysis and their IR spectra are displayed in Figure 3-23 to Figure 3-26. They all show 3 absorption bands as expected for cubic perovskite structures, these bands were found in good agreement with previous results.[33, 34] In this previous study, it was reported that the IR spectra of cubic perovskite should consist of an octahedral stretching vibration v_3 (which can be assigned to the highest frequency band, an octahedral bending vibration V_4 (middle frequency band), and a translation of the octahedral vs the 12-coordinated cation (lowest frequency band). The highest band at (400-500 cm^{-1}) is assigned to M-F stretching mode, in which F^- ions displace along the M-F-M line, whereas the second band at (200-300 cm^{-1}) is assigned to the M-F bending mode in which F^- ions displace perpendicular to the M-F-M line. The longest one is belong to the K^+ ions displaces relative to the consisting of the M^{2+} and F^- ions.[34]

In comparison to the FIR of $KMnF_3$, $KCoF_3$ and $KZnF_3$, the Far Infrared spectrum of $KFeF_3$ in Figure 3-24 showed a slight shift to higher wavenumbers (lower frequency), this could be due to the difference in the electronic configurations or ionic size between iron and manganese. Furthermore, a slight defect from the ideal perovskite structure could also be the reason for the observed shift for the $KFeF_3$ NPs, however a further work is needed to investigate the case.

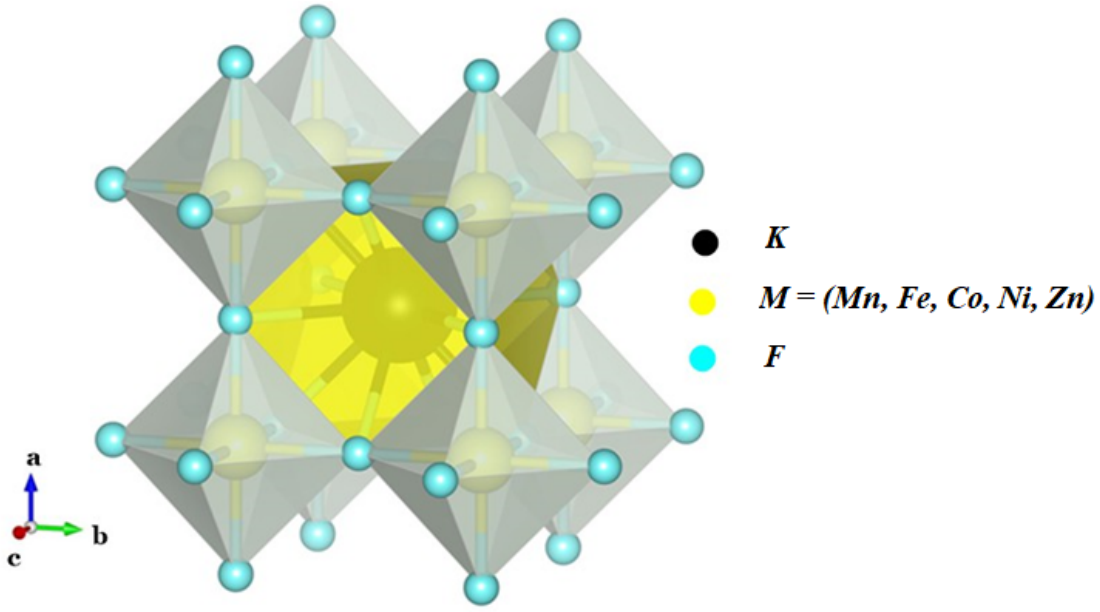

Figure 3-22 : Ideal cubic unit cell of the perovskite structure of KMF_3 where M = Mn, Fe, Co, Ni, Cu and Zn.

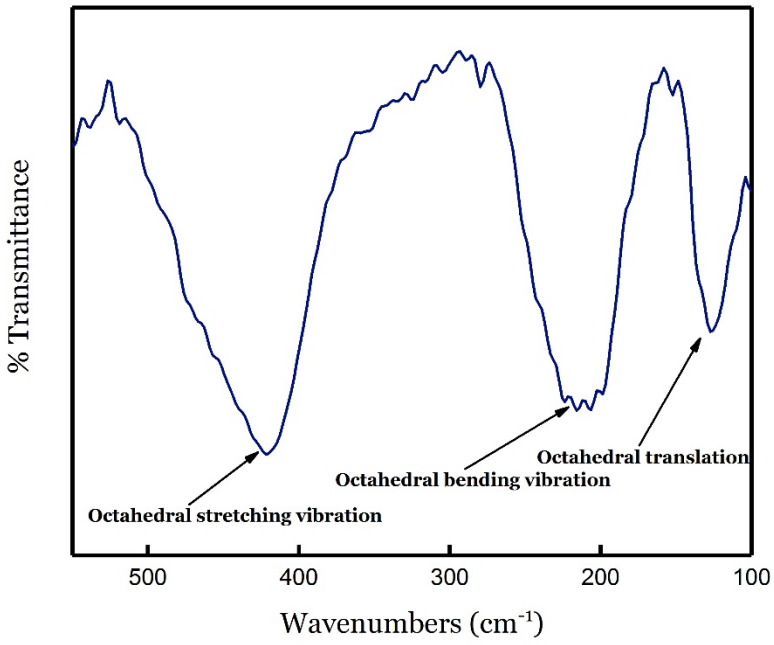

Figure 3-23: FIR spectrum of bare $KMnF_3$.

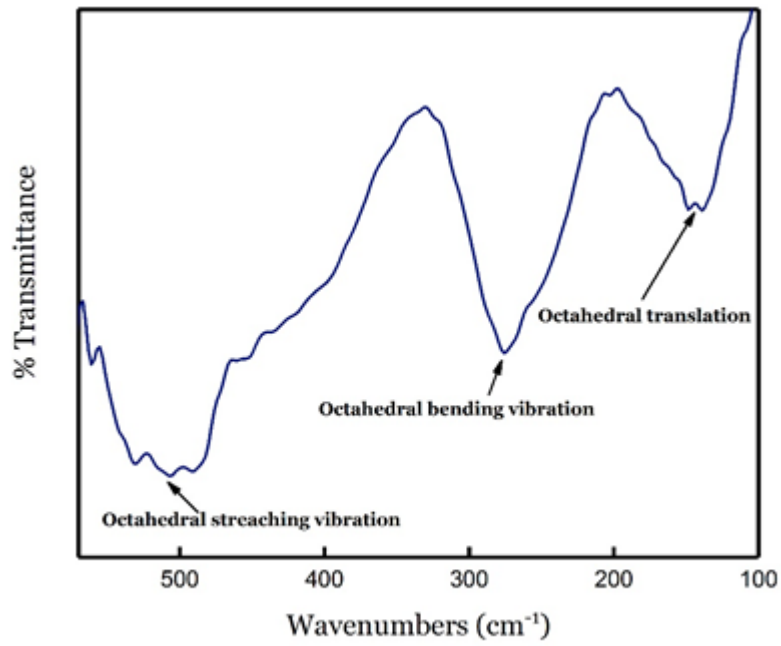

Figure 3-24: FIR spectrum of bare $KFeF_3$.

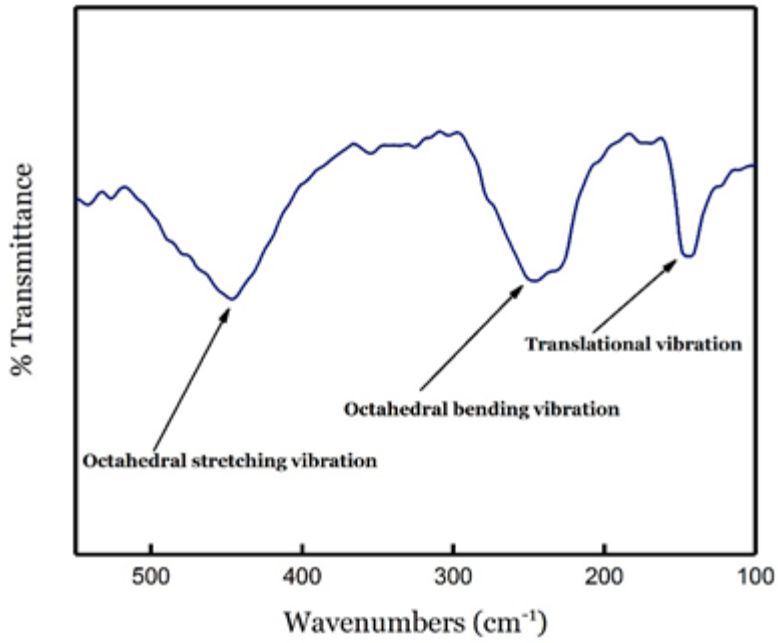

Figure 3-25: FIR spectrum of bare $KCoF_3$.

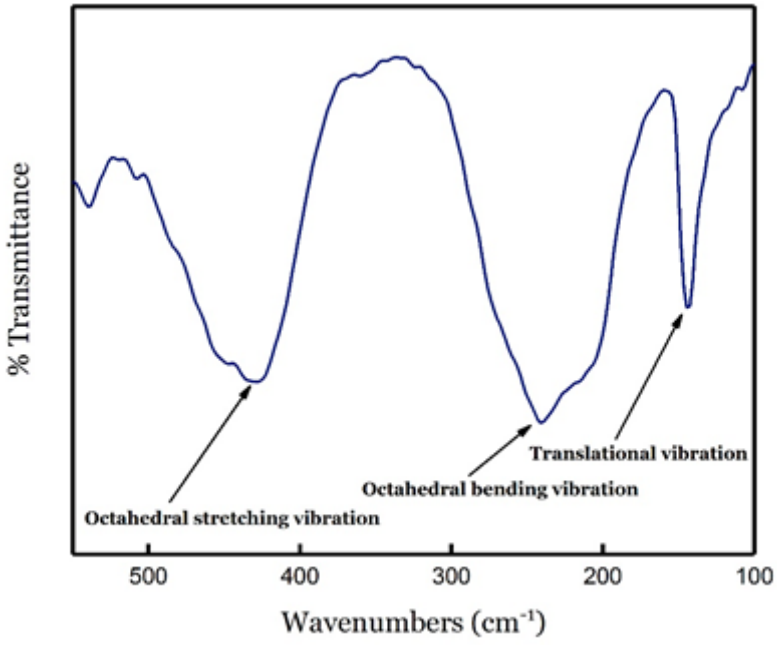

Figure 3-26: FIR spectrum of $KZnF_3$.

All the synthesised KMF_3 showed 3 stretching bands that confirmed the correct structure of these NPs.

3.3.3 Synthesis of $GdFeO_3$

Error! Reference source not found. represents a comparison in PXRD patterns between $GdFeO_3$ NP samples after being annealed at different temperatures and the standard PXRD pattern of the bulk material available in the literature.[35] The PXRD analysis reveals

that when the sample was heated from 500-600° C the products formed were Gd_2O_3 and $Gd_2O_2CO_3$. Utilizing synthetic precursors that were previously dried in air (and thus exposed to CO_2) might be the crucial reason for the formation of $Gd_2O_2CO_3$ in the reaction mixture. According to literature , $Gd_2O_2CO_3$ exists in a layered structure consisting of alternating ($Gd_2O_2^{2+}$) and carbonate groups ($(CO_3)_n^{2n-}$ layers.[36] Due to the increase of the thermal treatment temperature, decarbonation occurs, leading to formation of cubic crystallized active-reactive Gd_2O_3. A study showed that, $Gd_2O_2CO_3$ decomposes as follows: [36]

$$Gd_2O_2CO_3 \xrightarrow{650\,C^\circ} Gd_2O_3 + \uparrow CO_2 \qquad \textit{Equation 3-3}$$

According to the presented Powder X-ray pattern, starting from 700°C, the single phase orthorhombic $GdFeO_3$ perovskite structure is nearly formed, the unit cell parameter a = 5.3490(1) Å, b =5.6080(2) Å and c = 7.6687(1) Å which is in agreement with the model value.[37] However, some of the peaks available in the model pattern were not clearly observed in this pattern, therefore a judgment was made to not carrying any further characterisation for this NPs compound. From this PXRD pattern, clearly a gradual sharpness of the peaks increases as the incubating temperature increases was observed, indicating the growth and increase of crystallite size. Raising the temperature to 800°C, the perovskite structure was still retained with same orthorhombic $GdFeO_3$ structure, however increasing the temperature to 900°C leads to a different cubic structure which is $Gd_3Fe_3O_{12}$ with a unit cell constant a = b = c =10.7993337 Å and $\alpha = \beta = \gamma = 109.47°$.[38] E. A. Tugova *et al.* mentioned that the mean size of $GdFeO_3$ sample obtained after thermal treatment of the initial mixture at 700°C by same method was 40(4) nm.[39] The orthorhombic unit cell structure of $GdFeO_3$ is displayed in Figure 1-12

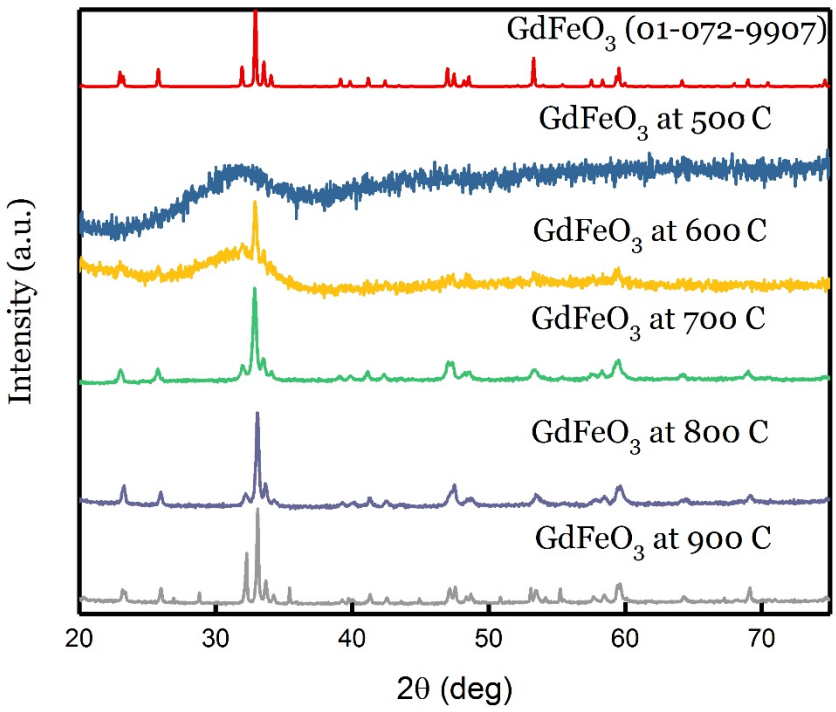

Figure 3-27: Powder X-Ray diffraction patterns of GdFeO3at different incubation temperature range from 500 to 900°C compared to the model.

Thus, when initial compositions were obtained by the co-precipitation method, the process for $GdFeO_3$ NPs formation can be represented as a scheme depicted in Figure 3-28, showed by the formation of $GdFeO_3$ nanocrystals. This diagram is well-known the literature.[40-43] As shown in the diagram the formation of the stable $GdFeO_3$ can be obtained by two mechanisms either by mixing FeO(OH) and $Gd(OH)_3$ hydroxides on the molecular level at the initial stages of synthesis with simultaneous dehydration of both components. The second mechanism involves both dehydration and decarbonation processes, where higher temperature is necessary for the decarbonation process. This process might leads to an increase in the size of the formed $GdFeO_3$ crystals if the localized in space Fe_2O_3 and Gd_2O_3 interact at the final stage.[39]

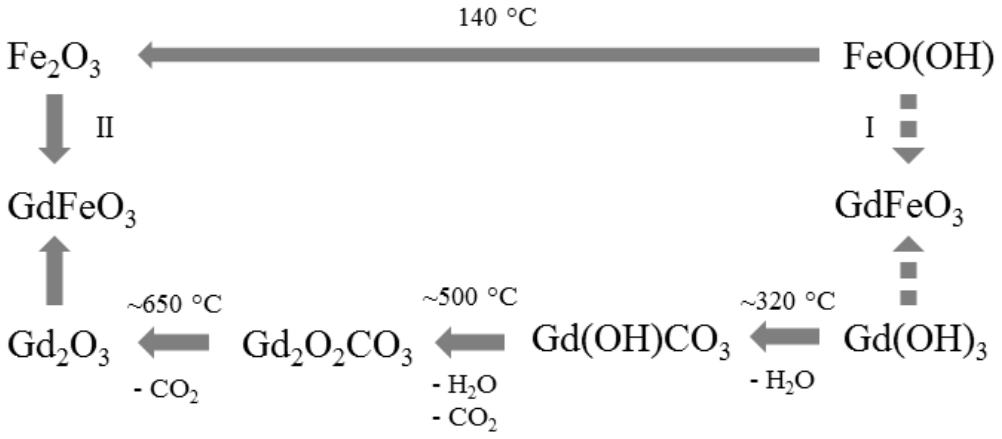

Figure 3-28: $GdFeO_3$ nanocrystal formation scheme exemplified by the forming of $GdFeO_3$ under the heat treatment of co-precipated initial mixture in air. I - the mechanism of co-precipated hydroxides simultaneous dehydration with $GdFeO_3$ formation; II - the scheme of step-by-step transformations of co-precipitated components with spatial-isolated Fe_2O_3 and Gd_2O_3 NPs formation followed by solid state interaction for $GdFeO_3$ production.[44]

3.4 Functionalisation of NPs

Compatibility with biological application require NPs to be soluble in aqueous medium. It was important to use more suitable bifunctional water soluble molecules to transfer the NPs from organic to aqueous solution, for this reason, and to examine the impact of ligands protecting/stabilising the NPs on the final relaxivity to be applicable as a contrast agents for Magnetic Resonance Imaging (*MRI*), the NPs were functionalised with the following ligands : 11-aminoundecanoic acid, a classic bifunctional carboxylic/amine small molecule and by alendronic acid a bifunctional, bisphosphonates/amine molecule). Bisphosphonates have not been investigated as much as carboxylates on iron oxide or perovskite fluorides, however they have additionally been appeared to render water soluble NPs with great magnetic properties and stability.[45] Amino acids are zwitterionic, they possess a negative charge on the carboxylate and positive charge on the amine throughout a wide range of pH. In acidic medium, the positively charged amine ligand has an electrostatic repulsion to the positively iron oxide charge. However, it is assumed that a coordinate bond is formed between the transition metals Mn, Co, Zn, and Ni that work as Lewis acids and the zwitterionic ligand which work as a Lewis base. In fact, the states of the OH functional groups available in the alendronic acid when chelate with divalent rare earth metals has been explained where P-OH groups gets deprotonated and

the amino group protonated. The others two P-OH groups remain in contact.[46] Figure 3-29 illustrates the chemical structures of both ligands used for this process.

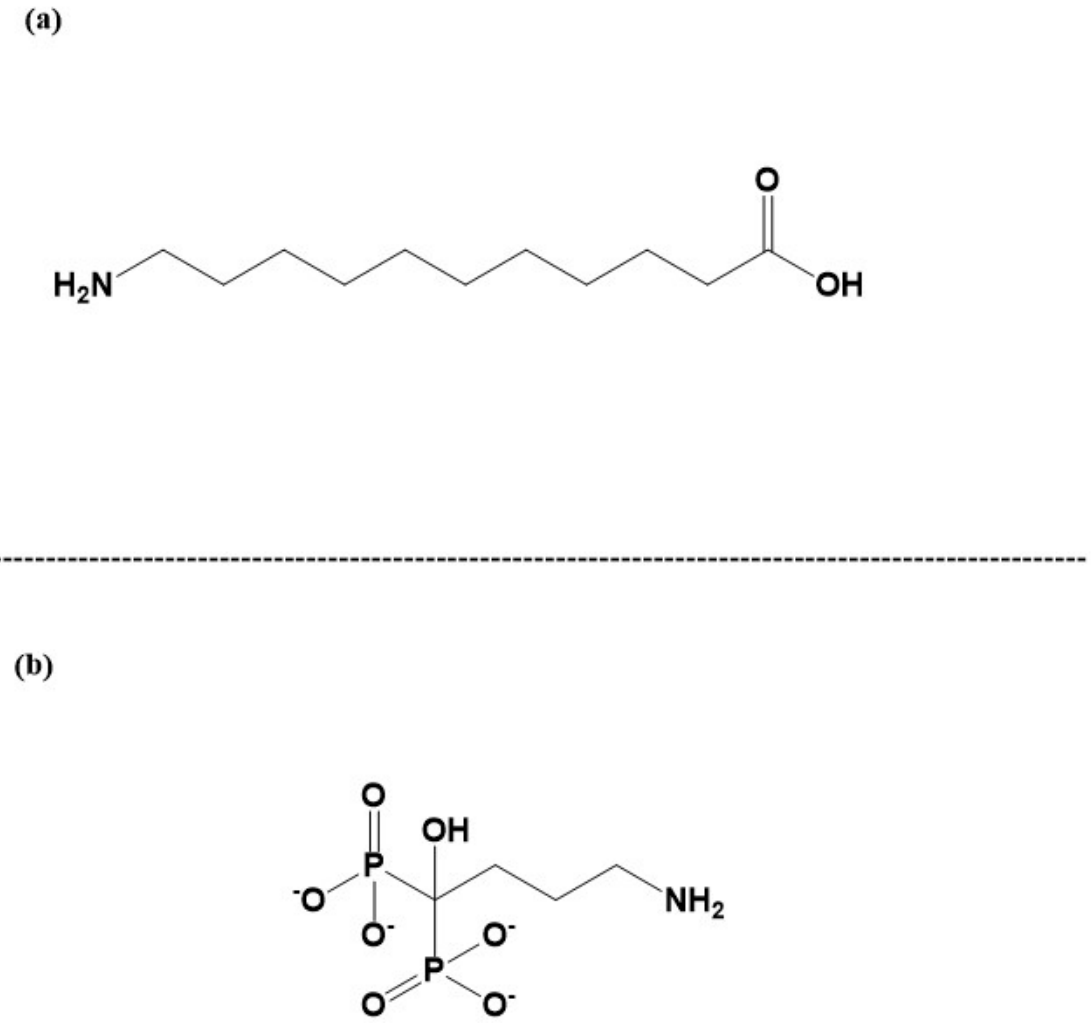

Figure 3-29: Chemical structures of ligands used in the functionalisation of the investigated NPs process: (a) 11-aminoundecanoic acid, (b) alendronate sodium trihydrate.

It is widely stated in the literature that carboxylic acids among the specific binding moieties which form bonds to gamma iron oxide as Fe^{3+}. They have a high charge-to-radius ratio and as a hard acid forms high-affinity complexes with hard oxygen ligands that work as hard Lewis bases.[47] According to Pearson, Fe^{2+}, Co^{2+} and Zn^{2+} are classified as intermediates between the hard and soft Lewis acids and the HSAB principle predicts that hard acids prefer hard bases, soft acids prefer soft bases, and borderline acids prefer borderline bases for complexation.[48] Therefore, 11-aminoundecanoic acid works as an

intermediate Lewis base due to its negatively charged oxygen donor atoms.[47] On the other hand, amines are non-specific binding moieties even in unfavourable pH medium. These are hard Lewis bases, they only form electrostatic or hydrogen bonds to the transition metals.[49] According to literature, the binding between the gamma iron oxide surface and ligand is expected exclusively through the carboxylic acid functional group, however few studies states that at high pH values, the amine groups adsorb on the gamma iron oxide surface. The following compounds displayed in Figure 3-30 demonstrates a successful functionalisation for the NPs by both ligands.

(a)

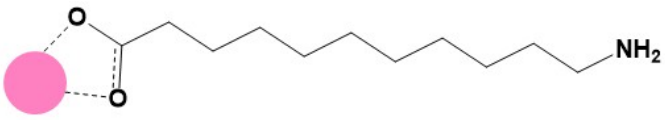

KMF_3---11-Aminoundecanoic acid

(b)

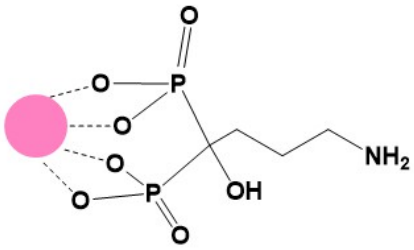

KMF_3---Alendronic Acid

Figure 3-30: Structures of NPs functionalised with (a) 11-aminoundecanoic acid and (b) Alendronic acid ligands.

In order to evaluate the ligand exchange efficiency, the NPs have to be characterised by infrared spectroscopy. Strong stretching frequencies of the functional groups, such as phosphonate resonance (strong P=O stretch around 1100 cm^{-1}) and C-O in the carboxylic group (around 1500 cm^{-1}) must be observed. These details will be explained in the next sections.

3.4.1 PXRD analysis for standard 11-aminoundecanoic acid and sodium alendronate trihydrate

Prior to the start of the functionalisation process, PXRD analysis was carried out for the pure 11-aminoundecanoic acid and alendronate sodium trihydrate ligands to confirm their purity as single-phase structures. PXRD patterns in Figure 3-31 and Figure 3-32 show that both ligands adopt same structures as their corresponding standard models structures available in the literature, although a slight decrease in some of the structure peak intensities were observed. The decrease in the peak intensity was attributed to the moisture existed in these ligands during analysis. However, work analysis using these ligands showed that reduction in intensity does not hinder the formation of the desired product.

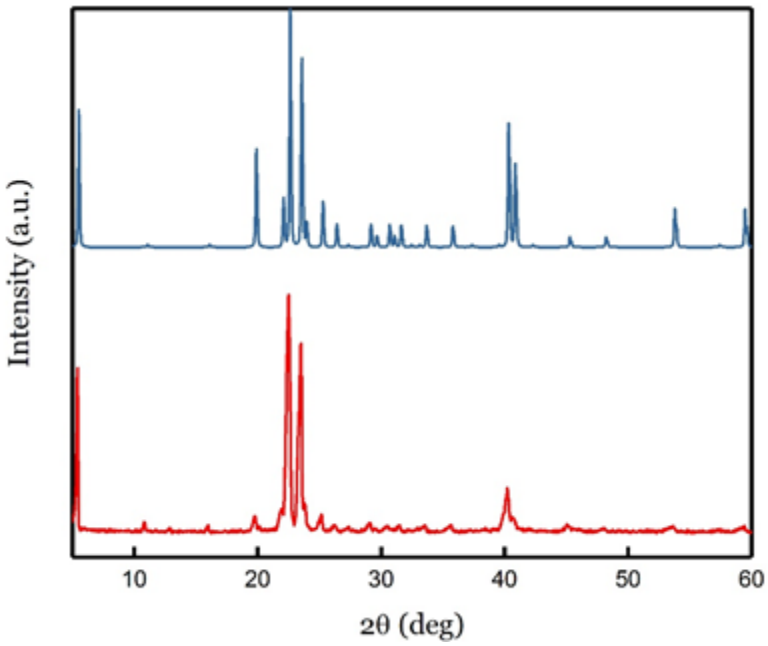

Figure 3-31: PXRD pattern of 11-aminoundecanoic acid ligand used (red) compared to its available model in literature (blue)

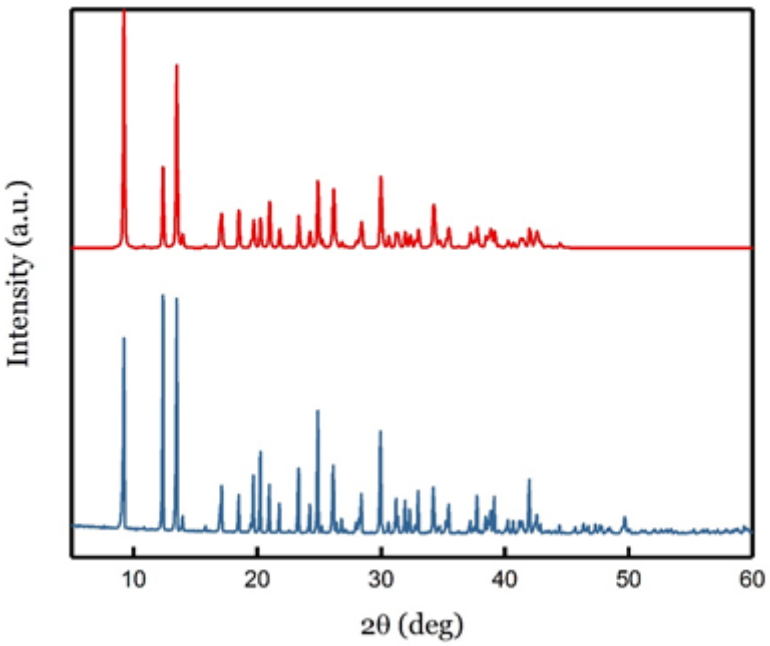

Figure 3-32: PXRD pattern of Alendronate sodium trihydrate ligand used (red) compared to its available model in literature (blue).

3.4.2 Functionalisation of NPs with 11-aminoundecanoic acid

Using the method described in the experimental section 3.2.3.1, the KMF_3 (M = Mn, Fe, Co, Zn) NPs were functionalised with the 11-aminoundecanoic acid ligand. The functionalisation process was done for 4 different stirring time, 48, 24, 2 and 1 hours. The produced PXRD patterns at 1 and 2 hours are displayed in Figure 3-33 to Figure 3-36. The PXRD patterns of the unfunctionalised NPs and the pure ligand are also combined within the same pattern for comparison. Other patterns obtained at other stirring time are displayed in the appendix.

Keasberry *et al.* outlined that functionalisation time required to coat the surface of $KMnF_3$ NPs by 11-aminoundecanoic acid while stirring the solution is 48h.[50] Unfortunately, our investigations at this stirring time and 24 hours revealed that the perovskite structure for all the synthesised NPs fall apart leading to a defect in their PXRD patterns where all of the main peaks related to the perovskite structure were not observed. Clearly this indicates, a decomposition in the perovskite structure takes place. On the other hand, reducing the functionalisation time to 2 or 1 h indicates a significant improvement in the successful coating of 11-aminundecanoic acid on the NPs surface due to the appearance of some of the perovskite structure main peaks. However, a slight difference was found in the PXRD patterns when functionalisation was performed at 1 and 2h. Hence the results of 1- and 2-hours functionalisation stirring time are discussed in this work.

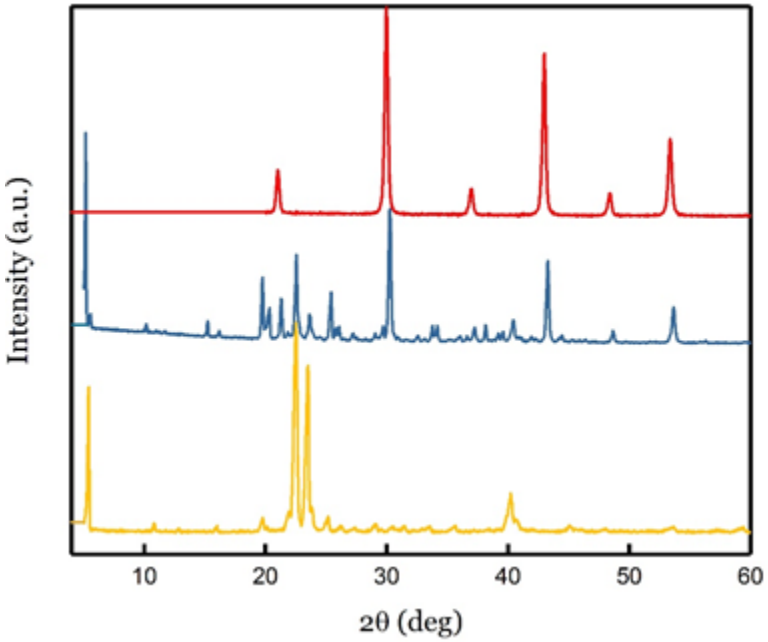

Figure 3-33: PXRD patterns of $KMnF_3$ 2-hours functionalisation with 11-aminoundeacnoic acid (blue) compared to bare $KMnF_3$ (red) and 11-aminoundecanoic acid (yellow).

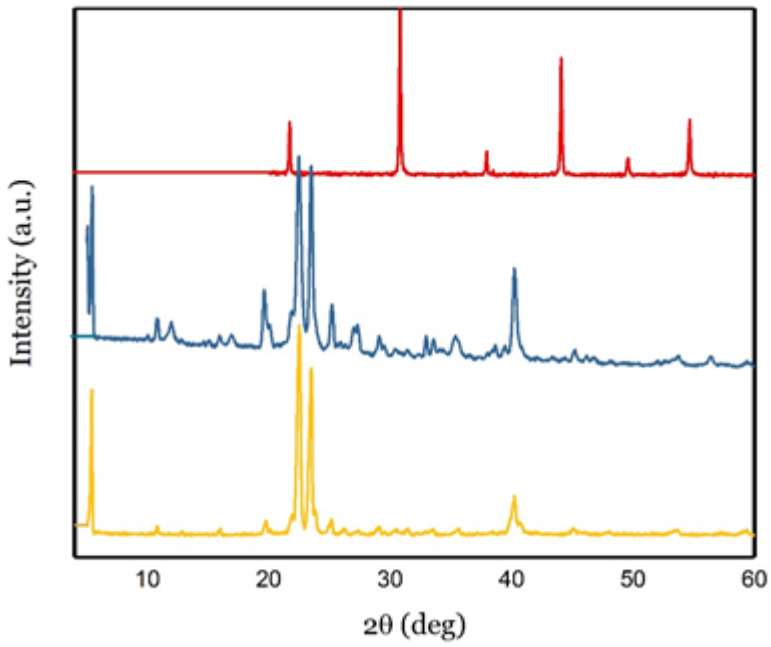

Figure 3-34: PXRD patterns of $KFeF_3$ 1-hour functionalisation with 11-aminoundeacnoic acid (red) compared to bare $KFeF_3$ (yellow) and 11-aminoundecanoic acid (blue).

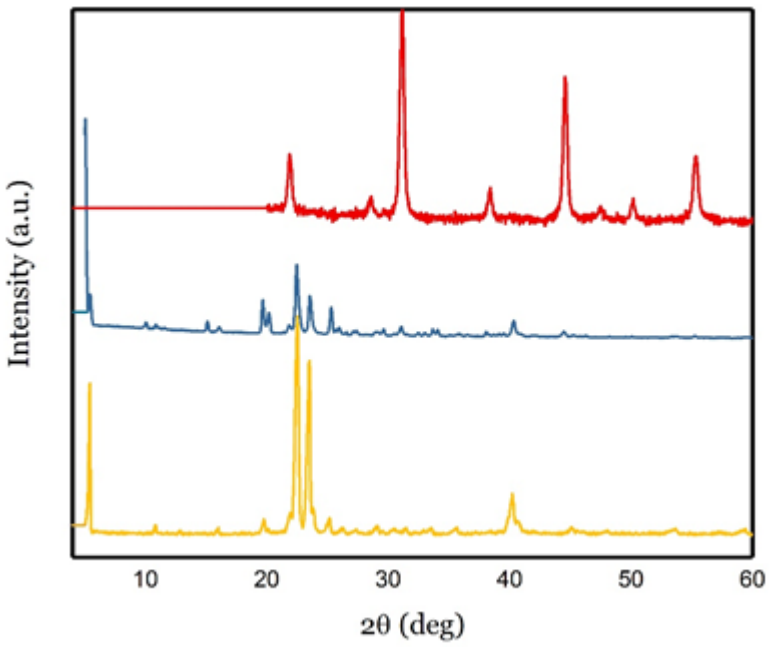

Figure 3-35: PXRD patterns of $KCoF_3$ 2-hours functionalisation with 11-aminoundeacnoic acid (red) compared to bare $KCoF_3$ (yellow) and 11-aminoundecanoic acid (blue).

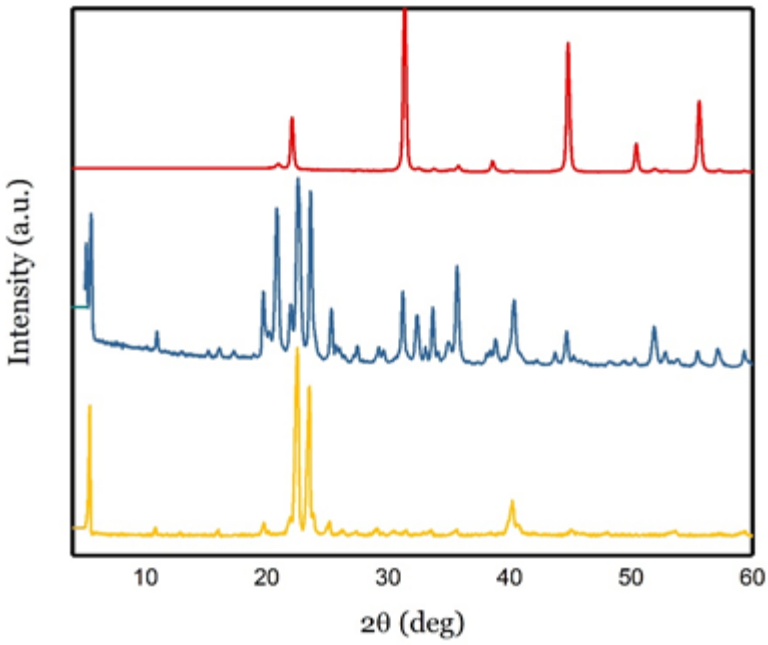

Figure 3-36: PXRD patterns of $KZnF_3$ 1-hour functionalisation with 11-aminoundeacnoic acid (red) compared to bare $KZnF_3$ (yellow) and 11-aminoundecanoic acid (blue).

As can be seen in the above PXRD patterns, it is clear that extra peaks in all the functionalised NPs have been observed. These observed peaks appear almost at similar 2θ to those found in the bare KMF_3 (M = Mn, Co and Zn) and bare amino ligand.

For Functionalised $KMnF_3$, the PXRD pattern in Figure 3-33 indicates that all peaks related to $KMnF_3$ perovskite structure are retained, however a new phase is observed due to the appearance of the extra peaks. It is possible that these extra peaks may be represent multiple attachment caused by 11-aminundecanoic acid on the perovskite surface of $KMnF_3$ NPs. On the other hand, the PXRD pattern of $KFeF_3$ in Figure 3-34 does not suggest that the perovskite structure has been retained due to the disappearance of the representive main peaks of perovskite structure. The functionalisation of $KCoF_3$ and $KZnF_3$ in Figure 3-35 and Figure 3-36 show a same trend as for $KMnF_3$.

The crystalline size for all the functionalised Nano particles were estimated by the same techniques used for the previously synthesised bare NPs. The observed increase in hydrodynamic diameter of the functionalised Nano particles of nearly 5 to 10 nm compared to those of the bare NPs as shown in Figure 3-37 provided a significant evidence that the particles are surrounded by the coating ligand. These particles can be used for cellular uptake due to their small sizes which enable them to escape from phagocytes in reticuloendothelial system (RES) and circulate through blood vessels with a long blood half-life.[51] On the other hand, bigger nanoparticles could yield in more rapid uptake by RES, such as liver and spleen.

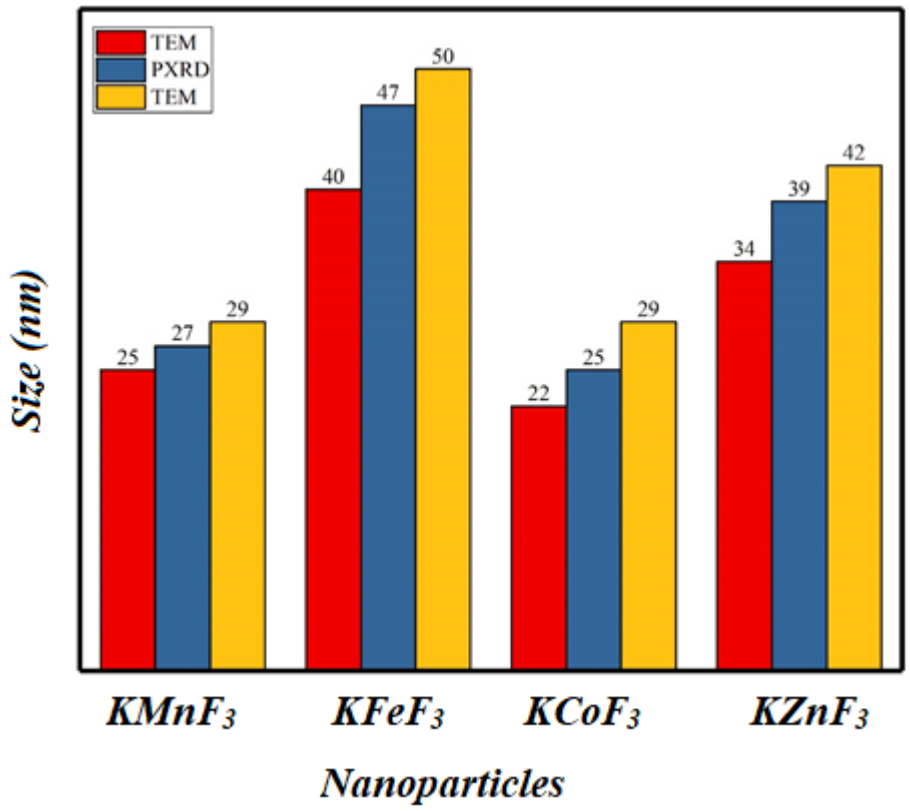

Figure 3-37: Crystal sizes obtained of functionalised NPs using 3 different techniques

The morphology of the NPs ($KMnF_3$, and $KFeF_3$, $KCoF_3$ and $KZnF_3$) attached to 11-aminoundecanoic acid ligand was examined with a high-resolution transmission electron microscope. The TEM images of the functionalised samples in water medium are shown in Figure 3-38.

In most of the images obtained, for $KMnF_3$, it was observed an obvious aggregation or formation of spherical macro clusters as illustrated in Figure 3-38(a). This existing aggregation phenomena may occur due to the lack in dispersing the samples using sonication or vortexing for a period of time prior to the analysis, the second reason for this property may be due to the delay in performing the analysis immediately at the microscopy suite room. However, it was obvious that these aggregations contain dark areas which represent regions of higher amounts of NPs compared to the lighter areas, giving a considerable indication for the existence of the retained perovskite structure. The average crystalline size of 25nm was obtained.

For $KFeF_3$, the TEM image in Figure 3-38 (b) shows a coating layer surrounded the $KFeF_3$ NPs. The observed geometry was cubic and the amount of the aggregation was less than that of the coated $KMnF_3$ NPs, although they have been functionalised with the

same method. The average crystalline size obtained For $KFeF_3$ was 40 nm, which is compatible for the biological applications.

For $KCoF_3$ coated with 11-aminoundecanoic acid, the TEM image in Figure 3-38 (c) shows a quasi-spherical particle with almost uniform particle sizes of about 22 nm. It can be seen from the morphology that the formed NPs have a smaller amount of aggregation comparing to the functionalised $KMnF_3$ NPs and the darker regions observed in most of the images that reveal the existence of the $KCoF_3$ NPs as a result of the retained perovskite structure. The obtained size values confirmed an increase of particle size compared to the bare $KCoF_3$ as a result of 11-aminoundecanoic acid coating, enabling their use for biological applications.

The TEM of the $KZnF_3$ coated with 11-aminoundecanoic acid ligand displayed in Figure 3-38(d) showed an interesting morphology in comparison to the other antiferromagnetic NPs where a rod-like shapes spreaded through some parts of the analysed sample. On some other parts of the sample a cubic morphology was observed using different magnification scales. The average crystalline size obtained was 34 nm. It is possible that the formation of rod-like shapes is related to the presence of the ZnO as reported by previous study.[52, 53]

The EDX spectra of the functionalised NPs was used to quantify the elemental analysis in their composition. The atomic percentages of the main elemental constituent and some impurities are plotted in the bar chart in Figure 3-39showed that all samples consist of their main elemental constituents, however the stoichiometry was not as expected compared to their theoretical values. This might be due to the same reasons discussed previously for the unfunctionalised NPs. The presence of the nitrogen in the functionalised NPs reflects the existence of the 11-aminoundecanoic acid ligand, therefore it was important to determine the amount of carbon in addition to hydrogen and nitrogen.

The results in Table 3-1represents the CHN measurements in the functionalised samples. These results show a high amount of carbon and small amounts of nitrogen which reflect the theoretical stoichiometric ratio of the elements present in the ligand structure that are existed in the functionalised NPs. This was an obvious evidence for successful functionalisation. The reason for the significant lower amount of hydrogen was unclear, however it could be due to the washing process as some of the sample's constituents were washed away.

The EDX results suggest that there is a wide variation of elemental composition throughout the sample. Furthermore, the estimated C, H and N for $KCoF_3$ NPs has lower amount of carbon and hydrogen and none of the nitrogen was present. This does not reflect the EDX results where 23% of carbon was detected. Therefore, this may be due to the excessive washing by THF that caused the ligand to be apart and none of the ligand molecules left on the nanoparticle surface.

Table 3-1: C, H and N analysis for functionalised NPs

NPs	*C %*	*H %*	*N %*
$KMnF_3$	35.85	8.54	6.04
$KFeF_3$	59.22	3.37	6.36
$KCoF_3$	0.27	1.10	0.00
$KZnF_3$	53.85	9.54	6.04

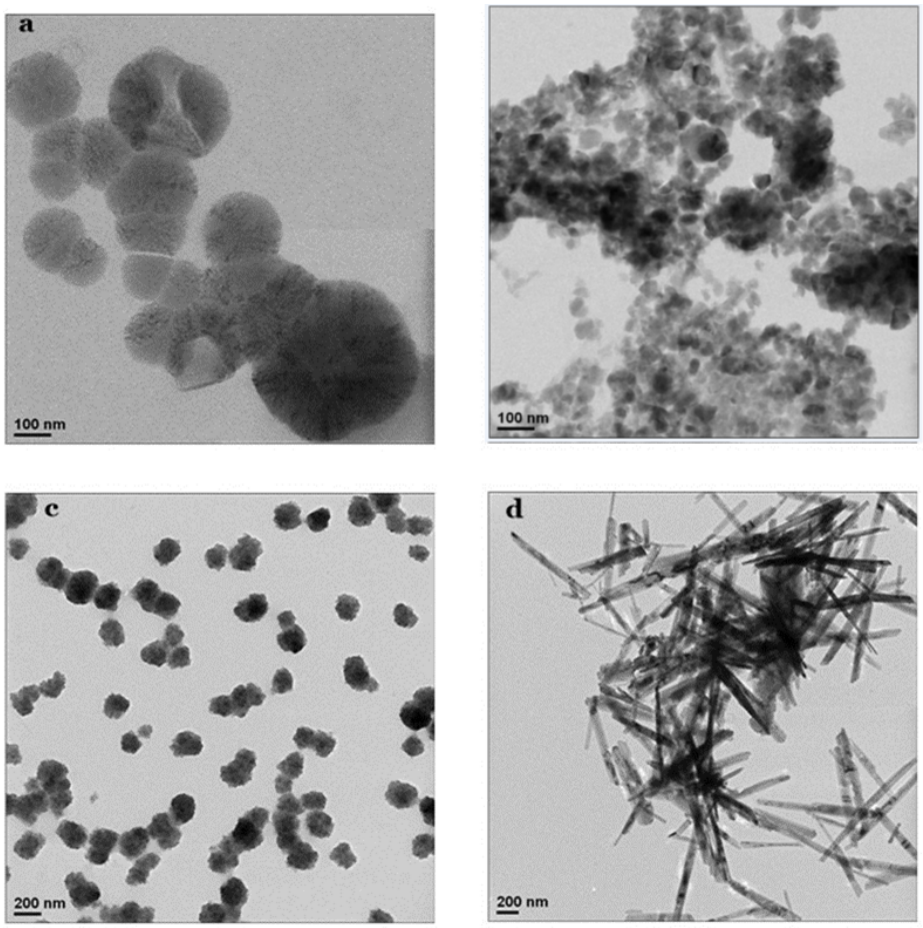

Figure 3-38: TEM images obtained for functionalised NPs with 11-aminoundecanoic acid: (a) $KMnF_3$, (b) $KFeF_3$, (c) $KCoF_3$ and (d) $KZnF_3$.

The surface chemistry for all functionalised NPs were also examined by FTIR spectroscopy. As can be seen in Figure 3-40 and Figure 3-41, when NPs were functionalised with 11-aminodecanoic ligand, the obtained spectra were almost identical. The peak at 2876 cm^{-1} and 2698 cm^{-1} were assigned to the stretching vibrational of the C-H bond. The band at 1678 cm^{-1} is related to the bending mode of N-H bond and the stretching mode of C=O bond which exist in the coating ligand. Another band appears at 1397 cm^{-1} which is assigned to C-C vibrational band of the ligand. It is assumed that the ligand is existed on the nanoparticle surface, however it is not sure that it is strongly bonded to the surface and its constituent did not overlap with nanoparticle content, causing the structure to decompose.

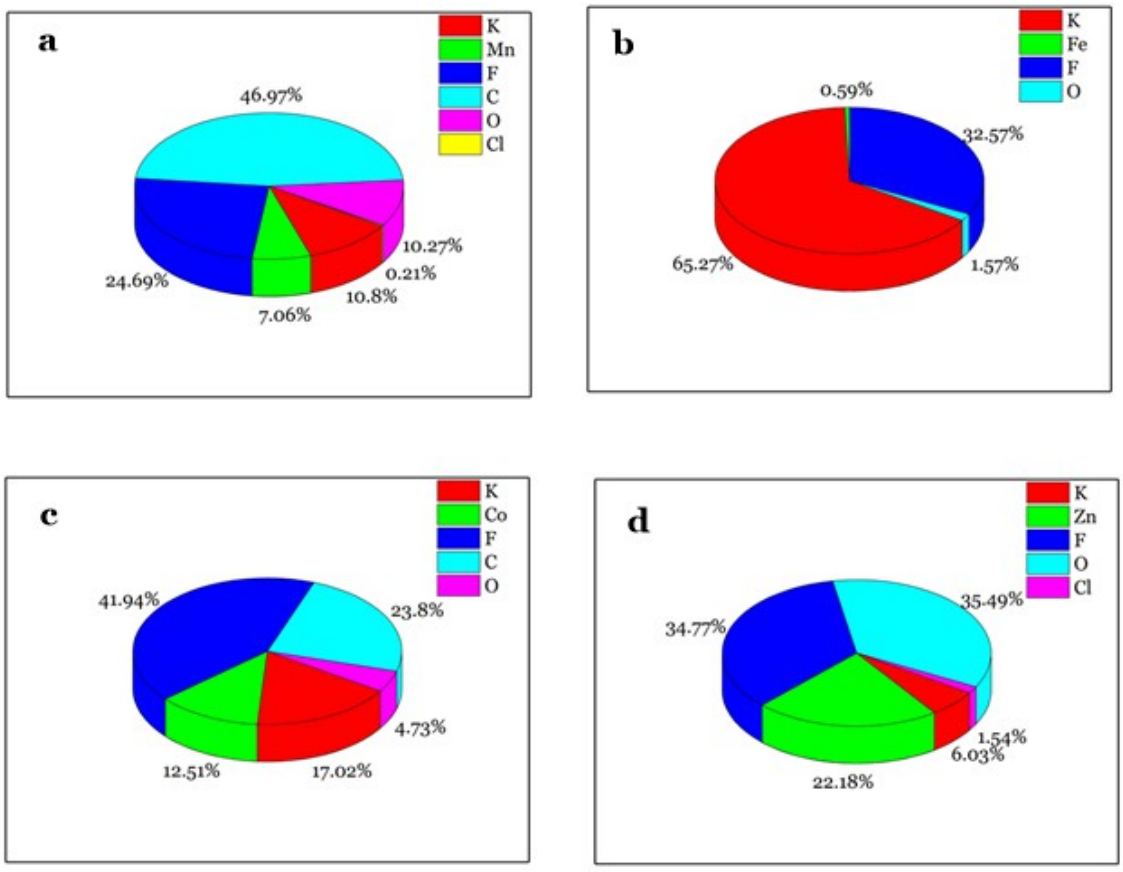

Figure 3-39: Atomic % of elemental composition obtained by EDX for functionalised NPs with 11-amino undecanoic acid (a) $KMnF_3$, (b) $KFeF_3$, (c) $KCoF_3$ and (d) $KZnF_3$

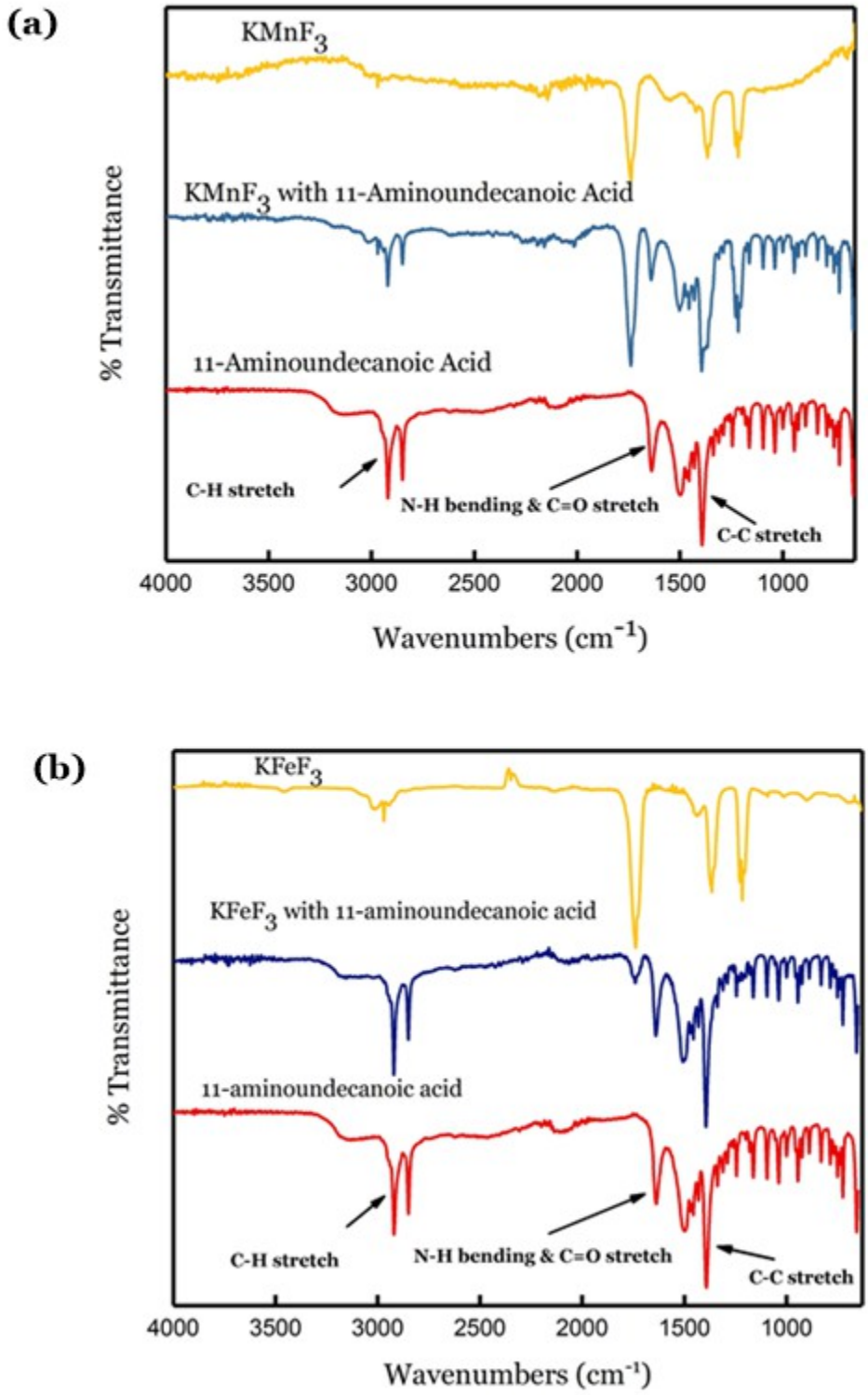

Figure 3-40: FTIR spectrum for functionalised $KMnF_3$ and $KFeF_3$ with 11-amino undecanoic acid compared to the bare compounds and ligand: (a) $KMnF_3$ and (b) $KFeF_3$ NPs

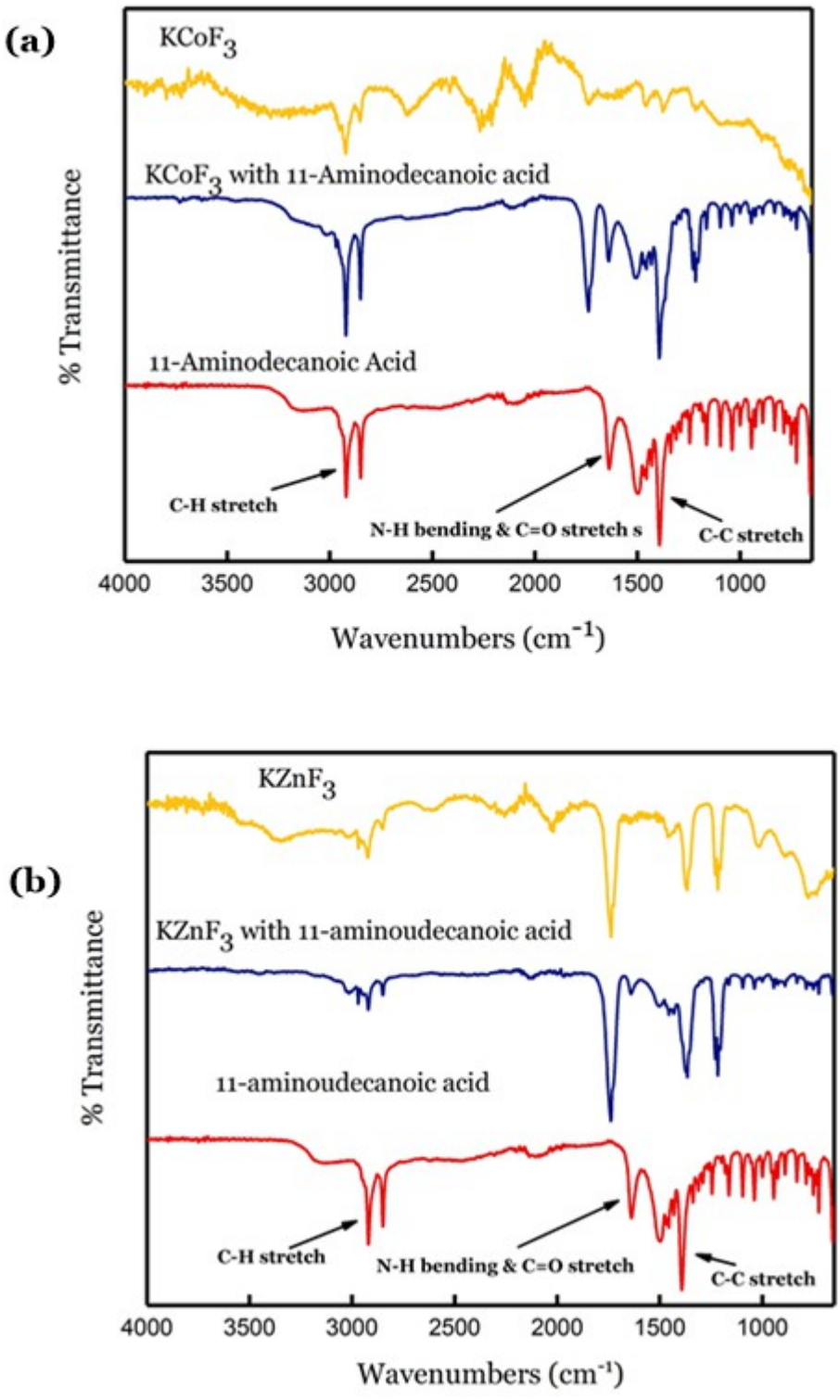

Figure 3-41: FTIR spectrum for functionalised $KMnF_3$ and $KFeF_3$ with 11-amino undecanoic acid compared to the bare compounds and ligand: (a) $KCoF_3$ and (b) $KZnF_3$ NPs

3.4.3 Zeta potential

Charge Stability of KMF_3 NPs plays a crucial role in their use in biological applications.[54] In order to evaluate the stability of synthesised NPs, the zeta potential of the different NPs

were measured. The zeta potential of NPs can affect the stability of NPs suspension. Table 3-2 illustrates the different zeta potential of NPs when they are coated with the 11-amino undecanoic acid. As can be seen in the data shown in Table 3-2, all the functionalised NPs exhibited negative charge with slight variation in the zeta potential compared to their corresponding naked NPs. $KFeF_3$ coated with 11-aminoundecanoic acid has the highest stability -17.6 ∓7.8 mV compared to the other NPs coated with the same ligand where almost have similar zeta potential, indicating a significant NPs coated ligand stability. Theoretically, the suspension of the coated NPs with 11-amino undecanoic acid was expected to be positively charged due to the bearing amino group terminal that exist in the coating ligand. This case was not observed for all the synthesised NPs. Previous study showed Similar negative zeta potential values for NPs coated with those ligands containing carboxylate and amino groups.[18] The reason for such a case may be linked to the different PK_a values related to the ligands that give rise to the overall negative values at the physiological conditions used for the measurements, where 11-aminoundecanoic acid has 2 PK_a values (amine) 11.15 and (carboxylate) 4.55. Another reason may be due to the excess unbounded carboxylate group that is available in the suspension due to insufficient washing during the functionalisation process. Since magnetic dipole interaction of ligand are very small or zero, so the existence of this ligand on the surface of NPs results in fine stable colloidal in aqueous medium. Thus, ligand coatings on NPs can play critical and efficient role in reducing agglomeration of particles, and modification of the stability and prolonging circulation times in the biological tissues. NPs carrying a positive charge could be logically the suitable canadate to penetrate the negatively charged cellular membrane, despite a previous study reported that the negatively charged NPs could also penetrate the cell membrane.[55]

Table 3-2: Zeta potential of functionalised and bare NPs.

NPs	*Functionalised Zeta potential (mV)*	*Bare Zeta potential(mV)*
$KMnF_3$	$-6.8(5.9)$	$-0.34(7.9)$
$KFeF_3$	$-17.6(7.8)$	$-5.66(11.3)$
$KCoF_3$	$-6.61(8.1)$	$2.28(10.7)$
$KZnF_3$	$-10.4(5.4)$	$0.22\ (13.44)$

3.4.4 Thermal Gravimetric analysis

To investigate the thermal stability of the bare and functionalised KMF_3 (M = Mn, Fe and Co) NPs, thermogravimetric analysis has been carried out. Initially the thermogravimetric analysis for the bare 11-aminoundecanoic acid ligand was performed, the decomposition of the ligand has two steps as shown in Figure 3-42. The weight loss at the first step from 200 to 300°C was 0.557 mg which contribute to about 10% from the total sample weight, whereas at the second step, a significant weight loss of 4.784 mg (87 %) occurred at the region from 400 to 480°C was observed.

Figure 3-42 illustrate the weight loss curves as a function of temperature for the bare and functionalised NPs. The observed initial weight loss in the temperature range 25-26°C for the bare $KMnF_3$ was 60% whereas for the bare $KFeF_3$ and $KCoF_3$ are relatively small percentage of 40% was observed. This weight loss was probably due to the moisture presents in the samples and/or hydroxyl groups attached at the NPs surface.

For the all functionalised NPs with 11-aminoundecanoic acid ligand, the decomposition and the phase transformation take place in 3 main steps. In the first step at lower temperature, the weight loss can be attributed to the removal of the water contents and hydroxyl groups adsorbed at the coated NPs surface. Clearly the same two steps of the decomposition of the bare ligand do present, reflecting the existence of the ligand where the first at 200-300°C step and the significant weight loss at higher temperature (400-480° C) could be linked to the evaporation and subsequent decomposition of the 11-aminoundecanoic acid ligand. The weight loss of the ligand in all of the synthesised NPs were found 2.81×10^{-7} % (2.81 , 6.66×10^{-6} % and 1.25×10^{-5}% for $KMnF_3$, $KFeF_3$ and $KCoF_3$ respectively.

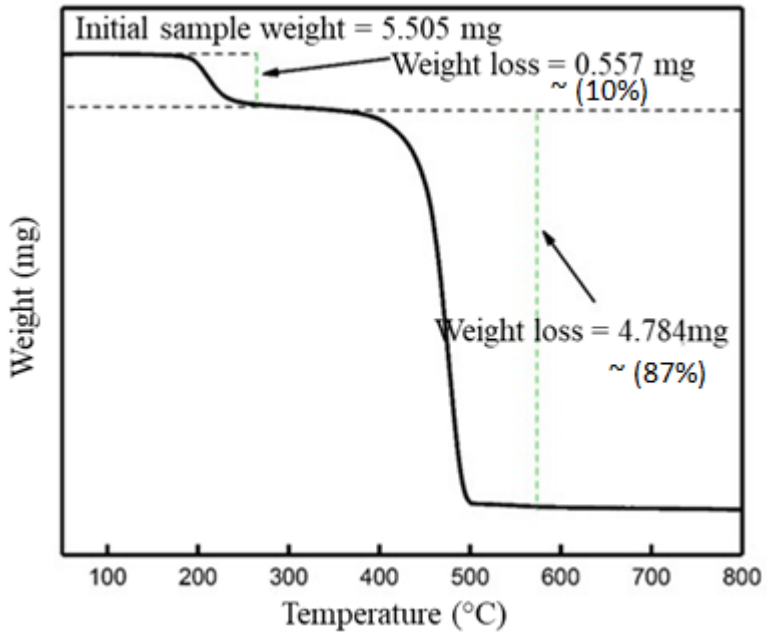

Figure 3-42: Thermogravimetric analysis for 11-aminoundecanoic acid.

The results confirmed that the synthesised NPs were coated with the 11-aminundecanoic acid. In addition, this experiment would have been better to be repeated to confirm the obtained current results or to validate the results by performing differential scanning calorimetric (DSC) analysis to obtain the heat flow curves as a function of temperature where we would be able to observe the endothermic peaks that are related to the removal of water contents and exothermic peaks that are linked to the phase transformation of the NPs.[56] Unfortunately, due to safety issue at the department concerning the spread of the NPs, TGA experiments were not repeated.

3.4.4.1 Calculating of density of ligands on NPs surface

Using the same TGA graphs in Figure 42, the density of the 11-aminoundecanoic acid on the NPs surface was calculated to determine the stoichiometry of the reaction. To calculate the number of ligands that coat the surface of one particle, the difference in mass after the evaporation of water when the sample is heated can be used. By subtracting the end mass which represents the mass of NP core only from the initial mass which represents the mass of (NP + ligand), the number of ligands that coat the surface of one particle can be calculated.

Assuming the NPs are spherical in shape, the volume (cm^3) of the NP, VNP can be calculated using the equation:

$$V_{NP} = \frac{4}{3}\pi r^3 \qquad \textit{Equation 3-4}$$

Where r is the average radii of the NPs measured by TEM image.

In order to obtain the molecular weight (M_W) of the core NP (no ligand), the mass of one particle (g) can be calculated using the density, d_{NP} [KMnF3 (3.41 g/cm^3), $KFeF_3$ (3.61 g/cm^3) and $KCoF_3$ (3.82 g/cm^3)] and the calculated volume, V_{NP} of the NP. The M_W (g/mol) of the core can be then calculated by multiplying the mass of one particle into the Avogadro number.

$$\textit{Mass of one particle} = d_{NP} \times V_{NP} \qquad \textit{Equation 3-5}$$

$$M_W = \textit{mass of one particle} \times \textit{Avogadro's number} \qquad \textit{Equation 3-6}$$

Knowing the mass of the core (mass at the end of the run), from TGA graph, the number of moles of the core can then be calculated;

$$\boldsymbol{n\,(core) = \frac{m\,(core)}{M_W(core)}} \qquad \textit{Equation 3-7}$$

Using the total mass of ligands lost from TGA curve, and the Molecular weight of the 11-aminoundecanoic acid ligand (MW = 201.13 g/mol), the number of moles of ligands per NPs can also be calculated;

$$\boldsymbol{n\,(ligand) = \frac{m\,(ligand)}{M_W\,(Ligand)}} \qquad \textit{Equation 3-8}$$

Dividing the number of moles per NP of ligand by the number of moles of the core per NP, the number of ligands per NP can be calculated

$$\boldsymbol{Number\ of\ ligands\ per\ NP = \frac{n(ligand)}{n(core)}} \qquad \textit{Equation 3-9}$$

The obtained results for the synthesised NPs are displayed in Table 3-3.

Table 3-3: Calculated ligands per one NPs for functionalised NPs with 11-aminoundecanoic acid

NPs	*Number of ligands per NP (ligands)*
$KMnF_3$	117
$KFeF_3$	124
$KCoF_3$	115

This obtained results correlates well with the previous literature measurements reported for same ligands coated on 5nm NPs surface.[18]

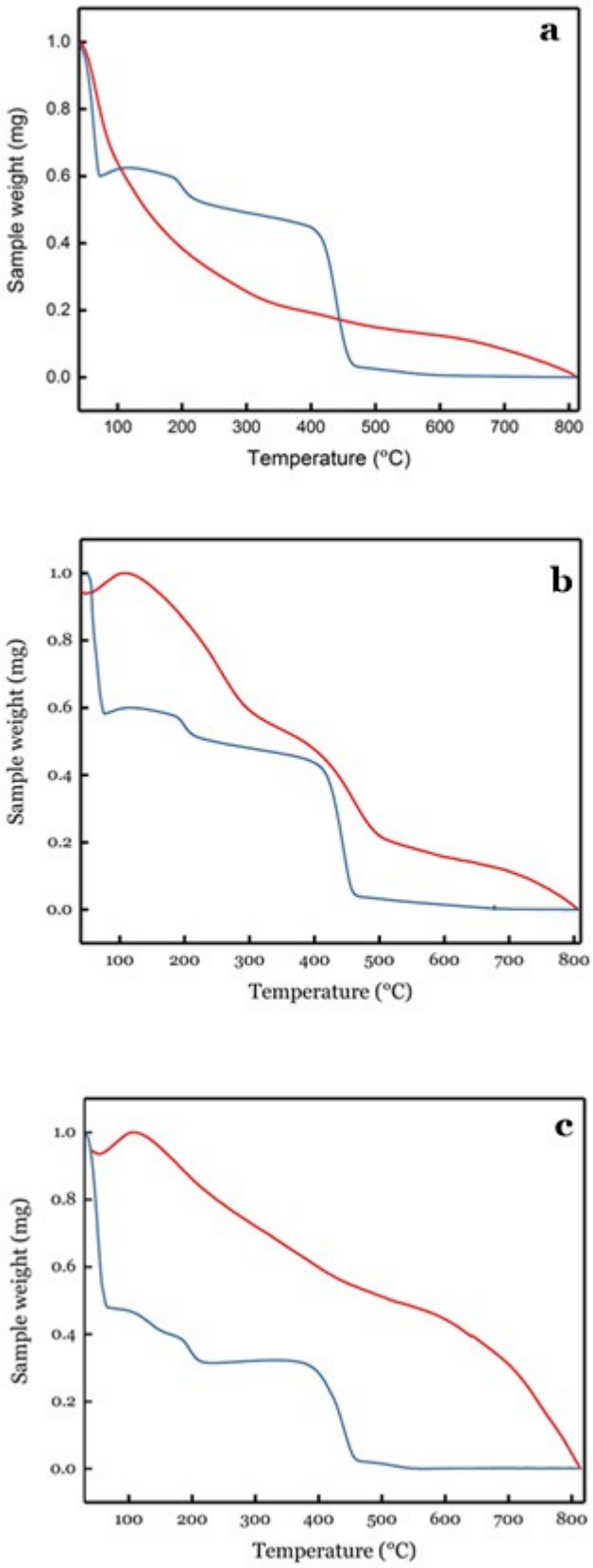

Figure 3-43: Thermal gravimetric analysis graphs for functionalised NPs (blue) compared to the bare NPs (red): a ($KMnF_3$), B ($KFeF_3$) and c ($KCoF_3$)

3.4.5 Rate of Relaxation measurements

3.4.5.1 Longitudinal and transverse relaxation rate of γ-Fe_2O_3

To investigate the efficiency of the prepared perovskite nanoparticle to work as T_1 and T_2 contrast agents, relaxation rates analysis was carried out using NMR at 9.4 T magnetic field. The longitudinal (r_1) and transverse (r_2) relaxivity values of NPs in water (determined by dividing the inverse of the relaxation time (T_1) and (T_2) over the concentration of Fe obtained by the ICP analysis). The data in Table 3-4 indicate that γ-Fe_2O_3 has small r_1 and high r_2 as shown in Figure 3-44 and Figure 3-45.

Table 3-4: The obtained longitudinal and transverse relaxitivity at 9.4 T for γ-Fe_2O_3

Relaxation rate	*Value ($mM^{-1}s^{-1}$)*
r_1	13.13
r_2	155

The calculated r_2 value obtained from Figure 3-45 is similar to that observed by other research groups for surface modified Fe_3O_4 NPs.[57] Significant change in the transverse relaxivity has been observed when a surface modification of Fe_3O_4 is made, making it a good candidate to use as an *MRI* contrasting agent. Recently Basly *et al.*[58] has synthesized Fe_3O_4 nanoparticle coated with PEGylated dendrons through a phosphonate group and observed r_2 relaxivity as high as 349 mM^{-1} s^{-1} at 1.5 T. Hence, the high relaxivity of γ-Fe_2O_3 observed in the present study may be attributed to the thin carboxyl decorated shell structure and good magnetization of γ-Fe_2O_3, giving rise to an effective magnetic relaxation to the water proton spins around the NPs. Thus, the high r_2 value, r_1/r_2 ratio (11.8) and the good colloidal stability make these NPs as promising candidates for high-efficiency T_2 contrast agent in *MR* imaging applications.

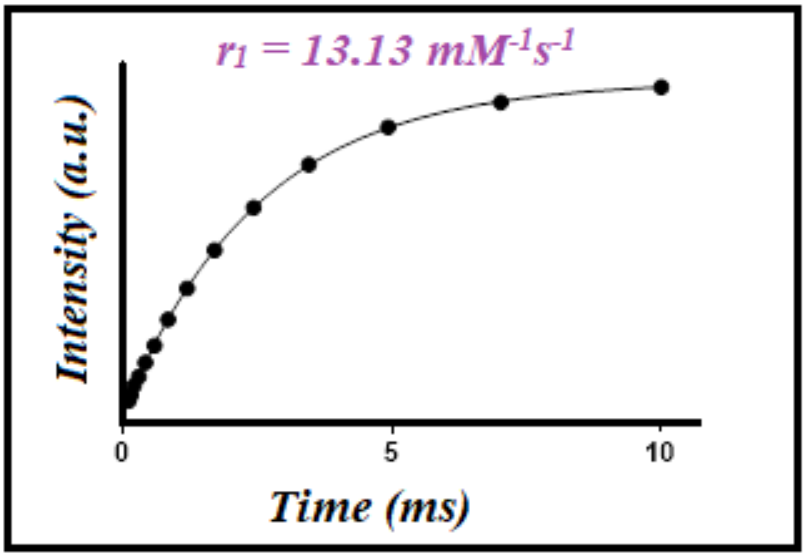

Figure 3-44: Longitudinal relaxation rate measurement for γ-Fe_2O_3 with 11-aminoundecanoic acid.

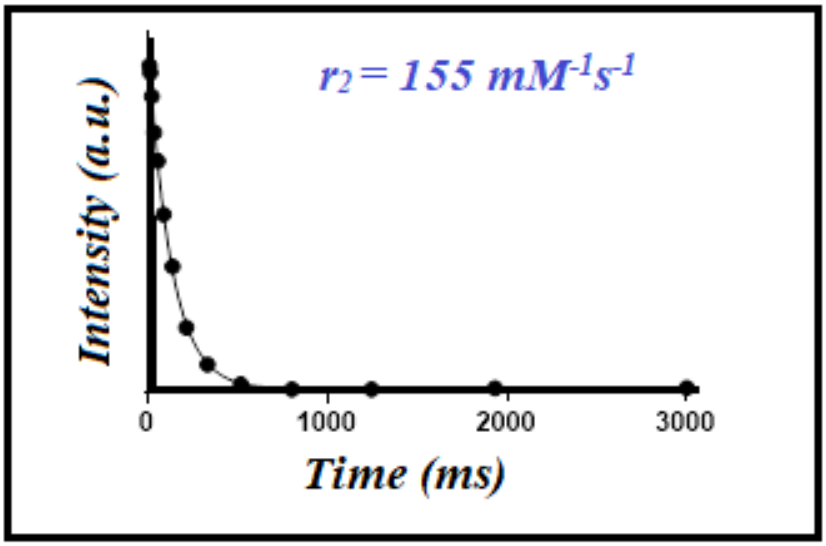

Figure 3-45: Transverse relaxation rate measurement for γ-Fe_2O_3 with 11-aminoundecanoic acid

3.4.5.2 Longitudinal and transverse relaxation rate of KMF_3 (M = Mn, Fe, Co, Zn)

Compared to the well-studied SPIONs for *MRI* , Only few literature papers has been considered Mn-based NPs.[59] Manganese can be formed in different oxidation state, (Mn^{2+}) divalent and (Mn^{3+}) trivalent. However the paramagnetic properties of Mn ions are attributed to the existence of unpaired electron (5) for Mn^{2+} or (4) for Mn^{3+}, with Mn^{2+} being the most powerful.[60] The paramagnetic $KMnF_3$ NPs coated with 11-aminoundecanoic acid ligand at room temperature exhibited enhanced relaxivity in both T_1 and T_2-relaxation, reflecting the efficiency of contrast enhancement by the coated magnetic NPs as *MRI* contrast agents. The calculated r_1 and r_2 values of the complex were obtained from Figure 3-46 and Figure 3-47 are displayed in Table 3-5. $KMnF_3$ contrast agent shows higher reflexivity r_1 and r_2 and the surface of the paramagnetic metal ion (Mn^{2+}) plays a significant role in shortening the longitudinal relaxation. The obtained results agree with the results obtained by Liu et al. who stated that $KMnF_3$ works as a T_1 contrast agent due to the spin inclination at the metal center that reduces the overall magnetic moment of the metal and results in lower magnetisation.[61]

Table 3-5: The obtained longitudinal and transverse relaxitivity at 9.4 T for $KMnF_3$.

Relaxation rate	*Value ($mM^{-1}s^{-1}$)*
r_1	42
r_2	244

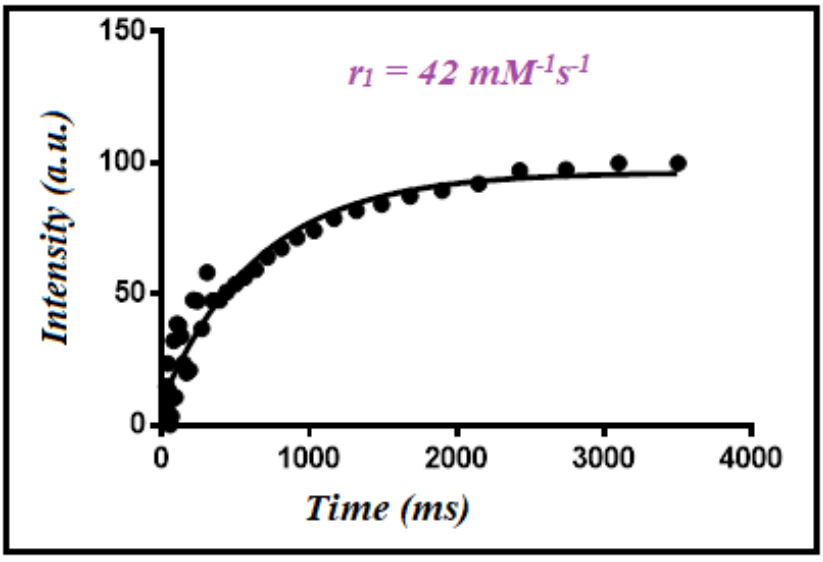

Figure 3-46: Longitudinal relaxation rate measurement for $KMnF_3$ with 11-aminoundecanoic acid

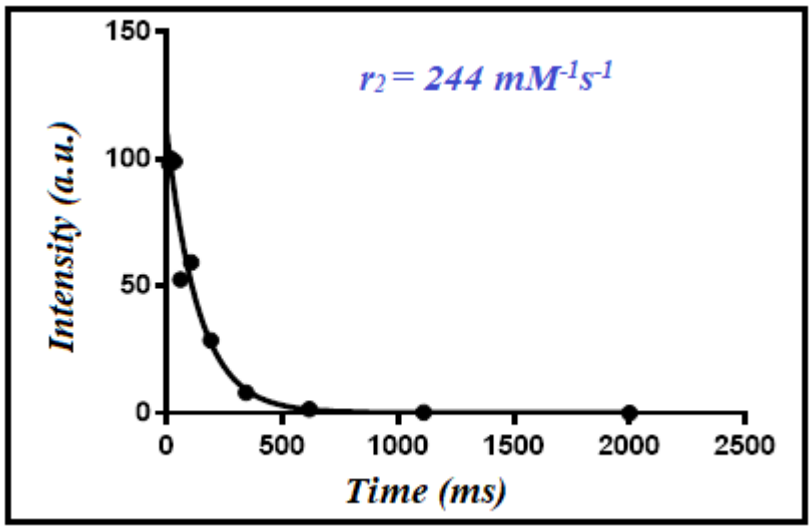

Figure 3-47: Transverse relaxation rate measurement for $KMnF_3$ with 11-aminoundecanoic acid.

Since iron oxide NPs are the commonly used as T_2 contrasting agents, $KFeF_3$ shows a potential for a contrast enhancement as T_2 contrasting agents. This was obvious from the obtained results in Table 3-6 where r_2 is nearly similar to those obtained for iron oxide particles. Although the longitudinal relaxation for $KFeF_3$ is high, the r_2/r_1 is less than 10 and higher than those of Resovist, which indicate that $KFeF_3$ could be considered as a highly efficient T_2 contrast agents.[62] The noticeable difference in transverse relaxation rate could be attributed to the small size and spherical morphology of the prepared NPs. The longitudinal and transverse decay of this contrast agent are illustrated in Figure 3-48 and Figure 3-49 respectively.

Table 3-6: The obtained longitudinal and transverse relaxitivity at 9.4 T for $KFeF_3$.

Relaxation rate	*Value ($mM^{-1}s^{-1}$)*
r_1	47
r_2	216

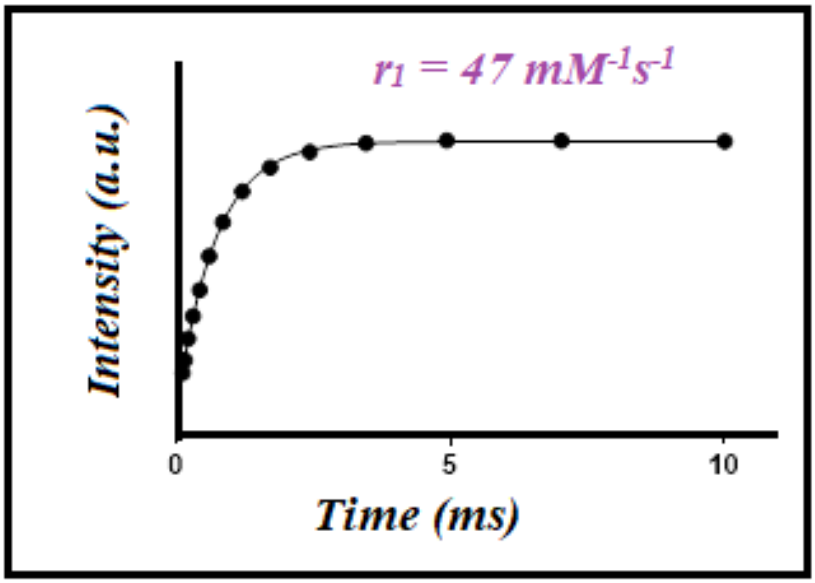

Figure 3-48: Longitudinal relaxation rate measurement for $KFeF_3$ with 11-aminoundecanoic acid

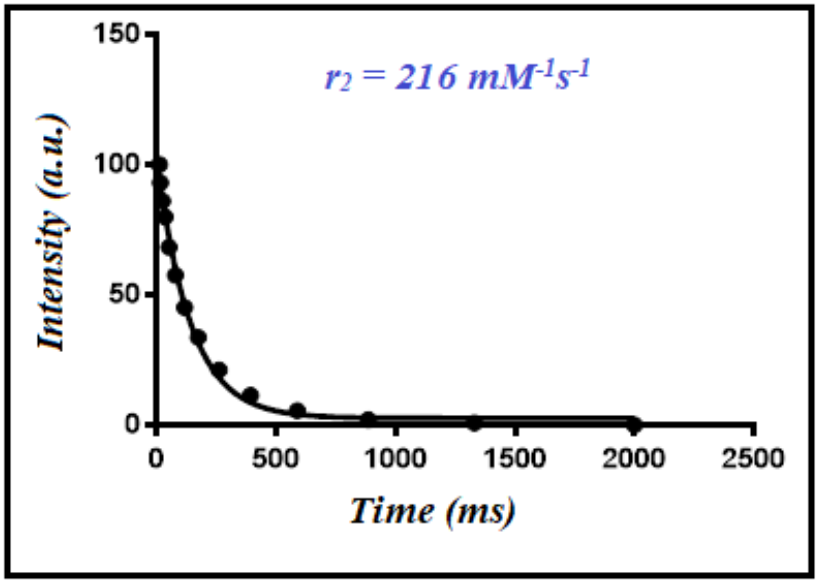

Figure 3-49: Transverse relaxation rate measurement for $KFeF_3$ with 11-aminoundecanoic acid

The results of the relaxation rate for $KCoF_3$ in Table 3-7 looks almost similar to those for $KFeF_3$. The values of r_1 and r_2 obtained by Figure 3-50and Figure 3-51 respectively are good enough to enable $KCoF_3$ to work as T_1 and T_2 contrast agents. Factors such as coating hydrophilic materials, small size and the spherical morphology have a dramatic impact on the $KCoF_3$ relaxitivities. Further *in-vitro* phantom study is needed to validate the obtained results.

Table 3-7: The obtained longitudinal, transverse relaxitivity at 9.7 T for $KCoF_3$.

Relaxation rate	*Value ($mM^{-1}s^{-1}$)*
r_1	26
r_2	220

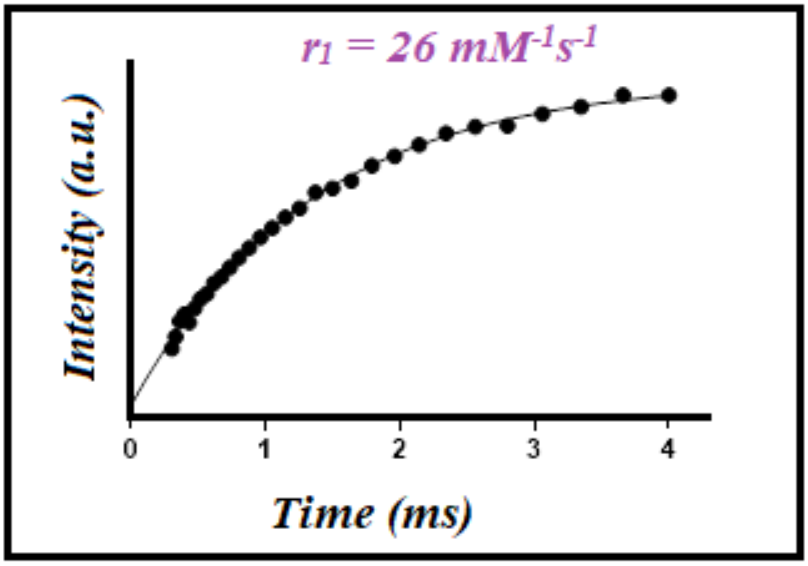

Figure 3-50: Longitudinal relaxation rate measurement for $KCoF_3$ with 11-aminoundecanoic acid

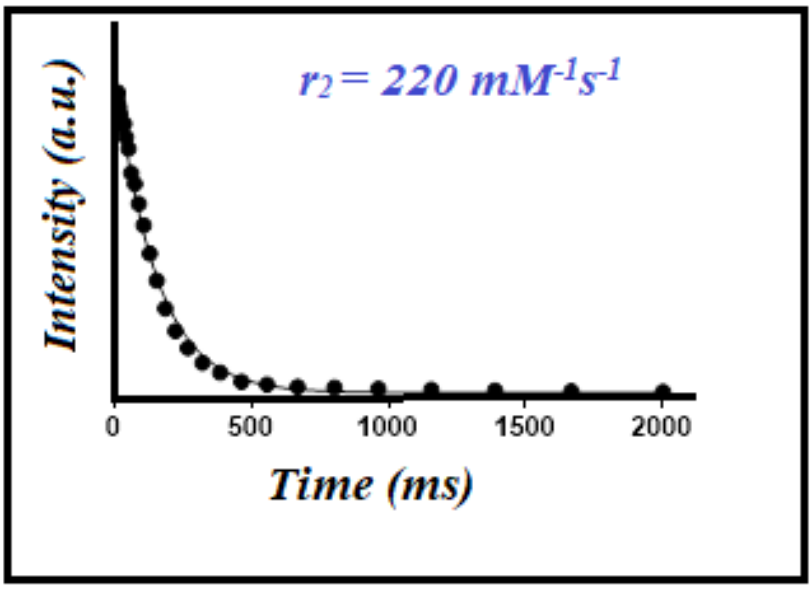

Figure 3-51: Transverse relaxation rate measurement for $KCoF_3$ with 11-aminoundecanoic acid

The most currently used contrast agents for clinical *MRI* investigations are gadolinium chelates for instant Gd-DTPA and Gd-DOTA which were previously reported to have r_1 relaxivity in the range 3-5 $mM^{-1}s^{-1}$.[63] In contrast, the results of r_1 obtained for this work were considerably high compared to some of the results obtained in previous studies for related gadolinium contrast agents as shown in Table 3-8. Furthermore, the spin-spin relaxation rate for the perovskite fluoride NPs are all higher than the reported gadolinium related contrasting agents (Table 3-9). In spite of the breakage in the perovskite structure during the surface modification with 11-aminoundecanoic acid ligand, these prepared NPs show a significant potential to work both as T_1 and T_2 contrast agents for Magnetic Resonance Imaging (*MRI*).

Table 3-8: r_1 and r_2 relaxivity for gadolinium related contrasting agents available in the literature.

Sample	*B_0 (T)*	*T (°C)*	*r_1 ($mM^{-1}s^{-1}$)*	*r_2 ($mM^{-1}s^{-1}$)*	*Ref*
Gd-DTPA	0.47	25	3.8	4.2	[64]
Gd-DOTA	0.47	25	4.2	4.6	[64]
Gd_2O_3-IC	1.5	25	28	52	[65]
Gd_2O_3-PVP	7	25	12.1	33.2	[66]
Gd_2O_3-SiPEG	7	25	4.4	28.9	[67]
Gd_2O_3 (cubic like)	3	25	19.5	89.4	[68]
Gd_2O_3 (sphere)	3	25	22.2	128.9	[68]
G4-5-Gd_2O_3-PEG	7	25	53.9	182.8	[63]

Table 3-9: r_1 and r_2 relaxitivity for the studied perovskite KMF_3 coated with 11-aminoundecanoic acid.

Sample	*B_0 (T)*	*T (°C)*	*r_1 ($mM^{-1}s^{-1}$)*	*r_2 ($mM^{-1}s^{-1}$)*
$KMnF_3$-11-aminoundecanoic acid	9.4	25	42	244
$KFeF_3$-11-aminoundecanoic acid	9.4	25	47	216
$KCoF_3$-11-aminoundecanoic acid	9.4	25	26	220

3.4.6 Functionalisation of KMF_3 (M = Mn, Fe, Co) with alendronate

Functionalisation processes for KMF_3 (M= Mn, Fe, Co) with sodium alendronate also leads to breakage of the perovskite structure, where extra peaks appeared in their PXRD

patterns, revealing unsuccessful encapsulation process. All PXRD patterns are available in the appendix. Due to this unsuccessful functionalisation with both 11-aminoundecanoic acid and sodium alendronate, it was important to look for an alternative strategy to encapsulate the bared NPs with other ligands such as potassium oleate, PEG, oleylamine or utilizing another method such as ligand exchange for a successful functionalisation. The next chapter will explain a new attempt using these strategies.

3.5 Conclusions

In summary, different NPs with different hydrodynamic sizes were synthesised using the well-known co-precipitation method. The PXRD analysis showed a pure single phase for these formed NPs except $KNiF_3$ and $KCuF_3$ before the functionalisation step, which reveal the retained perovskite structure, although some unknown impurities were detected. The formed nanoparticles were subjected to a functionalisation process with 11-aminoundecanoic acid and with sodium alendronate to transform them from the hydrophobic phase to water soluble phase for biocompatibility as *MRI* contrast agents. Unfortunately, this process was not successful due to the breakage of the perovskite structure that occurs due to the high energy absorbed which causes the perovskite structure bonds to break. The formed nanoparticles showed an effect on both r_1 and r_2 relaxitivities compared to the currently commercial and clinical agents. Therefore, these biocompatible NPs could have the potential to work as dual mode T_1 and T_2 contrast agents for *MRI* device simultaneously, due to the small hydrodynamic size, colloidal stability, and water dispersibility. To validate these obtained data, further *MR* phantom experiments are needed.

3.6 References

1. R. A. Taylor and L. H. Sansing, *Clinical and Developmental Immunology*, 2013, **2013**, 10.
2. S. F. Wang, X. T. Zu, G. Z. Sun, D. M. Li, C. D. He, X. Xiang, W. Liu, S. B. Han and S. Li, *Ceramics International*, 2016, **42**, 19133-19140.
3. T. Zargar and A. Kermanpur, *Ceramics International*, 2017, **43**, 5794-5804.
4. M. Goodarz Naseri, E. B. Saion and A. Kamali, *ISRN Nanotechnol.*, 2012, **2012**, 1-11.
5. H. Hong, N. K. Memon, Z. Dong, B. H. Kear and S. D. Tse, *Proceedings of the Combustion Institute*, 2019, **37**, 1249-1256.
6. S. Deka, V. Saxena, A. Hasan, P. Chandra and L. M. Pandey, *Materials Science and Engineering: C*, 2018, **92**, 932-941.
7. L.-N. Hao, K. Liu, S. Cheng, Y. Wang, Y.-J. Xu and H.-S. Qian, *Materials Letters*, 2017, **196**, 145-148.
8. J. Wan, X. Chen, Z. Wang, X. Yang and Y. Qian, *Journal of Crystal Growth*, 2005, **276**, 571-576.
9. Z. Yuanbi, Q. Zumin and H. Jiaying, *Chin. J. Chem. Eng.*, 2008, **16**, 451-455.
10. M. Faraji, Y. Yamini and M. Rezaee, *Journal of the Iranian Chemical Society*, 2010, **7**, 1-37.
11. E. Ruiz-Hernández, A. López-Noriega, D. Arcos, I. Izquierdo-Barba, O. Terasaki and M. Vallet-Regí, *Chemistry of Materials*, 2007, **19**, 3455-3463.
12. G. Kandasamy and D. Maity, *International Journal of Pharmaceutics*, 2015, **496**, 191-218.
13. R. A. Candeia, M. I. B. Bernardi, E. Longo, I. M. G. Santos and A. G. Souza, *Materials Letters*, 2004, **58**, 569-572.
14. N. E. Jones, *University of Hull*, 2015.
15. H. W. Lehui Lu, Hongjie Zhang, and Shiquan Xi, *Journal of cColloid and interface Science*, 2003, **266**, 115-119.
16. К. О. Н. Тугова Е. А., *Nanosystem: Phisics, Chemistry, Mathmatics*, 2014, **5(6)**, 854-860.
17. L. Li, X. Wang, Y. Lan, W. Gu and S. Zhang, *Industrial & Engineering Chemistry Research*, 2013, **52**, 9130-9136.
18. N. A. Keasberry, M. Banobre-Lopez, C. Wood, G. J. Stasiuk, J. Gallo and N. J. Long, *Nanoscale*, 2015, **7**, 16119-16128.
19. Y.-k. Sun, M. Ma, Y. Zhang and N. Gu, *Colloids and Surfaces A: Physicochemical and Engineering Aspects*, 2004, **245**, 15-19.
20. Brown, *X-Ray Identification and crystal structure of clay*.
21. A. Bee, R. Massart and S. Neveu, *Journal of Magnetism and Magnetic Materials*, 1995, **149**, 6-9.
22. R. L. H. Blake, R.E.; Zoltai, T.; Finger, L.W., *American Mineralogist*, 1966, **51**, 123-129.
23. S. Seraj, B. Mirzayi and A. Nematollahzadeh, *Advanced Powder Technology*, 2014, **25**, 1520-1526.
24. E. Darezereshki, *Materials Letters*, 2010, **64**, 1471-1472.
25. D. K. Kim, Y. Zhang, W. Voit, K. V. Rao and M. Muhammed, *Journal of Magnetism and Magnetic Materials*, 2001, **225**, 30-36.
26. R. H. Langley, C. K. Schmitz and M. B. Langley, *Journal of Chemical Education*, 1984, **61**, 643.
27. K. Knox, *Acta Crystallographica*, 1961, **14**, 583-585.
28. N. Tyagi, E. Ghanti, N. Gupta, N. P. Lalla and R. Nagarajan, *Bulletin of Materials Science*, 2009, **32**, 583-587.

29. N. B. o. S. Monograph, *Journal*, 1968, 6, 45.
30. N. B. o. Standards, *Journal*, 1968, 6,37.
31. A. Okazaki and Y. Suemune, *Journal of the Physical Society of Japan*, 1961, **16**, 671-675.
32. P. Hole, K. Sillence, C. Hannell, C. M. Maguire, M. Roesslein, G. Suarez, S. Capracotta, Z. Magdolenova, L. Horev-Azaria, A. Dybowska, L. Cooke, A. Haase, S. Contal, S. Manø, A. Vennemann, J.-J. Sauvain, K. C. Staunton, S. Anguissola, A. Luch, M. Dusinska, R. Korenstein, A. C. Gutleb, M. Wiemann, A. Prina-Mello, M. Riediker and P. Wick, *Journal of Nanoparticle Research*, 2013, **15**, 2101.
33. A. M. Hofmeister and K. Billups, *Spectrochimica Acta Part A: Molecular Spectroscopy*, 1991, **47**, 1607-1617.
34. I. Nakagawa, A. Tsuchida and T. Shimanouchi, *The Journal of Chemical Physics*, 1967, **47**, 982-989.
35. J. Blasco, J. Stankiewicz and J. García, *Journal of Solid State Chemistry*, 2006, **179**, 898-908.
36. H. S. Sheu, W. J. Shih, W. T. Chuang, I. Li and C. S. Yeh, *Journal of the Chinese Chemical Society*, 2010, **57**, 938-945.
37. J. Blasco, J. Stankiewicz and J. García, *Journal of Solid State Chemistry*, 2006, **179**, 898-908.
38. J. Weidenborner, *Acta Crystallographica*, 1961, **14**, 1051-1056.
39. E. Tugova and O. Karpov, *Nanosyst.: Phys., Chem., Math*, 2014, **5**, 854-860.
40. C. Chang and D. Mao, *International Journal of Chemical Kinetics*, 2007, **39**, 75-81.
41. V. Popov and A. Gorbunov, *Inorganic materials*, 2006, **42**, 275-281.
42. M. Shafer and R. Roy, *Journal of the American Ceramic Society*, 1959, **42**, 563-570.
43. J. Tareen and K. Krishnamurthy, *Bulletin of Materials Science*, 1981, **3**, 9-13.
44. K. Semenov, N. Charykov, A. Kritchenkov, I. Cherepkova, O. Manyakina, D. Tyurin, A. Shestopalova, V. Keskinov, K. Ivanova and N. Ivanova, *V. 5. N2. P. 315*, 2014, **319**.
45. C. Queffélec, M. Petit, P. Janvier, D. A. Knight and B. Bujoli, *Chemical Reviews*, 2012, **112**, 3777-3807.
46. M. Sikorska, M. Gazda and J. Chojnacki, *Acta Crystallographica Section E*, 2012, **68**, m820-m821.
47. K. L. Haas and K. J. Franz, *Chemical reviews*, 2009, **109**, 4921-4960.
48. R. G. Pearson, *Journal of the American Chemical society*, 1963, **85**, 3533-3539.
49. R. D. Hancock and A. E. Martell, *Chemical Reviews*, 1989, **89**, 1875-1914.
50. N. A. Keasberry, M. Bañobre-López, C. Wood, G. J. Stasiuk, J. Gallo and N. J. Long, *Nanoscale*, 2015, **7**, 16119-16128.
51. J. Kim, H. S. Kim, N. Lee, T. Kim, H. Kim, T. Yu, I. C. Song, W. K. Moon and T. Hyeon, *Angewandte Chemie*, 2008, **120**, 8566-8569.
52. Z. Jia, L. Yue, Y. Zheng and Z. Xu, *Materials Chemistry and Physics*, 2008, **107**, 137-141.
53. C. Wu, X. Qiao, J. Chen, H. Wang, F. Tan and S. Li, *Materials Letters*, 2006, **60**, 1828-1832.
54. G. Vanitha, K. Rajavel, G. Boopathy, V. Veeravazhuthi and P. Neelamegam, *Chemical Physics Letters*, 2017, **669**, 71-79.
55. J. M. a. A. S. B Clara Gnana Selvi, *Advances in Natural Sciences: Nanoscience and Nanotechnology*, 2016, **7**.
56. S. Anjum, R. Tufail, K. Rashid, R. Zia and S. Riaz, *Journal of Magnetism and Magnetic Materials*, 2017, **432**, 198-207.

57. H. S. K. Jaeyun Kim, Nohyun Lee, Taeho Kim, Hyoungsu Kim, Taekyung Yu, and W. K. M. In Chan Song, and Taeghwan Hyeon, *Angew. Chem. Int.*, 2008, **47**, 8438 –8441.
58. I. Lynch and K. A. Dawson, *Nano Today*, 2008, **3**, 40-47.
59. A. G. Melezhyk, *Nanosstem: Physics, Chemistry, Mathmatics, 2014, (2), P. 294–306*, 2014, **5(2)**, 294–306.
60. H. W. Wibeke Nodhey, Morten Bruvold, Per Jynge, Jostein Krane, Heidi Brurok, *NMR Biomed*, 2003, **16**, 82-95.
61. Z. J. Liu, X. X. Song and Q. Tang, *Nanoscale*, 2013, **5**, 5073-5079.
62. N. Schleich, P. Sibret, P. Danhier, B. Ucakar, S. Laurent, R. N. Muller, C. Jérôme, B. Gallez, V. Préat and F. Danhier, *International Journal of Pharmaceutics*, 2013, **447**, 94-101.
63. S. L. Mekuria, T. A. Debele and H.-C. Tsai, *ACS Applied Materials & Interfaces*, 2017, **9**, 6782-6795.
64. R. B. Lauffer, *Chemical Reviews*, 1987, **87**, 901-927.
65. W. X. Md. Wasi Ahmad, Sung June Kim, Jong Su Baeck, Yongmin Chang, Ji Eun Bae, Kwon Seok Chae, Ji Ae Park, Tae Jeong Kim, Gang Ho Lee, *Scientific reports*, 2015, **5**.
66. J. Fang, P. Chandrasekharan, X.-L. Liu, Y. Yang, Y.-B. Lv, C.-T. Yang and J. Ding, *Biomaterials*, 2014, **35**, 1636-1642.
67. J.-L. Bridot, A.-C. Faure, S. Laurent, C. Rivière, C. Billotey, B. Hiba, M. Janier, V. Josserand, J.-L. Coll, L. Vander Elst, R. Muller, S. Roux, P. Perriat and O. Tillement, *Journal of the American Chemical Society*, 2007, **129**, 5076-5084.
68. C.-H. S. I-Fang Li, Hwo-Shuenn Sheu, Hui-Chi Chiu, Yi-Wei Lo, Wei-Ting Lin, Jyh-Horng Chen, Chen Sheng-Yeh, *Advanced Functional Materials*, 2008, **18**, 766-776.

CHAPTER 4

Solvo-thermal synthesis of PEGylated and Alendronated KMF_3 (M = Mn, Fe, Co,) nanoparticles

4 Introduction

In the last chapter it was described that the functionalisation of KMF_3 (M = Mn, Fe, Co) formed by co-precipitation method with 11-aminoundecanoic acid and sodium alendronate were unsuccessful due to the instability of the perovskite structure. Here, the synthesis of KMF_3 (M = Mn, Fe, Co) NPs *via* solvothermal method using different encapsulation ligands is described. Surface coating of the NPs is mandatory to avoid aggregation and may provide a high degree of colloidal stability for NPs.[1] Several number of coating materials have been reported in literature including polyethylene glycol, chitosan and dextran, fatty acids and liposome, inorganic materials such as alumina and silica.[1-3] Oleic acid or potassium oleate have been reported to have a great affinity to bind iron oxide NP surface due to steric repulsion, providing a great stabilisation of NPs.[4] It is possible that these inorganic coating material provide a mono layer on the nanoparticle surface and transfer them from hydrophobic to hydrophilic, resulting in remarkable dispersity in organic solvents. It is also reported that the use of two surfactants as coating materials provide bilayers into the nanoparticle surface, enabling them to be easily dispersed in water. The mechanism of coating involves a unique adsorption of the primary layer on to the surface of the NPs through the carboxylic acid head terminal of the oleate surfactant. A second layer such as poly ethylene glycol or alendronic acid is adsorbed onto the primary layer due to hydrophobic interactions. This secondary layer provides hydrophilic groups that is capable to disperse magnetic nanoparticle in water.[5-9] In this chapter a new solvothermal method to prepare KMF_3 with different functionalisation strategy is described. Same metals salts (KF, MCl_2 or MBr_2) and different coating materials (oleate, poly ethylene glycol or alendronate) are used as starting materials. It is worth noting that the synthesis of the NPs and the functionalisation process with oleate take place in one step. After functionalisation with oleate, a ligand exchange protocol using alendronate ligand was performed, Alendronate binds NPs through its phosphate oxygen atoms, providing a great stability to make them compatible and well dispersed in aqueous medium to be applicable for biological application.[10]

4.1 Experimental

4.1.1 Synthesis of polyethylene glycol coated KMF_3 NPs (PEGylated KMF_3) (M = Mn, Fe, Co, Cu and Ni)

In a similar way described in ref (9).[11] The synthesis of KMF_3 (M = Mn, Fe, Co, Cu, and Ni) was carried out as follow: 5.75mmol potassium fluoride, 1.917mmol of the correspondence metal chloride $MCl_2.4H_2O$ was used for all the synthesis of the

PEGylated NPs compounds except $KCoF_3$ and $KNiF_3$ where 1.898 and 3.834mmol of $CoBr_2$ and $NiBr_2$ respectively were used. This was mixed with 3.834mmol potassium oleate, 5.915 ml absolute ethanol and 1.915ml n-hexane. The overall mixture was transferred to a stainless Teflon-line 23 ml-capacity autoclave. Once the autoclave containing the mixture was tightly closed, it was then transferred to an oven at a temperature of 160 °C for 24 hours. After cooling to room temperature, the entire mixture was transferred to a 15 ml centrifuge tube and centrifuged at 4500 RPM for 5 minutes. The supernatant was discarded. To remove the excessive potassium oleate and by-product KCl, the formed NPs was washed 3 times each 10 ml by a washing mixture of (1:1) (water: ethanol). To functionalise the NPs with PEG or alendronic acid, they were re-dispersed in 5 ml ethanol containing 0.0383 g PEG 1500 or sodium alendronate using the same stainless Teflon-line 23 ml-capacity autoclave and solvothermally treated in the same oven for 2 hours at 160°C. To remove the excess PEG 1500 or alendronic acid, the PEGylated KMF_3or $KMnF_3$ coated with alendronic acid product was transferred into centrifuge tube and washed 3 times (each 10 ml) by the same washing mixture used to remove the excessive PEG or alendronic acid. Eventually the final product was transferred to a centrifuge tube and quenched in liquid nitrogen by immersing the tube into a beaker containing 25 ml fresh liquid nitrogen to freeze it prior to the insertion into a dry freezer for 48 hours to dry. Freez-drying is an excellent technique that has been considered to improve the long-term stability of colloidal NPs.[12] On the other hand, the poor colloidal stability in aqueous medium could hinder their use in clinical application.[12] The dried NPs were collected and stored in a glass bottle for further use. Figure 4-1 represents the different steps involve in the synthesis of the coated NPs with PEG. The same steps were involved in the synthesis of KMF_3 coated with sodium alendronate.

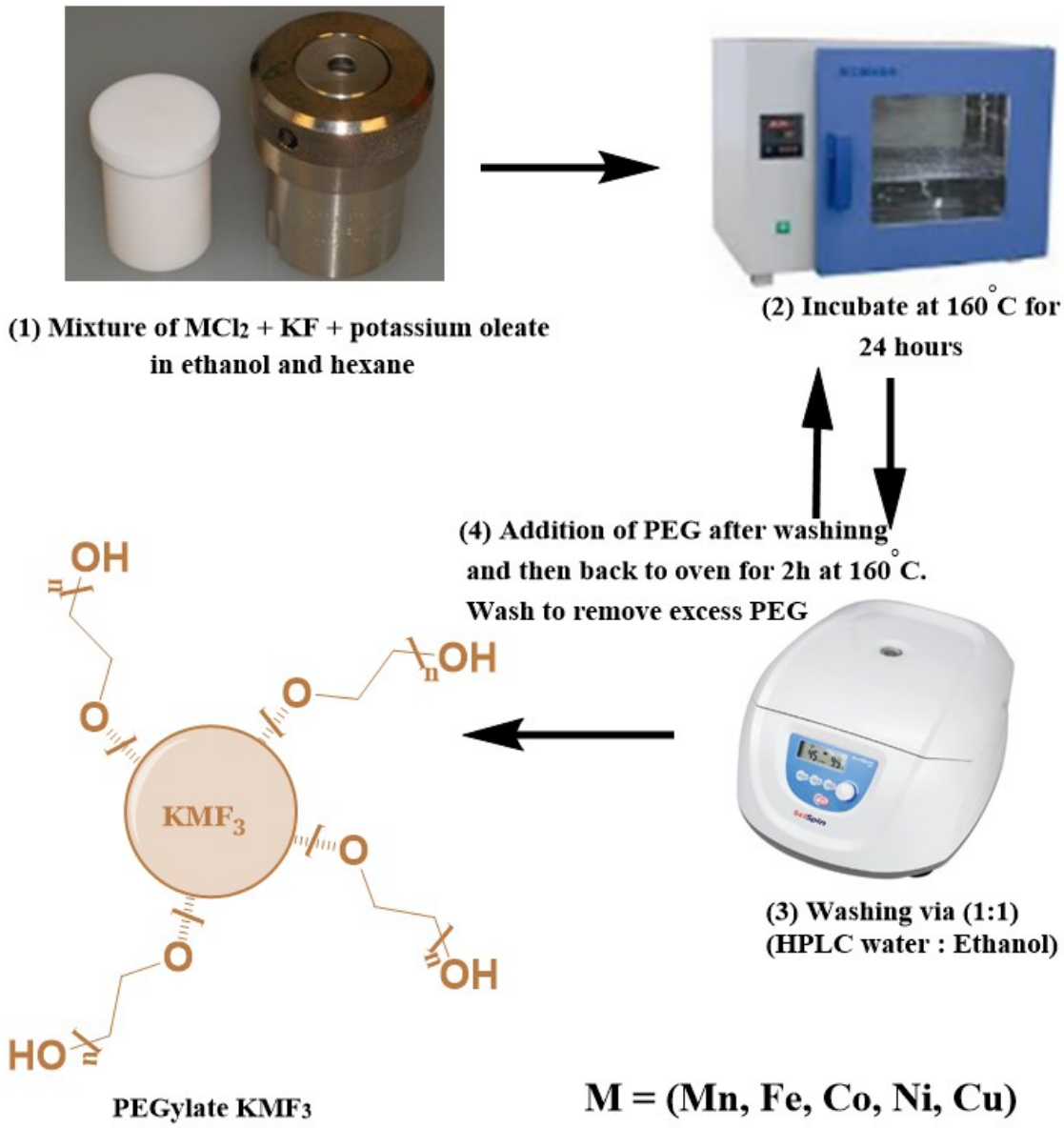

Figure 4-1: Different steps involve in the hydrothermal synthesis of PEGylated KMF_3 (M = Mn, Fe and Co)

4.2 Results and Discussion

4.2.1 PXRD analysis of PEGylated $KMnF_3$

Powder X-ray diffraction (PXRD) analysis was carried out to investigate the crystalline structures of the formed NPs. It was observed that the PXRD pattern for the as prepared nanoparticle before the functionalisation steps using the solvothermal method matches well with the bulk cubic spinel structure available in the database.[13] The as prepared compound is in its single phase and has no other contaminant produced as no other peaks appear in the obtained PXRD. The average crystalline size diameter estimated by Deby-Scherrer equation is 109 nm and the unit cell parameters are shown in Table 4-1.

From the PXRD pattern shown in Figure 4-2, it is obvious that the unit cell of the $KMnF_3$ coated with PEG is totally retained as the corresponding pattern exhibits all the peaks which appeared in the single-phase pattern. However, a few new peaks appear at 2θ = 31.6143 deg, 32.5710 deg and 36.2490 deg. A further washing attempts were made to remove these unknown contaminants, however all trials preformed were unsuccessful to wash them away and therefore to produce a single-phase perovskite structure.

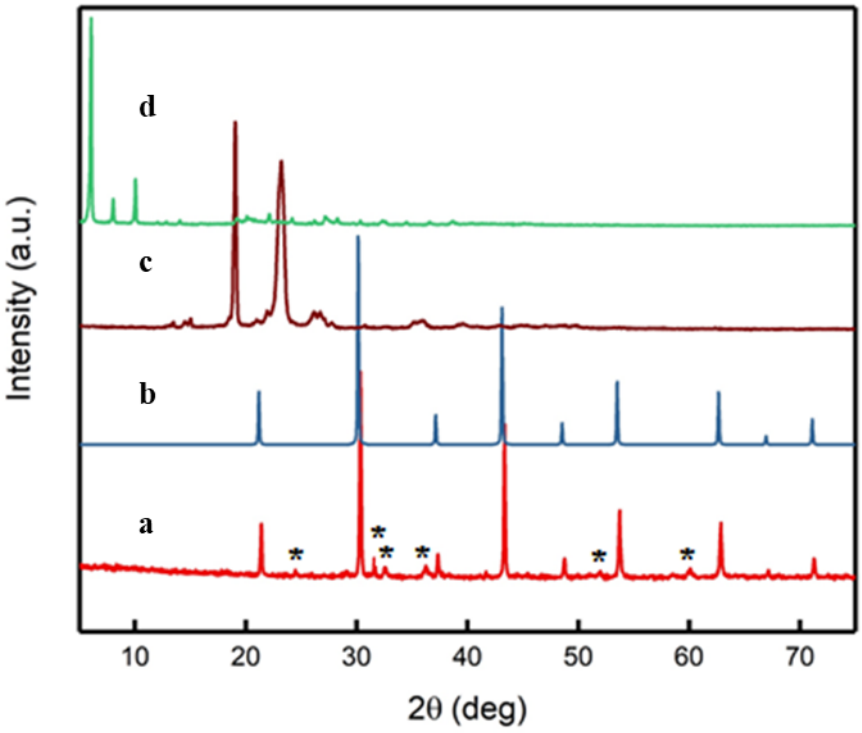

Figure 4-2: PXRD pattern of PEGylated $KMnF_3$ (a) compared to bare $KMnF_3$ (b), PEG (c) and K-Oleate (d). The peaks highlighted by * correspond to unknown impurities.

4.2.2 PXRD analysis of PEGylated $KFeF_3$

Figure 4-3 represents a PXRD comparison between PEGylated $KFeF_3$, model $KFeF_3$, PEG and K-oleate. As expected the PXRD pattern of PEGylated $KMnF_3$ NPs revealed a retained cubic primitive structure and small number of peaks at same 2θ (deg) as for PEGylated $KMnF_3$ were observed. These peaks were compared by the corresponding pattern coated with oleate as seen in Figure 4-3. Based on this comparison, these contaminants were exactly matched the extra peaks presented when the NPs were coated with oleate. Another evidence was observed when the NPs were formed *via* the solvothermal method using iron (II) chloride and potassium fluoride only, pure and single-phase NPs were formed without any impurities, these two reasons confirm the main source of the impurities existed in the PEGylated NPs. The crystal size was calculated using the Scherer equation and found 51 nm. The observed curvature of the baseline in the PXRD pattern occurs in the region at 2θ between 5 and 10 degrees is probably a significant sign for the encapsulation process by PEG ligand. This phenomena is commonly stated in literature where it is characteristic of ligands encapsulation.[14] The unit cell parameters calculated for the prepared NPs are illustrated in Table 4-1.

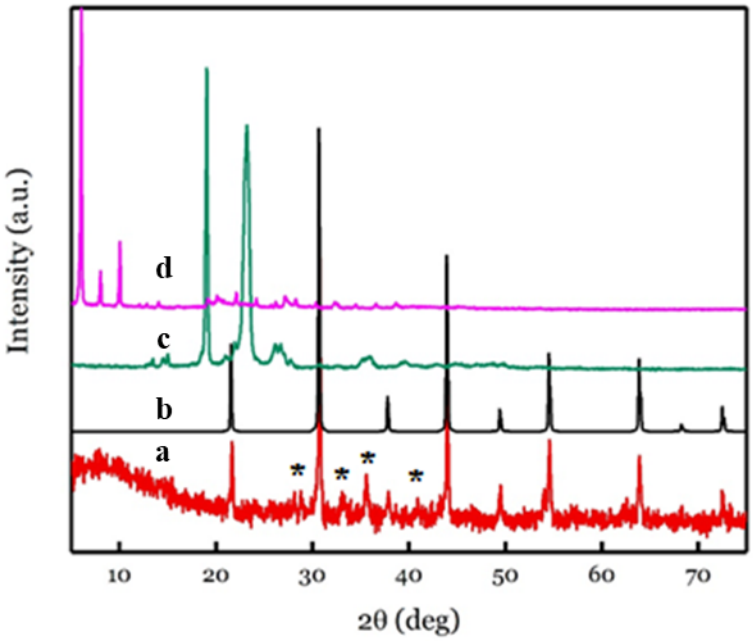

Figure 4-3: PXRD pattern of PEGylated $KFeF_3$ (a) compared to bare $KFeF_3$ (b), PEG (c) and K-Oleate (d). The peaks highlighted by * correspond to unknown impurities.

4.2.3 PXRD analysis of PEGylated $KCoF_3$

The PXRD pattern for $KCoF_3$ coated with PEG in Figure 4-4 showed a retained cubic structure that is in perfect agreement with the single phase $KCoF_3$.[13] Few extra peaks appeared at 36.907 (2θ) and this was attributed for the same reason described in section 4.3.2. The unit cell parameters for the formed NPs compared to the standard model are displayed in Table 4-1.

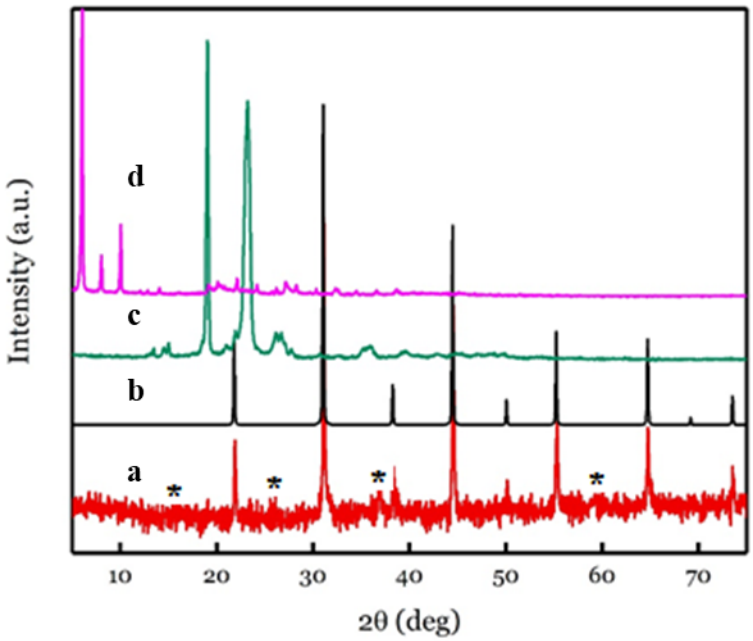

Figure 4-4: PXRD pattern of PEGylated $KCoF_3$ (a) compared to bare $KCoF_3$ (b), PEG (c) and K-Oleate (d). The peaks highlighted by * correspond to unknown impurities.

Table 4-1: The obtained unit cell parameters results for the investigated compounds compared to the literature reference standards.

	Formed NPs				*Model*			
NP	*Geometry*	*a=b=c*	*α*	*V*	*Geometry*	*a=b=c*	*V*	*Ref*
$KMnF_3$	Cubic	4.1790(3)	90	72.96	Cubic	4.1893	73.52	[15]
$KFeF_3$	Cubic	4.1159(3)	90	69.73	Cubic	4.1205	69.73	[16]
$KCoF_3$	Cubic	4.0666(8)	90	67.46	Cubic	4.0708	67.25	[17]

4.2.4 PXRD analysis of PEGylated $KZnF_3$ and $KCuF_3$

Figure 4-5 and Figure 4-6 represent the PXRD patterns for $KZnF_3$ and $KCuF_3$ coated with PEG respectively. Clearly the cubic perovskite structure for $KZnF_3$ was retained.

Unlike the PXRD patterns for $KMnF_3$ and $KFeF_3$, the pattern exhibited many peaks at many definite 2θ angles. Taking a close look at the PEG and oleate patterns in comparison to this pattern, a conclusion could be made that none of the peaks are related neither to oleate nor to PEG ligands. A complicated situation existed for $KCuF_3$, the tetragonal perovskite structure is not retained as seen in Figure 4-6 . This was expected due to the fact that during the washing step with (1:1) (H_2O:EtOH), a dark blue layer was formed in the discarded solution taking away most of the Cu (II) ions, thus making a disruption to the $KCuF_3$ unit cell structure by supplying more energy and forcing the bonds to break.

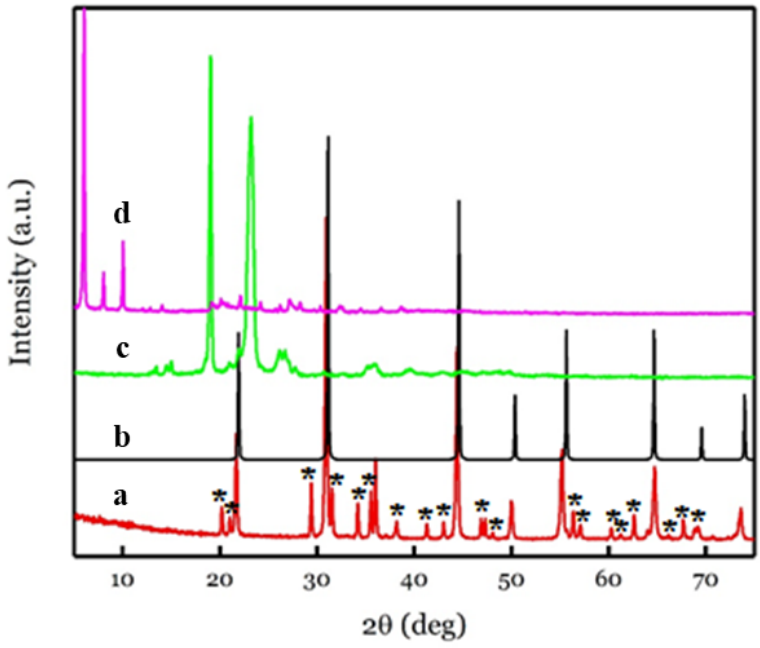

Figure 4-5: PXRD pattern of PEGylated $KZnF_3$ (a) compared to bare $KZnF_3$ (b), PEG (c) and K-Oleate (d). The peaks highlighted by * correspond to unknown impurities.

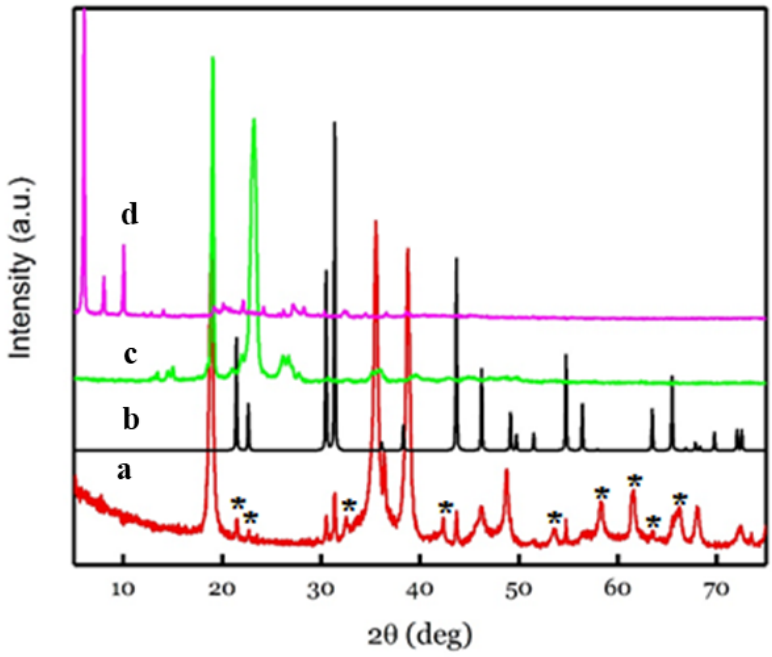

Figure 4-6: PXRD pattern of PEGylated $KCuF_3$ (a) compared to bare $KCuF_3$ (b), PEG (c) and K-oleate (d). The peaks highlighted by * correspond to unknown impurities.

4.2.5 FTIR analysis of coated K-oleate $KMnF_3$ NPs

In order to confirm the coating mechanism of the oleic acid into the surface of KMF_3 NPs before the ligand exchange with PEG. FTIR measurements were performed both for pure oleate and KMF_3 (M = Mn, Fe, Co) NPs coated with oleate. The FT-IR spectra of coated oleate $KMnF_3$ NPs compared to pure oleate is shown in Figure 4-7. Two intense bands were observed at 2936 and 2850 cm^{-1} in the pure oleate spectrum. These bands were assigned to the CH_2 asymmetric and symmetric stretches respectively. The sharp peak at 1560 cm^{-1} was assigned to the C=O stretch, while the stretching band appeared at 1272 cm^{-1} reflects the presence of C-O bond. There were also two bands exhibited at 1419 and 912 cm^{-1} were attributed to the presence of O-H group.

Referring to the coated KMF_3(M = Mn, Fe, Co) with K-oleate spectra in Figure 4-7 to Figure 4-9, it is worth to note that the expected two intense bands related to the asymmetric and symmetric CH_2 stretches appeared with less intensity compared to the same peaks in pure K-oleate, however it was observed a slight shift in their position towards lower energy region, in particular at 2917 and 2849 cm^{-1} respectively. K.Nakamoto attributed this shift to the fact that the monolayer carrying the long oleic acid hydrocarbon chains surrounding the NPs were in close-packed position in the crystal unit cell.[18, 19] These obtained results have given an evidence to confirm the adsorption of the K-oleate molecules on the crystal surface of KMF_3 (M = Mn,Fe,Co) as carboxylate.

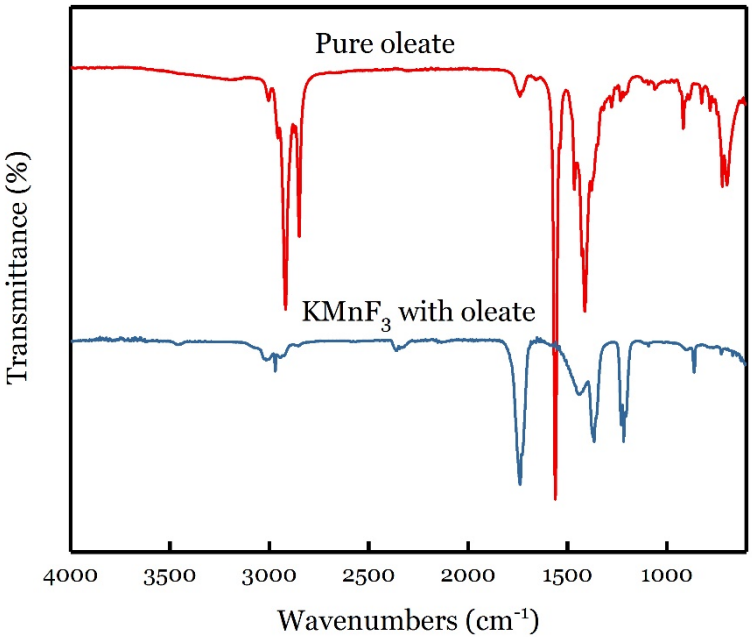

Figure 4-7: FTIR spectrum of $KMnF_3$ coated with oleic acid (blue) compared to pure oleic acid (red)

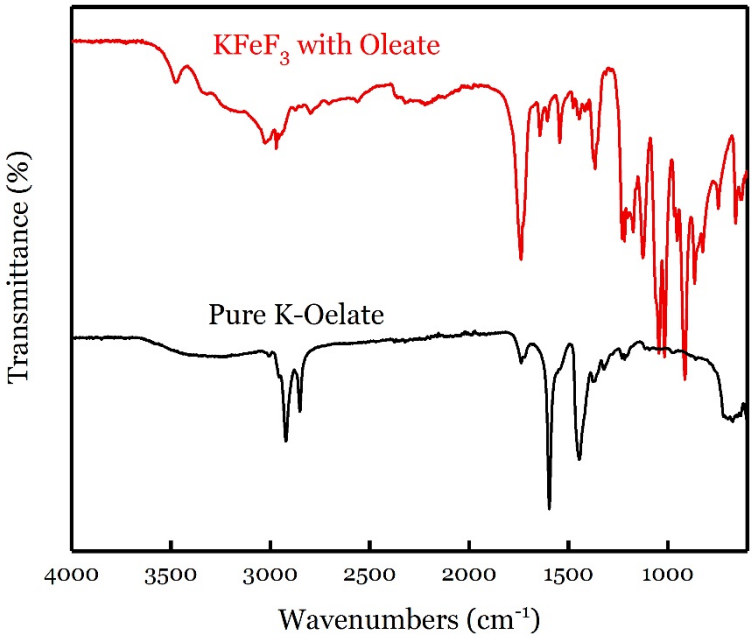

Figure 4-8: FTIR spectrum of $KFeF_3$ coated with K-oleate (red) compared to pure K-oleate (black)

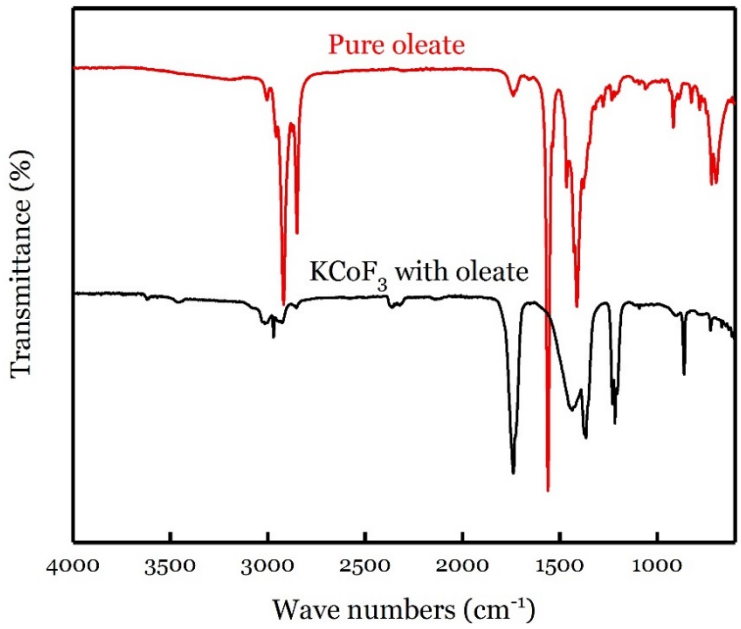

Figure 4-9: FTIR spectrum of $KCoF_3$ coated with K-oleate(black) compared to pure K-oleate (red)

4.2.6 FTIR analysis of PEGylated KMF_3 (M = Mn, Fe, Co) NPs

To utilize the PEGylated KMF_3(M= Mn, Fe, Co) NPs as a contrasting agent for Magnetic Resonance Imaging *(MRI),* it was crucial to modify their surface with a representative biocompatible polymer to transfer them from hydrophobic phase to hydrophilic phase in aqueous medium. There are many ligands that are well known to work as a coating ligand, among these ligands, polyethylene glycol (PEG) is a ligand that can be attached to the surface of the nanoparticle by exchange with passivated agent potassium oleate. Figure 4-10 represents a schematic diagram for ligand exchange process between PEG and oleate on the synthesised nanoparticle surface.

PEGs have been widely utilized as stabilizing ligands for various NPs used in biological application due to their nonfouling properties that enable the NPs to resist protein adsorption and bypass the reticuloentheial (RES) and natural barriers, for instant the nasal mucosa and therefore shielding them from immune detection.[20] The coating of the PEG ligand onto the surface of the KMF_3 NPs crystal was investigated by recording the FTIR spectrum for the synthesised NPs and comparing them with the FTIR spectra of the pure PEG. Form Figure 4-11to Figure 4-13, it can be seen that all the peaks assigned for the characteristics transmittance frequencies observed in pure PEG were observed in the coated NPs. The peak at 1123 cm^{-1} assigned to the asymmetric vibrational band for (C-O-C). Two extra peaks appeared on the fabricated NPs at 1375 and 2855 cm^{-1} and they are assigned to the asymmetric vibrational modes for C-C and C-H bonds respectively.

Theses evidences Confirmed the successful coating process; therefore, the formed compounds are expected to be stable in any aqueous biological media.

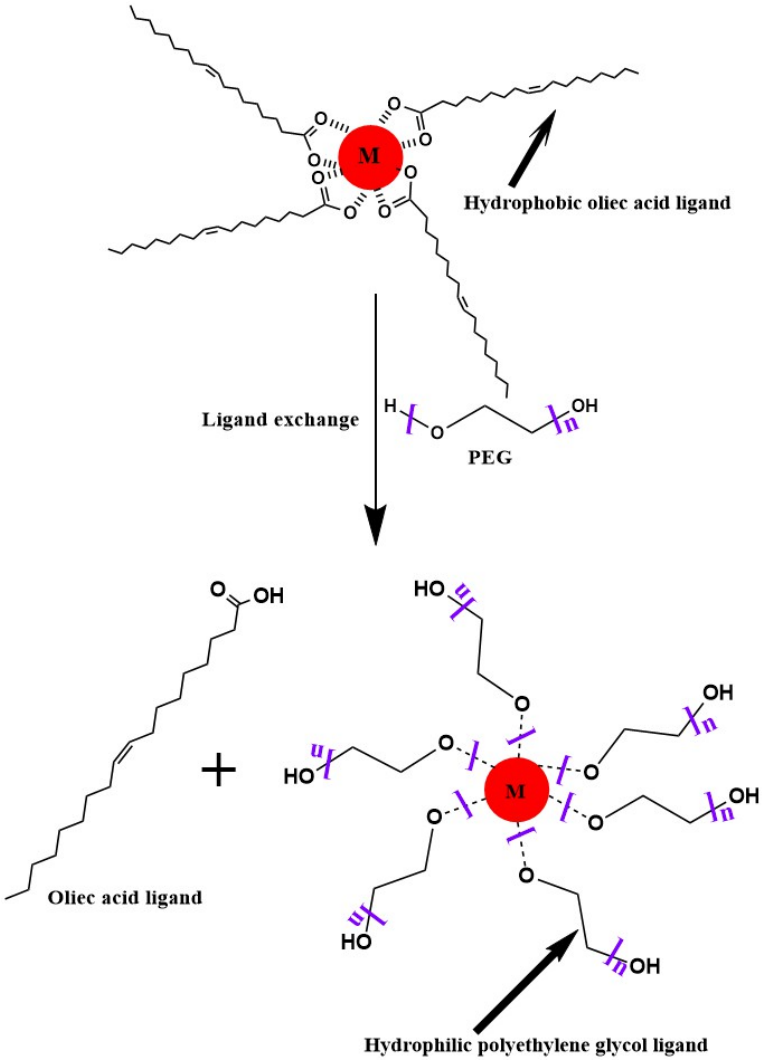

Figure 4-10: Ligand exchange mechanism between Poly Ethylene Glycol (PEG) ligand with potassium oleate

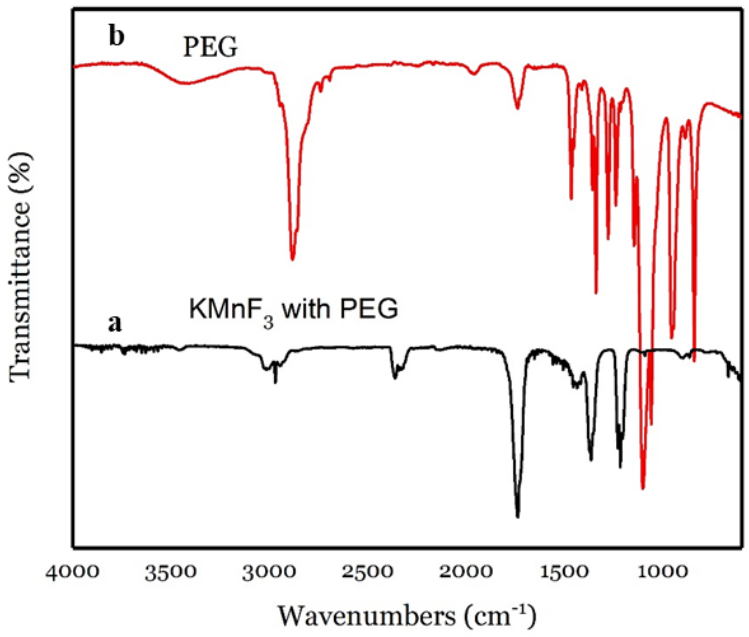

Figure 4-11: FTIR spectrum of $KMnF_3$ coated with PEG (a) compared to pure PEG (b)

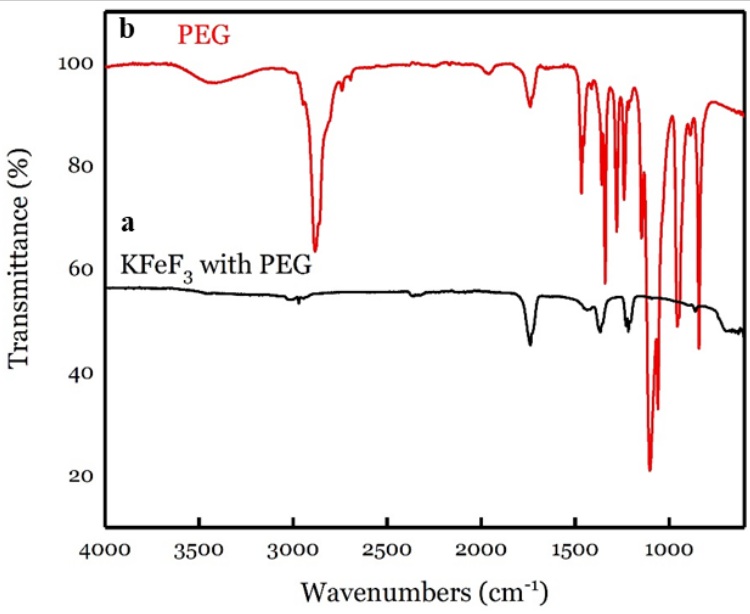

Figure 4-12: FTIR spectrum of $KFeF_3$ coated with PEG (a) compared to pure PEG (b)

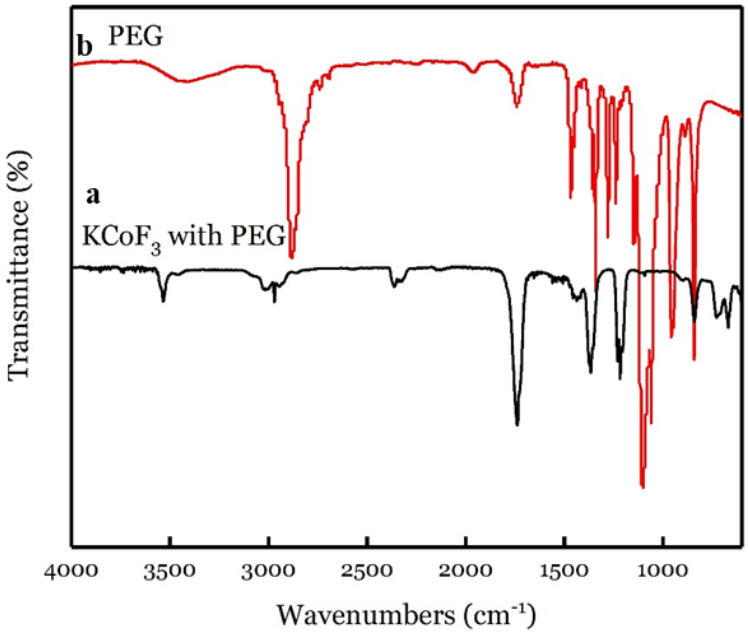

Figure 4-13: FTIR spectrum of $KCoF_3$ coated with PEG (black) compared to pure PEG (red)

4.2.7 Nano Tracking Analysis (*NTA*)

The size of NPs plays an important key role in their application. NPs with small diameters and narrow size distribution are considered to be the most desirable for biomedical applications. Various range of studies suggested that the recommended dimeter of the NPs should be in the range 10-100 nm to prevent rapid exertion from systemic circulation due to extravasation, renal clearance or uptake into the reticuloendothelial system, and emboli within capillaries.[21, 22]

The size distribution of the KMF_3 (M = Mn, Fe, Co) coated with PEG as measured by NTA are shown in Figure 4-14 to Figure 4-16. The mean hydrodynamic diameters of the synthesized NPs are 179, 149 and 134 nm for coated PEGylated $KMnF_3$, $KFeF_3$ and $KCoF_3$ respectively. These values are greater than the values obtained for the uncoated compounds using the same techniques 174,112, 57 nm. It is possible that the NPs aggregate prior to encapsulation is due to the higher surface to volume ratio. Another reason for the obtained bigger diameter could be related to the formation of the large layer of poly ethylene glycol into the nanoparticle surface. The observed polydispersity size distribution of the coated PEGylated NPs in Figure 4-14 to Figure 4-16 is another issue that might hinder their use as a contrast agents. NTA measurement of 100 nm silica particles Known standard shown in Figure 4-17 is carried out to calibrate the instrument and to make sure that a high accuracy for the crystal size measurements for all the prepared nanoparticle are obtained. The NTA size distribution graph obtained for this known silica standard showed a mean crystal size of roughly 113 nm, however the most

distributed size (mode) is about 104 which is in close agreement with the expected value of 100 nm. The higher mean value is attributed to the existence of few larger particles dispersed in the solution which are formed due to aggregation. The obtained results for this silica standard confirmed that all NTA measurements were accurate and have excellent reproducibility. On the other hand, the results obtained for the prepared NPs reveal that the hydrodynamic radius of these NPs are too big in size and have poor dispersity in aqueous medium, therefore cannot be used for medical application as contrast agents.

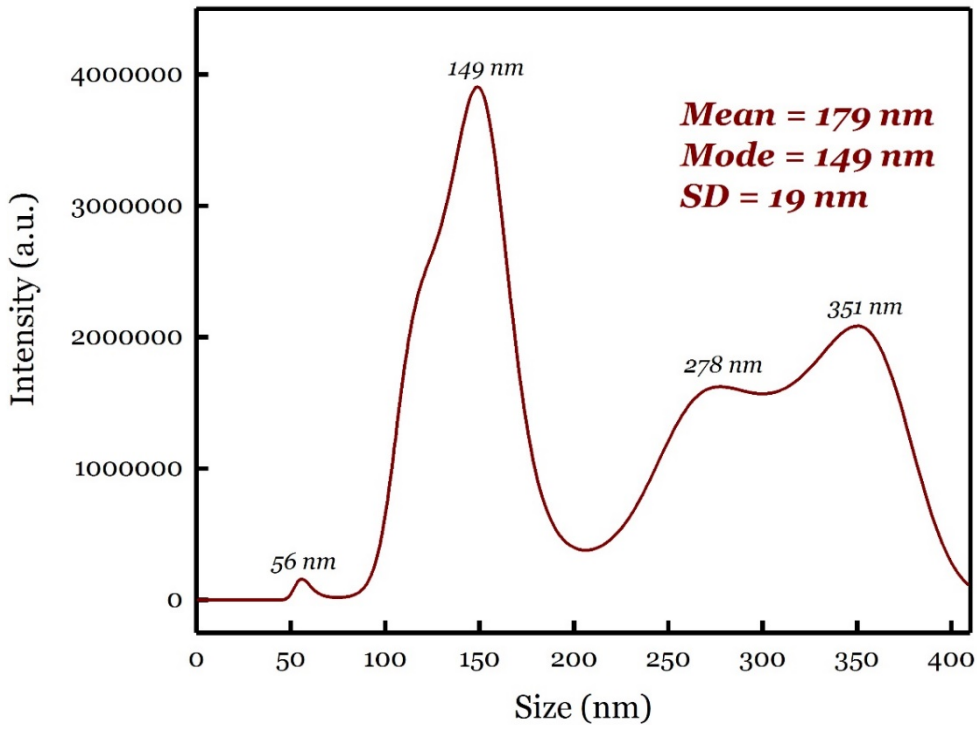

Figure 4-14: Nano Tracking analysis (NTA) size distribution graph obtained for the PEGylated $KMnF_3$ NPs.

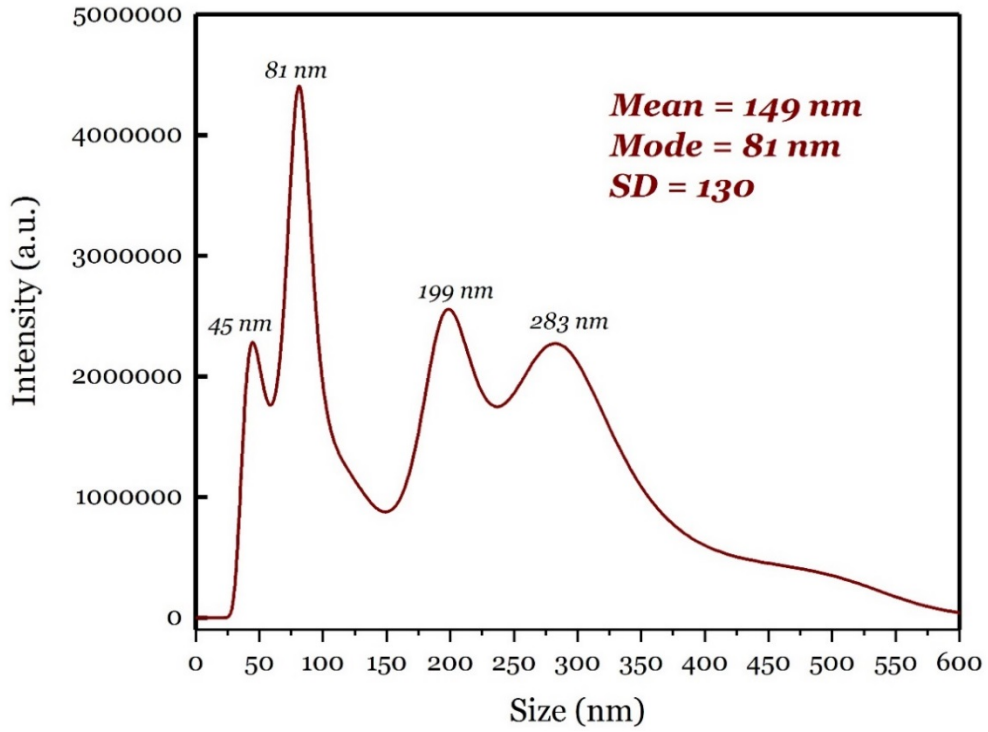

Figure 4-15: Nano Tracking analysis (NTA) size distribution graph obtained for the PEGylated $KFeF_3$ NPs.

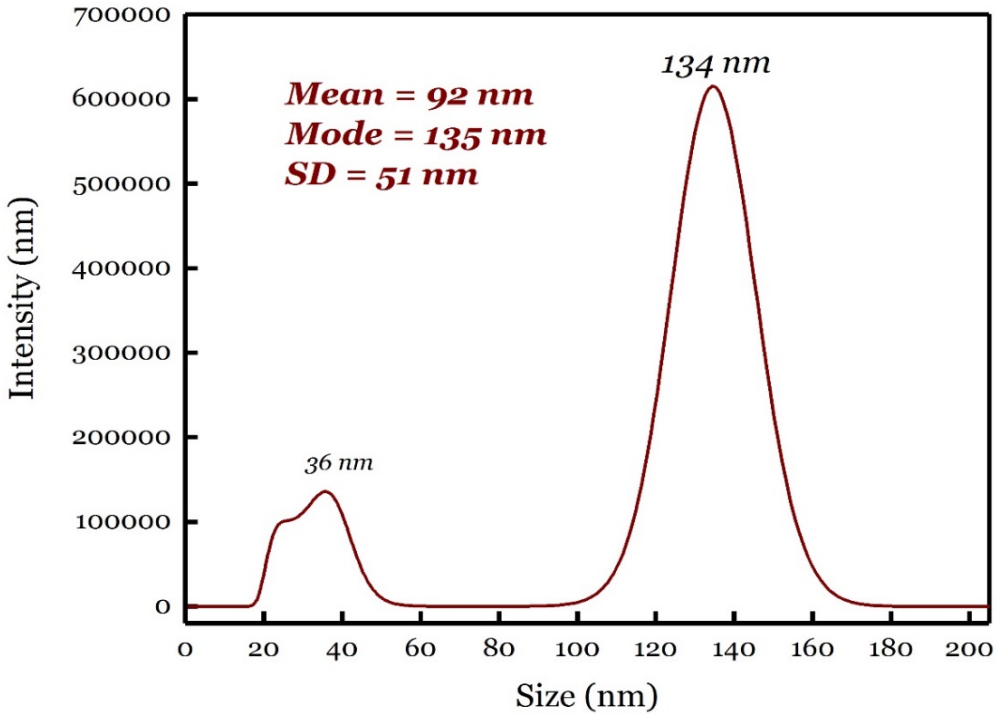

Figure 4-16: Nano Tracking analysis (NTA) size distribution graph obtained for the PEGylated $KCoF_3$ NPs.

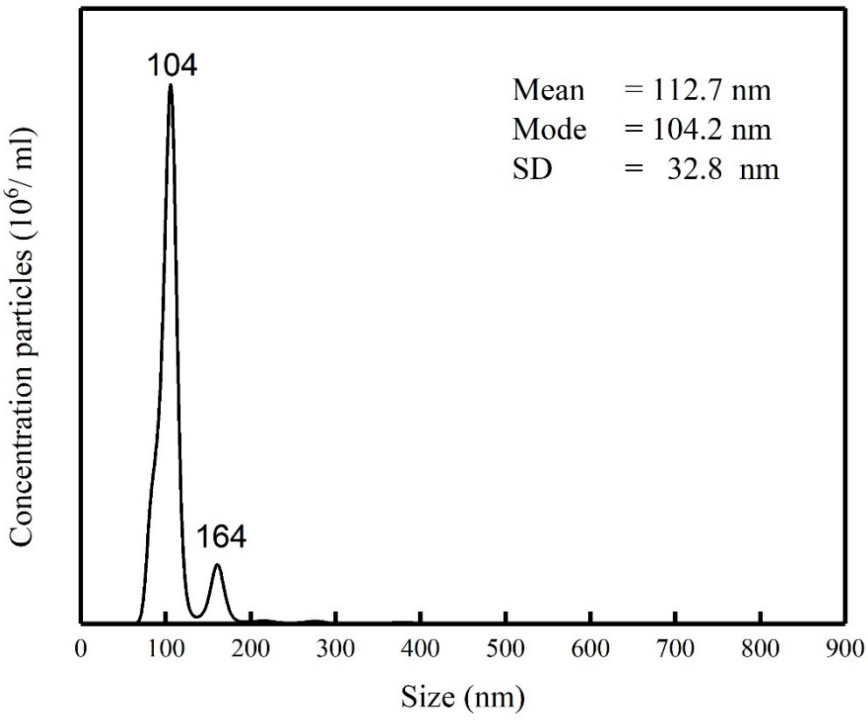

Figure 4-17: Nano Tracking analysis (NTA) size distribution graph obtained for the standard silica particles of 100 nm dispersed in water.

4.3 Synthesis and functionalisation of KMF_3 (M = Mn, Fe, Co) using ligand exchange between K-oleate and Na-alendronate

4.3.1 PXRD analysis of coated alendronate $KMnF_3$

PEGylated KMF_3 (M = Mn, Fe, Co) to be used as a contrast agent for Magnetic Resonance Imaging *MRI* using ligand exchange were shown to contain unknown impurities as well as a large hydrodynamic diameter. A new trial using a ligand exchange between K-oleate as a primary ligand and sodium alendronate as a secondary ligand was established. Figure 4-18 represents a comparison in the PXRD patterns obtained for coated alendronate $KMnF_3$ NPs in comparison to the pure $KMnF_3$, pure oleate and pure alendronate.

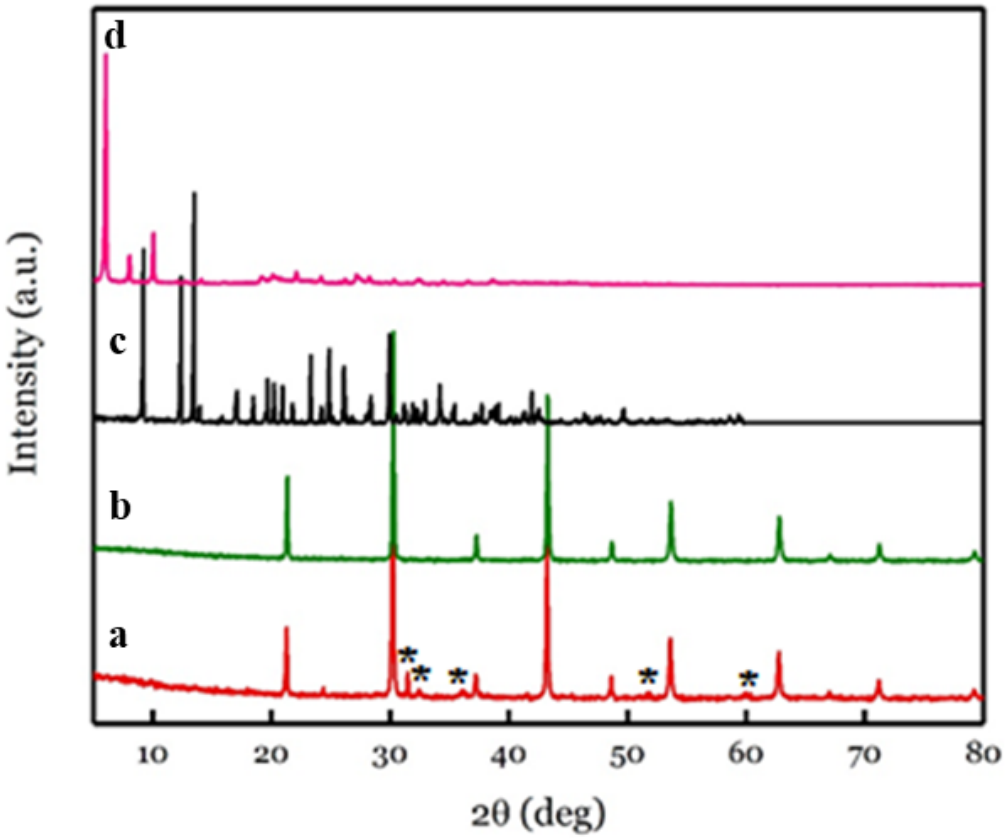

Figure 4-18: PXRD pattern of coated alendronate $KMnF_3$ (a) compared to bare $KMnF_3$ (b), alendronate (c) and K-Oleate (d). The peaks highlighted by * correspond to unknown impurities.

The analysis of the position and relative intensity of diffraction peaks suggests the formation of $KMnF_3$ NPs. However, some extra peaks appeared at 30, 32, 35, 54 and 60 2θ degrees due to unknown impurities. The unit cell parameters reported for $KMnF_3$ is 4.1893 Å. The PXRD analysis revealed the formation of NPs with lattice parameters of 4.1755(3) Å which is agreement with literature clear evidence for the successful synthesis of $KMnF_3$ and suggest that the surface coating did not alter or break down the main perovskite unit cell.[13] Samples were washed repeatedly to remove the unknown impurities in order to obtain a single phase coated alendronate $KMnF_3$. However, the unknown impurities could not be removed. After many unsuccessful attempts using these ligands to produce a single-phase unit cell for $KMnF_3$ NPs, a decision was made to change the synthesis method by using different coating ligands.

4.3.2 PXRD analysis of coated alendronate $KFeF_3$

PXRD patterns comparison is plotted for coated alendronate $KFeF_3$ with both pure ligands and the standard bulk $KFeF_3$ as seen in Figure 4-19. PXRD pattern for the coated alendronate $KFeF_3$ shows a good agreement with that of the pure $KFeF_3$ NPs where all of the cubic perovskite main peaks appeared. Revelling that the structure is retained and did

not changed after both functionalisation steps with K- oleate or after being ligand exchanged with Na-alendronate. However, more extra peaks appear at various 2θ degrees after the functionalisation with Na-alendronate, it is possible that some unknown impurities do exist as a secondary phase in the overall product. The unit cell parameters for the prepared coated NPs is 4.1231(3) Å. Since this value is closer to the theoretical value of the standard bulk $KFeF_3$ (4.1205 Å).[13] However some unknown impurities were observed in the formed products, a decision was made that this NPs cannot be used as a contrast agents.

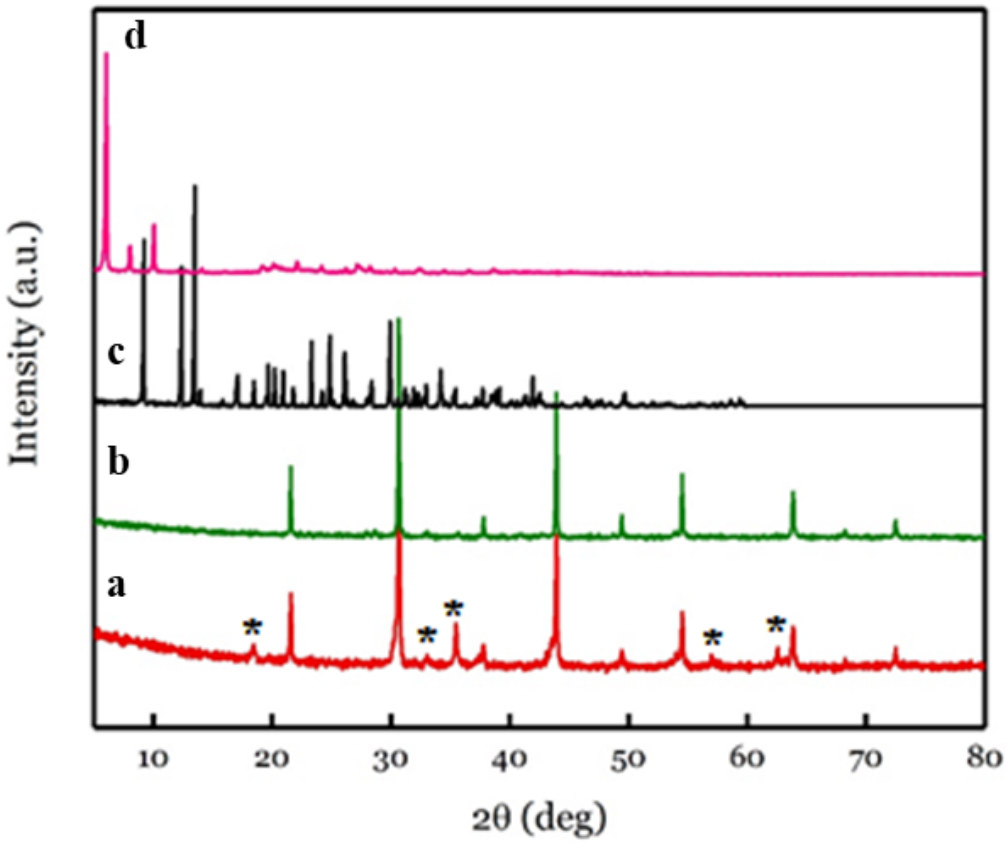

Figure 4-19: PXRD pattern of coated alendronate $KFeF_3$ (a) compared to bare $KFeF_3$ (b), alendronate (c) and K-Oleate (d). The peaks highlighted by * correspond to unknown impurities.

4.3.3 PXRD analysis of coated alendronate $KCoF_3$

PXRD patterns of coated alendronate $KCoF_3$ NPs, pure $KCoF_3$, pure oleate and pure alendronate ligands are presented in Figure 4-20. Similar issue as for coated alendronate $KMnF_3$ and $KFeF_3$ was observed. However higher amount of impurities is detected in this case. These impurities did not appear when ligands were not added as a starting material in the reaction vessel, thus a single phase $KCoF_3$ is obtained. It is more likely that the main source of these impurities is the K-oleate ligand or sodium alendronate ligands.

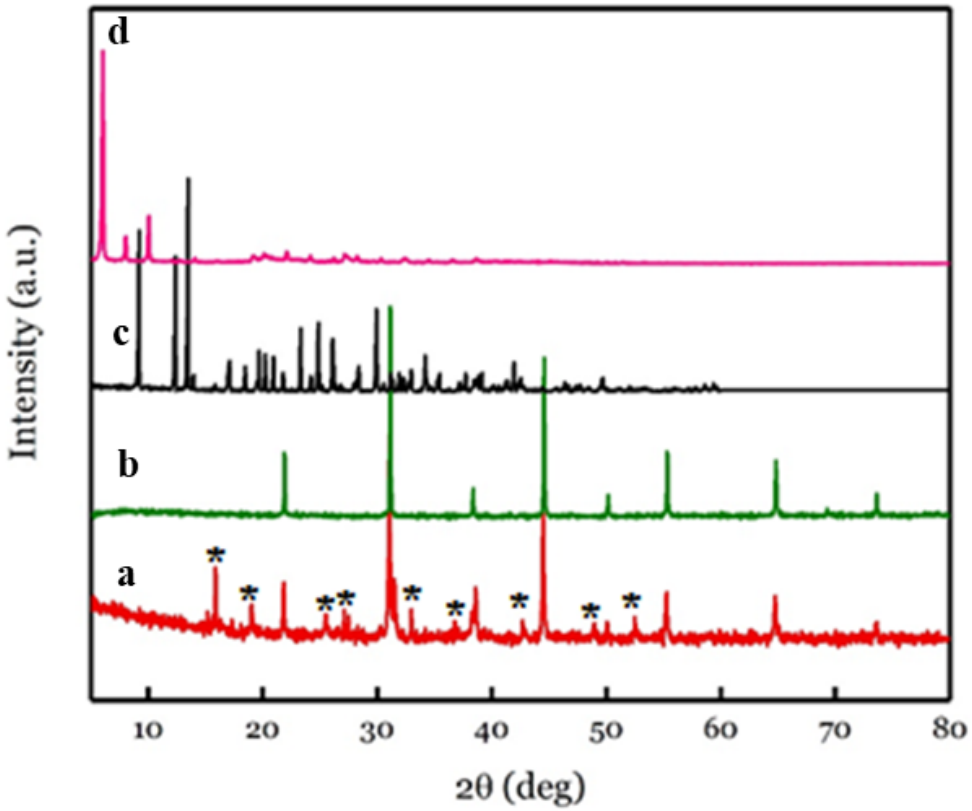

Figure 4-20: PXRD pattern of coated alendronate $KCoF_3$ (a) compared to bare $KCoF_3$ (b), alendronate (c) and K-Oleate (d). The peaks highlighted by * correspond to unknown impurities.

4.3.4 FTIR analysis

Figure 4-21 to Figure 4-23represent the FTIR spectrum of the alendronate coated KMF_3 (M = Mn, Fe, Co) respectively. In all figures, the prepared NPs spectrum are compared with pure alendronate and coated oleate NPs. It is clear that a ligand exchange mechanism take place, transforming the coated oleate NPs to coated alendronate NPs, where all peaks in the coated oleate product disappeared and exchanged by new peaks that are appeared due to the sodium alendronate ligand. The stretching band appeared at 1110 cm^{-1} in all figures is correlated to existence of P=O group and vibrational mode at 980 cm^{-1} is due to the carboxylic alcohol functional group, both stretching and vibrational bands reflect the attachment of alendronate at the surface of the NPs.

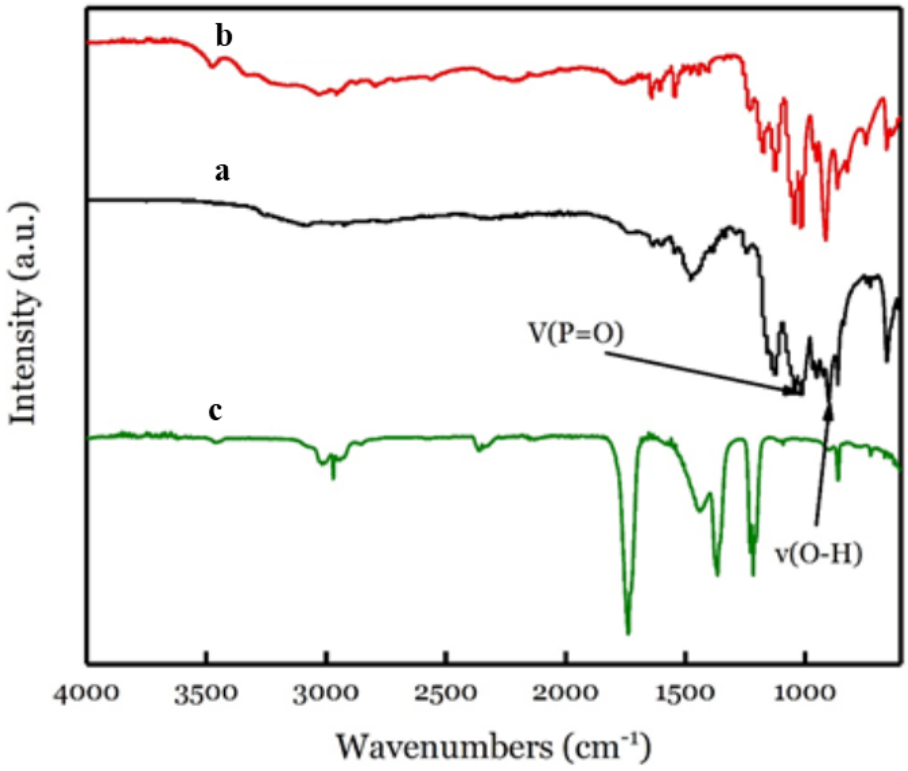

Figure 4-21: FTIR spectrum of $KMnF_3$ coated with alendronate (a) compared to pure alendronate (b) and coated oleate $KMnF_3$ (c).

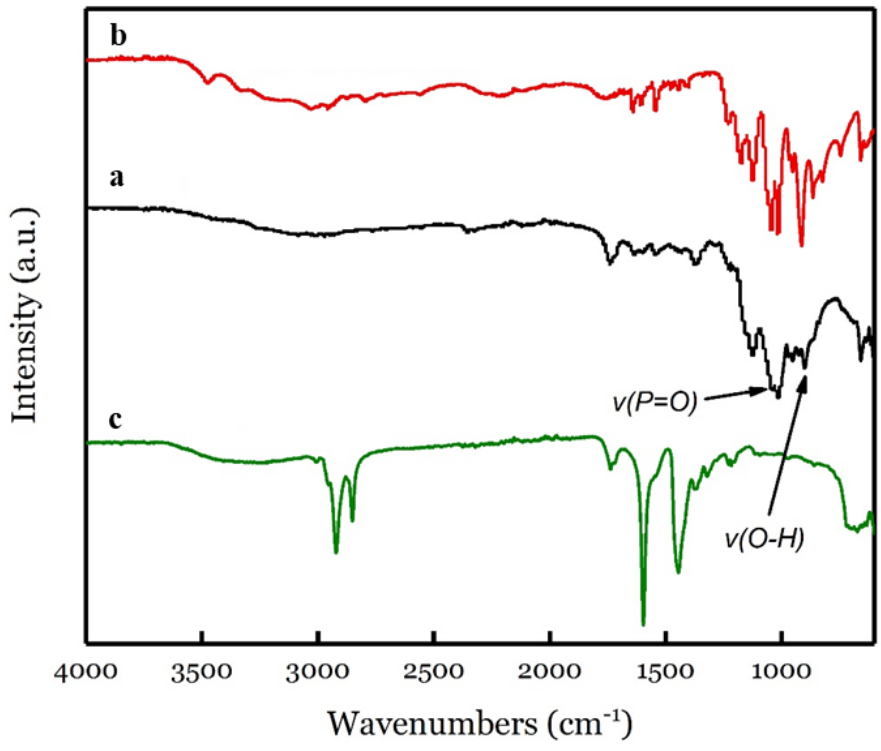

Figure 4-22: FTIR spectrum of $KFeF_3$ coated with alendronate (a) compared to pure alendronate (b) and coated oleate $KFeF_3$ (c).

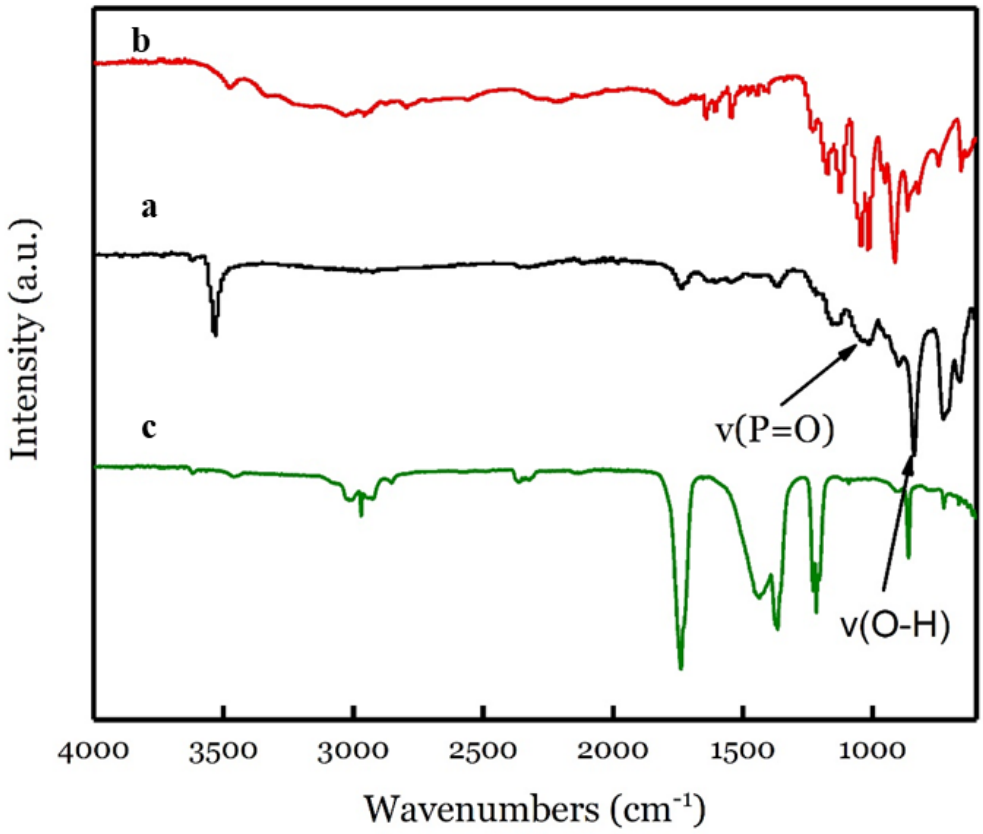

Figure 4-23: FTIR spectrum of $KCoF_3$ coated with alendronate (a) compared to pure alendronate (b) and coated oleate $KCoF_3$ (c).

4.3.5 Nano Tracking Analysis (NTA)

Figure 4-24 to Figure 4-26 display the Nano Tracking Analysis (NTA) spectrum for KMF_3 (M = Mn, Fe, Co) respectively. Since the perovskite structures of these prepared coated alendronate KMF_3 (M = Mn, Fe, Co) are retained, and despite of the existence of the unknown impurities formed, Nano tracking analysis (NTA) was still performed to investigate their crystal size diameters in order to make sure that they are in the applicable diameter to be used as contrast agents for medical application. Unfortunately, the analysis results reveal a large size in diameters of 180 nm, 182 nm and 189 nm for $KMnF_3$, $KFeF_3$ and $KCoF_3$ respectively. From these figures, it is also clear that all prepared NPs are aggregated, forming a poly dispersed solution in water, which is a clear evidence that these synthesised NPs are not suitable enough for biological application. A decision was made to change the hydrophobic K-oleate ligand to the hydrophilic oleylamine ligand prior to the ligand exchange with Na-alendronate ligand. The later will be discussed in chapter 5.

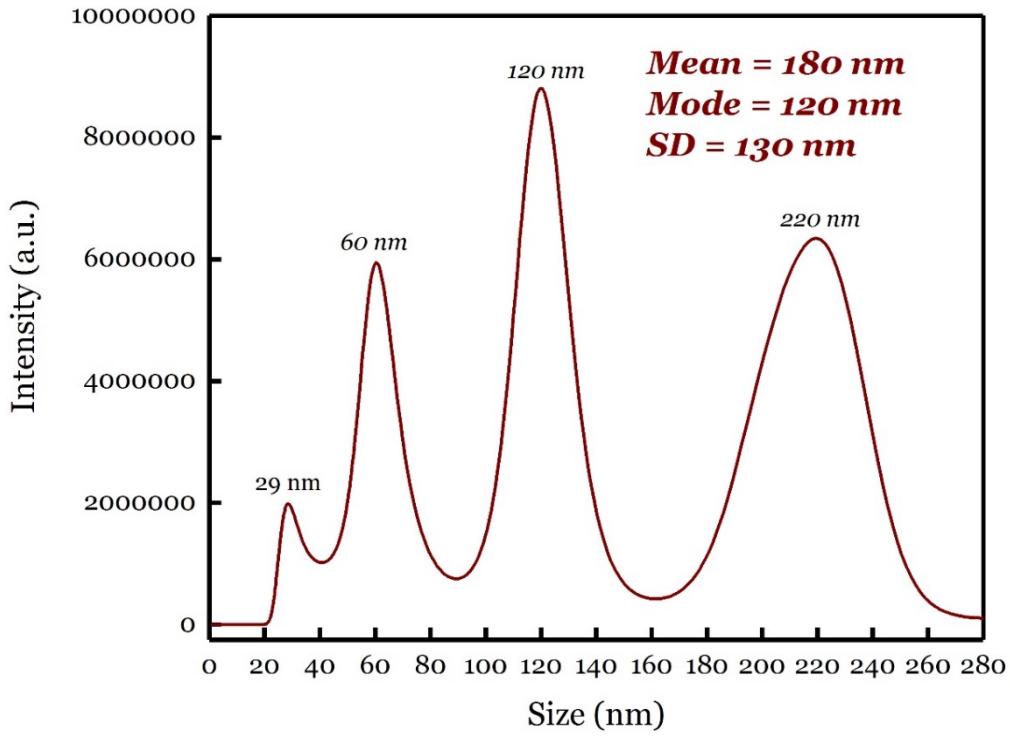

Figure 4-24: Nano Tracking analysis (NTA) size distribution graph obtained for the alendroted $KMnF_3$ NPs.

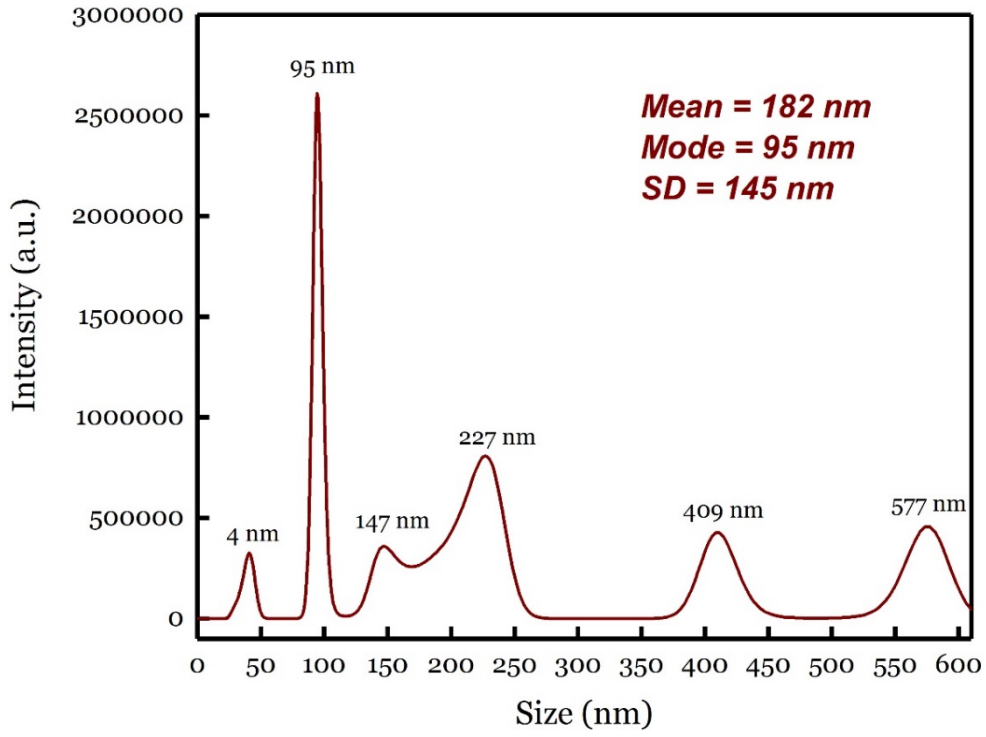

Figure 4-25: Nano Tracking analysis (NTA) size distribution graph obtained for the alendronated $KFeF_3$ NPs.

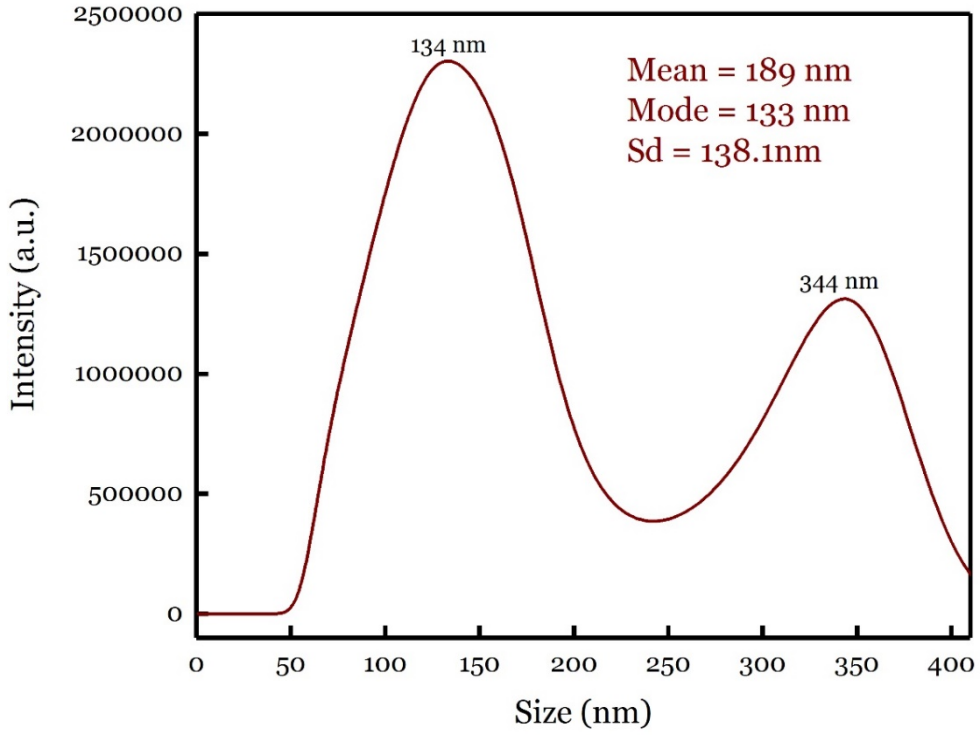

Figure 4-26: Nano Tracking analysis (NTA) size distribution graph obtained for the alendronated $KCoF_3$ NPs.

4.4 Conclusions

A simple and rapid solvothermal synthesis of PEGylated or ALENDronated KMF_3 (M = Mn, Fe, Co) has been developed. The synthesis is carried out in a thermal bomb. The prepared NPs were characterised by PXRD, FTIR, NTA to investigate their single-phase crystal structures, surface coating with the hydrophobic K-oleate ligand and after being ligand exchanged with PEG or alendronate ligands. The hydrodynamic diameters were measured. PXRD patterns showed retained cubic structures for all the prepared NPs, however unknown impurities were present following the K-oleate / PEG or alendronate ligand exchange.

NTA showed that the hydrodynamic diameter for the PEGylated NPs is around 100 nm or larger, hence the size is not conducive to application of the NPs as contrast agents. Furthermore, the size distribution is not homogeneous.

4.5 References

1. A. Tomitaka, T. Koshi, S. Hatsugai, T. Yamada and Y. Takemura, *Journal of Magnetism and Magnetic Materials*, 2011, **323**, 1398-1403.
2. J. K. Oh and J. M. Park, *Progress in Polymer Science*, 2011, **36**, 168-189.
3. Z. Karimi, L. Karimi and H. Shokrollahi, *Materials Science and Engineering: C*, 2013, **33**, 2465-2475.
4. S. Kango, S. Kalia, A. Celli, J. Njuguna, Y. Habibi and R. Kumar, *Progress in Polymer Science*, 2013, **38**, 1232-1261.
5. E. Tombácz, D. Bica, A. Hajdú, E. Illés, A. Majzik and L. Vékás, *Journal of Physics: Condensed Matter*, 2008, **20**, 204103.
6. B. Bateer, Y. Qu, X. Meng, C. Tian, S. Du, R. Wang, K. Pan and H. Fu, *Journal of Magnetism and Magnetic Materials*, 2013, **332**, 151-156.
7. W. Jiang, Y. Wu, B. He, X. Zeng, K. Lai and Z. Gu, *Journal of Colloid and Interface Science*, 2010, **347**, 1-7.
8. R. P. Araújo-Neto, E. L. Silva-Freitas, J. F. Carvalho, T. R. F. Pontes, K. L. Silva, I. H. M. Damasceno, E. S. T. Egito, A. L. Dantas, M. A. Morales and A. S. Carriço, *Journal of Magnetism and Magnetic Materials*, 2014, **364**, 72-79.
9. A. Tomitaka, K. Ueda, T. Yamada and Y. Takemura, *Journal of Magnetism and Magnetic Materials*, 2012, **324**, 3437-3442.
10. T. Muthukumaran and J. Philip, *Journal of Alloys and Compounds*, 2016, **689**, 959-968.
11. Z. J. Liu, X. X. Song and Q. Tang, *Nanoscale*, 2013, **5**, 5073-5079.
12. W. Abdelwahed, G. Degobert, S. Stainmesse and H. Fessi, *Advanced Drug Delivery Reviews*, 2006, **58**, 1688-1713.
13. K. Knox, *Acta Crystallographica*, 1961, **14**, 583-585.
14. Y. Do, I. Cho, Y. Park, D. Pradhan and Y. Sohn, *Bulletin of the Korean Chemical Society*, 2013, **34**, 3635-3640.
15. Y. Ivanov, T. Nimura and K. Tanaka, *Acta Crystallographica Section B*, 2004, **60**, 359-368.
16. N. Miyata, K. Tanaka and F. Marumo, *Acta Crystallographica Section B: Structural Science*, 1983, **39**, 561-564.
17. N. Miyata, K. Tanaka and F. Marumo, *Acta Crystallographica Section B: Structural Science*, 1983, **39**, 561-564.
18. L. Zhang, R. He and H.-C. Gu, *Applied Surface Science*, 2006, **253**, 2611-2617.
19. K. Nakamoto, *Infrared and Raman spectra of inorganic and coordination compounds*, John Wiley & Son, New York, 1997.
20. C. Leng, H.-C. Hung, S. Sun, D. Wang, Y. Li, S. Jiang and Z. Chen, *ACS applied materials & interfaces*, 2015, **7**, 16881-16888.
21. T. Neuberger, B. Schöpf, H. Hofmann, M. Hofmann and B. von Rechenberg, *Journal of Magnetism and Magnetic Materials*, 2005, **293**, 483-496.
22. M. E. Davis, Z. Chen and D. M. Shin, *Nature Reviews Drug Discovery*, 2008, **7**, 771-782.

CHAPTER 5

Solvothermal synthesis of KMF_3 (M = Mn, Fe, Co) with oleylamine

5 Introduction

Magnetic Resonance Imaging (*MRI*) is regularly used for clinical diagnosis due to its high spatial resolution and non-invasive nature. *MRI* images, are generated by the nuclear spin of protons, in the water within biological tissues. The images show high contrast differences between biological tissues, enabling clinicians to identify diseases. By manipulating the relaxation rates of the nuclear spins of the protons within a magnetic field using radio frequency pulses, the contrast images are generated. There are two types of relaxation mechanisms, T_1 relaxation (spin-lattice relaxation) and T_2 relaxation: (spin-spin relaxation). The signal produced is classified as being weighted to the predominant relaxation mechanism. Contrast agents are administered to patients to enhance differences in *MR* signal , thus improving the visibility of abnormal disease states.[1] These agents are described as T_1- or T_2-weighted agents based on which relaxation mechanism they most contribute to. This contribution is quantified by the relaxivity of a contrast agent (r_1 and r_2). T_1 contrast agents give rise to an increase in signal intensity (bright contrast) and are traditionally based on paramagnetic metal complexes, mainly Gd^{3+} complexes.[2, 3] However using Gd^{3+} based T_1 contrast agents have the potential for causing nephrogenic systemic fibrosis (NSF) in patients with impaired kidney function.[4] T_2 contrast agents give rise to a reduction in signal intensity (dark contrast) and are traditionally based on ferromagnetic or superparamagnetic NPs such as Fe_3O_4 and γ-Fe_2O_3.[3] However, most iron oxide NPs possess a large r_2/r_1 ratio causing almost negligible T_1 contrast and hence cannot be used as T_1 contrast agents.[4]

Magnetic NPs with perovskite structure have been extensively studied over the last two decades.[5] The perovskite structure has general formula ABX_3, with A as an electropositive metal (alkali, alkaline-earth or lanthanide), B a transition metal smaller than A and X an anion (Figure 5-1). It is one of the most encountered and best known structural types and thanks to its flexibility it includes he many compounds with enormous variety of fascinating electronic or magnetic properties.[6] $KMnF_3$ crystallises in the cubic perovskite structure with space group $Pm\bar{3}m$. The K^+ cation occupies the A crystal site and Mn^{2+} occupies the B cation and is coordinated by 6 F^- anions in an octahedral fashion.[7]

Mn^{2+} shows a d^5 outer electronic configuration with 5 unpaired spin, hence $KMnF_3$ shows paramagnetic properties down to its Neel Temperature (78 K).[8] $KMnF_3$ particles of 20 nm have been shown to act as T_1 contras agents.[9]

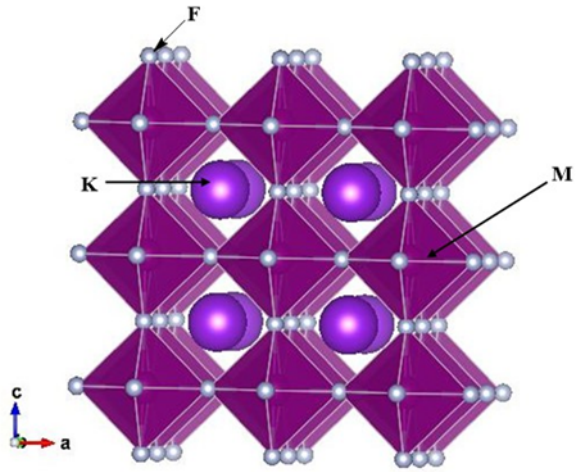

Figure 5-1: General Perovskite structure of KMF_3 (M = Mn, Fe, Co)

Magnetic properties of magnetic NPs are strongly dependent on the nature of these NPs. As the particle size decreases, the magnetization at room temperature tends to decrease.[10] In case of NPs that are smaller than 3 nm this is a result of the decreasing magnetic moment. Kim *et al* estimated that about 93.6% of surface spins in 3-nm sized iron oxide NPs were canted in comparison to 38.6% of surface spins in 12-nm sized NPs (by assuming 0.9 nm spin canting layer thickness). As a result of the increased canting effects in 3 nm sized iron oxide NPs, the magnetization values decreased correspondingly.[11] Furthermore, in a study conducted by Chen et al on 5 nm sized Fe_3O_4 NPs where a high magnetic moment of 27 emu/g was observed attributed to its ultra-small size.[12] This is related to the inclination effect or spin canting effect (inclination of the surface atomic spins of magnetic NPs to a particular angle), which results from the lack of full alignment of the spins in surface atoms. In other words, as the NP size decreases there is a lower number of atoms necessary for the formation of single magnetic moment and/or (ii) less organized spins at the surface as compared to the core of larger paramagnetic NPs (>10 nm). This spin canting is widely reported to be responsible for the low magnetization of small-sized magnetic NPs (small than 3 nm).[13]

It has been reported that size of magnetic NP is important on the relaxivity observed for *MRI* imaging.[14] Several studies have shown that as the degree of aggregation or the size of the aggregates increase, r_1 significantly drops due to strong interaction of the water

molecules with the core of the paramagnetic NP which results in a strong magnetisation, while r_2 dramatically increases.[15] In these iron oxide NPs, the r_2/r_1 ratios increase with size of the aggregates, indicating the T_2 effect becomes dominant with respect to size of NP. The effect of increasing r_2 relaxivity by aggregation of iron oxide NPs has been described previously.[16, 17] Since T_2 effects of aggregates start to dominate the signal behaviour, T_1 effects are decreased, resulting in the drop in longitudinal relaxivity when NPs agglomerate.[15] These results show that particle aggregation strongly affects relaxivities and the larger the aggregate the stronger the change in relaxivities. In contrast, according to a study conducted by Wang *et al* on different iron oxide NPs size, it concluded that magnetisation is highly dependent on size of the NPs. As the size decreases, the magnetisation at room temperature tends to decrease. It thus ultra-small NPs shorten the T_1 relaxation time and therefor exhibits a T_1 effect due to the decrease in magnetic moment. Previous works have been shown a development of various types of dual T_1/T_2 contrast agents. Fengqin Hu *et al* reported a facile synthesis of ultra-small PEGylated iron oxide NPs for dual-contrast T_1- and T_2-weighted *MRI*. The formed superparamagnetic iron oxide nanoparticles (SPIONs) are of high crystallinity and size uniformity with an average diameter of 5.4 nm, and can be individually dispersed in the physiological buffer with high stability.[18] Similarly, Soderlined *et al* synthesised ultra-small perovskite structured gadolinium orthoferrite NPs with an average size diameter of 4 nm, showing the potential to work as dual mode T_1/T_2 contrast agents with r_1 and r_2 values of 11.9 and 15.2 $mM^{-1}s^{-1}$ respectively.[19] Other types of dual-mode T_1 and T_2 contrast agents have been prepared by mixing lanthanide oxides to give a NP with an average diameter size of 1 nm and a r_2/r_1 ratio of 6.6. These NPs showed a clear dose-dependent in both R_1 and R_2 *MR* images.[20]

Most of the previous efforts to develop efficient dual –mode T_1 and T_2 contrast agents were based on iron oxide or gadolinium contrast agents. Therefore, to avoid their drawbacks, the development of a simple, low cost and environmentally friendly method to produce alternative contrast agents with modified surface, highly soluble in aqueous medium, ultra-small size and high affinity to work as T_1 and T_2 *MRI* with high crystallinity is a great challenge and highly demanded for medical application.

In this work, we develop high quality Ultra Small Nanoparticles (USNPs) $KMnF_3$ with an average diameter size of 2 nm by a modified solvothermal method in the presence of oleylamine and sodium alendronate ligands. The appropriate prepared USNPs were

successfully used as dual mode T_1 and T_2 *MRI* contrast agents, demonstrating its great contrast agents and potential clinical use.

5.1 Experimental

The synthesis of Ultra Small Nanoparticles KMF_3 (M = Mn, Fe, Co) was carried out using Liu *et al* method.[9] A simple modification was deliberately performed to obtain very small NPs.

5.1.1 Solvothermal synthesis of coated oleylamine KMF_3 (M = Mn, Fe, Co) NPs

Facile synthesis of Oleylamine KMF_3 NPs, in a typical procedure for the synthesis of KMF_3 NPs, 15 mmol potassium fluoride dehydrate ($KF.2H_2O$), 5 mmol M-chloride ($MCl_2.4H_2O$) (M= Mn, Fe, Co) and 10 mmol oleylamine ($(CH_3(CH_2)_7CH=CH(CH_2)_8NH_2$ approximate 80-90 % C_{18}-content were mixed. 5 ml ethanol mixed with 5 ml hexane were added to improve mixing and mobility of the reagents and the mixture was then transferred to a stainless-steel Teflon-line 45 ml capacity autoclave. The autoclave was maintained at the room temperature of 160° C for 24 hours and then cooled to RT. The oleylamine passivated NPs were centrifuged with alcohol and water to remove the by-product KCl and excessive oleylamine. This washing process was repeated 3 times.

5.1.2 Solvothermal synthesis of coated alendronate KMF_3 (M= Mn, Fe, Co) after being ligand exchanged with oleylamine ligand

Subsequently, the entire amount of the formed coated oleylamine KMF_3 NPs were then redispersed in ethanol with 0.1 g Na-alendronate. The mixture of oleylamine NPs with alendronate in ethanol was solvothermally treated for 2 h at a temperature of 160°C. After removing excessive sodium alendronate and then the solid obtained was dried using freeze dryer for 48 hours. The final product was dispersed in *HPLC* water for further use. The NPs were then characterised using PXED NTA, FTIR, TEM, ICP, EDS NMR and DLS.

5.2 Results and Discussion

5.3 Solvothermal Synthesis of KMF_3 NPs (M = Mn, Fe and Co)

5.3.1 Synthesis of coated alendronate $KMnF_3$

Our starting point was the preparation of $KMnF_3$ NPs carried out by Liu *et al*.[9] They prepared PEGylated $KMnF_3$ NPs *via* the reaction of 5 mmol potassium fluoride 5 mmol manganese chloride 10 mmol potassium oleate in 50 ml solvent composed by 45 ml ethanol and 5 ml hexane. The mixture was placed in an autoclave and heated at 160 °C for 24 hours. The synthesis reaction produced coated NPs on which carry out ligand

exchange to achieve functionalisation for application in *MRI*. Subsequently, the $KMnF_3$ NPs were PEGilated *via* oleate/PEG ligand exchange. The resulting NPs showed average size 20 nm and potential to be utilised as T_1-weighted contrast agents. By investigating this reaction in-depth, we concluded that the formation of $KMnF_3$ NPs derives from a co-precipitation reaction between the K^+ and Mn^{2+} salts dissolved in methanol. In fact, this has been the standard procedure for the preparation of KMF_3 (M = Mn-Zn) compounds.[21] We prepared three compounds of the KMF_3 series, $KMnF_3$, $KFeF_3$ and $KCoF_3$ and observed that the precipitation of the KMF_3 nuclei occurs immediately after the mixing of reagents. Liu *et al*. included K-oleate as a reagent to provide the NPs with an outer layer, with which PEGilation could occurr via ligand exchange. Therefore, we adopted the same general procedure reported by Liu *et al*. , the autoclave as reaction vessel, the temperature and time of the reaction and potassium fluoride and manganese chloride as starting reagents. However, in order to restrict the growth of the $KMnF_3$ NPs in size and prepare USNPs, we applied two modifications. We only used KF as a source of K^+ cations and used oleylamine to provide the outer layer on which carry out functionalisation of the particles *via* ligand exchange. Furthermore, oleylamine had the additional role of "restricting" the growth of the NPs. In fact, exploiting the observation that the formation of the KMF_3 nuclei from KF and a MBr_2 in methanol is immediate, hence the presence of a coating agent hinders the growth in size.[22] To maximise this effect, , the solvent was kept to the bare minimum to guarantee the mixing of the reagent and the occurrence of the co-precipitation reaction, but not to dilute the oleylamine. Only 5ml EtOH and 5 ml hexane were used to promote the mixing of the reagents. Oleylamine is widely used in reactions leading to the preparation of NPs.[23] Its role spans from solvent to surfactant, in some cases even reducing agent and there are reports of "triple role" (solvent, surfactant and reductant) in the synthesis of CoO NPs.[24] This approach produced ultra small NPs, with average size of approximately 2 nm, an order of magnitude smaller than those prepared by Liu *et al*.

The surface of the USNPs were functionalised with Na alendronate to make them water soluble and allowing for bio-compatibility in order to be investigated as contrast agent for *MRI*. The process of functionalisation occurred, as expected, *via* a mechanism of ligand exchange between the oleylamine and Na-alendronate. The additional advantage of the oleylamine layer is that it provides "protection" for the particles. In fact, we observed that bare $KMnF_3$ NPs, prepared *via* co-precipitation tend to decompose partially, when subjected to functionalisation. The ultra-small

size of the NPs is confirmed by HRTEM as shown in Figure 5-2 , where it is noticeable how the single USNPs are barely visible.

The morphology of the formed NPs is spherical and nearly monodispersed with uniform size of approximately 2 nm. In addition, TEM images were used to further confirm the crystallinity and structure of the nanocrystals. The lattice planes of the nanocrystals were observed which indicates their highly crystalline nature. The chemical compositions of these nanocrystal have been estimated from EDX measurements as shown in Figure 5-3. It was found that the average atomic weight ratios of (K: Mn) to be (25: 38), which is close to the theoretical values of (1:1). Furthermore, the appearance of C, P, O and N reflect the existence of the alendronate ligand surrounded the metal surface. The diffraction rings in Figure 5-2(a) and lattice planes that are discontinuous are clearly observed in the

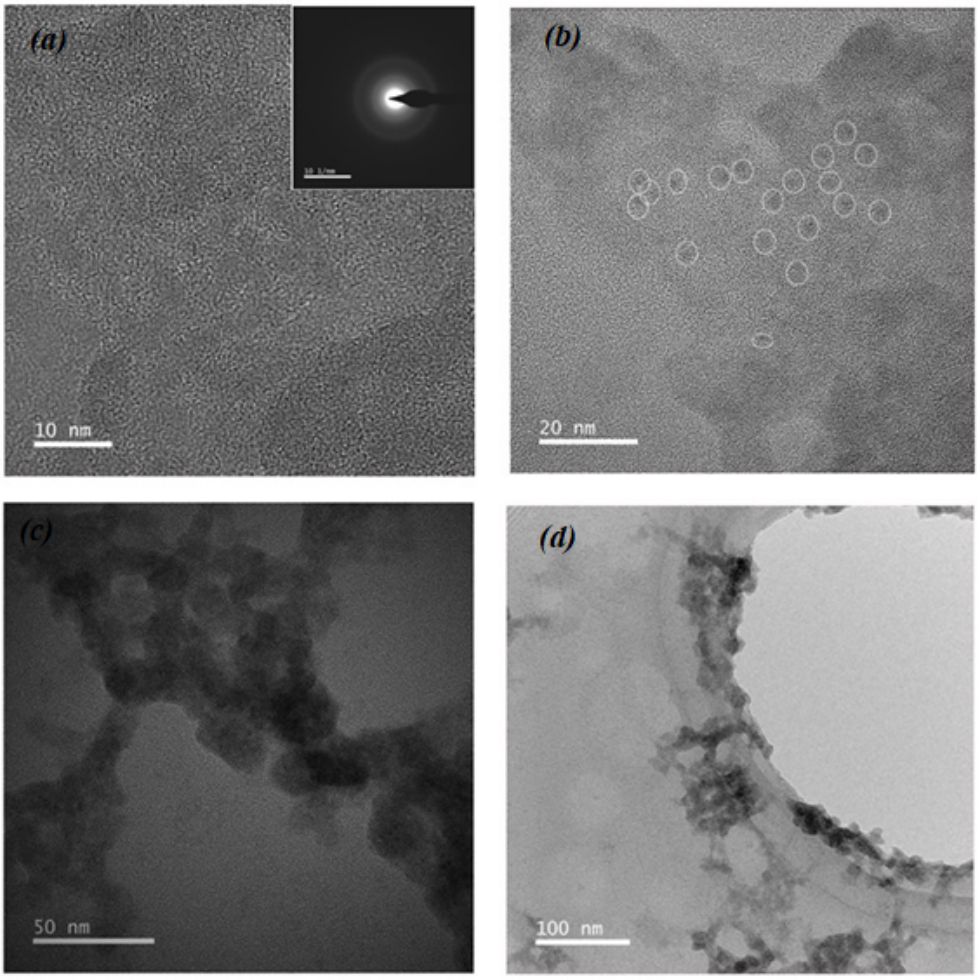

Figure 5-2: HERTEM images obtained for coated alendronate $KMnF_3$with different magnification scale obtained at different area

NPs unit cell as seen in Figure 5-4, this indicates a higher degree of crystallinity of these prepared NPs. The unit cell d-spacing for d_{110} was calculated using Image J

and found 2.93 Å, this is in perfect agreement with PXRD measurement and also with the value reported in literature and can be indexed to the crystal plane 110 for the bulk $KMnF_3$ at $2\theta = 30.14°$.[25]

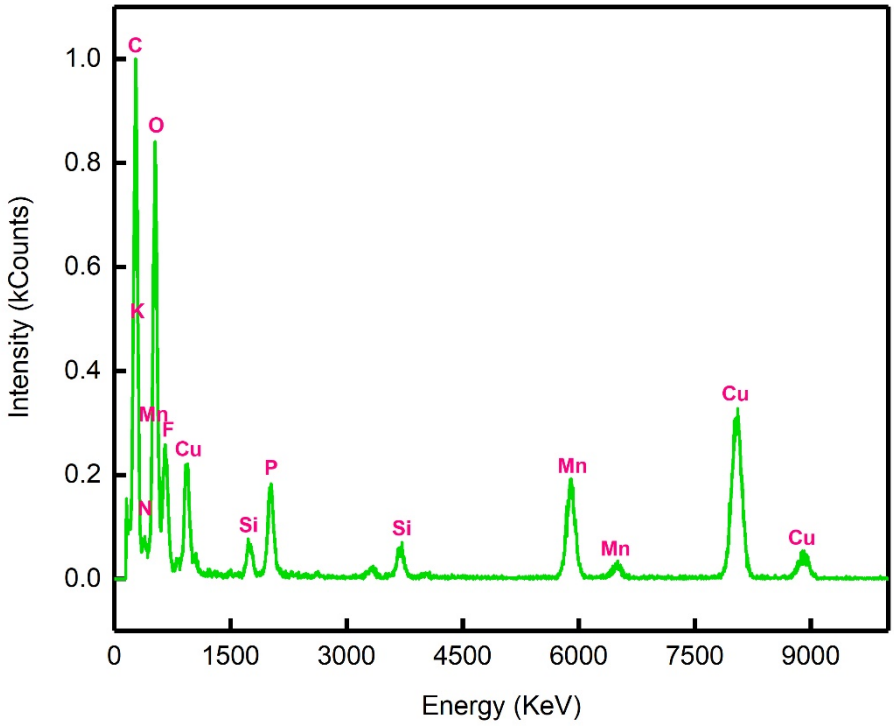

Figure 5-3: Elemental composition of alendronate coated $KMnF_3$ NPs obtained via EDS

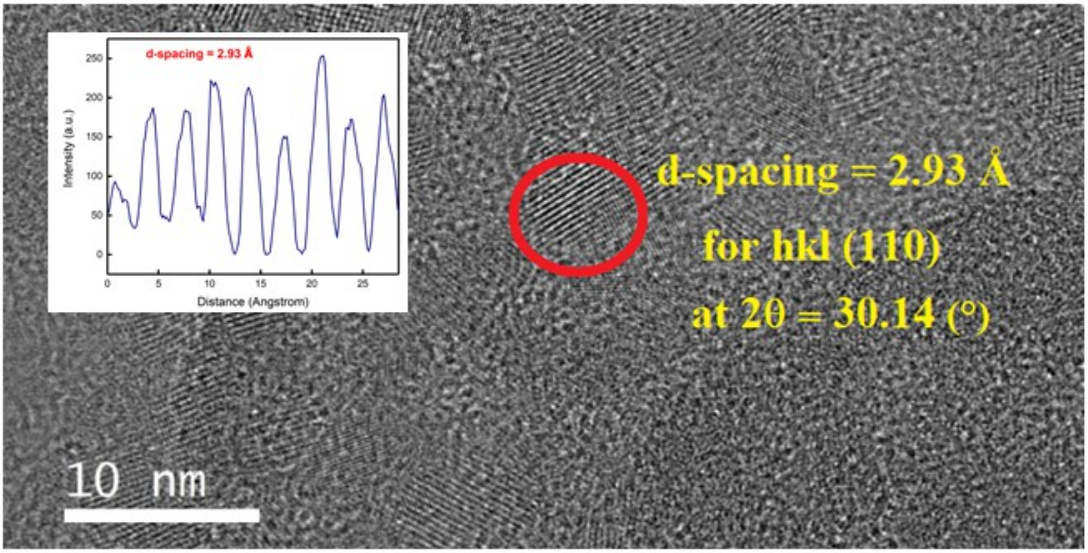

Figure 5-4: d-spacing measurement for the coated alendronate $KMnF_3$ crystal lattice.

5.3.2 PXRD analysis

$KMnF_3$ NPs prepared *via* solovothermal method and functionalised with alendronate after being ligand exchange from oleylamine were analysed with

PXRD. In literature there are common methods to functionalise NPs such as (i) direct encapsulation of hydrophobic NPs by hydrophilic polymer.[26] (ii) ligand exchange of hydrophilic ligand to the original surfactants such as thiol and oleic acid[27, 28] (iii) layer-by-layer deposition.[29] Ligand exchange between oleylamine and Na alendronate ligands strategy was used. All sets of $KMnF_3$ USNPs, as-prepared, coated with oleylamine and functionalised with alendronate were analysed *via* PXRD. The comparison between the three PXRD patterns are shown in Figure 5-5.

All PXRD patterns show that the samples are single-phase $KMnF_3$ cubic perovskite structure.[30] The unit cell parameter were calculated as a = 4.1843 (3) (Å) for as-prepared $KMnF_3$ USNPs and a = 4.1850 ±5Å for KMnF3 USNPs with alendronate. These lattice parameters are in agreement with those reported for KMnF3.[30] The average crystalline size of the $KMnF_3$ coated with Na-alendronate calculated using the Scherer's equation found to be approximately 2 nm.

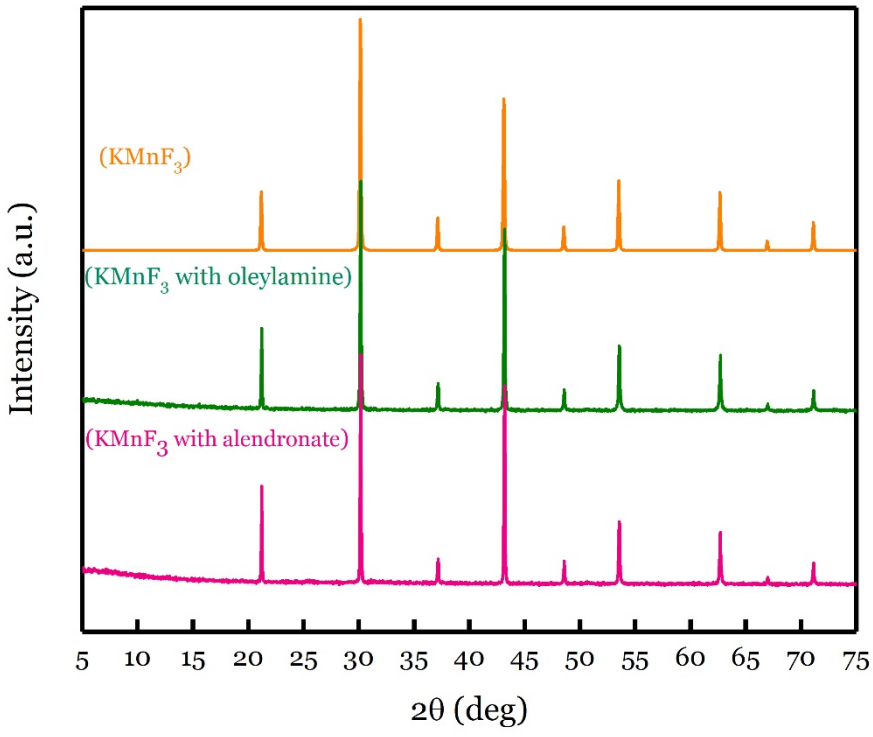

Figure 5-5: PXRD patterns of functionalised $KMnF_3$ with oleylamine and sodium alendronate compared to the standard $KMnF_3$ PXRD pattern.

5.3.3 FTIR analysis

The surface of the NPs was functionalised with Na alendronate to make them water soluble and allowing for bio-compatibly in order to be investigated as contrast agent for Magnetic Resonance Imaging (*MRI).*

Figure 5-6 shows a comparsion of FTIR spectrum for oleylamine and alendronate-functionalised $KMnF_3$ NPs, as well as the pure ligands oleylamine and Na alendronate. The comparison confirms the coating of $KMnF_3$ USNPs by the oleylamine and the subsequent ligand exchange between oleylamine and Na-alendronate.

The FTIR spectrum of oleylamine functionalised $KMnF_3$ NPs is very similar to that of the pure oleylamine ligand, both showing the strong amine N-H stretch at about 3000 cm^{-1} and a band at 1480 cm^{-1} assigned to CH_2 bending. The bands characteristic of $KMnF_3$ NPs are shifted towards higher wavelength supporting the ligand attachment to the surface. The FTIR spectrum of $KMnF_3$ coated with alendronate and after being ligand exchange with oleylamine was compared with that of the oleylamine-functionalised NPs. The vibrational frequencies bands related to $KMnF_3$ coated with oleylamine differ from that of $KMnF_3$ coated with alendronate. The most relevant intense peak of the c=c bond in oleylamine that appears at 1480 cm^{-1} is absent in the NPs coated with alendronate, indicating a successful ligand exchange. The FTIR spectrum of the bare Alendronate ligand was compared with that of $KMnF_3$ coated with alendronate. All bending and stretching bands in pure Na-alendronate can be seen in the final product, the peak at 1100 cm^{-1} is assigned to the strong stretching frequency of phosphonate resonance P=O. It is also observed that the characteristic stretching bands for the alendronate ligand shifted to lower wavelengths, supporting the functionalisation of $KMnF_3$ NPs with the alendronate ligand.

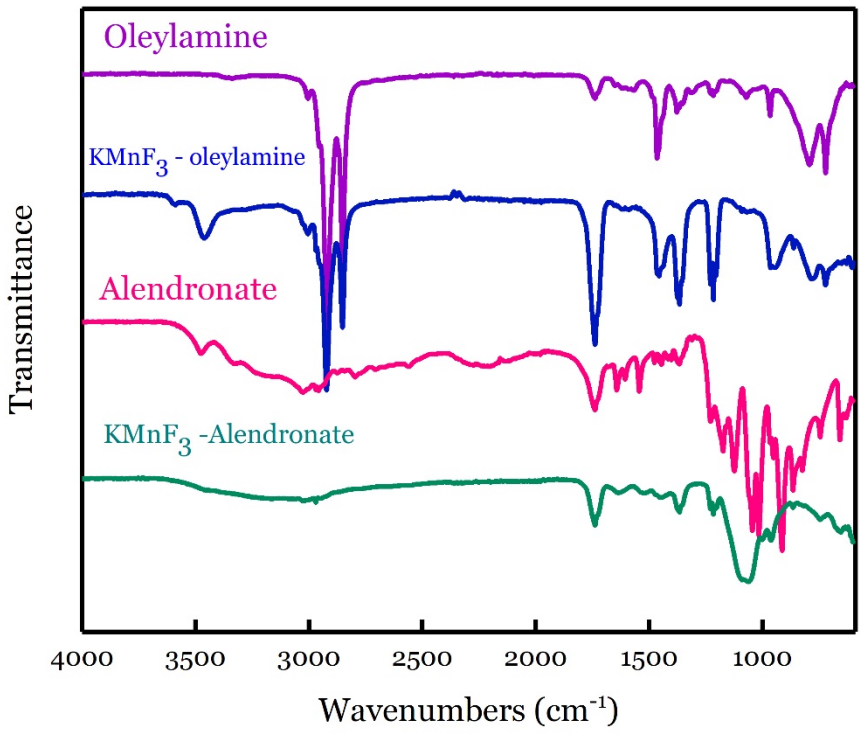

Figure 5-6: FT-IR spectra of the functionalised NPs compared to the pure oleylamine and sodium alendronate.

5.3.4 Nano Tracking Analysis (NTA)

Nano Tracking analysis has been used to measure the hydrodynamic size of the USNPs functionalised with alendronate. This is crucial parameter for understanding the NPs potential biodistibution when applied as contrast agents for biological application. The mean crystal size obtained for $KMnF_3$ coated with Na-alendronate was 7.5 nm as illustrated in Figure 5-7This number seems a little high to be including the diameter of the core NPs, the length of the alendronate molecule and water molecules in the liquid medium. The number probably includes a number of additional water molecules. Fluorometallates have been reported to contain crystal water, as the lone electron pairs of fluoride ions may act as powerful acceptors for acid hydrogen atoms of suitable donor groups such as the O-H group from water molecules.[31]

5.3.5 Zeta-potential measurements

Positive zeta potential value of 22.1 mV (Figure 5-8) was obtained for $KMnF_3$ coated with Na-alendronate at physiological conditions. This value reflects the presence of the positively charged amino group in the dispersed solution. In addition, this obtained positive value also could be correlated to the cationic functional groups or natural organic matter (NOM) having positive charge in water adsorbed onto nanoparticle surfaces and imparted positive charge to them, regardless of whether these NPs had positively or negatively charged surfaces originally.

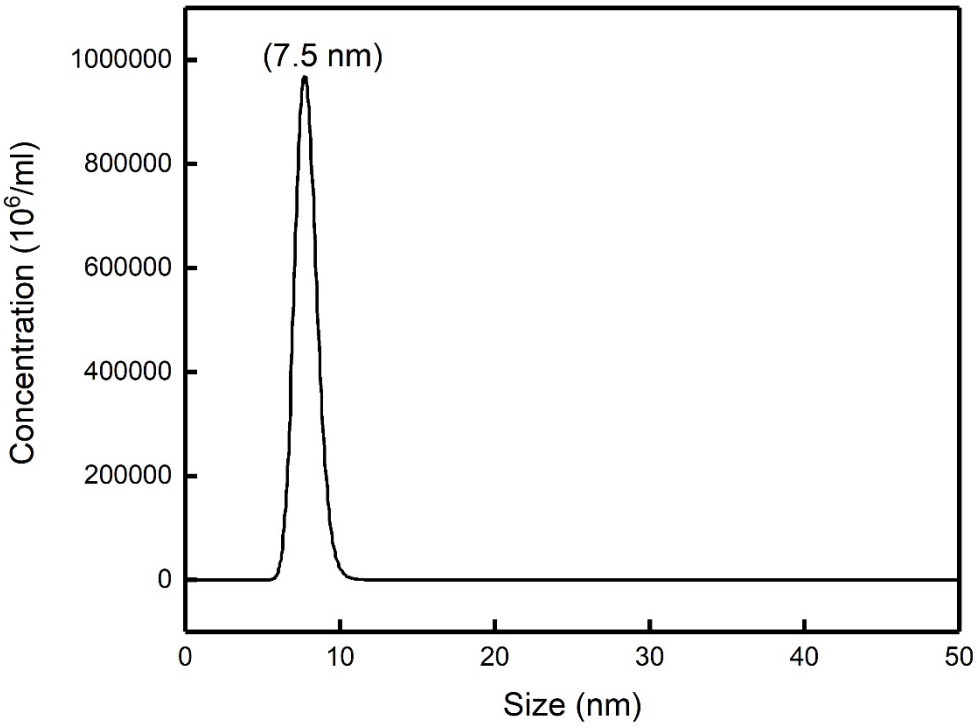

Figure 5-7: Hydrodynamic radius for $KMnF_3$ USNPs coated with Na-alendronate obtained by Nano tracking analysis (NTA).

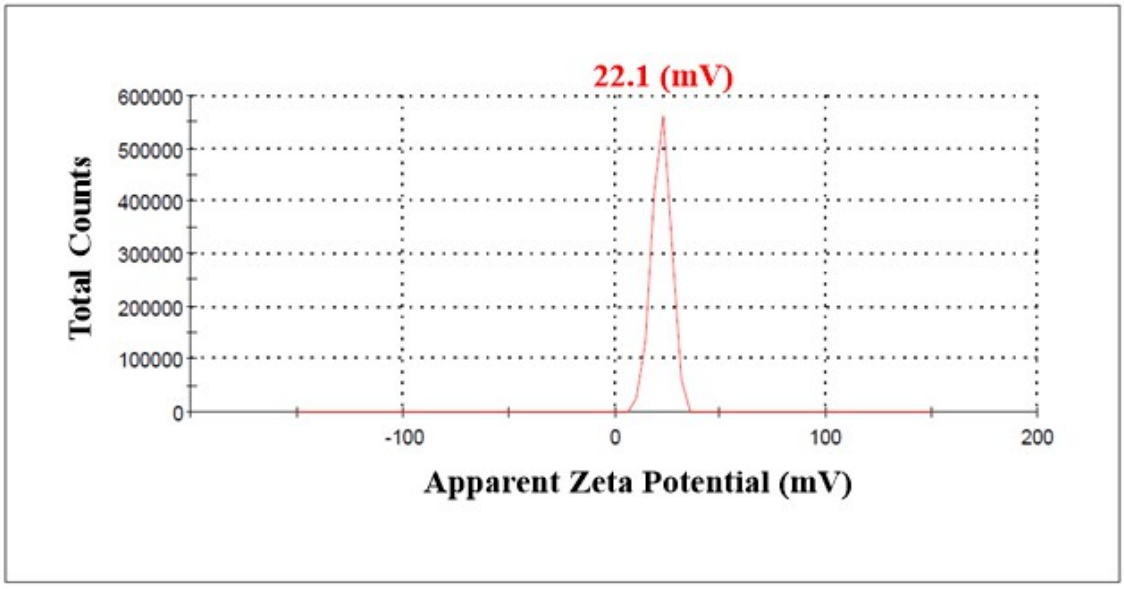

Figure 5-8: Zeta potential value obtained for coated alendronate $KMnF_3$ NPs.

5.3.6 Relaxation rates

The effectiveness of paramagnetic coated alendronate $KMnF_3$ NPs as T_1–T_2 dual model contrast agents were investigated by performing a phantom *MRI* experiment and compare it is *MRI* contrast with that of the agar which was used as a negative control. Relaxation rates were determined at 400 MHZ and 120 MHz by measuring the longitudinal and transverse relaxation times (T_1/T_2), at various NP concentrations. Figure 5-9 and Figure

5-10 show the absolute values of r_1 and r_2 (relaxivities) obtained for $KMnF_3$ ~ 6 and 51 $mM^{-1}s^{-1}$ respectively. The *MRI* T_1/T_2 images and mapping in Figure 5-11 and Figure 5-12 show clear and significant MR effect as the concentration of the Mn^{2+} increases, where each concentration gives rise to increasing enhancement in the MR image. The enhancement in both the T_1/T_2 image show that the USNPs act as a dual T_1 and T_2 contrast agent, this is confirmed by the low r_2/r_1 ratio of ~ 8.5. Alipour and his collaborators synthesised a new class of dual mode cubic super magnetic iron oxide (SPIONs) with an average diameter size of 11 nm.[32] The in-vitro relaxivity and contrast enhancement analysis show that, these NPs possess optimal molar relaxivities and contrast enhancement values, which can shorten the spin-lattice and spin-spin relaxation times, simultaneously. Tegafaw *et al* synthesised ultra-small mixed gadolinium-dysprosium oxide (GDO) NPs of 1 nm and their potential to act as a dual-mode T_1 and T_2 MRI contrast agent was investigated in vitro and in vivo.[20] The coated NPs showed large r_1 and r_2 values (r_2/r_1) ~ 6.6 and as a result clear dose-dependent contrast enhancements in R_1 and R_2 map images were obtained. Furthermore, considering that the 20 nm $KMnF_3$ NP were reported as potential T_1 contrast agents, the smaller size of the $KMnF_3$ USNPs is likely to be responsible for the different magnetic and relaxation behaviour. In fact it has been reported that NPs with the same chemical composition but different particle size show different magnetic and relaxivity behaviour, in particular, USNPs tend to show enhancement in both T_1 and T_2 images.[33]

In addition, the interaction of unpaired electrons of the paramagnetic metals with the protons of water molecules reduces the T_1 (longitudinal) relaxation time of the protons and results in *MRI* signal enhancement.[32]

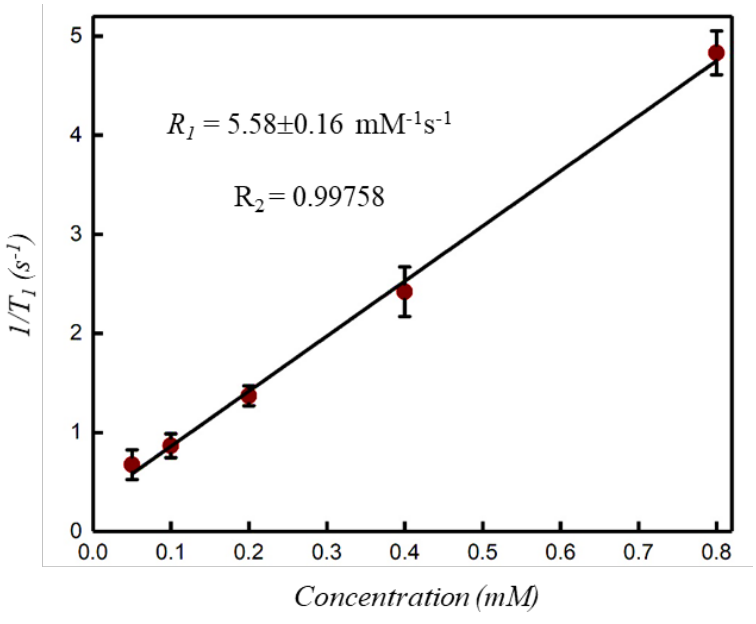

Figure 5-9: T_1 relaxation rate of coated alendronate $KMnF_3$

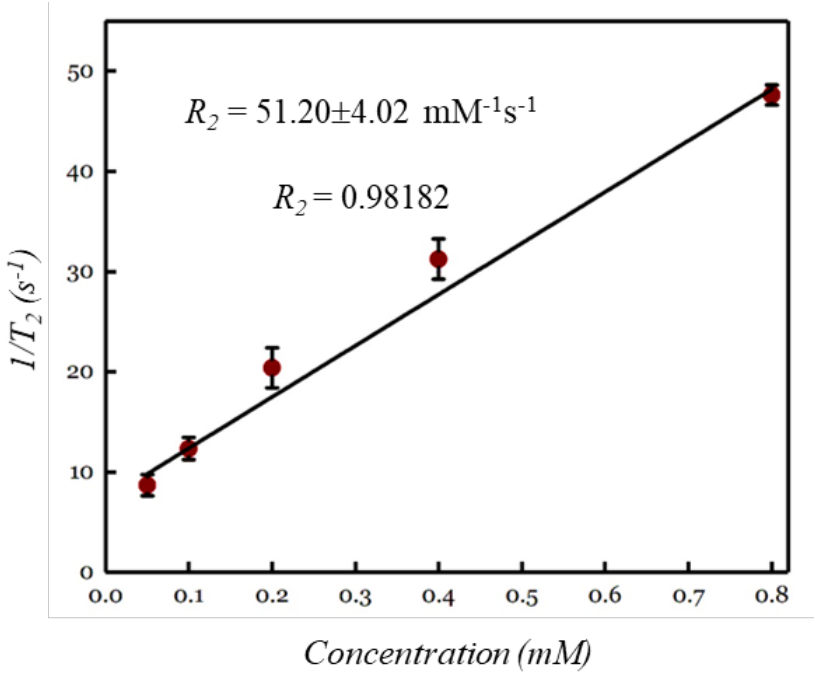

Figure 5-10: T_2 relaxation rate of coated alendronate $KMnF_3$

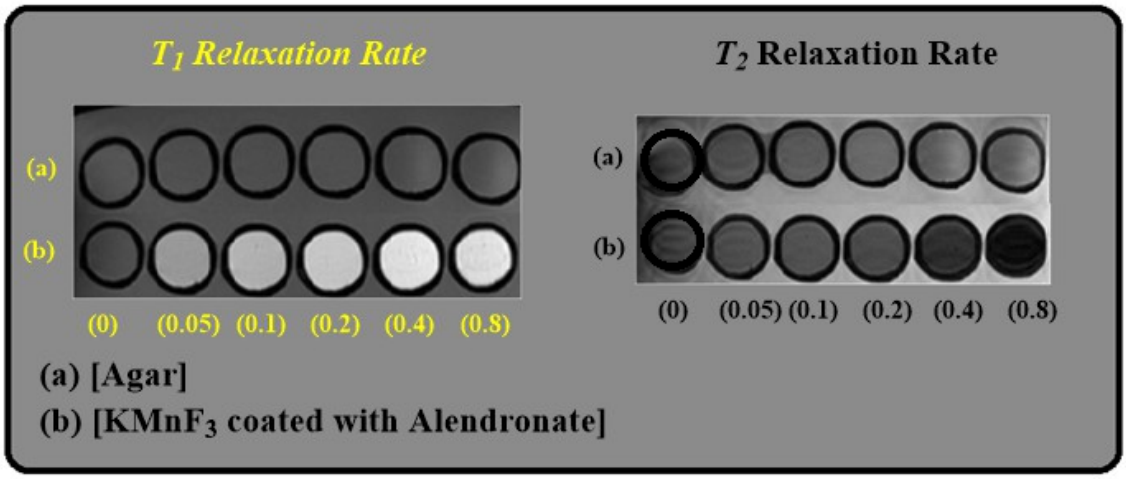

Figure 5-11: T_1/T_2 MRI effect of coated alendronate $KMnF_3$ at 3 T.

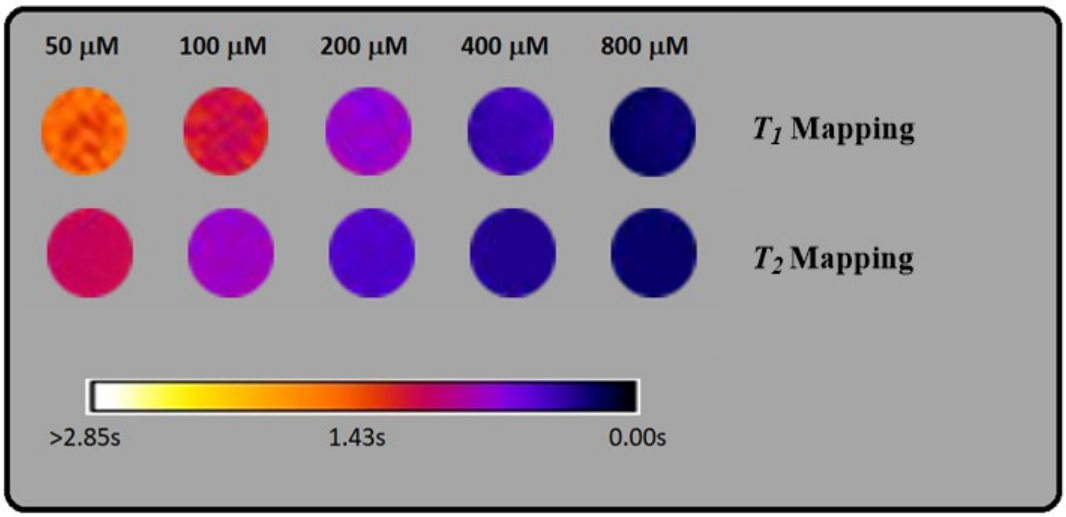

Figure 5-12: T_1 and T_2 mapping for coated alendronate $KMnF_3$ NPs.

5.3.6.1 Squid measurements

$KMnF_3$ coated with alendronate exhibits antiferromagnetic behaviours as shown in Figure 5-13. Antiferromagnetic properties exist only at low temperature and ultimately disappear at Neel temperature. Exceeding the Neel temperature, the NPs become paramagnetic. $KMnF_3$ coated with alendronate NPs show a Neel temperature of 48°C as identified in the ZFC curve in Figure 5-13 (a). This value is far less comparing to the previously reported value for $KMnF_3$ coated with polyethylene glycol (20 nm in size) NPs (80°C) and the bulk $KMnF_3$ value (88°C).[9, 34] This could be attributed to the smaller size of the particles of $KMnF_3$ and to the smaller molecular weight of the alendronate coating ligand comparing to the large molecular weight of poly ethylene glycol ligand. Therefore, tuning the hydrodynamic radius of the synthesised NPs could alter their chemical and physical properties dramatically.

The magnetisation versus external magnetic field (M/H) curve at 300 K is consistent with the one observed for the PEGilated $KMnF_3$ NPs reported previously.[9] However a wasp-waisted shape was observed for the obtained M-H hysteresis loop at 5 K which can be related to the existence of both the ferromagnetic phase and the antiferromagnetic phase at low temperature (Figure 5-13,c). At room temperature, the synthesised $KMnF_3$ NPs exhibits superparamagnetism and there is no spin coupling was observed at this condition. As a result, the M-H curve obtained at 300 K, represents the supermagnetic behaviours of the functionalised $KMnF_3$ (Figure 5-13,b). Similar curves were obtained for $MnFe_2O_3$@MnO janus nanosystem functionalised via Poly ethylene glycol nanosystem as a T_1-T_2 dual mode magnetic resonance imaging contrast agents reported by Deka *et al.*[35]

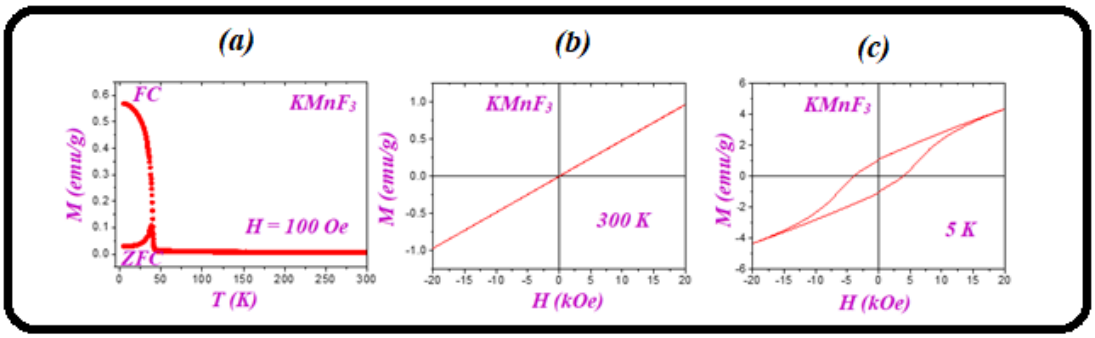

Figure 5-13: Squid measurements for perovskite coated alendronate $KMnF_3$ NPs

5.3.7 Synthesis of coated alendronate $KFeF_3$

In the case of $KFeF_3$, it was observed that the incorrect addition of the oleylamine amount to the reaction mixture can highly affect the purity of the formed NPs. Therefore, in order to obtain a single-phase coated alendronate $KFeF_3$ prior to the ligand exchange with alendronate, it was important to optimise the added amount of oleylamine ligand. This ligand can work as an electron donor at high temperatures.[36] A search in the literature shows that oleylamine can also work as a surfactant, it is greatly effective ligand for preparing small size NPs and has been shown to provide monodispersed gold and silver NPs.[36-38]Oleylamine can bind to perovskite $KFeF_3$ NPs through its amine functional group, forming a coordinate bond as shown in Figure 5-14. PXRD patterns for the optimisation process when different amount of oleylamine ligand was added are shown in Figure 5-15. It was observed that when 6 mmol of oleylamine is added, a single phase of $KFeF_3$ was obtained, however smaller amounts of oleylamine were not sufficient to coat $KFeF_3$ NPs, this was proved by the appearance of extra peaks in the PXRD patterns when 0.37 mmol or 1.87 mmol oleylamine were added, caused some impurities which could be associated to the decomposition of $KFeF_3$ to Fe_3O_4. Therefore, sample of $KFeF_3$ which coated with 6 mmol oleylamine was used for further characterisation.

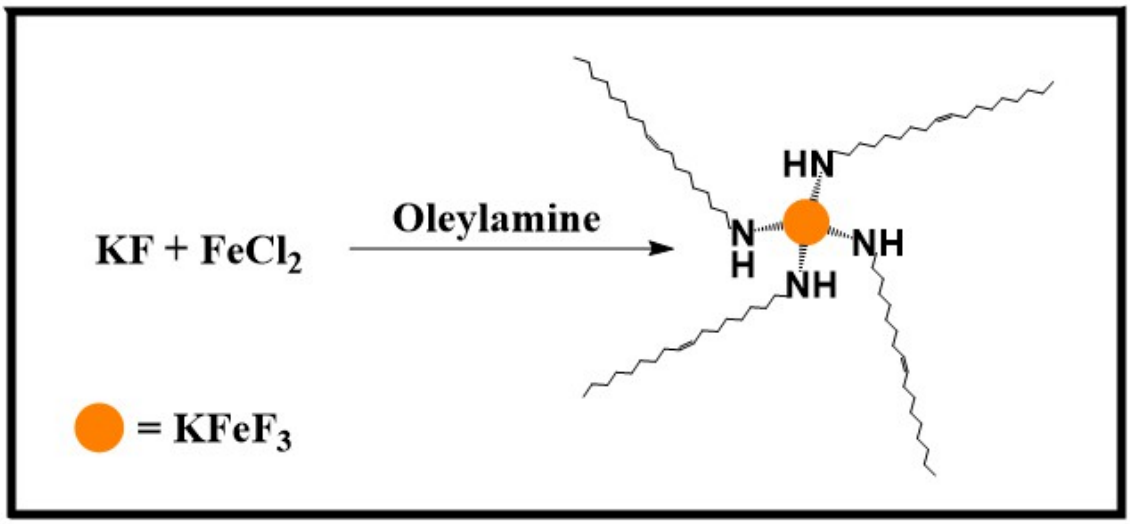

Figure 5-14: schematic diagram for the synthesis of coated oleylamine $KFeF_3$ NPs.

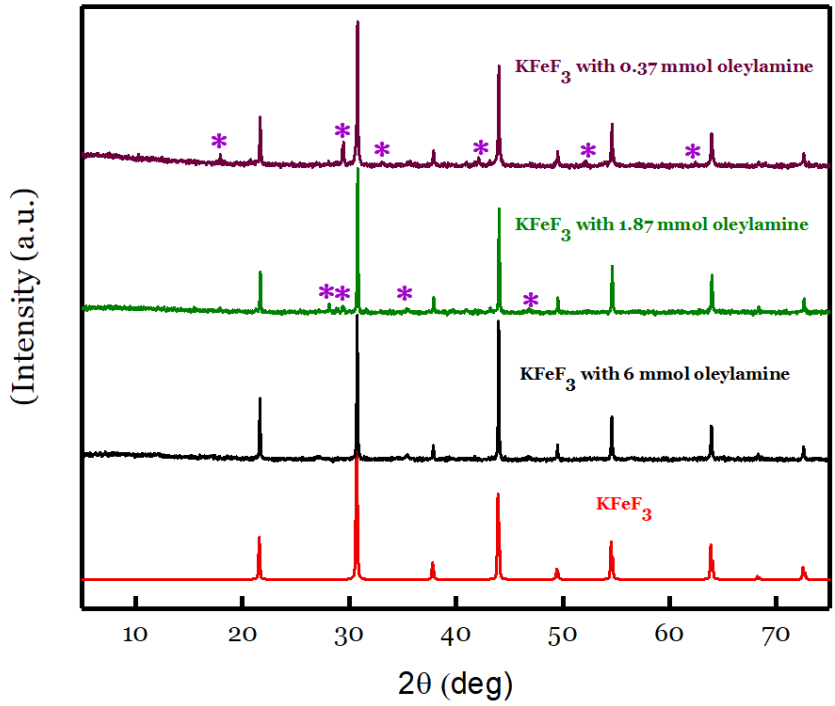

Figure 5-15: Optimisation of the long chain oleylamine ligand on $KFeF_3$ NPs surface.

5.3.7.1 Alendronate ligand exchange

After a successful functionalisation of $KFeF_3$ with oleylamine ligand, an attempt was made to functionalise $KFeF_3$ NPs with alendronate through ligand exchange method. To identify the crystal structure and phase purity of the formed NPs, the Powder X-ray Diffraction (PXRD) analysis was performed for alendronate coated $KFeF_3$ sample. The results obtained was compared to the bulk standard $KFeF_3$ and the single phase coated oleylamine prepared previously, presented in Figure 5-16. The PXRD pattern of the prepared NPs matches exactly with both patterns of bulk $KFeF_3$ and coated oleylamine

$KFeF_3$.[30] The retained peaks showed that single phase cubic with no detectable impurities was formed and the unit cell parameters was calculated and found to be 8.365±0.009 Å.

The d-spacing value shown in Figure 5-17 is constituent with standard d-spacing value obtained from PXRD analysis and that reported in the powder x-ray diffraction data.[25] The difference in the peak intensity in all patterns can indicate the difference in the structural composition of NPs.[39] The large crystal particles usually exhibits strong and sharp XRD peaks, on the other hand, Nano size crystals have relatively weak and broad peaks.[40] Therefore it is reasonable to conclude that the coated alendronate $KFeF_3$ NPs are retained and stable under these conditions. The observed curvature of the baseline of the pattern in range 5 to 15 degree for the prepared NPs is an indication for the existence of the alendronate ligand on the nanoparticle surface. This phenomenon is commonly observed for coated silica nickel and titanium NPs.[41]

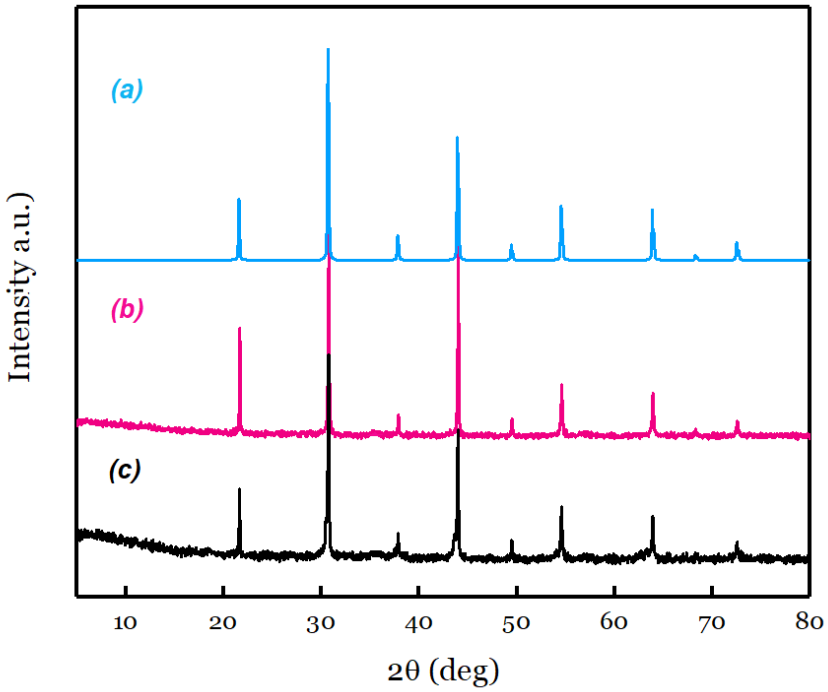

Figure 5-16: PXRD patterns obtained for $KFeF_3$ (a), coated oleylamine $KFeF_3$ (b) and coated alendronate $KFeF_3$ (c)

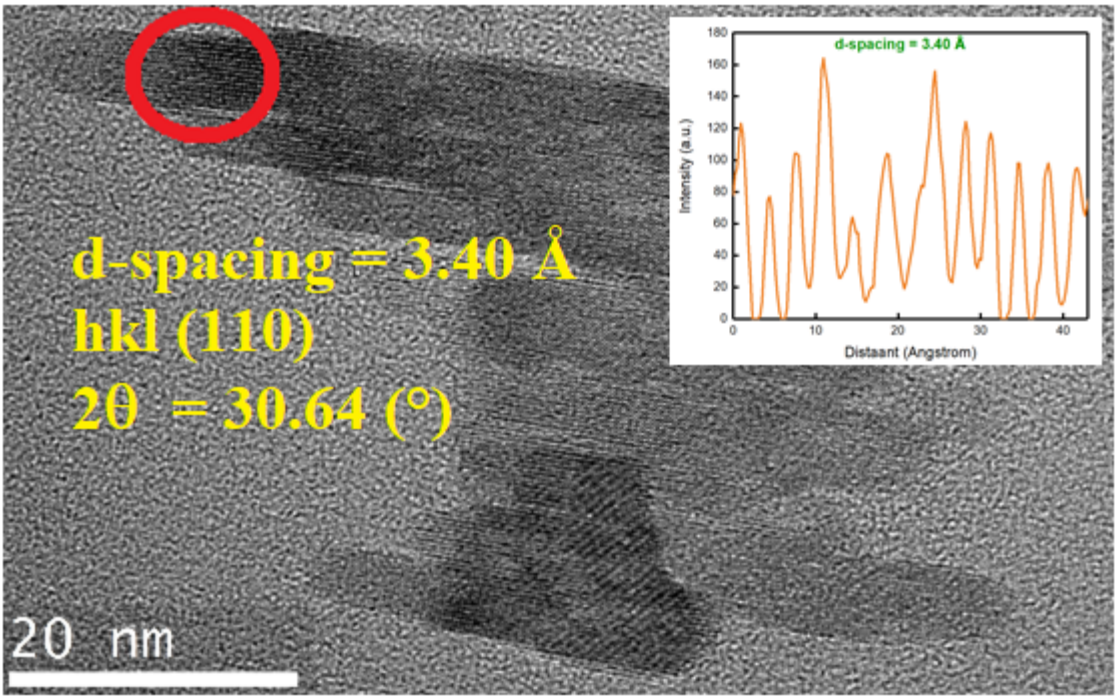

Figure 5-17: TEM picture to show the d-spacing of the coated alendronate $KFeF_3$ NPs.

5.3.7.2 FTIR analysis

The surface properties of the $KFeF_3$ NPs are vital to enable design and tailoring of magnetic drug delivery systems and magnetic resonance imaging contrast enhancement agents.

In order to prove the successful functionalisation process for both oleylamine and after being exchange with alendronate ligand and to confirm that they are adsorbed on the surface of the $KFeF_3$ NPs, FTIR spectroscopy was used to examine the surface composition of the synthesised NPs. The above two spectra (a&b) in Figure 5-18 represent a comparison between the pure oleylamine and coated oleylamine $KFeF_3$. Spectrum of the pure oleylamine shows a perfect agreement with spectrum reported in previous reports.[42, 43] . The characteristic absorption bands for pure oleylamine mainly include $\nu_{as}(NH_2)$ (3376 cm^{-1}) and $\nu_s(NH_2)$ (3295 cm^{-1}), $\nu(C-H)$ (3004 cm^{-1}), $\nu_{as}(C-H)$ and $\nu_s(C-H)$ (2925 cm^{-1}, 2853 cm^{-1}), $\delta(NH_2)$ (1604 cm^{-1}, 795 cm^{-1}), and $\nu(C-N)$ (1071 cm^{-1}).

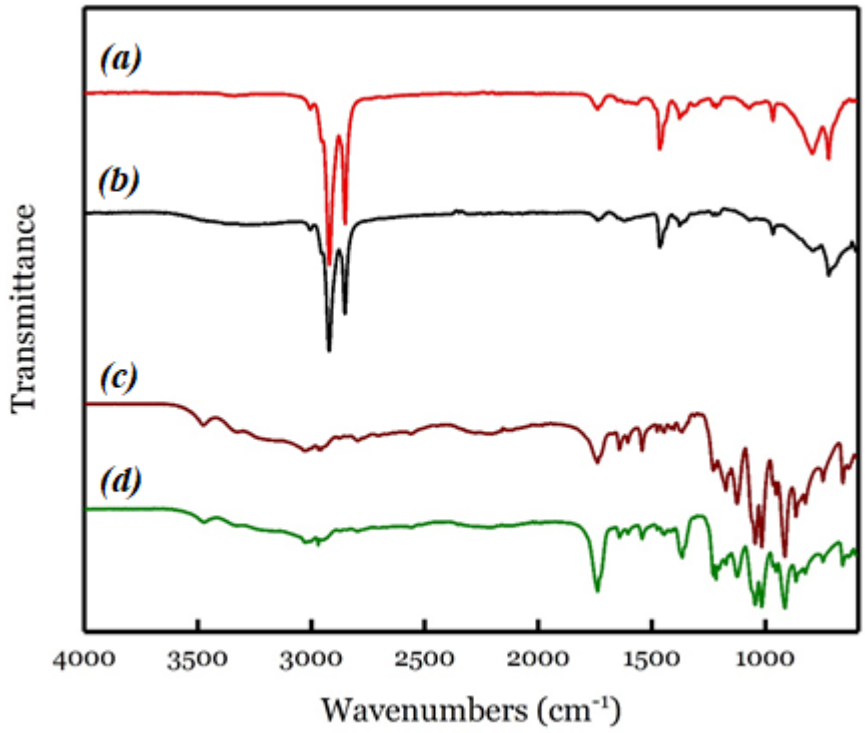

Figure 5-18: FTIR spectrum for oleylamine (red), coated oleylamine $KFeF_3$ (black), pure sodium alendronate (purple) and coated alendronate $KFeF_3$ (green)

For the coated oleylamine $KFeF_3$ spectrum, clearly all the charastrisitc absorption bands of oleylamine appears. A new absorption band at 1523 cm^{-1} is assigned to characteristic absorption of Fe − N bonds. This was also reported in a study conducted for the functionalisation of Fe_3O_4 with oleylamine which suggested that $-NH_2$ coordinates with Fe(III) on the surface of the particles.[44] This imply that oleylamine ligand was grifted on the $KFeF_3$ NPs surface succesfuly.

In the next step,functionalisation with alendronate after being exchanged with oleylamine was carried out. The FTIR spectra of both pure alendronate (c) compared to the coated alendronate $KFeF_3$(d) NPs are illustrated in in the lower two spctrum in Figure 5-18. Alendronate spectrum exhibited strong bands on the region 1200–900 cm^{-1} that correlated to C–O and P═O stretches.[45] For coated alendronate $KFeF_3$, almost identical spectra was observed to that of pure alendronate. These results confirm the existence of alendronate on the surface of NPs.

5.3.7.3 TEM analysis

The morphology of coated alendronate $KFeF_3$ NPs were investigated using TEM microscopy as seen in Figure 5-19. These images display a regular, uniform and spherical NPs with an average size of 1.5 nm as calculated from the distribution graph in Figure

5-20. As for coated alendronate $KMnF_3$, this size was unexpected in comparison with the size obtained from NTA of 31 nm (Figure 5-21) due to the same reasons mentioned in section 1.1.3. Because of high surface energy and large surface area, some of the prepared NPs aggregated. Clearly, when NPs were encapsulated with alendronate, well dispersed NPs was formed in some part of the dispersed solution. This hydrophilic ligand has a great influence in reducing the aggregates and enhanced the particle dispersion. In other words, It is the capping agent that facilitates monodispersing of $KFeF_3$ NPs.[46] It is also a crucial factor in *MRI* diagnosis as well as in drug delivery application that NPs are homogeneously dispersed and are not agglomerated due to the fact that aggregation could decrease the effective magnetic properties of NPs and therefore would causes a massive difficulties in delivering these particles to the targeted site in the body.[46] The well dispersed NPs shows clearly resolved lattice fringes of 101 planes with corresponding PXRD pattern.

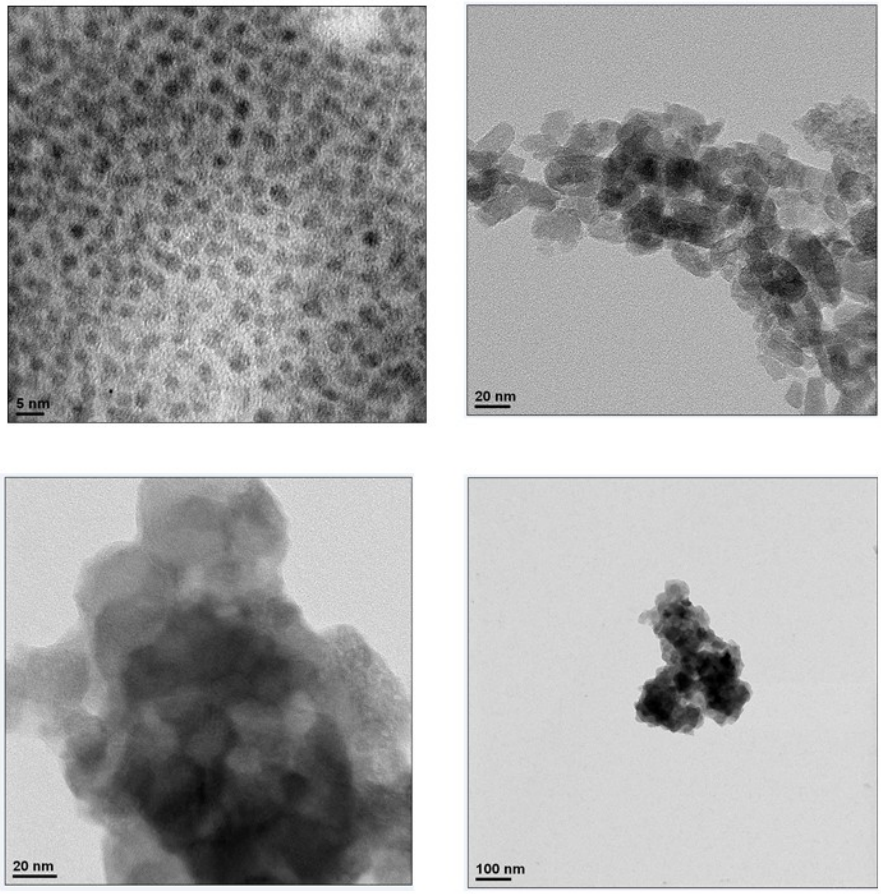

Figure 5-19: TEM images of the alendronate coated $KFeF_3$ of different magnification taken at different part of the dispersed NPs.

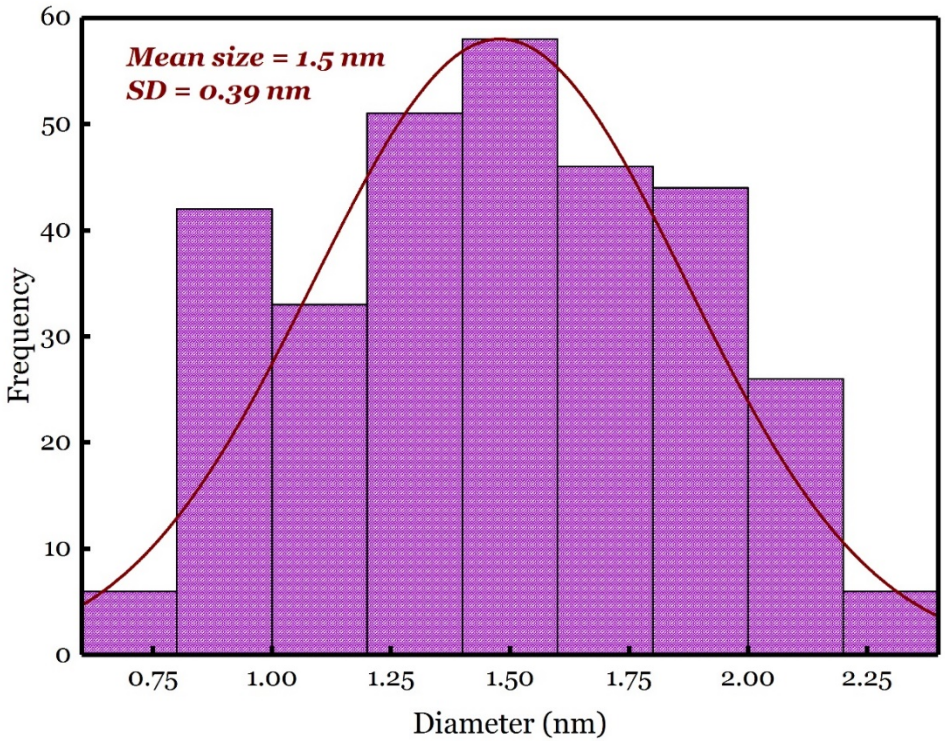

Figure 5-20: Size distribution graph for coated alendronate $KFeF_3$ NPs obtained by origin software.

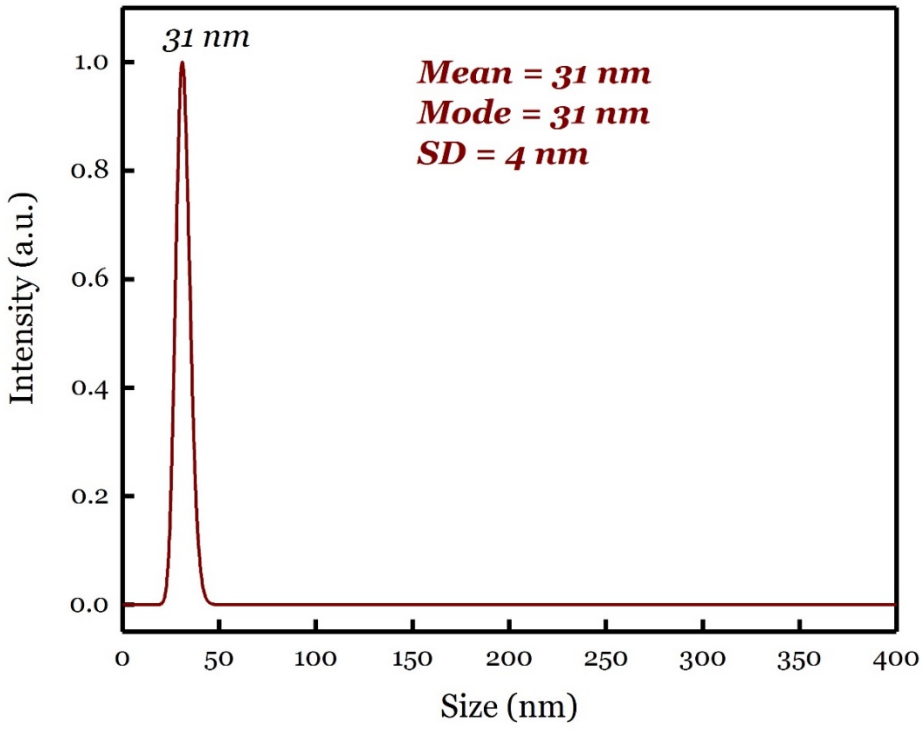

Figure 5-21: size of individual coated alendronate $KFeF_3$ NPs.

EDXanalysis of individual NPs (Figure 5-22) estimated K, Fe and F in an atomic weight ratio of approximately 1 : 0.98 : 2.85, which seems in good agrement with stochiometry

of $KFeF_3$. It also revealed some element corrolated to the alendronate ligand binded on the surface such as C, N, P and O. Some impurities such as Al and Si and Cu in minute amount were also detected which may arise due to the grid where the sample was presented for analysis. As perovskite $KFeF_3$ exhibits a symetric structure simillar to $KMnF_3$, however Fe metal ion has smaller atomic radius which may differ slightly from the typical cubic structure of $KMnF_3$. The Fe^{2+} ions coordinate to six F^- ions in an octahedral fashion, and FeF_6 octahedrons are binded at each corner to other FeF_6 octahedrons.[9] As for PEG ligand, Alendronate ligand may plays an important role in stablising the nanosystem sterically. The zeta potential of the alendronate stabilsed $KFeF_3$ as shown in Figure 5-23 was measured to be 25.5 mV. It is well known that alendronate ligand has five pKa values, and is completely ionised and possesses negative charges at the physiological pH (7.4). Alendronate binds to NPs through their phosphate functional group by steric interaction, leaving the positively charged amine group swimming in the dispersed solution, this could be a logical reason for the obtained positive zeta potential. Moreover, it is well known that cell membrane possess large negatively charge domains which have a great affinity to repel negatively charged NPs.[47] Furthermore NPs with positive charges are preferably taken up by tumours and retained for longer span time in comparison with negatively charge or neutral NPs, because the later NPs accumulate at the surface of the tumour cells, while positively charged nanoparticle localised inside the cancer tumour cells.[48, 49] Therefore this obtained positive value is suitable enough to supply steric stabilisation for the NPs, adsorped by the negatively charged cell membrane and evantually interact rapidly with the tuomer cells.[50]

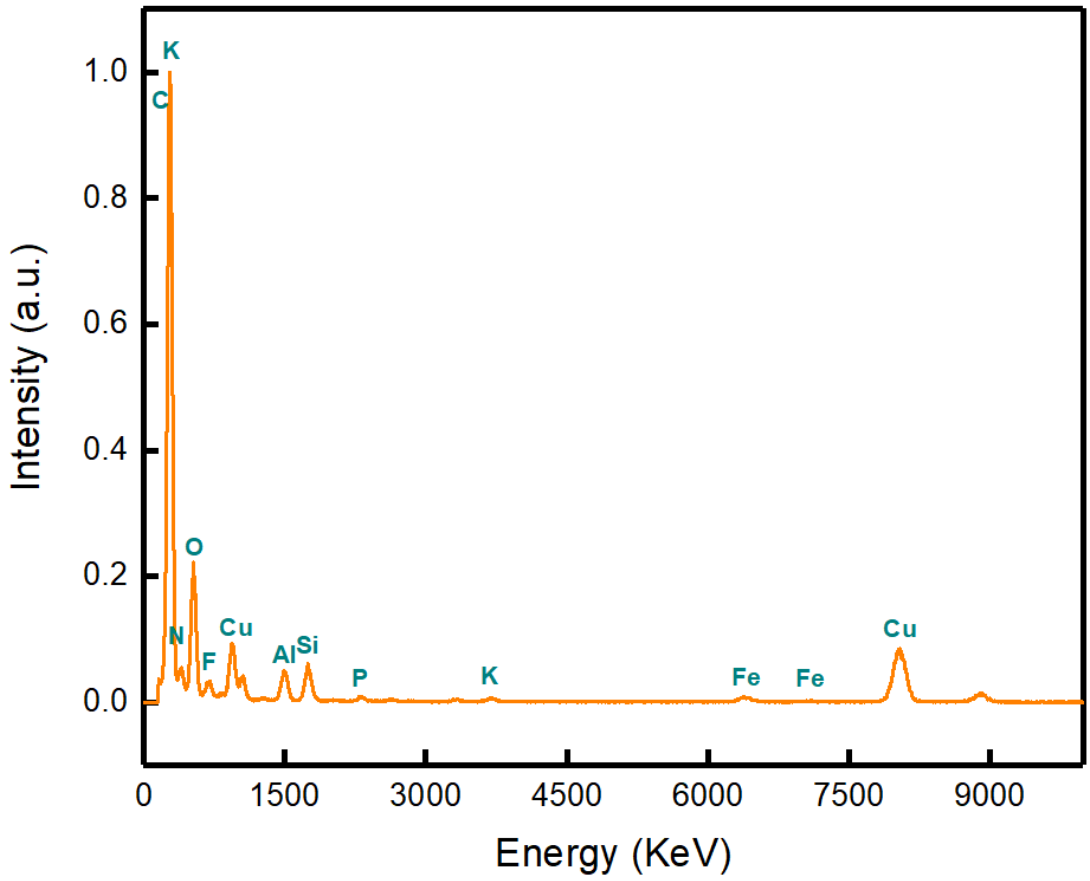

Figure 5-22: EDS analysis obtained for coated alendronate $KFeF_3$ NPs.

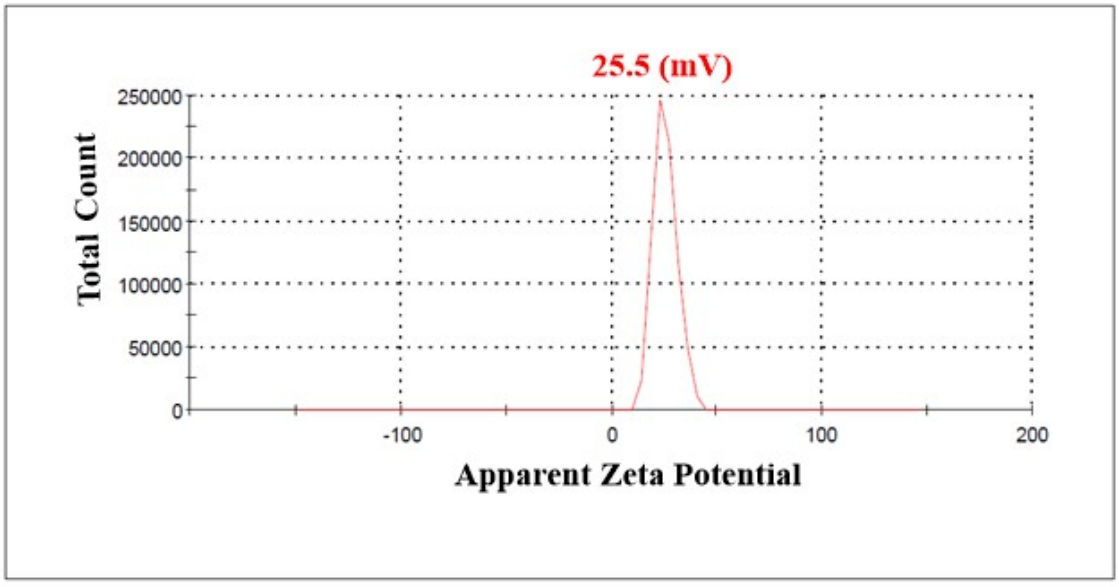

Figure 5-23: Zeta potential value measured for coated alendronate $KFeF_3$ NPs

5.3.7.4 Relaxation rate and *MR* imaging

In order to evaluate the performance of the coated alendronate $KFeF_3$ NPs prepared by solvothermal method in aqueous dispersions at physiological condition, as *MRI* contrast agents, T_1 and T_2 measurements were performed at 3T magnetic field. These values were calculated by linear fitting of $1/T$ versus Fe concentration as shown below in Figure 5-24 and Figure 5-25. At this particular field, r_1 and r_2 values are 0.167 and 25.168 $mM^{-1}s^{-1}$ respectively. Clearly, NPs have a significant impact in enhancing the $1/T_2$ values in a concentration dependent manner, which indicates a strong correlation with the paramagnetic metal ion. It is worth noting that the r_1 value is too small comparing to r_2 value and can be considered as a negligible value.

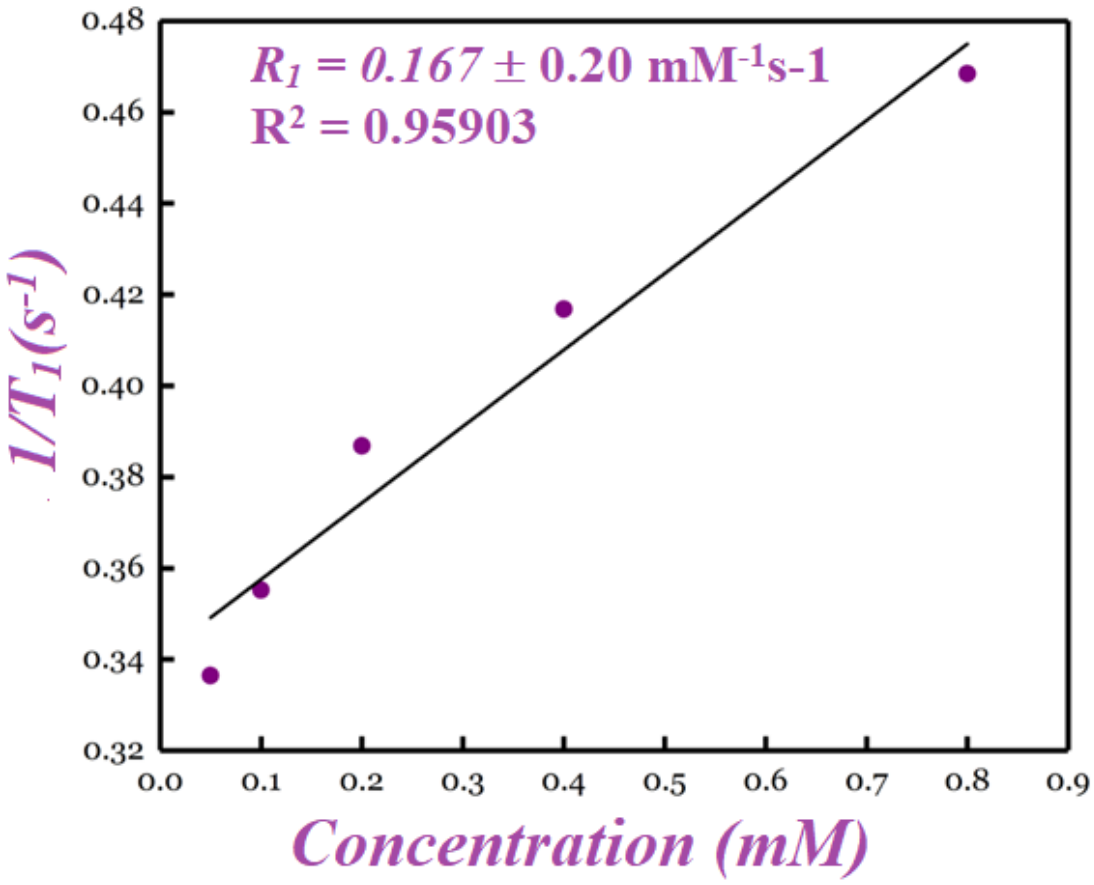

Figure 5-24: T_1 relaxation rate of coated alendronate $KFeF_3$.

Although the Values of r_1 and r_2 were low, the ratio of r_2 to r_1 indicated a positive potential of coated alendronate $KFeF_3$ T_1/T_2 dual-modal *MR* imaging. Normally, r_1 and r_2 are used to investigate the imaging performance as an *MRI* contrast agent, while the ratio of r_2 to r_1 is usually utilized to assess the imaging modality. T_1-weighted *MR* imaging has a ratio r_2/r_1 between 1 and 3, on the other hand, when r_2/r_1 ratio is higher than 10, it favours to work as the T_2 contrast agent. Generally, the contrast agent with the ratio of r_2 to r_1 in the range 3−10 is considered to be a good candidate to work as T_1/T_2 dual-modal MR imaging.[51, 52] The r_2/r_1 of the prepared NPs is 151 which is far high from the desired ratio suggested for T_2/T_1 dual mode contrast agent, thus illustrating the capability to work as T_2-weighted contrast agent only. T_1 and T_2 relaxation rate images in Figure 5-26 showed a minute difference in brightening as the concentration of Fe^{2+} increases for T_1-weighted image, while T_2 weighted image showed an obvious darkening as the concentration increases compared to the (agar) negative control used to illustrate the T_2 effect. T_1 and T_2 mapping in Figure 5-27 confirm same observations.

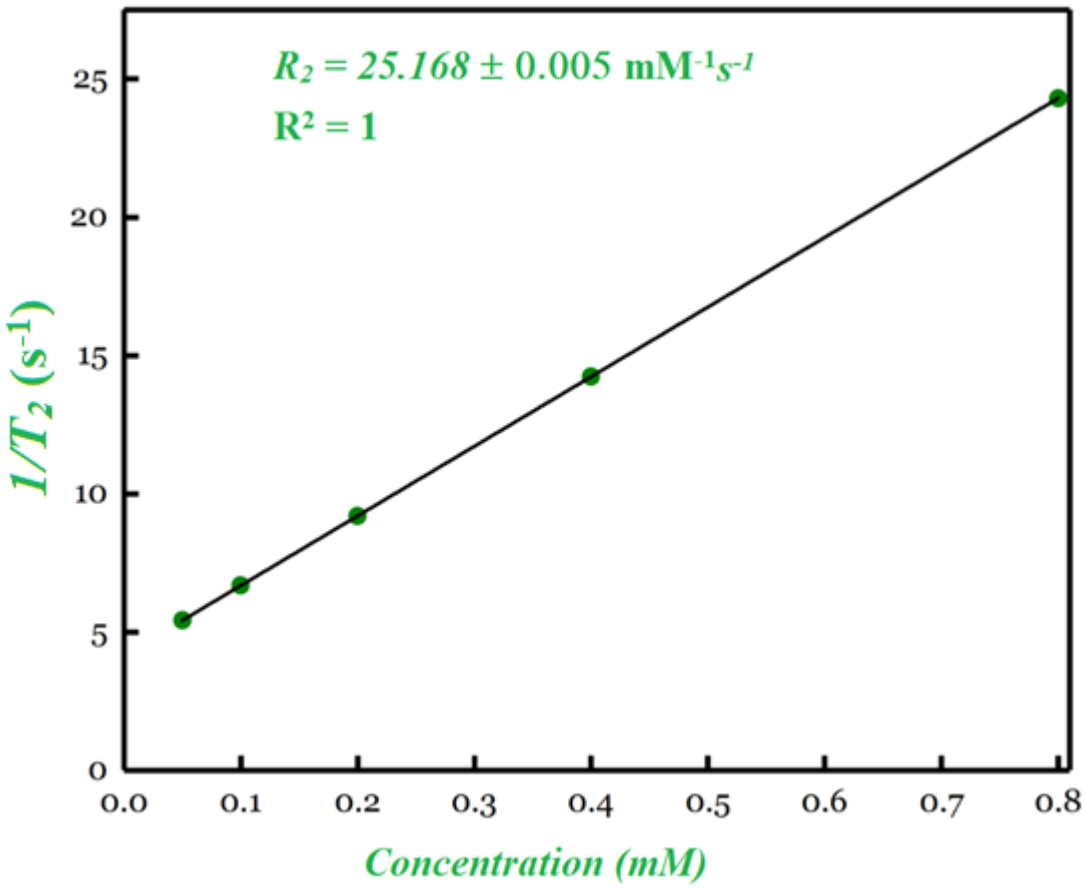

Figure 5-25: Transverse relaxation rate of coated alendronate $KFeF_3$ NPs

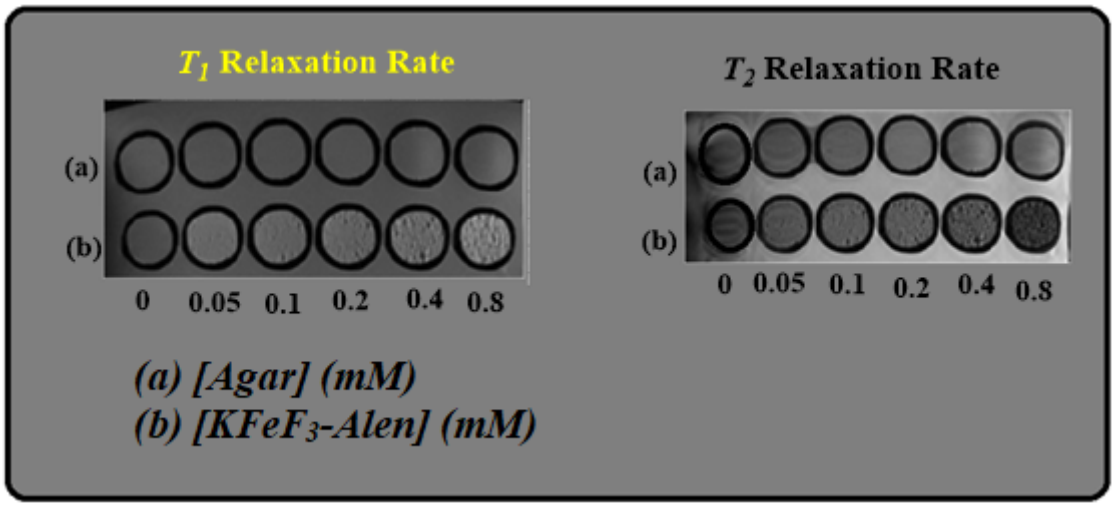

Figure 5-26: T_1 and T_2 weighted images obtained for coated alendronate $KFeF_3$ NPs as concentration of Fe ion increases

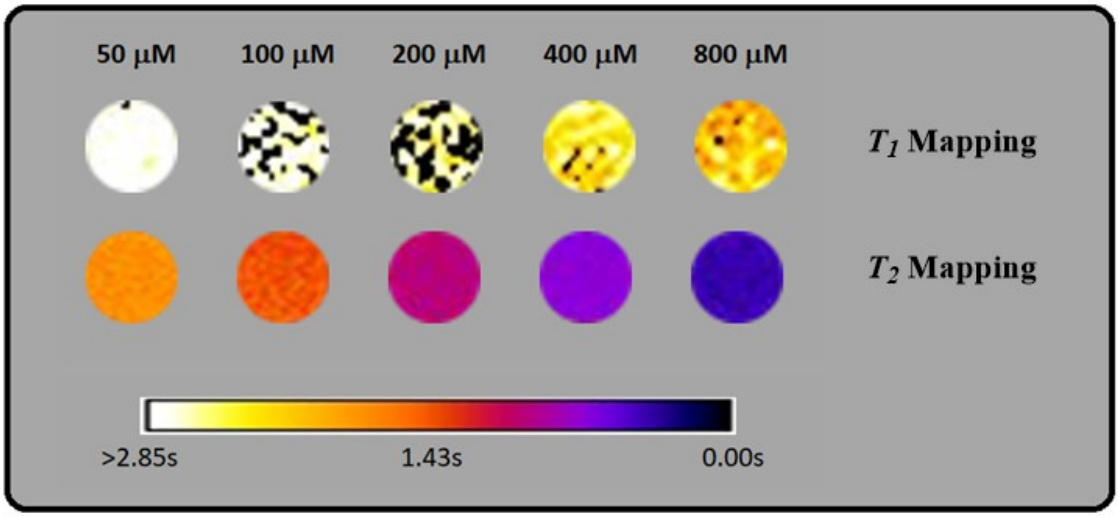

Figure 5-27: T_1 and T_2 mapping obtained for coated alendronate $KFeF_3$ NPs as concentration of Fe ion increases

Unfortunately, solvothermal method used to prepare alendronate coated $KFeF_3$ results in decomposition of $KFeF_3$ to metal oxide Fe_3O_4. This was confirmed by re-performing PXRD analysis for the same prepared compound after a month of preparation and compared to the Fe_3O_4 single phase PXRD pattern as seen in Figure 5-28. A new peak highlighted by * in the PXRD pattern are attributed to the formation of Fe_3O_4. The source

of the oxide was suggested to be a result of surface oxidation, occurring upon transfer of the sample in an open air, where Fe ion reacts with oxygen to form the corresponding metal oxide. This phenomenon is commonly observed for SPION such as γ-Fe_2O_3 NPs compounds due to the large surface to volume ratio exhibited.

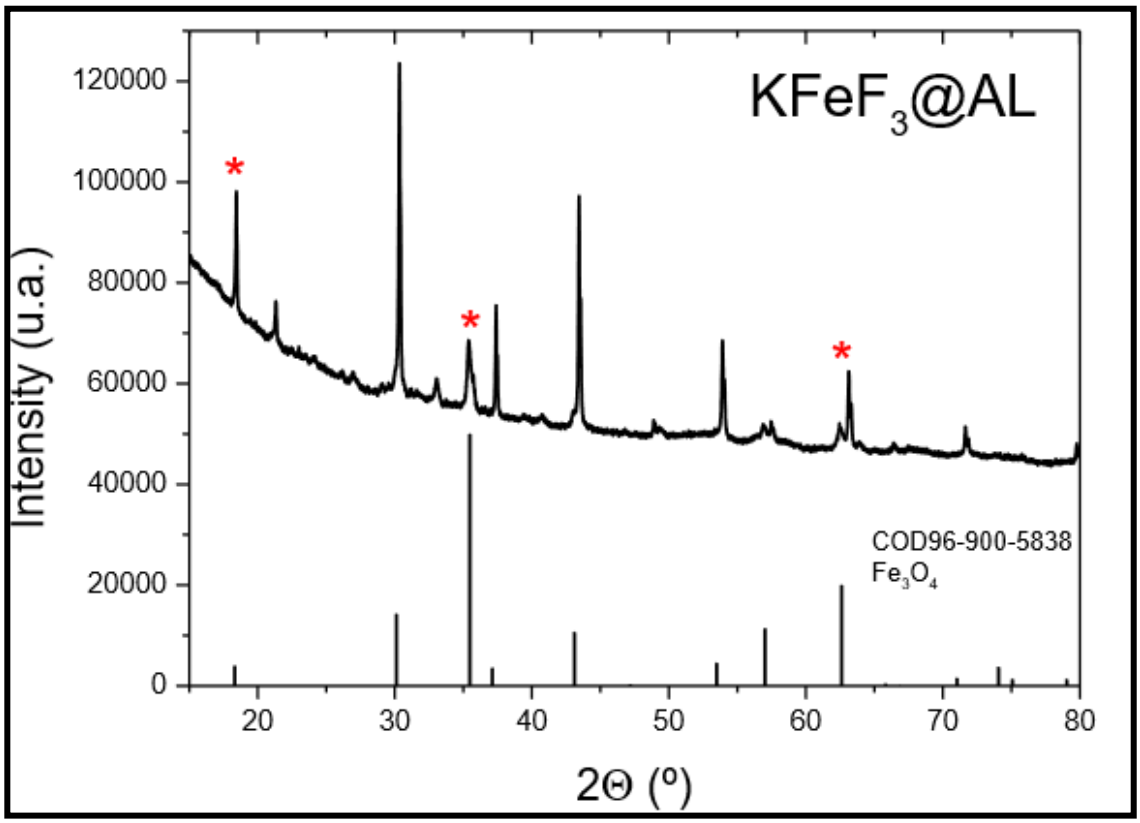

Figure 5-28: PXRD pattern comparison between the coated alendronate $KFeF_3$ and single phaseFe_3O_4 NPs

5.3.7.5 Squid measurements

To further confirm the oxidation of $KFeF_3$ to Fe_3O_4, magnetic measurement was performed. The collected results showed that the zero-field cooled curve exhibited a cusp, which is similar to that of 6 nm size coated oleate Fe_3O_4 nanoparticle obtained by co-precipitation method, prepared by Kim *et al.*[53] . The blocking temperature is estimated from ZFC curve to be 110 K. This value is less than that obtained for Fe_3O_4 (150 K), which could be attributed to the ultra-small size Nano system coated with alendronate ligand. When NPs is coated with surfactant, the attractive force between the NPs will decrease due to the decrease in the large ratio of surface area to volume, causing these NPs to be individually dispersed, hence a decrease in the blocking temperature occurs.[53] At room temperature, the prepared NPs exhibit zero coercivity and remanence in hysteresis loops as shown in Figure 5-29. This indicates a superparamagnetic behaviour.

Similar results was reported for 18 nm size magnetite.[54] At low temperature, the M-H hysteresis loop showed a wasp-waisted shape which indicate the presence of both antiferromagnetic phase of $KFeF_3$ and ferromagnetic Fe_3O_4 phases. It is logical that a compound having mixed magnetic components results in a mixture of magnetic properties, producing this type of M-H curves.

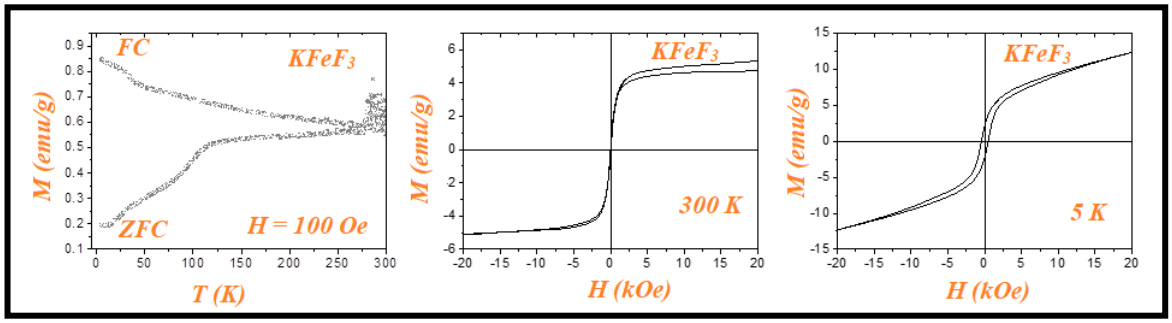

Figure 5-29: Squid measurements for the prepared coated alendronate $KFeF_3$.

5.3.8 Synthesis of coated alendronate $KCoF_3$

Figure 5-30 represents PXRD patterns for alendronate coated $KCoF_3$ after being ligand exchange from oleylamine (b) prepared by solvothermal method in comparison to the standard single phase $KCoF_3$(a) and coated oleylamine $KCoF_3$ NPs (c). From these patterns, the observed peaks for the oleylamine $KCoF_3$ are in perfect agreement with the $KCoF_3$ standard model, indicating a single phase with unit cell parameters. In spite of the shift in the position of the peaks in the PXRD pattern for alendronate coated $KCoF_3$ NPs to lower 2θ, the unit cell parameters for this prepared compound matches those obtained for the standard $KCoF_3$ and coated oleylamine $KCoF_3$. The shift in the peak positions indicates that small NPs with high degree of crystallinity were formed. The unit cell was completely retained and single-phase coated alendronate $KCoF_3$ was obtained. The calculated unit cell parameter was 4.0708±0003 which is in reasonable agreement with the standard $KCoF_3$.

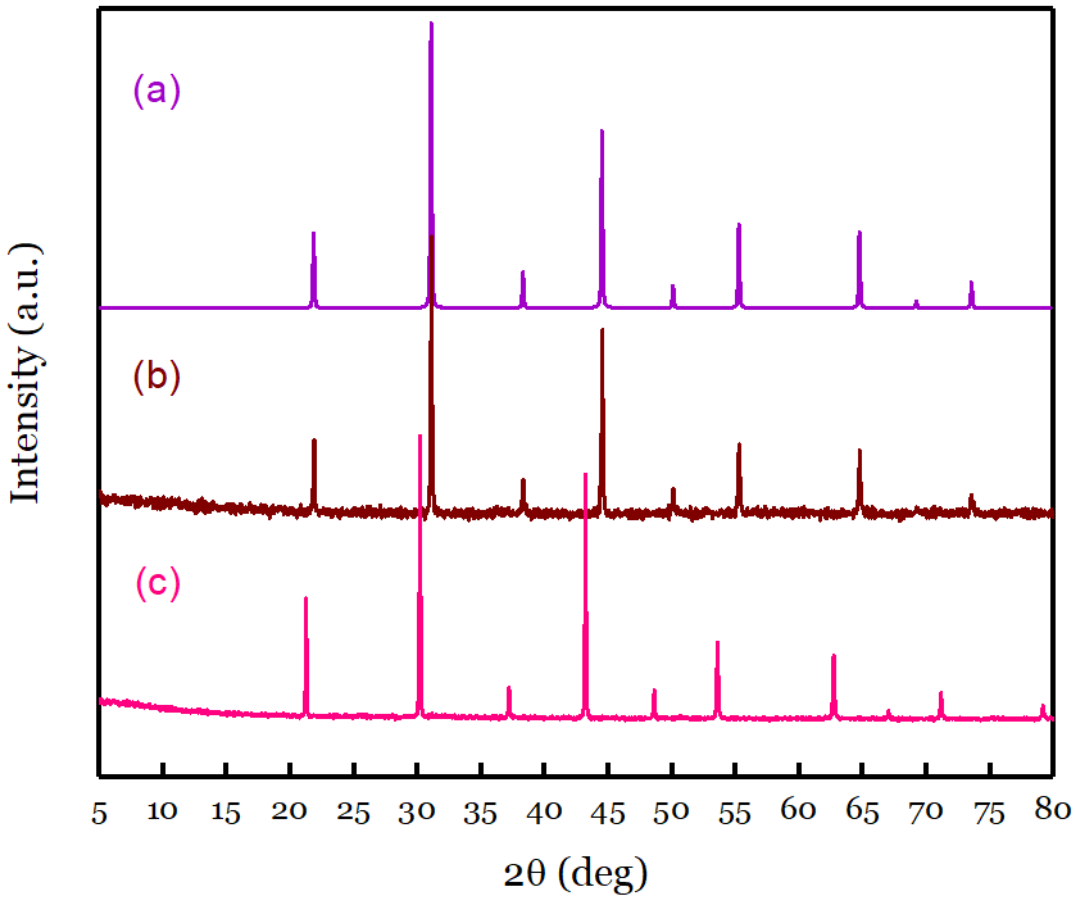

Figure 5-30: PXRD pattern of single phase $KCoF_3$ (a), coated oleylamine $KCoF_3$ (b) and Coated alendronate $KCoF_3$ after being ligand exchange with oleylamine ligand (c).

The average size diameter was calculated using Scherer equation and found to be 5 nm. Usually Cobalt NPs prepared by solvothermal method tend to oxidise readily to their corresponding oxide such as CoO.[55] However none of these oxides were detected, which might be due to the excellent protection given by the alendronate coating layer on the surface of the NPs.

5.3.8.1 FTIR analysis

The FTIR spectrum of single-phase sodium alendronate and the prepared coated alendronate $KCoF_3$ are displayed in Figure 5-31. Clearly, an interaction between the pure coating ligand and $KCoF_3$ takes place. The characteristic strong frequency band of P=O in the alendronate spectrum appears at 1100 cm^{-1}. The broad peak observed at 1242 cm^{-1} was assigned to the O=P-O group.[56] Existence of these peaks in both samples prove that the coordination of the capping ligand with $KCoF_3$ NPs surface was successful.

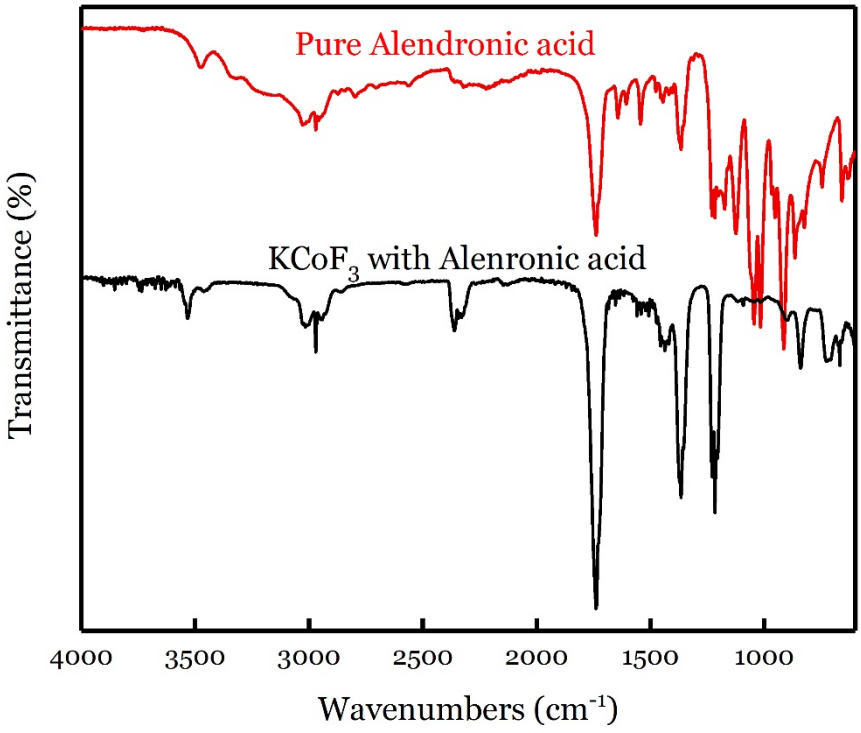

Figure 5-31: FTIR spectrum of single-phase coated alendronate $KCoF_3$ NPs and pure alendronate used as a coating ligand

5.3.8.2 TEM analysis

Figure 5-32 represents the TEM images taken at different parts of the dispersed coated alendronate $KCoF_3$ NPs. From TEM images, it is clear that some parts of the dispersed NPs contain individual dispersed spherical NPs which are fully isolated from each other. This could be due to the significant repulsion of the surface coordinated coating agent over the $KCoF_3$ NPs which hinder the formation of irreversible aggregation of NPs caused by the Van Der Waals attraction.[57] In contrast, some aggregation was observed on the other parts of the dispersed nanosystem, which could be attributed to the Smoluchoski ripening (a mechanism known for the growth of NPs during the nucleation stage) which is caused due to the excessive surface reactivity as a result of the lack in surface coating.[58] The formed polycrystals is believed to be as individual crystallites that have been incorporated into a larger particle through coalescence.[58] A second reason for the agglomeration might be that alendronate ligand utilized in capping NPs may not coat each individual nanoparticle separately but form clumps in each layer of coating. This will increase the aggregation of the NPs. The average crystalline size was obtained from the constructed size distribution curve (Figure 5-33) based on the measurement of the core NPs diameters using Image J.[59] The average core diameter was found 2.22 nm. Based on the close agreement between NPs diameter calculated from TEM images and PXRD data, a conclusion was made that the majority of the formed NPs are single crystalline with

high degree of mono dispersitivity. Unfortunately, unexpected average size value was obtained using NTA analysis of 83 nm in comparison to the values obtained from PXRD and TEM images as can be seen in Figure 5-34. This value was assumed to be for the hydrodynamic diameter which include the core diameter and the layer thickness surrounded the NPs surface which is caused by the coordination of the coating alendronate used and the binding of water molecules in the dispersive solution. On the contrary, the layer thickness of the organic coating material is not considered under bright TEM field.

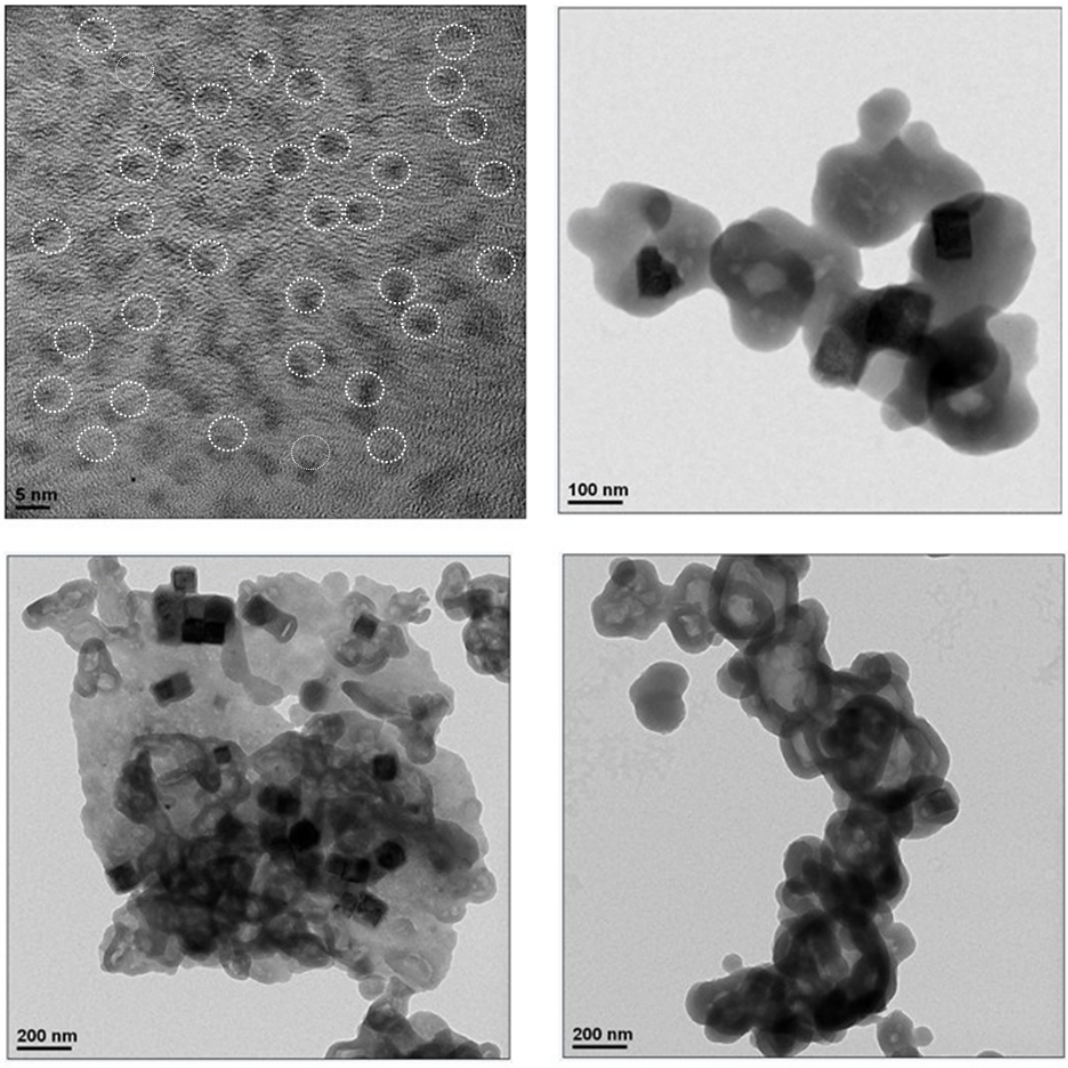

Figure 5-32: TEM images of coated alendronate NPs taken at different parts with different magnification

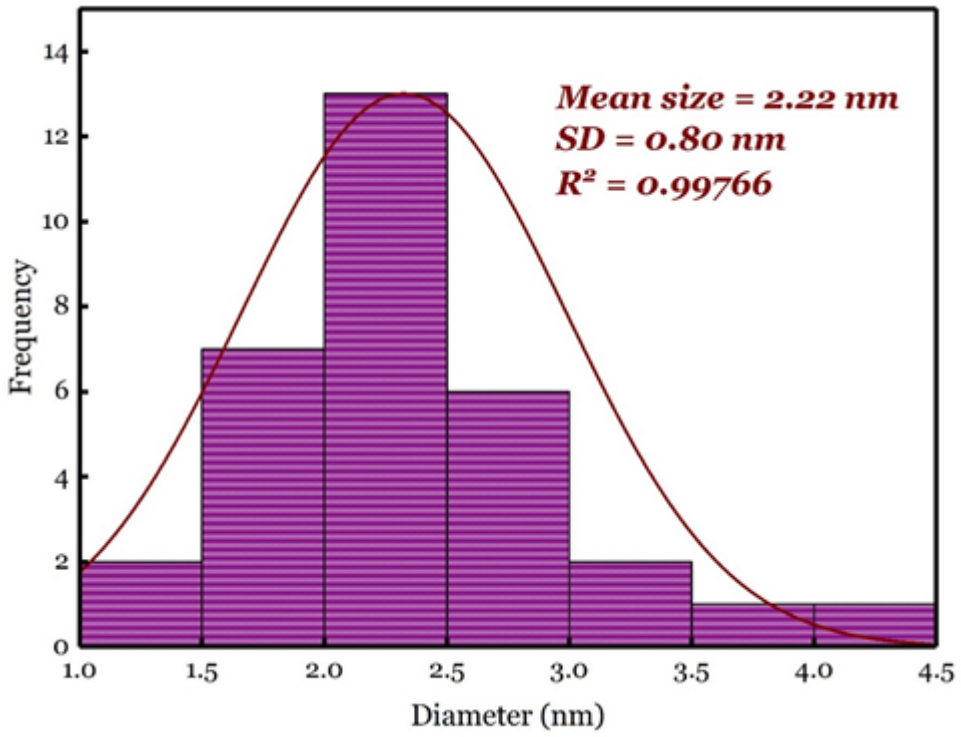

Figure 5-33: Distribution of NPs size for coated alendronate $KCoF_3$ constructed by origin software.

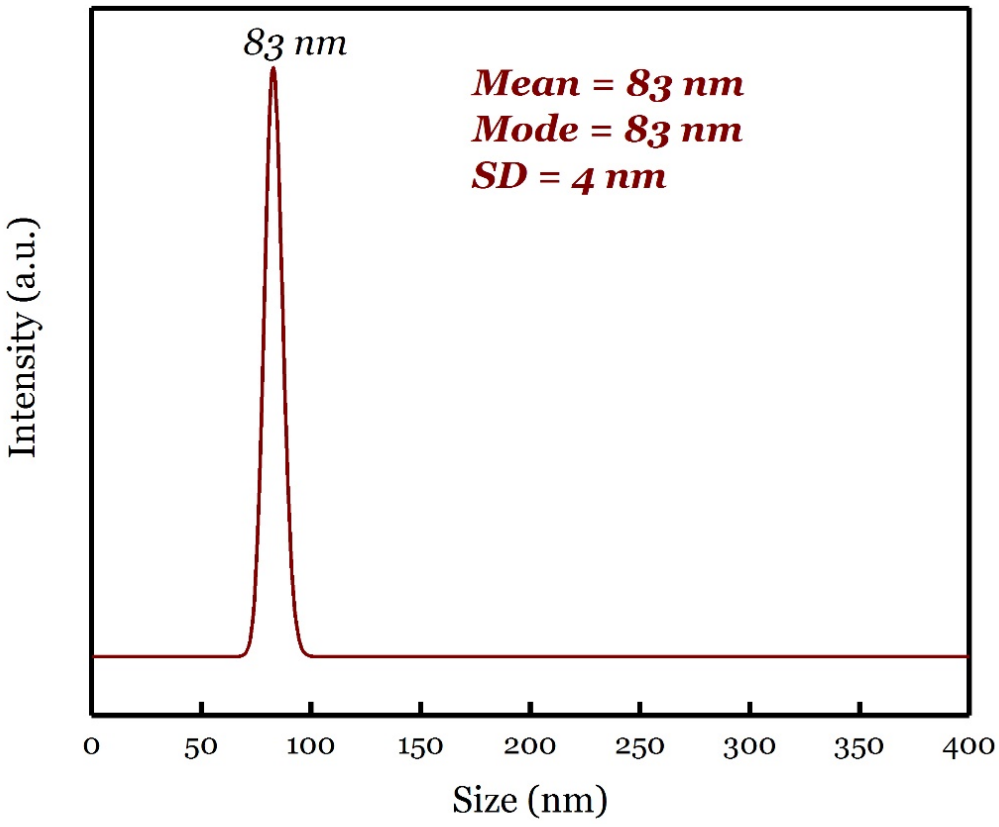

Figure 5-34: Hydrodynamic size of coated alendronate $KCoF_3$ obtained by NTA

Chemical purity and stoichiometry of the coated alendronate $KCoF_3$ was examined by EDX. The EDX spectrum of alendronate coated $KCoF_3$ is displayed in Figure 5-35.The main composition of the prepared NPs consists of K, Co and F with atomic ratio of nearly (1: 1.04: 2.01). The ratio of K to Co is in reasonable agreement to the stoichiometry of $KCoF_3$. The formation of the hydrofluoric acid is one of the issues attributed for the deficiency in the fluoride non-stoichiometry noticed in the average fluoride content and also for the hydroxyl groups observed in the final products as reported in previous reports.[21, 60, 61] The presence of phosphorous in the content is related to the alendronate coating ligand flourished at the nanoparticle surface.

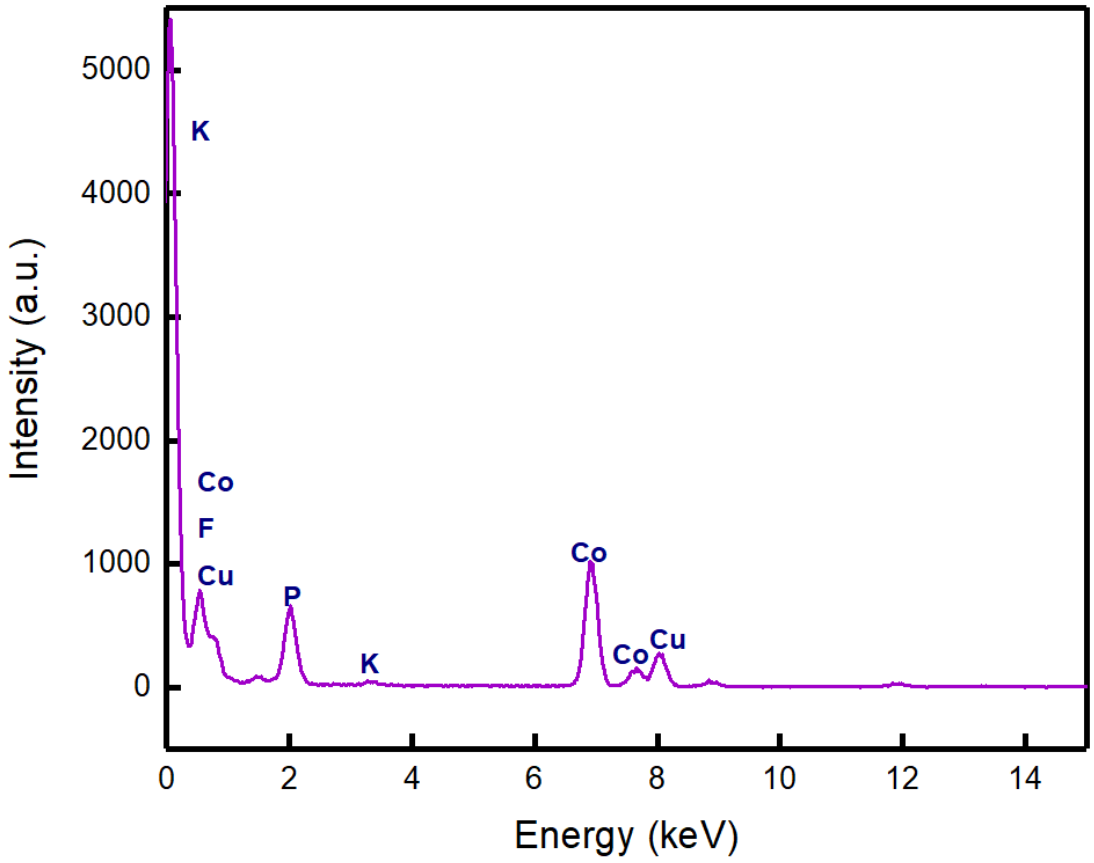

Figure 5-35: Elemental analysis of coated alendronate $KCoF_3$ NPs obtained by EDX

5.3.8.3 Relaxation rates

Figure 5-36 and Figure 5-37 show the longitudinal and transverse relaxation rate for coated alendronate $KCoF_3$ NPs prepared by solvothermal method. Relaxation measurements were performed at 3T external magnetic field across five concentrations which result in an r_1 = -0.63 $mM^{-1}s^{-1}$ and r_2 = -3.53418 $mM^{-1}s^{-1}$. However, the reliability of these two values is poor due to the unclear fit of the trend line. These values indicate

that the prepared NPs have no capability to induce magnetisation to the hydrogen spin in order to yield a sufficient relaxation time that would be able to enhance the contrast in T_1 and T_2 weighted images. Furthermore, the low r_2 value of coated NPs were due to their low magnetic moment, influenced by the small particle size and the presence of Co^{2+} ions.[62] As a results, the magnetic induction of local magnetic field inhomogeneities get gradually reduced and hinder the coated alendronate $KCoF_3$ from having a significant impact on T_2 relaxation.[62] This was clearly observed in the in-vitro *MRI* weighted images where no variation in the images contrast was observed as the cobalt concentration increases. Indeed, both of these images were identical to the images obtained from the negative agar standard that works as a negative control as can be seen in Figure 5-38. More evidence was obtained from T_2-*MRI* mapping where the colour remains unchanged as the cobalt concentration increases as shown in Figure 5-39. These finding are a clear evidence to judge that the alendronate coated $KCoF_3$ NPs do not have the potential to create a significant contrast enhancement in both T_1 and T_2 *MRI* images.

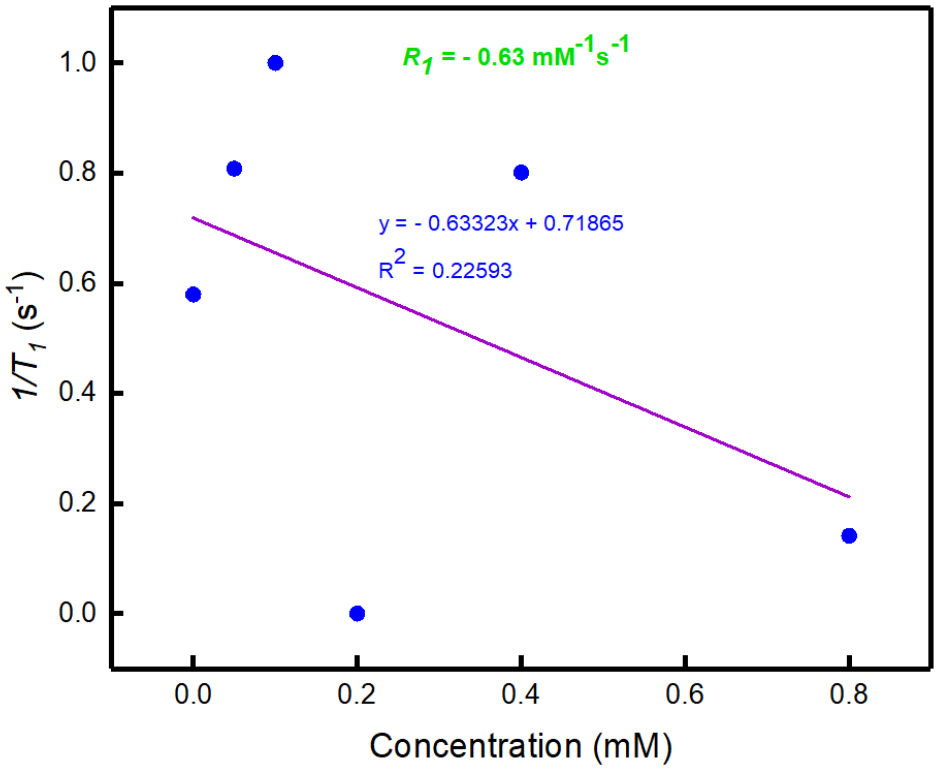

Figure 5-36: Longitudinal relaxation rate of coated alendronate $KCoF_3$ NPs.

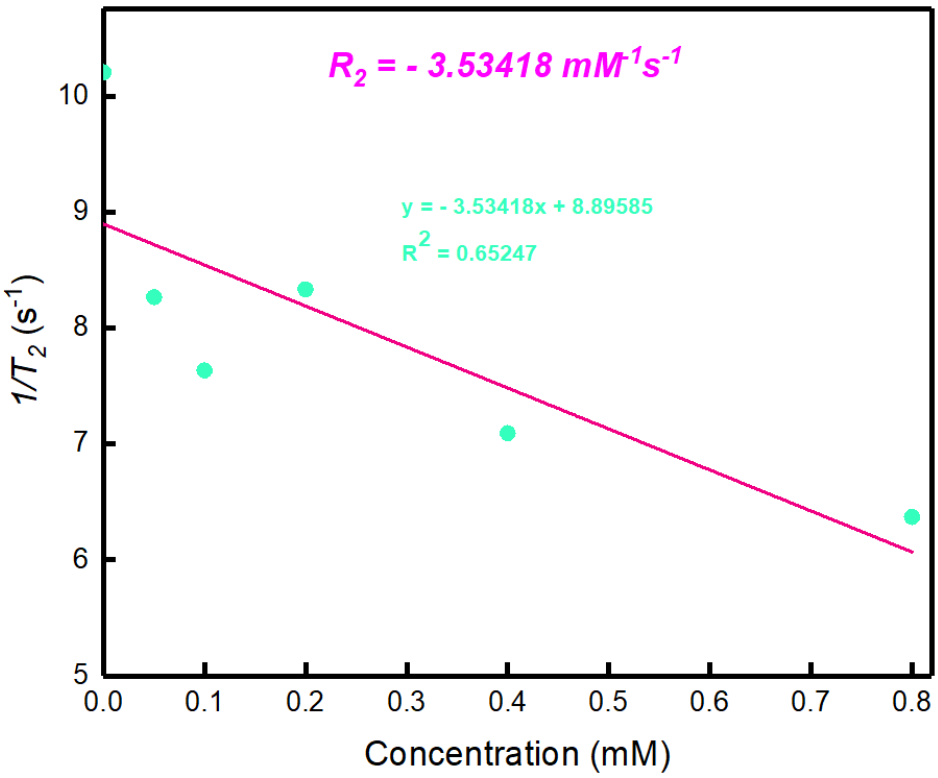

Figure 5-37: Transverse relaxation rate of coated alendronate $KCoF_3$ NPs.

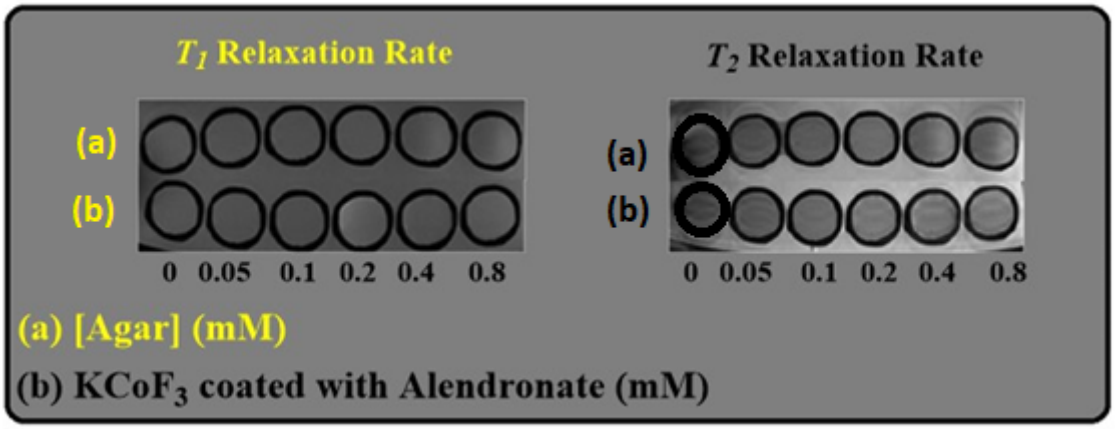

Figure 5-38: T_1 and T_2 weighted images obtained for the prepared coated alendronate $KCoF_3$ NPs (a) compared to negative standard image (b).

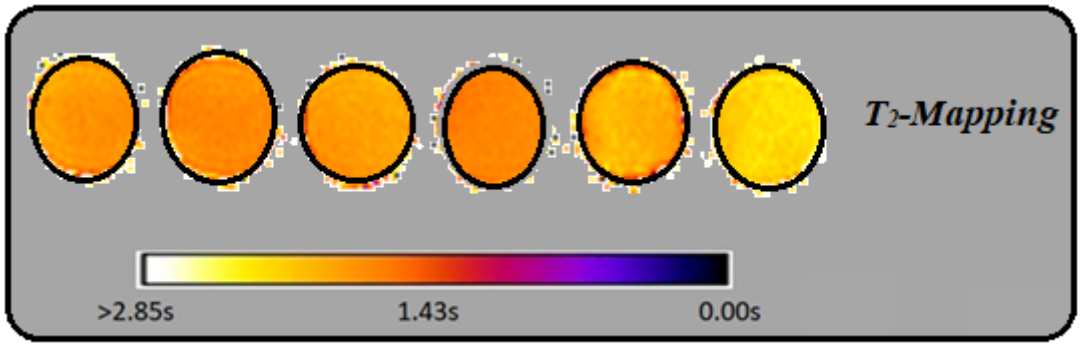

Figure 5-39: T_2-mapping image obtained for the prepared coated alendronate $KCoF_3$ NPs.

5.3.8.4 Squid measurement

Squid measurements of the coated alendronate $KCoF^6$ NPs are shown in Figure 5-40. ZFC-FC and hysteresis loops has been collected to provide the magnetisation saturisation data. From ZFC curve, it was very hard to indicate the blocking temperature of the synthesised NPs, the temperature where compound possess higher magnetisation value at room temperature. Early reports suggested that the value of blocking temperature diminishes as the NPs size decreases.[63-65] This match well with the data obtained for the small average size of these prepared NPs from TEM images and PXRD patterns. The FC curve indicates that at lower temperature, NPs behaves like a soft magnet and exhibited antiferromagnetic properties with maximum M of 0.08 emu/g. This value is extremely low compared to the bulk $KCoF_3$ (110 emu/g). Usually, the magnetization property has a strong relationship with the EDX results and the content of the paramagnetic ions with the obtained magnetisation of the materials. Previous studies showed that when nonmagnetic elements contribute to the total contents of the NPs containing magnetic elements, the magnetic ability of the entire system gradually declines.[66] It is well known that NPs materials have lower saturation magnetization (MS) when compared to those of their corresponding bulk analogues.[67] The main reason for this fact is related to the existence of spin canting over the particle surface of the NPs. As evidenced by EDX analysis, the paramagnetic cobalt ion was homogeneously mixed with other non-magnetic elements , which suggests that the magnetic grains were shielded by these elements, thus a small magnetisation value would be observed.[68]

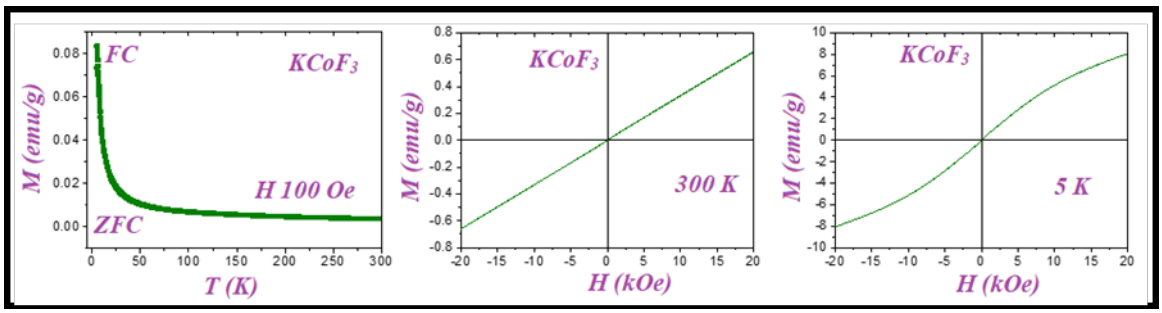

Figure 5-40: Squid measurements for coated alendronate $KCoF_3$ NPs.

5.4 Conclusions

In this chapter a successful synthesis of ultra-small KMF_3 (M = Mn, Fe, CO) nanoparticle was developed. The method used was based on the previously published method by Liu et al. Based on our scientific knowledge, this method was deliberately modified to fabricate the surface of the formed NPs and controlling the NPs size. This includes using different ligands (oleylamine and sodium alendronate) and minimising the solvent volume to 10 ml. This modification plays a crucial role in obtaining ultra-small NPs with an average diameter size of 1 to 3 nm. Co-precipitation method used to synthesis these NPs proved that the precipitation of the formed NPs occurs immediately, Hence, small volume of solvent in the reaction mixture did not dilute the oleylamine concentration. Within this concentration, oleylamine works as a surfactant which was able to encapsulate the formed NPs rapidly by providing a coating layer that restrict the growth of the NPs. Ligand exchange process was carried out to transfer the hydrophobic nature of the NPs to hydrophilic phase using sodium alendronate hydrophilic ligand. The formed NPs were characterised by PXRD, FTIR, TEM, EDX, NTA, Squid, NMR and MRI phantoms studies.

Based on the relaxation rates and phantom studies, the efficiency of the formed NPs to work as a contrast agent was assessed. The results obtained indicate that the ultra-small alendronate coated $KMnF_3$ exhibits a potential to work as Dual-mode T_1 and T_2 *MRI* contrast agents where r_1 = 6 $mM^{-1}s^{-1}$ and r_2= 51 $mM^{-1}s^{-1}$ with r_2/r_1 ratio of 8.5

Ultra-small coated alendronate $KFeF_3$ showed a potential to work as T_2 contrast agents, however the stability of this formed NPs was a major issue that restrict its use as a contrast agent as they tend to decompose to magnetite (Fe_3O_4) as the time prolonged. On the other hand, ultra-small coated $KCoF_3$ has not shown and potential to work neither as T_1 nor to T_2 contrast agents due to the observed negative *MRI* effect on the *MRI* T_1, T_2 and mapping images obtained.

5.5 References

1. J. Ward, *Radiography*, 2007, **13**, e54-e72.
2. Y. Cao, L. Xu, Y. Kuang, D. Xiong and R. Pei, *Journal of Materials Chemistry B*, 2017, **5**, 3431-3461.
3. N. A. Keasberry, M. Bañobre-López, C. Wood, G. J. Stasiuk, J. Gallo and N. J. Long, *Nanoscale*, 2015, **7**, 16119-16128.
4. Z. Li, P. W. Yi, Q. Sun, H. Lei, H. Li Zhao, Z. H. Zhu, S. C. Smith, M. B. Lan and G. Q. Lu, *Advanced Functional Materials*, 2012, **22**, 2387-2393.
5. M. Penchal Reddy, X. B. Zhou, L. Jing and Q. Huang, *Materials Letters*, 2014, **132**, 55-58.
6. K. S. Aleksandrov and V. V. Beznosikov, *Physics of the Solid State*, 1997, **39**, 695-715.
7. Hayatullah, G. Murtaza, R. Khenata, S. Muhammad, A. H. Reshak, K. M. Wong, S. Bin Omran and Z. A. Alahmed, *Comput. Mater. Sci.*, 2014, **85**, 402-408.
8. A. Okazaki and Y. Suemune, *Journal of the Physical Society of Japan*, 1961, **16**, 176-183.
9. Z. J. Liu, X. X. Song and Q. Tang, *Nanoscale*, 2013, **5**, 5073-5079.
10. C. Rümenapp, B. Gleich and A. Haase, *Pharmaceutical Research*, 2012, **29**, 1165-1179.
11. G. H. Im, S. M. Kim, D.-G. Lee, W. J. Lee, J. H. Lee and I. S. Lee, *Biomaterials*, 2013, **34**, 2069-2076.
12. W. Chen, P. Yi, Y. Zhang, L. Zhang, Z. Deng and Z. Zhang, *ACS Applied Materials & Interfaces*, 2011, **3**, 4085-4091.
13. C. Sun, J. S. H. Lee and M. Zhang, *Advanced Drug Delivery Reviews*, 2008, **60**, 1252-1265.
14. N. J. J. Johnson, W. Oakden, G. J. Stanisz, R. Scott Prosser and F. C. J. M. van Veggel, *Chemistry of Materials*, 2011, **23**, 3714-3722.
15. H. T. Ta, Z. Li, Y. Wu, G. Cowin, S. Zhang, A. Yago, A. K. Whittaker and Z. P. Xu, *Materials Research Express*, 2017, **4**, 116105.
16. S. Meier, G. Pütz, U. Massing, C. E. Hagemeyer, D. von Elverfeldt, M. Meißner, K. Ardipradja, S. Barnert, K. Peter, C. Bode, R. Schubert and C. von zur Muhlen, *Biomaterials*, 2015, **53**, 137-148.
17. N. Liao, M. Wu, F. Pan, J. Lin, Z. Li, D. Zhang, Y. Wang, Y. Zheng, J. Peng, X. Liu and J. Liu, *Scientific Reports*, 2016, **6**, 18746.
18. F. Hu, Q. Jia, Y. Li and M. Gao, *Nanotechnology*, 2011, **22**, 245604.
19. F. Söderlind, M.-A. Fortin, R. M Petoral Jr, A. Klasson, T. Veres, M. Engström, K. Uvdal and P.-O. Käll, *Nanotechnology*, 2008, **19**, 085608.
20. T. Tegafaw, W. Xu, M. W. Ahmad, J. S. Baeck, Y. Chang, J. E. Bae, K. S. Chae, T. J. Kim and G. H. Lee, *Nanotechnology*, 2015, **26**, 365102.
21. D. S. Crocket and H. M. Haendler, *Journal of the American Chemical Society*, 1960, **82**, 4158-4162.
22. L. Lu, H. Wang, H. Zhang and S. Xi, *Journal of Colloid and Interface Science*, 2003, **266**, 115-119.
23. S. Mourdikoudis and L. M. Liz-Marzán, *Chemistry of Materials*, 2013, **25**, 1465-1476.
24. W. S. Seo, J. H. Shim, S. J. Oh, E. K. Lee, N. H. Hur and J. T. Park, *Journal of the American Chemical Society*, 2005, **127**, 6188-6189.
25. T. N. B. O. STANDARDS, *Journal*, 1968.
26. N. L. Rosi and C. A. Mirkin, *Chemical Reviews*, 2005, **105**, 1547-1562.

27. J. Aldana, N. Lavelle, Y. Wang and X. Peng, *Journal of the American Chemical Society*, 2005, **127**, 2496-2504.
28. K. Davis, B. Qi, M. Witmer, C. L. Kitchens, B. A. Powell and O. T. Mefford, *Langmuir*, 2014, **30**, 10918-10925.
29. A. Sedlmeier and H. H. Gorris, *Chemical Society Reviews*, 2015, **44**, 1526-1560.
30. K. Knox, *Acta Crystallographica*, 1961, **14**, 583-585.
31. W. Massa and D. Babel, *Chemical Reviews*, 1988, **88**, 275-296.
32. A. Alipour, Z. Soran-Erdem, M. Utkur, V. K. Sharma, O. Algin, E. U. Saritas and H. V. Demir, *Magnetic Resonance Imaging*, 2018, **49**, 16-24.
33. G. Huang, H. Li, J. Chen, Z. Zhao, L. Yang, X. Chi, Z. Chen, X. Wang and J. Gao, *Nanoscale*, 2014, **6**, 10404-10412.
34. Y. Suemune and H. Ikawa, *Journal of the Physical Society of Japan*, 1964, **19**, 1686-1690.
35. K. Deka, A. Guleria, D. Kumar, J. Biswas, S. Lodha, S. D. Kaushik, S. A. Choudhary, S. Dasgupta and P. Deb, *Dalton Transactions*, 2019, **48**, 1075-1083.
36. R. Lontio Fomekong, J. Ngolui Lambi, G. R. Ebede, P. Kenfack Tsobnang, H. M. Tedjieukeng Kamta, C. Ngnintedem Yonti and A. Delcorte, *Journal of Solid State Chemistry*, 2016, **241**, 137-142.
37. H. Hiramatsu and F. E. Osterloh, *Chemistry of Materials*, 2004, **16**, 2509-2511.
38. Y. Tan, X. Dai, Y. Li and D. Zhu, *Journal of Materials Chemistry*, 2003, **13**, 1069-1075.
39. N. Nezafati, F. Moztarzadeh, S. Hesaraki and M. Mozafari, *Ceramics International*, 2011, **37**, 927-934.
40. C. Jiang, Z. Wang, H. Lin, Y. Wang, C. Luo, B. Li, R. Qi, R. Huang, X. Tang and H. Peng, *Colloids and Surfaces A: Physicochemical and Engineering Aspects*, 2017, **529**, 403-408.
41. J. R. Sohn and J. S. Lim, *Catalysis Letters*, 2006, **108**, 71-78.
42. Z. Wang, C. Jiang, R. Huang, H. Peng and X. Tang, *Journal of Physical Chemistry C*, 2014, **118**, 1155-1160.
43. J. L. Zhang, R. S. Srivastava and R. D. K. Misra, *Langmuir*, 2007, **23**, 6342-6351.
44. S. Sun, H. Zeng, D. B. Robinson, S. Raoux, P. M. Rice, S. X. Wang and G. Li, *Journal of the American Chemical Society*, 2004, **126**, 273-279.
45. K. Miladi, S. Sfar, H. Fessi and A. Elaissari, *Journal of Drug Delivery Science and Technology*, 2015, **30**, 391-396.
46. J. Zhang, S. Rana, R. S. Srivastava and R. D. K. Misra, *Acta Biomaterialia*, 2008, **4**, 40-48.
47. S. Ran, A. Downes and P. E. Thorpe, *Cancer Research*, 2002, **62**, 6132-6140.
48. R. Yang, S.-G. Yang, W.-S. Shim, F. Cui, G. Cheng, I.-W. Kim, D.-D. Kim, S.-J. Chung and C.-K. Shim, *Journal of Pharmaceutical Sciences*, 2009, **98**, 970-984.
49. S. Cafaggi, E. Russo, R. Stefani, R. Leardi, G. Caviglioli, B. Parodi, G. Bignardi, D. De Totero, C. Aiello and M. Viale, *Journal of Controlled Release*, 2007, **121**, 110-123.
50. S. Honary and F. Zahir, *Tropical Journal of Pharmaceutical Research*, 2013, **12**, 265-273.
51. P. Caravan, J. J. Ellison, T. J. McMurry and R. B. Lauffer, *Chemical Reviews*, 1999, **99**, 2293-2352.

52. Q. Zou, R. Tang, H.-x. Zhao, J. Jiang, J. Li and Y.-y. Fu, *ACS Applied Nano Materials*, 2018, **1**, 101-110.
53. D. K. Kim, Y. Zhang, W. Voit, K. V. Rao and M. Muhammed, *Journal of Magnetism and Magnetic Materials*, 2001, **225**, 30-36.
54. M. Aliahmad and N. Nasiri Moghaddam, *Materials Science-Poland*, 2013, **31**, 264-268.
55. M. Salavati-Niasari, Z. Fereshteh and F. Davar, *Polyhedron*, 2009, **28**, 1065-1068.
56. Y. Kiritoshi and K. Ishihara, *Polymer*, 2004, **45**, 7499-7504.
57. T. Muthukumaran and J. Philip, *Journal of Alloys and Compounds*, 2016, **689**, 959-968.
58. A. J. Barker, B. Cage, S. Russek and C. R. Stoldt, *Journal of Applied Physics*, 2005, **98**, 063528.
59. C. T. Rueden, J. Schindelin, M. C. Hiner, B. E. DeZonia, A. E. Walter, E. T. Arena and K. W. Eliceiri, *BMC Bioinformatics*, 2017, **18**, 529.
60. H. M. Haendler and A. W. Jache, *Journal of the American Chemical Society*, 1950, **72**, 4137-4138.
61. N. Tyagi, E. Ghanti, N. Gupta, N. P. Lalla and R. Nagarajan, *Bulletin of Materials Science*, 2009, **32**, 583-587.
62. D. Piché, I. Tavernaro, J. Fleddermann, J. G. Lozano, A. Varambhia, M. L. Maguire, M. Koch, T. Ukai, A. J. Hernández Rodríguez, L. Jones, F. Dillon, I. Reyes Molina, M. Mitzutani, E. R. González Dalmau, T. Maekawa, P. D. Nellist, A. Kraegeloh and N. Grobert, *ACS Applied Materials & Interfaces*, 2019, **11**, 6724-6740.
63. V. Kusigerski, E. Illes, J. Blanusa, S. Gyergyek, M. Boskovic, M. Perovic and V. Spasojevic, *Journal of Magnetism and Magnetic Materials*, 2019, **475**, 470-478.
64. J. Chatterjee, Y. Haik and C. J. Chen, *Journal of Magnetism and Magnetic Materials*, 2003, **257**, 113-118.
65. H. Shim, P. Dutta, M. S. Seehra and J. Bonevich, *Solid State Communications*, 2008, **145**, 192-196.
66. R. S. Yadav, I. Kuřitka, J. Vilcakova, J. Havlica, L. Kalina, P. Urbánek, M. Machovsky, M. Masař and M. Holek, *Journal of Materials Science: Materials in Electronics*, 2017, **28**, 9139-9154.
67. Z. Kozakova, I. Kuritka, N. E. Kazantseva, V. Babayan, M. Pastorek, M. Machovsky, P. Bazant and P. Saha, *Dalton Transactions*, 2015, **44**, 21099-21108.
68. Z. K. Karakaş, R. Boncukcuoğlu and I. H. Karakaş, *J Magn Magn Mater*, 2015, **374**, 298-306.

CHAPTER 6

Sol-gel synthesis of $DyFeO_3$

6 Introduction

Rare earth orthoferrite compounds which have the general formula RBO_3, where R is rare earth metal and B is transition metal. Depends on R metal, these compounds can exhibits one of the three well known structure classes: Perovskite, bixbyite and corundum.[1] Dysprosium oxide belongs to the bixbyite class, a derivation of fluorite crystal structure, and has a space group of *Ia3*.[1]The 4F orbitals for Dy^{3+} are partially filled with five unpaired electrons, making it an ideal paramagnetic T_2 contrast agent. The structure of rare earth (lanthanide) perovskites, $R^{3+}M^{3+}O_3$ (where R represents a rare earth metal and M a transition metal) have a Jahn-teller distorted, orthorhombic structure. The space group of this structure is Pbnm at room temperature.

Due to RBO_3 magnetic and physical properties, these compounds can be utilized in different application such as catalysts, gas sensors, semiconductors, magneto-optic materials and magnetic resonance imaging (*MRI*) in biomedicine.[2-5]

In particular, $DyFeO_3$ NPs is one of the interesting RBO_3 materials which exhibits antiferromagnetic properties under the ambient temperature due to the strong interaction between Fe^{2+} and Dy^{3+} through the oxygen atoms.[6] On the other hand, above the ambient temperature, $DyFeO_3$ shows paramagnetic properties.[6] The crystal structure of $DyFeO_3$ is displayed in Figure 1-12 .

Several methods have been reported for the synthesis of ultrapure and ultrafine of $DyFeO_3$ NPs. This includes co-precipitation method, combustion synthesis, hydrothermal method, microemulsion synthesis and sonochemical method.[7-11] Among these methods, Sol gel method is one of the most efficient and effective technique for preparation of multioxides which involves atomic scale mixing and known by its high reaction rate. In addition, the method is simple, environmentally friendly, easy and involves a rapid reaction with citric acid and polyacrylamide typical chelating reagents that has a strong chelating affinity to bind with the metals due to it is multi carboxylate functional groups. The structure of citric acid is shown in Figure 6-1

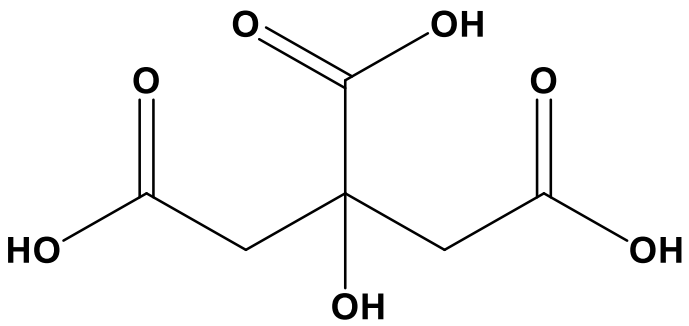

Figure 6-1: Chemical structure of citric acid

In this chapter, a synthesis of the $DyFeO_3$ was performed through the well-known polyacrylamide modified sol gel method in order to be investigated as a contrast agent for Magnetic Resonance Imaging (*MRI*). Dy_2O_3 and $Fe(CH_3COO)_2$ were the starting materials precursors used. NPs formed were characterised using PXRD, TEM, EDX, ICP, magnetic properties, NMR and zeta potential.

$DyFeO_3$ NPs were then functionalised with silica (TEOS). The core NPs did not decompose. This was confirmed by PXRD. The coating process following was investigated *via* FTIR, TEM and EDX and zeta potential.

Finally, the attachment of DOX was attached to the NPs after APTES functionalisation. The resulting NPs were characterised by PXRD, FTIR, TEM and EDX.

6.1 Experimental

6.1.1 Synthesis of $DyFeO_3$

In this chapter, a modified polyacrylamide sol-gel method to synthesize orthorhombic $DyFeO_3$ NPs was used.[12]

In 500 ml beaker, Dy_2O_3 (1.25 g, 3.35×10^{-3} moles) was dissolved in 100 ml *HPLC* water. Nitric acid (1.80 M) was added dropwise under constant stirring until a white clear solution was obtained. Subsequently, $Fe(CH_3COO)_2$(1.17 g, 6.73×10^{-3} moles) was added to form 1:1 ratio of dysprosium and iron cations. Citric acid (6.43 g, 0.0335 moles) was added to form 1:1:5 ratio of cations and complexant, with respect to the cation mentioned previously. The obtained solution is then adjusted to pH 3 using ethylene diamine anhydrous then acrylamide monomers (10 g per 100 ml) were added. The resulting mixture was left under constant stirring for 30 minutes and then heated at 80°C until a viscous pale orange gel was produced. This gel was then transferred to a furnace and heated for 24 hours at 150°C. A dried black xerogel was obtained which was ground using a pestle and mortar to a light orange fine powder. This resulting powder was divided into 3 samples and heated separately at 500°C for 23, 25 and 30 hours respectively. The

produced samples were then annealed at 800°C for 2 hours. These obtained 3 samples of orange $DyFeO_3$ were then characterised by Powder x-ray diffraction (PXRD) for optimisation, hence sample possessing single phase was chosen and characterised by FTIR, NTA, ICP, NMR and DLS. The average crystalline size of the bare $DyFeO_3$ was calculated using Scherer equation;

$$L = 0.9\lambda/\beta cos\theta \qquad \textit{Equation 6-1}$$

Where λ is the wavelength of the x-ray radiation is, β is the width of PXRD peak at its half maximum intensity (FWHM) and θ is the Bragg diffraction angle.

6.1.2 Functionalisation with tetra ethyl orthosilicate

$DyFeO_3$ (0.15 g) NPs were dispersed in a mixture consisting of absolute ethanol (30 ml) and HPLC water (6 ml) in 3 necks round bottom flask. The mixture was refluxed and constantly stirred for 2 hours under a nitrogen atmosphere. Subsequently TEOS (0.685 g, 3.30×10^{-3}) was dropwise introduced to the mixture and continued to stir for further 30 minutes. Aqueous ammonia (2.5 ml, 35%) was added and the dispersive solution was left stirring for 2 hours. The resulting $DyFeO_3/SiO_2$ core shell NPs were separated from the solution via a centrifuge at 45000 round per minute for 5 minutes. The Coated $DyFeO_3$ was washed with HPLC water to remove any unbounded excessive silicate.

In order to optimise the amount of silica on the $DyFeO_3$ NPs surface, various parameters such as altering the amount of the coating silica ligand added, effect of TEOS addition time and by filtering the coated silica $DyFeO_3$ suspension using a 45 µl filter. Table 6-1 describes the optimisation of the above parameters in details.

Table 6-1: Different samples prepared to optimise the hydrodynamic size of the prepared coated silica $DyFeO_3$ NPs.

S. No	*Sample (g)*	*TEOS (g)*	*NH_3 (ml)*	*H_2O (ml)*	*EtOH (ml)*	*Addition time of TEOS*	*NPS F/unF*
1	0.15	0.6	2.5	6	30	1h	unfiltered
2	0.15	0.6	2.5	6	30	1h	filtered (0.45µl)

3	0.15	0.3	2.5	6	30	24h	Unfiltered
4	0.15	0.3	2.5	6	30	24 h	filtered (0.45µl)

In the above table, all samples were characterised by TEM and EDS.

6.1.3 Functionalisation of silica core shell $DyFeO_3$ with APTES

0.2 g $DyFeO_3/SiO_2$ core-shell NPs were suspended in 12.5 ml toluene. 3 ml APTES was then added and the dispersion was left to stir under nitrogen for 12 hours at 75°C. The coated NPs were separated from solvent using a centrifuge running at a speed of 45000 RPM for exactly 10 minutes. The resulting product was analysed by PXRD and FT-IR.

6.2 Results and discussions

6.2.1 PXRD analysis

PXRD Scanning of the formed $DyFeO_3$ samples at different calcination time, displayed in Figure 6-2 indicates that the major composition of the sample calcinated for 25 hours is well matched with the standard bulk $DyFeO_3$ available in the literature.[13] No impurities was detected. However, small impurities were observed at 2θ (29 deg) for both samples calcinated at 23 and 30 hours. These were attributed to Dy_2O_3. It is possible that some of the unreacted Fe^{3+} ions have been washed away during the washing process and some of Dy_2O_3 starting material left unreacted in the obtained $DyFeO_3$. This might be a reason for the fact that no peaks were observed for any excessive Fe_2O_3 phase in the PXRD pattern. Therefore, sample heated for 25 hours is used in this study. An orthorhombic structure with *Pnma* space group was obtained. This is similar to the results reported in literatures for perovskite-type oxide.

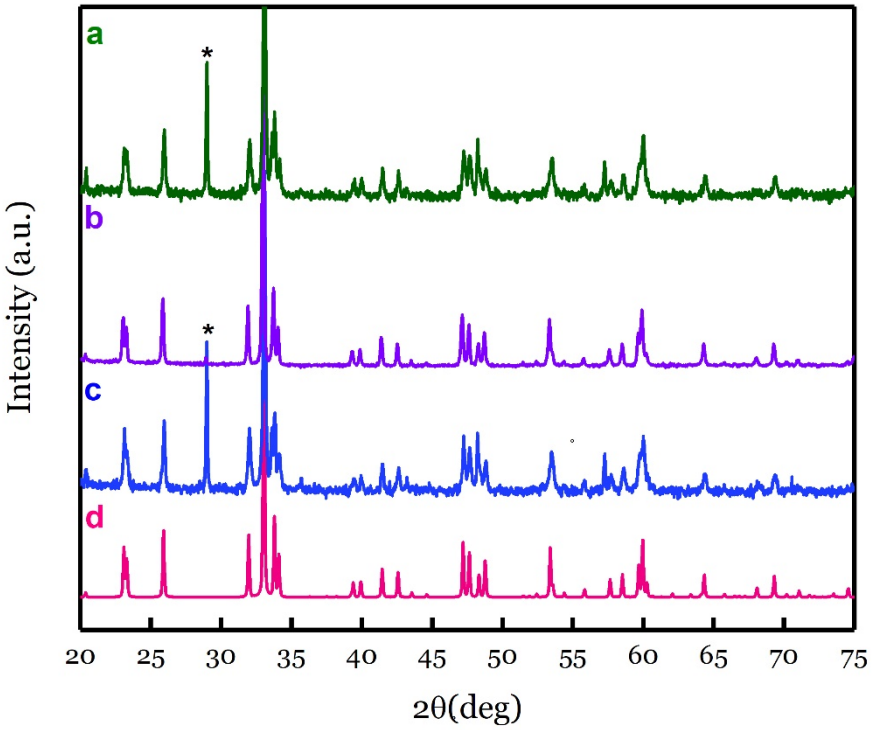

Figure 6-2: PXRD patterns of $DyFeO_3$ heated at 500°C for different times (a) 23h, (b) 25h and (c) 30 h compared to the (d) standard pattern for bulk $DyFeO_3$

The unit cell parameters of the synthesised NPs samples at different calcination time are displayed in Table 6-2. These values are agreed with the previously reported values for $DyFeO_3$ documented in the literature.[13, 14]

Table 6-2: The refined unit cell parameters of $DyFeO_3$ NPs calcinated at 500°C for different time compared to the model values obtained by High score software

NPs	*a (Å)*	*b (Å)*	*c (Å)*
Model	5.3051	5.5966	7.6243
NPs at 23 h	5.309(6)	5.592(6)	7.620(8)
NPs at 25 h	5.305(3)	5.595(2)	7.621(4)
NPs at 30 h	5.302(3)	5.598(3)	7.623(5)

The average crystalline size of the bare $DyFeO_3$ was calculated using Scherer equation and found to be approximately 32 nm. It is worth noting that as the annealing time and temperature were increased, the mean dimeter size of the obtained NPs increases. A same phenomenon was observed by Zhu et al.[14]

6.3 TEM images

The morphology and size of the $DyFeO_3$ NPs were investigated by high resolution TEM microscopy. TEM images of the prepared NPs were taken in different area of the samples and with different magnification as seen in Figure 6-3. One of the main characteristics of magnetic NPs that they tend to agglomerate. Agglomeration is a phenomenon in which single particles in a dispersion medium are clumped into a cluster. Due to this phenomenon, it was really difficult to measure the precise size of the prepared NPs. However nearly spherical morphology could be observed.

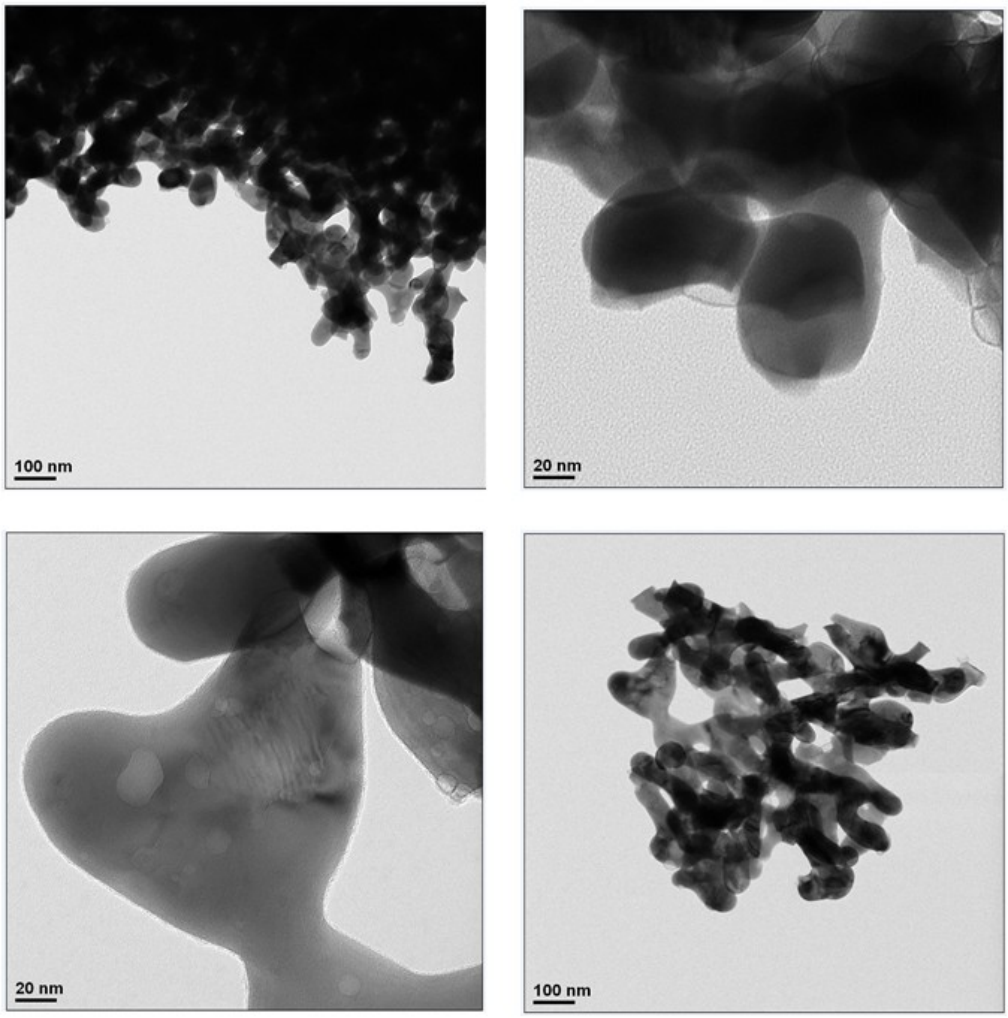

Figure 6-3: TEM images for bare $DyFeO_3$ at different magnifications.

In order to produce a monodispersed $DyFeO_3$ NPs and reduce the NPs agglomeration, many studies suggested different strategies to enhance the colloidal stability of the NPs. For inorganic materials, the NPs usually encapsulated by an inorganic layer such as silica.[15] The coated layer could protect magnetic NPs from direct contact with different

environments and thus decrease the chance of oxidation and agglomeration. For instance, the anionic silica layer on the NPs surface could play a crucial role in improving the electrostatic repulsion between the particles, hence, a shielding is provided to reduce the magnetic dipole interaction.[16]

6.4 Zeta potential

Zeta potential value is an important concept used to determine the surface charge of NPs. This value is closely related to the stability of NPs in suspensions and particles surface morphology.[17] For this reason, the influence of the surface charge of the as prepared $DyFeO_3$ was measured. As can be seen form Figure 6-4, the zeta potential of this prepared NPs is measured at pH = 7 is -21.4 mV. Generally, a suspension that exhibits a zeta potential less than ± 20 mV tends to form aggregates and will results in particle precipitating in the solution.[18] The negative zeta potential value obtained might also reflects the coordination of the negative OH^- groups in the water suspension. In a study conducted on silver NPs, it was highlighted that as pH increases from 2-10, the concentration of OH^- increases. This allows OH^- to more strongly compete for the surface sites, resulting in the formation of the negative surface charge in alkaline pH environment.

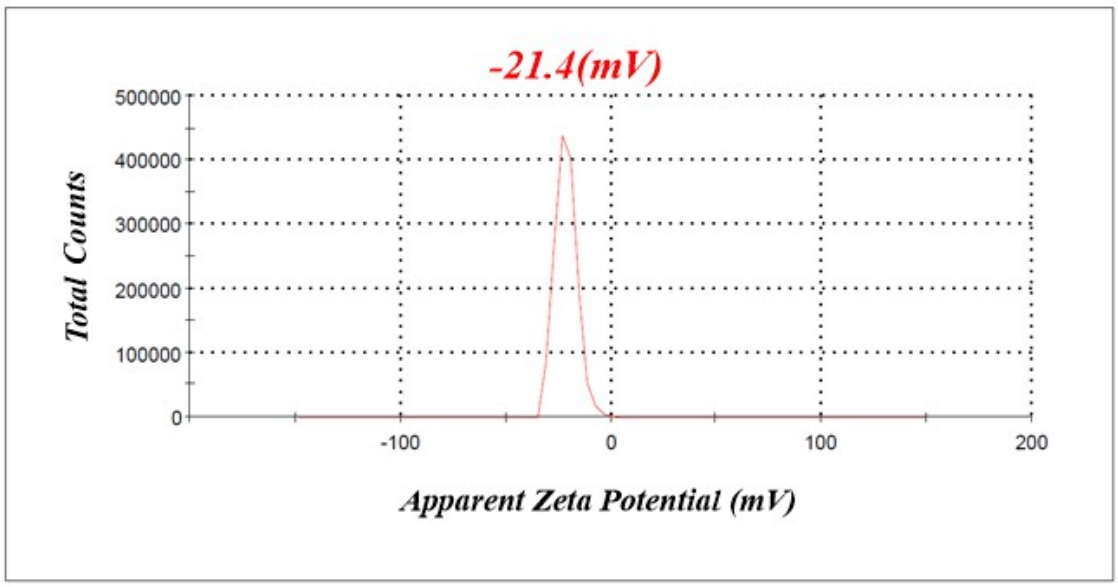

Figure 6-4: Apparent zeta potential of $DyFeO_3$ NPs surface prior to coating with TEOS

6.5 Functionalisation of $DyFeO_3$ with silica

For better biological compatibility and stability, the synthesised $DyFeO_3$ was coated with silica. The use of silica as a coating materials to improve the colloidal stability has been

used in various application such as semiconductors, nanoscale metals and magnetic and ceramic NPs, with high surface area and magnetic and optical properties.[19] The use of silica as a coating materials has a long history in colloidal science. This rely on it is high stability, especially in aqueous medium. In addition, other reasons such as easy control of the deposition process (and the shell thickness), chemical inertness, its processability, controllable porosity and optical transparency make silica an ideal, low-cost material to tailor surface properties, while basically maintaining the physical integrity of the underlying core nanocrystals.[20] The important two factors favouring the remarkable stability of silica sols are that i) van derWaals interactions between the silica and surface of NPs are much lower than those involving other NPs, and ii) cations and positively charged molecules can be tightly attached to the characteristic polymeric silicate layer at silica–water interfaces under basic conditions. Thus, this silicate layer can confer both electrostatic and steric protection on different cores, and act as dispersing agent of many electrostatic colloids.[21]

In order to investigate the stability of the synthesised $DyFeO_3$ after being functionalised with silica, PXRD analysis was carried out and compared to the PXRD results of the uncoated NPs. The PXRD pattern obtained for this sample indicated that $DyFeO_3$ is stable under SiO_2 coating as there were no detectable peaks corresponding to impurities as well as no detectable 2θ shift in the position of these peaks, although amorphous impurities cannot be excluded. PXRD patterns of the coated sample with silica compared to the bare $DyFeO_3$ and model is depicted in Figure 6-5

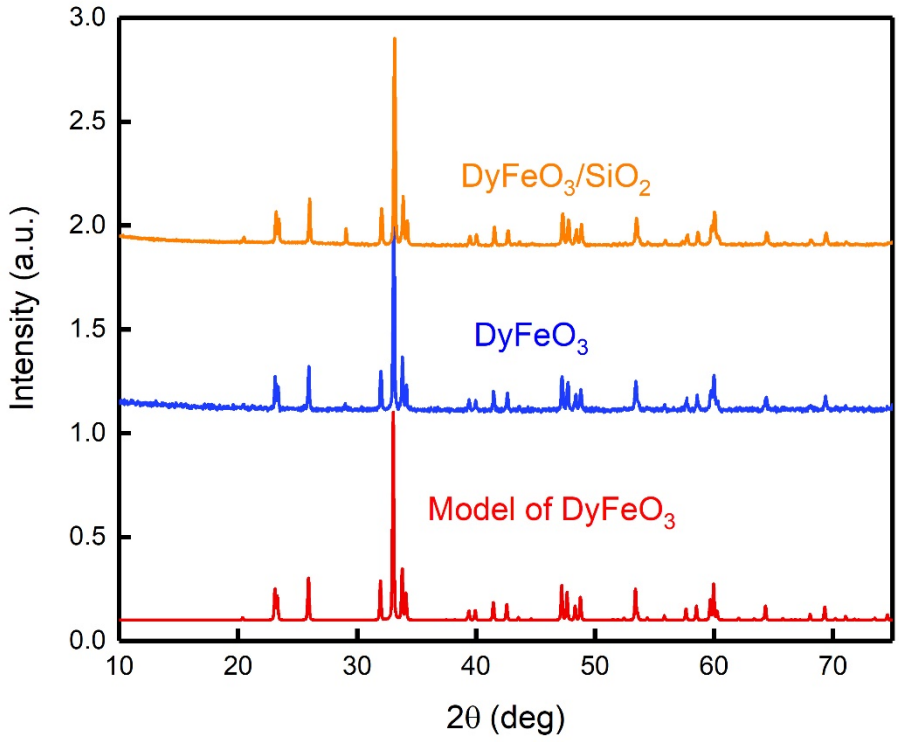

Figure 6-5: PXRD pattern of silica coated $DyFeO_3$ compared to bare $DyFeO_3$ and standard $DyFeO_3$

The average crystal size of the silica coated NPs calculated using Scherer formula found to be 39 nm. The increase in the crystal size compared to the bare nanoparticle size was a significant evidence that the synthesised $DyFeO_3$ is successfully coated with silica ligand.

6.6 FTIR analysis

For further confirmation, the surface coating of $DyFeO_3$ NPs was evaluated by FTIR spectroscopy. In Figure 6-6, clearly the bare TEOS ligand displays two characteristic bands at 1080 cm^{-1} and 800 cm^{-1}. These two bands are assigned to Si-O(-Si) stretching vibrations. Another band appeared at 950 cm^{-1} which is attributed to the Si-O(H) stretching vibrations. All of these bands appeared in the FTIR spectrum of the coated silica $DyFeO_3$. However, a small shift to lower wavelength was observed. On the other hand, the FTIR spectrum of the bare $DyFeO_3$ does not contains these three bands. This indicates that the silica ligand was deposited on the NPs surface.

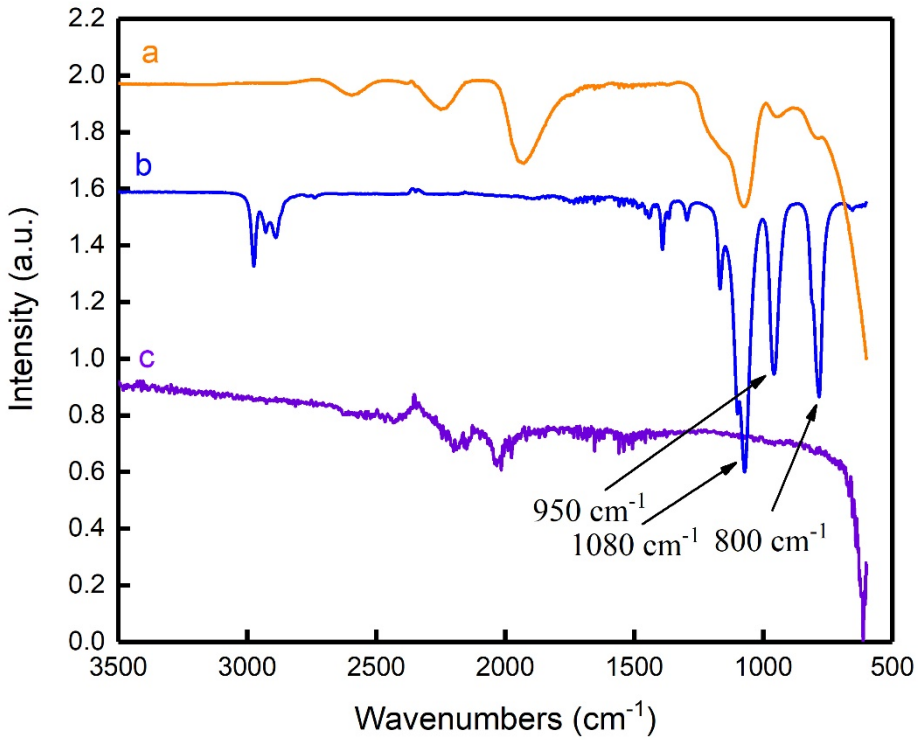

Figure 6-6: FTIR spectrum of silica coated $DyFeO_3$ (a) compared to bare ligand (b) and bare $DyFeO_3$ (c).

6.7 TEM analysis

Many studies have shown that the kinetics of interaction of metal ions with reducing agents, experimental conditions and adsorption processes of stabilizing agent with metal NPs have a strong impact on the morphology, stability, size and (chemical and physical) properties of the metal NPs.[22] In reality, specific control of the size, shape and distribution of the produced NPs can be obtained by changing the methods of synthesis, reducing and stabilizing factors. For the above reasons, the coating processes of the synthesised $DyFeO_3$ NPs were performed many times and optimised by altering the amount of the coating silica ligand added, effect of TEOS addition time and by filtering the coated silica $DyFeO_3$ suspension using a 45 µl filter. This was done to adjust the amount of the coating silica layer on the NPs surface. Therefore, the desired optimum diameter size applicable for biological application (1-100 nm) can be obtained. Thus, a set of different samples, as shown in Table 6-1displayed in section 6.2.2 were characterised using TEM and elemental analysis EDX.

Representive TEM images for all filtered and unfiltered coated silica $DyFeO_3$ samples are all displayed in Figure 6-7 to Figure 6-10. Clearly, $DyFeO_3$ NPs cores are surrounded by a thick layer of silica. It is worth noting that at any experimental conditions used, no uncoated NPs are observed.

It was proposed that the rate of the silica layer formation into the surface of NPs influenced by the amount of TEOS added into the reaction vessel and the reaction time taken for this addition. For sample number 1where 0.6 g silica was added over an hour and no filtration treatment was performed, TEM images displayed in Figure 6-7 showed an overall average diameter of 63.88 nm for the silica coated $DyFeO_3$ NPs, where the average diameter of 36.19 nm for the NPs core and an average diameter size of 27.69 nm for the silica coating layer as seen in Figure 6-7 (a). This overall diameter size makes the NPs shell applicable for the use of biological application. However, the formation of NPs clusters due to agglomeration goes against this assumption as the prepared NPs not well-dispersed state and not totally separated from each other are inapplicable. Therefore, a second experiment was performed where the NPs suspension was filtered using 0.45 µl micro filter. The resulting TEM images obtained in

Figure 6-8: TEM images for filtered silica coated $DyFeO_3$ NPs when 0.6 g ETOS added over an hour

(b) showed an average size of 39.81 nm and 20.16 nm for the core NPs and the coating silica layer respectively. In this experiment, no significant results were obtained in terms of the NPs agglomeration in comparison with sample 1. Silica particles predominantly attached directly to the surface of the NPs forming a multi layers and aggregates. This indicates that there were not well dispersed in the original solution.

The third attempt was performed for sample 3, where half the amount of silica was added over 24 hours using burette and the dispersed NPs were not filtered. TEM images in Figure 6-9 showed a high degree of NPs agglomeration and the silica coating layer increased to 51.27 nm, Figure 6-9 (a). In addition, the agglomeration of the NPs increased to form a large cluster. This indicates that the growth of the silica layer on the NPs surface increases due to the increase in the rate of the reaction. This might also give a positive indication that the molar ratio correlation between the silica and the dispersed NPs has an effective impact on the formation of the coated silica layer. As a final attempt to overcome this agglomeration issue, sample 4 was filtered while keeping all parameters constant as for the sample 3. Surprisingly, few individual NPs of 39.09 nm as shown in Figure 6-10 were observed, despite the formation of clusters and thick layer of silica surrounding these NPs compared to the previous silica optimisation attempts. Generally, in NPs synthesis, agglomeration usually occurs due to the high surface area to volume ratio of NPs which provides a very high surface energy and higher instability. Due to attractive van der Walls forces between particles, NPs tend to agglomerate in order to minimize their surface energy, thus stable NPs are formed.[23] Agglomeration is also an ordinary property for

magnetic NPs occurs due to magnetic dipole–dipole attractions between these particles. NPs prone to agglomerate forming large clusters and resulting in increased particle size.[24] Synthesis of isolated and well- dispersed NPs for nanotechnology is still in its initial developing steps and has been an interesting topic for researchers and thus the total removal of this aggregation phenomena may not be possible.

To improve the dispersion of silica coated $DyFeO_3$ NPs in order to synthesise well-defined and an ideal silica layer on the surface of NPs, further investigation is needed to study the rate of TEOS hydrolysis, the correlation between the TEOS hydrolysis rate and the silica-particle growth rate and the impact of the concentration of water and ammonia on the kinetics of silica-particle growth in aqueous suspension.

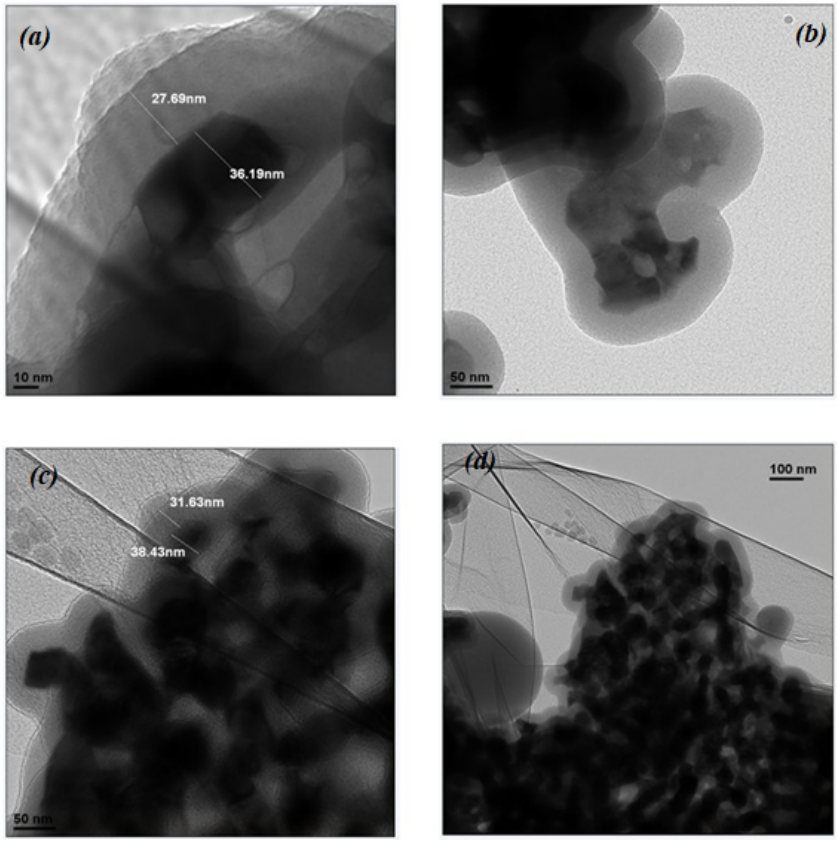

Figure 6-7: TEM images for unfiltered coated silica $DyFeO_3$ NPs when 0.6 g ETOS added over an hour.

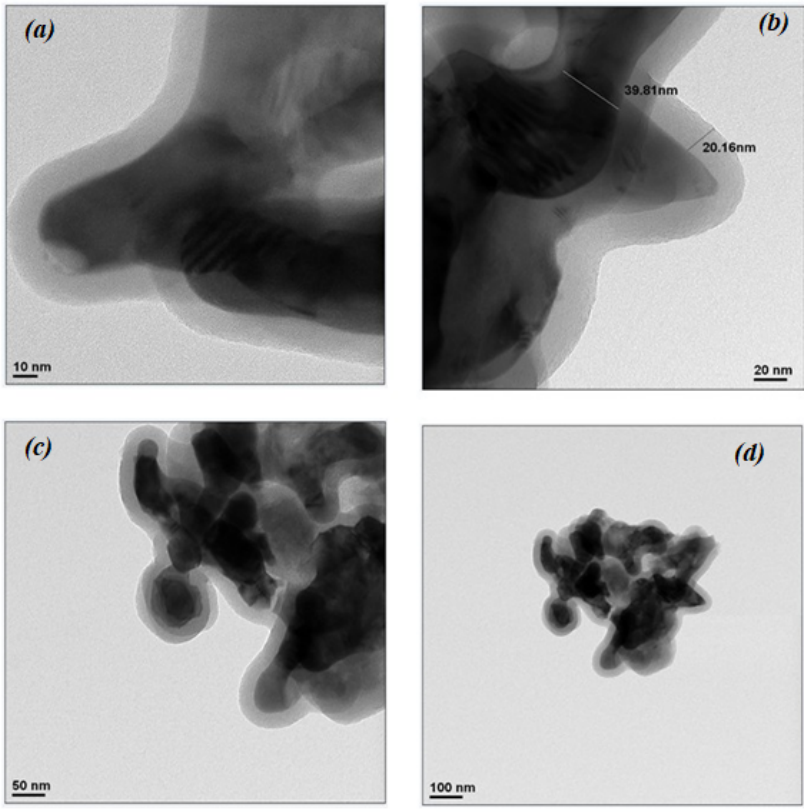

Figure 6-8: TEM images for filtered silica coated $DyFeO_3$ NPs when 0.6 g ETOS added over an hour

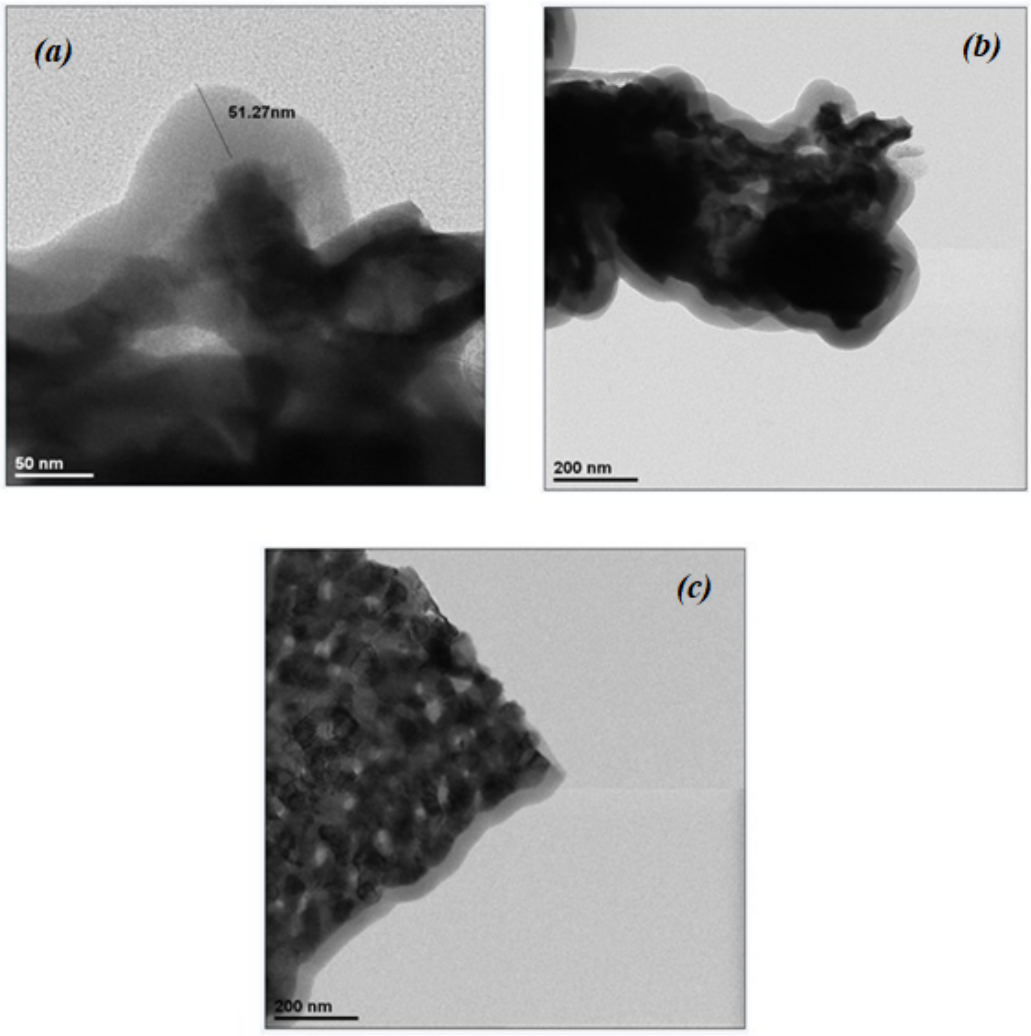

Figure 6-9: TEM images of unfiltered $DyFeO_3$ with half amount of silica added over 24 hours using a burette.

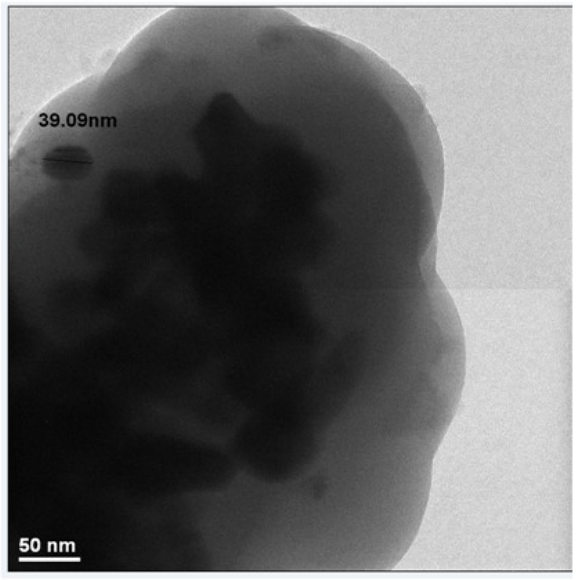

Figure 6-10: TEM images of filtered $DyFeO_3$ with half amount of silica added over 24 hours using a burette

The chemical composition of the $DyFeO_3$ NPs was determined by Energy Dispersive X-ray spectroscopy (EDX). The elemental analysis confirms the existence of Dy, Fe O and Si in their composition as seen in the spectra shown in Figure 6-11 and Figure 6-12 for both filtered and unfiltered samples respectively. Interestingly, all silica coated NPs prepared during the TEOS optimisation process showed a reasonable atomic weight ratio for Dy and Fe by (1:1). This agrees with their theoretical values and also matched well with the results obtained by inductively coupled plasma analysis. It is worth noting that the atomic weight percentages of silicon in all filtered and unfiltered samples are far high than Dy and Fe atomic weight percentages. This might be also a reasonable reason for the presence of the thick silica layer on the NPs surface.

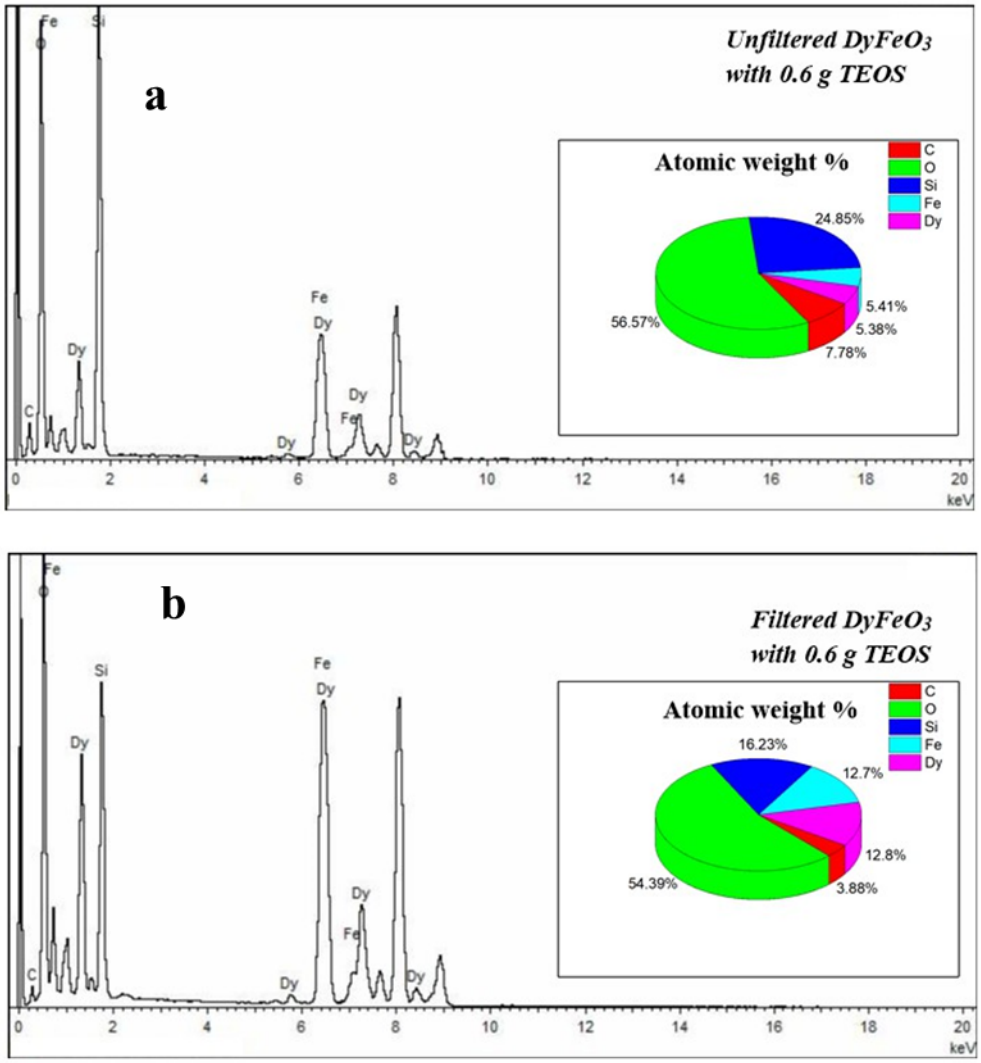

Figure 6-11: Elemental composition of unfiltered(a) and filtered(b) silica coated $DyFeO_3$ NPs when 0.6 g ETOS added over an hour.

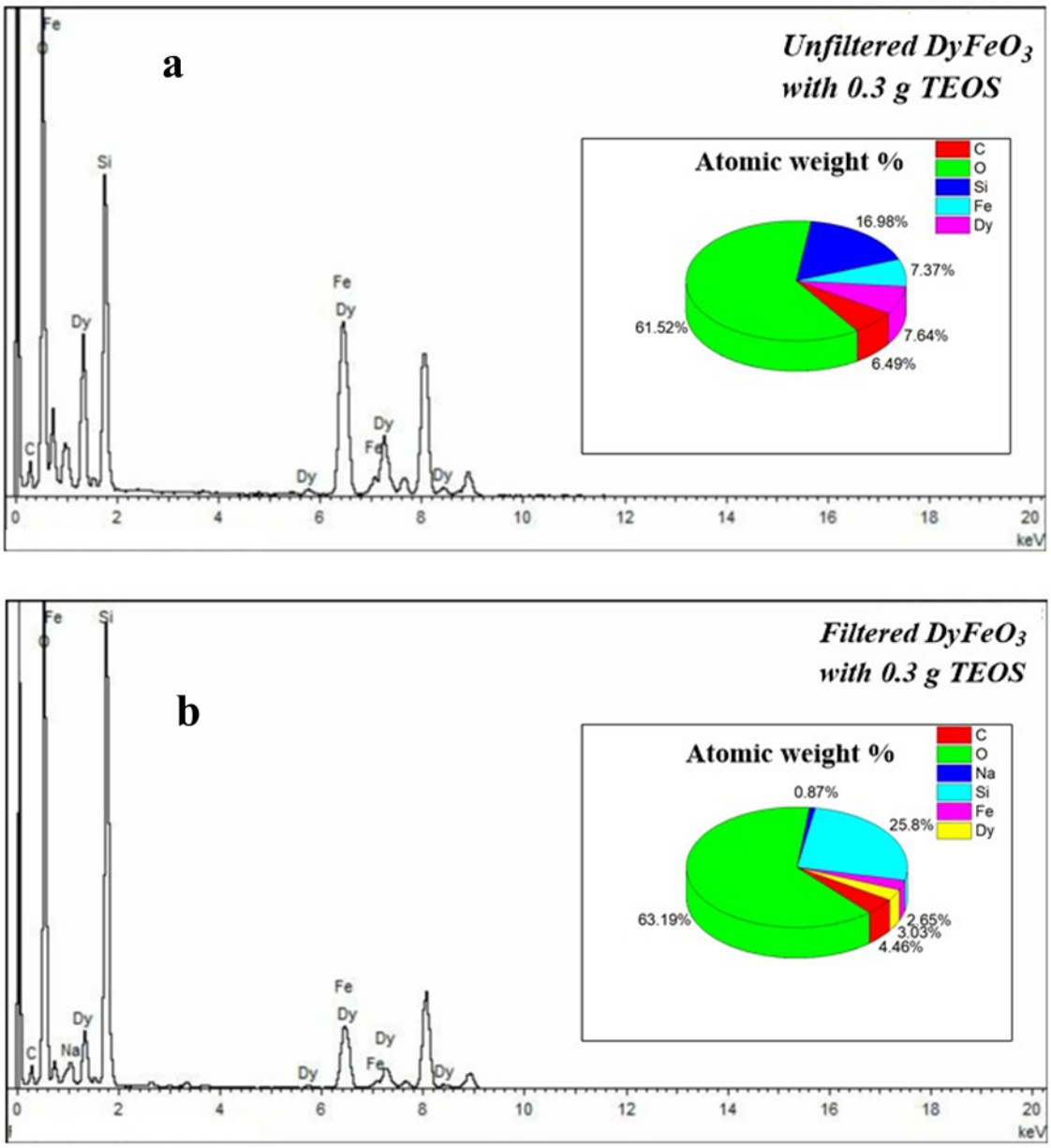

Figure 6-12: Elemental composition of unfiltered and filtered silica coated $DyFeO_3$ NPs when 0.3 g ETOS added over 24 hours.

6.8 Zeta potential

Hypothesis of specific interaction between inorganic NPs and silica have been intensively reported in literature. The homogenous dispersity of the NPs in the silica matrices may take place due to various types of electrostatic and covalent interactions, for instant, electrostatic, between negatively charged Si-O terminal ligands and positively charged groups on the particle surface, covalent, through Si-O-Fe bond formation or hydrogen-bond interactions between hydration layers of silanol groups and the particle surface.[17] At pH = 7 the obtained value of zeta potential for the silica coated $DyFeO_3$ NPs is 5.06

mV as shown in Figure 6-13. The obtained positive value is more likely due to the coordination of the silica to the Fe^{3+} or Dy^{+3} ions *via* oxygen, allowing the Si-O-Fe or Si-O-Dy bonds to form. The positive zeta potential magnitude also indicates that the elimination of the negatively charged OH^- ion and replaced by the silica Si ion. Since TEM images for the prepared silica $DyFeO_3$ showed a high degree of aggregation, it could be more likely related to the instability of the formed NPs as the zeta potential value is less than the value recommended for the formation of stable NPs of ± 20.[18]

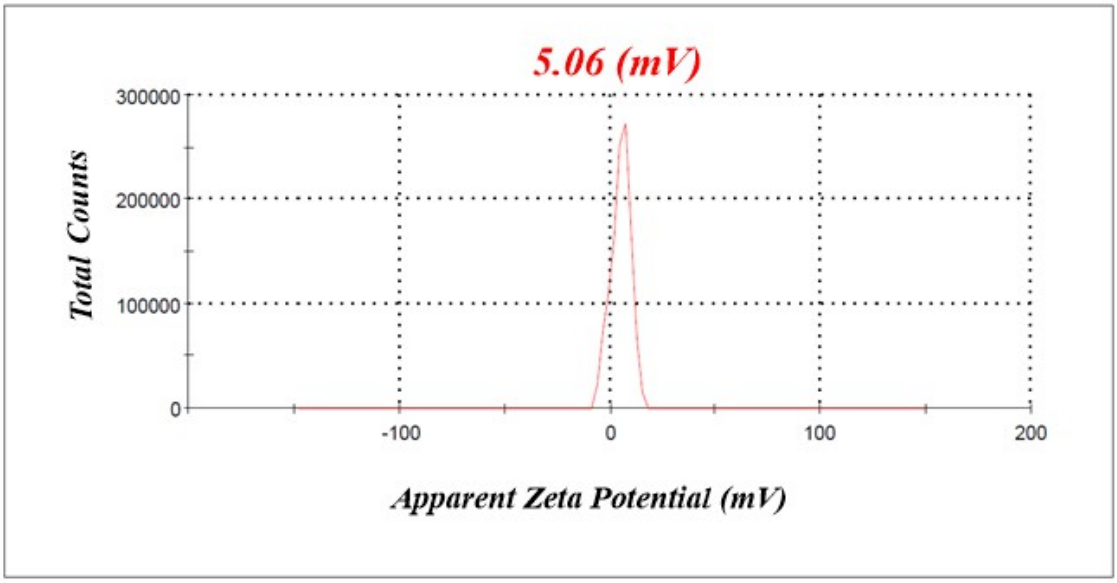

Figure 6-13: Apparent zeta potential of the silica coated $DyFeO_3$ nanoparticle surface

6.9 Relaxitivity

To evaluate the efficiency of the synthesised NPs as *MRI* contrast agents, longitudinal and transverse relaxation rate measurements were carried out at external magnetic field strength 9.4T.

$DyFeO_3$ as prepared and silica coated $DyFeO_3$ NPs were suspended in water, and sets of samples with different concentrations were prepared to study the relaxation rates of the bare NPs and the effects of the coating upon the relaxitivity. The obtained results for longitudinal relaxation rates in (Figure 6-14) and transverse relaxation rates (Figure 6-15) were subsequently compared against each other. For $DyFeO_3$ NPs at 9.4T, r_1 = 2.92829 mM^{-1} s^{-1} whereas silica coated $DyFeO_3$ NPs r_1 = 9.18894 mM^{-1} s^{-1}. The observed increase by 28 % in the longitudinal relaxation rate of the silica coated NPs could be due to the silica hydrophilic layer which facilitate the interaction between the surrounding water protons and the core NPs. It is also more likely that the Si-O polar groups in the silica have an extreme contribution towards the enhancement of the spin-lattice relaxation rate

by allowing the water molecules to penetrate the coating layer and interact with the core NPs, thus contribute in shortening the relaxation time. Furthermore, the neighbouring Dy and Fe metals ions in the coated silica $DyFeO_3$ NPs could further accelerate the r_1 relaxation rate of the water protons *via* their cooperative interaction. On the other hand, for the coated NPs at 9.4T, spin-spin relaxation rate for uncoated $DyFeO_3$ r_2 = 6.61143 mM^{-1} s^{-1} and for silica coated $DyFeO_3$ NPs r_2 = 37.64756 mM^{-1} s^{-1}. Many studies have indicated that the thickness of the coating on the NPs surface have a significant role in determining the net relaxation rates of magnetic iron oxide NPs.[25] Generally, a higher thickness of the coating layer leads to a low relaxation rate value. Although, optimisation of the silica coating process performed in this study showed unsatisfied measurements for the coating thickness, a significant increase by 82% in the transverse relaxation rate take place for the silica coated nanoparticles in comparison to the uncoated NPs. It is also worth to note that the silica coating does not influence the initial structures and compositions of the NPs as shown by PXRD patterns displayed previously in Figure 6-5 . However, the increase in the relaxation rate for the coated $DyFeO_3$ could be attributed to the improvement in the magnetic properties by SiO_2 layer, which may stabilise the spin order on the surface of the NPs, by avoiding surface oxidation, as reported for silica coated Fe_3O_4 NPs.[26]

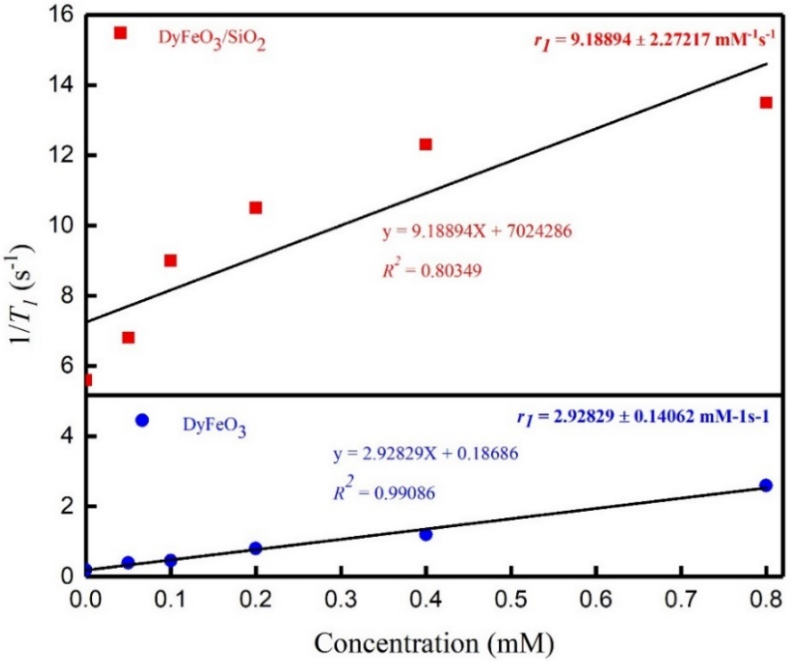

Figure 6-14: Longitudinal relaxation rates of $DyFeO_3$ and silica coated $DyFeO_3$

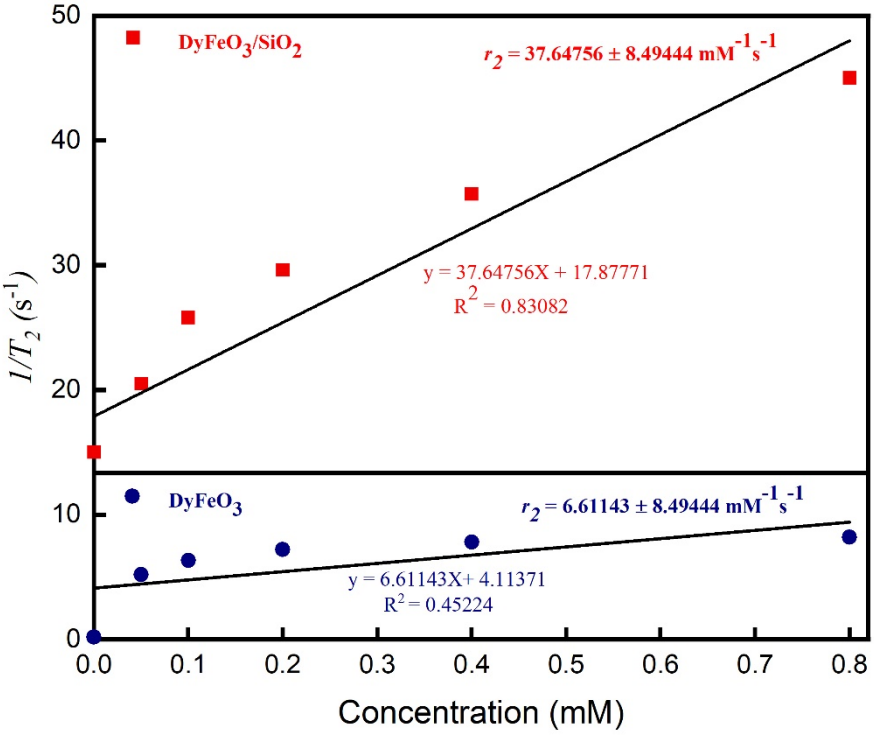

Figure 6-15: Transverse relaxation rates of $DyFeO_3$ and silica coated $DyFeO_3$

6.10 Conjugation of APTES with silica coated $DyFeO_3$

To use the coated silica $DyFeO_3$ NPs as a drug delivery carrier for a cancer cells treatment. It was important to functionalise it with APTES, thus a bearing NH_2 group would be formed on the nanoparticle surface, making it easier to be used as a conjugation terminal to bind the drug.

Gentle heating of the prepared silica coated $DyFeO_3$ with APTES gives rise to the formation of NH_2 group on the NPs surface as can be seen in the schematic diagram in Figure 6-16. The 3-aminopropyltriethoxysilane (APTES) is a ligand that is most frequently used organosilane coupling agents that may connect chemically reactive amino on Si substrate.[27-30] The reaction at room temperature results in the chemical modification of APTES ethoxy groups $(OC_2H_5)_3$-Si-$(CH_2)_3$-NH_2 to hydroxyl groups $(OH)_3$-Si-$(CH_2)_3$-NH_2 hydrolysis.[31] To confirm the stability of the coated nanoparticle by APTES, PXRD analysis indicates that $DyFeO_3$ NPs were retained, as all peaks appeared in their same 2θ positions. Figure 6-17 represents the PXRD pattern of the APTES coated NPs compared to silica coated and standard PXRD patterns. Small amount

of Dy_2O_3 impurities were observed as a second phase. These impurities could be formed due to the incomplete hydrolysis of APTES where some of the oxygen reacted with the dysprosium metal to form the undesired product. To get an ultra-pure single phase, an optimisation process to investigate the exact amount of APTES needed to overcome this issue.

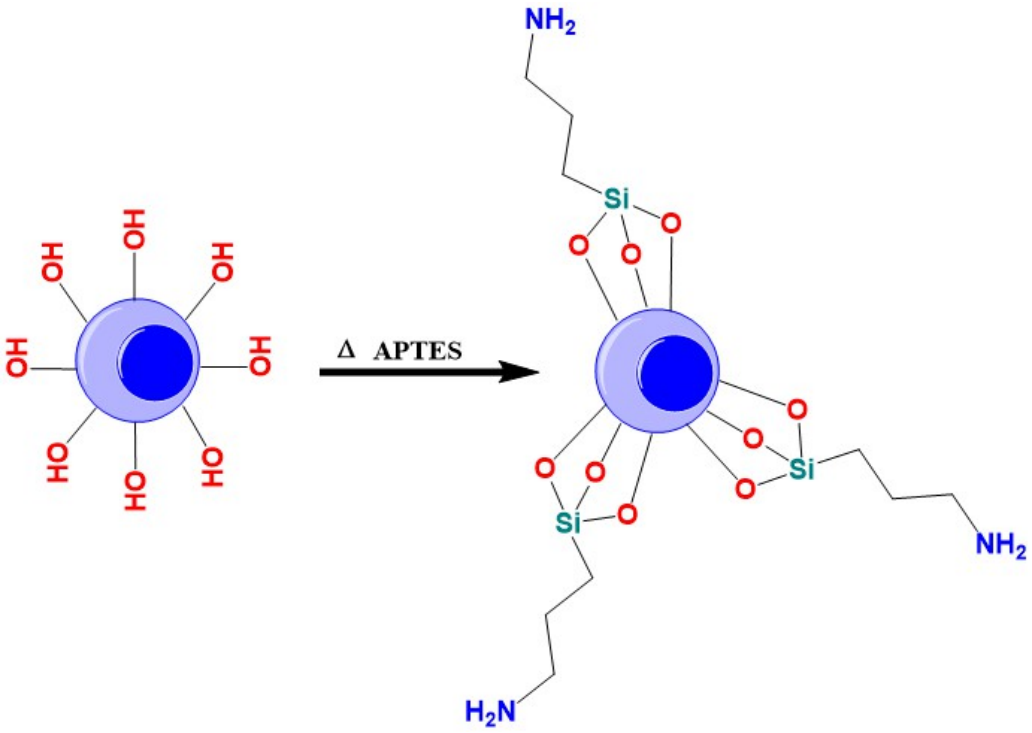

Figure 6-16: Functionalisation of $DyFeO_3$ with APTES ligand.

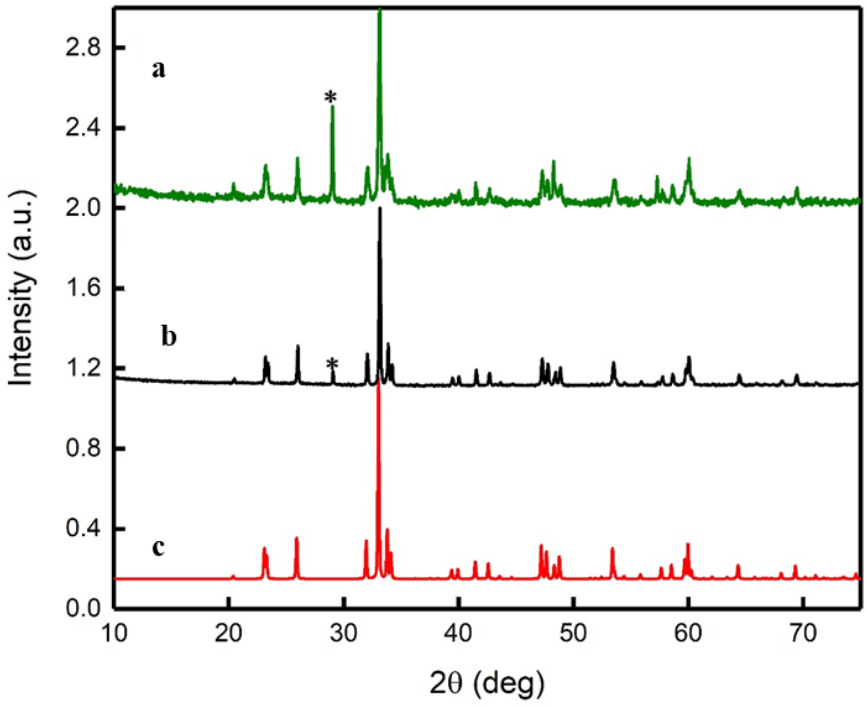

Figure 6-17: PXRD patterns of APTES coated $DyFeO_3$ (a) compared to silica coated $DyFeO_3$ (b) and standard $DyFeO_3$ (c).

To confirm the bonding of APTES ligand on the $DyFeO_3$ surface, FTIR spectrum for the functionalised NPs was obtained and compared with that of pure APTES and bare $DyFeO_3$ as displayed in Figure 6-18.The absorption bands associated to the hydrolysed APTES layer, are due to different bending and stretching modes assigned to the NH_2, CH_2 and SiO bonds. The 1562 cm^{-1} and 1484 cm^{-1} peaks are assigned to the NH_2 modes of the amine groups, which are very strongly hydrogen bonded to the silanol groups to form cyclic structures. Also, one may observe the mode of the Si-CH_2 peak at 1410 cm^{-1} and the asymmetric stretching modes of the Si-O-Si bond peaking at 1130 cm^{-1} and 1044 cm^{-1}. The peak at 1622 $cm^{-1}$is related to the stretching vibrational band of the OH group. No bands are observed near 2975, 1104 and 1089 cm^{-1} from the Si-O-C_2H_5 groups proving that APTES was completely hydrolysed. These results confirm that APTES was successfully anchored into the NPs surface.

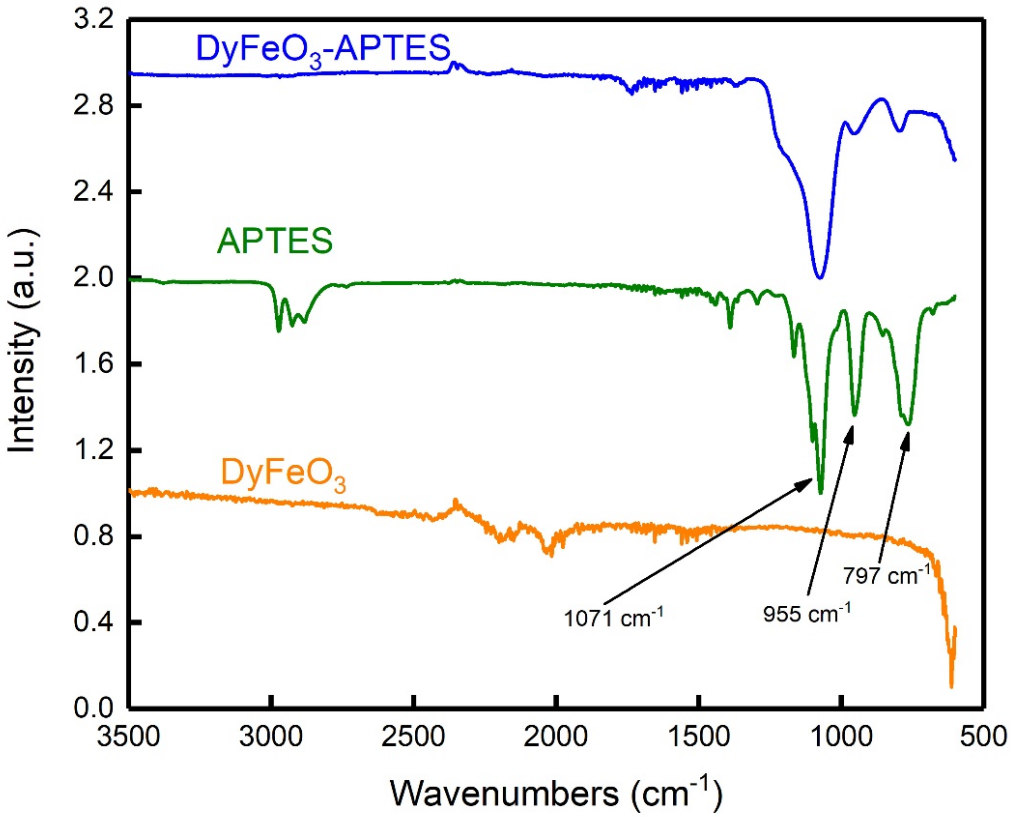

Figure 6-18: FTIR spectrum of APTES coated $DyFeO_3$ compared to silica coated $DyFeO_3$ and standard $DyFeO_3$.

6.11 TEM images

After functionalisation with APTES, $DyFeO_3$ NPs were characterised by TEM microscopy. Figure 6-19 shows no individual particles were observed and NPs agglomeration was predominant. As a result of this agglomeration, it was very difficult to measure the NPs diameter. On the other hand, the NPs were surrounded by a thick layer of APTES ligand, possibly through Si-OH groups, confirming that NPs are successfully functionalised by APTES in an aqueous medium. The thickness of APTES layer was almost similar to that observed in the coated TEOS $DyFeO_3$. EDX elemental analysis showed the Dy, Fe, Si, O, N and C elements in the sample as shown in the spectra displayed in Figure 6-20 . The atomic ratio for (Dy: Fe) is 1:1, which perfectly agrees with their theoretical ratio in $DyFeO_3$. The atomic percentage of oxygen in the structure content is roughly 1-fold higher than that of the theoretical atomic percentage. This increase might be due to the existence of the APTES ligand on the surface of the NPs, which contains oxygen, causing a significant increase in the oxygen content. Elements such as N and C are also related to the coating ligand content existed on the NPs surface,

these elements showed a real evidence for the successful functionalisation of the prepared NPs with APTES ligand.

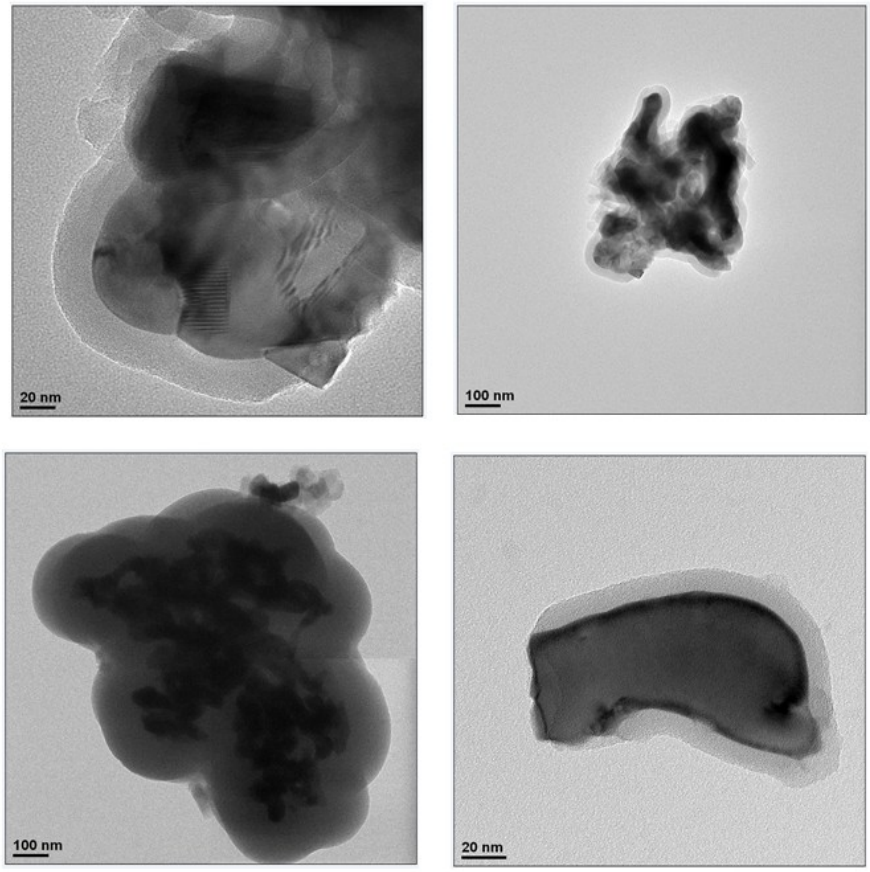

Figure 6-19: TEM images obtained for APTES conjugated $DyFeO_3$ at different crystal parts.

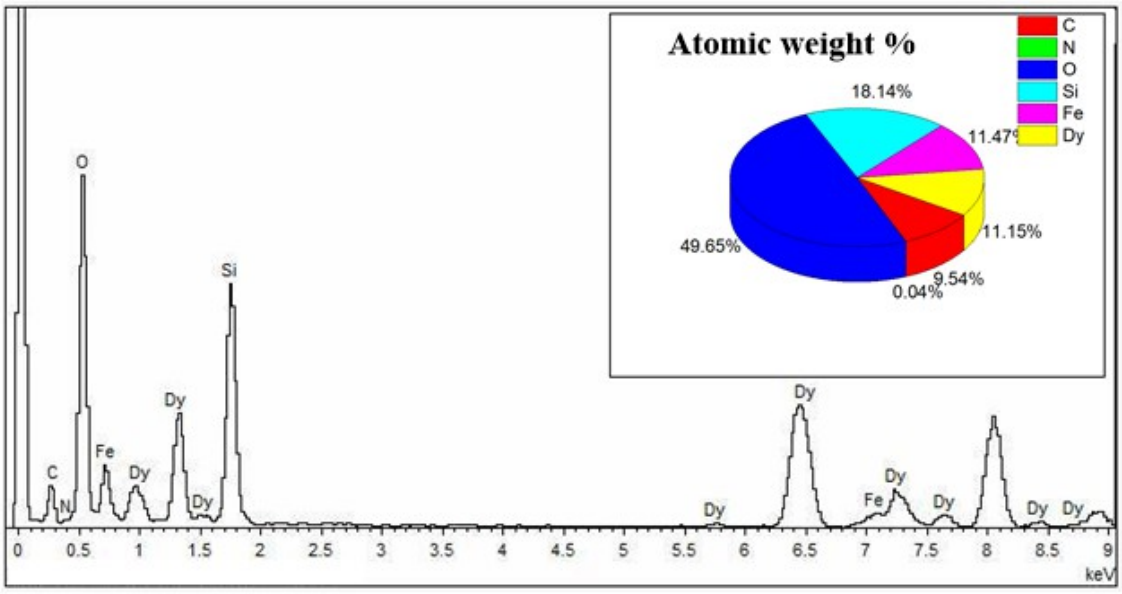

Figure 6-20: EDX spectra obtained for APTES conjugated DyFeO3 at different crystal parts.

6.12 Conjugation with doxorubicin (DOX)

An attempt was made to link APTES coated $DyFeO_3$ with DOX. The drug used as anti-cancer for the treatment of human cancers such as breast cancer and leukaemia, which ultimately leads to apoptosis. However, one of the serious problems in using this drug in chemotherapy is its massive toxicity to normal tissues. To minimise this side effect, many carriers' technologies have been developed, in which DOX is conjugated with polymers, protein, antibodies. This conjugation relays on acid labile linkers such as ester, hydrazone, acetyls and amide, which enable DOX to cross the blood-brain barriers. The crucial reason behind this conjugation is that the pH within cancer cells and tumour environments is often lower than that of healthy cells and tissues. As a result, the acid-labile linker will undergo cleavage within the cancer cell environment. This enable DOX to be in its free form. Dox is highly fluorescent, its release from the conjugate can often be detected optically. As illustrated in the schematic diagram in Figure 6-21. The reaction mechanism involves hydroxide nucleophilic attack by DOX into the amine group in the functionalised NPs to form an amide bond. The conjugation was assessed by running FTIR spectrum.

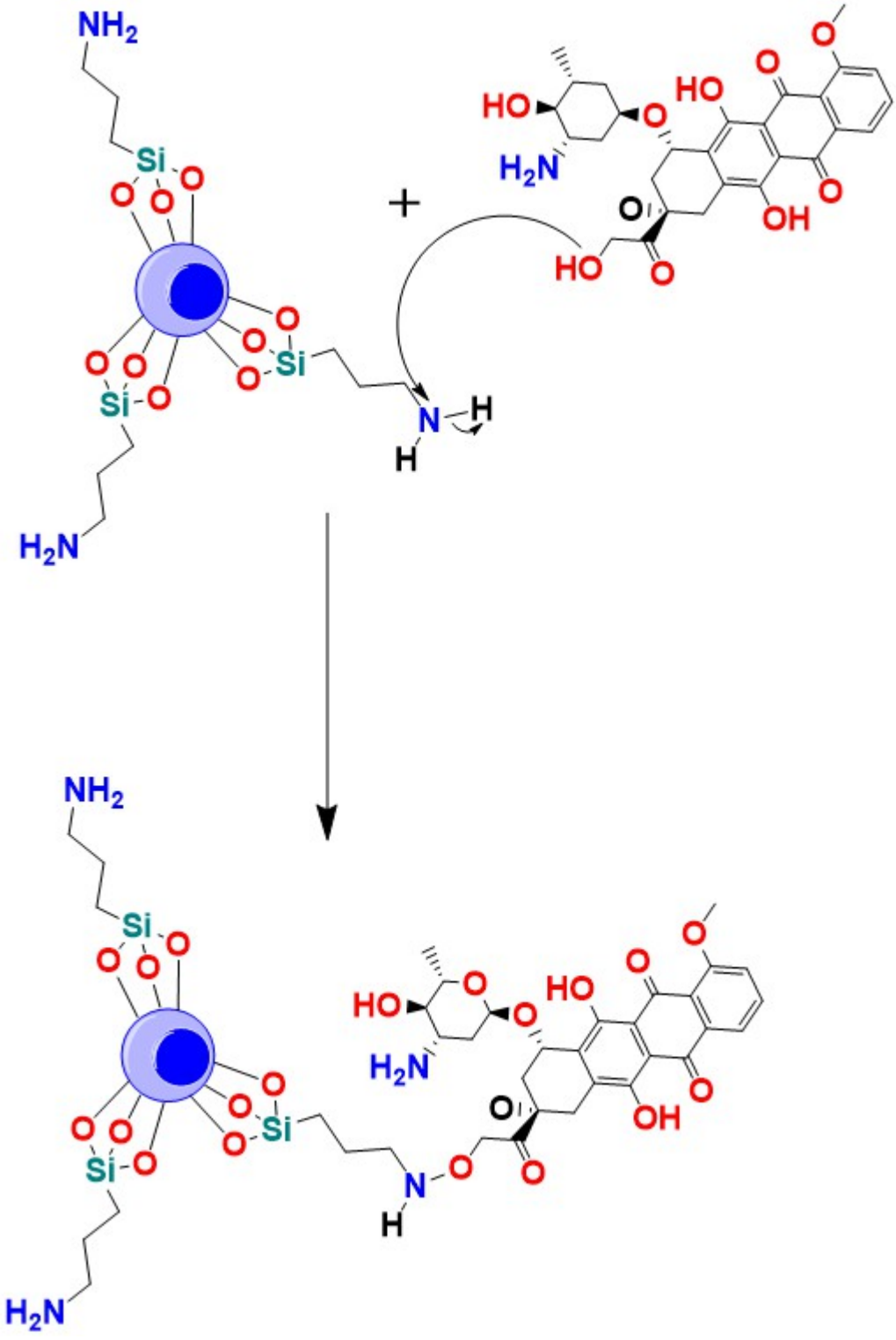

Figure 6-21: Conjugation of DOX with APTES coated $DyFeO_3$ mechanism

6.13 FT-IR spectrum of conjugated DOX/$DyFeO_3$ NPs

FT-IR is an applicable technique to prove the conjugation of DOX with the coated APTES $DyFeO_3$.Figure 6-22 shows the FT-IR spectra of APTES coated $DyFeO_3$, pure DOX and conjugation of DOX with $DyFeO_3$.

FTIR spectrum of pure DOX shows peaks at 3450 cm^{-1} due to N–H stretching vibrations for the primary amine structure and at 3330 cm^{-1} due to O–H stretching vibrations (Figure 6-22). On the other hand, DOX-conjugated APTES coated $DyFeO_3$ NPs, both peaks assigned to N–H stretching vibrations and O–H stretching vibrations overlap, are shifted to the lower frequency range (~3317 cm^{-1}). The bands observed at 870 cm^{-1} and 805 cm^{-1} due to N–H in pure DOX appear in the FTIR spectrum of DOX-conjugated APTES coated $DyFeO_3$ NPs. From this FTIR result, it can be proved that conjugation of DOX to the APTES coated $DyFeO_3$ NPs occurs *via* the interaction of –OH groups of DOX with $–NH_2$ groups of APTES through hydrogen bonding which is consistent with previous work reported by Kayal et al.[32] It is worth to note that all the stretching bands of pure DOX did not observed in the coated APTES $DyFeO_3$.

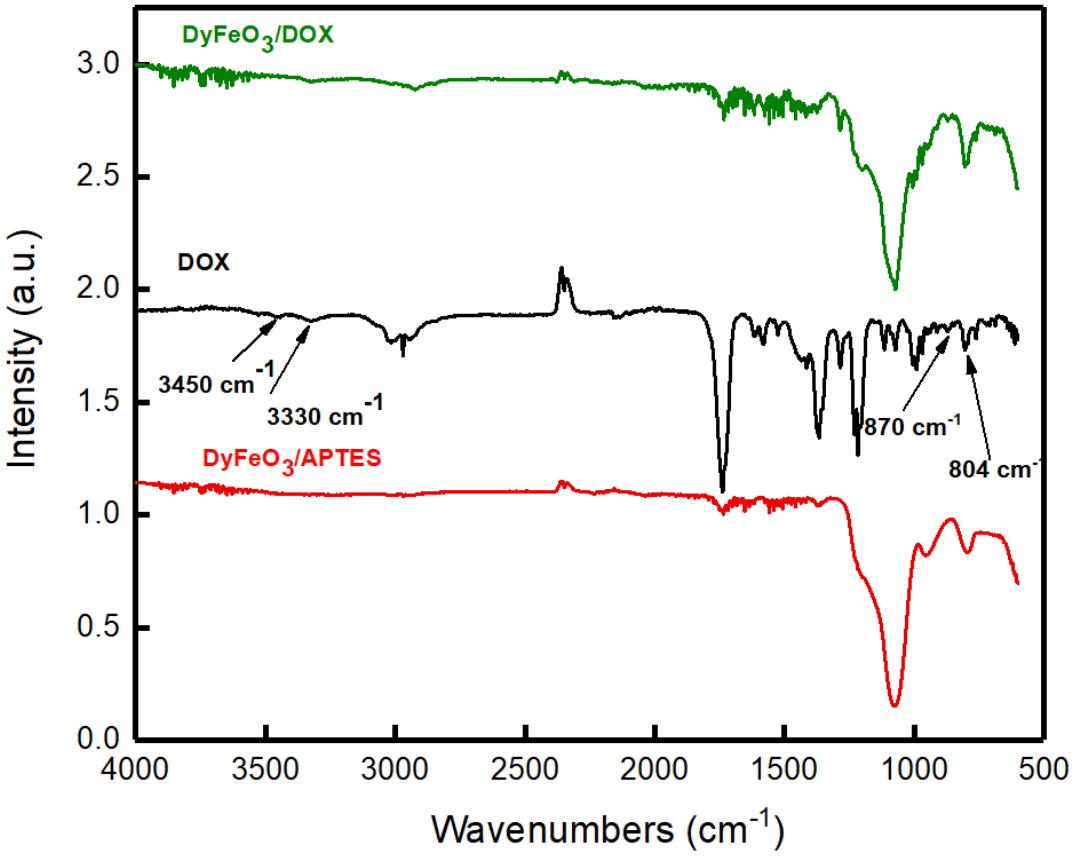

Figure 6-22: FTIR spectrum of $DyFeO_3$/DOX compared to DOX and $DyFeO_3$/APTES

6.14 Zeta potential of DOX conjugated $DyFeO_3$

To examine the stability of the DOX conjugated $DyFeO_3$ NPs, zeta potential was measured. Colloidal dispersions with ζ-potential absolute values larger than 20 mV (i.e., >+20 mV or <−20 mV) indicates suitable and appropriate physical stability due to the strong electrostatic repulsion between the dispersed particles. The zeta potential for the dispersed NPs was found to be -4.10 as shown in Figure 6-23. This value is a clear evidence for the formation of the aggregates observed by TEM images.

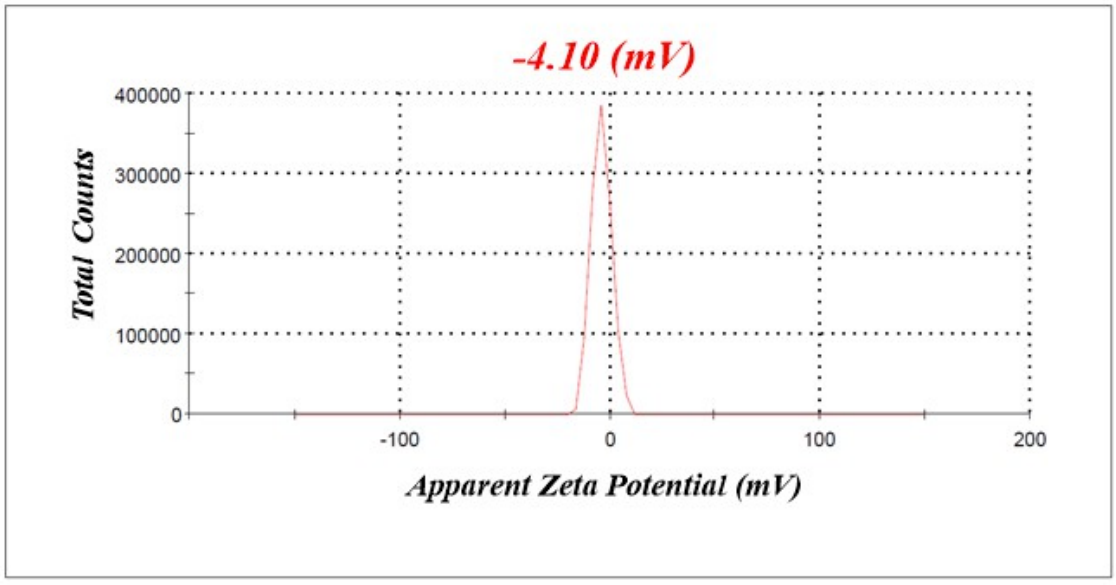

Figure 6-23: Zeta potential of $DyFeO_3$ conjugated with DOX

6.15 Conclusions

The main goal of this chapter was to prepare a dual probe contrast agent for magnetic Resonance Imaging (*MRI*) and utilise it as a DOX drug carrier to colorectal cancer HT-29, HCT-116 and Colo320 tumour cell lines (Theranostic).

The first step involved in achieving this goal was the preparation of DyFeO3 NPs by sol-gel method, using an acrylamide and citric acid as combustion reagents. The stability of the formed NPs was interpreted by Powder X-Ray Diffraction (PXRD). The PXRD pattern produced at 800°C annealing for 25 hours was single phase and almost matches to the standard for the bulk $DyFeO_3$ documented in the literature.

Silica core-shell (ETOS) was added to modify the surface of the formed NPs to make them biocompatible in aqueous medium using the well-known the Stőber process and their existence was confirmed by PXRD, TEM, FT-IR and EDX. TEM showed ETOS

coated NPs to be in the range 60 nm to 75 nm, however NPs tend to cluster, forming a large mass surrounded by a thick layer of silica.

An attempt was made to reduce the thickness of the silica by reducing the amount of ETOS added and filtering the suspension. Insignificant results were obtained where the thick layer of ETOS has not been affected and almost same thickness was observed in each attempt.

The longitudinal (r_1) and transverse relaxation rate (r_2) and transverse of the silica coated $DyFeO_3$ were found to be 9.2 mM-1s-1 and 37.6 mM-1s-1at 9.4 Tesla respectively. The silica coating layer plays an important role in improving the sensitivity of the *MRI* machine by shortening the relaxation time. From the r_2/r_1 ratio *(4.09),* it was possible to interpret that the coated silica $DyFeO_3$ predominantly works as T_1 contrast agents.

Functionalisation with APTES and subsequently with DOX was performed for a theranostic purpose, FT-IR confirmed the successful conjugation. However, TEM images reveals a large thick layer surrounding the NPs. The colloidal stability of the formed NPs was measured by DLS and the zeta potential was found to be -4.10. This value is not appropriate for a perfect stability.

Over all, both the large silica layer surrounded the formed NPs and the lower stability of these NPs were the two main obstacles that hider their use as a theranostic agents for biological application.

6.16 References

1. E. N. Maslen, V. A. Streltsov and N. Ishizawa, *Acta Crystallographica Section B*, 1996, **52**, 414-422.
2. S. Jauhar, M. Dhiman, S. Bansal and S. Singhal, *Journal of Sol-Gel Science and Technology*, 2015, **75**, 124-133.
3. L. Jiang, W. Liu, A. Wu, J. Xu, Q. Liu, L. Luo and H. Zhang, *Journal of Sol-Gel Science and Technology*, 2012, **61**, 527-533.
4. Z. Lu, J. Liu, Y. Tang and Y. Li, *Inorganic Chemistry Communications*, 2004, **7**, 731-733.
5. S. Santra, D. Dutta and B. M. Moudgil, *Food and Bioproducts Processing*, 2005, **83**, 136-140.
6. L. Jiang, W. Liu, A. Wu, J. Xu, Q. Liu, L. Luo and H. Zhang, *Journal of Sol-Gel Science and Technology*, 2011, **61**.
7. H. N. Pandya, R. G. Kulkarni and P. H. Parsania, *Materials Research Bulletin*, 1990, **25**, 1073-1077.
8. W. Haron, T. Thaweechai, W. Wattanathana, A. Laobuthee, H. Manaspiya, C. Veranitisagul and N. Koonsaeng, *Energy Procedia*, 2013, **34**, 791-800.
9. W. Zheng, R. Liu, D. Peng and G. Meng, *Materials Letters*, 2000, **43**, 19-22.
10. A. E. Giannakas, A. K. Ladavos and P. J. Pomonis, *Applied Catalysis B: Environmental*, 2004, **49**, 147-158.
11. M. Sivakumar, A. Gedanken, W. Zhong, Y. H. Jiang, Y. W. Du, I. Brukental, D. Bhattacharya, Y. Yeshurun and I. Nowik, *Journal of Materials Chemistry*, 2004, **14**, 764-769.
12. X. Cai, L. Shi, S. Zhou, J. Zhao, Y. Guo and C. Wang, *Journal of Applied Physics*, 2014, **116**, 103903.
13. L. Yuan, K. Huang, S. Wang, C. Hou, X. Wu, B. Zou and S. Feng, *Crystal Growth & Design*, 2016, **16**, 6522-6530.
14. L. Zhu, N. Sakai, T. Yanoh, S. Yano, N. Wada, H. Takeuchi, A. Kurokawa and Y. Ichiyanagi, *Journal of Physics: Conference Series*, 2012, **352**, 012021.
15. S. P. Yeap, J. Lim, B. S. Ooi and A. L. Ahmad, *Journal of Nanoparticle Research*, 2017, **19**, 368.
16. S. Laurent, D. Forge, M. Port, A. Roch, C. Robic, L. Vander Elst and R. N. Muller, *Chemical Reviews*, 2008, **108**, 2064-2110.
17. R. Xu, *Particuology*, 2008, **6**, 112-115.
18. F. Ghiasi, M. H. Eskandari, M.-T. Golmakani and S. M. H. Hosseini, *Journal of Colloid and Interface Science*, 2019, **541**, 65-74.
19. L. M. Liz-Marzán and P. Mulvaney, *The Journal of Physical Chemistry B*, 2003, **107**, 7312-7326.
20. G. Vigil, Z. H. Xu, S. Steinberg and J. Israelachvili, *Journal of Colloid and Interface Science*, 1994, **165**, 367-385.
21. A. Guerrero-Martínez, J. Pérez-Juste and L. M. Liz-Marzán, *Advanced Materials*, 2010, **22**, 1182-1195.
22. H. R. Ghorbani, A. A. Safekordi, H. Attar and S. M. R. Sorkhabadi, *Chemical and Biochemical Engineering Quarterly*, 2011, **25**, 317-326.
23. Y. Zare, K. Y. Rhee and D. Hui, *Composites Part B: Engineering*, 2017, **122**, 41-46.
24. Y. Ge, Y. Zhang, J. Xia, M. Ma, S. He, F. Nie and N. Gu, *Colloids and Surfaces B: Biointerfaces*, 2009, **73**, 294-301.
25. L. E. W. LaConte, N. Nitin, O. Zurkiya, D. Caruntu, C. J. O'Connor, X. Hu and G. Bao, *Journal of Magnetic Resonance Imaging*, 2007, **26**, 1634-1641.

26. S. H. Lee, D. H. Lee, H. Jung, Y.-S. Han, T.-H. Kim and W. Yang, *Current Applied Physics*, 2015, **15**, 915-919.
27. M. Arroyo-Hernández, J. Pérez-Rigueiro, M. Manso-Silván and J. M. Martínez Duart, *Materials Science and Engineering C*, 2007, **27**, 1211-1214.
28. N. Lorrain, M. Hiraoui, M. Guendouz and L. Haji, *Materials Science and Engineering B: Solid-State Materials for Advanced Technology*, 2011, **176**, 1047-1053.
29. S. Li, W. Ma, Y. Zhuo, X. Chen, M. Ma, Y. Xu, Z. Ding and X. Wu, *International Journal of Electrochemical Science*, 2013, **8**, 1802-1812.
30. N. S. K. Gunda, M. Singh, L. Norman, K. Kaur and S. K. Mitra, *Applied Surface Science*, 2014, **305**, 522-530.
31. N. Majoul, S. Aouida and B. Bessaïs, *Applied Surface Science*, 2015, **331**, 388-391.
32. S. Kayal and R. V. Ramanujan, *Materials Science and Engineering: C*, 2010, **30**, 484-490.

CHAPTER 7

Theranostics application for $KMnF_3$ nanoparticles

7 Introduction

7.1 Conjugation of Doxorubicin (DOX) to coated alendronate $KMnF_3$ NPs

DOX is one of the most common drugs used for chemotherapy. It is belonging to the anthracyclines – antineoplastic antibiotics. DOX is the first drug administered to patients in hospitals to treat many type of cancer.[1] It is recognized by the World Health Organization (WHO) as a crucial medicine.[2] Its usage covers but is not limited to many types of lymphomas, sarcomas, colon, breast and bladder cancer. Sadly, apart from its activity as an intercalating agent, it causes a huge toxic side effect due to the negative effect on mitochondrial respiration and elevative reactive oxygen species (ROS) production.[3] Patients treated with DOX exhibits side effects such as vomiting and nausea, decrease in the number of platelet cells in the blood and temporary hair loss. Furthermore, it has been reported that cardiotoxicity is the most significant side effect of DOX.[4] In order to minimize this toxicity, accumulating the drug into the tumour only and increase the therapeutic index, DOX must be encapsulated in several carriers such as NPs[5, 6], polymersoms[7], liposomes[8], micelles[9, 10] and nanogels.[11, 12]

In this chapter, a strategy to conjugate DOX to the prepared coated alendronate $KMnF_3$ NPs as a carrier targeting the cancer tumour will be reported. The process involves linking DOX to the NPs through Suberic. The loading of the DOX on to the NPs is determined via UV-visible method, the *in-vitro* cytotoxicity against cervical (HeLa cell line) and colon cancer cells such a HT-29, and HCT116 were examined. Finally, confocal studies were performed to assess their localisation in these cells.

7.2 Experimental

This section describes the method used to prepare the conjugation of DOX with the prepared coated alendronate $KMnF_3$ NPs. The formed NPs are then tested for cytotoxicity against colorectal cancer cell lines such as HeLa, HT-29 and HCT-116.

In order to target the epidermal growth factor and vascular epidermal growth factor that are over-expressed in many cancer cells, these proteins were first detected in all cervical and colorectal cancer cells. After confirming their existence in these cell lines, the NPs are attached to EGFR and VEGFR antibodies to specifically targeting these proteins.

7.2.1 Conjugation of sodium alendronate coated $KMnF_3$ with DOX

Figure 7-1 illustrates the synthesis steps involved in the preparation of conjugated DOX-$KMnF_3$ NPs. DOX.HCl (14 mg, 2.4×10^{-5} mole) and *O*,*O*′-Bis[2-(*N*-Succinimidyl-

succinylamino)ethyl]polyethylene glycol linker (18 mg, 9×10^{-6} mole) were placed in a Schlenk flask and dissolved in 15 ml anhydrous dimethylformamide (DMF). The mixture was stirred in the dark at room temperature for 48 hours under nitrogen atmosphere. Then 100 µl of a solution of 7.5 mg $KMnF_3$ coated with alendronate in 1 ml HPLC water was added. Finally, 100 µl triethylamine (TEA) was added and the mixture was left to stir for further 48 hours. The solvent was evaporated using a vacuum pump and the final product was obtained. UV visible spectroscopy was used to confirm the chemical structure of the obtained product. Figure 7-1 represents a schematic diagram for the conjugated DOX) into the coated alendronate $KMnF_3$ *via* and *O*,*O*′-Bis[2-(*N*-Succinimidyl-succinylamino)ethyl]polyethylene glycol linker.

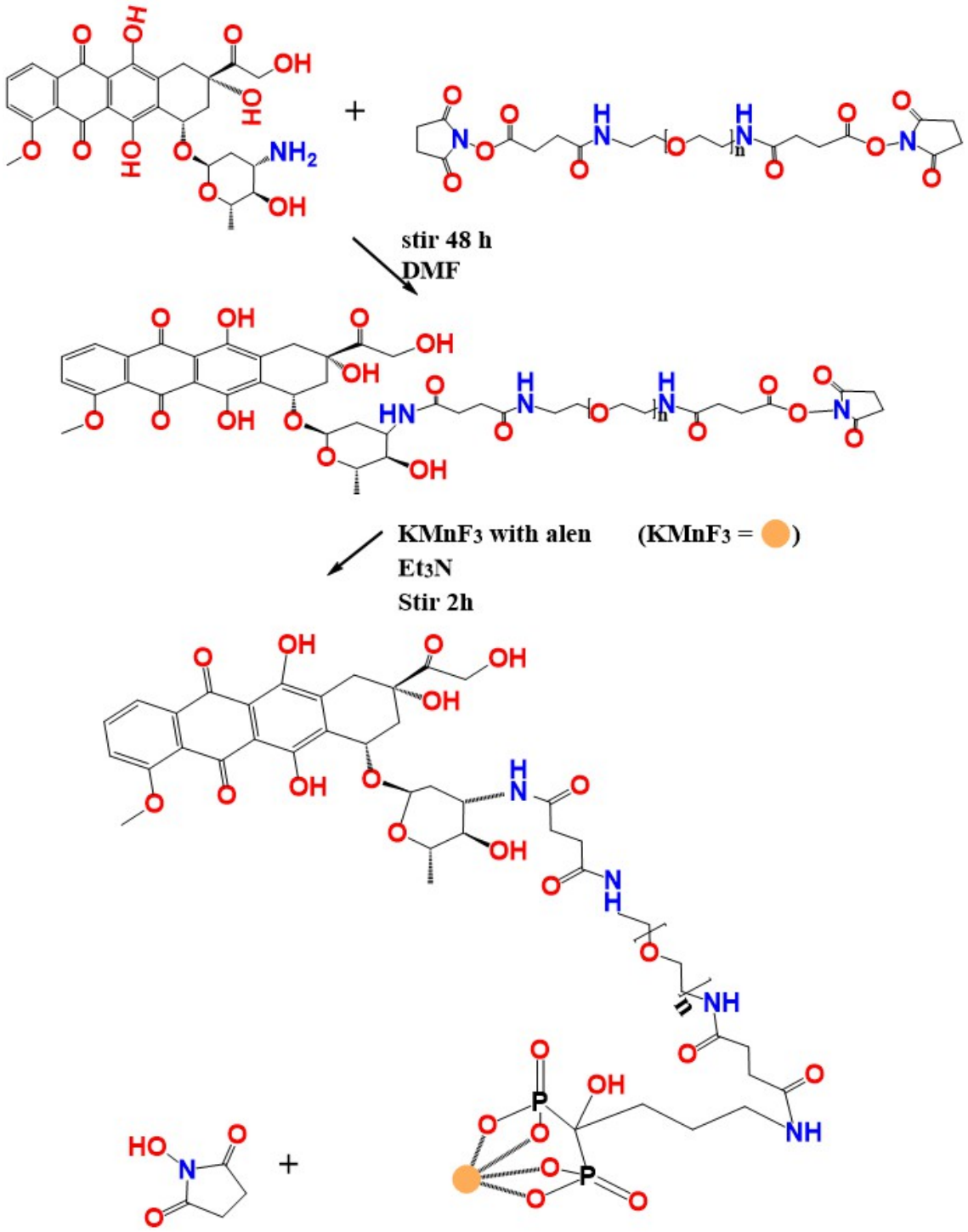

Figure 7-1: Schematic diagram for the synthesis for conjugated DOX into the coated alendronate $KMnF_3$ via and O,O'-Bis[2-(N-Succinimidylsuccinylamino)ethyl]polyethylene glycol linker that activates the carbonyl group .

7.2.2 MTS Assay

The synthesised KMF_3 (M = Mn, Fe, Co, Cu, Zn) NPs were tested for cytotoxic activity against human cervical (HeLa) and colorectal (HT-29 and HCT-116) cancer cell lines. The cells were split and counted to achieve a concentration of 1×10^5 cells/ml. Following the strategy illustrated in Figure 7-2, 190 µl of cells was then added to the middle cells of three 96 well plates, the remaining cells were filled with 180 µl PBS. The plates were then transferred to an incubator at 37°C 5% CO_2 for 24 hours to allow the cells to adhere to the base of the wells.

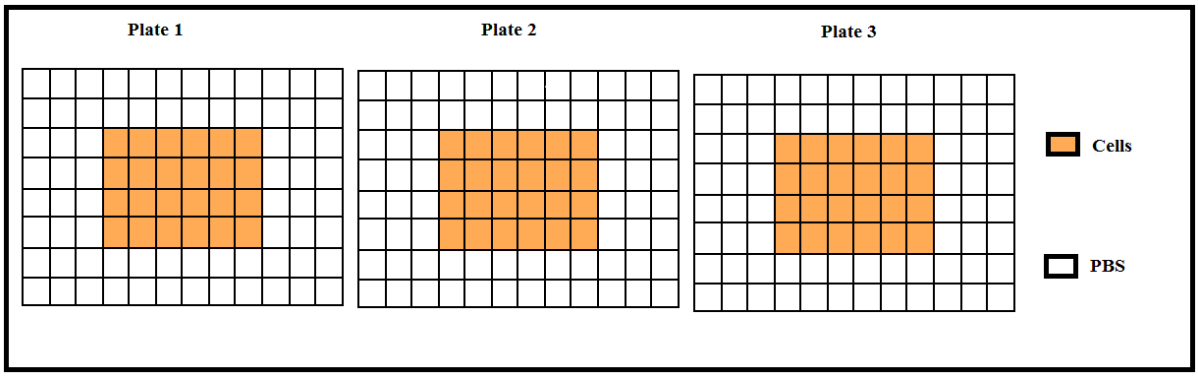

Figure 7-2: The appearance of the three 96 well plates when MTS assay was performed

After the incubation, the media was removed and the treatment were applied with different concentration of manganese and DOX to achieve 3125 to 0.006 uM. The plates were then returned back to the incubator for 24 hours.

MTS solution was defrosted in a thermostatic water bath at 37°C one hour before the experiment was ready to perform. After the 24 hours, the plates were transferred to the cabinet and all contents of media and probes were removed using a multi micro pipette. 180 µl of PBS was added to the cells followed by the addition of 20 µl MTS solution.

The conversion of MTS into the aqueous soluble formazan product is accomplished by dehydrogenase enzymes found in metabolically active cells. A schematic representation of the process is shown in Figure 7-3. The plates were then returned back to the incubator for further two hours before the absorbance reading in maximum optical density were taken *via* BIO-TEK synergy HT instrument at 490 nm. Graphs of various probe

concentrations verses maximum optical density at 490 nm were constructed using excel and graph pad prism 7 with sigmoidal graph fit.

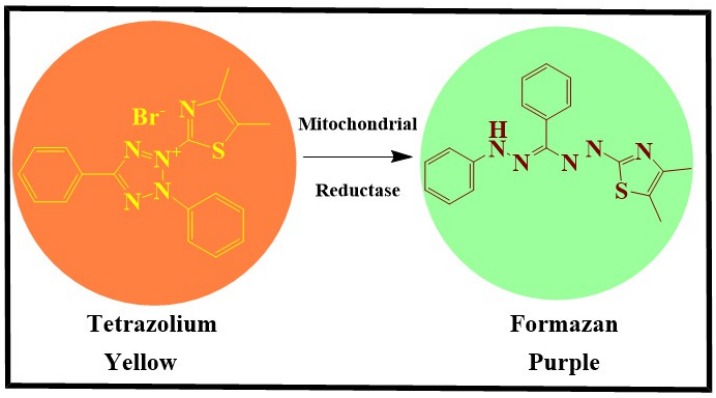

Figure 7-3: Reduction of yellow Tetrazolium compound to water soluble purple Formazan for alive cells using MTS protocol

7.2.3 Fluorescence properties measurement of DOX

In order to record fluorescence spectra, Horiba Fluoromax-4P spectrofluorometer in a 10 mm quartz cuvette was used. The fluorescence spectra of DOX dissolved in water were measured. The excitation and emission spectra of DOX were collected by scanning the sample at wavelengths from 200 nm to 600 nm and from 580 nm to 800nm respectively.

7.2.4 Detection of EGFR and VEGFR-1 on Hela, HCT116 and HT-29 cell lines determined by FACS

Cervical cancer cell line (Hela), both colon cancer HCT-116 and (HT-29) were grown in Dulbecco's Modified Eagle's Medium (DMEM) with L-glutamine and McCoy's, with L-glutamine respectively, to 80% confluence, cells were then trypsinized and returned to incubator for 3 minutes and then transferred into 15 ml centrifuge tube. 5 ml media were added and then centrifuged at 1500 round per second for 3 minutes. The media was discarded and pellets were washed twice by cold PBS. 175 µl cell was transferred into a new centrifuge tube and 2 ml PBS was added. From this suspension, 50 µl was transferred into a FACS tube. This gives approximately 200,000 cells. 5 µl Primary Rabbit Anti-EGFR antibody [E235] (Alexa Flour ® 488) (ab205731) was then added. Cells were then incubated for 30 minutes in the dark at room temperature, centrifuged and then washed twice by PBS to remove any unbounded antibodies. Cells were then suspended in 1 ml

PBS and 5 µl secondary Donkey Anti-Rabbit JgG H&L (Alexa Flour ® 647) antibody was added and incubated for further 30 minutes in the dark at room temperature. Cells were then washed twice by PBS to remove excess antibody. Finally, cells were suspended into 300 µl PBS and immediately underwent FACS analysis (BD FACS calibur, USA) with the help of cell quest pro software (Becton Dickinson). Same procedures were applied to detect VEGFR using Primary antibody Anti-VEGFA antibody [EP1176Y] (Alexa Flour ® 488) (ab206886). Non-specific EGFR and VEGFR was used as a negative control (Rabbit IgG, Monoclonal [EPR 25 A] Iso type control (Alexa- Fluor ® 488) (ab199091)

7.2.5 Cellular uptake studies

HT-29 and HCT116 colon cancer cell lines HeLa cervical cancer cell lines were seeded in a McCoy's with L-glutamine media at a density of 150×10^3 cells per well on three 35 mm imaging dish with four compartments and the ibidi polymer coverslip bottom for 24 hours. Media was discarded and cells were washed twice with 1 ml cold PBS. Each cell compartment was then treated individually, cells only, $KMnF_3$, DOX, DOX conjugated $KMnF_3$ and DOX-$KMnF_3$-VEGFR-anti-body nanoconjugates incubated for 1 hour at 37°, 5% CO_2. Treatment was removed and cells were washed with cold PBS. Cells were then fixed by paraformaldehyde for 10 minutes at room temperature and then washed by 1 ml PBS buffer twice. Finally, the coverslip was fixed and viewed under an inverted fluorescence microscopy ZEISS AXIO Vert.

7.3 Results and discussion

7.3.1 Conjugation of DOX to coated alendronate $KMnF_3$ NPs

DOX was conjugated to the coated alendronate $KMnF_3$ NPs using *O*,*O*′-Bis[2-(*N*-Succinimidyl-succinylamino)ethyl]polyethylene glycol linker by forming a peptide bond between the DOX NH_2 group and the carbonyl group of the linker. The conjugation of DOX into the surface of the coated $KMnF_3$ was confirmed by FT-IR spectra as shown in Figure 7-4. The main feature of the loading of DOX on the surface of the coated alendronate $KMnF_3$ NPs is the stretching band of the NH_2 group of the peptide bond appeared at 2860 cm^{-1}. The vibrational stretching band of the aromatic carbonyl group also appeared at 1714 cm^{-1}. The P=O stretching band at 1100 cm^{-1} appears giving a clear signal for the existence of the coated alendronate $KMnF_3$ NPs. These stretching

vibrational frequencies were a direct evidence that DOX was loaded into the surface of the synthesised coated alendronate $KMnF_3$ NPs.

To further investigate the in-vitro DOX loading on the surface of the NPs, UV-visible spectroscopy was performed. DOX can easily incorporated into the NPs as can be seen by the absorption study in Figure 7-5. This is due to electrostatic interaction between the positively charged amino or the carbonyl groups of DOX with the negatively charged ester or carboxylic groups of the linker.[13] Furthermore, many studies have been reported that DOX having an aromatic rings utilises its π delocalised electrons via hydrophobic interaction and π-π stacking to efficiently loaded into the NPs surface.[14]

In this study a UV-visible spectrum for the synthesised coated alendronate, DOX, linker and loaded DOX coated alendronate $KMnF_3$ NPs were compared. Clearly Both free DOX and the loaded DOX alendronate coated $KMnF_3$ NPs exhibited similar λ maximum at 233 nm, 255 nm and 493 nm as can be seen in Figure 7-5 . However, unloaded coated alendronate $KMnF_3$ and the linker do not show these absorption bands. These results suggest that DOX drug has been incorporated into the NPs surface.

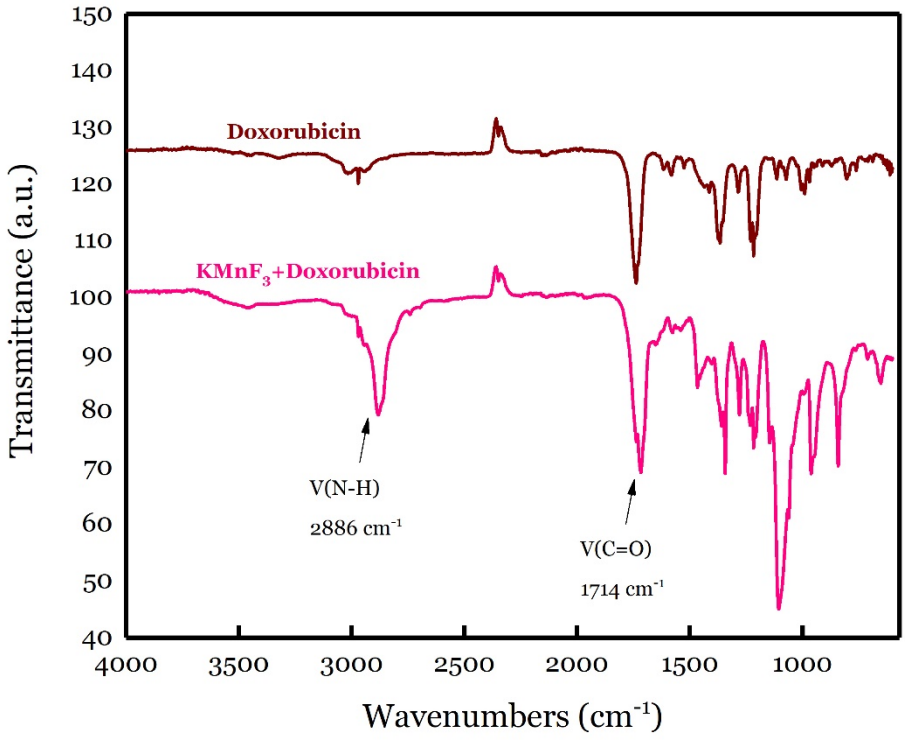

Figure 7-4: FT-IR spectrum for conjugated DOX with coated alendronate $KMnF_3$ NPs compared to DOX spectrum.

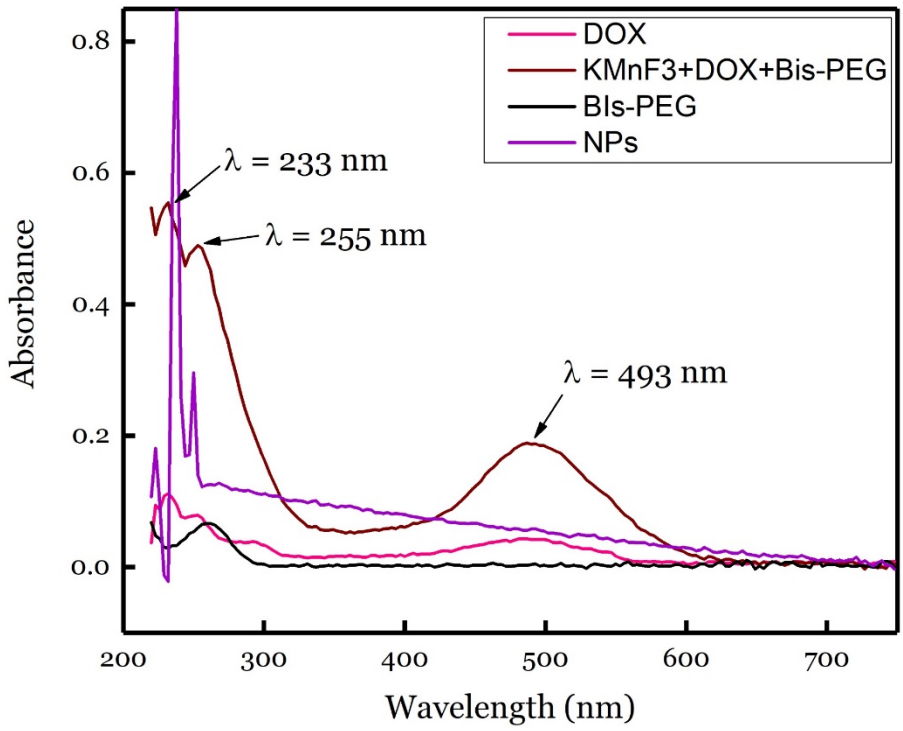

Figure 7-5: comparison of UV-visible spectrum for DOX, loaded DOX NPs, linker and unloaded DOX NPs.

The concentration of the loaded DOX was calculated from the calibration curve obtained from the UV-vis spectroscopy with different concentrations of standard pure DOX using 493 λ as illustrated in Figure 7-6 and Figure 7-7. An increase in the absorbance of DOX was observed as the DOX concentration increases.

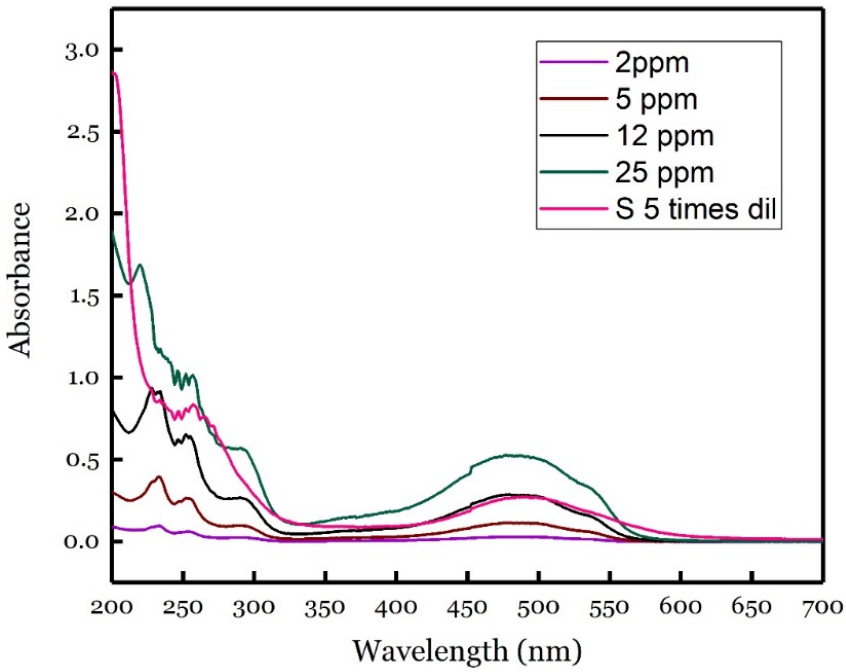

Figure 7-6: Determination of loaded DOX into coated alendronate $KMnF_3$ NPs using UV-visible spectroscopy

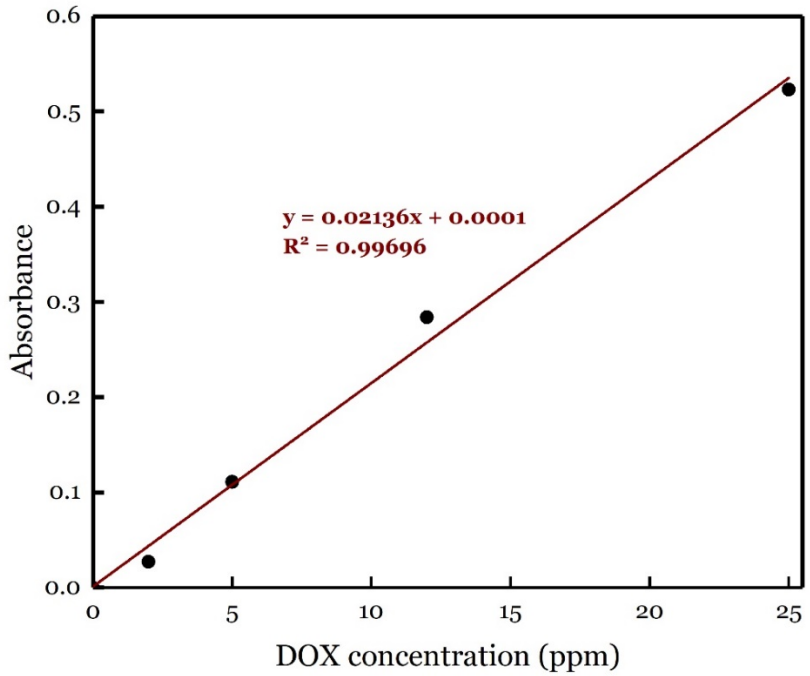

Figure 7-7: Calibration curve obtained for the determination of loaded DOX into coated alendronate $KMnF_3$ NPs using UV-visible spectrometry measurements.

The amount of the diluted loaded DOX sample was calculated from the calibration curve obtained and the original concentration was calculated using the equation 1-5 and found 25%.

Concentration of loaded DOX in NPs surface = (Concentration of DOX in diluted sample $\times$ $\boldsymbol{dilution\ factor}$***)/ weight of sample taken*** ***Equation 7-1***

The loading amount of DOX was significantly higher than that reported for Nano gels used as smart carriers for improving the therapeutic index of DOX for breast cancer.[1] This suggest that the loading and encapsulation efficiency of coated alendronate $KMnF_3$ is higher due to the nature of these small NPs.

7.3.2 Dynamic Light Scattering (DLS) and Nano Tracking Analysis (NTA)

NTA were performed to investigate the hydrodynamic size of the loaded DOX coated alendronate $KMnF_3$ NPs as shown in Figure 7-8. The average hydrodynamic diameter was found to be (29 nm). NPs with the size up to 400 nm are preferred as nanocarriers for drug delivery due to the "enhanced permeability and retention (EPR)" effect stated by Bhushan et al.[15] Therefore, this obtained size is suitable as carriers for drug delivery. The analysis of the NTA video shows a monodispersity with nearly uniform size of NPs. This is in perfect agreement with the results obtained from DLS. However, a straight forward correlation between the particles hydrodynamic diameters obtained by NTA and DLS can hardly be deduced due to the fact that NTA experiments were performed in HPLC water while DLS were carried out in ethanol, which might be the main reason for affecting the swelling degree due to the aggregation and therefore increasing the diameter size. The hydrodynamic size obtained by NTA seems to be the correct size with an acceptable difference due to the small increase in the NPs coating layer, since the size of the nanoparticle before loading DOX was 2 nm.

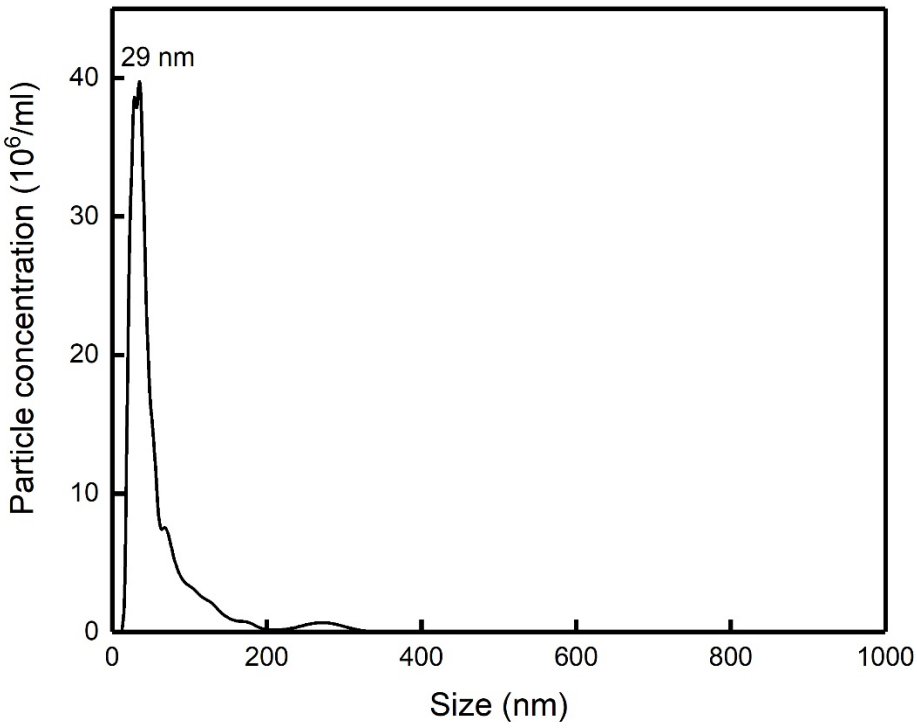

Figure 7-8: Hydrodynamic size of conjugated DOX with coated alendronate $KMnF_3$ obtained by NTA

7.3.3 Zeta potential

The stability of the DOX conjugated $KMnF_3$ NPs could be related to the considerably higher zeta potential. The obtained zeta potential value was found to be −16.9 mV as can be seen in Figure 7-9. This value is different than the positive value obtained for the NPs before DOX was loaded (24 mV), providing a further evidence that DOX has been loaded into the NPs surface. Furthermore, the value lies within the stable range, signifying that the loaded DOX NPs formation lead to the formation of stable system. In addition, the electrostatic repulsive force among the negatively charged surface of the NPs affords high stability to the colloidal solution by preventing them from agglomerating in the colloid state.[16] Therefore, NPs with negative zeta potential are desirable for drug delivery systems.

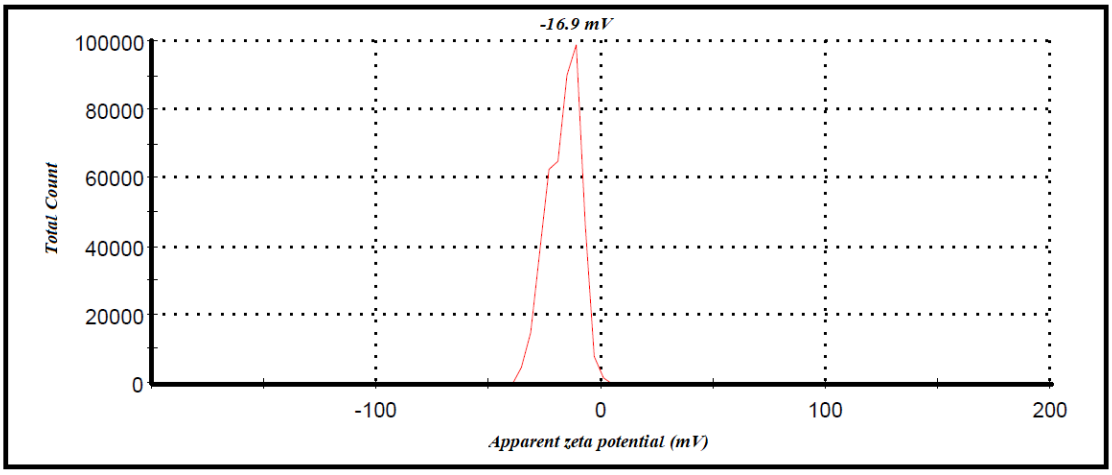

Figure 7-9: Apparent zeta potential for conjugated DOX with coated alendronate $KMnF_3$ NPs.

7.3.4 Cytoxicity study

The anticancer effect of coated alendronate $KMnF_3$, DOX and loaded DOX coated alendronate $KMnF_3$ NPs were studied against cervical Hela cell line and colorectal cancer cell lines HT-29 and HCT-116 using colorimetric MTS assay, which relies on the reduction of the yellow MTS into dark brown formazan by the active dehydrogenase in viable cells, through measurement of cell growth inhibition rate after 24 h of treatment. A cytotoxicity comparison for the coated $KMnF_3$ NPs, DOX and conjugated DOX $KMnF_3$ NPs against each of the examined cancer cell lines were carried out. Alendronate coated $KMnF_3$ revealed no cytotoxicity effect against HeLa cells and they remained more than 97% viable (Figure 7-10). The low toxicity could be related to the fact that alendronate is hydrophilic, and it protects surfaces from interacting with cells or protein. Similar observation was obtained for coated PEG iron oxide NPs of 40-50 nm against human dermal fibroblast.[17] This result reveals the safety use of coated alendronate $KMnF_3$ NPs as contrast agents for *MRI*. On the other hand, when HeLa cells were treated by free DOX (Figure 7-11), a significant cell survival loss was observed as the concentration increases, and IC_{50} obtained was 7.757 uM. The decrease in the cell viability is probably due to the strong affinity of DOX to bind the cell membrane. Furthermore, treating HeLa cells with $KMnF_3$-DOX decreases the cell viability by almost 50% (IC_{50}, 4.179 uM) compared to free DOX treatment (Figure 7-12). This further decrease in the cell viability might be due to the cytotoxic effect of improved DOX enhancement which are located inside the cells due to the NPs effect and triggered by the acidic endocytic environment. Therefore, greatly enhancing the cells cytotoxicity.

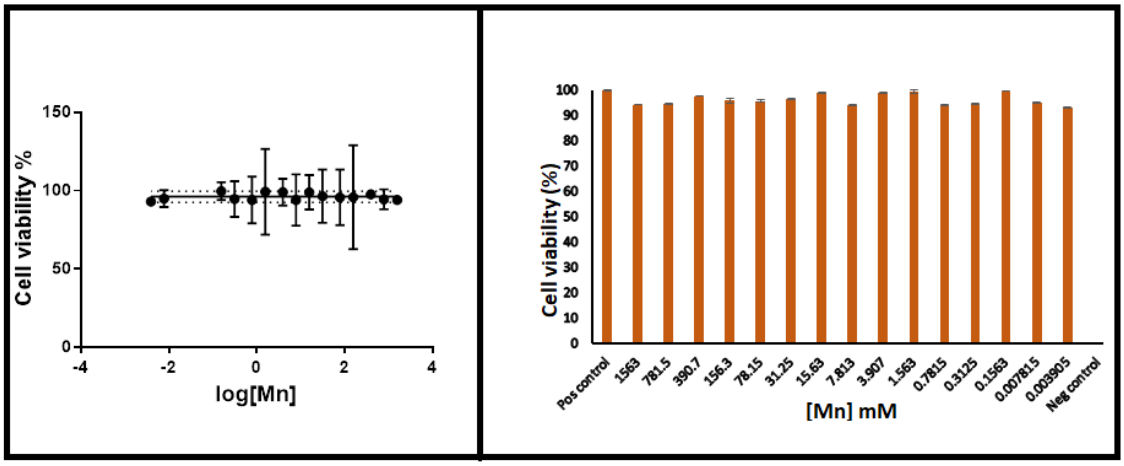

Figure 7-10: Cytotoxicity effect of synthesised coated alendronateKMnF3 NPs against HeLa cervical cancer cell lines.

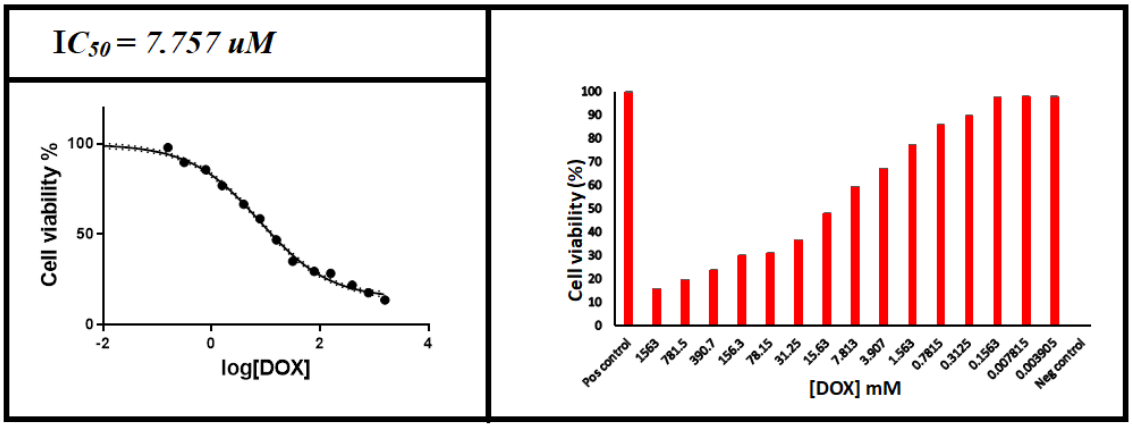

Figure 7-11: Cytotoxicity effect of DOX against HeLa cervical cancer cell lines.

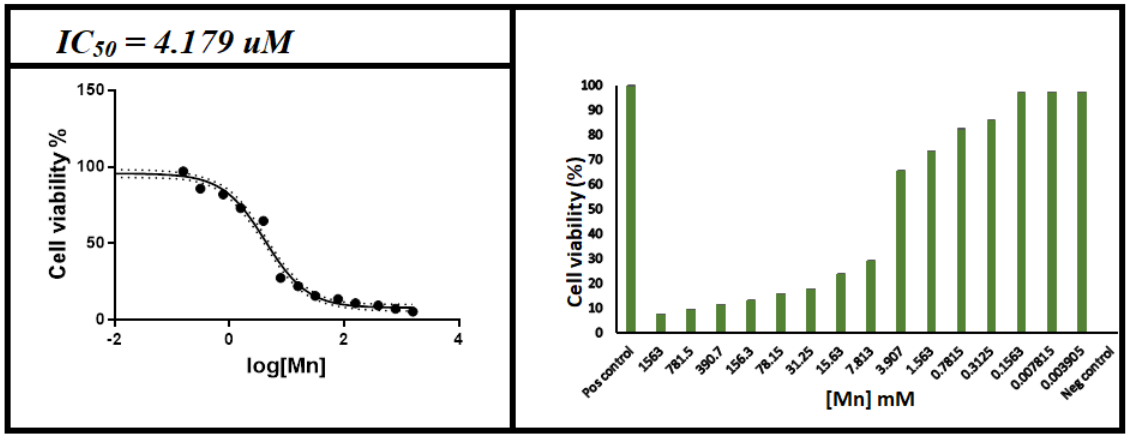

Figure 7-12: Cytotoxicity effect of DOX-conjugated $KMnF_3$ NPs against HeLa cervical cancer cell lines.

Treating HT-29 cells lines with the synthesised coated alendronate $KMnF_3$ do not show any significant effect on the cell viability and about 98% of viable cells were obtained over the concentration range studied (Figure 7-13). This indicates the safety use of NPs as a contrast agent for *MRI* only. On the other hand, treating HT-29 cell lines with Free DOX has a significant negative effect on the cell viability at higher concentrations (63 uM to 3125 uM) and the IC_{50} obtained was 49 uM (Figure 7-14). DOX conjugated $KMnF_3$ NPs, caused the cytotoxicity to increase further more at the same concentration ranges with lower IC_{50} of 42 uM as seen in Figure 7-15. The obtained results reveal that cytotoxicity enhances as the concentrations of DOX conjugated $KMnF_3$ increases, demonstrating a dose-dependent effect in vitro. This increased cytotoxicity could be due to the improved DOX cellular uptake by DOX conjugated $KMnF_3$ nanocomposites through the endocytosis pathway, which is a well-known phenomenon of NPs-based drug delivery systems.[18] Hence, an adequate high concentration of DOX would be adsorbed within tumour cells by coated alendronate $KMnF_3$ NPs, thereby highly enhancing the cytotoxic effects.

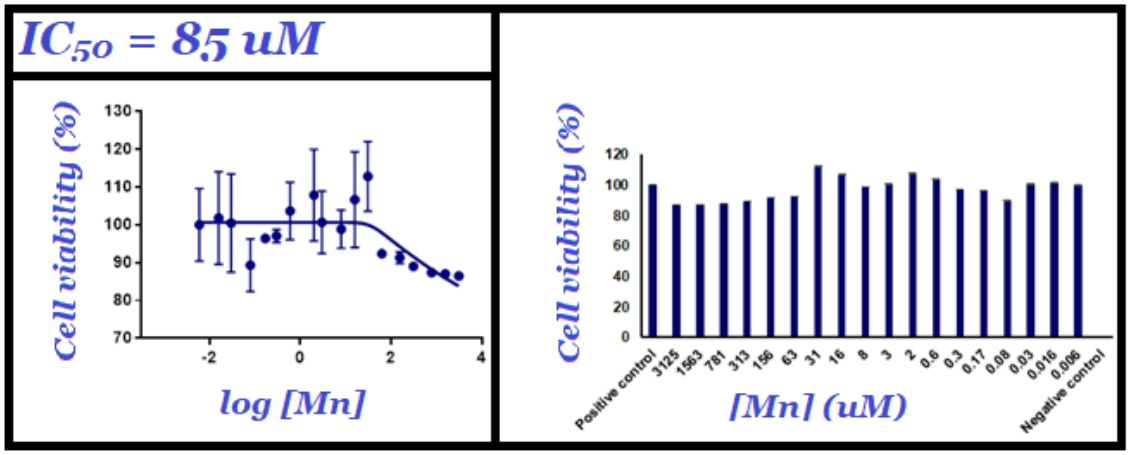

Figure 7-13: Cytotoxicity effect of synthesised coated alendronate$KMnF_3$ NPs against HT-29 colorectal cancer cell lines.

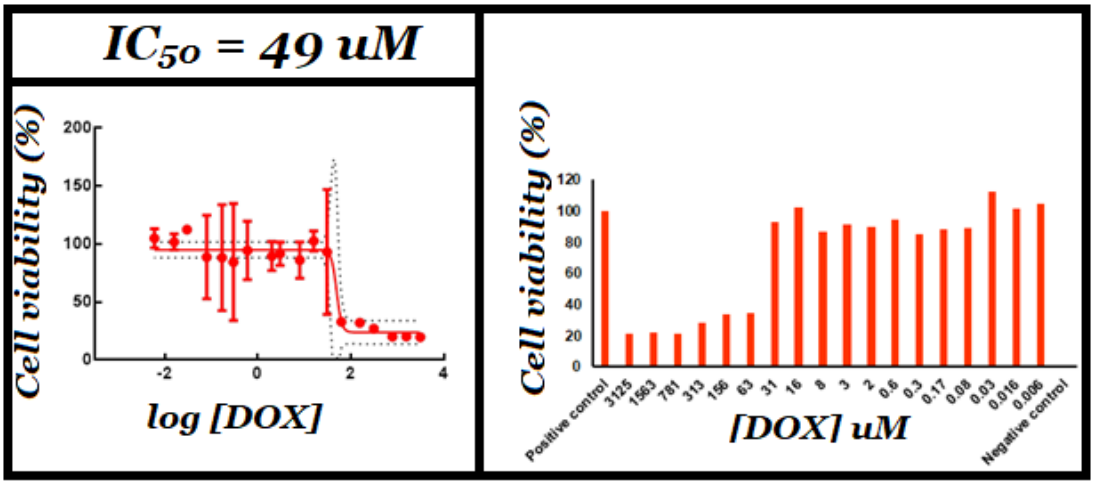

Figure 7-14: Cytotoxicity effect of DOX against HT-29 colorectal cancer cell lines.

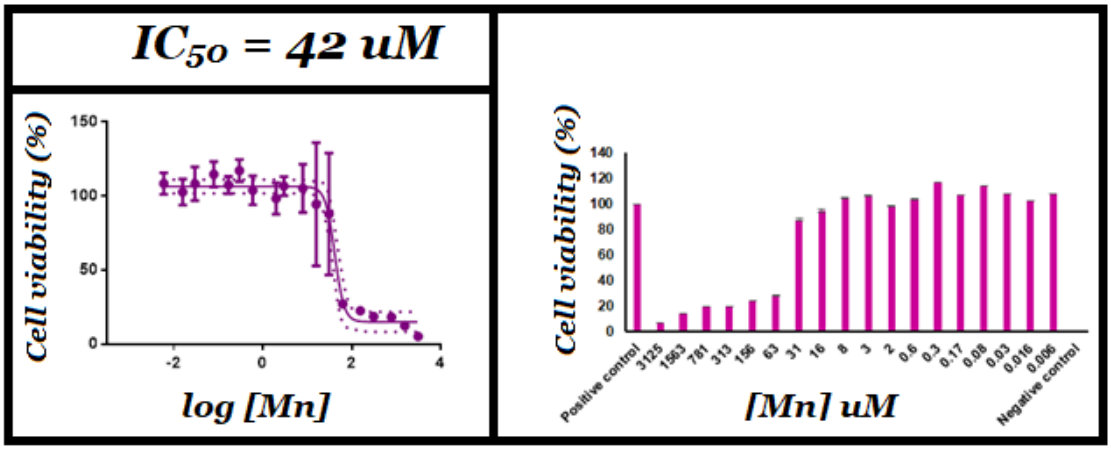

Figure 7-15: Cytotoxicity effect of DOX-coated alendronate $KMnF_3$ NPs against HT-29 colorectal cancer cell lines.

In the case of HCT-116 colorectal cancer, *in vitro* cytotoxicity tests of the coated alendronate $KMnF_3$ NPs demonstrated that at higher concentration from 3125 to 3 uM, the coated NPs showed a significant toxicity effect. However, at lower concentrations, the probe was non-toxic to the cells even when used down to very low concentration (0.006 uM) (Figure 7-16). This could be due to the insufficient coating by the alendronate ligand, where some of the Mn^{2+} was uncoated. Previous studies on MIONs reported that uncoated MIONs act as a main source for ferrous ions and highly reactive hydroxyl radicals that are highly toxic to cells.[19] Therefore, a further coating could overcome this issue or a low concentration that would not exceed 3 uM of this probe can only be used for biological application, in particular as a contrast agents for *MRI*.

Furthermore, it was observed that when HCT-116 cells were treated by free DOX or $KMnF_3$-DOX, the activity of the drug was dose dependent, where cell death gradually

increases as the concentration of the drug increases either in the form of free DOX or conjugated $KMnF_3$-DOX. These results are logical and in consistent with previous results.[20] However, for this particular colorectal cancer cell line, the anti-cancer activity were lower when they were treated by conjugated DOX-$KMnF_3$ NPs compared to free DOX and coated $KMnF_3$ (Figure 7-17 and Figure 7-18). The reason for this observation could be due to the delayed release of the DOX from the NPs during the tested time. Therefore, increasing the incubation time to more than 24 h might cause a significant change in the anti-cancer activity.

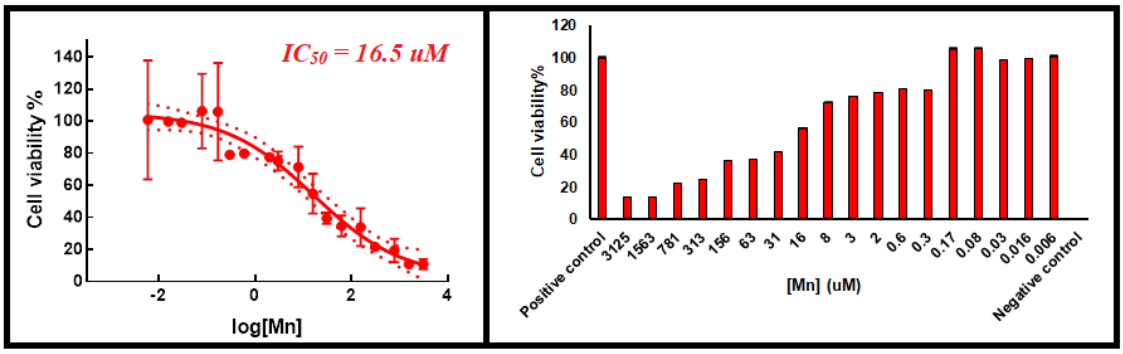

Figure 7-16: Cytotoxicity effect of synthesised coated alendronate$KMnF_3$ NPs against HCT-116colorectal cancer cell lines.

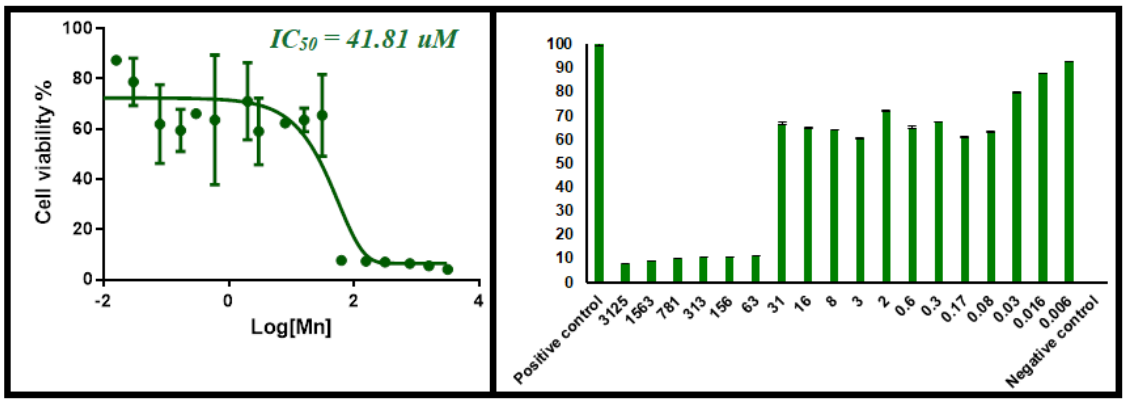

Figure 7-17: Cytotoxicity effect of DOX against HCT-116 colorectal cancer cell lines.

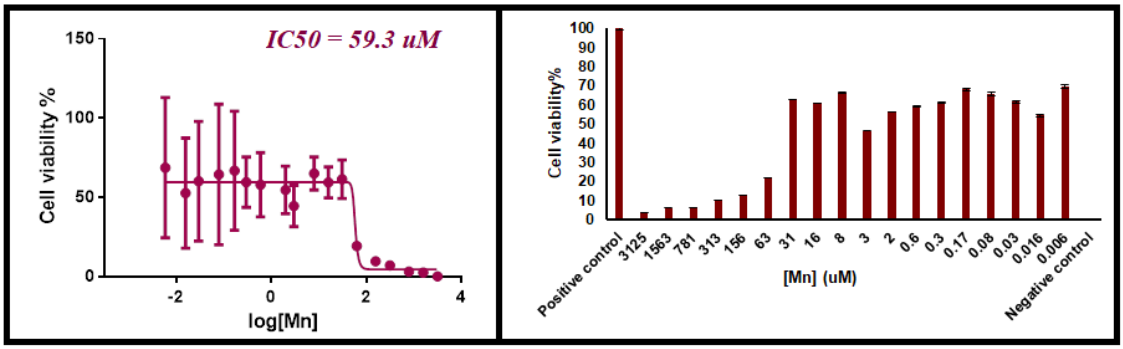

Figure 7-18: Cytotoxicity effect of DOX-coated alendronate $KMnF_3$ NPs against HCT-116 colorectal cancer cell line

Generally, these results indicated the higher affinity of the loaded DOX into the prepared $KMnF_3$ NPs to enhance the cervical HeLa cancer cell lines, colorectal HT-29 cancer cell lines death than Free DOX. Furthermore, the higher viability rates of the cells after treatment with different concentrations of coated alendronate $KMnF_3$ NPs is a clear evidence that these components are not toxic and have no undesirable interferences on the designed drug delivery system as was reported in the previous study.[21] Further incubation time is needed to increase the capability of $KMnF_3$-DOX against HCT-116 colorectal cancer cell lines.

7.3.5 Fluorescence DOX

In order to detect DOX and achieve highly sensitive detection of DOX fluorescence during flow cytometry and confocal microscopy analysis, the fluorescence spectra of this compound in water was first investigated. This can estimate the feasibility of the method. DOX showed typical excitation and emission spectra as illustrated in Figure 7-19. The maximum wavelengths of the excitation and emission were obtained at 499 nm and 594 nm respectively. DOX provides much better and sufficient fluorescence to be detected and quantified directly without the need of any fluorescence derivatization.

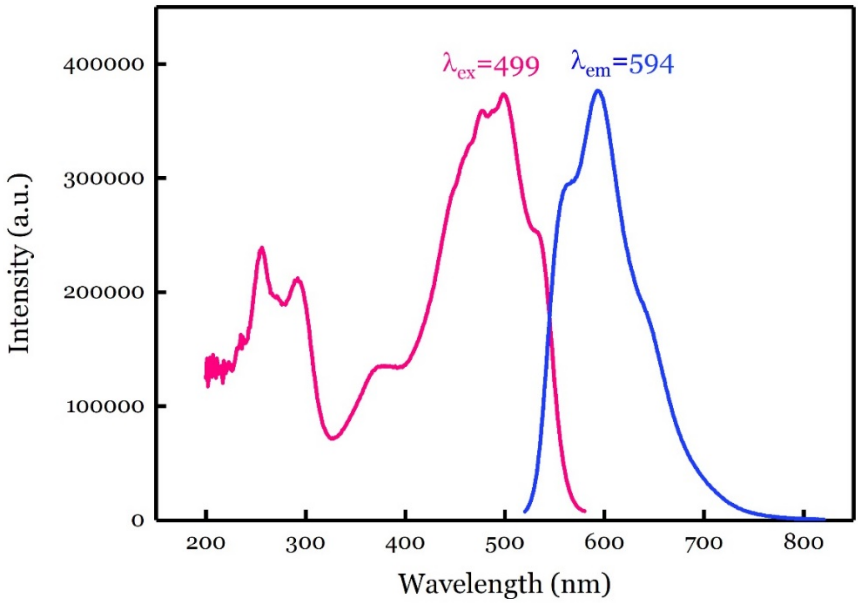

Figure 7-19: Emission and excitation fluorescence spectra of DOX.

7.3.6 Detection of over expressed EGFR and VEGFR proteins by flow cytometry

To assess whether VEGFR antibody maintains its binding affinity and specificity for VEGFR upon conjugation with DOX and $KMnF_3$ NPs. Expression level of EGFR and VEGF proteins in the human cervical cancer cell lines, Hela, and colorectal cancer cell lines, Colo320, HCT116 and HT29 were examined by systematic flow cytometry where a negative control of Rabbit IgG, monoclonal [EPR25A] - Isotype Control (Alexa Fluor® 488) (ab199091) was used. Flow cytometry confirms the cell surface protein expression of VEGF. HeLa cell have strong expression (Figure 7-20), HT-29 and HCT116 have minimal expression (Figure 7-21Figure 7-22), whereas Colo320 has no expression (Figure 7-23) as evidenced by background levels of fluorescence signal of all cells when compared with the unstained cells (Negative control). Most human cancer such as breast, colon, ovarian oesophageal and pancreatic cancer, are widely recognized to highly express VEGF protein.[22-28] Furthermore, it is expression often plays a crucial role in tumour progression and poor prognosis. Ahluwalia and his collaborators reported in their *in vitro* study using western blotting that both HT-29 and HCT116 colon cancer cell lines express VEGF, VGF-R1 and VGF-R2 up to concentration of 2000 pg/ml.[29]

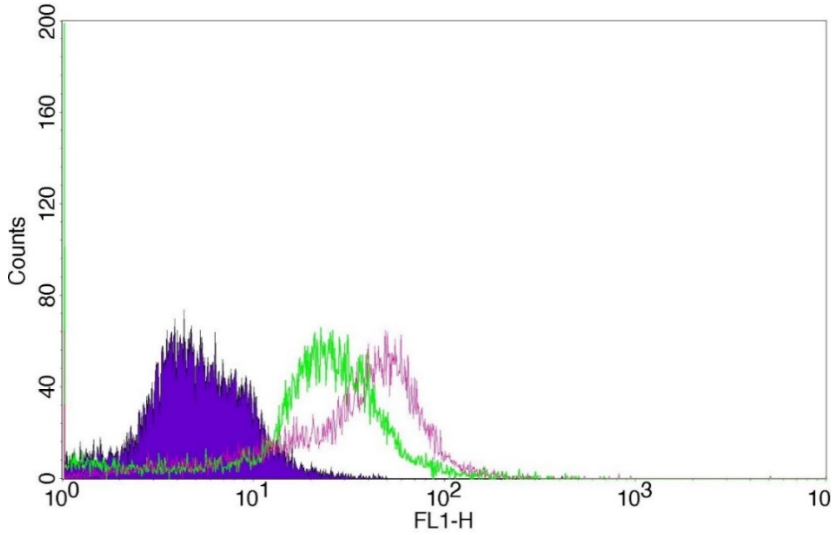

Figure 7-20: FACS analysis to show the existence of EGFR (green) and VEGFR (pink) compared to the negative control (purple) on Hela cells lines

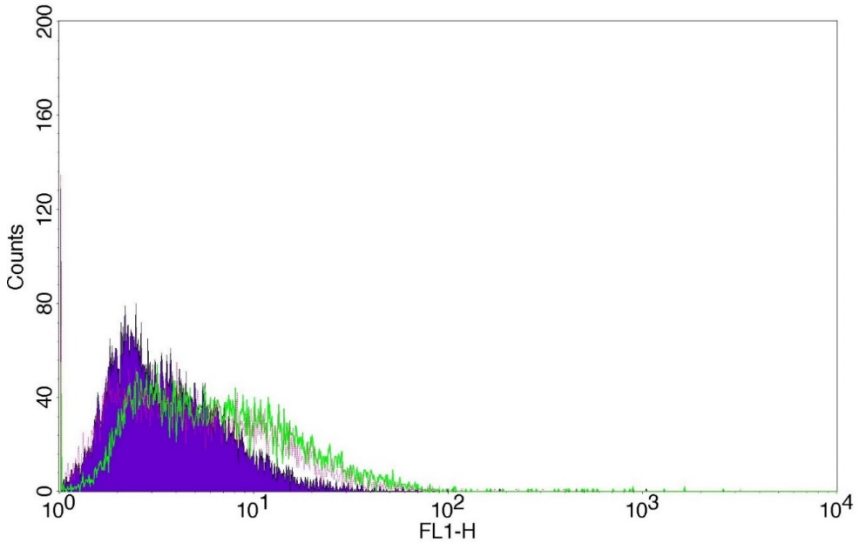

Figure 7-21: FACS analysis results to show the existence of negative control (dark purple), EGFR (green) and VEGFR (Indigo) on HCT-116 colorectal cells lines.

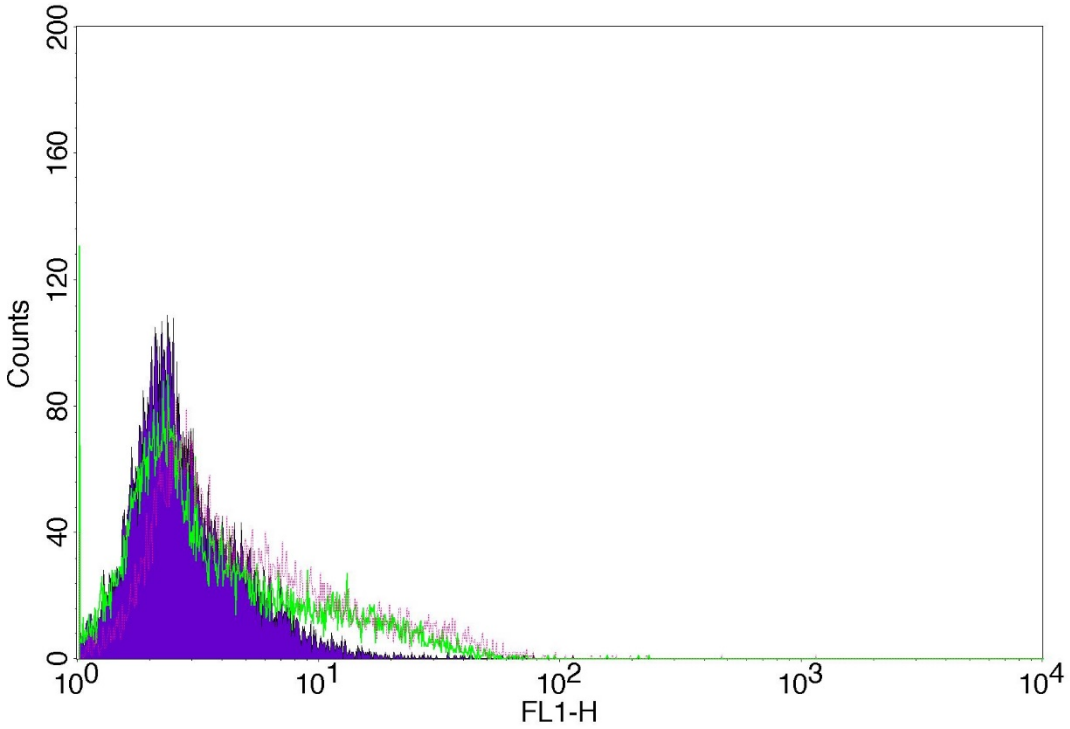

Figure 7-22: FACS analysis results to show the existence of negative control (dark purple), EGFR (green) and VEGFR (Indigo) on HT-29 colorectal cells lines.

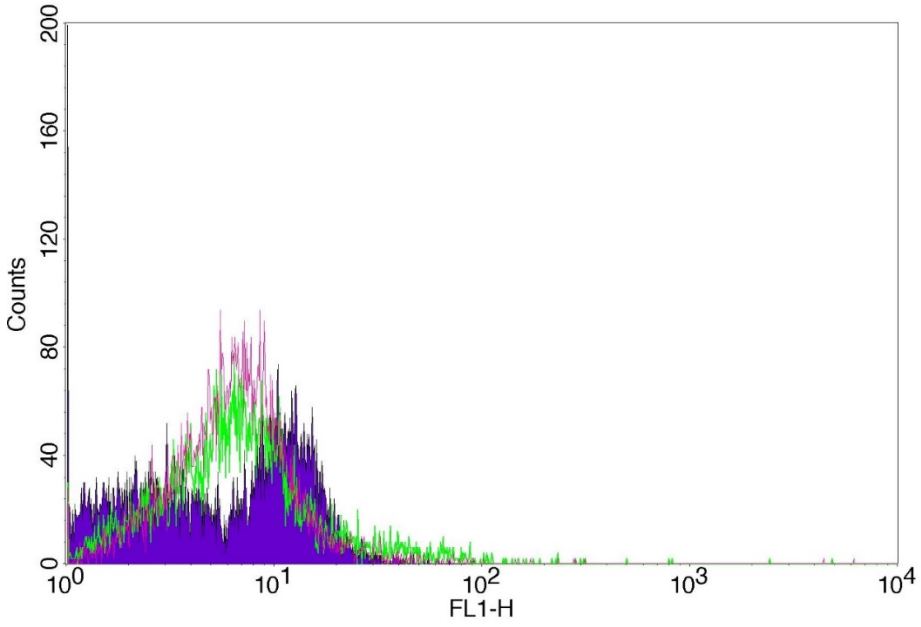

Figure 7-23: FACS analysis to show the existence of EGFR (green) and VEGFR (pink) compared to the negative control (purple) on Colo 320 cells lines

7.3.7 Conjugation of anti-VEGFR to DOX-$KMnF_3$

After the successful loading of DOX into the mesosphere channel of $KMnF_3$ NPs. Further reaction of the DOX conjugate NPs with VEGFR antibody was carried out to yield DOX-$KMnF_3$-Anti-VGFR nanoconjugate. The average hydrodynamic diameters and surface charge of synthesised nanoconjugates were measured using dynamic light scattering (DLS) and zeta-potential. The average size measurement is depicted in Figure 7-24. As expected, DLS measurements showed larger size of 49 nm when compared with alendronate coated $KMnF_3$ NPs and DOX conjugated $KMnF_3$ NPs. This could be due to the successful addition of targeting moieties VEGFR antibody and the presence of the hydrated shell on the surface of $KMnF_3$ NPs. It also might be due to the presence of aggregation that formed by the electrostatic interaction between the NPs. Furthermore, surface charge of the nanoconjugate increased to -12.9 mV and vary from the value obtained for pure VEGFR anti body dissolved in water -9.50. This was expected due to the subsequent VEGFR anti-body conjugation. The stability of the formed nanoconjugates were monitored over 3 months with no obvious aggregation observed. Hence, this nanoconjugate is expected to be stable and applicable for medical applications. Figure 7-25 and Figure 7-26 display the zeta potential measurements for both pure VEGFR anti-body dissolved in water and the formed nanoconjugate respectively.

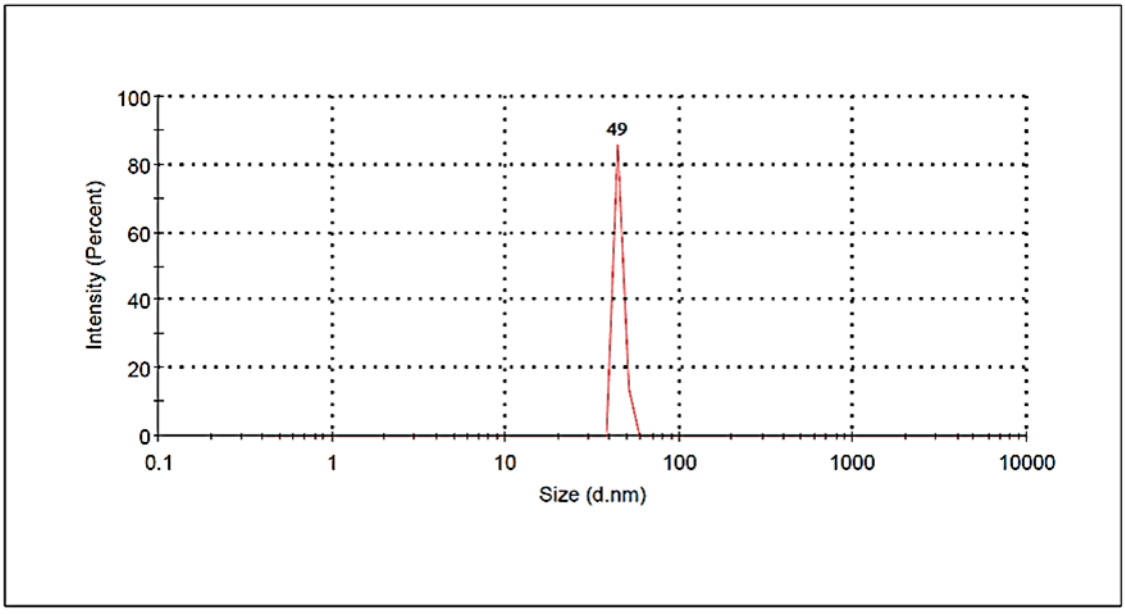

Figure 7-24: Average hydrodynamic size of DOX-$KMnF_3$-antiVEGFR nanoconjugate.

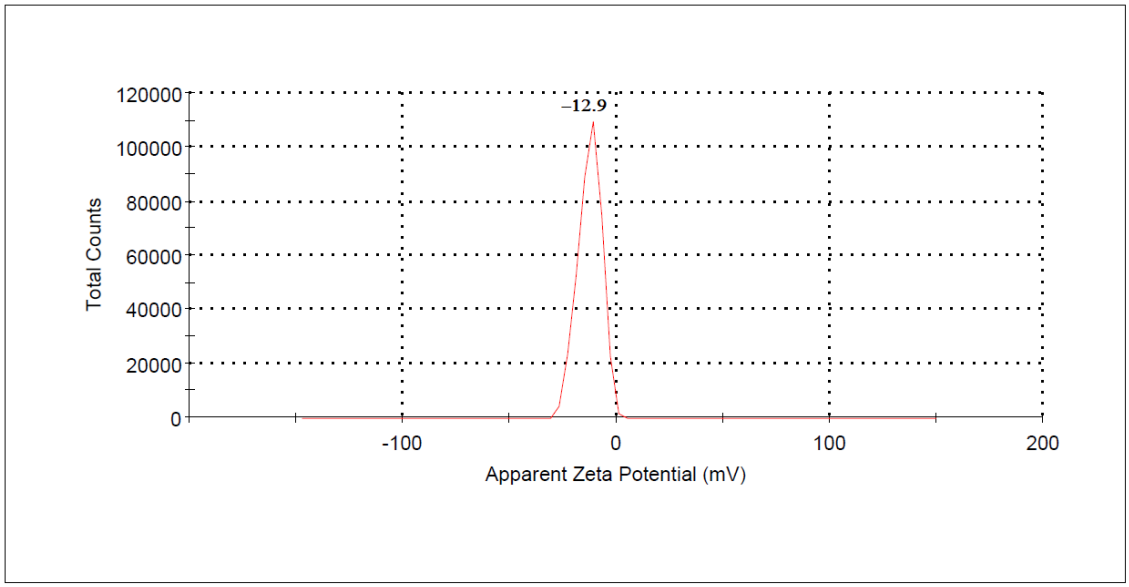

Figure 7-25: Zeta potential of VEGFR dissolved in HPLC water

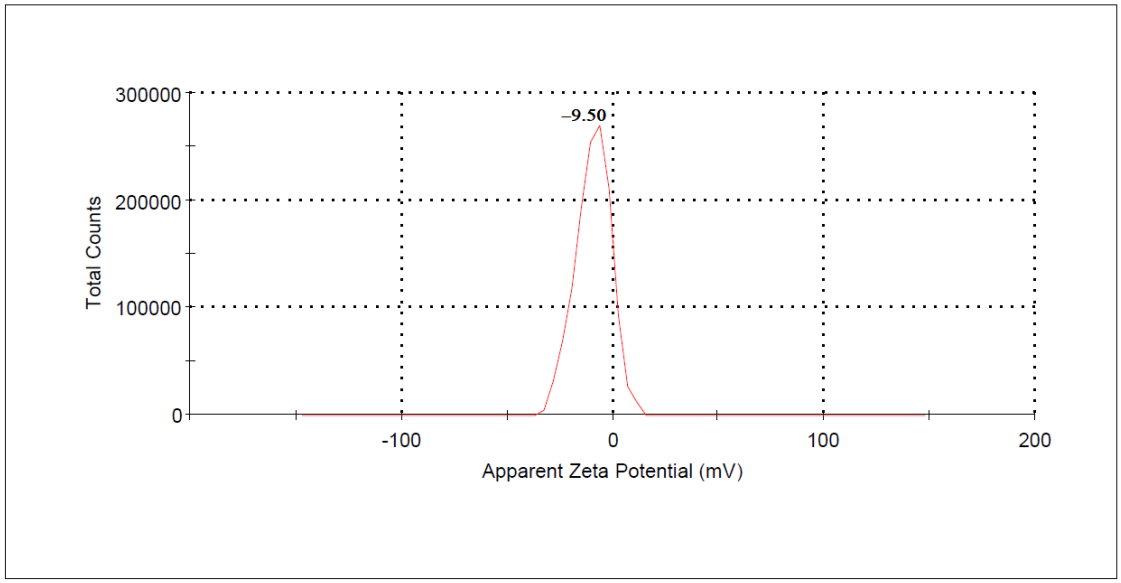

Figure 7-26: Zeta potential of conjugated DOX-KMnF₃-VEGFR anti-body.

7.3.8 Cellular uptake

The ability of $KMnF_3$-DOX-antiVEGFR probe to selectively recognize target cancer cells was confirmed using systematic flow cytometry analysis. To assess whether VEGFR antibody maintains its binding affinity and specificity for VEGFR upon conjugation with $KMnF_3$-DOX in Cervical (HeLa) and colorectal cancer cell lines (HT-29 and HCT-116). Flow cytometry using FL2 channel was carried out. Each cell line was incubated with

different probe, $KMnF_3$, DOX, $KMnF_3$-DOX and $KMnF_3$-DOX-anti-VEGFR. Each probe was aspirated separately to flow cytometry instrument.

The results obtained for all cell lines revealed that a minimum fluorescence was observed when the prepared $KMnF_3$ NPs were incubated with HeLa and HCT-116 cell lines (Figure -7-27 and Figure -7-29), whereas no fluorescence was observed from HT-29 cell line (Figure-7-28). A strong fluorescence signals which is attributed to the higher binding of both DOX and VEGFR anti-body to the $KMnF_3$ NPs was observed, compared to control (cell only). The higher fluorescence associated with the binding of NPs with DOX and VEGFR anti-body could also be attributed to the variation in the amount of VEGFR receptors on the surface of each cancer cells examined. It is worth to note that, the increase in the cell-associated fluorescence for $KMnF_3$-DOX-VEGFR anti-body compared to $KMnF_3$, DOX and $KMnF_3$-DOX, could be explained by the active binding to VEGFR which inhibits its proliferation. According to Hurwitz *et al* that anti-VEGFR therapy enhances the effect of standard chemotherapy in patient with metastatic colorectal cancer.[30] Therefore, the obtained results have potential amplifications for designing and constructing new therapy to specifically target the over expressed VGFR protein receptor pathway.

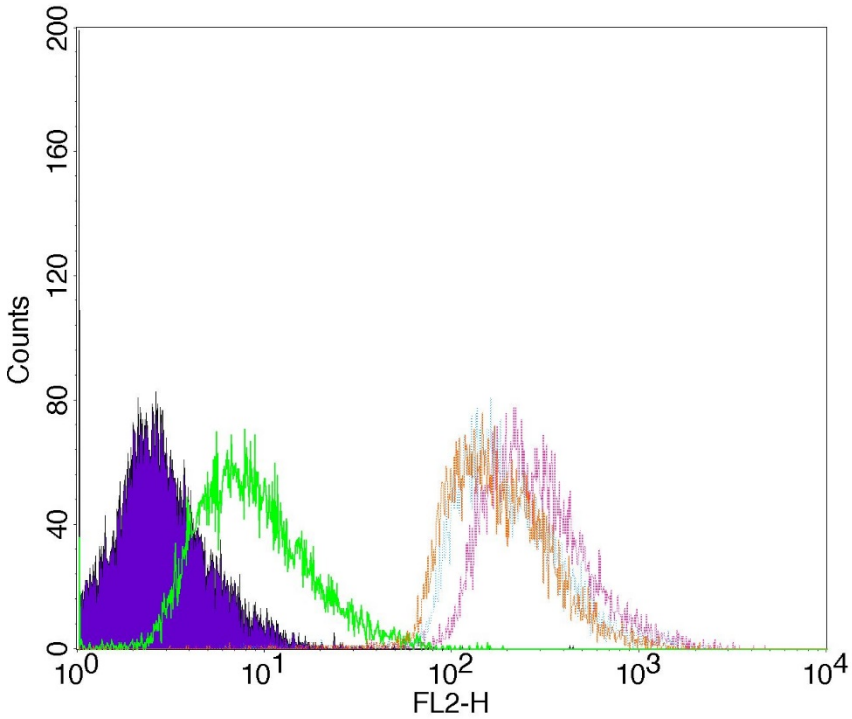

Figure -7-27: Hela cells uptake by (Violet) cell only, (green) $KMnF_3$ NPs, (brown) DOX only, (blue) $KMnF_3$ and DOX, (Purple) $KMnF_3$-DOx-VEGFR anti body using FL_2 flow cytometry channel

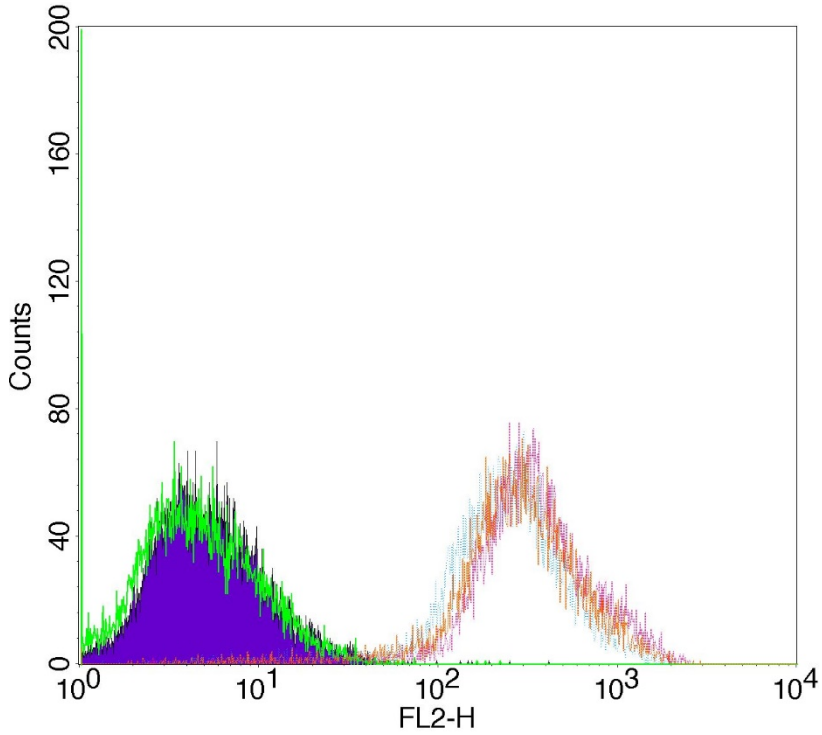

Figure-7-28 Colorectal HT-29 cells uptake by (Violet) cell only, (green) $KMnF_3$ NPs, (brown) DOX only, (blue) $KMnF_3$ and DOX, (Purple) $KMnF_3$-DOx-VEGFR anti body using FL_2 flow cytometry channel

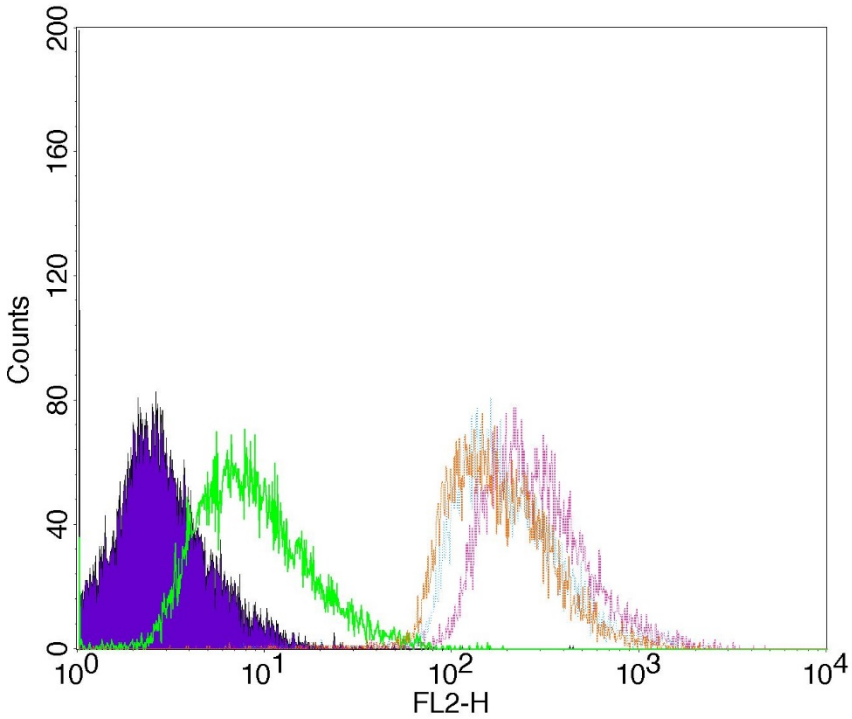

Figure -7-29: HCT116 cells uptake by (Violet) cell only, (green) $KMnF_3$ NPs, (brown) DOX only, (blue) $KMnF_3$ and DOX, (Purple) KMnF3-DOx-VEGFR anti body using FL2 flow cytometry channel

7.3.9 Confocal microscopy

To further explore the mechanism of $KMnF_3$, Dox, $KMnF_3$-DOX and $KMnF_3$-DOX-VEGFR internalization and intracellular drug delivery. Hela, HT-29 and HCT-116 were observed by laser scanning confocal fluorescence microscopy after incubation with coated $KMnF_3$, free Dox, $KMnF_3$-DOX and $KMnF_3$-DOX-VEGFR for 1 hour. The intracellular localisation of nanomaterials has been proofed to involve lysosomes once the materials enter the cells.[31, 32] Images obtained for treating all cell lines with $KMnF_3$ NPs do not show any fluorescence and was really hard to observe their localisation in all of the tested cell lines (Figure 7-30 to Figure 7-32). Free Dox rapidly accumulated inside the cells. They look like vascular within body, which might be localised in the mitochondria (Figure 7-33 to Figure 7-35). In contrast, $KMnF_3$-DOX have well defined shape that are distributed inside the cell and possibly accumulate in the nucleus Figure 7-36 to Figure 7-38). Treating cells with $KMnF_3$-DOX- VEGFR result in more distributed NPs, which might be localised in the cytosol of the cell (Figure 7-39 to Figure 7-41). It is worth noting that the $KMnF_3$-DOX-VEGFR is also observed inside the cell and could be localised in the nucleus. These results suggest that Dox accumulation in the lysosomes, where the lysosomes acidic environment and enzyme catalysis assisted the faster degradation of the NPs and released the loaded DOX and anti-VEGFR into the cytoplasm. Following that, DOX and VEGFR-anti-body migrated to the nucleus and specifically induced cervical and colorectal cancer cells apoptosis. Furthermore, the correct dose of loaded DOX anti-VEGFR-$KMnF_3$ NPs causes an enhancement in killing colorectal and cervical cancer cells and therefore inhibition of metastasis. Moreover, we assume that the specific delivery of DOX to the tumours *via* these anti-VEGFR-$KMnF_3$ targeted NPs would minimize the potential toxic side effect towards the health cells. Similar reason was reported for CSA, the exclusively expressed protein in the placental trophoblast-targeted in-vivo study reported by Zhang *et al*.[33] Due to this improvement, it is expected that DOX-$KMnF_3$-VEGFR antibody would result in a substantial enhancement of human survival compared to the pure DOX or $KMnF_3$-DOX. In correlation with previously reported work, DOX-$KMnF_3$-VEGFR-antibody could a novel probe for the targeted drug delivery to cervical and colorectal human cancer.[34, 35]

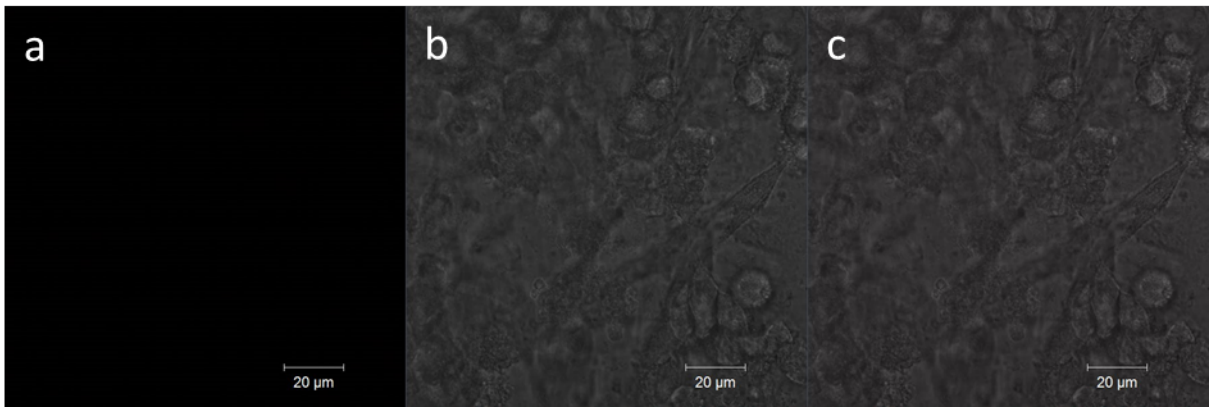

Figure 7-30: Bright field (c), dark field(a) and merge (b) images of HeLa cells incubated with coated alendronate $KMnF_3$ NPs only for one hour

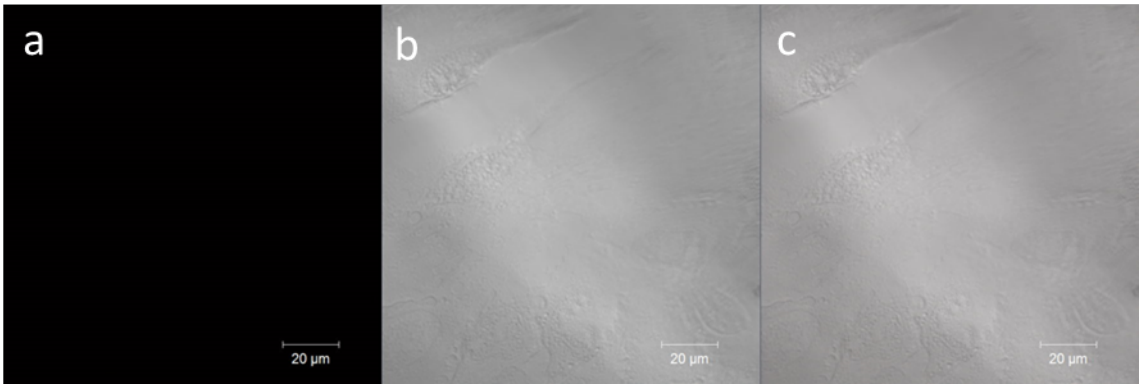

Figure 7-31: Bright field (c), dark field(a) and merge (b) images of HT-29 cells incubated with coated alendronate $KMnF_3$ NPs only for one hour

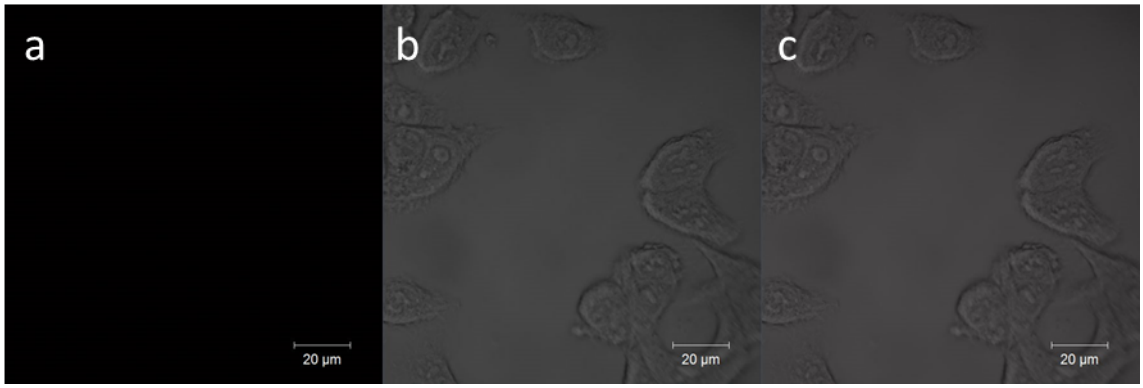

Figure 7-32: Bright field (c), dark field(a) and merge (b) images of HCT-116 cells incubated with coated alendronate $KMnF_3$ NPs only for one hour

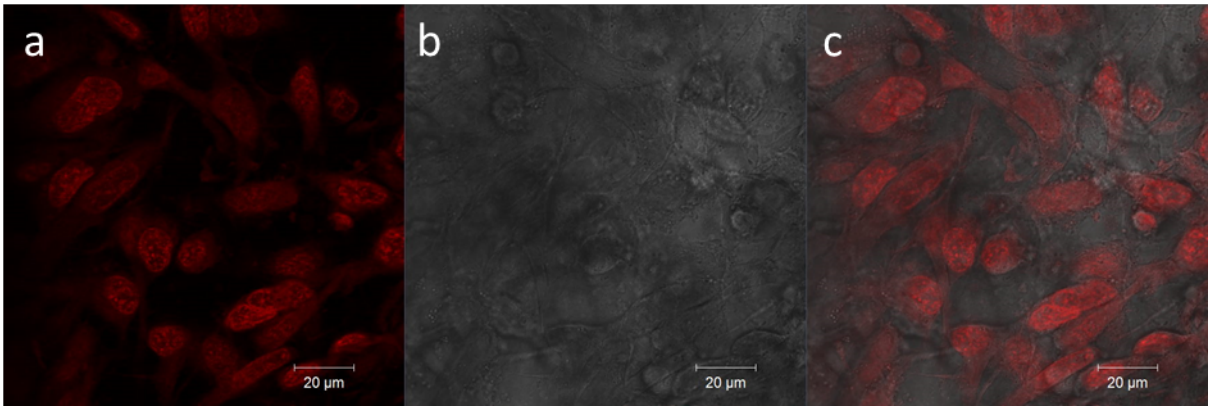

Figure 7-33: Bright field (c), dark field(a) and merge (b) images of HeLa cells incubated with coated DOX only for one hour

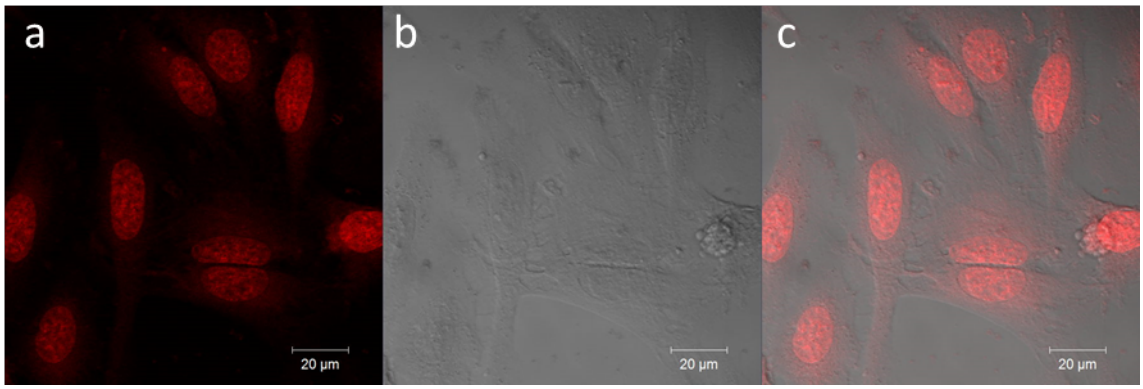

Figure 7-34: Bright field (c), dark field(a) and merge (b) images of HT-29 cells incubated with DOX only for one hour

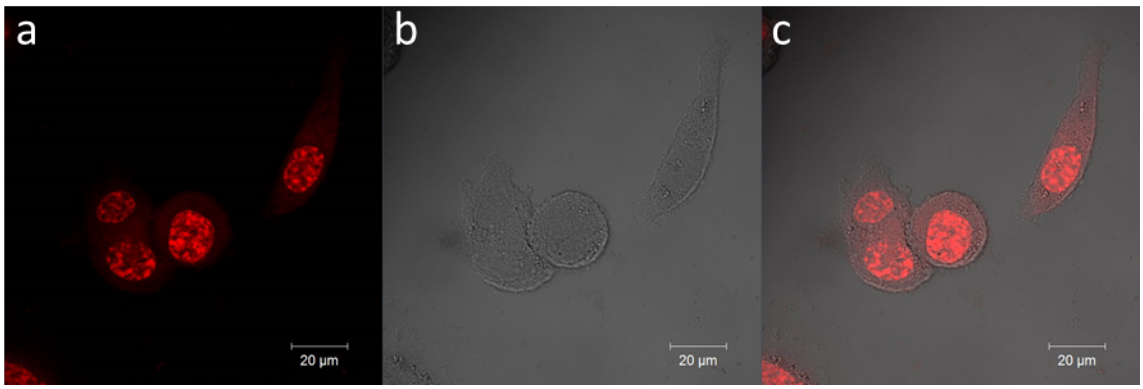

Figure 7-35: Bright field (c), dark field(a) and merge (b) images of HCT-116 cells incubated with DOX only for one hour

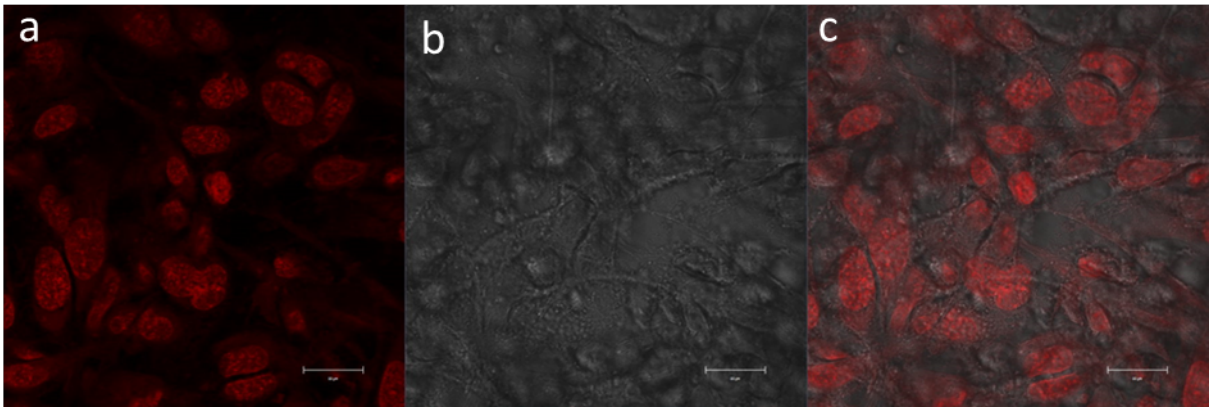

Figure 7-36: Bright field (c), dark field(a) and merge (b) images of HeLa cells incubated with $KMnF_3$-DOX for one hour

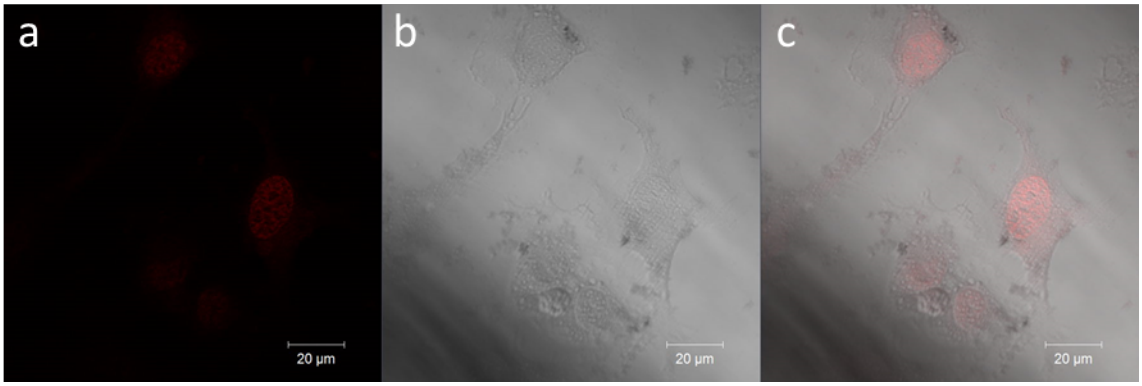

Figure 7-37 Bright field (c), dark field(a) and merge (b) images of HT-29 cells incubated with $KMnF_3$-DOX for one hour

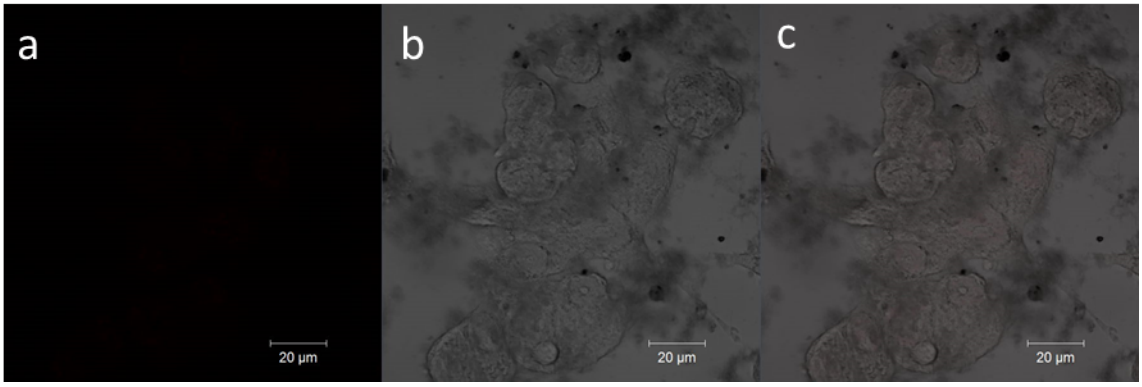

Figure 7-38: Bright field (c), dark field(a) and merge (b) images of HCT-116 cells incubated with $KMnF_3$-DOX for one hour

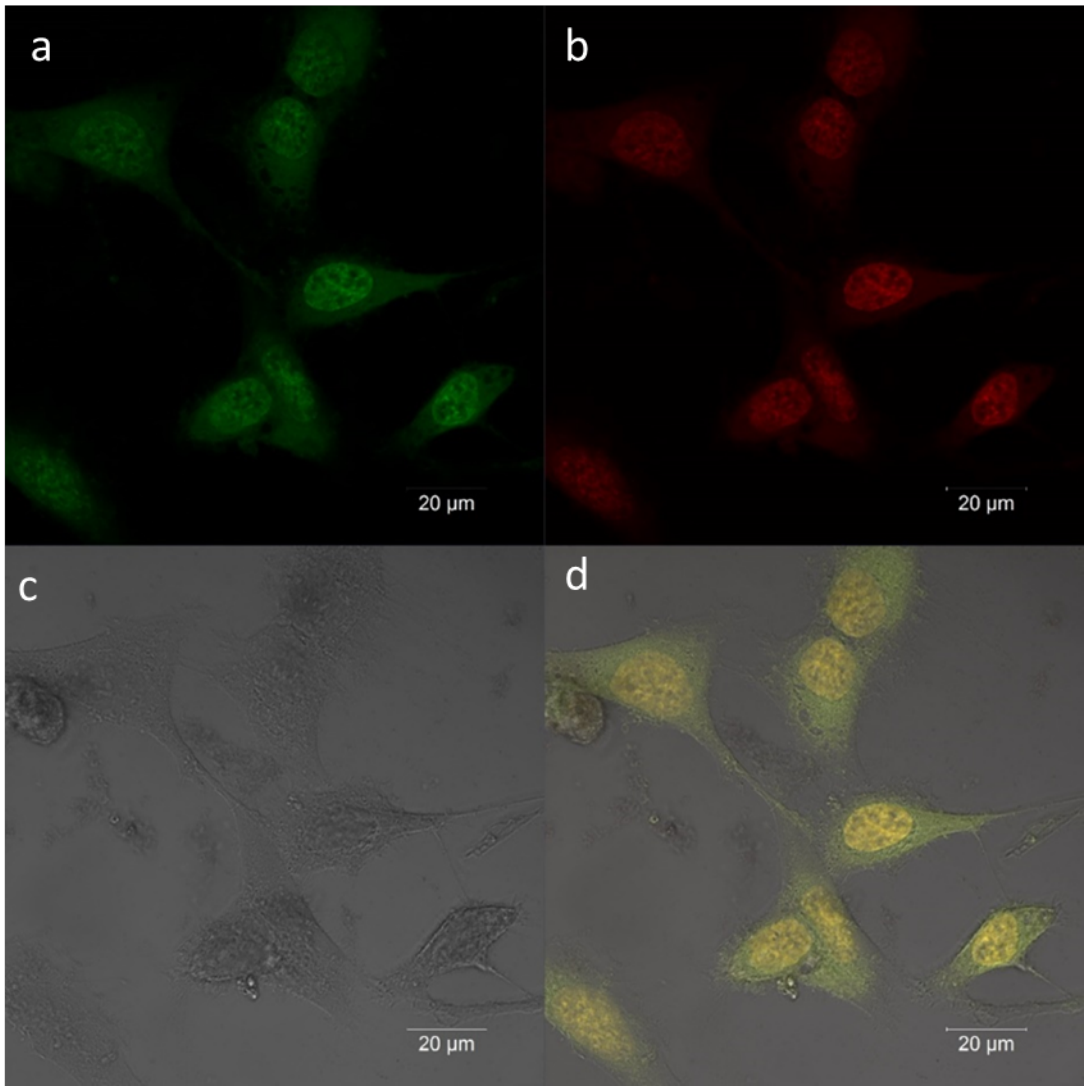

Figure 7-39: Bright field (c), dark field of Alex Flour 488 anti-VEGF(a), dark field of DOX(b) and merge (d) images of HeLa cells incubated with $KMnF_3$-DOX-anti-VEGFR for one hour

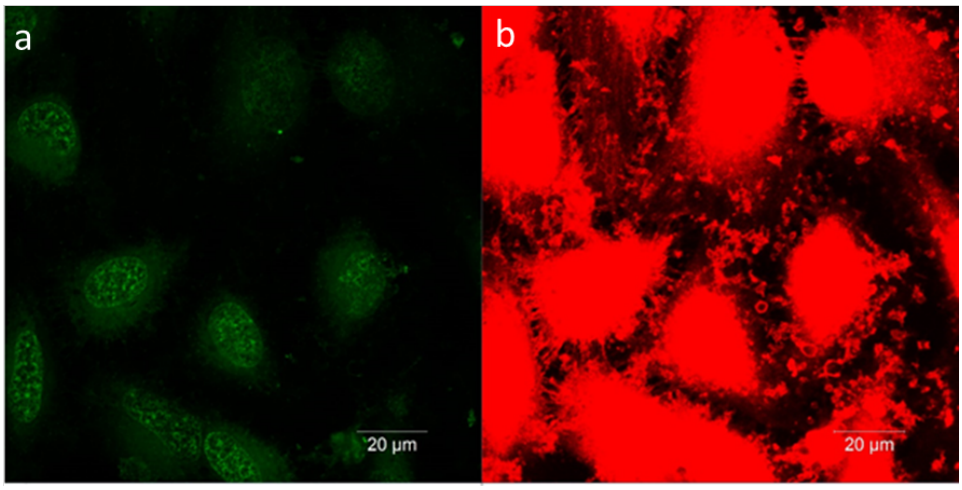

Figure 7-40: Dark field of Alex Flour 488 anti-VEGF(a), dark field of DOX(b)images of HT-29 cells incubated with $KMnF_3$-DOX-anti-VEGFR for one hour

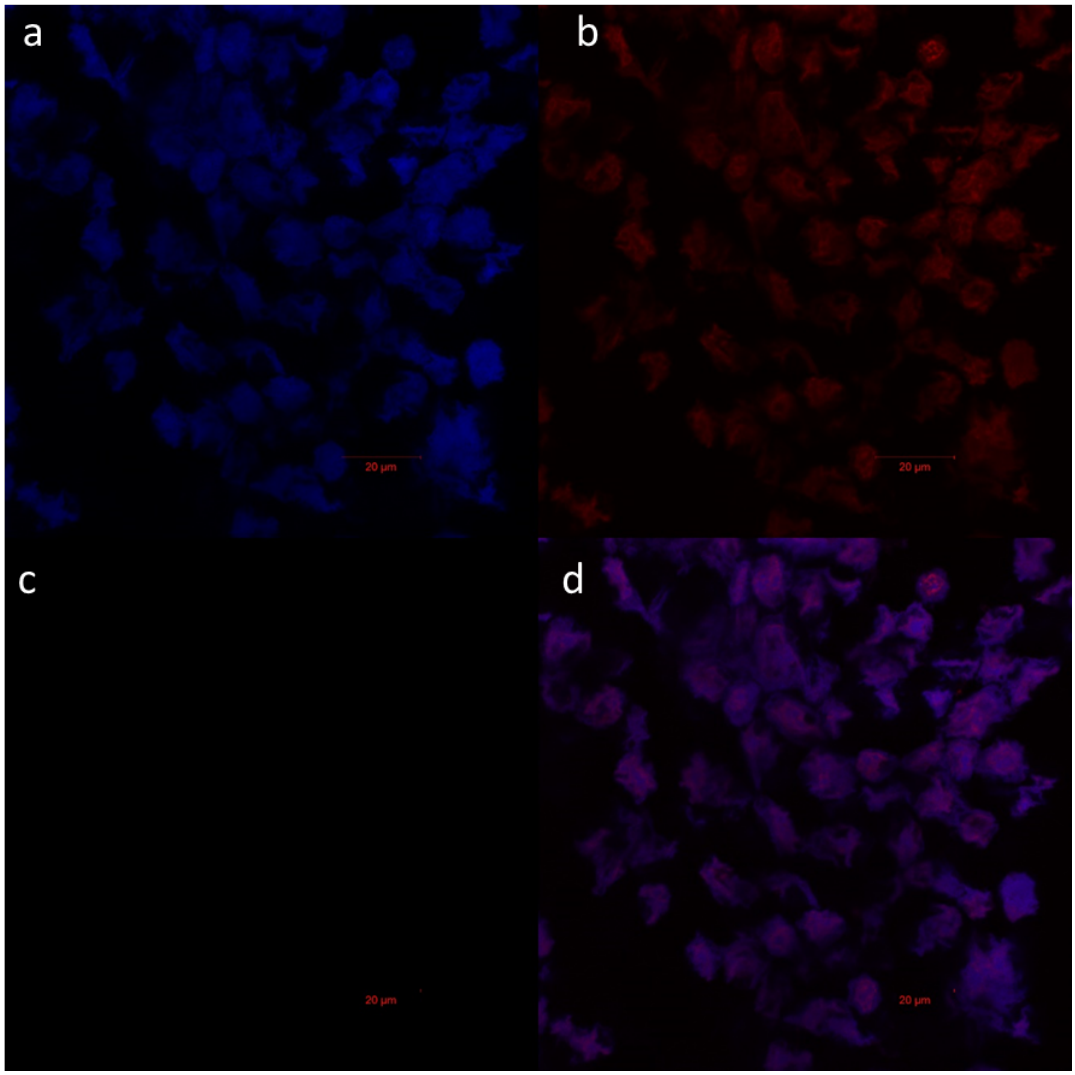

Figure 7-41: Bright field Alex Flour 488 anti-VEGF(a), bright field of DOX(b), dark field (c) and merge (d) images of HT-116 cells incubated with $KMnF_3$-DOX-anti-VEGFR for one hour

7.3.10 Cytotoxicity of $KMnF_3$-DOX-anti-VEGFR

The toxic side effects of anticancer drug due to the lack of specificity of conventional therapies, normally require the increase in the amount of drug dose to eradicate or inhibit the tumour growth. In the last few decades, many strategies have been developed for the enhancement of the tumour specific delivery of DOX loaded NPs, *via* targeting them through monoclonal antibodies. This would facilitate the delivery of NPs with DOX and cargos them into the site drug action and therefore minimizing the unwanted side effects.

Based on the ability of anti-VEGFR to specifically interact with highly expressed VEGFR protein on the cervical and colorectal cancer cell. The cytotoxicity of $KMnF_3$-DOX-VEGFR anti-body against cervical HeLa cell line, HT-29 and HCT-116 colorectal

cancer cell lines was further studied using MTS test and the cell survival rates were compared to the same cell lines when incubated by free DOX or $KMnF_3$-DOX.

From Figure 7-42 to Figure 7-44, it can be seen that treating HeLa, HT-29 and HCT-116 cells with $KMnF_3$-DOX-anti-VEGFR reduces the IC_{50} to 3.75, 6.147 and 42.34 uM for HeLa, HT-29 and HCT-116 cells respectively. These values represent higher cancer activity compared to the values obtained for free DOX and the covalently conjugated DOX-$KMnF_3$. It may be attributed to the specific binding of the anti-VEGF conjugates $KMnF_3$-DOX to the over expressed VEGFR receptors in these cells. These preliminary data show that the conjugation of anti-VEGF molecules to the surface of the NPs, which favours anti-VEGF receptor recognition, was responsible for the targeting ability of anti-VEGF-$KMnF_3$-DOX and in turn facilitate their entry into the cells through endocytosis or micropinocytosis, therefore enhances the concentration of the drug in the targeted site. In addition, it is apparently known that anti-VEGF conjugated NPs showed efficient receptor-mediated endocytosis in anti-VEGF receptor-overexpressing cancer cells, compared with nontargeted NPs.[36]

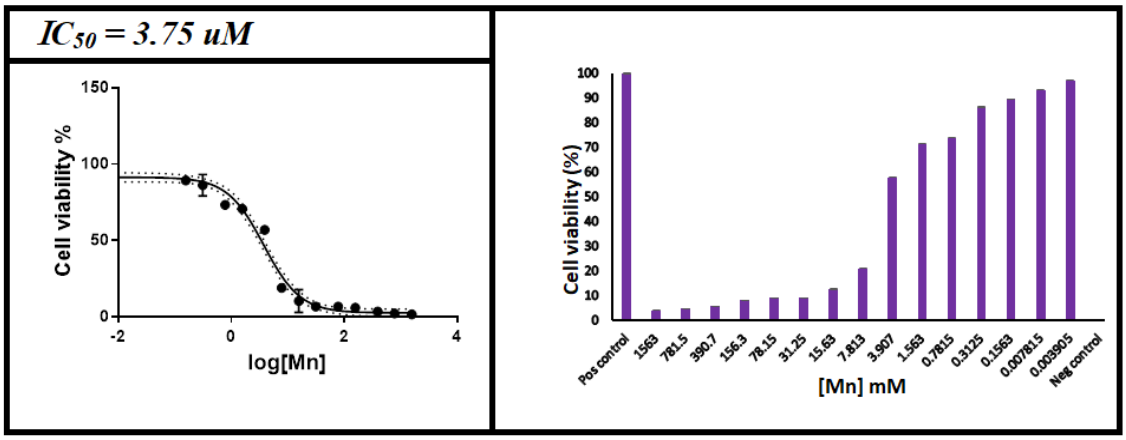

Figure 7-42: Cytotoxicity effect of DOX-coated alendronate $KMnF_3$ NPs and anti-VEGFR against Hela cervical cancer cell lines.

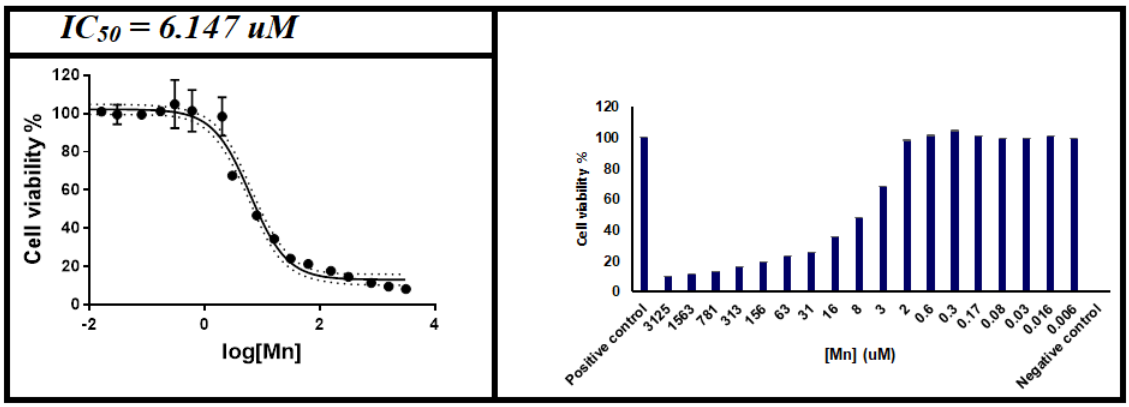

Figure 7-43: Cytotoxicity effect of DOX-coated alendronate $KMnF_3$ NPs and anti-VEGFR against HT-29 colorectal cancer cell lines.

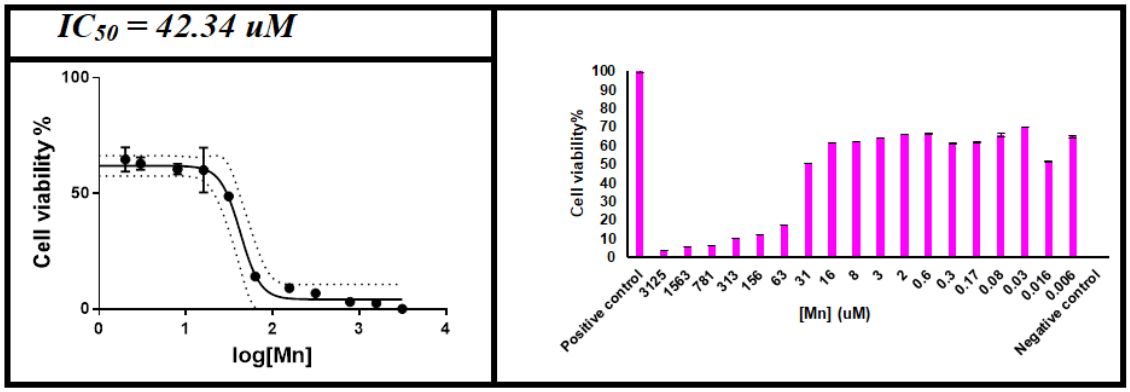

Figure 7-44: Cytotoxicity effect of DOX-coated alendronate $KMnF_3$ NPs and anti-VEGFR against HCT-116 colorectal cancer cell line

7.4 Conclusions

In the present study, DOX was successfully loaded into $KMnF_3$ NPs through polyethylene glycol linker. This Nano conjugate had an average hydrodynamic size of 29 nm. The successful conjugation of the DOX was confirmed by FT-IR and UV spectroscopy. The amount of the loaded DOX was determined using UV-spectroscopy and found 25%. Furthermore, DOX conjugated $KMnF_3$ showed a significant anti-cancer activity with lower IC_{50} of 4.179 and 42 uM against cervical HeLa and colorectal and HT-29 cancer cell lines respectively, when compared to $KMnF_3$ NPs and pure DOX *In-vitro*. This suggest that $KMnF_3$ NPs could be a promising tool for cancer cell targeting.

In an attempt to increase the cellular-uptake of chemotherapeutic DOX drug to improve the anti-cancer activity against the tested cell lines, the loaded doxorubicin $KMnF_3$ NPs

was further conjugated with VEGFR-antibody that have high affinity and specificity for cell surface over-expressed VEGFR receptor normally expressed by cervical and colorectal cancer cells. A successful conjugation process and cellular-uptake were confirmed by flow cytometry and confocal studies. Interestingly, DOX-$KMnF_3$-VEGFR-anti-body NPs showed a significant change in the anticancer-activity for all cells where IC_{50} dropped down to 3.75, 6.147 and 42.34 uM for HeLa, HT-29 and HCT-116 respectively compared to the conjugated DOX-$KMnF_3$ NPs. The most probable reason for this change is the higher affinity of the VEGFR anti-body for specifically binding the VEGFR receptor, and markedly stimulate the internalization of the drug into the cells. Upon the localisation of the drug at the cell surface, the anti-body may use its cytosolic interaction probably either at cell membrane or following internalisation.[37] Increasing the concentration of DOX at the cell surface or, in lysosome by lysosomal enzymes, would results in the anti-cancer activity enhancement.[37]

7.5 References

1. J. C. Cuggino, G. Gatti, M. L. Picchio, M. Maccioni, L. M. Gugliotta and C. I. Alvarez Igarzabal, *European Polymer Journal*, 2019, **116**, 445-452.
2. M. Psurski, B. Filip-Psurska, M. Cuprych, J. Wietrzyk and J. Oleksyszyn, *Life Sciences*, 2019, **231**, 116530.
3. K. Renu, A. V.G, T. P. P.B and S. Arunachalam, *European Journal of Pharmacology*, 2018, **818**, 241-253.
4. A. U. Buzdar, C. Marcus, G. R. Blumenschein and T. L. Smith, *Cancer*, 1985, **55**, 2761-2765.
5. M. Brzeziński, S. Wedepohl, B. Kost and M. Calderón, *European Polymer Journal*, 2018, **109**, 117-123.
6. J. Park, P. M. Fong, J. Lu, K. S. Russell, C. J. Booth, W. M. Saltzman and T. M. Fahmy, *Nanomedicine: Nanotechnology, Biology, and Medicine*, 2009, **5**, 410-418.
7. D. Kim, E. S. Lee, K. T. Oh, Z. Gao and Y. H. Bae, *Small*, 2008, **4**, 2043-2050.
8. Y. Barenholz, *Journal of Controlled Release*, 2012, **160**, 117-134.
9. K. K. Upadhyay, A. N. Bhatt, A. K. Mishra, B. S. Dwarakanath, S. Jain, C. Schatz, J. F. Le Meins, A. Farooque, G. Chandraiah, A. K. Jain, A. Misra and S. Lecommandoux, *Biomaterials*, 2010, **31**, 2882-2892.
10. W. Cheng, J. N. Kumar, Y. Zhang and Y. Liu, *Biomaterials Science*, 2015, **3**, 597-607.
11. J. C. Cuggino, M. Molina, S. Wedepohl, C. I. A. Igarzabal, M. Calderón and L. M. Gugliotta, *European Polymer Journal*, 2016, **78**, 14-24.
12. J. Huang, Y. Xue, N. Cai, H. Zhang, K. Wen, X. Luo, S. Long and F. Yu, *Materials Science and Engineering C*, 2015, **46**, 41-51.
13. N. Singh, J. Nayak, S. K. Sahoo and R. Kumar, *Materials Science and Engineering: C*, 2019, **100**, 453-465.
14. C. Wang, H. Xu, C. Liang, Y. Liu, Z. Li, G. Yang, L. Cheng, Y. Li and Z. Liu, *ACS Nano*, 2013, **7**, 6782-6795.
15. M. Baneshi, S. Dadfarnia, A. M. H. Shabani, S. K. Sabbagh, S. Haghgoo and H. Bardania, *International Journal of Pharmaceutics*, 2019, **564**, 145-152.
16. B. Bhushan, P. Dubey, S. U. Kumar, A. Sachdev, I. Matai and P. Gopinath, *RSC Advances*, 2015, **5**, 12078-12086.
17. A. K. Gupta and S. Wells, *IEEE Transactions on NanoBioscience*, 2004, **3**, 66-73.
18. H. S. Yoo, K. H. Lee, J. E. Oh and T. G. Park, *Journal of Controlled Release*, 2000, **68**, 419-431.
19. N. Singh, G. J. Jenkins, R. Asadi and S. H. Doak, *Nano reviews*, 2010, **1**, 5358.
20. Y. Qin, L. Sun, X. Li, Q. Cao, H. Wang, X. Tang and L. Ye, *Journal of Materials Chemistry*, 2011, **21**, 18003-18010.
21. C. Yan, N. Liang, Q. Li, P. Yan and S. Sun, *Carbohydrate Polymers*, 2019, **216**, 129-139.
22. J. Adams, P. J. Carder, S. Downey, M. A. Forbes, K. MacLennan, V. Allgar, S. Kaufman, S. Hallam, R. Bicknell and J. J. Walker, *Cancer research*, 2000, **60**, 2898-2905.
23. G. Gasparini, E. Bonoldi, C. Gatti, O. Vinante, M. Toi, T. Tominaga, M. Gion, R. Dittadi, P. Verderio and P. Boracchi, *Journal of the National Cancer Institute*, 1997, **89**, 139-147.
24. T. J. Duncan, A. Al-Attar, P. Rolland, I. V. Scott, S. Deen, D. T. Liu, I. Spendlove and L. G. Durrant, *Clinical Cancer Research*, 2008, **14**, 3030-3035.

25. S. Ishigami, S. Arii, M. Furutani, M. Niwano, T. Harada, M. Mizumoto, A. Mori, H. Onodera and M. Imamura, *British journal of cancer*, 1998, **78**, 1379.
26. Y. Zhang, X. Liu, J. Zhang, L. Li and C. Liu, *Oncology letters*, 2012, **4**, 763-766.
27. C. Huang, R. Huang, W. Chang, T. Jiang, K. Huang, J. Cao, X. Sun and Z. Qiu, *Neoplasma*, 2012, **59**, 52-61.
28. M. Kozłowski, W. Laudański, B. Mroczko, M. Szmitkowski, R. Milewski and G. Łapuć, *Advances in medical sciences*, 2013, **58**, 227-234.
29. A. Ahluwalia, M. K. Jones, S. Szabo and A. S. Tarnawski, *Biochemical and biophysical research communications*, 2013, **437**, 515-520.
30. H. Hurwitz, L. Fehrenbacher, W. Novotny, T. Cartwright, J. Hainsworth, W. Heim, J. Berlin, A. Baron, S. Griffing and E. Holmgren, *New England journal of medicine*, 2004, **350**, 2335-2342.
31. F. Zhao, Y. Zhao, Y. Liu, X. Chang, C. Chen and Y. Zhao, *small*, 2011, **7**, 1322-1337.
32. P. Zhao, M. Zheng, Z. Luo, X. Fan, Z. Sheng, P. Gong, Z. Chen, B. Zhang, D. Ni and Y. Ma, *Advanced healthcare materials*, 2016, **5**, 2161-2167.
33. B. Zhang, G. Cheng, M. Zheng, J. Han, B. Wang, M. Li, J. Chen, T. Xiao, J. Zhang and L. Cai, *Drug delivery*, 2018, **25**, 461-471.
34. A. Salanti, T. M. Clausen, M. Ø. Agerbæk, N. Al Nakouzi, M. Dahlbäck, H. Z. Oo, S. Lee, T. Gustavsson, J. R. Rich and B. J. Hedberg, *Cancer cell*, 2015, **28**, 500-514.
35. R. Seiler, H. Z. Oo, D. Tortora, T. M. Clausen, C. K. Wang, G. Kumar, M. A. Pereira, M. S. Ørum-Madsen, M. Ø. Agerbæk and T. Gustavsson, *European urology*, 2017, **72**, 142-150.
36. B. Yang, Y. Li, X. Sun, X. Meng, P. Chen and N. Liu, *Journal of Chemical Technology & Biotechnology*, 2013, **88**, 2169-2175.
37. R. Sinha, G. J. Kim, S. Nie and D. M. Shin, *Molecular cancer therapeutics*, 2006, **5**, 1909-1917.

CHAPTER 8

Conclusion and future work

8 Conclusion

The aim of this work was to prepare new theranostics systems for the detection and treatment of colon cancer. Theranostics systems are composed by core NPs functionalised with molecules which act as receptors for cancer cells and as drugs to be deliver in situ to the tumour. Paramagnetic perovskite metal fluoride and metal oxide NPs, KMF_3 (M = Mn, Fe, Co) and $DyFeO_3$, were prepared *via* co-precipitation, hydrothermal and so-gel methods. $KMnF_3$ USNPs were prepared via a modified hydrothermal method and showed potential as dual mode T_1/T_2 *MRI* contrast agents. Following functionalisation with DOX and VEGF antibody, this has shown a targeted Theranostics in colon cancer cells.

Chapters 1 presents a general introduction that highlight the crucial aspects involved in this project, such as underlying the key points of the magnetic metal oxides and fluorides NPs and discus their physical and chemical properties that enable them to be an excellent candidate for various number of applications. This chapter also describes the perovskite structure of ABX_3 materials and highlighted the difference between the cubic and the other distorted symmetry adopted by this structure with illustration of some common examples. Furthermore, various preparation methods used to prepare NPs are also described. The basic mechanisms of the contrast agents to shorten the relaxation time of the water molecules in human tissues for clear *MRI* images are explained and supported by different examples available in the literature. The last part of the introduction defines the term theranostics as diagnosis and drug delivery, either by NPs carriers or by a specific recognition to the targeted site in the human body for an effective therapy, this includes various examples from literature.

Chapter 2 introduces the basic principles of the instrumentation techniques used to characterise the as prepared and functionalised NPs. These techniques include Powder X-ray Diffraction (PXRD), Fortier Transform Infra-Red Spectroscopy (FT-IR), Electron Transform Microscopy (TEM), Inductively Coupled Plasma (ICP), Ultraviolet Visible Spectroscopy (UV-visible) and Nuclear Magnetic Resonance (NMR). Basic principles of flow cytometry and confocal microscopy were also discussed. The second part of this chapter describes the various chemical methods used to prepare and functionalise the different NPs used as well as the biological methodology and techniques used in cell culturing. This includes, tissue culture, cell passaging, and cell counting.

In chapter 3, spherical and cubic γ-Fe_3O_4, cubic $KMnF_3$, $KFeF_3$, $KCoF_3$, $KNiF_3$, $KCuF_3$, $KZnF_3$ and orthorhombic $GdFeO_3$ NPs were synthesised by controlled co-precipitation

methods. Novel route was designed to hinder the oxidation of Fe^{3+} to Fe^{2+} by the addition of $SnCl_2$ as a reducing agent. The synthesised NPs were fully characterised *via* PXRD, FT-IR, ICP and DLS. The single phase of the as-prepared NPs was confirmed by PXRD analysis.

The surface of the formed NPs was coated with 11-aminoundecanoic acid to increase the hydrophilicity and compatibility for biological application. Different functionalisation times at 48, 24, 2 and 1 hours were investigated. PXRD analysis were performed after the functionalisation process to make sure that the perovskite structure did not decomposed. The perovskite structures functionalised at 1 or 2 hours were partially retained, where their PXRD patterns show some of their major peaks, however some unknown impurities were observed. Functionalisation for 48 and 24 hours causes the compounds to decompose completely. On the other hand, an attempt was made to functionalise these NPs with sodium alendronate using the same functionalisation times. Unfortunately, PXRD patterns obtained did not show any of the main peaks related to the perovskite structure, hence it was concluded that the $KMnF_3$ phase had decomposed. Therefore, a decision was made not to go any further with this functionalisation methodology.

In chapter 4, a new solvothermal method was adapted to achieve a successful synthesis and functionalisation strategy for KMF_3 (M = Mn, Fe, Co) NPs. The synthesis of the NPs and the coating process were performed in one step and involved mixing the starting material with potassium oleate as a surfactant in a closed system (thermal bomb). The formed NPs was then functionalised using PEG or sodium alendronate. PXRD patterns confirmed the retained perovskite structure, however unknown impurities were observed in the patterns of the functionalised NPs. Furthermore, Nano Tracking Analysis (NTA) reveals that these functionalised NPs were inhomogeneous and possess large hydrodynamic sizes >100 nm. Therefore, these crucial reasons hamper their use as contrast agents in medical applications.

In chapter 5, a new method was developed to synthesise KMF_3 (M= Mn, Fe, Co) Ultra-Small NPs (USNPs), based on a previously published method. Simple modifications involved a large reduction of the solvent and the use of oleylamine as coating layer and surfactant. $KMnF_3$ USNPs show promise as dual-mode T_1 and T_2 *MRI* contrast agents. The method involves the use of the highly concentrated hydrophobic oleylamine surfactant that restrict the growth of the NPs after their nucleation. The formed NPs are then functionalised with sodium alendronate for a high degree of hydrophilicity and

biocompatibility to work as T_1 and T_2 *MRI* dual probe contrast agents. The successful formation and functionalisation with both oleylamine and sodium alendronate was confirmed by PXRD and TEM analysis. No impurities were present in the PXRD patterns. KMF_3 (M = Mn, Fe, Co) USNPs showed average diameter size of 2 nm. Longitudinal and transvers relaxation rates showed a promising result for $KMnF_3$ NPs to work as dual-mode T_1 and T_2 *MRI* contrast agents. The relaxitivities values obtained at 3 T are 6 and 51 $mM^{-1}s^{-1}$ for r_1 and r_2 respectively, the r_2/r_1 ratio is 8.2. The capability of these NPs to work as dual-mode T_1 and T_2 was confirmed by T_1 and T_2 weighted images. On the other hand, PXRD pattern showed that $KFeF_3$ started to decompose to Fe_3O_4 after a month from preparation, whereas $KCoF_3$ showed a negative effect on both T_1 and T_2 weighted images.

In Chapter 6, $DyFeO_3$ NPs were synthesised using polyacrylamide and citric acid sol-gel method. The single phase of the prepared NPs was confirmed by PXRD. The surface of the NPs was coated with silica using Stŏber process. The presence of the silica shell on the NPs surface was proved by PXRD, TEM, EDX and FT-IR. The core size of the silica coated $DyFeO_3$ NPs was measured using TEM microscopy. Large clusters of NPs with a thick silica layer surrounded them were observed. Different strategies were conducted to optimise the addition of the silica to reduce the silica diameter during the functionalisation process in order to produce optimum hydrodynamic size applicable for biological application. Relaxitivites study was performed, $DyFeO_3$ showed longitudinal relaxation rate values of 9.2 and 37.6. $mM^{-1}S^{-1}$ at 4.9 T for longitudinal relaxation rate and transverse relaxation respectively and r_2/r_1 value of 4.09. Based on these values, coated silica $DyFeO_3$ has a capability to work as dual- mode T_1 and T_2 contrast agents for *MRI*, however more MR phantoms experiments are needed to investigate and confirm this case.

Chapter 7 discuss the applicability of coated alendronate $KMnF_3$ NPs to be used as a theranostics agents. The as prepared NPs cytotoxicity was checked at various concentrations in the range of 0.006 to 3125 uM in order to investigate the safe concentration used as a contrast agent in medical application. $KMnF_3$ was then conjugated with DOX, a drug used in chemotherapy to treat various cancer diseases. Upon successful conjugation, the cytotoxicity of the probe was tested for cytotoxicity against cervical HeLa and colorectal HT-29 and HCT-116 cancer cells using MTS Assay and compared with the results obtained for coated alendronate $KMnF_3$ and pure DOX. The MTS results of the DOX conjugated $KMnF_3$ NPs confirm the higher anticancer activity

against these cancer cell lines in comparison to those of coated alendronate $KMnF_3$ NPs and pure DOX.

After the detection of VEGFR on HeLa, HT-29 and HCT-116, DOX conjugated $KMnF_3$ NPs was attached to VEGFR antibody to specifically target the over expressed VEGFR protein. Targeting a specific molecule on the cell surface or nucleus allows selective delivery of the probe to the cervical and colorectal cells as confirmed by confocal microscopy, where the drug was localised in the cytosol and possibly on the cell membrane. MTS results confirm the highest anticancer activity towards these cells compared to the results obtained for as prepared NPs, pure DOX and DOX conjugated $KMnF_3$.

Future work

Future work will focus on improving the coating uniformity of the KMF_3 (M = Mn, Fe, Co, Ni, Cu) NPs by attaching different hydrophilic ligands that could shorten the relaxation time further and therefore produce efficient contrast agents for clear *MRI* images. $KFeF_3$ coated with alendronate *via* oleylamine ligand exchange showed a promising results as dual T_1/T_2 contrast agents, however the decomposition of this NPs to Fe_3O_4 was a major issue and hindered further investigation, hence a further work is needed to stabilise $KFeF_3$ NPs.

The addition of KF and MBr_2 salts precursors in solvothermal synthesis of KMF_3 (M = Mn, Fe, CO) NPs as well as the coating ligands play a crucial role in controlling the particles size, whereas the reaction temperature and time determines the particles size distribution. To solve this important issue, an optimisation for such factors has to be addressed in the next future work.

$DyFeO_3$ NPs coated with silica have shown the potential to work as T_1/T_2 contrast agents despite the formation of the large layer of silica surrounding the NPs surface, that have high impact on increasing their average crystal size. Thus, optimisation of the technique for silica coating material should be considered.

Since alendronate coated $KMnF_3$ synthesised by solvothermal method demonstrates an excellent potential as dual probe *MRI* contrast agents, it could be tested *in vivo* by conducting pharmacokinetic studies to validate the results obtained in the *in vitro* tests. Furthermore, testing this probe on different cancer cell lines rather than cervical HeLa cancer cell lines, colorectal HT-29 and HCT116 cell lines and targeting their specific over

expressed receptors on their surface would be a great trial to assess the NPs efficiency as drug delivery carriers for an effective and enhanced therapeutic chemotherapy treatment.

Appendix

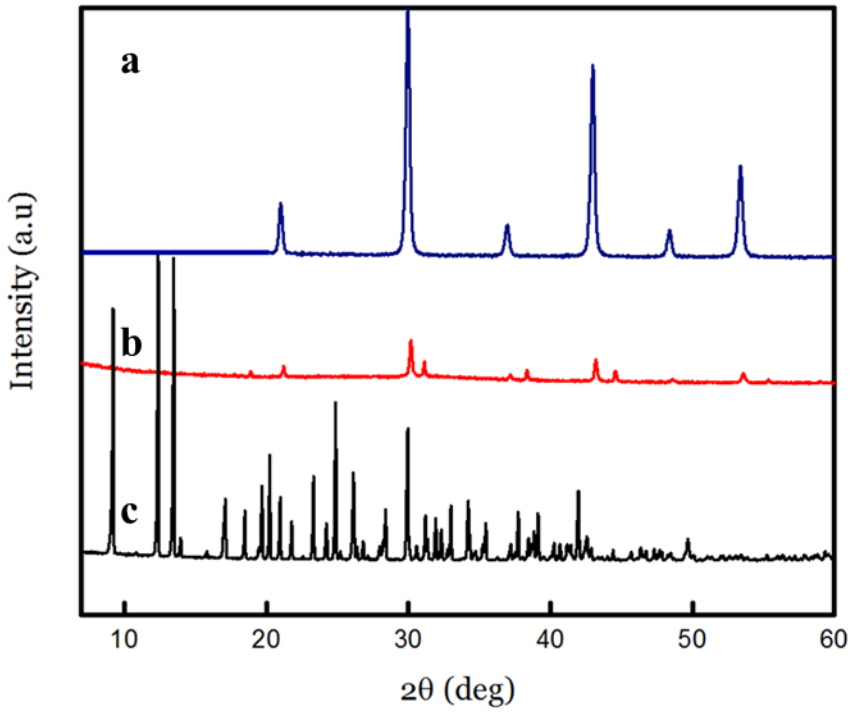

Figure 0-1: PXRD patterns for standard $KMnF_3$ (a) compared to coated alendronate $KMnF_3$ (b) and sodium alendronate trihydrate (c) obtained at 2 hours.

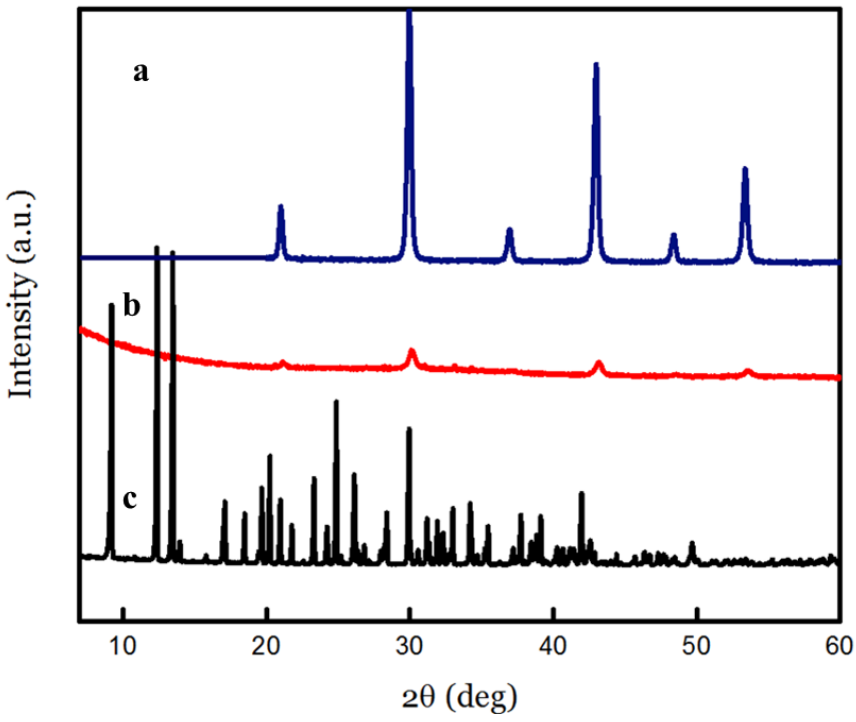

Figure 0-2: PXRD patterns for standard $KMnF_3$ (a)compared to coated alendronate $KMnF_3$ (b) and sodium alendronate trihydrate (c) obtained at 1 hour.

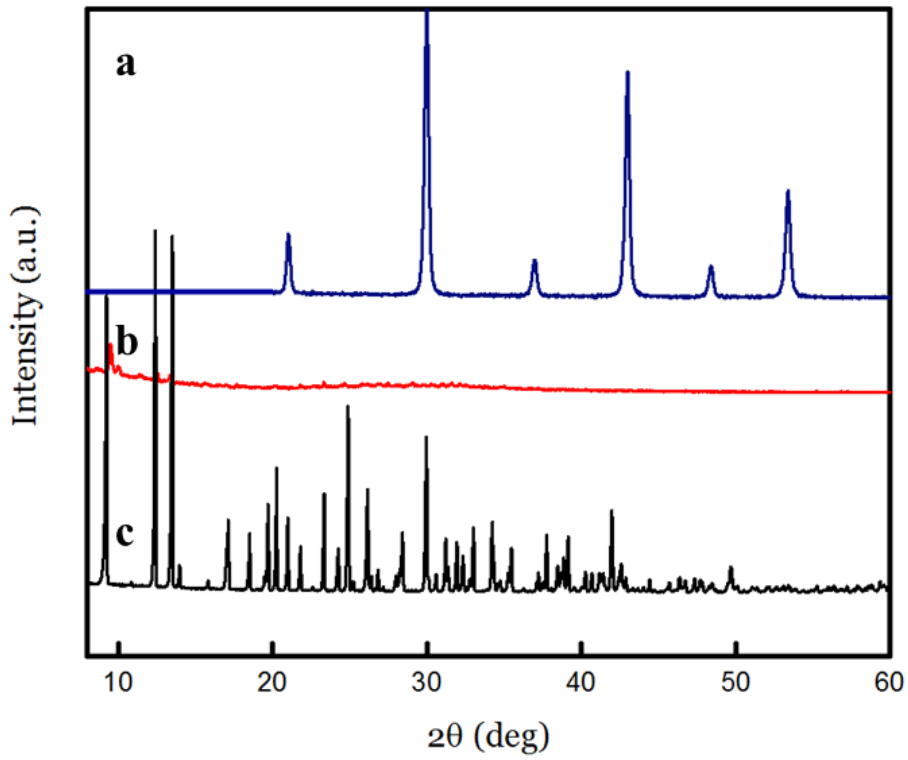

Figure 0-3: PXRD patterns for standard $KMnF_3$ (a)compared to coated alendronate $KMnF_3$ (b) and sodium alendronate trihydrate (c) obtained at 48hours

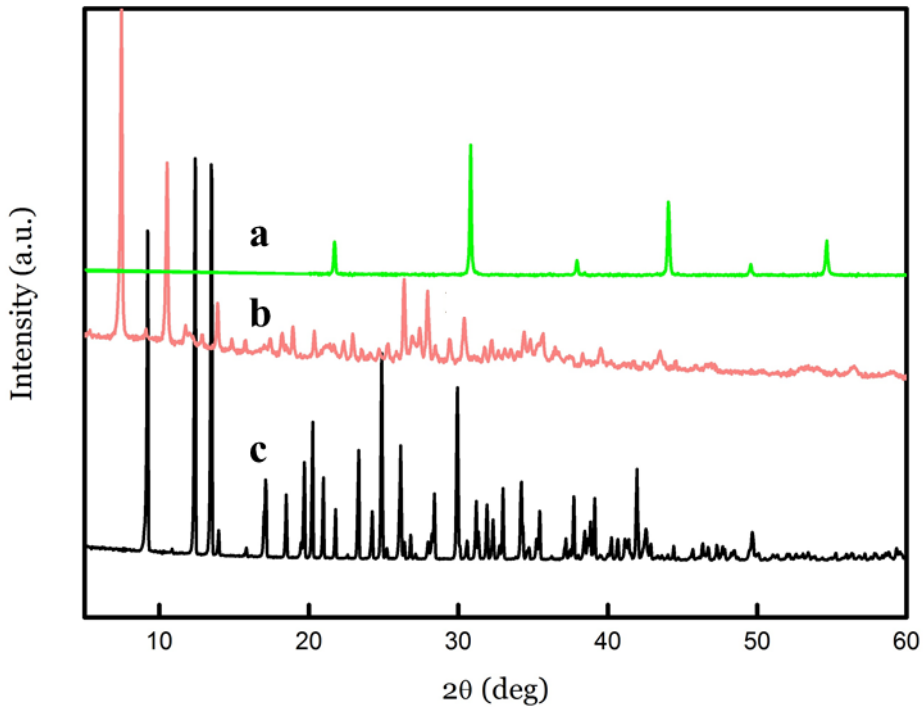

Figure 0-4: PXRD patterns for standard $KFeF_3$ (a) compared to coated alendronate $KFeF_3$ (b) and sodium alendronate trihydrate (c) obtained at 1hour.

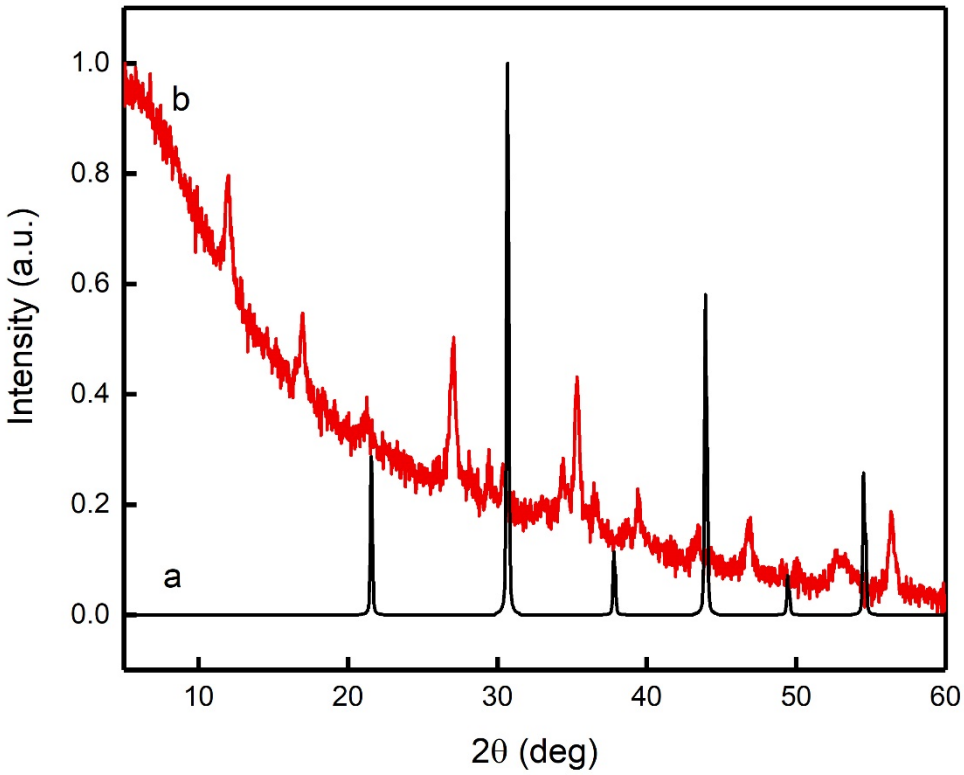

Figure 0-5: PXRD patterns for standard $KFeF_3$ (a) compared to coated alendronate $KFeF_3$ obtained at 2hours.

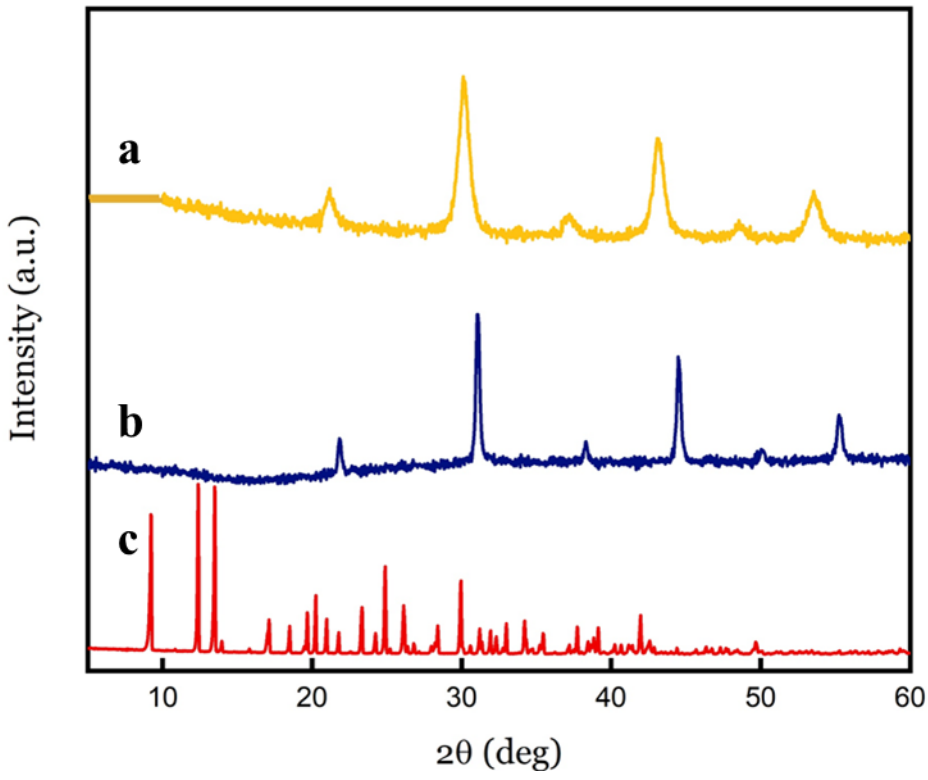

Figure 0-6: PXRD patterns for standard $KCoF_3$ (a) compared to coated alendronate $KCoF_3$ obtained at 2hours and sodium alendronate trihydrate (c).

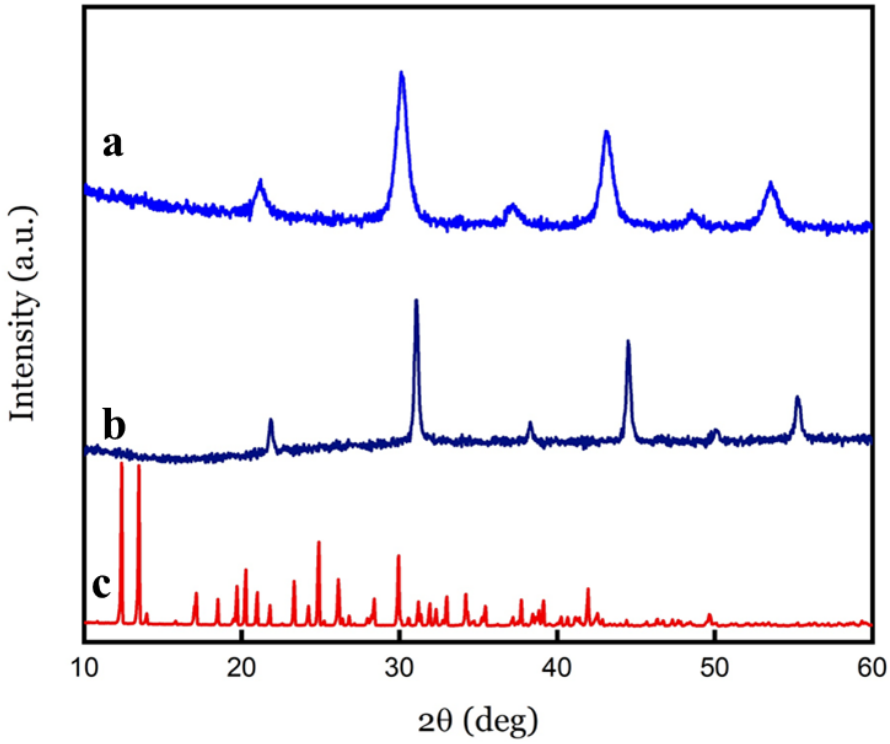

Figure 0-7: PXRD patterns for standard $KZnF_3$ (a) compared to coated alendronate $KZnF_3$ obtained at 2hours and sodium alendronate trihydrate (c)

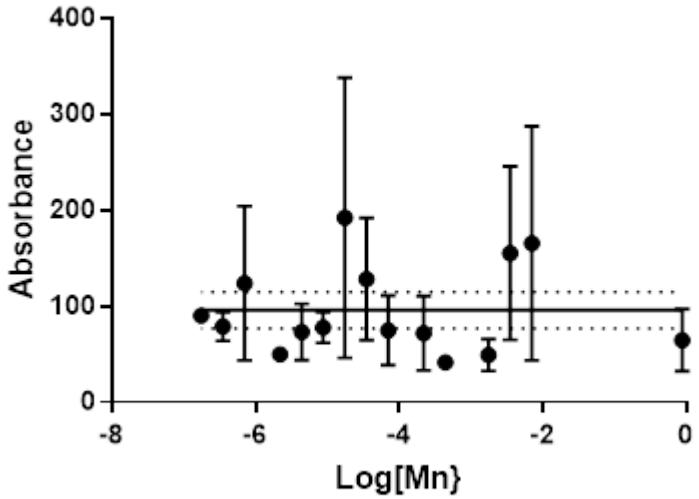

Figure 0-8: MTS graph for coated alendronate $KMnF_3$ against Colo320 cancer cell line plotted by graph prism pad software

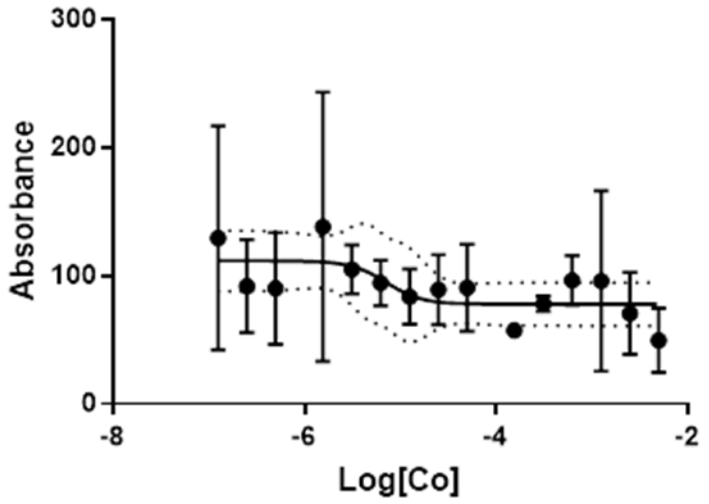

Figure 0-9: MTS graph for coated alendronate $KCoF_3$ against Colo320 cancer cell line plotted by graph prism pad software

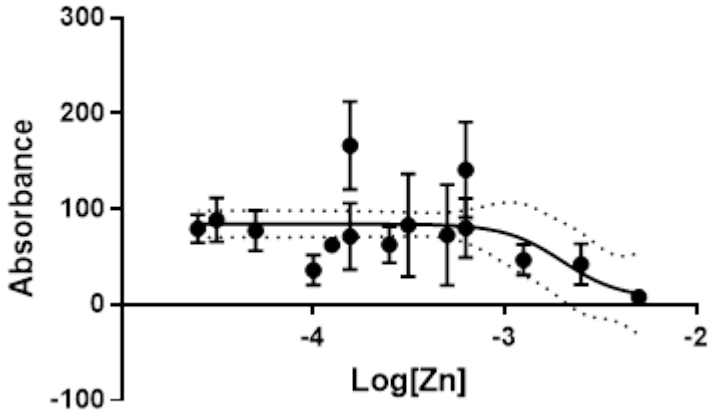

Figure 0-10: MTS graph for coated alendronate $KZnF_3$ against Colo320 cancer cell line plotted by graph prism pad software

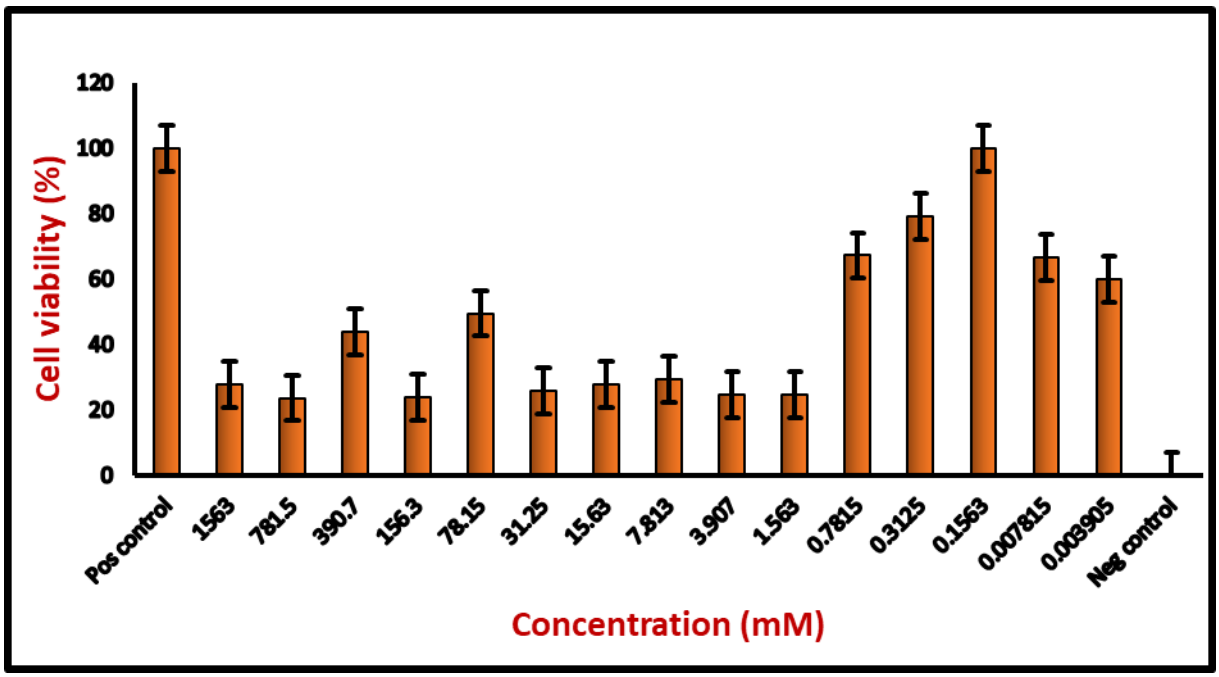

Figure 0-11: MTS graph for coated alendronate $KMnF_3$ against Caco cancer cell line plotted by Excel.

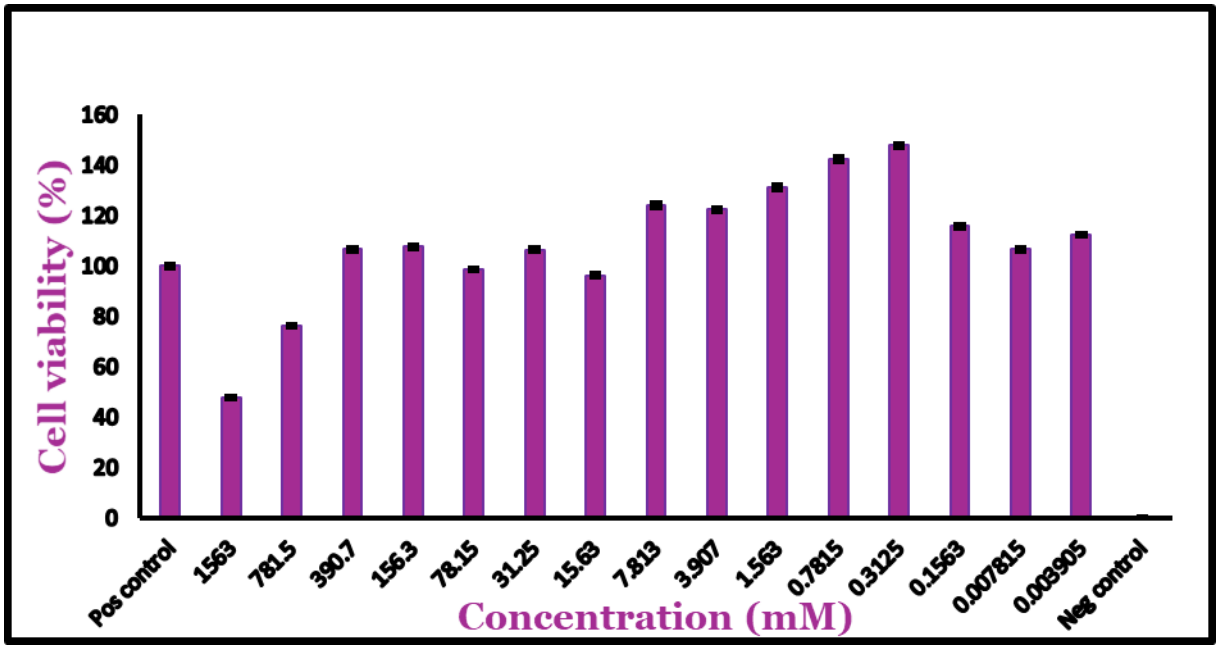

Figure 0-12: MTS graph for coated alendronate $KFeF_3$ against Caco cancer cell line plotted by Excel.

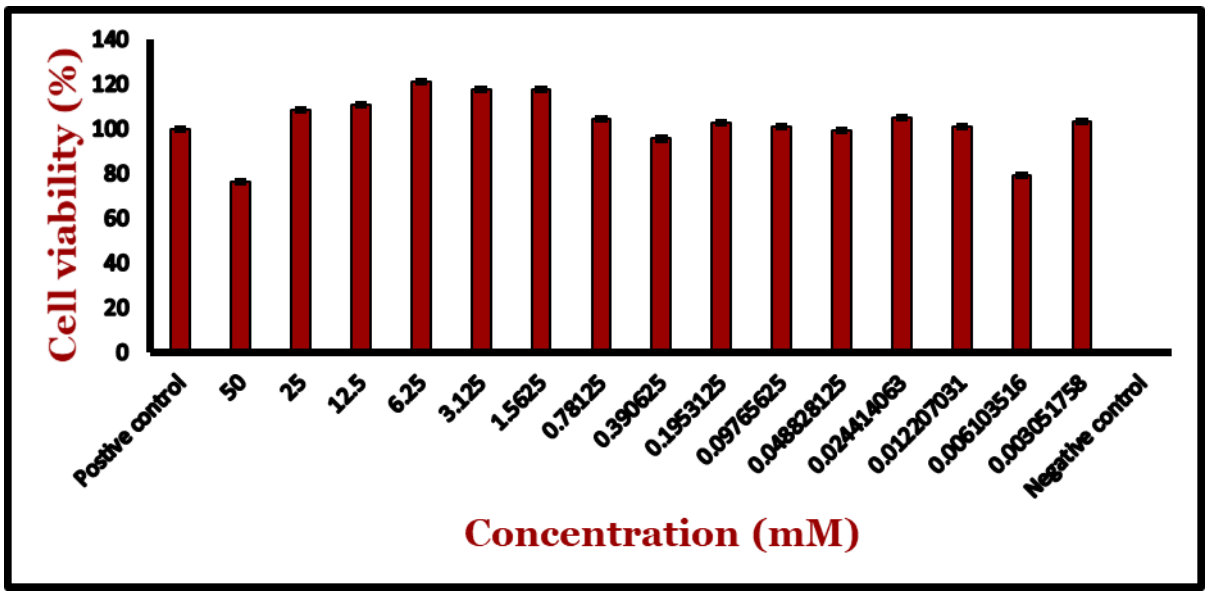

Figure 0-13: MTS graph for coated alendronate $KFeF_3$ against Colo320 cancer cell line plotted by Excel.